Nuclear Science
NEA/NSC/R(2015)3
June 2015
www.oecd-nea.org

Shielding Aspects of Accelerators, Targets and Irradiation Facilities – SATIF 12

Workshop Proceedings
Batavia, Illinois, United States
28–30 April 2014

OECD
BETTER POLICIES FOR BETTER LIVES

NEA
NUCLEAR ENERGY AGENCY

Organisation de Coopération et de Développement Économiques
Organisation for Economic Co-operation and Development

19-Jun-2015

English - Or. English

OECD Nuclear Energy Agency
Steering Committee for Nuclear Energy

NEA/NSC/R(2015)3
Unclassified

Nuclear Science Committee

Shielding Aspects of Accelerators, Targets and Irradiation Facilities-SATIF-12

Batavia, Illinois, US
28-30 April 2014

This document exists only in PDF

yukio.nakahara@oecd.org

JT03379180

English - Or. English

Nuclear Science

Shielding Aspects of Accelerators, Targets and Irradiation Facilities – SATIF-12

Twelfth Workshop Proceedings

Hosted by the
Fermi National Accelerator Laboratory (FNAL)
Batavia, Illinois, US
28-30 April 2014

NUCLEAR ENERGY AGENCY
Organisation for Economic Co-operation and Development

ORGANISATION FOR ECONOMIC CO-OPERATION AND DEVELOPMENT

The OECD is a unique forum where the governments of 34 democracies work together to address the economic, social and environmental challenges of globalisation. The OECD is also at the forefront of efforts to understand and to help governments respond to new developments and concerns, such as corporate governance, the information economy and the challenges of an ageing population. The Organisation provides a setting where governments can compare policy experiences, seek answers to common problems, identify good practice and work to co-ordinate domestic and international policies.

The OECD member countries are: Australia, Austria, Belgium, Canada, Chile, the Czech Republic, Denmark, Estonia, Finland, France, Germany, Greece, Hungary, Iceland, Ireland, Israel, Italy, Japan, Luxembourg, Mexico, the Netherlands, New Zealand, Norway, Poland, Portugal, the Republic of Korea, the Slovak Republic, Slovenia, Spain, Sweden, Switzerland, Turkey, the United Kingdom and the United States. The European Commission takes part in the work of the OECD.

OECD Publishing disseminates widely the results of the Organisation's statistics gathering and research on economic, social and environmental issues, as well as the conventions, guidelines and standards agreed by its members.

NUCLEAR ENERGY AGENCY

The OECD Nuclear Energy Agency (NEA) was established on 1 February 1958. Current NEA membership consists of 31 countries: Australia, Austria, Belgium, Canada, the Czech Republic, Denmark, Finland, France, Germany, Greece, Hungary, Iceland, Ireland, Italy, Japan, Luxembourg, Mexico, the Netherlands, Norway, Poland, Portugal, the Republic of Korea, the Russian Federation, the Slovak Republic, Slovenia, Spain, Sweden, Switzerland, Turkey, the United Kingdom and the United States. The European Commission also takes part in the work of the Agency.

The mission of the NEA is:

- to assist its member countries in maintaining and further developing, through international co-operation, the scientific, technological and legal bases required for a safe, environmentally friendly and economical use of nuclear energy for peaceful purposes;
- to provide authoritative assessments and to forge common understandings on key issues, as input to government decisions on nuclear energy policy and to broader OECD policy analyses in areas such as energy and sustainable development.

Specific areas of competence of the NEA include the safety and regulation of nuclear activities, radioactive waste management, radiological protection, nuclear science, economic and technical analyses of the nuclear fuel cycle, nuclear law and liability, and public information.

The NEA Data Bank provides nuclear data and computer program services for participating countries. In these and related tasks, the NEA works in close collaboration with the International Atomic Energy Agency in Vienna, with which it has a Co-operation Agreement, as well as with other international organisations in the nuclear field.

Foreword

The transport of radiation through shielding materials is a major consideration in the safety design studies of nuclear power plants, and the modelling techniques used may be applied to many other types of scientific and technological facilities. Accelerator and irradiation facilities represent a key capability in R&D, medical and industrial infrastructures and can be used in a wide range of scientific, medical and industrial applications. High-energy ion accelerators, for example, are now used not only in fundamental research, such as the search for new super-heavy nuclei, but also for therapy as part of cancer treatment.

While the energy of the incident particles on the shielding of these facilities may be much higher than that in nuclear power plants, much of the physics associated with the behaviour of the secondary particles produced is similar, as are the computer modelling techniques used to quantify key safety design parameters, such as radiation dose and activation levels. Clear synergies exist, therefore, with other technical work being carried out by the OECD Nuclear Energy Agency (NEA), and its Nuclear Science Committee continues to sponsor activities in this domain.

One of these activities concerns "Shielding Aspects of Accelerators, Targets and Irradiation Facilities" (SATIF). A series of workshops have been held over the last 18 years: SATIF-1 was held on 28-29 April 1994 in Arlington, Texas; SATIF-2 on 12-13 October 1995 at CERN in Geneva, Switzerland; SATIF-3 on 12-13 May 1997 at Tohoku University in Sendai, Japan; SATIF-4 on 17-18 September 1998 in Knoxville, Tennessee; SATIF-5 on 17-21 July 2000 at the NEA in Paris, France; SATIF-6 on 10-12 April 2002 at the Stanford Linear Accelerator Center (SLAC), Menlo Park, California; SATIF-7 on 17-18 May 2004 at ITN, Sacavém, Portugal; SATIF-8 on 22-24 May 2006 at the Pohang Accelerator Laboratory in the Republic of Korea; SATIF-9 on 21-23 April 2008 at Oak Ridge National Laboratory (ORNL), Oak Ridge, Tennessee; SATIF-10 on 2-4 June 2010 at CERN in Geneva, Switzerland; SATIF-11 on 11-13 September 2012 at the High-energy Accelerator Research Organisation (KEK) in Tsukuba, Japan.

The 12th workshop on Shielding Aspects of Accelerators, Targets and Irradiation Facilities took place in Batavia, US and was jointly organised by the Expert Group on Radiation Transport and Shielding (EGRTS) of the Working Party on Scientific Issues of Reactor Systems (WPRS) of the NEA and Fermi National Accelerator Laboratory (FNAL).

The workshop was sponsored by the NEA and its Nuclear Science Committee (NSC) and co-sponsored by the Office of Science of the US Department of Energy and FNAL.

The current proceedings provide a summary of the discussions, decisions and conclusions as well as the text of the presentations made at the twelfth workshop.

Acknowledgements

The following members of the SATIF-12 Scientific Committee and the Local Organising Committee are thanked for their contribution to shaping the technical programme and organising the workshop: S. Ban (KEK), M. Bruce (FNAL), M. Brugger (CERN), D. Cossairt (FNAL), R. Grove (ORNL), J. Gulliford (NEA), H. Hirayama (KEK), G. Hughes (LANL), B. Kirk (honorary), H.S. Lee (PAL), S. Mashnik (LANL), N. Mokhov (the general chairman of SATIF-12, FNAL), G. Muhrer (ESS), T. Nakamura (honorary), H. Nakashima (JAEA), V. Pronskikh (FNAL), I. Rakhno (FNAL), S. Roesler (CERN), S. Rokni (SLAC), E. Sartori (honorary), C. Sazama (FNAL), M. Silari (CERN), T. Valentine (ORNL), K. Vaziri (FNAL), P. Vaz (IST), S. Weber (FNAL), and A. Yamaji (NEA).

Dedicated to Dr. Dick Prael

Our friend and colleague Dick Prael passed away in 2014. He earned his PhD in 1971, worked at ANL, and was then associated with the Los Alamos Monte-Carlo code-development group from 1978. He created the LAHET code and made other critical contributions to Monte-Carlo high-energy particle transport, specifically in MCNP. Dick was a participant at and a contributor to many SATIF meetings including the first one in Arlington. Dick's scientific accomplishments, personality and sense of humour will be sorely missed.

Dedicated to Dr. Klaus Tesch

Our friend and colleague passed away in 2013. Klaus joined DESY in 1963. He was the leader of the Radiation Protection group there from 1971 until his retirement in 1996. He was a major force in shaping the radiation protection for DORIS, PETRA and HERA. His scientific contributions included experiments on the development and shielding of electro-magnetic cascades, muon shielding, calculation and measurement of high-energetic neutrons behind the shielding of proton accelerators, research and development of passive and active neutron detectors, measurement of pulsed neutrons. Klaus was a contributor to SATIF meetings including the first one in Arlington. The community will miss him dearly.

Table of contents

Executive summary

The twelfth SATIF workshop (SATIF-12) took place at the Fermi National Accelerator Laboratory (FNAL), Batavia, US on 28-30 April 2014. The workshop was chaired by N. Mokhov and was attended by 65 participants representing 29 organisations of 10 countries.

Support for the SATIF workshop is now part of the mandated activity of the Expert Group on Radiation Transport and Shielding (EGRTS, chaired by R. Grove from ORNL) of the Working Party on Scientific Issues of Reactor Systems (WPRS) of the NEA Nuclear Science Committee (NSC). The EGRTS also co-ordinates maintenance and development of the Shielding Integral Benchmark Archive and Database (SINBAD) of Reactor Shielding, Fusion Neutronics and Accelerator Shielding benchmark experiments.

More information on the activities of the WPRS can be found at: http://www.oecd-nea.org/science/wprs/index.html.

The main objectives of the SATIF Workshops are to:

- promote the exchange of information among experts in the field of accelerator shielding and related topics;
- identify areas where international co-operation can be fruitful;
- undertake a programme of work in order to achieve progress in specific priority areas.

SATIF-12 is sponsored by the NEA and its Nuclear Science Committee (NSC) and co-sponsored by the Office of Science of the US Department of Energy and FNAL. The workshop consisted of 7 technical sessions (including a poster session) and a wrap up session summarising achievements and defining further work for the next two years. The highlight of the workshop was a tour to the Fermilab ASTA and PXIE Facilities, Tevatron A/E sector and D0 detector, Pbar Rings, the Neutron Therapy Facility and a face-to-face meeting with the Fermilab radiation experts.

There were 7 technical sessions:

- Source Term and Related Topics
- Induced Radioactivity
- Radiation Shielding
- Medical Accelerators
- Status of Codes and Data Bases
- Code Benchmarking and Inter-comparison
- Poster Session

The first session was chaired by H. S. Lee (POSTECH) and focused on source term and related topics. Six presentations were made, including introductions on the installation of new facilities and discussions on evaluations related to radiation protection as well as techniques being employed in the development of new detectors. As more facilities are being made available for external users around the world, the participants recognised

that more information, such as beam availability and field property of the relevant facility, needs to be easily accessible for external users to help identify the facilities which would most suit the needs. There has been growing interest in utilising new types of radiation sources in evaluations for radiation protection purposes to reflect the latest trend in high power lasers. Estimation of environmental effect due to radioactive material released from the Hadron Experimental Facility of J-PARC was also reported.

The second session was chaired by H. Nakashima (JAEA) and S. Rokni (SLAC) and targeted induced radioactivity. The session contained eleven presentations. The main themes of discussions consisted of issues associated with estimation and evaluation of residual activity (and cool down) and handling and storage of activated materials (e.g. leaching of tritium from shielding and soil with or without ground water, different scenario studies for temporary storage, etc.) from the viewpoint of radiation protection. Estimation of residual activity requires a vast accumulation of measured data with various irradiation conditions (particle, energy), various atomic composition, and chemical types as well as analyses. Extensive measurements, benchmarking of models and codes enable optimisation in many applications, such as in designing nuclide inventory in accelerators or designing target chambers. On the other hand, the recent trend of increase in the power or the use of heavy ions is bringing new challenges in shielding and radiation protection and further development in modelling and validation is needed for improved accuracy in analyses to meet the requirements.

The third session was chaired by H. Hirayama (KEK) and V. Vylet (TJNAF) and focused on radiation shielding of different types of facilities including spallation neutron sources, radioactive ion beams, heavy-ion accelerators, and electron accelerators. There were ten presentations in the session. Monte Carlo calculations (together with empirical models) are now extensively utilised in shielding analyses and designs, especially in upgrading the existing facilities and designing new facilities (with high energy and luminosity, heavy ions). However, they require not only large computation power, but also considerable man-power for preparations. Recent advances in the development of a tool drew a lot of interests on the part of the participants as it saves substantial amounts of analyst time as well as achieving well-converged solutions in substantially less computer time. Also, it was suggested that users should not rely on such powerful tools without understanding the physics of the subject. The participants also shared risks associated with the use of powerful Monte Carlo programmes, such as the risk of being over-confident with the calculated results and overlooking the complexity of the problem in simulations.

The fourth session was chaired by V. Mares (HZM) and focused on medical accelerators. The session contained four presentations. Today, most radiation therapies are performed using with high-energy X-rays due to cost and availability. However, different technologies are being developed to improve the efficacy of radiotherapy treatments and ultimately the overall quality of life of the patients. In this session, the success and challenges of such technologies were presented including neutron therapy and various particle beam radiation therapies (protons and ions). It was discussed and agreed that a simulation bridge between physical processes and biological processes is needed.

The fifth session was chaired by A. Ferrari (CERN) and the status of codes and databases was discussed. There were four presentations in the session. The participants showed interest in potential contribution to the activities of NEA Expert Group on Radiation Transport and Shielding. For example, accelerator benchmarks (e.g. on deuteron beam experiments) and contribution to review the current SINBAD benchmarks may be made available for the Shielding Integral Benchmark Archive and Database (SINBAD) supported by the SATIF experts. The latest developments of the FLUKA and MARS codes were presented. Some requests were made for inclusion in the future SATIF workshops of presentations on developments of other Monte-Carlo particle transport

simulation codes, which were not presented this time (e.g. PHITS, MCNP) and of discussions on safety factors applied in design and licensing of facilities.

The sixth session was chaired by R. Grove (ORNL) and focused on code benchmarking and inter-comparison exercises. The session contained four presentations. Extensive benchmarking and inter-comparisons were presented for the codes FLUKA, GEANT4, MARS15 and PHITS and phenomena. The results on the inter-comparison proposed at the last workshop (SATIF-11) revealed some unexpected discrepancies among results from different codes (in the energy range of 10-100GeV and with increasing angle) and indicated that further comparisons and analyses were needed for the next workshop (possibly, comparison with experimental measurements).

For the first time in the history of SATIF, a poster session was held, due to the high number of submitted contributions that could not be accommodated in the oral session. The session attracted 11 contributions from ESS (2), HZDR (2), Fermilab (4), FRIB (1), JLab (1), and KEK (1) in the topics of radiation protection (7), design of instrumentation (3), and code development (1).

The last session was dedicated to summarising the workshop, identifying areas of co-operation for the next two years, identifying actions required in order to achieve desired progress in the different research areas and monitoring the progress achieved in actions decided in past workshops. Several comments and suggestions were made by the participants and by N. Mokhov and P. Vaz in particular. Some participants showed interest and were encouraged to participate in NEA EGRTS activities and in particular, to participate in the compilation of new experimental data and review of SINBAD.

There were on-going investigations on possible causes of the systematic underestimation or overestimation of code-computed results compared with experimental results (by factors ranging up to a factor of 10 in some cases). The participants agreed on the need to perform further analyses to better understand the reasons for the underestimations and inform the community on their findings. This need was also supported by the outcome results of the computational benchmark proposed by H. Hirayama at SATIF-11. The results from the benchmark indicated a further need to compare total cross-sections used by each code as well as compare total neutron fluence, and total energy fluence emitted from the target. Furthermore, comparison with experimental measurements seemed essential.

Discussions were undertaken on the available computational methods to perform radiation damage assessment and to compute displacement per atom (dpa), helium production, etc. The need to validate models currently used for dpa calculation, using measurements already identified at the SATIF-11 meeting, was re-stated. Suggestions for topics to be addressed in the future SATIF workshops included discussions on state-of-the-art of radiation transport in molecular dynamics and multi-scale modelling.

It was suggested that the next SATIF workshop (SATIF-13) be held in 2016 in Europe following the tradition of rotating the venue between America, Europe and Asia. Anna Ferrari (HZDR) presented that Helmholtz-Zentrum Dresden-Rossendorf is ready to organise SATIF-13 with the support of the Technische Universität Dresden in Dresden, Germany. A technical tour to ELBE (Electron Linac for beams with high Brilliance and low Emittance) may be arranged. A. Ferrari agreed to explore details of the potential arrangements. An interest in hosting SATIF-13 was also expressed by P. Ortego (SEA) at the fourth EGRTS meeting of WPRS held in February 2014 at the NEA. Final confirmation will be provided well in advance of the next meeting. Participants thanked the General Chairman N. Mokhov and FNAL for hosting SATIF-12, for the outstanding scientific programme, for the friendly atmosphere that contributed to foster intense scientific discussion and for their kind hospitality. The Chairman adjourned the meeting.

The members of the Scientific Committee of SATIF-12 were:

S. Ban (KEK), M. Brugger (CERN), R. Grove (ORNL), J. Gulliford (NEA), H. Hirayama (KEK), G. Hughes (LANL), B. Kirk (honorary), H.S. Lee (PAL), S. Mashnik (LANL), N. Mokhov (the general chairman of SATIF-12, FNAL), G. Muhrer (ESS), T. Nakamura (honorary), H. Nakashima (JAEA), S. Roesler (CERN), S. Rokni (SLAC), E. Sartori (honorary), M. Silari (CERN), T. Valentine (ORNL), P. Vaz (IST), and A. Yamaji (NEA).

The members of the Local Organising Committee (from FNAL) were:

M. Bruce, D. Cossairt, N. Mokhov, V. Pronskikh, I. Rakhno, C. Sazama, K. Vaziri, and S. Weber.

Session I: Source Term and Related Topics

Chair: Hee-Seock Lee

The CERN High Energy Accelerator Mixed Field (CHARM) Facility in the CERN PS East Experimental Area

Robert Froeschl, Markus Brugger, Stefan Roesler
CERN European Organisation for Nuclear Research, Switzerland

Abstract

The CERN High Energy Accelerator Mixed Field (CHARM) Facility is currently being constructed in the CERN PS (Proton Synchrotron) East Experimental Area to study radiation effects on electronic components. The chosen location has become available due to the decommissioning and subsequent dismantling of the DIRAC experiment and the CHARM Facility will share it with a proton irradiation facility that is situated further upstream.

The CHARM Facility will receive a primary proton beam from the CERN PS at a beam momentum of 24 GeV/c and a maximum average beam intensity of 6.7E10 protons/second with a maximum pulse intensity of 5E11 protons/pulse and a respective pulse length of 350 ms. The beam will impinge on one out of a set of dedicated targets to produce the desired radiation fields at several experimental positions. These radiation fields can be adjusted by insertion of up to four moveable shielding walls, two made out of concrete and two made out iron. The main purpose of the CHARM Facility will be the investigation of the effects of these radiation fields on electronic components in the framework of the Radiation to Electronics (R2E) project.

First, the radiation field requirements on the CHARM facility by the R2E project are discussed. Then, the radiological assessment of the facility is presented, including the shielding design for the prompt radiation and the optimisation of the residual radiation. Furthermore, the air activation calculations, the resulting radiological impact from the release of radionuclides to the environment and the derived requirements for the dynamic confinement of the air inside the CHARM facility are illustrated.

The shielding of the CHARM facility will also include the CERN Shielding Benchmark Facility (CSBF) situated laterally above the target. This facility will allow deep-penetration benchmark studies of various shielding materials. The current plans for the construction and the commissioning of the CSBF are outlined.

Introduction

The CERN High Energy Accelerator Mixed Field (CHARM) Facility [1] is currently being constructed in the CERN Proton Synchrotron (PS) East Experimental Area. The purpose of the CHARM Facility is to provide test locations for electronic equipment with well understood, mixed radiation fields that are typical of the CERN accelerators and other applications of interest. This facility will complement the existing irradiation facilities at CERN such as CERF and IRRAD.

The location of the CHARM Facility on the CERN site and its connection to the CERN PS are shown in Figure 1.

Figure 1. Location of the CHARM Facility connected to the CERN PS

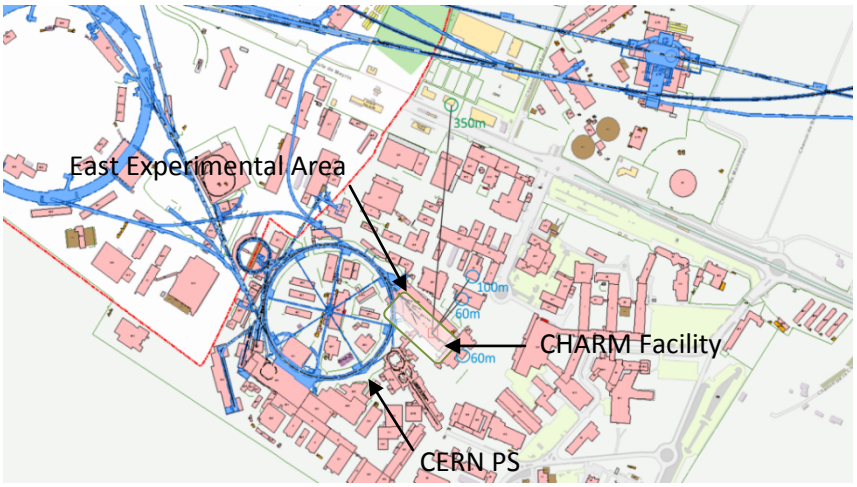

The CHARM Facility will provide test locations for electronic equipment with well understood, mixed radiation fields to the CERN Radiation2 Electronics (R2E) project [2][3][4]. The R2E project was initiated by the observation of significant downtime of the CERN Large Hadron Collider (LHC) due to Single Event Effects (SEE) in electronic devices in the LHC tunnel that triggered the dumping of the LHC beams. This fact is illustrated in Figure 2.

To be able to reach the goal of the R2E project of 0.5 SEE induced beam dumps/fb-1 after the start-up ending the Long Shut-down 1 (LS1) in 2015, extensive testing of electronic equipment that is installed in the LHC tunnel is necessary. The CHARM Facility will provide this testing capability even for tests of entire electronic systems up to dimensions of 1m x 1m x 2m.

Figure 2. LHC beam dumps induced by Single Event Effects (SEE) in electronic devices

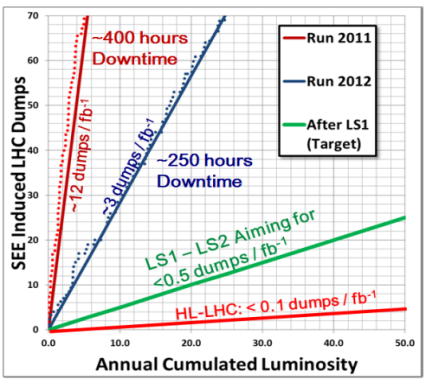

This facility is not only useful for testing devices within accelerator representative environments, but its available radiation fields will also be characteristic of ground and atmospheric environments (neutron energy spectra) as well as the space environment (representative for the inner proton radiation belt). In addition, the size of the available test area is such that also larger objects, and ultimately even objects requiring special services (power, cooling, etc.) to be connected for operation, can be irradiated.

Table 1. Annual High Energy Hadron (HEH) fluences for different radiation environments

Spectrum	HEH fluxes (>20MeV/cm2/year)
Ground level	$1\text{-}2\times10^{5}$
Avionic	2×10^{7}
ISS orbit	1×10^{9}
LHC machine	1×10^{6} - 1×10^{11}
LHC detectors	$> 10^{11}$

The irradiation chamber is large enough to host a complete accelerator control system (e. g. power converters) but can also host full satellites, and part of cars or planes. For SEEs caused by High Energy Hadrons (HEH) present in the various radiation environments, Table 1 provides a generalised overview of annual fluences, later to be put in the context of what can be achieved in terms of test-time acceleration factor at CHARM. In this respect, so far only few mixed field test areas exist, which often do not provide sufficient beam-intensity or flexible test conditions (e.g two CERN test areas, CNRAD and H4IRRAD, but have significant limitations in beam availability, intensity and flexibility).

Layout and operational parameters

As indicated in Figure 1, the CHARM Facility will be located in one of the experimental halls at CERN. Its surrounding layout is composed of iron and concrete blocks in order to reduce maximum radiation outside the shielding structure. A three-dimensional view of the facility and a horizontal cut of the inner target chamber are shown in Figure 3 (a) and (b), respectively. As shown in Figure 3 (a), the target chamber is large enough to host bulky and complete systems (e.g. satellites) as around 70 m^3 of space will be available for radiation tests.

Figure 3: (a) Three-dimensional view of the facility and (b) FLUKA geometry for the target area

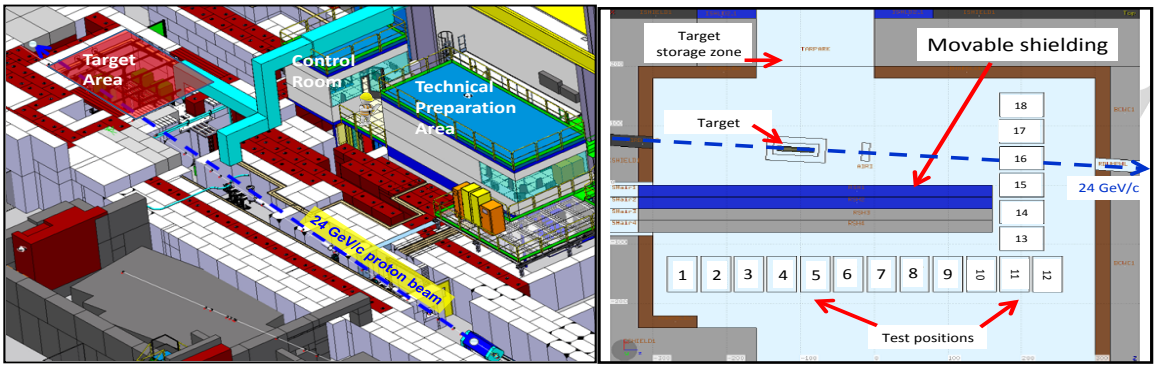

Racks 1 to 18 are the regions representing the test locations. The blue, grey and brown plates are iron, concrete and marbles blocks.

Within the facility, a 24 GeV/c proton beam extracted from the Proton Synchrotron (PS) accelerator impacts on a cylindrical copper or aluminum target and the created secondary radiation field is used to test electronic equipment installed at predefined test positions. Copper and aluminum as material choices for the primary beam target are good compromises not only because of their mechanical and thermal properties, but together with the mobile shielding configuration they also allow the creation of a secondary particle spectra representative for the source term of those present in the atmospheric, space and accelerators environments.

To model and choose between the various representative spectra, different shielding configurations are thus available in the facility. Four movable layers of an individual thickness of 20 cm made of concrete and iron can be placed between the target and the test locations in different combinations, thus allowing to modulate the test spectra and adopt them as closely as possible to the radiation field (energy and intensity) aimed for during the tests. The shielding plates are motorised with remote control. The intensity of the radiation field can be modulated by varying the primary beam intensity, the choice of target head, e.g. two massive ones (Al or Cu – the yield of the massive Al target is about 2.5 times smaller than for the massive Cu target) or one with reduced effective density (Al target with holes – it gives an additional reduction by a factor 4), allowing for an overall reduction factor (including beam intensity reduction) of the primary radiation field of 10-100, in total.

In summary, the CHARM Facility will receive a pulsed proton beam from the CERN PS with a beam momentum of 24 GeV/c. There will be 5e11 protons per pulse with a pulse length of 350ms. Under nominal conditions, 2 spills per 45.6 seconds, i.e. per PS super-cycle, will be sent to the CHARM Facility. This is the foreseen operation mode of the facility for the next years. Theoretically, up to 6 spills per 45.6 seconds will be possible in case the East Experimental Area is the only user of the test beam cycles of the PS. Table 2 shows the operational parameters accounting for the number of days of operation per year and machine availability.

Table 2. Operational parameters of the CHARM Facility

Scenarios	Average proton beam intensity on target	Annual number of protons on target
Nominal (2spills/45.6s)	2.2E10 p/s	3.3E17 p/y
Maximum (6spills/45.6s)	6.7E10 p/s	1e18 p/y

A sketch of the CHARM Facility is presented in Figure 4. Figure 5 shows the comparison of a representative radiation spectrum in the LHC tunnel and the selected location in the CHARM Facility.

Figure 4. Layout of the CHARM Facility

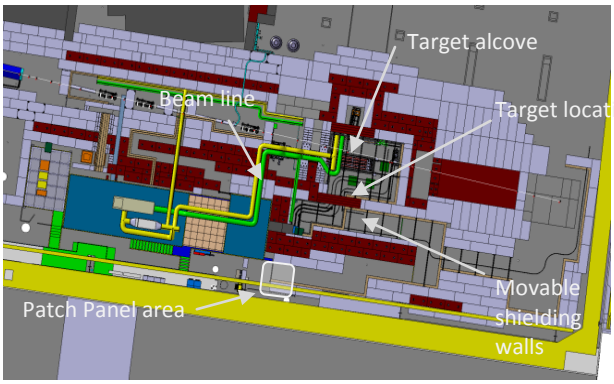

Figure 5. Reverse integral (defined as the integral starting from a given energy up to infinite energy) of the high-energy hadron fluence normalised to the total high-energy hadron fluence above 20 MeV (left) for the LHC tunnel and location 13 in the CHARM Facility

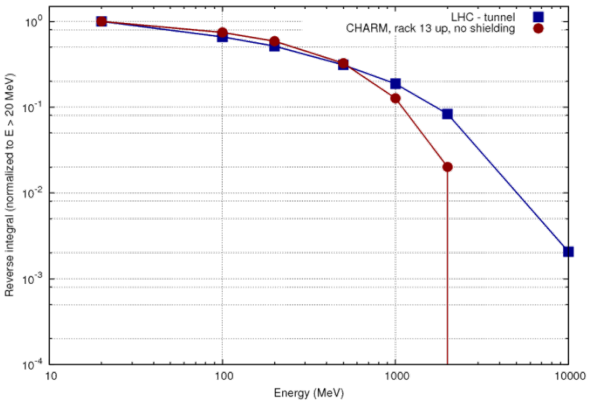

Radiation protection assessment approach

The radiation protection assessment of the facility has been divided into 3 categories that are discussed in the following sections, namely the shielding design for the prompt radiation, the optimisation of the residual radiation and the activation of air and its subsequent release to the environment. The characterisation of the facility with respect to the categorisation of its various parts in terms of radioactive waste classes and their corresponding elimination pathways will be performed in the future.

Prompt radiation

The shielding of the CHARM Facility was designed to respect the CERN area classification. This means that the ambient dose equivalent rates should be below 3 µSv/h for the control rooms inside the East Hall and less than 15 µSv/h (low occupancy area) at 40 cm outside the shielding walls for maximum average beam intensity of 6.7E10 protons per second. In addition, the ambient dose equivalent rates should be below 2.5 µSv/h outside the hall for maximum average beam intensity. These requirements meant that all shielding passages (access chicanes, ventilation ducts, cable ducts) had to be designed in an optimised way. The locations of the area monitors were chosen to verify compliance with these area classification limits.

In addition, the shielding had to be designed so that the annual effective dose to members of the public, combined of prompt radiation (sky-shine) and releases to the environment, would be less than 1 μSv for the nominal annual protons on target.

The design of the shielding tried to make use of as many existing concrete and iron shielding blocks as possible as well as magnet yokes that had been part of the former LEP accelerator. In total, approximately 2000 tonnes of iron and 4000 tonnes of concrete have been used. The design had also to accommodate the fact that design choices were limited due to the presence of existing facilities in the East Experimental Area.

Monte Carlo simulations with the FLUKA code [5] [6] have been performed to estimate the prompt ambient equivalent dose rate levels for the CHARM Facility. The prompt ambient equivalent dose rate is shown at the beam-line level in Figure 6 and at 40 cm above the top of the shielding roof in Figure 7, demonstrating the compliance of the shielding design with the design goals with respect to the CERN area classification. The annual effective dose to members of the public due to sky-shine is shown in Figure 8 to be 1.25 μSv for the current design. Since this value is above the design goal of 1 μSv/y, the design of the shielding roof will be modified to respect this design goal. The predicted ambient dose equivalent rate level on the shielding roof will be verified by dedicated measurements during the commissioning of the CHARM Facility because of the large sensitivity of the ambient dose equivalent rate behind thick shielding to the uncertainties of the attenuation properties of the shielding material. This will also be part of the measurement programme for the CERN Shielding Benchmark Facility that is described below.

Figure 6. Prompt radiation at beam-line level with colour-coded area classification (blue covering the acceptable control room levels and green the acceptable low occupancy area levels)

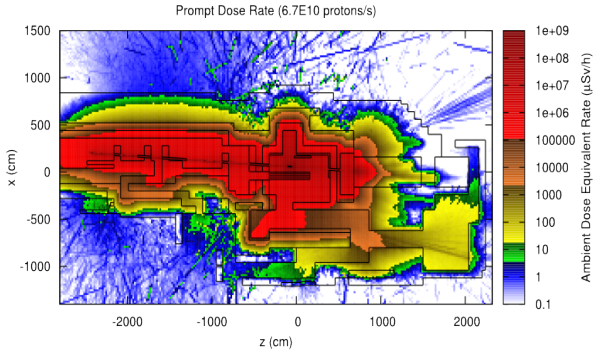

Figure 7. Prompt radiation at 40 cm above the shielding roof with colour-coded area classification (blue covering the acceptable control room levels and green the acceptable low occupancy area levels)

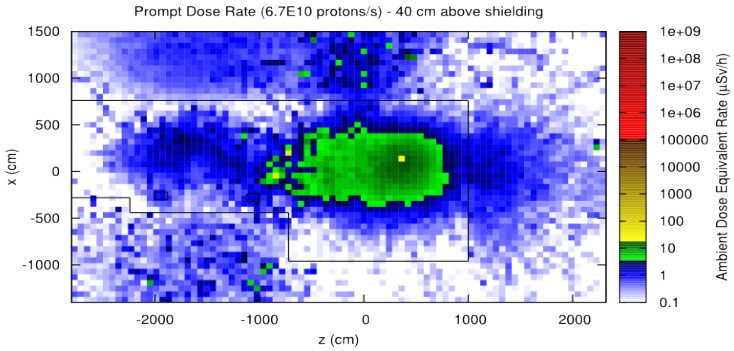

Figure 8. Annual effective dose to members of the public due to sky-shine with nominal beam parameters

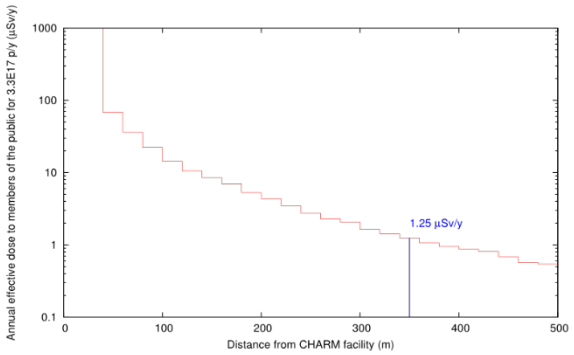

Residual radiation

The reduction of the residual ambient radiation levels is an important optimisation following the ALARA principle. In addition, reducing the residual ambient radiation levels to lower, the effective dose to personnel during interventions will also decrease the administrative requirements for the interventions and, as a consequence, result in a more efficient exploitation of the facility.

The main optimisation measures have been:

- Starting from the beginning, the radiation protection assessment was integrated in the design process of the facility.
- Parts of the concrete walls and the iron ceiling structure in the vicinity of the target have been covered with marble. This will reduce the production of ^{24}Na and ^{22}Na in this area and the marble will act as a shielding material reducing the radiation from the iron ceiling structure.
- The target will be moved to a dedicated alcove during access to the CHARM Facility. This alcove will be closed by a 20 cm thick movable marble shielding reducing the radiation exposure due to the target.
- Extensive studies for different shielding configurations during access have been performed to optimise the access procedures.
- An ambient dose equivalent rate objective of 100 µSv/h for the Patch Panel area (see Figure 4) has been defined. This area will be the most frequently accessed part of the facility.

To predict the ambient dose equivalent rate levels for various operational scenarios and cool-down times, Monte Carlo simulations have been performed with FLUKA and the DORIAN code [7]. The ambient dose equivalent rate levels for 200 days of operation with maximum beam intensity followed by cool-down periods of 1 hour and 1 day are shown in Figure 9. The evolution of the ambient dose equivalent rate for the Patch Panel area for various shielding configurations is presented in Figure 10 as a function of the cool-down time. The ambient dose equivalent rates for the Patch Panel area at cooling time less than 1 day are approximately 3 times higher for the configuration where the movable shielding walls have been retracted from the facility during irradiation than for the configuration where the movable shielding walls have been inside the facility during irradiation. The objective of 100 µSv/h for the Patch Panel area can be achieved for a cooling time of 1 hour for the maximum beam intensity when the movable shielding walls have been inside the facility during irradiation and for the nominal beam intensity

(lower by a factor of 3) when the movable shielding walls have been retracted from the facility during irradiation.

Figure 9. Residual radiation levels after 200 days of operation with maximum beam intensity followed by 1 hour (left) and 1 day (right) of cool-down

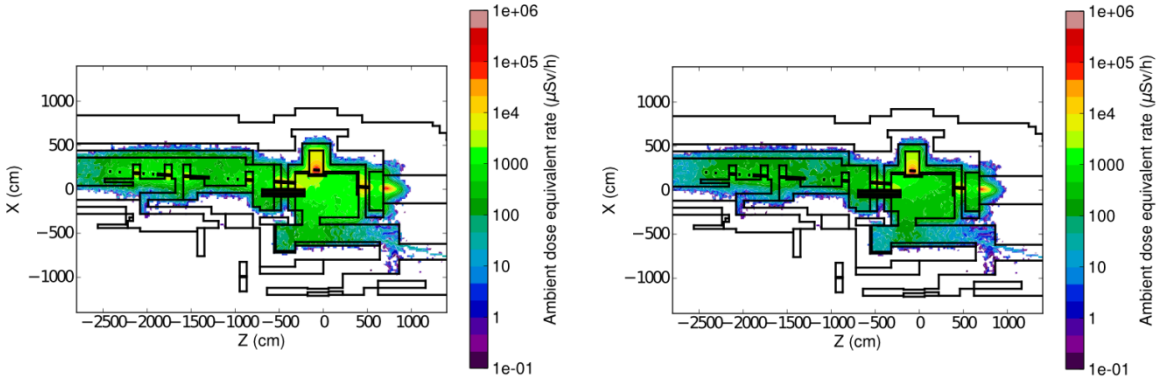

Figure 10. Time evolution of the residual radiation in the Patch Panel area after 200 days of operation with maximum beam intensity

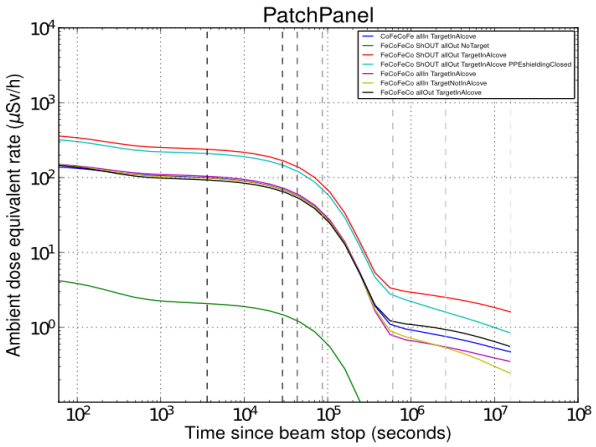

Air activation and subsequent release to the environment

The operation of the CHARM Facility will result in the activation of the air inside the facility. The design goals for the ventilation system of the CHARM Facility are:

- The committed effective dose due to inhalation has to be less than 1 μSv for a 1-hour access. The reason for this requirement is that the inhalation component of the effective dose is not directly monitored. The external exposure due to the activated air is monitored, is not larger for the given geometries than the internal exposure and is normally much smaller than the external exposure from the activated components of the facility.
- Effective dose to members of the public (reference group) has to be less than 1 μSv per year, combined from prompt radiation (sky-shine) and from releases to the environment.

The following methodology has been used to obtain the radionuclide concentrations, the annual release to the environment and the resulting annual effective dose to members of the public:

- The track-length spectra for protons, neutron and charged pions have been scored in the air volumes inside the CHARM Facility (and the upstream proton facility) in the FLUKA Monte Carlo simulation.
- These track-length spectra have been folded with a dedicated set of air activation cross-sections [8] [9] to obtain the radionuclide production yields.
- The radionuclide concentrations in the facility and the release term to the environment have been calculated from the radionuclide production yields taking the time evolution and the characteristics of the ventilation circuit into account.
- The radionuclide concentrations in the facility after beam stop have been converted to the committed effective dose due to inhalation without flush for a 1-hour access by application of exposure-to-dose conversion coefficients for inhalation [10]. The decrease of the radionuclide concentrations due to decay during the 1 hour period has been taken into account.
- The release term has been converted to the effective dose to members of the public by application of release to effective dose conversion coefficients, computed with a dedicated Monte Carlo integration program EDARA [11].

The obtained committed effective dose due to inhalation and the effective dose to members of the public are given in Table 3 for static confinement with one flush every week and dynamic confinement with an extraction rate of 1 air volume per hour. To meet design goal 1, dynamic confinement with a flush before access has been chosen. As shown in Figure 11, to meet design goal 2, the effective dose to members of the public has been calculated as a function of the air tightness, which corresponds to the extraction rate to ensure dynamic confinement of the facility. A design goal for the air tightness of 2 air volumes per hour has been set to preserve enough margin for the overall design goal of 1 µSv per year for the effective dose to members of the public (reference group).

Table 3. Radiological impact of air activation for different confinement types

Confinement type	Committed effective dose due to inhalation without flush* for 1 hour access µSv	Release to the environment TBq/y	Effective dose to members of the public µSv/y
Static (1 flush/week)	14	0.026	0.0072
Dynamic (1 volume/h)	1.9	2.4	0.10

*These are hypothetical values used only in the assessment. A flush will always be performed before access.

Figure 11. Annual effective dose to members of the public as a function of the air tightness

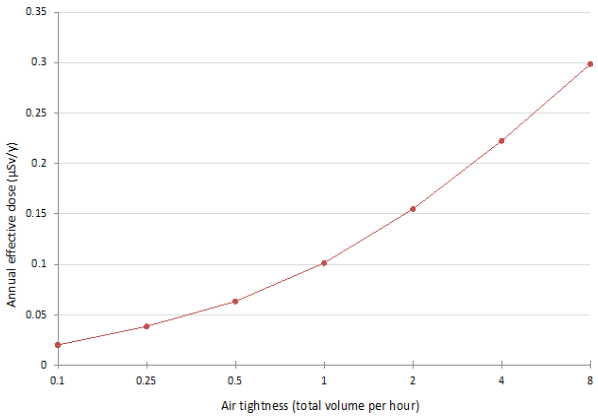

CERN Shielding Benchmark Facility (CSBF)

The CERN Shielding Benchmark Facility (CSBF) will be incorporated into the roof shielding structure of the CHARM Facility. The main purpose of the CSBF is the characterisation of the shielding properties of various materials for radiation fields laterally from a target after deep shielding penetration. In addition, these radiation fields can be used for detector calibration and detector inter-comparison studies.

The CSBF will make parasitic use of the radiation field generated by the impact of the beam on the CHARM target. The detailed design is still on-going and aims to minimise the impact on the operation of the CHARM Facility.

Figure 12 shows a side view and a top view of the first part of the CSBF. Situated vertically above the CHARM target and embedded into the roof shielding structure, the first part of the CSBF consists of a stack of 9 layers. Each layer is 40 cm high and consists of 2 concrete slabs of 80 cm x 80 cm area. Below the CSBF are cast iron of 80 cm thickness and marble of 10 cm thickness. The first part of the CSBF starts at a distance of 320 cm from the centre of the CHARM target. A second stack with identical layout will be placed further downstream.

Some concrete slabs can be replaced by slabs of the shielding material to be characterised. It will also be possible to place detectors inside the CSBF into hollow spaces created by dedicated support structures. These support structures will also provide cable feed-throughs. The characterisation studies of the inserted shielding materials will be performed with neutron detectors and activation samples.

Figure 12. Side and top view of the first stack of the CERN Shielding Benchmark Facility (CSBF)

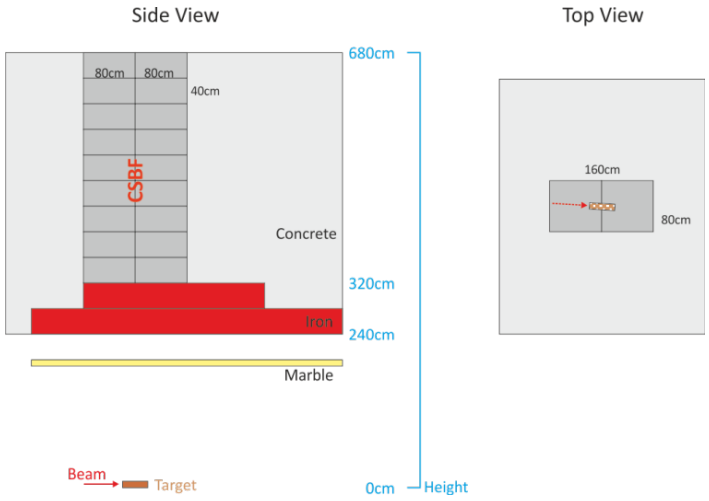

Conclusions

The CERN High Energy Accelerator Mixed Field (CHARM) Facility is currently constructed in the CERN PS East Experimental Area and will provide test locations for electronic equipment with well understood, mixed radiation fields to the CERN Radiation2 Electronics (R2E) project to study radiation effects on electronic components.

The radiation protection assessment of the facility has been presented. It has been split into the shielding design for the prompt radiation, the optimisation of the residual radiation and the activation of air and its subsequent release to the environment. It has been demonstrated that the CHARM will fulfill the CERN radiation protection requirements.

The CERN Shielding Benchmark Facility (CSBF) will be incorporated into the roof shielding structure of the CHARM Facility and will make parasitic use of the beam on the CHARM target for characterisation studies of the shielding properties of various materials for radiation fields laterally from a target after deep shielding penetration.

According to the current schedule, the CHARM Facility was expected to receive beam from the PS in July 2014.

Acknowledgements

We would like to thank the team members of the PS East Experimental Upgrade project for their support.

References

[1] www.cern.ch/charm.

[2] www.cern.ch/r2e.

[3] M. Brugger (2012), “Radiation Damage to Electronics at the LHC”, May 2012, *Conf.Proc.* C1205201, 3734-3736, Presented at Conference, C12-05-20.1, *Proceedings IPAC-2012-THPPP006.*

[4] M. Brugger et al. (2011), "FLUKA Capabilities and CERN Applications for the Study of Radiation Damage to Electronics at High-Energy Hadron Accelerators", presented at the SNA+MC, 17-21 October 2010, Tokyo, Japan, published by Atomic Energy Society of Japan in *Progress in NUCLEAR SCIENCE and TECHNOLOGY*; 948-954.

[5] A. Ferrari, P.R. Sala, A. Fassò, J. Ranft (2005), "FLUKA: a multi-particle transport code", CERN 2005-10 (2005), INFN/TC_05/11, SLAC-R-773.

[6] G. Battistoni, S. Muraro, P.R. Sala, F. Cerutti, A. Ferrari, S. Roesler, A. Fassò, J. Ranft (2007), "The FLUKA code: Description and benchmarking", *Proceedings of the Hadronic Shower Simulation Workshop 2006*, Fermilab 6-8 September 2006, M. Albrow, R. Raja eds., *AIP Conference Proceeding* 896, 31-49.

[7] R. Froeschl (2013), "The DORIAN code for the prediction and analysis of residual dose rates due to accelerator radiation induced activation", *Proceedings of the AccApp13 Conference 2013*, Brugge, 5-8 August 2013.

[8] M. Huhtinen (1997), "Determination of cross-sections for assessments of air activation at LHC", CERN Internal Report CERN/TIS-RP/TM/97-29.

[9] M. Brugger, D. Forkel-Wirth. S. Roesler, P. Vojtyla (2004), "Effective Dose to the Public from Air Releases at LHC Point 7", CERN-SC-2004-064-RP-TN.

[10] Swiss Federal Council (1994), "Swiss Radiological Protection Ordinance (RPO)", Status as of 1 January 2014, Reference 814.501.

[11] P. Vojtyla (2006), "Calculation of the external effective dose from a radioactive plume by using Monte Carlo dose kernel integration", *Applied Modeling and Computations in Nuclear Science*. Semkow, T. M., Pomme´, S., Jerome, S. M. and Strom, D. J. Eds. *A.C.S. Symposium Series* 945 (Washington, DC: American Chemical Society) pp. 104-114.

Radiation skyshine calculation with MARS15 for the Mu2e Experiment at Fermilab

A.F. Leveling
Fermi National Accelerator Laboratory, US

Abstract

The Fermilab Antiproton source is to be repurposed to provide an 8 kW proton beam to the Mu2e experiment by 1/3 integer, slow resonant extraction. Shielding provided by the existing facility must be supplemented with in-tunnel shielding to limit the radiation effective dose rate above the shield in the AP30 service building. In addition to the nominal radiation shield calculations, radiation skyshine calculations were required to ensure compliance with Fermilab Radiological Controls Manual. A complete model of the slow resonant extraction system including magnets, electrostatic septa, magnetic fields, tunnel enclosure with shield, and a nearby exit stairway are included in the model. The skyshine model extends above the beam enclosure surface to 10 km vertically and 5 km radially.

Facility overview

The dominant source of radiation dose during Mu2e operation is the delivery ring extraction system, located in the beam enclosure below the AP30 service building. The AP30 anti-proton source service building was originally designed in conjunction with the accumulator/debuncher rings for a mW power, secondary anti-proton beam and could be operated nominally at up to 13 watts of 8 GeV primary proton beam. The shield between the beam tunnel and service building is 10 feet thick (3.048 m). The anti-proton source debuncher ring (now, the delivery ring) is being reconfigured to condition and extract an 8 kW, 8 GeV proton beam by 1/3 integer, slow resonant extraction, a relatively lossy process. If this facility was to be built in a “green field”, a shielding thickness of 18 to 22 feet might be chosen. To compensate for the shielding deficit, an in-tunnel steel shielding system has been designed. A MARS model of the existing facility was created which includes a portion of the delivery ring, the slow resonant extraction system, extration beam line, and a nearby exit stairway. A longitudinal elevation view of the facility model is shown in Figure 1 while transverse elevations views which illustrate details of the exit stairway are shown in Figure 2.

Extraction system configuration and alignment

Details of the MARS model for the extraction system including a portion of the delivery ring, the electrostatic septa, various quadrupoles, extraction Lambertson magnet, C magnet, and vertical bending magnet are shown in Figure 3. The model includes magnetic fields in the quadrupole and bending magnets. The electric fields of the electrostatic septa are approximated by a magnetic field vector at 90 degrees to the nominal electric field. A total of 850 graphite and tungsten foils are included in the model.

Figure 1. Longitudinal elevation view of the MARS model

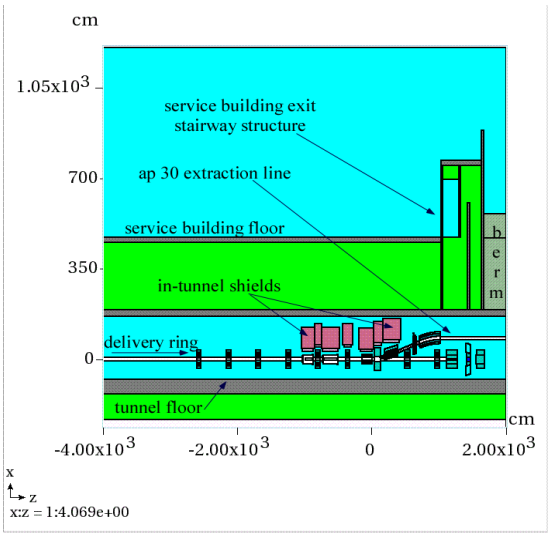

The shielding berm increases to 13 feet (3.96 m) just downstream of the indicated stairway. The AP 30 Service Building walls and roof are not shown in the figure.

Figure 2. Shielding details of the exit stairway

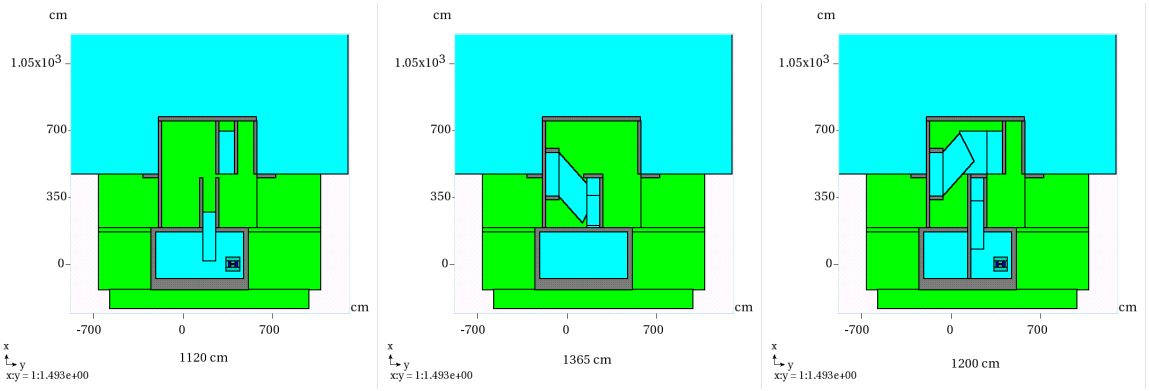

Figure 3. Delivery ring and extraction system details in a series of expanded views

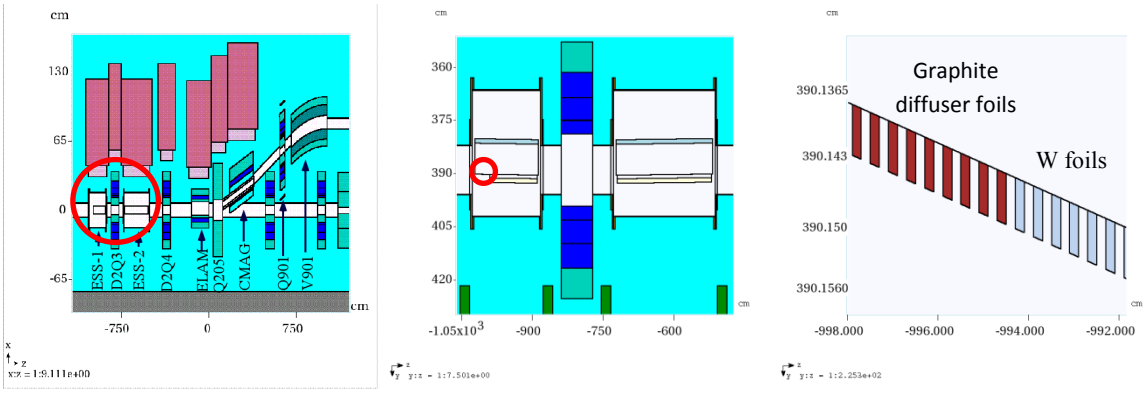

Horizontal scales for the images are left, 20 m; middle, 6 m, and right, 0.06 m.

The 2 m long Lambertson magnet (ELAM in Figure 3) is the limiting aperture in the extraction system. Cross-section views of the circulating and extraction apertures are illustrated in Figure 4. The circulating beam in the delivery ring passes through the non-field region of the Lambertson magnet while the extracted beam passes through the field region where it is deflected vertically upward. A part of the beam which intersects the foil plane scatters and is lost in the Lambertson magnet at the septum, a 3 mm wide steel divides the circulating and extraction channels. The septum acts as a magnetic field flux return; consequently, its design thickness is a constraint, which results in unavoidable beam loss.

Figure 4. Beam position at the upstream and downstream ends of the Lambertson magnet apertures (left)

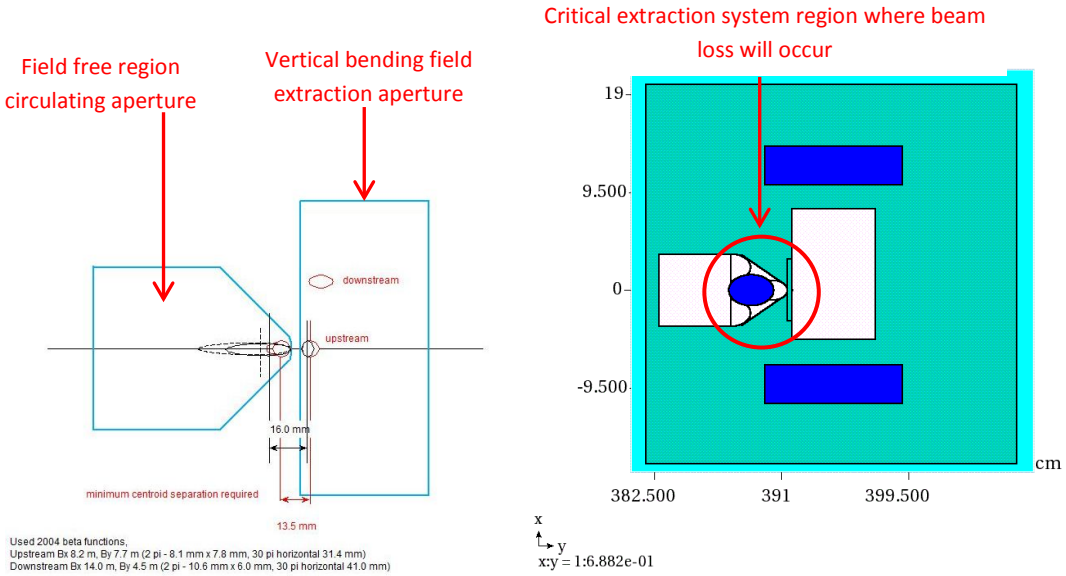

Beam scattered by the electrostatic septa foils is stopped in the steel in the region depicted by the circle in the right image.

In the MARS model, alignment of the extraction system components is necessary to optimise beam transmission and minimise beam loss. Scattering of the proton beam incident on the electrostatic septa foil planes is unavoidable. Losses from scattering in the foils are indistinguishable from losses due to misalignment of extraction system magnets. Therefore, to aid in the alignment process, the wire plane foils are temporarily treated as black holes. This permits the positioning of the extraction Lambertson, C-magnet, and other extraction line components to minimise beam loss. Once loss-free extraction positions are determined, the foil planes are returned to their normal material properties to establish conditions for normal beam loss. Surface detectors were also included in the model to determine the fraction of the beam lost in the tracking studies shown in Figure 5. The total beam loss for the region is estimated to be 1.25% or about 100 watts.

Figure 5. Extraction system component alignment

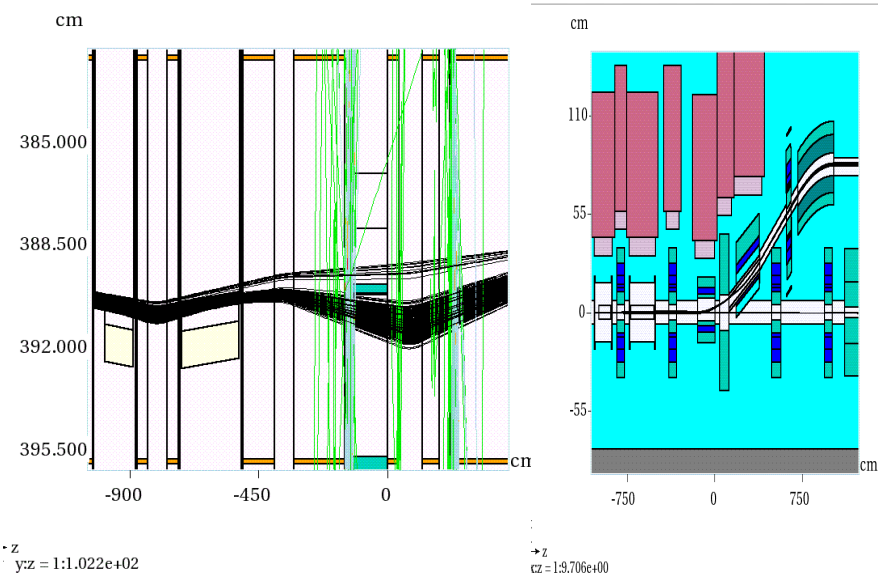

At the left of the figure, the electrostatic septa foil planes are treated as black holes. The separated beams scrape on the misplaced Lambertson magnet resulting in a particle shower indicated by the green neutron traces. The Lambertson magnet is then repositioned so that the separated beams pass cleanly through the circulating and extraction orbits as shown on the right.

Supplemental shielding system

The AP30 service building shielding is limited to 10 feet (3.048 m). Various schemes have been examined to supplement the shielding externally but all options explored were found to be either impracticable or cost prohibitive. An in-tunnel, supplemental shielding system was devised as an alternative. The modular shield design can be adopted on a location by location basis as required. The design features of such a system are illustrated in Figure 6. Seven of the supplemental systems were incorporated in the MARS model to shield extraction beam losses resulting from the electrostatic septa, Lambertson magnet, C-magnet, and three quadrupoles in Figures 3 and 5.

In addition to the steel shield shown in Figure 6, a composite concrete/marble shield is to be located in the aisle of the tunnel adjacent to the extraction devices. Residual radiation dose rates due to the unavoidable 100 watt extraction beam loss will be shielded to limit worker exposure during delivery ring maintenance periods. Figure 7 shows an illustration of the aisle shield.

Figure 6. Supplemental in-tunnel shielding is shown above the Lambertson magnet

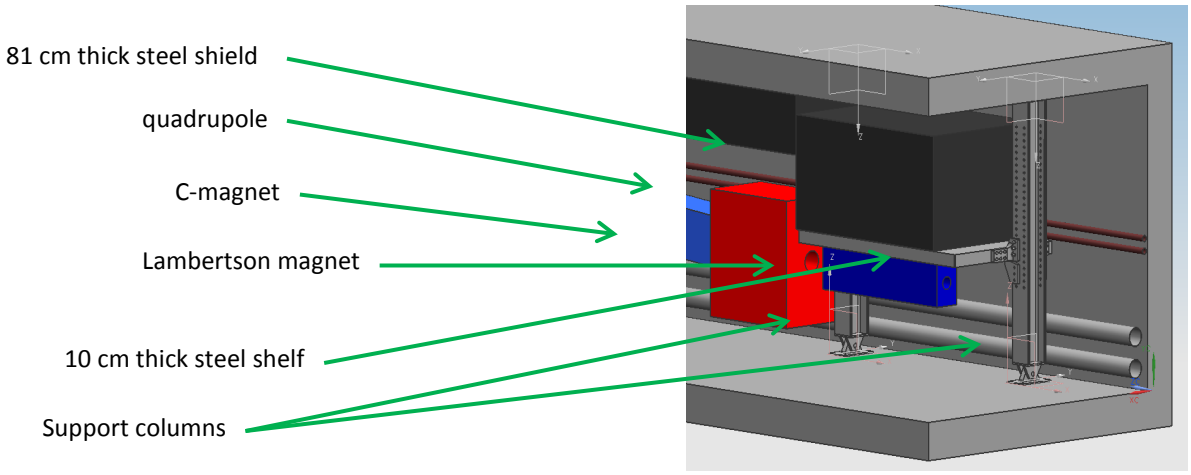

Figure 7. A concrete/marble shield is to be placed in the tunnel adjacent to extraction system components to limit worker radiation exposure during maintenance periods

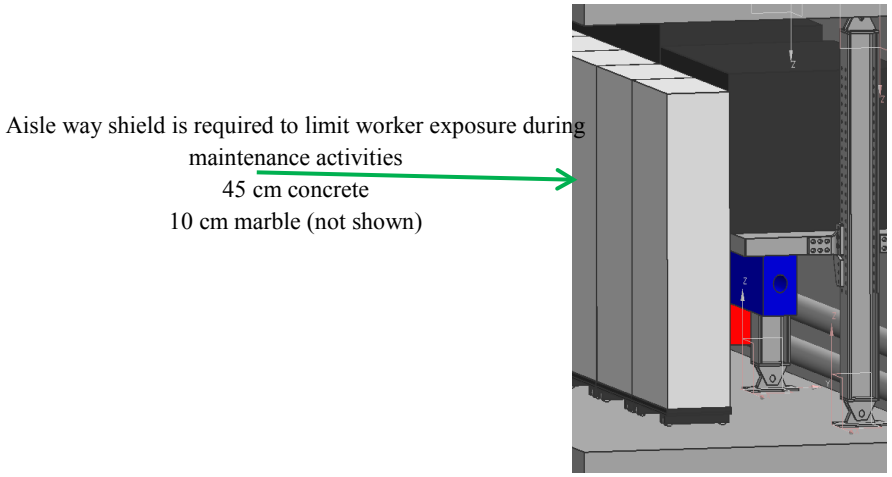

The shields are mounted on movable platforms to facilitate access to extraction system components.

Radiation skyshine model

The radiation skyshine model eventually developed for this work is a cylindrical volume with a radius of 5 km and a height of 10 km. Initially, the goal in making the model was to understand radiation effective dose at a radial distance of 500 metres and a height of up to 500 metres. As work on the calculation proceeded, and because grid computing resources were being employed, it became apparent that a significantly larger atmospheric model could be used without the need for extraordinary calendar time to complete the calculation. Therefore, the dimensions of the model were increased.

The base of the model is a concrete disk 2 m thick and 5 km radius. A tissue equivalent (TE) layer of detector, 0.3 m in height, covers the concrete disk. For the first 50 m, the TE layer is subdivided into 1 metre radial bins. From 50 m to 5,000 m, the TE disk is divided into 10 m radial bins. A MARS histogram volume (air), 100 m long by 100 m wide by 1.7 m high was placed in the atmosphere just above the TE detector at the model centre. The purpose of this histogram is to determine radiation effective dose rate due to direct and skyshine sources in the service building, the adjacent parking lot, and the nearby service road. Details of the model are shown in Figures 8 and 9.

The placement of the particle source between the TE detector and histogram volumes was intentional. The source propagates upward through the histogram volume, which gives a measure of the direct component. Reflected sky shine passes downward through the histogram volume and provides a pure skyshine component in the TE detector.

Figure 8. Skyshine model feature for radius = 500 m and height = 10 m

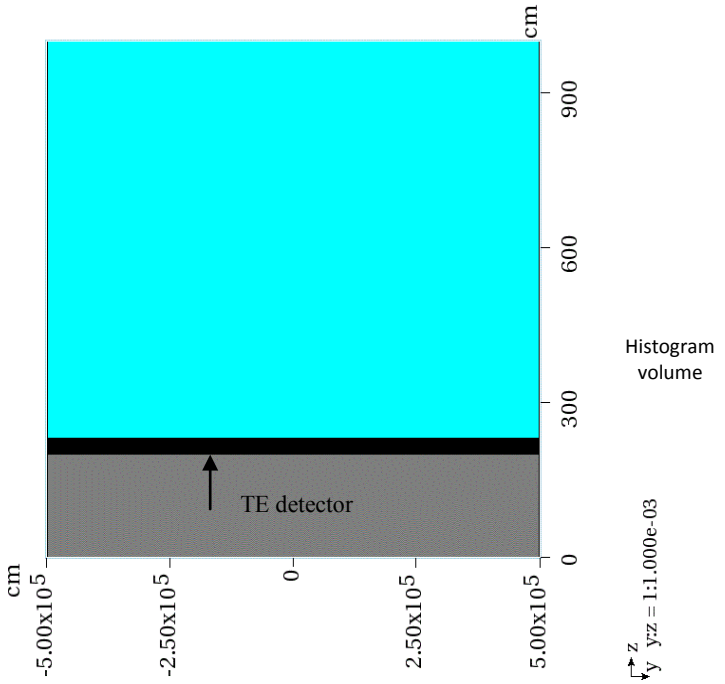

Figure 9. Cross-section of the full model (left), plan view of the model through the TE detector for the first 50 m in radius (right)

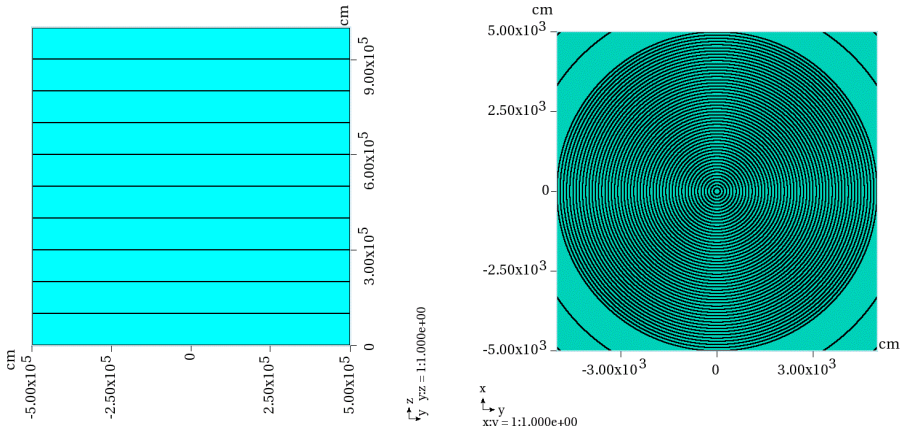

The density of the atmosphere as a function of height was calculated using the NASA earth atmosphere model for the troposphere for altitudes less than 11,000 m [4]. The temperature corrected density was calculated at the elevation for the centre of each of ten 1 km layers (local ground elevation at the AP30 service building is 744 feet) and

assumed to be constant throughout each layer. The atmosphere was modelled with weight fractions of the following elements: nitrogen (0.746), oxygen (0.24), argon (0.013), and hydrogen (0.001). The density of the atmosphere was found to have a profound effect on the shape of the plume.

Wilson Hall, the 16 story central laboratory building, is sited approximately 500 m from the AP30 service building. This building would be exposed to radiation directly emitted from the surface of the AP30 service building floor. A second MARS skyshine model, referred to as the DIRECT model, was also employed to determine radiation effective dose rate as a function of floor at Wilson Hall, due to direct and skyshine radiation sources. The model, created in root geometry, consists of at TE cylindrical shell centred on the AP30 service building with a radius of 500 m and a height of 70 m corresponding to the height of Wilson Hall. The TE cylinder was subdivided into 16 layers representing the approximate division of floors within Wilson Hall. Each of the layers was subdivided into 10 degree bins in azimuth. The details of the model are illustrated in Figure 10.

Figure 10. The blue arrow points to the approximate location of the slow resonant extraction system in the AP30 service building

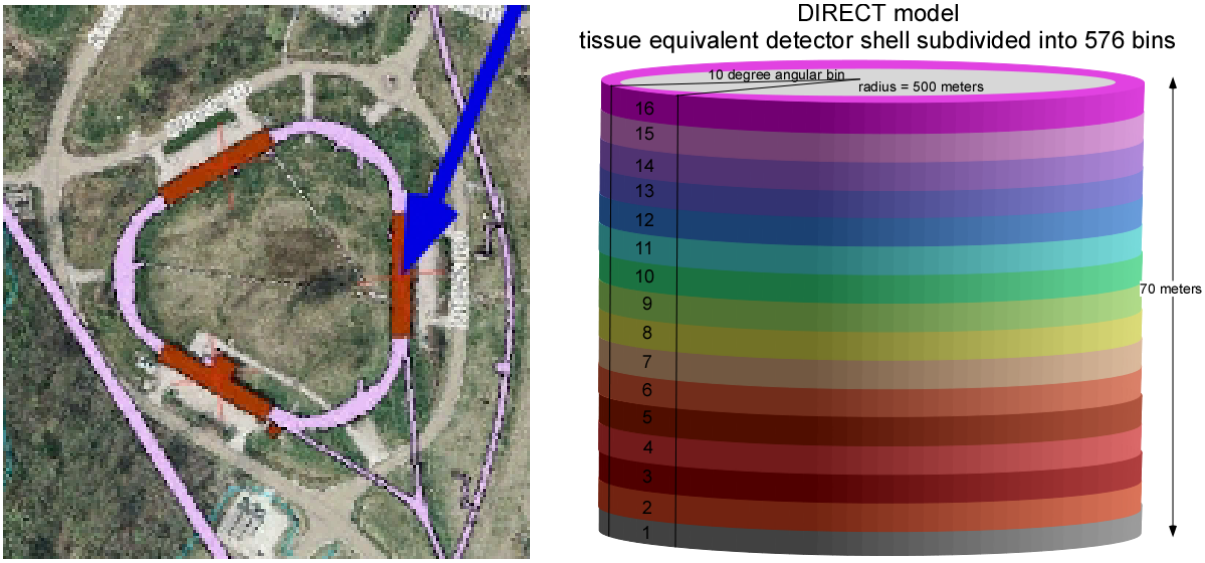

The tail of the arrow is directed towards Wilson Hall, an angle of 23 degrees relative to the direction of the incident beam. The figure at right shows a representation of the DIRECT model. The layers represent approximate floor locations at Wilson Hall and are further subdivided into 36 angular bins of 10 degrees azimuth. The cylindrical shell is centred at the AP30 service building.

MARS simulations

A series of four MARS simulations was required for this work. In the first run (called stage 1), the 8 GeV proton beam is introduced to the slow resonant extraction system. The resulting shower is propagated through the slow resonant extraction system, the in-tunnel shielding system, and to a surface just outside the tunnel. The goal of the first run is to write a file of shower particles at a surface defined outside the tunnel containing the slow resonant extraction system. The particle file consisting of 2×10^5 to 1×10^6 particles contains the particle type, the weight, energy, positions in x, y, and z and the direction cosines. In the second run (called stage 2), the stage 1 particle file is used as a source term to continue propagation of the shower through the remaining shield above the tunnel. A second set of surfaces, the service building floor and the top surface of the stairway structure, were established to collect a new set of shower particles for the stage 2 run.

The stage 2 run particle files were used as source terms for the third (skyshine) and fourth (direct) calculations. Figure 11 shows the location in elevation at which the particle source files were written. Histograms indicating the total flux during the stage 1 and stage 2 runs are shown in Figure 12.

Figure 11. Elevation view of AP 30 service building showing elevations at which stage 1 and stage 2 particle showers were collected

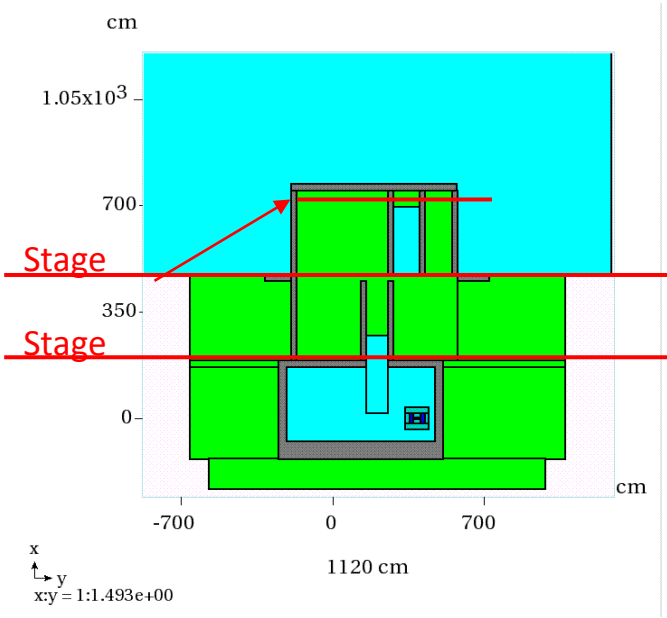

Figure 12. Longitudinal elevation views in the plane of the proton beam

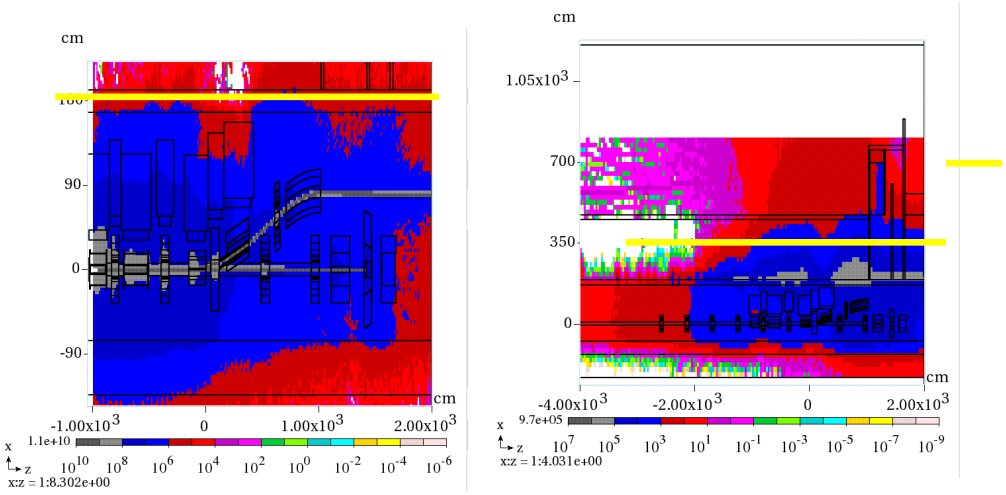

Histograms of total flux created during the stage 1 (left) and stage 2 (right) runs are indicated. The yellow lines indicate particle collection surfaces for the two runs.

MARS skyshine and direct results

Histograms in elevation view of total effective dose rate for the 8 kW proton beam extraction with a 1.25% beam loss are shown in Figure 13. The plume in the xz plane is tipped due to the forward momentum tendency of the emerging particle shower. The plume in the yz plane is tipped to beam left due to the proximity of the beam transport system adjacent to the tunnel wall at beam right; i.e. the tunnel wall suppresses the plume at beam right.

Figure 13. The prompt total effective dose rate in mrem/hr is shown for the xz plane on the left and the yz plane on the right

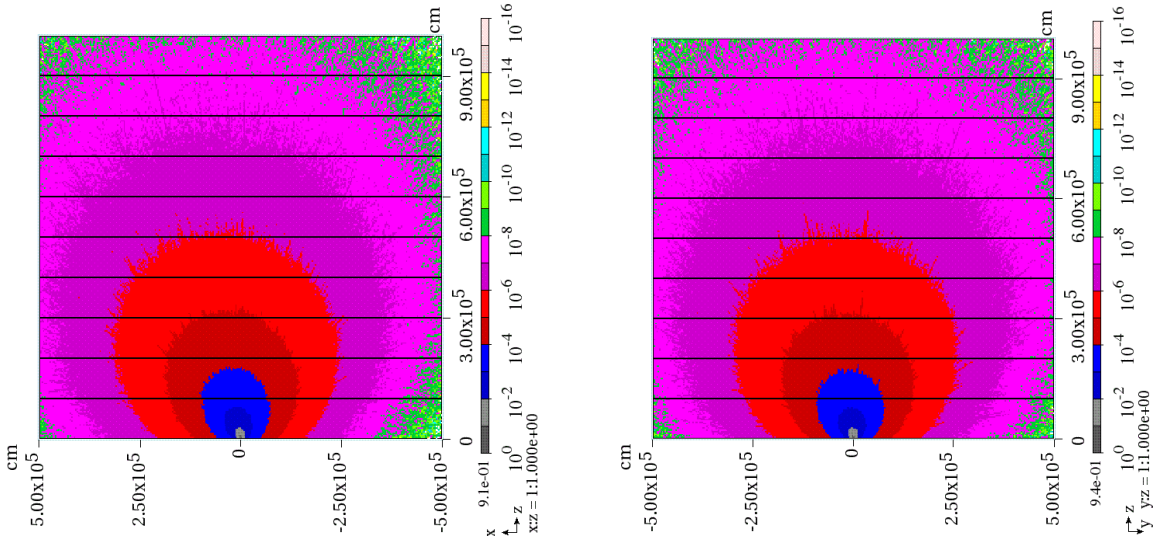

Histograms in a plan view of total effective dose rate for the 8 kW proton beam extraction with a 1.25% beam loss are shown in Figure 14. The non-symetric nature of the plume is further amplified in these images.

The result of total effective dose rate in the 5 km radius TE detector is shown in Figure 15. The dose rate at Wilson Hall (500 m) is 0.17 mrem per year

The result for prompt effective dose rate in the volume histogram in the vicinity of the AP30 service building is shown in Figure 16.

Figure 14. Plan view of average total effective dose rate in mrem/hr for ten 1 km layers of atmosphere above the AP30 service building

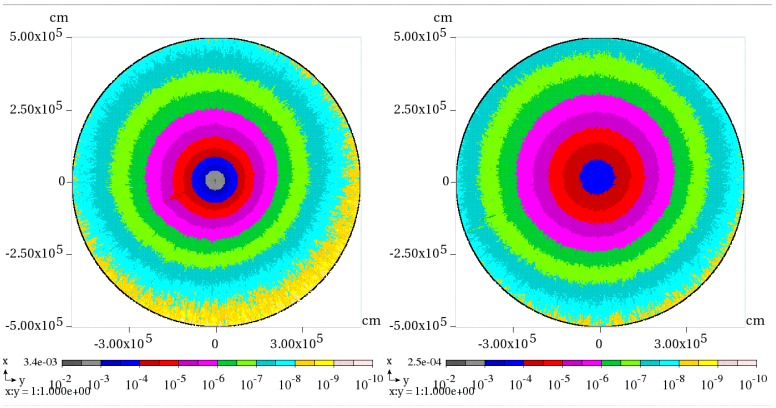

Layer 1 and 2

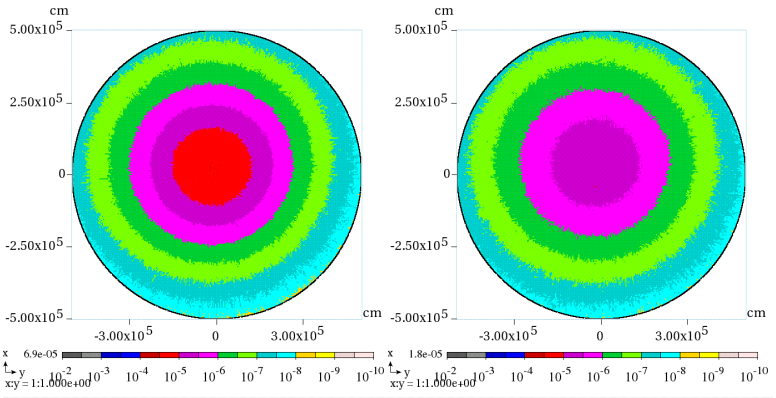

Layer 3 and 4

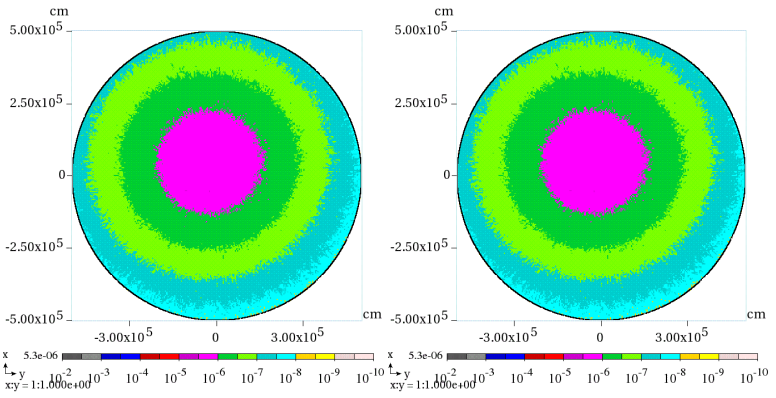

Layer 5 and 6

Figure 14. Plan view of average total effective dose rate in mrem/hr for ten 1 km layers of atmosphere above the AP30 service building (continued)

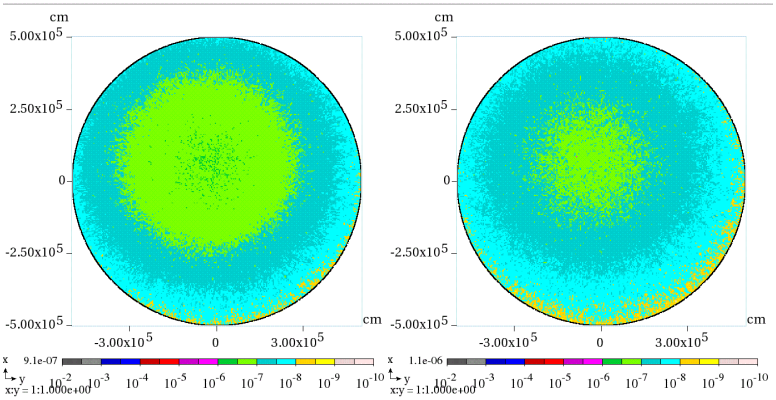

Layer 7 and 8

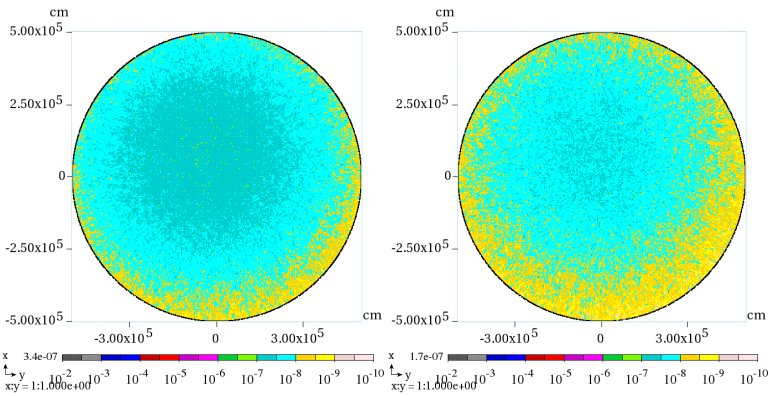

Layer 9 and 10

Figure 15. The annual radiation effective dose rate for continuous Mu2e operation in the 5 km TE detector is shown in blue while statistical errors are shown in red as a function of distance from the centre of the model

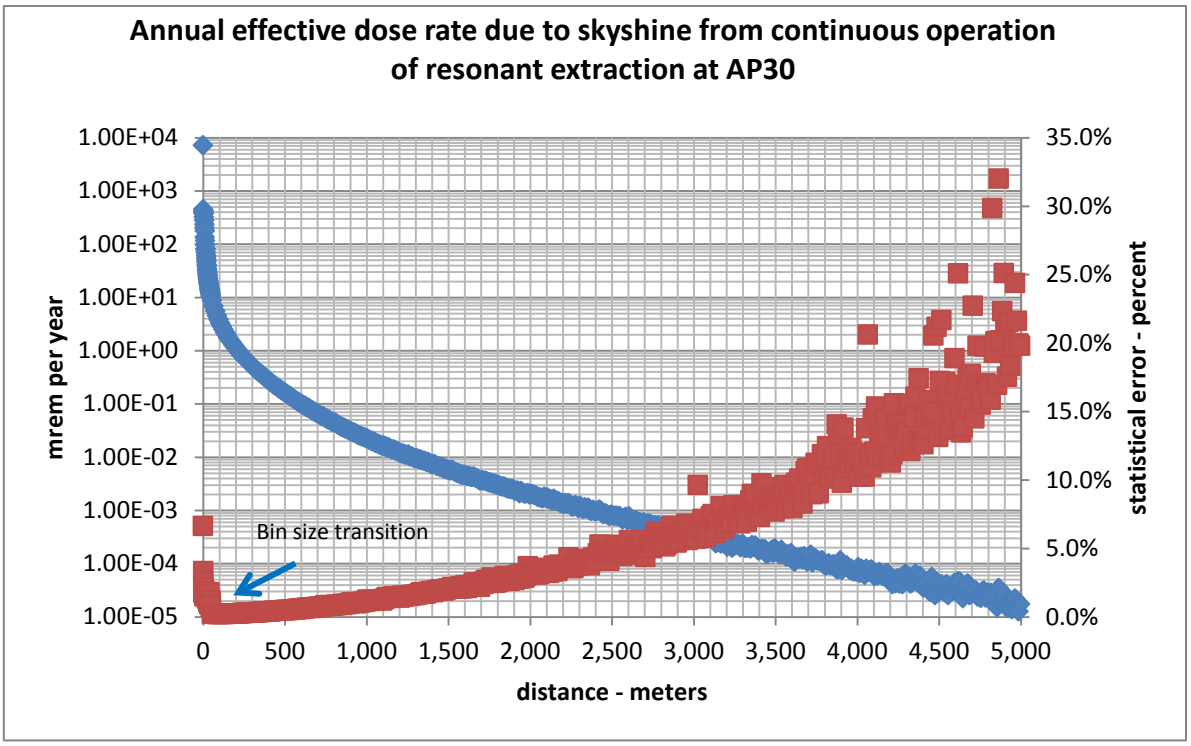

Figure 16. Histogram of prompt effective dose rate in mrem/hr for slow resonant extraction of 8 GeV, 8 kW beam loss with 1.25% beam loss

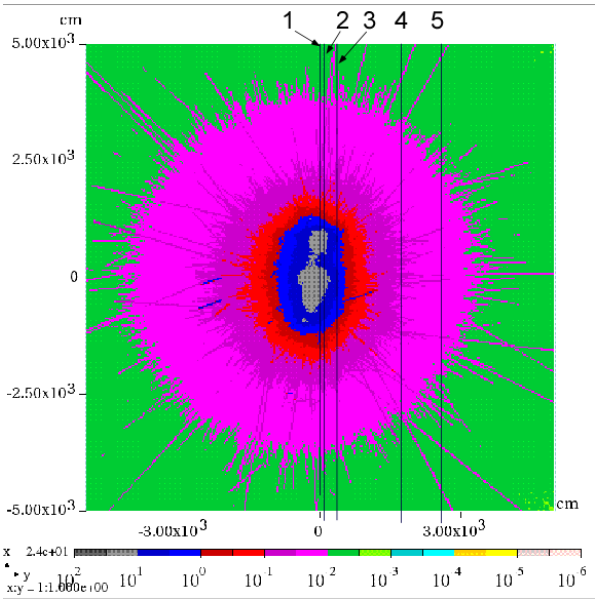

Enumerated lines legend is: 1. Delivery Ring centreline, 2. Tunnel outer concrete edge, 3. Edge of service building; 3/4. Parking Lot; 5. Edge of Indian Road.

Finally, the result of the direct calculation, which includes direct and skyshine sources as a function of floor in Wilson Hall, corresponding to an angle of 23 degrees in azimuth relative to the forward incident beam direction, is shown in Figure 17. The first floor does not receive a direct contribution from the AP30 service building since the areas share a common elevation. The direct effective dose rate contribution at a given floor can be approximated by subtracting the first floor rate from the combined rate. Wilson Hall is a massive concrete structure. No credit is taken for the shielding provided by the building. Consequently, the calculations are conservative except perhaps where offices are located in the glass-walled cross-overs at the south face of Wilson Hall.

Figure 17. The combined skyshine/direct effective dose rate as a function of floor elevation in Wilson Hall is shown at the arrow in the plot

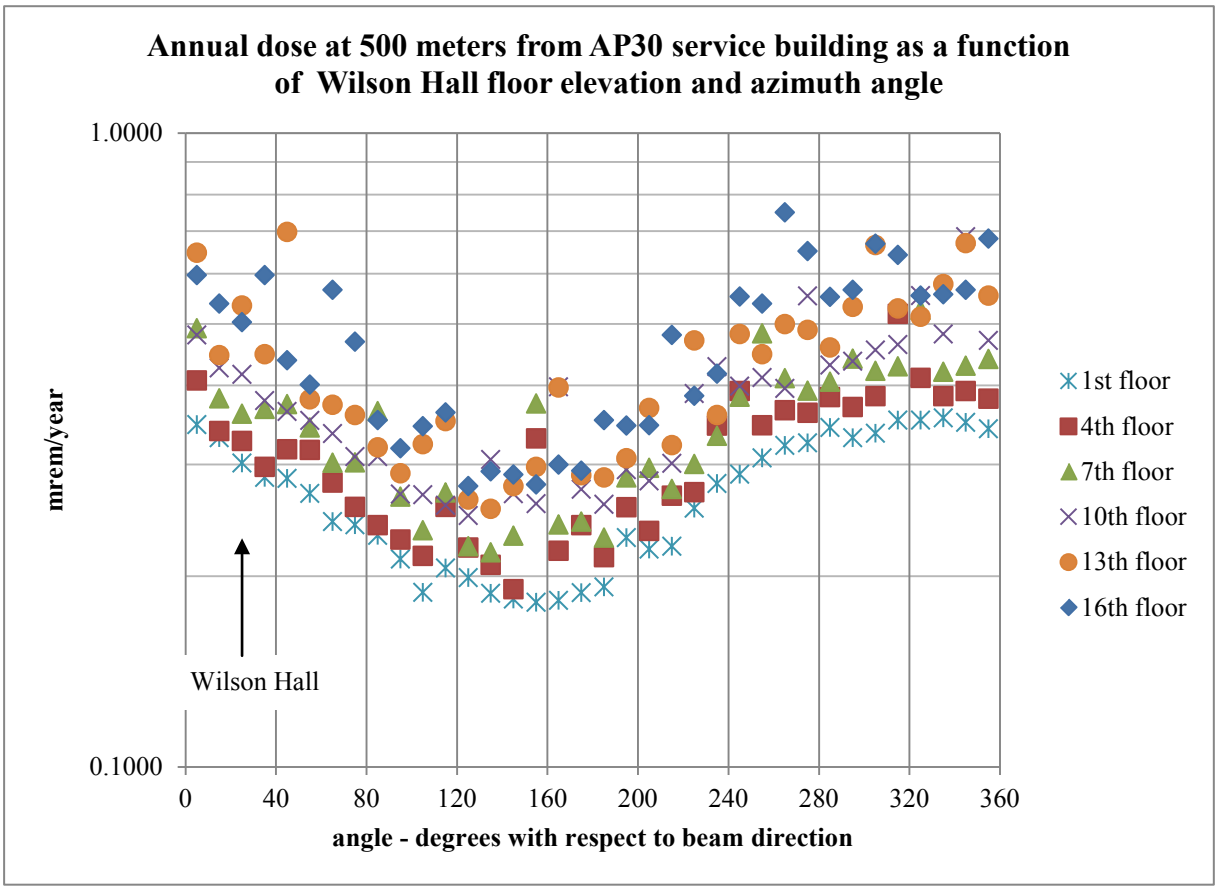

The difference between the 1st floor and other floor effective dose rates is due to the direct effective dose rate.

Conclusions

A model of the resonant extraction system has been created in which 1.25% beam losses are realistically distributed. A supplemental shield system design has been produced. The resulting calculated skyshine and direct effective dose rates fall within all limitations of the Fermilab Radiological Controls Manual. However, an active protection system will be required to limit radiation effective dose rates significantly higher than those calculated in the work reported here. Additional sources of beam loss at the antiproton source facilities could lead to additional sources of skyshine. Those additional sources must be included with the results reported here when/if they are observed. Based upon the beam

loss scenario considered here, it will be prudent to exclude personnel access to the AP30 service building during mu2e beam operations.

Acknowledgements

Consultation with a rather large group of people was required to produce this work. First and foremost, the author acknowledges the contributions by Don Cossairt and Nikolai Mokhov for insights into the skyshine problem and for application of the MARS code to solve it.

Vladimir Nagaslaev provided the incident beam parameters for the resonant extraction system as well as the layout of the ESS septa placement and angles. Jim Morgan provided the design layout of the extraction system along with beam line coordinates and magnet currents. Carol Johnstone provided starting alignment data for the extraction line components. Corey Crowley designed the modular in-tunnel shielding system. Brian Hartsell provided the preliminary electrostatic septa mechanical design adapted for the model. Mike Vincent provided the C-magnet geometry. Rob Kutschke and Andrei Gaponenko made advances in MARS grid job submission procedures and taught the author to use them. Steve Werkema provided general help and consul in the development and execution of this model and the many previous versions. He also reviewed this paper and is partly responsible for whatever clarity of thought it may provide. Finally, the calculations used to produce results presented here required many years of process time. This work would not have been possible without the support of the Fermilab grid computing system.

References

[1] Mu2e Collaboration (2012), Mu2e Conceptual Design Report, arXiv:1211.7019 [physics.ins-det].

[2] Fermilab Radiological Controls Manual, http://esh.fnal.gov/xms/FRCM.

[3] N.V. Mokhov (1995), "The Mars Code System User's Guide", Fermilab-FN-628, N.V. Mokhov, S.I. Striganov, "MARS15 Overview", Fermilab-Conf-07/008-AD (2007); *Proc. of Hadronic Shower Simulation Workshop*, Fermilab, September 2006, *AIP Conf. Proc.* 896, pp. 50-60 (2007); http://www-ap.fnal.gov/MARS/.

[4] http://www.grc.nasa.gov/WWW/k-12/airplane/atmosmet.html.

Measurements of high-intensity laser induced ionising radiation at SLAC

Taiee Liang[1,2], Johannes Bauer[1], Maranda Cimeno[1], Anna Ferrari[3], Eric Galtier[1], Eduardo Granados[1], James Liu[1], Bob Nagler[1], Alyssa Prinz[1], Sayed Rokni[1], Henry Tran[1], Mike Woods[1]
[1]SLAC National Accelerator Laboratory, Menlo Park, CA US
[2]Georgia Institute of Technology, Atlanta, GA US
[3]Institute of Radiation Physics, Dresden, Germany

Abstract

A systematic study of measurements of photon and neutron radiation doses generated in high-intensity laser-target interactions is underway at SLAC National Accelerator Laboratory using a femtosecond pulsed Ti:sapphire laser (800 nm, 40 fs, up to 1 J and 25 TW) at the Linac Coherent Light Source's (LCLS) Matter in Extreme Conditions (MEC) facility. Preliminary results from recent measurements with the laser-optic-target system (peak intensity $1.8x10^{18}$ W/cm^2) are presented and compared with results from calculations based on analytical models and FLUKA Monte Carlo simulations.

Introduction

The number and use of high-intensity (multi-terawatt and petawatt) lasers in research facilities has seen a rapid rise in recent years. These lasers can now be used in conjunction with research programmes in III- and IV-generation light sources to study matter under extreme conditions [1], or as sources of particle acceleration [2].

High-intensity laser-matter interaction in vacuum can create a plasma, and further laser interactions with the plasma can accelerate electrons in the plasma up to 10's to 1000's of keV [3-9]. These "hot" electrons will interact with the laser target and the target chamber and generate bremsstrahlung X-rays [10-11]. This mixed field of electrons and photons can be a source of ionising radiation hazard for personnel working on or near such systems if sufficient radiological controls are not implemented. Currently, there is limited information on the ionising radiation hazards associated with such laser-matter interactions, and on controls for such hazards. Characterisation of the radiation source term, understanding the radiological hazards, and development of appropriate measures to ensure personnel safety in this rapidly rising field are needed.

SLAC Radiation Protection (RP) Department, in conjunction with the Linac Coherent Light Source (LCLS) Laser Division, has embarked on a systematic study to measure ionising radiation under controlled experiments using the high-intensity, short-pulse laser of the LCLS's Matter in Extreme Conditions (MEC) instrument [12].

As part of this on-going effort, SLAC RP has also been developing analytical models to estimate radiation yield (Sv/J) and performing Monte Carlo simulations to characterise the measured data more accurately [13-16]. Another goal from the measurements is to evaluate the performance of various types of active and passive detectors in the laser-induced radiation fields. The purpose of these studies is to evaluate the efficacy of shielding for protection of personnel from the ionising radiation and to develop accurate

methods and tools to estimate the required shielding at various intensities for different targets.

Experiments performed to-date include radiation measurements at the Lawrence Livermore National Laboratory's Titan laser Facility in 2011 and measurements at SLAC's MEC Facility in 2012 and 2014. In the Titan measurements, the laser beam intensity and pulse energy were ~10^{20} W/cm^2 and 400 J, respectively. Targets included 3-5 mm thick hydrocarbon foam and 1 mm gold foil. The 2012 experiment at SLAC's MEC laser facility was performed with laser intensities between 3x10^{16} and 6x10^{17} W/cm^2 (40 fs and up to 0.15 J per pulse). Targets for the MEC 2012 experiment included gold foils (0.01 and 0.1 mm) and copper (1 mm). The results of these two measurements have been reported elsewhere [14] [16]. Preliminary results of the latest MEC experiment in February 2014 are compared with results from analytical models and Monte Carlo simulations.

SLAC RP dose model

The bremsstrahlung photon yield due to hot electrons generated from laser-matter interaction is characterised by the temperature (or energy) of hot electrons, T_h, and the laser energy to electron energy conversion efficiency, α. The hot electron temperature T_h is a function of laser parameters and increases with the normalised laser intensity, $I\lambda^2$, where I (W/cm^2) is the laser intensity, λ the laser wavelength (μm) [17] [18].

Electron temperature and energy distribution

At lower laser intensities, inverse bremsstrahlung and resonance absorption are the dominant mechanisms for producing hot electrons, and SLAC RP uses Meyerhofer's empirical scaling of Equation (1) to calculate T_h in units of keV for normalised laser intensity $I\lambda^2 < 1.6\text{x}10^{17}$ W-μm^2/cm^2 [17].

$$T_h = 6\times10^{-5}\left(I\lambda^2\right)^{\frac{1}{3}} \quad (1)$$

At higher laser intensities, when $I\lambda^2 \geq 1.6\text{x}10^{17}$ W-μm^2/cm^2, the ponderomotive force is the primary electron heating mechanism, and it is defined as the force that a dipole experiences in an oscillating electromagnetic field. In the case of a laser-plasma interaction, the free electrons in the plasma experience the oscillating electric field of the incident laser. Equation (2) is used to calculate T_h-based on the ponderomotive force where M_e is the electron rest mass (511 keV) [18] [19].

$$T_h = M_e \times \left(\sqrt{1.0 + I\lambda^2/1.37\times10^{18}} - 1.0\right) \quad (2)$$

Figure 1 shows the distinct inflection point at $I\lambda^2$ = 1.6x10^{17} W-μm^2/cm^2 from the combination of Equations (1) and (2) for calculating T_h. The value of T_h is directly proportional to the photon dose generated through bremsstrahlung of hot electrons with the laser's target and target chamber's walls. The SLAC RP model for T_h provides a conservative approach at estimating the photon dose yield from laser-matter interaction.

Figure 1. SLAC RP model for T_h (keV) as a function of I (W/cm²) with λ=0.8 µm

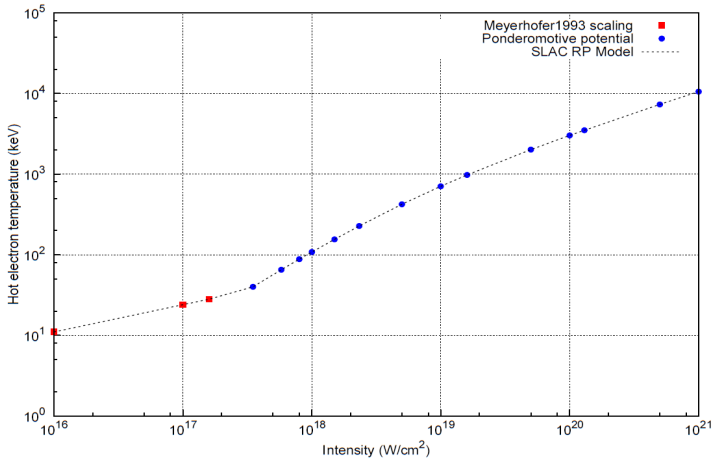

The energy distribution of electrons is also characterised by T_h. Equations (3) and (4) give two distributions used by RP to characterise the energy of the hot electrons for I below and above 10^{18} W/cm², respectively [20-22]. The Relativistic Maxwellian case with an average electron energy of $3T_h$ is a harder electron spectrum than the Maxwellian case with an average energy of $1.5T_h$.

$$N_e \propto E_e^{1/2} \exp\left(-\frac{E_e}{T_h}\right) \text{ for } I \le 10^{18} \text{ W/cm}^2 \text{ (Maxwellian)} \quad (3)$$

$$N_e \propto E_e^{2} \exp\left(-\frac{E_e}{T_h}\right) \text{ for } I > 10^{18} \text{ W/cm}^2 \text{ (Relativistic Maxwellian)} \quad (4)$$

Photon dose calculation

Monte Carlo codes such as FLUKA can predict the photon dose from a hot electron spectrum described by Equation (3) or (4), the hot electron temperature T_h, the laser energy to electron energy conversion efficiency α, and the angular and spatial distribution of the electrons. However, it is desired to have a simple empirical formula based on the above parameters that can provide a quick estimate of the photon dose yield due to laser-matter interaction.

The SLAC RP model for photon dose utilises Equations (5) and (6) from Y. Hayashi [23] that are derived for the maximum bremsstrahlung photon dose (occurring at 0° along laser axis) generated through interaction between a short pulse high-power laser and a solid target. The equations are based on a laser-generated electron spectrum with a Relativistic Maxwellian distribution as described earlier in Equation (4).

$$H_x \approx 1.8 \times \left(1.10 \times \frac{\alpha}{R^2}\right) \times T_h^2 \text{ for } T_h < 3 \text{ MeV} \quad (5)$$

$$H_x \approx 1.8 \times \left(3.32 \times \frac{\alpha}{R^2}\right) \times T_h \text{ for } T_h \ge 3 \text{ MeV} \quad (6)$$

The 0° photon dose yield H_x is in units of Sv/J, and R is the distance between the laser-target interaction point and the dose point in cm. Equations (5) and (6) from Hayashi were derived based only on the ponderomotive force theory for I between 10^{19} to 10^{21} W/cm². To adapt for lower laser intensities, the RP model uses the T_h from Equations (1) and (2) to calculate H_x. The SLAC RP model for the laser conversion efficiency α is 30% for I ≤ 10^{19} W/cm²

and 50% for I > 10^{19} W/cm^2 [1] [24]. Because Hayashi equations only account for the 0° photon dose yield at very high-intensity lasers with no shielding, the SLAC RP model may overestimate the photon dose outside 0° and when accounting for the shielding effects of the target chamber itself.

Experimental set-up and beam parameters

The February 2014 experiment was performed at the LCLS Hutch 6 (MEC hutch) using the 0.8 µm Ti:Sapphire short pulse laser on a 100 µm thick copper target. Figure 2 shows the layout of MEC Hutch 6 with its short and long pulse laser systems and the aluminium target chamber.

Figure 2. Layout of SLAC LCLS Hutch 6

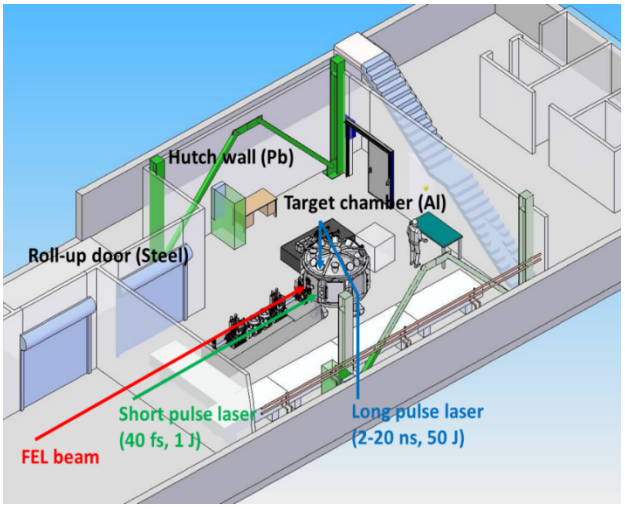

MEC target chamber layout

Figure 3 shows a horizontal cross-section of the MEC target chamber. The target chamber has a radius of about 1 meter, and its aluminium walls vary in thickness, but are typically 2.54 cm thick (5.08 cm for chamber doors). For the 2014 MEC experiment described here, the unfocused short pulse laser entered the target chamber from the left and was directed with a series of mirrors to an Al-coated off-axis parabolic (OAP) mirror. The OAP mirror focused the laser beam to a horizontal and vertical 1/e2 radius spot size of 13 µm × 8 µm with a peak intensity of 1.8x1018 W/cm2 at 192 mJ. The focused laser beam was incident on the target material at an angle of 15o relative to target normal. Copper foils of thickness 100 µm served as the laser targets and were positioned at the chamber centre and perpendicular to the FEL axis.

The lenses and mirrors located downstream of the laser-matter interaction point were used before the start of the experiment for characterising laser beam parameters. Pulse energy measurements were taken with a Coherent J50 50M-IR sensor and a Coherent LabMax-TOP meter. The pulse duration was measured twice with two separate instruments, a Coherent single-shot autocorrelator (SSA) and an APE LX Spider autocorrelator, before and after the experiment, and both instruments reported the same result. An Adimec OPAL-1000 CCD camera, calibrated before the experiment, determined the spot size by imaging the beam. The measured profile of the focused beam on target was a complicated distribution with multiple peaks, and this contributes to the uncertainty associated with laser intensity calculations.

With the laser system operating at 1 Hz, a target rastering system ensured each laser shot interacted with fresh copper material. Furthermore, as seen in Figure 3, two 12 cm

thick steel shields were deployed inside the MEC chamber in the forward and backward direction of the laser beam to evaluate their effectiveness in shielding the generated ionising radiation. Their efficacy is discussed later in the measurement results.

Figure 3. Layout inside MEC chamber for February 2014 experiment

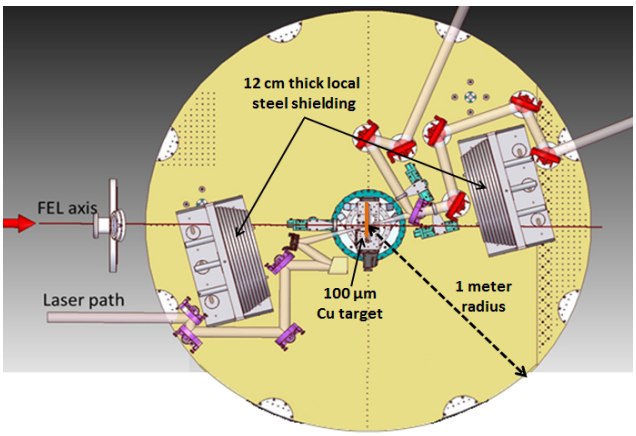

Table 1 lists key laser and optic parameters for the experiment and their associated uncertainties (one standard deviation). A total of 540 laser shots on target were taken during the course of the experiment. Due to the damage to the Al-coated OAP focusing mirror from the high-energy laser beam, only a limited number of shots could be taken. Future experiments using the MEC laser system will utilise other metal mirror coatings with higher reflectivity.

Table 1. Parameters from February 2014 MEC experiment (uncertainties in parentheses)

Parameters	MEC 2014
Target material	Copper
Target thickness (µm)	100
Energy before compressor (mJ)	1400 (5%)
Transmission fraction of compressor	0.68 (2%)
Transmission fraction of Al-coated OAP	0.87 (5%)
Fraction of energy in main peak	0.23 (20%)
Energy on target in main peak (mJ)	192 (21%)
FWHM pulse duration (fs)	70 (5%)
Horizontal $1/e^2$ radius spot size of main peak (µm)	13 (10%)
Vertical $1/e^2$ radius spot size of main peak (µm)	8 (10%)
Calculated peak intensity (W/cm^2)	1.8×10^{18} (27%)

Detectors and instruments

A combination of passive dosimeters and active detectors were deployed inside and outside the Al MEC target chamber and around Hutch 6 for radiation measurements. The passive dosimeters included electrostatic pocket ion chambers (PIC) with a full scale of 0.02 or 2 mSv and Landauer personnel dosimeters (nanoDot, Luxel+ Ja, and InLight). Only nanoDots were approved for use in the MEC under vacuum conditions, and these were expected to record high-dose values from the mixed electron and photon field inside the target chamber. All other dosimeters (0.02 and 2 mSv PICs, Luxel+ Ja, and Inlight) were

deployed outside the target chamber to measure the photon doses that escape the target chamber.

The active instruments included RADOS electronic dosimeters, two HPI-6031 styrofoam-walled ion chambers, two PTW-7262 pressurised argon ion chambers, Victoreen-451 handheld ion chambers, and two polyethylene-moderated BF_3 neutron detectors (a quasi-remmeter design). The RADOS were added to the passive dosimeters outside the target chamber at their respective locations. The two HPI ion chambers, HPI-01 and HPI-02, were positioned directly outside the target chamber. One of the PTW ion chambers, PTW-01, was located in the Hutch 6 control room on the roof, the other, PTW-02, was at the Hutch 6 steel roll up door. The Victoreen-451 meters and BF_3 detectors were deployed at various angles and distances around the target chamber. The active instruments provided real-time dose monitoring information throughout the experiment. These detectors are described in detail in [16].

Measurement results

The amount of ionising radiation generated from laser-matter interaction depends heavily on the intensity and energy of laser and less on the solid target material and thickness. For a laser interacting with a solid high Z target, the radiation field inside the target chamber is composed of the accelerated hot electrons and bremsstrahlung photons originating from either the copper target itself or the walls of the Al chamber. The varying 2.54 to 5.08 cm thick Al wall of the target chamber is expected to attenuate the large majority of the low-energy electrons and photons. However, electrons and photons of sufficiently high energy can penetrate the wall, or the chamber's thin 5 mm glass view ports. The following sections provide preliminary measurements results from active and passive detectors used during the MEC experiment.

Dose inside target chamber

Passive nanoDot dosimeters inside the MEC chamber measured very high integrated doses from the experiment. The nanoDot results presented here are based on ^{85}Kr shallow dose calibration that accounts for the high fluence electron field inside the chamber. Figure 4 presents a polar plot of dose from nanoDots located 30 cm radially from the laser-target interaction point.

Figure 4. Dose (cGy) from nanoDots inside MEC chamber at 30 cm (I=1.8x10^{18} W/cm^2 for 540 shots)

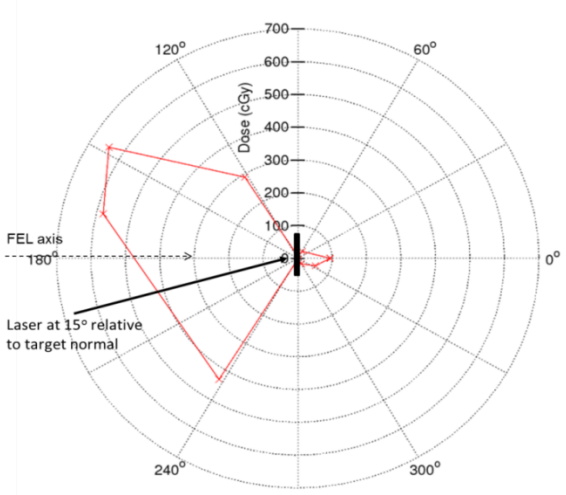

The maximum measured dose is 650 cGy in the backward direction and 100 cGy in the forward. The angular distribution of dose suggests that the dose is peaked towards 0°, whereas the dose in the backward direction spreads over a wide angle. Two possible factors may contribute to the difference between the measured forward and backward dose: target thickness and laser intensity. Studies at other facilities have shown that the dose is dominantly in the forward direction [25]. However, these studies utilise filters to measure only electrons of 100 keV and greater, or they use a very high laser intensity between 10^{19}-10^{20} W/cm^2. On the other hand, the February 2014 MEC measurements presented here include dose from low-energy electrons along with high energy, and the laser intensity is also comparatively low at 1.8x10^{18} W/cm^2. In addition, the 100 µm thick copper target used in this experiment can be considered a thick target shielding to low-energy electrons in the forward direction. This shows the complexity of energy and angular distributions of hot electrons and their implications on photon doses outside the target chamber.

Radiation levels outside target chamber

Figure 5 shows the maximum photon and neutron dose rates (ambient dose equivalent) measured above background with the active instruments outside the MEC chamber, excluding PTW pressurised ion chambers. Each BF_3 station also included a Victoreen 451 to measure photon dose rate at that location. All active detectors performed well at the laser intensity of 1.8x10^{18} W/cm^2 at 1 Hz and were not affected by any electromagnetic pulse effects as experienced in experiments [14].

Figure 5. Maximum dose rates from active detectors at target chamber (I=1.8x1018 W/cm2 at 1 Hz)

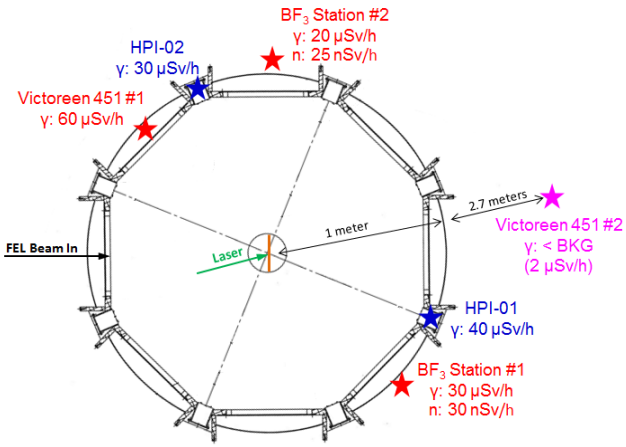

The maximum photon dose rate outside the target chamber of 60 µSv/h was measured by Victoreen #1 in the backward direction of the laser. This location outside the chamber corresponds with the mostly backward-directed nanoDot doses shown earlier in Figure 4. On the other hand, Victoreen #2 was shielded by 12 cm of steel shielding inside the chamber and did not measure greater than background during the experiment. This result demonstrates the effectiveness of localised shielding (designed for up to ~1x10^{20} W/cm^2 and 8 J) inside the target chamber for a laser intensity of 1.8x10^{18} W/cm^2.

As shown in Figure 5, the photon dose rates from active detectors outside the MEC chamber agree well. Differences between the photon dose rates may be due to self-shielding effects of the optics equipment and lenses inside the chamber as seen earlier in Figure 3. Comparing results from active detectors suggests the photon dose rate outside

the MEC chamber is directionally dependent and dependent on the dose inside the chamber.

PTW-01 was located inside the Hutch 6 control room above the hutch roof. The control room is 3 m above the MEC target chamber and shielded by about 25 cm of concrete roof. This combination of distance and shielding caused PTW-01 to only measure a maximum dose rate of 0.01 µSv/h above background. PTW-02 was located outside the Hutch 6 steel roll up door about 6 meters from the target chamber and measured a maximum dose rate of 0.1 µSv/h above background.

Figure 6 shows a marked drop in photon dose rates over the course of 540 laser shots at 1 Hz. The same decreasing pattern was also observed by the BF_3 neutron detectors. The left bunch represents 140 shots, and right bunch represents 400 for a total of 540 laser shots on the copper target with a starting peak intensity of 1.8×10^{18} W/cm^2. The drop in dose rates is linked with the progressive damage of the Al-coated OAP focusing mirror. In addition, the sudden dips in the dose rate are due to the target rastering system shifting the copper foil to provide fresh material for laser shots.

Figure 6. Photon dose rates from Victoreen 451 #1

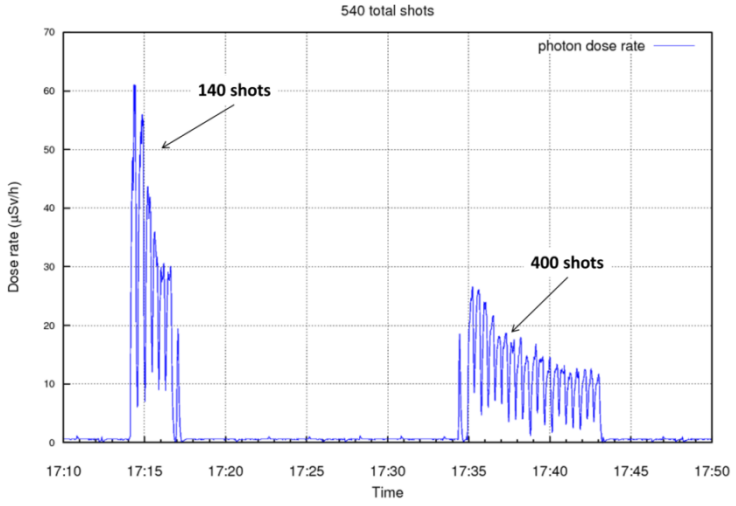

Most passive dosimeters such as the 2 mSv PIC, InLight, and Luxel+ that measure integrated dose were not sensitive enough and did not read above background. Measurements with more sensitive dosimeters (RADOS and 0.02 mSv PIC) did provide dose results that agreed well with each other. The maximum integrated doses measured on the passive dosimeters outside the target chamber were 4 µSv around the sides and 6 µSv above the chamber roof. The passive dosimeters on the roof measured higher doses because the chamber roof is thinner than the sides.

Photon dose yield

Figure 7 presents the maximum measured dose yield from this and two past experiments [14] [16], and error bars represent one standard deviation. Dose yield (ambient dose equivalent generated per laser shot energy) is in units of mSv/J at a distance of 1 meter. The blue triangles are from the 2012 MEC experiment [16], and the purple pluses are the 2011 measurements performed by SLAC RP at the LLNL Titan laser Facility [14]. The Titan results are shown with no error bars, since they were obtained parasitically from another experiment, and thus the laser-optic parameters were not well characterised and subject to large uncertainties.

Figure 7. Photon dose yield (mSv/J) at 1 meter

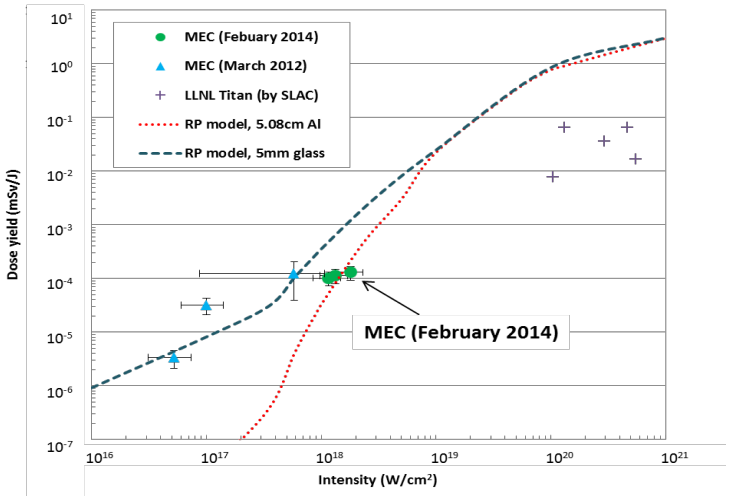

The three green circles are measurements from the February 2014 MEC experiment presented earlier and represent detector locations outside the target chamber wall (5.08 cm Al). The right point at 1.8×10^{18} W/cm^2 is the dose yield generated from the peak laser intensity before OAP mirror damage. The left point at about 1.1×10^{18} W/cm^2 is the final intensity inferred from the drop in dose rate observed in Figure 6. This laser intensity is calculated assuming the energy transmission fraction of the OAP mirror decreases proportionally with the observed decrease in dose rate. The middle point is associated with the integrated dose measurements by passive dosimeters and is a shot-weighted average of the two other laser intensities.

The two lines for the RP model represent the analytical calculation of photon dose as described earlier. The MEC target chamber is primarily Al wall with thin glass viewports. The dashed blue line estimates the photon dose yield through the thin 5 mm glass viewport of the MEC target chamber. Similarly, the dotted red line estimates the photon dose yield transmitted through a 5.08 cm thick Al chamber door. After converting the dose rates and integrated doses measured by active and passive instruments from earlier, the dose yields outside the MEC target chamber are about 10^{-4} mSv/J. This is in agreement with the RP model adjusted for attenuation of 5.08 cm of aluminium wall.

Neutron dose outside target chamber

As seen earlier in Figure 5, the results of the two neutron detectors agreed with each other, measuring a maximum neutron dose rate of 30 nSv/h. The neutron dose rate also translates to a dose yield of about 5×10^{-8} mSv/J at 1 m and a neutron-to-photon yield fraction of about 2×10^{-3} for I=1.8×10^{18} W/cm^2. Figure 8 compares the neutron results from the February 2014 MEC experiment to other experiments where neutrons were also measured [16] [20].

Figure 8. Neutron dose results from BF_3 detectors

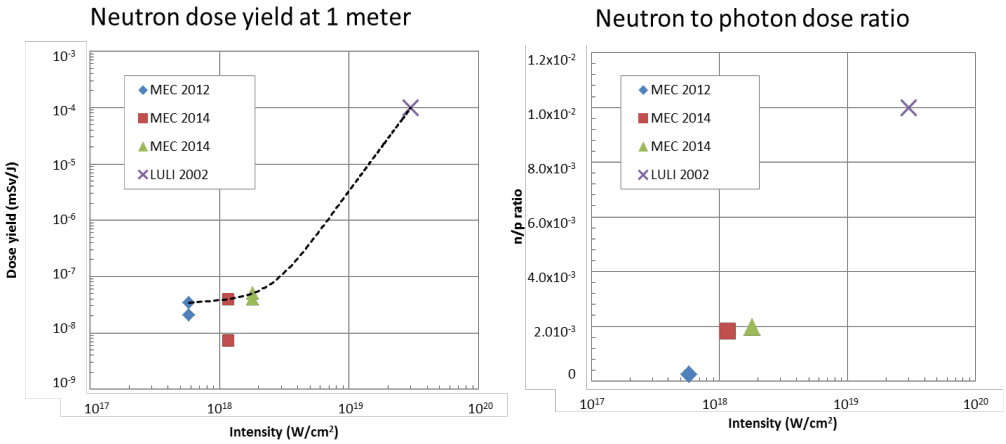

FLUKA simulations

Monte Carlo simulations with the radiation transport code FLUKA were used to calculate the bremsstrahlung photon yield outside the MEC target chamber from hot electron interactions inside the chamber and to compare with experimental measurement results. FLUKA2011 Version 2b.5 was used for all simulations [26-28]. The energy thresholds for electron and photon production and transport in FLUKA were both set at 1 keV.

Electron source term

The information on angular distribution of the electrons source term is limited. Thus, two opposite scenarios for the electron angular distribution were considered in the FLUKA simulations: mono-directional and isotropic.

For the mono-directional case, the electron source is modelled as a pencil beam and directed along the path of the laser. The electron beam (with energy sampled from a distribution characterised by Equation 4 and T_h from Equation 2) interacts with the laser target (100 µm thick copper foil). Figure 9 shows the FLUKA-calculated one-dimensional ambient dose equivalent $H^*(10)$ yield projected along the direction of the mono-directional electron beam (+x axis). The asymmetrical 1-D dose profile is a result of the simulated directional electron pencil beam interacting with the copper target at x=0 cm. The 12 cm local steel shields at x=±40 cm effectively reduce the ambient dose (mixed electron and photon field) by at least two orders of magnitude, and the Al walls of the chamber itself serve to further reduce the dose (dominated by photons) that may escape the target chamber.

For the isotropic beam case, the electrons are again sampled from an energy distribution characterised by Equation 4, but instead of being modelled as a pencil beam like the mono-directional case, the electrons are emitted isotropically as a point source from the surface of the copper target.

Figure 9. 1-D ambient dose equivalent H*(10) projection

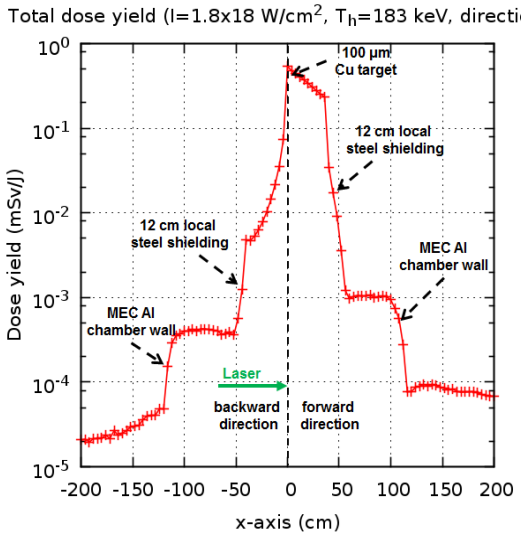

Source of dose outside target chamber

Simulations in FLUKA are used to gain additional insight on where the photon dose measured outside the MEC target chamber during the experiment originates from. Figure 10 presents results from two separate FLUKA simulations where bremsstrahlung photon production was suppressed in either the Al chamber wall or the Cu target using a high-energy (1 GeV) threshold for photon production. In Figure 10, the dose map on the left shows the total ambient dose equivalent for the target chamber when there is no bremsstrahlung photon production in the Al walls. The dose map on the right shows the ambient dose equivalent when there is no bremsstrahlung production in the Cu target. For both scenarios, the ambient dose equivalent inside the target chamber remains relatively unchanged because of dominance of electrons.

Figure 10. Suppression of bremsstrahlung photon production in FLUKA ($I=1.8\times10^{18}$ W/cm^2, T_h=183 keV, isotropic)

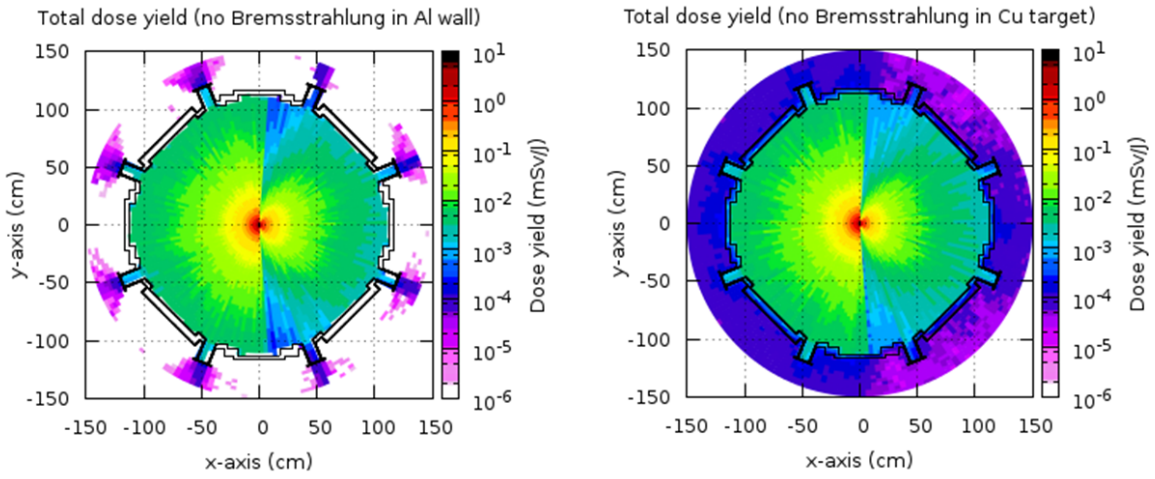

The comparison in Figure 10 appears to indicate that the dose outside the MEC target chamber is dominated by bremsstrahlung photons from electron interactions with the Al chamber wall for $I=1.8\times10^{18}$ W/cm^2. When photon production is suppressed in the Al walls, only a slight amount of dose escapes the chamber via the thin glass viewports.

Whereas when bremsstrahlung is suppressed only in the target, the dose is seen all around the outside of the target chamber and agrees well with photon yield measured by the active instruments. This is especially noticeable in the backward (-x axis) direction outside the chamber where the dose is about 10^{-4} mSv/J.

Figure 11 shows the 1-D dose yield projection for electrons and photons when simulating either a mono-directional or isotropic electron beam scenario in FLUKA with energy thresholds of 1 keV for both electrons and photons. The 1-D slice is in the backward direction, extending radially from the laser-target interaction point at R=0 cm. As before, the target is a 100 μm thick copper foil. Also, the FLUKA calculation did not implement any local steel shielding inside the target chamber because measurement locations of interest were unshielded during the actual experiment.

Figure 11. Comparison of 1-D FLUKA H*(10) projection with measured photon dose ($I=1.8x10^{18}$ W/cm^2, T_h=183 keV)

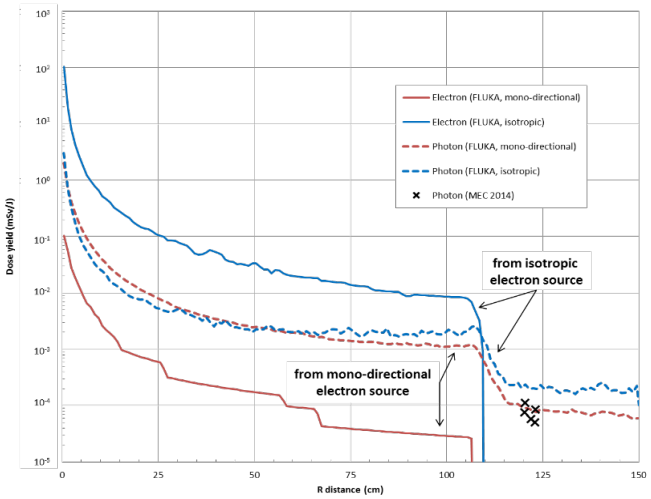

When observing a 1-D slice in the backward direction, the electron and photon dose yields differ between the isotropic or mono-directional electron beam scenarios. For an isotropic electron beam in FLUKA, the electron dose contribution dominates over the photon. However, this relation is reversed for a mono-directional source where the photon dose is greater. This behaviour is expected due to the fact that source electrons are emitted in all directions, including backwards, for the isotropic case, and only in the forward direction for the mono-directional case. Thus, the electron dose seen in Figure 11 for the mono-directional case is primarily due to back-scattered electrons from interactions with the copper target, whereas both source electrons and scattered electrons contribute to the electron dose in the backward direction for an isotropic electron beam scenario.

On the other hand, bremsstrahlung photons from electrons interacting with the copper target or aluminium chamber is the dominant mechanism that contributes to the photon dose yield for both electron beam direction scenarios, but a few interesting observations can be made from their slight differences in Figure 11. Inside the chamber at about R<50 cm, the photon yield from a mono-directional source is greater than the yield from an isotropic source because all the mono-directional source electrons in FLUKA can experience bremsstrahlung with the copper target. Near the Al chamber wall (R=100 cm), the photon yield is greater for the isotropic case due to source electrons now interacting with the Al chamber wall and producing bremsstrahlung photons. Photon build-up in the chamber wall can even be observed for the isotropic case at about R=105 cm. The photon dose outside the MEC chamber (R>110 cm) is also greater for the isotropic case.

Active and passive instruments measured photon dose yields of about 10-4 mSv/J outside the MEC target chamber. As seen in Figure 11, these experimental results agree well with the 1-D ambient dose equivalent projection calculated in FLUKA simulations.

Summary

As part of an on-going study, recent experiments at SLAC MEC focused a high-intensity laser (1.8×10^{18} W/cm^2, T_h=183 keV, 0.2 J at 1 Hz) onto 100 µm thick copper targets. Active and passive detectors measured the ionising radiation generated inside and outside the target chamber. Preliminary results show photon and neutron dose yields of around 10^{-4} and 5×10^{-8} mSv/J, respectively, outside the MEC target chamber. Inside the chamber, passive dosimeters measured very high integrated doses, primarily due to low-energy electrons, up to 650 cGy after 540 laser shots. Analysis of the complex electron source term and mixed electron/photon dose results inside the chamber are on-going, and particle-in-cell plasma code studies are planned to better characterise the energy and angular distribution of the electron source term generated from the laser plasma.

Analytical models appear to provide a good estimate of the photon dose yield outside the target chamber generated from laser-matter interactions. Measurements of photon H*(10) outside the MEC target chamber also agree with results of FLUKA simulations. Future plans are underway at SLAC to further upgrade the MEC laser to a pulse energy of 8 J, and dedicated radiation measurements at higher laser intensities up to 2×10^{20} W/cm^2 (T_h=3.5 MeV) with different targets (including gas acceleration) will be performed.

Acknowledgements

This work was supported by Department of Energy contract DE-AC02-76-SFO0515. The authors wish to acknowledge support from William White (SLAC), Philip Heimann (SLAC), and Thomas Cowan (HZDR).

References

[1] J. Hastings et al. “Physics Requirements for MEC Instrument”, LCLS RPD SP-391-001-89 R0.

[2] W. P. Leemans et al. (2006), “GeV electron beams from a centimetre-scale accelerator”, *Nat. Phys.*, 2, pp. 696-699.

[3] T. Tajima, J. M. Dawson (1979), “Laser Electron Accelerator”, *Phys. Rev. Lett.*, 43, pp. 267-270.

[4] G. Malka, J.L. Miquel (1996), “Experimental Confirmation of Ponderomotive-Force Electrons Produced by an Ultrarelativistic Laser Pulse on a Solid target”, *Phys. Rev. Lett.*, pp. 75-78.

[5] F. Brunel (1987), “Not-So-Resonant, Resonant Absorption”, *Phys. Rev. Lett.*, 59, pp. 52-55.

[6] S.C. Wilks et al. (1992), “Absorption of Ultra-Intense Laser Pulses”, *Phys. Rev. Lett.*, 69, pp. 1383-1386.

[7] S.C. Wilks, W.L. Kruer (1997), “Absorption of Ultrashort, Ultra-Intense Laser Light by Solids and Overdense Plasmas”, *IEEE J. Quantum Electron.*, 33, pp. 1954-1968.

[8] F. Amiranoff et al. (1998), “Observation of Laser Wakefield Acceleration of Electrons”, *Phys. Rev. Lett.*, 81, pp. 995-998.

[9] M.I.K. Santala et al. (2000), “Effect of the Plasma Density Scale Length on the Direction of Fast Electrons in Relativicstic Laser-Solid Interactions”, *Phys. Rev. Lett.*, 84, pp. 1459-1462.

[10] T. Guo et al. (2001), "Generation of hard x rays by ultrafast terawatt lasers", *Rev. Sc. Instr.*, 72, pp. 41-47.

[11] L.M. Chen et al. (2004), "Study of hard x-ray emission from intense femtosecond Ti:sapphire laser-solid target interactions", *Phys. Plasmas*, 11, pp. 4439-4445.

[12] R. Qiu et al. (2010), "Preliminary Radiation Hazard Analysis of X-ray Generated by High Intensity Laser Systems", SLAC RP Note RP-10-11.

[13] R. Qiu et al. (2011), "Analysis and mitigation of X-ray hazard generated from high intensity laser-target interaction", SLAC-PUB-14351.

[14] J. Bauer et al. (2011), "High intensity laser induced radiation measurements at LLNL", SLAC RP Note RP-11-11.

[15] M. Woods (2010), "Laser Beam Focusing and Propagation", SLAC LSO Memo 2010-10.

[16] J. Bauer et al. (2013), "Measurements of Ionizing Radiation Doses Induced by High Irradiance Laser on Targets in LCLS MEC Instrument", SLAC PUB-15889.

[17] D.D. Meyerhofer et al. (1993), "Resonance absorption in high-intensity contrast, picosecond laser-plasma interactions", *Phys. Fluids B*, 5, pp. 2584-2588.

[18] H. Chen et al. (2009), "Hot Electron Energy Distributions from Ultraintense Laser Solid Interactions", *Phys. Plasmas*, 16, 020705.

[19] P. Mulser, D. Bauer (2010), *High Power Laser-Matter Interaction*, Springer, Berlin Heidelberg, 416 p.

[20] F. Borne et al. (2002), "Radiation protection for an ultra-high intensity laser", *Radiat. Prot. Dosim.*, 102, pp. 61-70.

[21] K.W.D. Ledingham et al. (2000), "Photonuclear Physics when a Multiterawatt Laser Pulse Interacts with Solid Targets", *Phys. Rev. Lett.*, 84, pp. 899-902.

[22] M. D. Perry et al. (1997), "Laser Driven Radiography", Lawrence Livermore National Laboratory UCRL-ID-129314.

[23] Y. Hayashi et al. (2006), "Estimation of photon dose generated by a short pulse high power laser", *Radiat. Prot. Dosim.*, 121, pp. 99-107.

[24] M.H. Key et al. (1998), "Hot electron production and heating by hot electrons in fast ignitor research", *Phys. Plasmas*, 5, 1966-1972.

[25] Y. Ping et al. (2008), "Absorption of Short Laser Pulses on Solid Targets in the Ultrarelativistic Regime", *Phys. Rev. Lett.*, 100, 085004.

[26] G. Battistoni, S. Muraro, P.R. Sala, F. Cerutti, A. Ferrari, S. Roesler, A. Fassò, J. Ranft (2007), "The FLUKA code: Description and benchmarking", *Proceedings of the Hadronic Shower Simulation Workshop 2006*, Fermilab 6-8 September 2006, M. Albrow, R. Raja eds., AIP Conference Proceeding 896, 31-49.

[27] A. Ferrari, P.R. Sala, A. Fassò, and J. Ranft (2005), "FLUKA: a multi-particle transport code", CERN-2005-10, INFN/TC_05/11, SLAC-R-773.

[28] V. Vlachoudis (2009), "FLAIR: A Powerful But User Friendly Graphical Interface For FLUKA" *Proc. Int. Conf. on Mathematics, Computational Methods and Reactor Physics* (M&C 2009), Saratoga Springs, New York.

Fast neutron measurements at the Booster Neutrino Beamline for a future Coherent Neutrino-Nucleus Scattering (CENNS) Experiment at Fermilab

S.J. Brice, R.L. Cooper[1], F. DeJongh[1], A. Empl[3], L.M. Garrison[2], A. Hime[4], E. Hungerford[3], T. Kobilarcik[1], B. Loer[1], G. Mariani[5], M. Mocko[4], G. Muhrer[4], R. Pattie[6], Z. Pavlovic[4], E. Ramberg[1], K. Scholberg[7], R. Tayloe[2], R.T. Thornton[2], J. Yoo[1], A. Young[6]

[1]Fermi National Accelerator Laboratory, Batavia, US
[2]Indiana University, Bloomington, IN, US
[3]University of Houston, Houston, US
[4]Los Alamos National Laboratory, Los Alamos, NM, US
[5]Virginia Tech, Blacksburg, VA, US
[6]North Carolina State University, NC, US
[7]Duke University, Durham, NC, US

Abstract

Low-energy neutrinos (E<50 MeV) have a standard model predicted, but unobserved, coherent elastic neutrino-nucleus scattering (CENNS) mode. Coherent neutrino scattering has important physics reach for understanding supernovae dynamics, direct supernova neutrino detection, standard model tests, nuclear form factors, direct dark matter search backgrounds, and reactor monitoring. The CENNS collaboration proposes to deploy a 1-tonne fiducial volume, single-phase, liquid argon scintillation detector at a far off-axis location at the Fermilab Booster Neutrino Beam (BNB) in order to produce a flux of low-energy neutrinos from decay-at-rest pions. The CENNS detector must be placed relatively close to the BNB target (approximately 20 m) in order to maximise the detected neutrino flux. Because the detector is relatively close to the BNB target, a major concern is the beam-correlated fast neutron fluxes that give the same signal as a coherently scattering neutrino. In order to understand these fluxes, the Indiana-built SciBath detector was deployed to measure fast neutron fluxes 20 m from the BNB target in the BNB target building. The SciBath detector is a novel 80-liter liquid scintillator, particle tracking detector that is read out by a three-dimensional grid of 768 wavelength-shifting fibers. The fiber readout allows SciBath to measure neutral particle fluxes by tracking the recoiling charged particles with uniform efficiency in all directions. This paper will describe the SciBath detector and summarise our previous measurement of the flux of 10 to 200 MeV neutrons at the BNB. This paper will also highlight a plan to improve these neutron measurements at the BNB with the SciBath detector and other neutron detectors. We will systematically change a concrete shielding structure around the detectors to modulate the neutron background fluxes. In this way, we will validate a shielding Monte Carlo simulation of the neutron flux.

Introduction

Coherent Elastic Neutrino-Nucleus Scattering (CENNS) has never been observed despite its standard model prediction by Freedman in 1974 [1]. In order to satisfy the coherence condition for CENNS, the neutrinos must have sufficiently low energy such that very little momentum is transferred in a collision. In this way, the scattered waves off each nucleon

in the nucleus are all in-phase and add up coherently. The de Broglie relation can be used to estimate the neutrino energy required to satisfy the coherence condition. The coherence condition requires an incoming neutrino wavelength that is comparable to or larger than the size of a target nucleus. For a typical, medium-A nucleus (nuclear radius $R_N \approx$ few fm), the neutrino energy $\boldsymbol{E_\nu}$ that satisfies the coherence condition is:

$$\boldsymbol{E_\nu < hc/R_N \approx 50}\ \text{MeV} \qquad (1)$$

where h is Planck's constant and c is the speed of light. The experimental signature for a CENNS interaction is the elastic scattering of the target nucleus within the bulk of the target material. It is a simple kinematics problem to calculate the maximum energy imparted to the recoiling nucleus E_r^{max}, and it is:

$$\boldsymbol{E_r^{max} \approx 2E_\nu^2/M \approx 50}\ \text{keV} \qquad (2)$$

where M is the mass of the target nucleus. The direct detection of CENNS has been hampered largely by the development of large-scale, low-background detectors that are capable of low-threshold detection. However, recent progress in direct detection dark matter experiments has made it possible to attempt a first CENNS measurement.

In this paper, we will subsequently describe the physics motivation for measuring CENNS and the unique method we are developing in order to measure it at Fermilab. A CENNS measurement is tantamount to developing a low-energy neutrino source, a large low-energy neutrino detector, and a background rejection scheme. The most troublesome backgrounds are beam-correlated fast neutrons whose elastic scatters resemble the CENNS signal. We will describe the Fermilab Booster Neutrino Beam (BNB) as a viable, low-energy neutrino source. As previously noted, fast neutrons near the BNB are an indistinguishable background, and we will briefly describe our 2012 measurement of these fast neutrons in the BNB target building. This measurement featured an innovative fast neutron detector called SciBath, which is sensitive to up to 10-200 MeV neutrons. Finally, we will conclude with a description of additional measurements that are planned to further characterise the neutron fluxes around the BNB target building.

Physics motivation

The recent Snowmass process has identified CENNS as a fundamentally important interaction for particle physics, direct dark matter searches, astrophysics and supernovae, and as a novel technique for monitoring nuclear reactors [2]. Moreover, the recent P5 report strongly supports the "small neutrino experiment portfolio" in all budget scenarios [3]. Below, we outline some important physics motivations and refer the reader to [4] and the references therein for a more detailed examination of these physics motivations.

The neutral weak current via the Z boson mediates CENNS in the standard model. The standard model cross-section for CENNS interactions is:

$$\boldsymbol{\sigma_{\nu A} = {}^{4}/_{\pi}\, E_\nu^2 \left(Zw_p + Nw_n\right)^2 \approx {}^{G_F}/_{\pi}\, E_\nu^2 N^2} \qquad (3)$$

where wn, wp are the neutral current weak charges for the protons (Z) and the neutrons (N), and GF is the Fermi constant of weak interactions. We see that the cross-section is the coherent addition of all the nucleons, and that because wp ≈ 0, the CENNS interaction rate scales roughly as the number neutrons squared. Of course, bigger nuclei with more neutrons have a larger interaction rate, but its average recoil energy necessarily drops. For medium-A nuclei, the cross-section is approximately 10-39 cm^2, which dominates all other interactions at low energies for a given nucleus.

CENNS is also independent of the neutrino flavour. This is relevant for neutrino disappearance measurements to study short baseline neutrino oscillations and constrain possible sterile flavours of neutrinos. Because neutrinos have mass, they can possess a

magnetic moment. An anomalously large magnetic moment (order 10-10 Bohr magnetons) would be measureable in future CENNS experiments by precisely measuring the nuclear recoil spectrum. CENNS is also sensitive to possible non-standard interactions, which could show up as different interaction strength with a particular neutrino flavour when all flavours should be equal. Low-energy neutrino interactions give supernova their positive pressure, and CENNS is a vital contribution. A programme to measure the CENNS interactions on a variety of nuclear targets can help to understand supernova dynamics. A CENNS detector, like dark matter detectors, can also be used as a sensitive supernova observatory. In fact, the sensitivity to CENNS interactions means that CENNS from solar and atmospheric neutrinos is an irreducible background for 10-tonne-scale dark matter detectors. CENNS can also be used probe nuclear form factors because the finite distribution of nucleons alters the coherence condition slightly. Finally, nuclear reactors are a copious source of low-energy neutrinos. A CENNS detector with very low thresholds could be used to monitor reactors at a distance for non-proliferation applications.

Low-energy neutrino source at the booster neutrino beamline at Fermilab

Fermilab currently operates a pair of GeV-scale neutrino beamlines for a suite of neutrino experiments. These GeV-energy beams are too high energy on-axis to satisfy the CENNS coherence condition. Beam Monte Carlo simulations for the less energetic Booster Neutrino Beamline (BNB) have shown that moving far off-axis (> 45°) leads to a nearly isotropic flux of < 50 MeV neutrinos from stopped pions [4].

The BNB delivers a 32 kW, 8 GeV proton beam to a beryllium target. This, in turn, produces positive pions that decay with a 26 ns lifetime to a positive muon and a muon neutrino. The muon neutrinos are prompt with respect to the 1.6 μs beam and are monoenergetic at 29.9 MeV. The resulting muons then decay with a 2.2 μs lifetime into a positron, muon antineutrino, and an electron neutrino. These neutrinos have a continuous, three-body energy spectrum from 0 MeV to half the muon mass (approximately 50 MeV). Because the beam is 8 GeV, a small fraction of neutrinos are from heavier kaon decays or from muon capture in the surrounding materials. Simulations have shown that the level of contamination from these high-energy neutrinos is tolerable in a CENNS measurement.

To satisfy Fermilab radiation safety regulations, the BNB beam target is surrounded by many tonnes of steel and concrete. The target itself is located about 7 m underground and there is 40 tonnes of steel above and below the target. Around the target are 1600 tonnes of iron blocks and 300 tonnes of concrete shielding above this iron structure. Approximately 30 forward-peaked neutrons are produced per proton on target (approximately 10^{21} POT per year), and simple neutron dosimetric attenuation factors predict that about 3.6×10^{8} neutrons per m^2 per 10^{21} POT emerge 20 m from the target. These estimates predict that 90% of these neutrons have energies below 50 MeV with a tail extending up to 8 GeV. Linearly scaling this attenuation suggests that an additional 8 m of concrete is sufficient neutron shielding for a future CENNS experiment. It is well known that neutron shielding simulation is notoriously difficult, and a programme was started to measure the neutron flux, energy spectrum and direction spectrum in the BNB target building.

Previous neutron measurements

In spring 2012, a pair of neutron detectors were deployed in the BNB target building to measure the fast neutron fluxes correlated with the beam [4]. A portable EJ-301 [5] liquid scintillator detector was first used to survey the fission-energy neutron fluxes in multiple areas around the building. This detector facilitated finding the best location of the larger, 70-kg neutron detector called SciBath [6-7]. Figure 1(a) shows the running location of

these detectors in the BNB target building. SciBath was located at position A and the EJ-301 was run for a significant amount of time after its survey at position B.

Figure 1. (a) BNB target building: SciBath operated in position A and the EJ-301 collected data at position B, (b) a schematic diagram of the SciBath detector

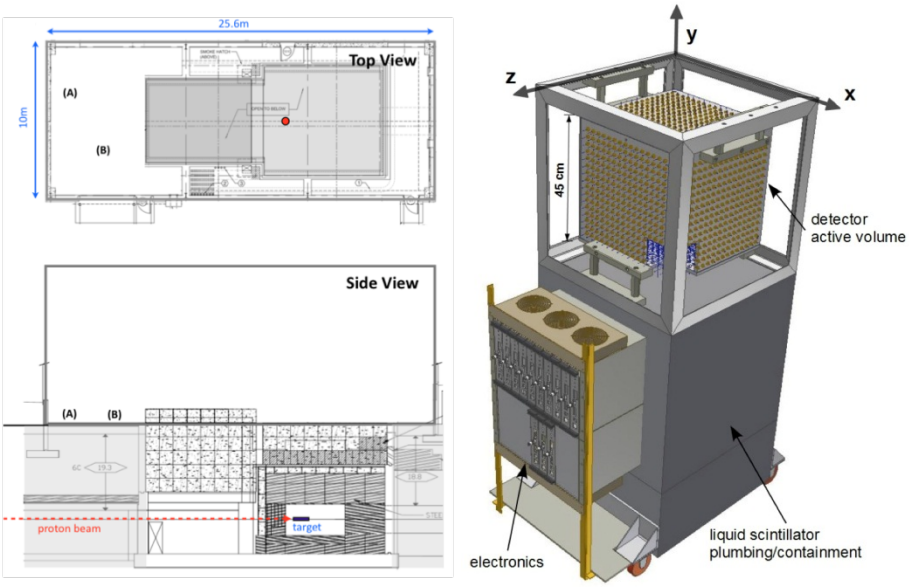

EJ-301 liquid scintillator detector

In order to obtain a rough estimate of the neutron fluxes at various locations in the BNB target building, a small, encapsulated, 1-kg neutron detector was deployed. This detector assembly uses 1-kg of Eljen EJ-301 liquid scintillator and is read out by a single, 5-inch PMT. PMT pulses collected around the BNB beam window were digitised and analysed off-line. The electron-recoil energy scale was calibrated with a variety of gamma ray sources. Manufacturer tabulations of the proton-recoil quenching factors for EJ-301 were used to understand the low-energy neutron scatters on hydrogen. For 1 MeV proton recoils, the quenching factor is ~0.16 compared to a 1 MeV electron recoil from a gamma ray.

EJ-301 can discriminate proton recoils from electron recoils using the pulse shape discrimination (PSD). We used the F90 PSD parameter to discriminate proton and electron recoils. The F90 PSD parameter is the fraction of the photons collected in the first 90 ns of a pulse to the total number of photons collected out to 1 μs. Using a ^{252}Cf source, we found that proton recoils have an F90 that is approximately 0.76-0.91, while electron recoils from gamma ray sources have “faster” pulses with an F90 that is above 0.91. Because of low light levels and digitizer saturation, the effective proton recoil energy range we used was 0.3-1.6 MeV.

The 1-kg detector was moved to various locations in the building in order to scope out an ideal location for the larger SciBath detector (see below). Once a site was located for SciBath, the EJ-301 detector was placed 19 m behind the beam target. Without a precise Monte Carlo simulation of the detector response to neutrons, we roughly estimate that the neutron flux above 0.3 MeV is about 2 neutrons per beam pulse. During our measurements, each BNB beam pulse delivers about 4.5×10^{12} protons on the beryllium target.

SciBath detector

The Indiana University-built SciBath detector is a particle-tracking detector using 70 kg of mineral oil-based liquid scintillator (15% by volume pseudocumene and 1.5 g/L PPO). The liquid scintillator is contained in a roughly cubic volume (0.5 m × 0.5 m × 0.5 m) that is read out by 768 wavelength-shifting (WLS) fibers. Each of the three cubic axes is readout by a 16×16 square array of fibers with 2.54 cm spacing. The scintillator does not contain a secondary wavelength shifter (e.g. *bis*-MSB or POPOP) because the SciBath principle requires a wavelength shift to occur inside the WLS fiber. In this way, a fraction of the re-emitted, wavelength-shifted light is optically trapped in the fiber and transported to a PMT. Twelve 64-anode PMTs were used to read out each individual WLS fiber. A schematic drawing of SciBath is shown in Figure 1(b).

The SciBath detector electronics and single photoelectrons were calibrated with an LED pulser system. A stable, low-light LED was pulsed at the opposite end of the WLS fiber from the PMT readout during monthly calibration runs. The energy-to-light yield conversion factor was calibrated with minimum-ionising cosmic ray muons. These muons deposited approximately 65 MeV of energy and yielded about 400 total photoelectrons; the energy-to-light yield conversion factor is about 6 p.e./MeV. Cosmic ray muons were also an excellent calibration of the SciBath tracking capabilities, and we were able to reproduce the angular muon flux at the surface. More importantly, we developed topology algorithms that can separate track-like muons from point-like proton recoils with similar light yields. These were essential for reporting the high-energy neutron direction spectrum.

Figure 2(a) shows the background subtracted light output in 3 μs window around the beam. The discontinuity above 1000 p.e. is due to rebinning for added statistical power. It is clear that the beam duty factor significantly reduces the beam-uncorrelated background rates to negligible levels. Figure 2(b) shows the timing around the beam window for various light output groups. The group with the highest light output (blue) is consistent with fast neutrons in time with the beam interacting with the detector. The middle light output group (red) shows a similar beam turn-on, but there is a noticeable few-μs tail that is consistent with slower neutrons taking longer transit times and longer path lengths from scattering in the target building shielding. Finally, the lowest light output group (black) has a similar turn on and few-μs tail, but its post-beam rate is significantly higher than its pre-beam rate. Extending the time scale shows a characteristic lifetime of ~200 μs, which is consistent with neutrons thermalising in SciBath and our tagging on the 2.2 MeV gamma ray from the $n(p, d)\gamma$ neutron-capture reaction. Unfortunately, total event rates at the surface are too high to use this capture-gating technique to uniquely tag neutrons.

Figure 2. (a) The background-subtracted photoelectron spectrum collected in the beam time window, (b) the timing spectrum around the beam time spectrum for various groups of total photoelectrons

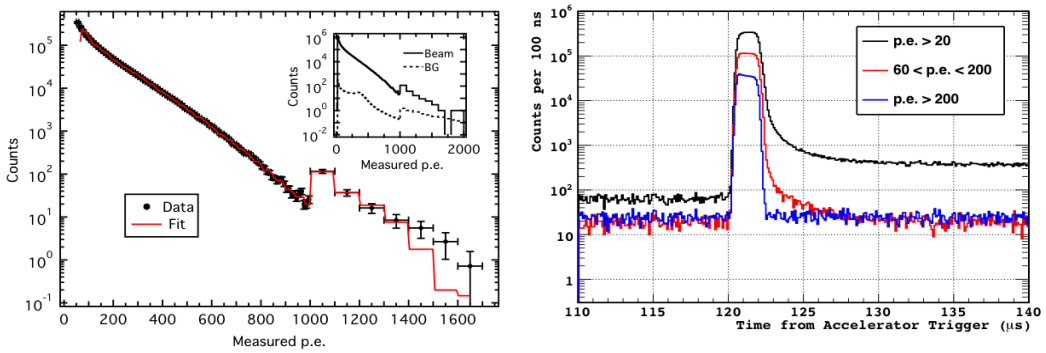

Results

Using a Monte Carlo simulation, the incident neutron flux was unfolded from the light output spectra in Figure 3(a). Because SciBath has no ability to discriminate gamma rays from neutrons below 5 MeV, a conservative threshold was placed on the light output to remove most gamma rays. This cut leads to a 10 MeV neutron threshold. At higher energies, the low statistics and finite size of SciBath effectively limit its neutron sensitivity to approximately 200 MeV. Above 10 MeV, 6.3±0.7 neutrons were measured per m^2 per BNB pulse (4.5×10^{12} POT per pulse). Figure 3(b) reports the reconstructed direction spectrum for the highest energy proton recoils. Additional track-like cuts are applied with our topology algorithms. The peak of the direction spectrum is in line with the beam direction but points upstream of the BNB beam target.

Figure 3. (a) The unfolded neutron energy spectrum, (b) the direction spectrum of high-energy recoiling protons

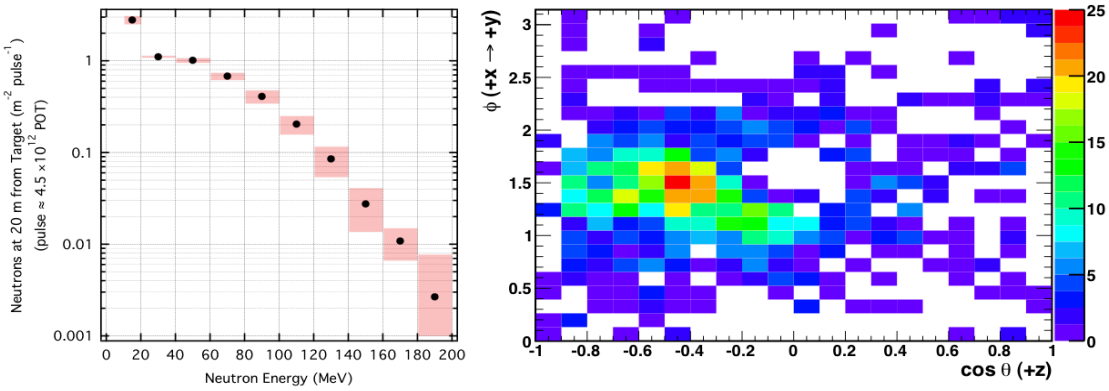

They tend to back-project upstream of the BNB target.

Proposed CENNS experiment at the BNB

Liquid argon (LAr) has several advantages as a detector medium. It has a high light yield, is transparent to its own scintillation light, can be purified, and is relatively inexpensive. This scintillation light has a wavelength of 128 nm, and it comes from the de-excitation of dimers in the form of trapped exciton states. These states can form in a singlet or triplet state and they have very different lifetimes in LAr, 6 ns and 1600 ns, respectively. LAr is also advantageous because the relative amount of the singlet and triplet states produced in an ionising radiation event will depend upon the recoiling particle. Electron recoils from gamma rays will have relatively more triplet state than nuclear recoils from CENNS neutrinos and neutron backgrounds. Therefore, electron recoils will tend to have slower pulses than nuclear recoils. Pulse-shape discrimination (PSD) is then able to separate electron recoils from the desired nuclear recoil signal from CENNS.

For a first CENNS measurement, we are proposing to use a 1-tonne fiducial volume, single-phase, LAr scintillation detector. The single-phase scintillation approach has the advantage of simplicity. The only signal-collecting element is an array of PMTs surrounding the LAr tank. Therefore, signal collection time is only limited by the time-scale of the triplet state. This is in marked contrast to dual-phase systems or time-projection chambers, which collect the ionised electrons over many milliseconds. Fast timing in the single phase allows us to take advantage of the 5×10^{-5} beam duty factor to reject cosmogenic backgrounds, radon progeny, and ^{39}Ar beta decays. ^{39}Ar is naturally occurring and leads to a natural radioactivity of about 1 Bq/kg of LAr. Because of LAr PSD rejection and the beam duty factor, this natural radioactivity should not be problematic.

The MiniCLEAN experiment has shown that a high level of PSD rejection is possible in large volumes of LAr [8].

For a 1-tonne detector with a 50% detection efficiency (mostly from PSD efficiency) and a low-energy threshold of 25 keV_{nr} (the quenching factor for nuclear recoils at these energies is approximately 25%), we expect about 300 CENNS events to be detected per year at the BNB (nominally 10^{21} POT). Our estimates indicate that the backgrounds should be controllable to a few per cent, and with adequate shielding, the beam-induced neutrons can be adequately attenuated. Our calculations from the previous neutron measurements show that about 7 m of concrete is sufficient to discover CENNS with negligible neutron contamination.

A first measurement of CENNS therefore requires a new LAr detector and a new neutron shielding system. Currently, the MiniCLEAN detector is operating underground searching for dark matter, but it may become available in a few years after its initial dark matter search concludes. This detector satisfies most of our operating requirements, though is only 500 kg. We are exploring options to bring it to Fermilab once a neutron shielding structure is designed. The neutron shielding design will require more input measurements of the neutron flux.

Future neutron measurements

In summer 2014, an effort started to improve neutron measurements at the BNB. The goal of these measurements is to deliver a comprehensive set of neutron measurements at viable locations for a future CENNS experiment (see Figure 4(a)). Because our previous measurements in 2012 were performed with no additional neutron shielding, our proposed measurements seek to modulate the measured neutron spectrum by systematically reconfiguring the surrounding concrete shielding structures. Therefore, we can precisely test our neutron shielding Monte Carlo simulations through a few metres of concrete. With these tests, we will deliver the neutron energy spectrum and flux, direction spectrum, and modulated shielding parameters.

Improved EJ-301 detector array

Three additional EJ-301 neutron detectors were procured from Eljen and have been combined into a single 5-kg detector array. The four-detector configuration is shown in Figure 4(b). These detectors and their data acquisition system are extremely portable, and we will measure the neutron fluxes at a variety of locations around the BNB target building. Until September 2014, the BNB is in an off-target configuration to support a low-mass dark matter search with the MiniBooNE detector [9-10]. This presents a unique opportunity to compare, contrast, and understand the specific processes that govern neutron transport through the BNB radiation shielding with the beam on- and off-target.

The neutron energy sensitivity of an EJ-301 neutron detector was found to be 0.3-1.6 MeV in the previous measurement. A series of precise calibrations were performed in spring 2014 at Indiana University to understand the full energy sensitivity range. We are extending the neutron reconstruction energy range through the full fission-energy-range (approximately 0.5-10 MeV). If the energy range of SciBath does not change, then in tandem, these detectors will be sensitive to 0.5-200 MeV neutrons. These represent the most dangerous neutron energies for a first CENNS experiment in LAr.

Figure 4. (a) Proposed site for a future CENNS experiment, (b) the 5-kg array of EJ-301 neutron detectors

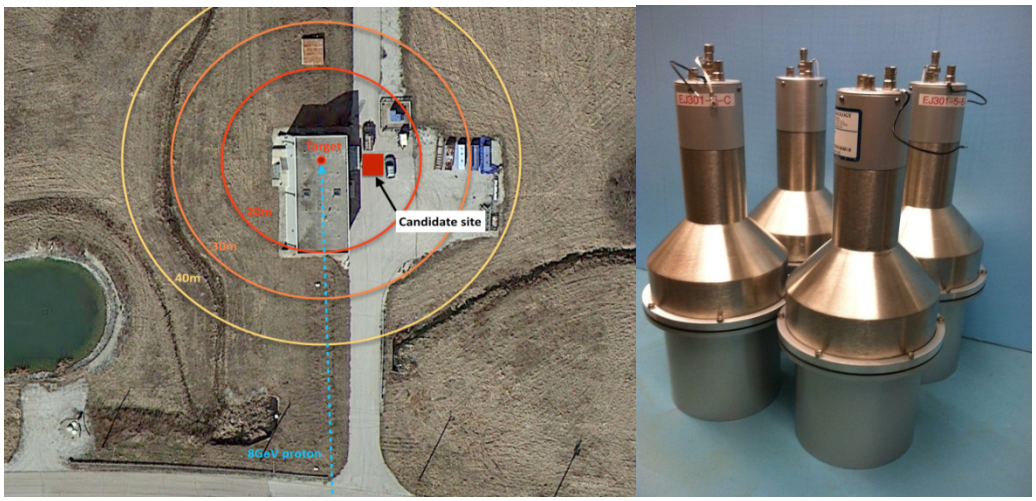

Improved SciBath detector

In the previous measurement, the limiting systematic error was our understanding of the detector gain and calibrations. Before delivering SciBath to the BNB in August 2014, we will improve our knowledge of this systematic. The light output of our current mineral oil-based scintillator will be measured with a series of off-line sample tests. We will also perform similar light yield tests by replacing our current scintillator with EJ-309 or linear alkylbenzene (LAB). Oxygenation is known to significantly reduce organic scintillator light yield. Therefore, nitrogen bubbling to remove any dissolved oxygen is an important systematic to control during these tests. Concurrently, a rigorous calibration programme to more precisely extract the energy-to-light yield conversion factor will be performed.

A custom, transport trailer is being designed to facilitate moving SciBath to other interesting locations. We will produce a map of the high-energy neutron flux and direction at multiple points around the BNB target building and will use a combination of pre-existing concrete blocks on the Fermilab campus to rapidly assemble a shielding structure to surround the SciBath trailer. We will also use large, commercially available tanks of water to modulate the incoming neutrons. With these shielding structures, we hope to validate the potentially complex neutron shielding simulations with neutron measurements.

CENNS-10 detector

The CENNS-10 detector is a 10-kg fiducial volume, single-phase LAr scintillation detector. The main goal of the CENNS-10 detector is to understand the detector response and necessary experimental configurations at the practical site of the experiment: detector energy thresholds, beam-induced background response, timing characteristics of the in-beam and out-of-beam events, shielding performance, etc. CENNS-10 consists of a 9-inch diameter inner chamber and a 12-inch diameter outer vacuum jacket. A cooling head equipped with a cryocooler and a heat exchanger module consistently circulate the argon through a hot-getter for argon purification. Two 8-inch PMTs (HAMAMATSU R5912-02MOD) view the active LAr detector volume for the scintillation light readout. The PMT siganal waveform will be used to discriminate between electron- and nuclear-recoil events. The cryogenic components of the detector are currently being commissioned. The full commissioning of the entire detector system and a calibration programme started in summer 2014. The detector operation at the BNB site is expected to begin in spring 2015.

Summary

CENNS is extremely important for particle and nuclear physics and astrophysics. We are developing the Fermilab BNB at Fermilab as a low-energy neutrino facility for a first measurement of CENNS. We plan to operate a 1-tonne-scale, single-phase, LAr scintillation detector (possibly the MiniCLEAN detector) at a far-off-axis location. We performed fast neutron measurement in 2012 to survey the beam-induced neutron flux near the BNB target. Our calculations based upon these results suggest that a few metres of concrete are sufficient to attenuate these neutrons to acceptable levels for a first CENNS measurement. A second set of neutron measurements was scheduled for summer 2014 to more precisely assess the neutron energy spectrum, flux, and direction and to validate shielding design Monte Carlo simulations for the future experiment.

The CENNS experiment at the BNB represents a new class of accelerator-driven rare search physics experiments. A typical feature of all these experiments is the reduction of beam-induced backgrounds, namely neutrons. We have developed techniques to precisely measure high-energy neutron fluxes, energy spectra, and direction spectra. These techniques are valuable to the radiation shielding community. Our proposed technique to systematically configure shielding to modulate the detected neutron spectrum is unique.

References

[1] D. Z. Freedman (1974), *Phys. Rev. D*9, 1389.

[2] A. de Gouvea, K. Pitts, K. Scholberg, and G.P. Zeller (conveners), et al. (2013), "Neutrinos", Intensity Frontier Neutrino Working Group response to the Snowmass charge; arXiv:13010.4340v1.

[3] http://science.energy.gov/~/media/hep/hepap/pdf/May%202014/FINAL_DRAFT2_P5Report_ P5 Report (2004).

[4] S. Brice et al. (2014), CENNS Collaboration, *Phys. Rev. D*89, 072004; arXiv:1311.5958.

[5] Eljen Technology, Sweetwater, TX 79556, www.eljentechnology.com.

[6] R. Tayloe et al. (2006), *Nucl. Instrum. Meth. A*562, 198.

[7] R. Cooper et al. "SciBath: A Novel Tracking Particle Detector for Measuring Neutral Particles Underground", *Proceedings of the DPF-2011 Conference*, Providence, RI; arXiv:1110.4432.

[8] A. Hime (2011), "The MiniCLEAN Dark Matter Experiment", Proceedings of the DPF-2011 Conference, Providence, RI; arXiv:1110.1005.

[9] A.A. Aguilar-Arevalo, et al. (2012), "Low Mass WIMP Searches with a Neutrino Experiment: A Proposal for Further MiniBooNE Running"; submitted to the Fermilab PAC; arXiv:1211.2258.

[10] R. Dharmapalan, et al. (2013), "A Proposal to Search for Dark Matter with MiniBooNE", www.fnal.gov/directorate/program_planning/Jan2014PACPublic/MB_Request_2013_v2.pdf.

Session II: Induced Radioactivity

Chairs: Hiroshi Nakashima and Sayed Rokni

Induced radioactivity in accelerator materials and soil-shield samples

Francesco Paolo La Torre, Marco Silari
CERN European Organisation for Nuclear Research, Switzerland

Abstract

Several samples of materials used for accelerator components and shielding structures were irradiated in the high-energy stray radiation field of the H4IRRAD Facility, installed in one of the secondary beam lines (H4) from the SPS at CERN. After irradiation, the induced radioactivity of the samples was measured by gamma spectrometry at various cooling times up to 2 years, allowing identification of isotopes with a wide range of half-lives. The activation of soil-shield samples was also studied in detail. In particular, the mechanism and probability that the radioactivity produced in soil and ground water may transfer from the site of activation to the environment was investigated. Two techniques were used to quantify the amount of radioactivity leaching in the groundwater. Furthermore, the isotope production and their specific activities measured in the soil were simulated with the FLUKA Monte Carlo code.

Introduction

The operation of high-energy accelerators leads to nuclear activation of the surrounding material due to particle interactions in accelerator components, beam transfer line elements and shielding structures. A detailed estimation of the induced radioactivity is required in order to keep the impact on personnel and environment as low as reasonably achievable. A total of 30 material samples were collected from machine and shielding components manly used in the Large Hadron Collider (LHC) as well as in other CERN accelerator environments [1,2]. The samples were irradiated in a high-energy stray radiation field in a series of experiments recently performed at the H4IRRAD Facility at CERN.

The preliminary results on measured specific activities for seven samples are presented in this work. Conversion coefficients from unit lost beam power to induced specific activity at saturation for five metallic samples are shown. The activation of soil-shield samples was also studied in detail [3]. In particular, the mechanism and probability that the radioactivity produced in soil and ground water may transfer from the site of activation to the environment was investigated. Two techniques were used to quantify the amount of radioactivity leaching in the groundwater.

Material sample description

The AISI 304L steel is a general-purpose grade widely used for vacuum applications. At CERN it is mainly used in flanges and interconnections of the LHC vacuum vessel [4,5]. The AISI 316L steel is a molybdenum-containing grade. Due to its corrosion resistance, ductility and increased austenitic stability, this grade is used for specific application in the LHC interconnections. AISI 316LN is a nitrogen containing stainless steel. Both 316L and 316LN grades are widely used in the LHC main dipole cold masses (shell, insert, cover, plate, cold bore tubes, etc.) [4,5]. MUMETAL is a nickel-steel alloy with high magnetic

properties, high magnetic permeability for low magnetic fields and small hysteresis effect. Vacuum chambers in the LHC injection and extraction septa were manufactured with MUMETAL [6]. The last sample is a Ni-Fe alloy called INVAR and used for the LHC helium transfer lines [7]. Table 1 shows the chemical composition of the metallic samples.

The soil samples were collected on the Prévessin site of CERN at a depth of 24 m. CERN is located in the Geneva basin, which is filled by sedimentary deposits called "molasse". The chemical analysis of the molasse rock was carried out by the EMPA laboratory in Dübendorf (Switzerland) via X-ray fluorescence spectrometry (WD-XRF). The results of the chemical analysis are shown in Table 2. The natural water content of the soil (moisture) was measured in CERN Environmental laboratory by drying a known amount of earth. The soil moisture content may be expressed by weight as the ratio of the mass of water present to the dry weight of the soil sample. To determine this ratio, the samples and container were weighed in the laboratory both before and after drying, the difference being the mass of water originally in the sample. The water content measured in the soil specimen was 5% by weight.

Table 1. Chemical composition in mass fraction (g/100 g) of metallic samples irradiated at H4IRRAD [2]

Element	Steel 304L	Steel 316L	Steel 316LN	INVAR	MuMetal
Density	8	7.99	8	8	8.75
C	0.03	0.03	0.03	/	0.011
Co	< 0.2	< 0.2	< 0.2	/	0.01
Cr	17 - 20	16 – 18.5	16 – 18.5	/	0.03
Cu	/	/	/	/	5.04
Fe	balance	balance	balance	64	13.8
Mg	/	/	/	/	0.015
Mn	2	2	2	/	0.57
Mo	/	2 – 2.5	2 - 3	/	4.02
N	/	0.05	0.14 – 0.2	/	/
Ni	10 – 12.5	11 - 14	12 - 14	36	76.4
P	< 0.045	< 0.03	< 0.045	/	0.002
S	< 0.03	< 0.01	< 0.015	/	/
Si	1	1	1	/	0.05

Table 2. Chemical composition of dried soil (density: ~1.4 g/cm^3)

Element	O	Si	Ca	Al	C	Fe	Mg	K	Na	Ti
(g/100 g)	38.8*	24	16	6.8	5*	4	2	1.9	0.7	0.42
Element	Mn	Ba	P	Sr	Zn	Cr	Zr	Eu	Ni	S
(g/100 g)	0.11	0.06	0.06	0.05	0.03	0.02	0.02	0.01	0.01	0.01

*Extrapolated value, not quantifiable by XRF analysis.

Irradiation facility and sample activation

The activation experiment was carried out at the H4IRRAD Facility which is installed in one of the secondary beam lines (H4) from the SPS in the CERN North Area [8]. The samples were installed under the copper target (8 cm in diameter and 100 cm in length) struck by the SPS primary proton beam with momentum of 400 GeV/c and average intensity of about 3×10^9 protons per pulse (over a supercycle of about 45 seconds and an extraction length of ~5 seconds). An argon ionisation chamber (XION) placed in the H4 beam line just upstream of the copper target monitored the intensity of the primary beam. Figure 3 shows the beam intensity profile and the accumulated number of protons

as a function of the irradiation time as recorded during the experiment: for the long-lived radionuclides of interest in the present study, the irradiation can be considered constant over the entire period (about 18 days).

Figure 1. Irradiation profile of the samples

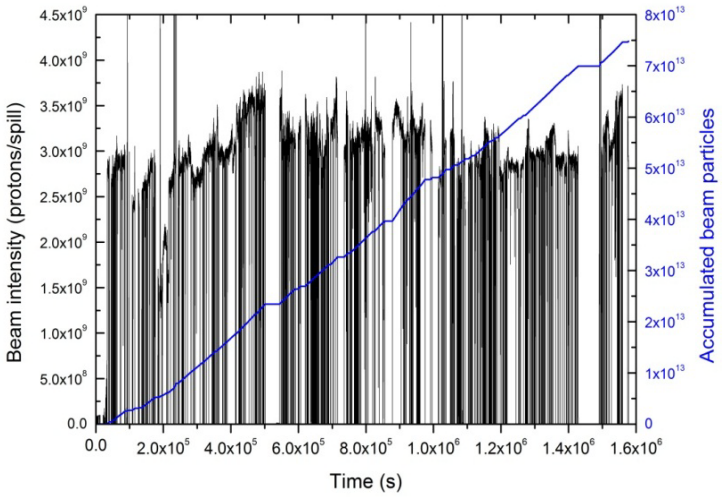

The number of protons in each spill (left scale) is shown together with the accumulated total number of protons (right scale).

Gamma spectrometry results

Immediately after irradiation with ~7.5×10^{13}accumulated protons, the dose rate of the samples was of the order of a few mSv/h. Most of this radioactivity was due to very short half-life radioisotopes. Since the radioisotopes of interest to this study have medium or long half-life, the samples were allowed to decay for at least 10 days before counting. The activated samples were measured with a high sensitivity, low-background, high-purity germanium (HPGe) detector by Canberra. The data acquisition and analysis was carried out using Canberra's Genie-2000 spectrometry software and the PROcount-2000 counting procedure software. This is a comprehensive software package for data acquisition, display and analysis, which includes a set of advanced spectrum analysis algorithms providing a complete analysis of gamma ray spectra. Several gamma spectrometry analyses were performed for each sample at various cooling times up to 2 years.

The soil samples could not be directly counted for ^{3}H due to the low beta-particle endpoint energy (18 keV), which is absorbed in the sample. For this reason, the tritium activity in the soil was estimated via Monte Carlo calculations with the FLUKA code [9,10]. The tritium activity in the water was determined using a liquid scintillation counter (Packard TRI-CARB 3180TR/SL), measuring a mixture of 8 ml of activated water and 12 ml of so-called liquid scintillation cocktail (Packard Ultima Gold LLF). In the case of high precision measurements, distillation is usually recommended requiring well controlled conditions where other radionuclides present in the sample (e.g. ^{22}Na) may significantly increase the result for tritium. This was not needed in the present case, as the potential interference of other radionuclides in the tritium pulse-height window was negligible.

The results of the gamma spectrometry for all samples and of the tritium measurement for the irradiated water after 10 days of cooling time are shown in Table 3. Quoted errors include statistical and systematic uncertainties of the gamma spectrometry analysis and liquid scintillation analysis.

Table 3. Specific activity of material samples irradiated at H4IRRAD, after 10 days of cooling time

Nuclide	$t_{1/2}$	Specific Activity (Bq/g)						
		304L	316L	316LN	INVAR	MUMETAL	Soil	Water
^{3}H	12.32 y	/	/	/	/	/	14.1 ± 0.3*	28.9 ± 2.6
^{7}Be	53.1 d	30.4 ± 10.7	/	17.7 ± 5.8	87.8 ± 27	102 ± 25	425 ± 32	523 ± 48
^{22}Na	2.6 y	0.49 ± 0.08	0.34 ± 0.07	0.21 ± 0.04	0.47 ± 0.11	0.76 ± 0.15	12.5 ± 0.8	/
^{46}Sc	83.8 d	101 ± 9	77. ± 7.7	48.2 ± 3.7	75.7 ± 7.6	47.1 ± 4.2	3.02 ± 0.19	/
^{48}V	16 d	554 ± 97	497 ± 99	501 ± 100	524 ± 152	516 ± 139	9.33 ± 0.50	/
^{51}Cr	27.7 d	2048 ± 307	1619 ± 259	1004 ± 161	1744 ± 366	1176 ± 282	25.0 ± 2.3	/
^{52}Mn	5.59 d	273 ± 87	294 ± 91	534 ± 144	653 ± 287	396 ± 174	6.01 ± 0.43	/
^{54}Mn	312 d	287 ± 29	239 ± 24	138 ± 14	336 ± 34	151 ± 15	6.02 ± 0.42	/
^{56}Co	77.3 d	74.4 ± 6.0	74.1 ± 6	58.7 ± 4.1	323 ± 23	620 ± 43	0.40 ± 0.04	/
^{57}Co	272 d	76.4 ± 9.2	81.5 ± 9.8	64.0 ± 7.7	464 ± 56	746 ± 82	/	/
^{58}Co	70.9 d	270 ± 27	318 ± 32	256 ± 26	1451 ± 145	2639 ± 237	0.22 ± 0.05	/
^{59}Fe	44.5 d	/	2.93 ± 1.1	1.90 ± 0.66	9.67 ± 2.9	15.1 ± 3.8	/	/
^{60}Co	5.27 y	1.48 ± 0.15	1.40 ± 0.14	0.71 ± 0.07	3.88 ± 0.39	6.97 ± 0.63	/	/
^{75}Se	120 d	/	/	0.41 ± 0.18	/	1.94 ± 0.73	/	/
^{83}Ru	86.2 d	/	/	2.10 ± 0.59	/	6.60 ± 1.98	/	/
^{88}Y	107 d	1.03 ± 0.19	7.20 ± 0.72	6.30 ± 0.63	/	22.8 ± 2.0	/	/
^{88}Zr	83.4 d	0.64 ± 0.34	4.93 ± 0.79	4.03 ± 0.60	/	15.3 ± 2.29	/	/
^{95}Nb	115 d	/	13.0 ± 2.4	10.5 ± 2.4	/	41.2 ± 9.1	/	/
^{133}Sn	115 d	0.62 ± 0.33	/	/	/	14.5 ± 2.3	/	/

*From FLUKA simulations.

Conversion coefficients for metallic samples

The conversion coefficients obtained in this work should be regarded as an upper limit of the induced radioactivity that can be expected in materials irradiated by the secondary radiation generated by high-energy protons (beam losses) stopped in target-like objects (e.g. collimators). Since the samples were exposed very close (~ 1 cm) to the target, which is thick enough to develop most of the hadronic cascade, these coefficients should be considered conservative. In cases where the material exposed to the secondaries is at a larger distance and/or the component where the beam loss occurs is not so thick, the specific activity induced in the material will be lower.

The induced radioactivity in the materials nearby the beam loss evolves with time according to the well-known expression:

$$A(t) = A_S[1 - exp(-t_{irr}/\tau)]exp(-t_{cool}/\tau) \quad (1)$$

where $A(t)$ is the activity at time $t = t_{irr} + t_{cool}$, A_S is the saturation activity, τ is the mean life of the radionuclide of interest, t_{irr} and t_{cool} are the irradiation time and the cooling time.

Let us assume a continuous loss of 1 W of beam power, on average, on a collimator. The value of 1 W is a fairly representative figure and the results can easily be scaled to a different power loss. Using Equation (1) one can calculate the specific activity at saturation A_S for the radionuclides of Table 3. Normalising A_S to 1 W of beam loss, we obtain the conversion coefficients from unit lost beam power to induced specific activity at saturation for the radionuclides produced in each material (Table 4).

Table 4. Conversion coefficients from unit lost beam power to induced specific activity at saturation

Nuclide	$t_{1/2}$	Conversion coefficient $A_S(Bq/g/W)$				
		304L	316L	316LN	INVAR	MUMETAL
^{7}Be	53.1 d	5.43E+04	/	3.16E+04	1.56E+05	1.81E+05
^{22}Na	2.6 y	1.23E+04	8.47E+03	5.20E+03	1.17E+04	1.90E+04
^{46}Sc	83.8 d	2.59E+05	1.98E+05	1.23E+05	1.94E+05	1.21E+05
^{48}V	16 d	5.30E+05	4.75E+05	4.80E+05	5.01E+05	4.94E+05
^{51}Cr	27.7 d	2.40E+06	1.90E+06	1.18E+06	2.04E+06	1.38E+06
^{52}Mn	5.59 d	3.71E+05	3.98E+05	7.25E+05	8.86E+05	5.38E+05
^{54}Mn	312 d	2.43E+06	2.03E+06	1.17E+06	2.84E+06	1.27E+06
^{56}Co	77.3 d	1.78E+05	1.78E+05	1.41E+05	7.73E+05	1.48E+06
^{57}Co	272 d	5.67E+05	6.05E+05	4.75E+05	3.44E+06	5.53E+06
^{58}Co	70.9 d	6.03E+05	7.10E+05	5.71E+05	3.24E+06	5.89E+06
^{59}Fe	44.5 d	/	4.60E+03	2.98E+03	1.52E+04	2.38E+04
^{60}Co	5.27 y	7.41E+04	7.00E+04	3.57E+04	1.95E+05	3.50E+05
^{75}Se	120 d	/	/	1.43E+03	/	6.78E+03
^{83}Ru	86.2 d	/	/	5.49E+03	/	1.73E+04
^{88}Y	107 d	3.25E+03	2.27E+04	1.99E+04	/	7.19E+04
^{88}Zr	83.4 d	1.64E+03	1.26E+04	1.03E+04	/	3.89E+04
^{95}Nb	115 d	/	1.74E+04	1.41E+04	/	5.53E+04
^{133}Sn	115 d	2.07E+03	/	/	/	4.87E+04

Leaching techniques for activated soil

Two leaching possibilities were investigated: water stagnation with irradiated soil (mixing system) and water percolation through the irradiated soil (flowing system). To measure the amount of radioactivity passed from the irradiated soil to the water in both systems, leach water samples were systematically measured by gamma spectrometry and by scintillation analysis.

In the mixing system, 100 g of the irradiated soil was placed in a graduated flask together with 1 litre of distilled (tritium free) water. After vigorous shaking to disperse the soil in the water, the mixture was stirred for 8 hours. To measure the radioactivity leached out, a 100 ml sample of the hazy water was filtered through a Millipore filter (0.45 µm). The gamma activity in the water was measured with a Germanium detector as discussed above while β emitters were measured with a liquid scintillation spectrometer after distillation. Activated soil and water were in contact for 4 months and the analyses on the leached water were repeated after 1, 2 and 4 months. The results for the mixing system are shown in Table 5.

In the flowing system, a sample of 100 g of irradiated soil was placed in a funnel with a Millipore filter (0.45 µm) connected to a graduated container. A glass separatory funnel was placed over the funnel and filled with 1 litre of distilled (tritium free) water. The glass stopcock allowed controlling the rate of addition of the water to 125 ml/hr. The gamma activity in the water was measured with a Germanium detector while β emitters were measured with a liquid scintillation spectrometer after distillation. The whole procedure was repeated after 1, 2 and 4 months. The results for the flowing system are shown in Table 6.

Table 5. Specific activity of ^{3}H and ^{22}Na measured in leached water after correction for the decay and the concentration for the mixing system

Mixing time	Specific Activity (Bq/l)	
	^{3}H $(t_{1/2} = 12.32\ \mathrm{y})$	^{22}Na $(t_{1/2} = 2.6\ \mathrm{y})$
8 hours	518 ± 31	96.7 ± 5.8
1 month	541 ± 32	131 ± 8
2 months	542 ± 32	136 ± 8
4 months	542 ± 33	144 ± 9

Table 6. Specific activity of ^{3}H and ^{22}Na measured in the leached water including decay correction for the flowing system

Wash	Specific Activity (Bq/l)	
	^{3}H $(t_{1/2} = 12.32\ \mathrm{y})$	^{22}Na $(t_{1/2} = 2.6\ \mathrm{y})$
1	384 ± 23	126 ± 6
2	3.23 ± 0.93	12.7 ± 0.9
3	1.67 ± 0.90	3.15 ± 0.22
4	2.05 ± 1.09	4.71 ± 0.54

Fraction of radioactivity leached out

The activity concentration of the leached water for both systems was compared with the radioactivity measured in the activated soil in order to estimate the fraction leached out. Figure 2 shows the ratio between the total activity measured in the leached water and the total activity measured in the activated soil for ^{3}H and ^{22}Na, the two radionuclides of major interest in this study. Since the liquid scintillation analysis cannot be performed on the soil, the tritium activity measured in the leached water was compared with the tritium estimated in the soil by the FLUKA simulations. Most of the radioactivity leached into the water just after 8 hours of mixing time (mixing system) or after the first wash (flowing system). In the first case, the longer the soil is mixed with the water, the more radioactivity leaches out. After two months of stirring, 39% of the ^{3}H and 11% of the ^{22}Na are leached by water. For the flowing system, the leachable fraction after one wash is 27% for ^{3}H and 10% for ^{22}Na. As from the second wash, the leachable fraction falls down to a fraction of per cent for both radioisotopes.

Figure 2. Cumulative fraction of ^{3}H and ^{22}Na activities extracted by water from the activated soil for both systems

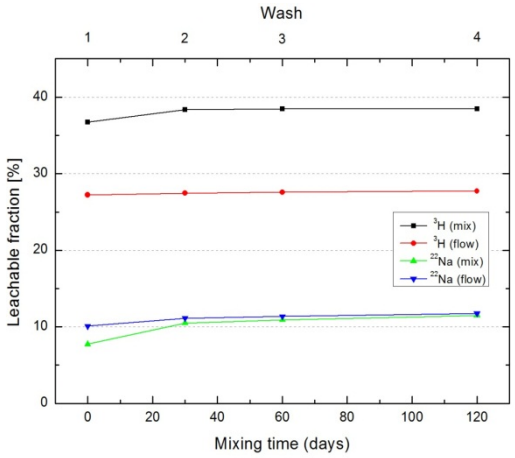

Conclusions

Several metallic and soil samples were irradiated at the H4IRRAD test facility. Gamma spectrometry and beta scintillation analysis (leached water only) were performed to determine the radioactivity induced in the samples. Conversion coefficients from unit lost beam power to induced specific activity at saturation were calculated for each radionuclide produced in metallic samples. FLUKA simulations were carried out to estimate the concentration of ^{3}H in the soil. Two leaching procedures were used and compared to quantify the amount of radioactivity leached out of the soil into the water. The mixing system was able to remove up to 39% of ^{3}H and 12% of ^{22}Na from the irradiated soil.

Acknowledgements

The authors would like to thank A. Dziewa, F. Malacrida and A. El Gares for performing the gamma spectrometry and the liquid scintillation measurements. The authors are grateful to M. Calviani, M. Brugger and the H4IRRAD team for allowing the irradiation of the samples and for providing the FLUKA geometry of the facility.

References

[1] R. Froeschl, F.P. La Torre and N. Walter (2012), "The ActiWiz material composition catalogue", CERN Technical Report, CERN-RP-2012-002-REPORTS-TN.

[2] R. Froeschl, FP. La Torre, S. Sgobba, C. Theis, H. Vinke, N. Walter (2012), "Radiological Hazard classification of material in CERN's accelerators", CERN Technical Report, CERN-DGS-2012-003-RP-IR.

[3] F.P. La Torre, M. Silari (2014), "Leaching of radionuclides from activated soil into groundwater", CERN Technical Report, CERN-RP-2014-012-REPORTS-TN.

[4] S. Sgobba (2006), "Material for high vacuum technology: an overview", CERN-TS/2006-004 (MME), EDMS 773904.

[5] S. Sgobba (2009), "Physics and measurements of magnetic materials", CERN Accelerator School CAS 2009: Specialised Course on Magnets, Bruges, 16-25 June 2009.

[6] J.M. Jimenez, B. Henrist (2004), "Vacuum Chambers for the Circulating Beams in the LHC Injection and Extraction Septa", Functional Specification, LHC-VCRS-ES-0001 rev. 1.0, EDMS 405734, (MUMETAL).

[7] S. Claudet et al. (2004), "Two 100 m Invar transfer Lines at CERN: design principles and operating experience for helium refrigeration", CERN-AT-2004-021-ACR.

[8] B. Biskup, M. Brugger, M. Calviani, I. Efthymiopoulos, R. Kwee, J. Mekki, F.P. La Torre, E. Lebbos, P. Mala, G. Manessi, A. Nordt, F. Pozzi, K. Roeed, C. Severino, M. Silari, A. Thornton (2011), "Commissioning and Operation of the H4IRRAD Mixed-Field Test Area", CERN Technical Note, CERN-ATS-Note-2011-121 PERF.

[9] A. Ferrari, P.R. Sala, A. Fasso, J. Ranft (2005), "FLUKA: A Multi-particle Transport Code", CERN-2005-10, INFN/TC_05/11, SLAC-R-773.

[10] G. Battistoni, S. Muraro, P.R. Sala, F. Cerutti, A. Ferrari, S. Roesler, A. Fasso, J. Ranft (2007), "The FLUKA code: description and benchmarking", *Proceedings of the Hadronic Shower Simulation Workshop 2006*, Fermilab 6-8 September 2006, M. Albrow, R. Raja Eds., AIP Conference Proceeding 896, 31-49.

Evaluation of radiation environment at FRIB linac

Mikhail Kostin[1], Robert Lowrie[1,2], Reginald Ronningen[1]
[1]Facility for Rare Isotope Beams, US
[2]URS Corporation, US

Abstract

The Facility for Rare Isotope Beams (FRIB) at Michigan State University is a project jointly funded by the US Department of Energy and Michigan State University with the construction started in March 2014. This accelerator facility will use a broad range of primary ion beams from ^{16}O to ^{238}U with a beam power of up to 400 kW and energy of 200 MeV/nucleon for ^{238}U in its baseline configuration to produce rare isotopes. A possible facility upgrade will include increase of the beam energy up to 400 MeV/nucleon for ^{238}U and the addition of new light ion beams down to ^{3}He and protons for ISOL operations.

The work presented here is an overview of radiation transport calculations aimed to evaluate the radiological environment at the FRIB linac and adjacent areas. A number of calculations have addressed the impact on environment (activation of soil and ground water, evaluation of radionuclide releases); prompt radiation to the workers and general public due to normal beam losses and beam loss incidents; and activation of services.

This material is based on work supported by the US Department of Energy Office of Science under Cooperative Agreement DE-SC0000661.

Introduction

The Facility for Rare Isotope Beams (FRIB) is a new national user facility at Michigan State University (MSU). The facility is being built for the research in the fields of physics of nuclei, nuclear astrophysics, fundamental interactions, and applications for society. In its baseline configuration the facility will offer separation of isotopes in-flight for fast, stopped and reaccelerated secondary beams. A broad range of the primary ion beams will be utilised, from ^{16}O to ^{238}U with a beam power of up to 400 kW and energy of 200 MeV/nucleon for ^{238}U (higher for lighter primary beams) to produce rare isotopes. A possible facility upgrade will include an increase in the primary beam energy up to 400 MeV/nucleon for ^{238}U and the addition of new light ion beams down to ^{3}He and protons for Isotope-Online (ISOL) operations. A multi-user operation with simultaneous light and heavy primary beams is also considered.

FRIB will consist of two major systems: a double-folded linear accelerator which will deliver a primary ion beam to a rare isotope production facility, consisting of a high-power target connected to a fragment separator for providing secondary rare isotope beams for science experiments (see Figure 1). This paper provides an overview of the radiation transport calculations performed in support of the design of the FRIB linear accelerator and its radiation shielding with focus on human and environmental impact issues rather than on the design of specific beam line elements.

Figure 1. Schematics of the FRIB Facility and the experimental areas

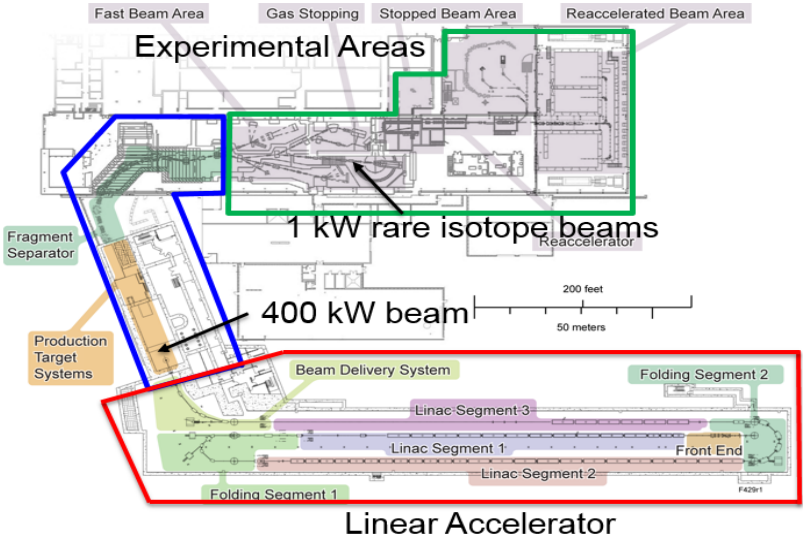

Regulatory protection criteria applied to FRIB

One of the goals of the radiation transport calculations is to provide input to the designers to verify that the facility meets the limits from various regulatory agencies and satisfy the MSU ALARA (As Low As Reasonably Achievable) goals both for the general public and the radiation workers. One key factor for this analysis is that FRIB is situated on the MSU campus where the general public is immediately outside the facility walls and not in a remote location. Although FRIB is largely funded by the US Department of Energy, the regulatory agencies include the US Nuclear Regulatory Commission (NRC), whose limits are the applicable regulations for this study. FRIB will be under an independent NRC license. Table 1 summarises various limits. The MSU ALARA goals are in general set to 10% of the limits imposed by the regulatory agencies. One distinctive difference is the self-imposed limits for the ground water activation. The limits for effluent water shown in Table 1 show the significant margin being applied to the design by using the drinking water limits. Groundwater near FRIB is not in contact with any source of drinking water nor public access. FRIB is relatively distant from the closest drinking water well and the aquifer is relatively deep under FRIB. Nonetheless, the design goal is to assure radiation protection for the ground water activation level by meeting the limits established for the drinking water.

Table 1. Regulatory radiation protection limits and MSU ALARA goals

Type of limit	Limits and goals	
Radiation dose – Worker	Standard [1]: 5,000 mrem/yr MSU ALARA Goal [2]: 500 mrem/yr	
Radiation dose – Public	Standard [1]: 100 mrem/yr and < 2 mrem/(any one hour) MSU ALARA Goal [2]: 10 mrem/yr and < 2 mrem/(any one hour)	
Air – maximum exposure to nearest receptor	Standard [1]: 10 mrem/y MSU ALARA Goal [2]: 1 mrem/yr	
Groundwater - effluent	^{3}H Standard [1]: 1,000 pCi/ml FRIB Design Goal: 20 pCi/ml (drinking water standard [3])	^{22}Na Standard [1]: 6 pCi/ml FRIB Design Goal: 0.4 pCi/ml (drinking water standard [3])

Activation of soil and ground water

Some activation of the soil and the ground water is expected at the FRIB linac due to normal beam losses. Whereas the actual beam losses will be determined during facility operation, the design requirement for the linac is to keep it below 1 W/m. The level of activation was evaluated for an assumed beam loss rate of 1 W/m and radiologically bounding beam of protons at 200 MeV in the first linac segment (see Figure 1), 611 MeV in the second segment, and 1 GeV in the third segment. The calculations were carried out in two steps. As the first step, the star density distribution was calculated around the linac tunnel using the radiation transport code MARS15 [4-6]. The concentrations of dominant radionuclides ^{3}H and ^{22}Na were estimated from the star density using Radionuclide Concentration Model [7] after that.

Star density distribution due to normal beam losses

Figure 2 shows a cross-section of the double-folded FRIB linac, the tunnel walls and the surrounding soil. The associated proton beam energies are also indicated in the figure. Fermilab-type wet dirt [6] with a density of 2.24 g/cm^3 was used as the soil (standard MARS15 material "SOIL"). The tunnel wall thickness used in the calculations was 30 in, and that of the tunnel roof is 42 in. The linac segments were represented with a stainless steel pipe surrounded with a box as cryogenic modules. The angle at which the beam particles entered the beam pipe material was set to 3 mrad with respect to the beam pipe surface, and the entry position is uniformly distributed both longitudinally and azimuthally. These assumptions are a simplification. In reality, a broader angular spectrum is possible, with the beam loss rate higher in focusing elements where the beam size is larger. The effect of the incident angle on the ground water activation was tested for angles 0.1 mrad, 3 mrad and 1 degree and no significant difference was found.

The resulting star density distribution with contribution from beam losses in all the segments is shown in Figure 3. The distribution is presented in units of 1/cm^3/y assuming that one operational year is 2×10^7 s (5556 h). It is recognised that a gradient in activity will be present from the edge of the facility. The soil and groundwater activation is assessed by assuming uniform mixing of the activated water over the assumed analysis volume. Activated soil and groundwater next to the tunnel wall poses no risk to the environment or the public. It must flow from this location to the "facility boundary" or "point of compliance" for the facility as described in the regulations. Therefore, the region can be assumed to effectively mix. The mixing of the water is taken into account by assessing the average star density over a volume that contains either 99% or 99.9% of the entire radioactivity generated in the soil. The 99% and 99.9% volumes were found to be restricted by isocontours located approximately 2 m and 3 m respectively from the concrete walls of the tunnel. These distances of 2 m and 3 m are measured against the segment 2 (611 MeV) and segment 3 (1 GeV) which are locations where the soil activity is maximum. In other places these isocontours are located even closer to the tunnel walls. The averaged star densities are summarised in Table 2.

Figure 2. Cross-section of linac model with surrounding soil and tunnel walls

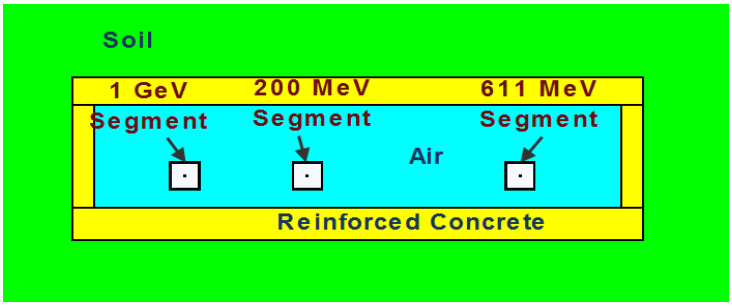

Figure 3. Resulting star density distribution

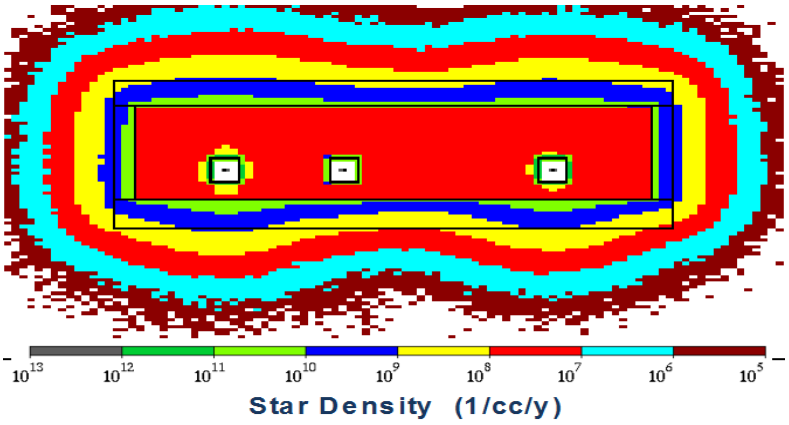

Table 2. Averaged star densities and limiting isocontour levels corresponding to 99% and 99.9% volumes

Volume	Averaged star density [1/cm^3/y]	Isocontour level [1/cm^3/y]
99%	2.99×10^8	1.13×10^7
99.9%	1.87×10^8	1.24×10^6

The isocontours levels can be used to determine "points of compliance" from Figure 3.

Nuclide concentrations

The averaged star densities are converted in radionuclide concentration using Radionuclide Concentration Model [7]. In the original model, the concentration C_i (in *pCi* per *ml*) for a radionuclide of the type *i* in water in proximity to the beam enclosure is expressed by:

$$C_i(t) = N_p \cdot S_{\max} \cdot G \cdot K_i \cdot L_i \cdot (1.17\times10^6 \cdot \rho \cdot w_i)^{-1} (1 - e^{\lambda_i t}) \quad (1)$$

or, in the limit of radionuclide saturation, by:

$$C_i(t=\infty) = N_p \cdot S_{\max} \cdot G \cdot K_i \cdot L_i \cdot (1.17\times10^6 \cdot \rho \cdot w_i)^{-1} \quad (2)$$

where:

N_p is the number of incident protons per year;

S_{max} is the maximum star density (in 1/cm^3) per incident proton in the soil or rock obtained from calculations carried out with radiation transport codes;

G is the geometry factor which takes into account mixing of the activated water in some volume;

K_i is the radionuclide production probability per star (0.075 atoms/star for ^{3}H, 0.02 atoms/star for ^{22}Na in the original model, calculated in simulations in our case and presented in Table 3);

L_i is the *leachability* factor for the radionuclide (0.9 for ^{3}H and 0.135 for ^{22}Na in soil);

ρ is the material density;

w_i is the weight of water divided by the weight of soil needed to leach 90% of the leachable radioactivity that is present (0.27 for ^{3}H and 0.52 for ^{22}Na);

λ_i is the inverse mean lifetime of the radionuclide of the type *i*, measured in units consistent with those of time *t* (e.g. years);

1.17×10^{6} is the numerical factor that converts disintegrations per second into *p*C*i* (0.037) and years into seconds (3.15×10^{7}).

The averaging of the activated water is taken into account by the geometry factor, *G*. A typical value of *G* found in the literature is 0.19 for beam lines and 0.019 for target stations not followed by long beam lines [8]. The factor was analytically calculated as a ratio of the star density averaged out to a radius where the star density has fallen to 1% of its peak value over the peak star density. The calculations were performed for a system with a certain cylindrical symmetry. Sometimes this approach is erroneously called a "99% volume" approach assuming that in these calculations 99% of all the activation is contained in the volume over which this procedure is performed. This is only approximately correct, especially for systems where there is no cylindrical symmetry. In the present calculations, however, we do not rely on the knowledge of the geometry factor. The previously calculated averaged star density is used as described above. This changes Equations (1) and (2) to:

$$C_i(t) = N_p \cdot S_{aver} \cdot K_i \cdot L_i \cdot (1.17\times10^{6} \cdot \rho \cdot w_i)^{-1} (1 - e^{\lambda i\, t}) \quad (3)$$

or in the limit of radionuclide saturation

$$C_i(t=\infty) = N_p \cdot S_{aver} \cdot K_i \cdot L_i \cdot (1.17\times10^{6} \cdot \rho \cdot w_i)^{-1} \quad (4)$$

In these equations, S_{aver} is the star density averaged over volumes containing either 99% or 99.9% of all the activity, and is $S_{max}\times G$. The rates of radionuclide production per star, K_i, are also calculated. We do not rely on the values originally presented in the radionuclide concentration model. The number of lost particles N_p is energy dependent and is calculated assuming a beam loss rate of 1 W/m.

As discussed in [7] and [9], only two radionuclides ^{22}Na and ^{3}H are of importance for FNAL soil types based upon the production rates, half-life time and the leachability by water. The leaching factor, L_i, is probably the most uncertain parameter of the model. It is a fraction of radionuclides that can be washed out by a representative amount of water. As discussed in [9], measurements were made of the number of radionuclides washed out of a sample of material exposed to a known amount of beam, by successive mixings of known amounts of water. For ^{22}Na, the amount washed out with each batch of water can be totalled and compared to the amount of activity initially present. This is not possible with the ^{3}H leaching measurements, due to the low energy of its beta decay and the analytical techniques employed. Only a product of the leachability and radionuclide production probability per star, K_i, can be measured for tritium.

The concentration model chooses to use the quantity of water that removes 90% of the leachable radionuclides, and uses this amount of the water as the basis for conversion from the soil density,ρ, to the density of water in the soil, ($\rho\ w_i$). The leachability for tritium in soil is 0.9, and has the meaning that the volume of water considered removes 90% of the amount of tritium that could be removed by continuing the washes to the necessary limit.

Table 3 summarises some parameters for the dominant radionuclides. *K*-factors were obtained from the simulations. Tables 4 and 5 show dominant radionuclide concentrations averaged over different volumes. The concentrations were calculated for three irradiation times: 10 years, 20 years and an infinite irradiation time ("saturation"). Beside the concentrations, the values $\Sigma_i C_i/C_{i,max}$ are also shown. The values are the sums of concentrations of all radionuclides of importance divided by maximum allowed concentrations in drinking water. The regulatory requirements stipulate that the value

$\Sigma_i C_i/C_{i,max}$ must be less or equal to 1. The values of $C_{i,max}$ for drinking water are found in [3] and also summarised in Table 3. As the calculations for the considered model showed, the radionuclide concentrations calculated in the 99.9% volume are expected to stay below the regulatory limits for drinking water standards for all radionuclides of importance both separately and in sum. These calculations are conservative for a number of reasons. The thickness of the tunnel walls has been increased from 30 in to 36 in after these calculations where completed; ion beams will be used instead of radiologically bounding proton beams in the baseline configuration of the facility, and heavier beams are expected to produce even less activity in the ground water; and in addition to that, we do not expect that the saturation conditions will even be achieved due to the seasonal variations of the water table.

Table 3. Dominant radionuclide parameters and regulatory limits C_{max}

Nuclide	Half-life [y]	C_{max} [pCi/ml]	Atoms per Star (*K*-factor)
^{3}H	12.32	20	0.0250
^{22}Na	2.6027	0.4	0.00732

Table 4. Concentrations of radionuclides averaged over the volume containing 99% of activity

Irradiation 10 years			Irradiation 20 years			Saturation		
$C(^{3}H)$ [pCi/ml]	$C(^{22}Na)$ [pCi/ml]	$\Sigma_i C_i/C_{i,max}$	$C(^{3}H)$ [pCi/ml]	$C(^{22}Na)$ [pCi/ml]	$\Sigma_i C_i/C_{i,max}$	$C(^{3}H)$ [pCi/ml]	$C(^{22}Na)$ [pCi/ml]	$\Sigma_i C_i/C_{i,max}$
4.10	0.20	0.71	6.44	0.22	0.86	9.54	0.22	1.02

Table 5. Concentrations of radionuclides averaged over the volume containing 99.9% of activity

Irradiation 10 years			Irradiation 20 years			Saturation		
$C(^{3}H)$ [pCi/ml]	$C(^{22}Na)$ [pCi/ml]	$\Sigma_i C_i/C_{i,max}$	$C(^{3}H)$ [pCi/ml]	$C(^{22}Na)$ [pCi/ml]	$\Sigma_i C_i/C_{i,max}$	$C(^{3}H)$ [pCi/ml]	$C(^{22}Na)$ [pCi/ml]	$\Sigma_i C_i/C_{i,max}$
2.56	0.13	0.44	4.02	0.13	0.54	5.95	0.14	0.64

Comparison of FNAL and FRIB soil

Although the evaluation of the soil and ground water activation was performed using FNAL-type soil, a comparison between this type of soil and actual FRIB soil was also carried out. NTH Consultants, Ltd. [10] performed a geological survey taking a number of samples at various locations and depths (up to 75 ft) on the FRIB site. The moisture content and the element composition were determined. It was found that although the soil composition varies from sample to sample, the averaged composition and the density is somewhat similar to those of the FNAL-type soil. The soil compositions are compared in Table 6. The averaged density of the FRIB soil was found to be 2.257 g/cm^3 versus that of 2.24 g/cm^3 for the FNAL soil. To further validate the similarity, Monte Carlo calculations were conducted using a simple cylindrically symmetrical model with dimensions that resemble those found in the actual FRIB tunnel. Star density was calculated for both soil types. A beam of 1 GeV protons was used.

Figure 4 shows two star density distributions as a function of soil depth for both types of soil. Both distributions are similar which validates that the results previously obtained with the FNAL-type wet dirt are applicable to the FRIB site.

Table 6. Composition of averaged FRIB soil and FNAL-type wet dirt

Element	Z	A	Weight fraction (FNAL)	Weight fraction (FRIB)	Atomic fraction (FNAL)	Atomic fraction (FRIB)
H	1	1.00794	0.023	0.016	0.31	0.23
C	6	12.01100		0.028		0.035
O	8	15.99940	0.57	0.61	0.49	0.56
Mg	12	24.30500		0.020		0.012
Al	13	26.98154	0.071	0.034	0.036	0.018
Si	14	28.08550	0.33	0.21	0.16	0.11
K	19	39.09830		0.0094		0.0036
Ca	20	40.07800		0.060		0.022
Ti	22	47.88000		0.0022		0.00069
Fe	26	55.84500		0.014		0.0038

Figure 4. Star density distribution as a function of the soil depth

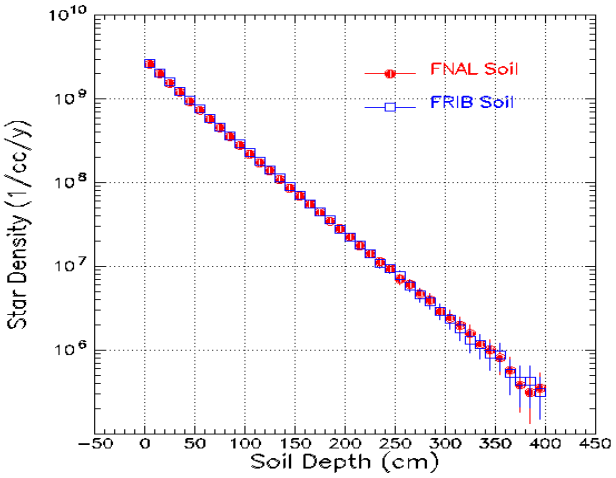

Effect of major penetrations

The linac tunnel will be located approximately 6 m under the surface. This shielding of 6 metres (concrete and soil) is not solid, however. There is a number of small penetrations through the shielding like those for radio-frequency wave guides, cables and services, and several big penetrations. These major penetrations (see Figure 5) are the front-end drop; heating, ventilation and air conditioning inlet (HVAC-In); second (smaller) HVAC inlet ("Small" HVAC-In); HVAC outlet (HVAC-Out); hatch on the east side of the linac tunnel (East Hatch); stairwell on the north-east side of the linac tunnel; and cryogenic distribution shaft (Cryoline). Due to their substantial size, one expects an enhanced radiation streaming through them which, in turn, will increase the level of the soil and ground water activation. An effect of the major penetrations on the ground water activation was studied in two sets of calculations. The star densities were calculated in volumes surrounding these penetrations (see Figure 6). The volume size was chosen to be 3 m which approximately corresponds to the 99.9% volume as described in the previous sections. The star densities were compared to values obtained in the second set of calculations using the same model but with the major penetrations removed (Figure 7). The direct comparison between the two sets of star density values allows us to estimate the effect of the penetrations on the ground water activation. The calculations were performed for a constant beam loss of 1 W/m for radiologically bounding beams: protons at 611 MeV in the second linac segment and the second folding segment, and protons at 1 GeV in the third linac segment. The beam losses in the first linac segment and the first folding segment were ignored due to the fact that these segments would not be used for the proton beams, and that the energy of other ion beams in this segment will be as low as 20 MeV/nucleon or below. Table 7 provides the comparison between those two sets of star density values for each of the major penetrations. One can see that the values are less than 33% different. Thus the conclusions of our previous studies are not affected.

Figure 5. Three-dimensional rendering of the concrete structure of the linac tunnel and the service building

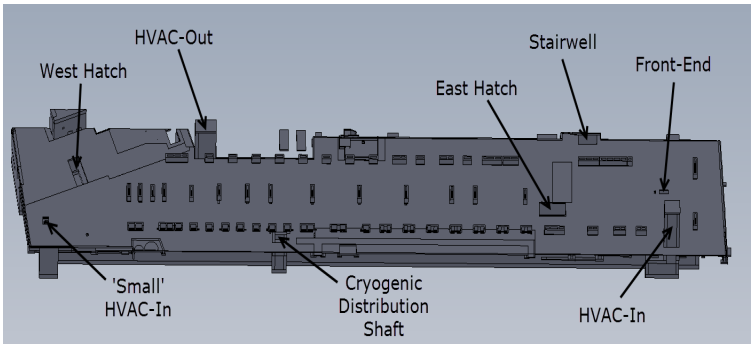

The area above the surface level is clearly seen. The major penetrations are indicated.

Figure 6. Plan view of model above the tunnel

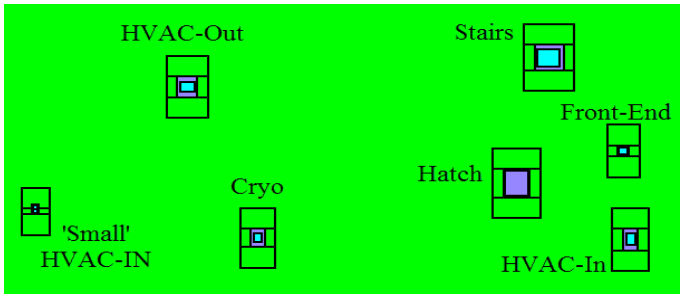

Volumes around the penetrations in which the star densities were calculated are shown.

Figure 7. Plan view of model above the tunnel

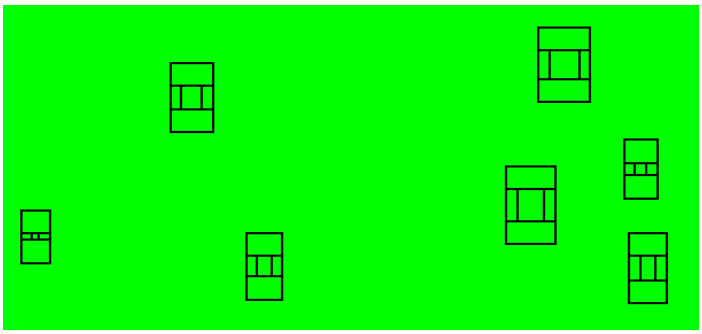

Volumes around the penetrations in which the star densities were calculated are shown. The model is similar to that shown in Figure 6, but the major penetrations were removed from it.

Table 7. Averaged star densities calculated in 3 m-thick volumes located around the major penetrations

Penetration	Averaged star density in model with major penetrations [1/cm^3/y]	Averaged star density in model with major penetrations removed [1/cm^3/y]	Star density increase due to penetration [%]
Front end	8.79E+07	8.15E+07	7.3
HVAC-In	4.52E+07	3.99E+07	11.7
East Hatch	1.89E+08	1.27E+08	32.5
Cryoline	6.68E+07	5.92E+07	11.3
Stairs	2.35E+06	1.87E+06	20.2
HVAC-Out	8.95E+07	7.76E+07	13.3
'Small' HVAC-In	5.83E+06	5.61E+06	3.8

Also shown are the averaged star densities calculated in the same volumes but in the model where the penetrations were removed.

Prompt dose rates

As part of the design process, we need to ensure that the facility provides an adequate shielding so that the dose equivalent rates stay below the MSU ALARA goals for both the workers and the general public. In the case of prompt dose radiation at the FRIB linear accelerator, the limits apply to the areas above the surface (grade) only, because the machine was not designed to allow access into the beam enclosure during the operation. It is important to note that the facility is located on the MSU campus, and that the members of the general public can be present close to the facility walls. The dose rates must be evaluated for both the normal operation (1 W/m beam loss rate) and beam loss incident scenarios, and compared to both the personnel and general public dose limits. All the calculations for this purpose were performed with the MARS15 code [4-6] using a model that includes the linear accelerator, tunnel, all major penetrations and other conduits, and the walls of the service building above grade.

Prompt dose rates during normal operation

MSU ALARA stipulates that the annual doses should not exceed 500 mrem for the workers, and 10 mrem for members of the general public. These numbers translate into 0.25 mrem/h and 0.0018 mrem/h ALARA goals assuming that one working year during which the exposure of the workers to the radiation is possible is 2000 hours, and one operational year during which the general public can be exposed to is 5556 hours. We do not claim any credit for the general public to be around FRIB for only part of the year.

The dose equivalent rate above grade was calculated for the radiologically bounding beams: protons at 611 MeV in the second linac segment and the second folding segment, and protons at 1 GeV in the third linac segment. In addition, we added the beam losses for ^{18}O beam at 35 MeV/nucleon in the first linac segment and the first folding segment. These segments would not be used for protons. The resulting dose rate distribution is shown in Figure 8. The distribution is overlaid with a plan view of the facility. A number of recommendations were made based on this distribution for the purpose of protection of the general public: the walls of the service building constructed with CMU blocks should be filled with grout in several locations (see Figure 9); the fence on the north side of the building should be realigned to restrict access of the general public to that area; and the shielding above the surface for the cryogenic distribution shaft must be redesigned.

The dose map also confirmed that the dose rate is below 0.1 mrem/h everywhere in the service building with exception of the vicinity of the major penetrations. The dose rate of 0.1 mrem/h is in fact the MSU ALARA goal for the workers with additional safety margin of 2.5. A closer look at the dose rate around the major penetrations revealed that it is only a small numerical factor higher than 0.1 mrem/h and in relatively small areas with size in a scale of a meter. A number of mitigation strategies can be applied in these areas such as active monitoring, local shielding that would not impact the operation, stand-offs, and occupancy factors in locations where the workers are not expected to be during the entirety of their shift. Other penetrations such as conduits for radio-frequency wave guides appear to be small enough and well shielded to keep the dose rates in their vicinity below 0.1 mrem/h.

Figure 8. Dose equivalent rate distribution calculated above grade and expressed in units of mrem/h

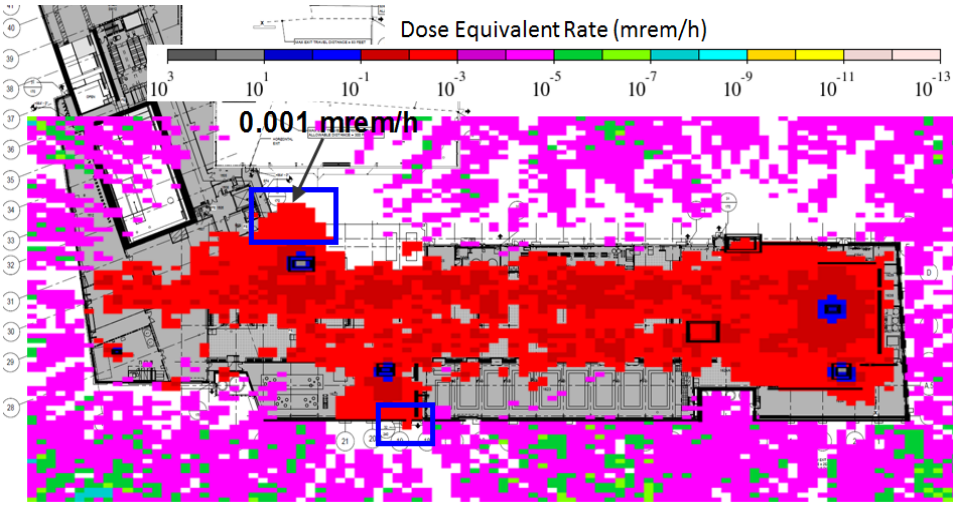

The blue boxes indicate publically accessible areas where the dose rate exceeds 0.001 mrem/h.

Figure 9. Plan view of the service building at the grade level

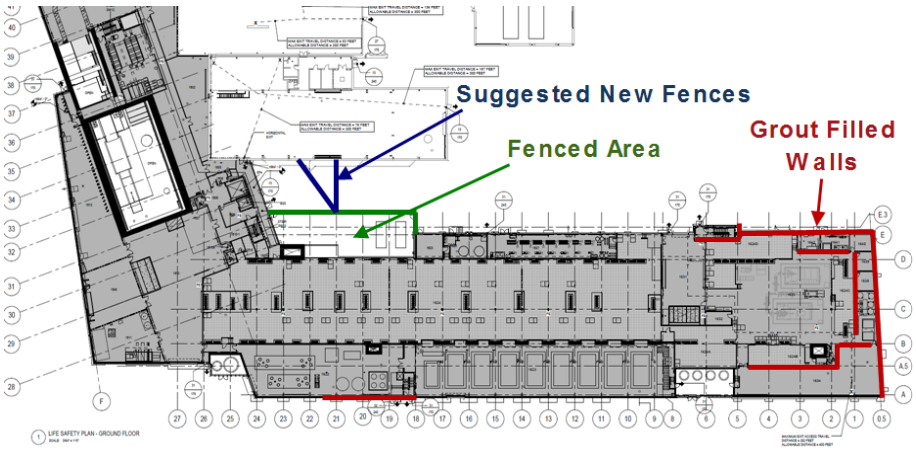

The red lines indicate building walls that are suggested to be filled in with grout. The green lines limit an area outside the service building that is planned to be fenced out. The blue lines show fence locations which will limit the public access to the area because the expected dose rate will exceed 0.001 mrem/h.

Prompt dose rates due to beam loss incidents

The dose equivalent rates in the service building above grade due to beam loss incidents were also evaluated. Radiologically bounding proton beams were used. We also assumed that the beam is completely stopped in a stopping target. This is rarely the case, however. Particle beams are not normally lost locally but rather on a stretch of accelerator because an actual beam has a size and particles in the beam have angular distribution. And, if the beam is lost due to a magnet failure, the field in the magnet changes slow enough to spread the beam losses over a section of the machine. Therefore, the assumption of the local beam losses will result in conservative estimates. The positions of the stopping target were selected to maximise to dose rates around the major penetrations, since the dose rate increase due to smaller conduits is not substantial. The intensity of the stopped

beam was 2.5×10^{15} 1/s, which corresponds to 400 kW of 1 GeV protons (beam power on the production target). It was found that the maximum dose rate reaches 1.8×10^{4} mrem/h. This dose rate is found at the front-end drop when the beam is lost in one of the locations in the second folding segment. The MSU ALARA stipulates that the dose rate stays below 2 mrem in any one hour for the workers. The limit of 2 mrem in any one hour is also a regulatory limit for the general public. Further assuming that the accelerator will be shut down after such an incident to investigate the reasons for the lost beam and therefore no more than one beam loss incident in any one hour is possible, we will need to detect such beam loss event and shut down the machine in 0.4 s. Note that the machine protection system is being designed to do so in just 35 μs. Therefore the beam loss incidents should not pose a risk to people from the standpoint of the prompt dose.

Activation of water services

There are several thousand gallons of water in two closed-loop systems at the FRIB linac. The LCA system (Low Conductivity Activated) will hold ≈6435 gallons to cool various beam line elements and magnets. Approximately, 1425 gallons in the CHA system (Chilled Activated) will be used for the HVAC units in the tunnel. Both systems will have an extensive plumbing and various purpose tanks in the linac tunnel and the service building above grade. Since this water is directly exposed to the radiation from the linac, we need to know both radionuclide concentrations and the total amount of radioactivity produced in these systems. These values are used in spill analyses of the activated water and in calculations of the doses to the workers from the activated water contained in the plumbing.

Radionuclide inventories in LCA and CHA systems

The dominant radionuclides produced in water in the accelerator environment are ^{3}H (tritium), ^{7}Be, ^{11}C, ^{13}N and ^{15}O [12]. These radionuclides are produced via spallation reactions induced by nucleons with the energy above 20 MeV. Fluxes of such nucleons were calculated in the LCA and CHA systems with MARS15 [4-6] for the normal beam losses (1 W/m) and the radiologically bounding proton beam. The fluxes were then converted into concentrations of the radionuclides of importance using a model described in [12]. The concentrations were calculated for broad ranges of the irradiation time (from 1 month to saturation) and the cooling time (from 0 to 1 year). The activities produced by ion beams at the same beam loss rate of 1 W/m are expected to be lower. The total activities were also calculated since the volumes of water directly exposed to the radiation in both systems are known. Both activities per unit volume and the total activities in the case of unlimited irradiation (saturation) and no cooling time allowed are summarised in Table 8. This case is the worst case scenario. The activities will decrease if a cooling time is assumed. For accident scenarios involving spills or leaks, the saturation case with no decay time should be used.

Table 8. Activities per unit volume and total activities of dominant radionuclides produced in water in the LCA and CHA systems for unlimited irradiation time (saturation) and no cooling time allowed

Radionuclide	LCA		CHA	
	Activity per unit volume [μCi/ml]	Total activity [μCi]	Activity per unit volume [μCi/ml]	Total activity [μCi]
^{3}H	1.53E-02	3.73E+05	1.59E-03	8.57E+03
^{7}Be	2.55E-03	6.21E+04	2.65E-04	1.43E+03
^{11}C	3.57E-04	8.70E+03	3.71E-05	2.00E+02
^{13}N	4.59E-03	1.12E+05	4.77E-04	2.57E+03
^{15}O	2.04E-02	4.97E+05	2.12E-03	1.14E+04

Dose rates at LCA and CHA systems

A further analysis allows calculations of the dose rates at the various components of the LCA and CHA systems using the estimated radionuclide concentrations. This was carried out with the code MicroShield6 [13]. Both the LCA and CHA systems have four types of cylindrically shaped tanks. These are air separators (Gas Liquid Separators, GLS), carbon filter tanks, ion exchangers (DI), and expansion tanks. There are two tanks of each type in each system. The tanks are located in a designated room in the service building. The tanks are not completely filled with activated water and have components inside which provide additional shielding against photons emitted from decaying radionuclides in water. In our calculations we assume that the tanks are filled with the water entirely. Thus, our calculations are conservative. There are also three heat exchangers in the LCA system and two in the CHA system, and regular pipes.

We assumed that a possible build-up of ^{7}Be anywhere in the LCA and CHA systems is insignificant and can be ignored. The build-up might occur due to ^{7}Be ions attaching to the plumbing if the water dynamics allows it. There are two factors, however, that suggest the low level of the build-up. First, the ions of ^{7}Be will be continuously removed from the systems by the ion exchange columns with efficiency of approximately 95% per cycle. Second, our collaborators from Spallation Neutron Source (SNS) reported that the build-up of ^{7}Be in their similar systems was insignificant. The dose rates were calculated, however, assuming that no ^{7}Be is removed from the LCA and CHA systems. Thus our calculations are conservative.

The dose equivalent rates at various components of the LCA and CHA systems are summarised in Tables 9 and 10. The dose rates were calculated at a distance of one foot from the components, assuming that the water in the system was irradiated for an infinite amount of time (saturation). The calculations were carried out for a moment immediately after the beam shut-down (0 hour delay), and 4 hours after the beam shut-down. We also assumed that no radionuclides are removed from water by any filters. The dose rates were calculated in two locations for each cylindrical tank assuming that these tanks are placed vertically: one foot from the cylindrical surface in the middle plane of the tank ("Side" in the tables); and one foot from the flat surface of the tanks ("Top" in the tables). Similarly, the dose rates were calculated in two locations for the heat exchangers: one foot from the middle point of the side surface ("Side" in the tables, the largest surface of the heat exchangers); and one foot from the middle point of the front or end surface ("Face" in the tables). Generally, the dose rates at the LCA components are more than an order of magnitude higher than those at the CHA components. The highest dose rate is

observed on the sides of the heat exchangers due to their significant size and small amount of shielding.

The contributions to the dose rates with no decay time allowed come mostly from short-lived nuclides ^{11}C, ^{13}N, and ^{15}O. Letting the radionuclide decay for 4 hours reduces the dose rates by more than two orders of magnitude, and ^{3}H and ^{7}Be become the dominant nuclides. However, as long as tritium remains contained by the plumbing, only ^{7}Be will be contributing to the dose rate outside the plumbing due to a low energy of electrons produced in the tritium decay.

Table 9. Dose equivalent rates (mrem/h) at a one foot distance from various components of the LCA system

– Tank/Device	– Side		– Top ("Face" for Heat Exchanger)	
	– 0 hours decay	– 4 hours decay	– 0 hours decay	– 4 hours decay
– Air Separator/GLS	– 4.801	– 2.373E-02	– 3.228	– 1.596E-02
– Heat Exchanger	– 2.307E+01	– 1.139E-01	– 2.918E-01	– 1.306E-03
– Expansion Tank	– 5.657	– 2.793E-02	– 4.320	– 2.135E-02
– DI	– 7.829	– 3.856E-02	– 7.605	– 3.756E-02
– Carbon Filter	– 7.829	– 3.856E-02	– 7.605	– 3.756E-02
– Pipe in Tunnel	– 2.190	– 1.086E-02	–	–

Table 10. Dose equivalent rates (mrem/h) at a one foot distance from various components of the CHA system

– Tank/Device	– Side		– Top ('Face' for Heat Exchanger)	
	– 0 hours decay	– 4 hours decay	– 0 hours decay	– 4 hours decay
– Air Separator/GLS	– 3.038E-01	– 1.506E-03	– 1.806E-01	– 8.898E-04
– Heat Exchanger	– 1.861	– 9.169E-03	– 3.121E-02	– 1.392E-04
– Expansion Tank	– 2.934E-01	– 1.449E-03	– 1.805E-01	– 8.894E-04
– DI	– 3.515E-01	– 1.735E-03	– 1.808E-01	– 8.904E-04
– Carbon Filter	– 3.515E-01	– 1.735E-03	– 1.808E-01	– 8.904E-04
– Pipe in Tunnel	– 7.780E-02	– 3.845E-04	–	–

Low-level liquid waste

There will be two more sets of tanks in the service building for Low Level Liquid Waste (LLLW). One set will store low-level activity water that is assumed to be condensed and collected on the HVAC cooling coils in the tunnel. The other set is for the condensed water from the tunnel walls and the magnets. Unlike the tanks in the two closed-loop systems, the LLLW tanks release activated vapour (humidity above the free surface) when additional water is added to the tanks and is released through the SMOG system to the environment. The activated water collected in LLLW will be removed as the tanks get filled, releasing the activated water vapour that has had a chance to decay in the LLLW tank. It was estimated that in the worst case mode as much as 9400 gallons of condensed water can be collected from the HVAC units in a full year operation. This mode of operation is unlikely, however, in the controlled climate of the facility.

Two sources of radionuclides in LLLW are possible: a direct production in water that has been already condensed, and production of the nuclides in the tunnel air with their

consequent capture by the water condensate. The concentrations of the nuclides produced by the first mechanism were calculated using the same approach as used for water in the LCA and CHA systems. Similar model was also used for the production of ^{3}H, ^{7}Be, ^{11}C, ^{13}N and ^{15}O in the tunnel air via spallation reactions caused by the nucleons with the energy above 20 MeV. A yield of ^{41}Ar in air was estimated directly by taking into account a capture of thermal neutrons. All the nuclide concentrations were found to be quite low, and thus this low-activated water can be processed with the existing MSU systems.

Independently validated design basis air effluent

FRIB operation inherently activates air in the linac tunnel and the target building hot cell. Additionally gaseous releases associated with activated water in the facility result in normal operational effluent from the facility. This effluent is filtered with both activated charcoal and HEPA filters to remove a significant portion of the activated material from the gaseous effluent. This effluent is released to the environment through high velocity exhaust stacks on the top of the FRIB target building. The potential impact on the public from these releases must be conservatively evaluated to assure that regulatory release limits and ALARA goals (Table 1) can be met during operation. Actual exposure will be determined by monitoring and is anticipated to be significantly lower than these conservatively estimated releases.

Airborne consequence analysis was performed in two steps. First, the various sources of air activation and gaseous activated products were determined from radiation transport calculations. These included the tunnel air HVAC exhaust and hot cell air HVAC exhaust, as well as the gaseous releases from activated systems from the target facility hot off-gas system (HOG) and service building special mechanical off-gas system (SMOG). These sources were then evaluated for potential public consequence based on both decay and dispersion from the stack [11]. A key factor in this evaluation is the potential wind conditions at FRIB accounting for the normal annual variations in wind, the impact of surrounding buildings, and the potential location of public receptors. This evaluation was performed using scale model wind tunnel testing (Figure 10) and the local historical wind data for this area. An appropriate set of receptor locations were identified to provide a representative sample of receptor location (Figure 11). The results of the evaluation accounting for the conservative source term, radioactive decay in the time to reach the receptors, and dispersion as defined by the wind tunnel data show that the regulatory limits and MSU ALARA goals can be easily met.

Figure 10. Wind tunnel scale model

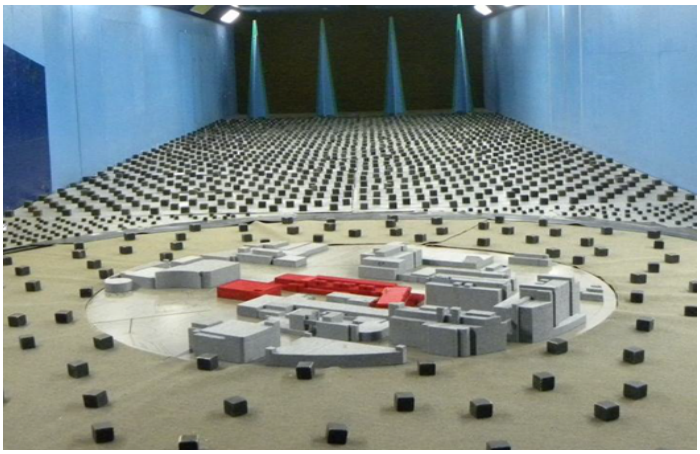

Figure 11. Receptor locations evaluated

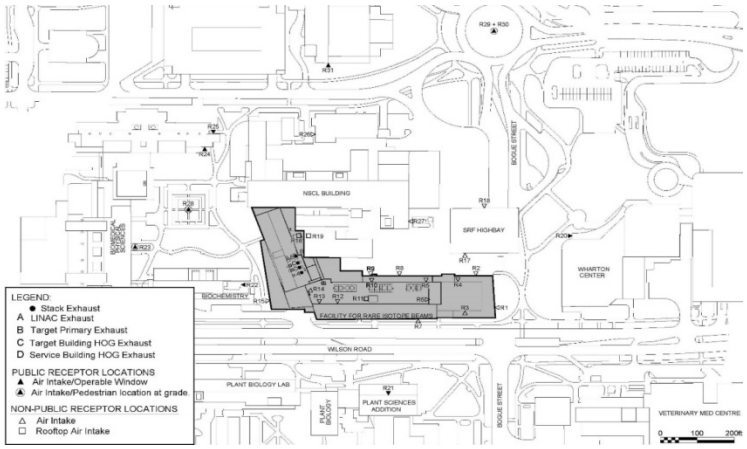

Conclusions

This paper provides an overview of the range of conservative radiation transport analyses performed in support of the FRIB design. The focus is on analyses that demonstrate compliance with NRC limits and MSU ALARA goals for postulated human and environmental exposure. Actual exposure will be based on measurements during commissioning and operation. These radiation calculations demonstrate anticipated acceptability and support the start of technical construction. Radiation transport will continue to support the designers, to ensure the completion of the final design, commissioning and operations.

Acknowledgements

This material is based on work supported by the US Department of Energy Office of Science under Cooperative Agreement DE-SC0000661.

References

[1] Standards for sump water, Nuclear Regulatory Commission, 10 CFR 20.

[2] MSU ALARA – NRC License Number 21-00021-29, MSU Type A Broad Scope License. MSU operates as a fully-licensed, non fuel cycle R&D Type A, NRC broad-scope licensee since 1977.

[3] Standards for drinking water, Entironmental Protection Agency, 40 CFR 141.

[4] N.V. Mokhov (1995), “The Mars Code System User's Guide”, Fermilab-FN-628.

[5] N.V. Mokhov, S.I. Striganov (2007), “MARS15 Overview”, Fermilab-Conf-07/008-AD; *Proc. of Hadronic Shower Simulation Workshop,* Fermilab, September 2006, AIP Conf. Proc. 896, pp. 50-60.

[6] http://www-ap.fnal.gov/MARS/.

[7] A. Wehmann, W. Smart, S. Menary, J. Hylen and S. Childress (1997), “Groundwater Protection for the NuMI Project”, FERMILAB-TM-2009.

[8] Bill Freeman (1996), "A NuMI Wide-Band Beam Shield Design That Meets the Concentration Model Groundwater Criteria", NuMI Note B-155.

[9] A.J. Malensek, A.A. Wehmann, A.J. Elwyn, K.J. Moss and P.M. Kesich (1993), "Groundwater Migration of Radionuclides at Fermilab", FERMILAB-TM-1851.

[10] NTH Consultants, Ltd.; http://www.nthconsultants.com/.

[11] RWDI; http://www.rwdi.com/.

[12] J.D. Cossairt (2000), "Calculation of the Radioactivity Produced in the Cooling Loops of the CDF SVX II Detector", Fermilab-TM-2112.

[13] MicroShield6 code; http://www.radiationsoftware.com/.

The use of ActiWiz in operational radiation protection

Christian Theis, Helmut Vincke
CERN European Organisation for Nuclear Research, Switzerland

Abstract

The ActiWiz code was originally developed at CERN for easy and quick assessment and comparison of the radiological hazard of materials used in the environment of high-energy accelerators. Due to its foundations on nuclide production terms, extensions have recently been developed which allow for expanding the scope of its application also to the field of operational radiation protection. An isotope build-up and decay engine has been developed to calculate nuclide inventories for arbitrary irradiation- and cooling period patterns. Automatic analysis of the dominating contributors to various quantities like radiotoxicity, clearance levels, photon dose-rate, gamma emission spectra etc. is provided. In addition, shielding of activated equipment, including the treatment of photon dose build-up factors, can be calculated within a few seconds even for nuclide sets with many thousands of gamma lines. The utilised initial nuclear inventories, including radioisotope production terms, can either originate directly from ActiWiz, from Monte Carlo codes like FLUKA, PHITS, MARS, MCNP or gamma spectroscopy measurements. In this paper an overview of these new features and a benchmark comparison to shielding calculations with FLUKA and the analytic Nucleonica code are given.

Introduction

The ActiWiz code [1] was originally developed to assess the radiological hazard of materials that are used in the environment of CERN's accelerators. It is based on a large number of FLUKA [2,3] calculations yielding nuclide inventories for the exposure of 69 basic constituents (chemical elements and a few radioisotopes) to various irradiation scenarios typically found at high-energy proton accelerators. These nuclide inventories constitute the foundation for ActiWiz' risk model that is applied to compare the radiological hazard of compounds that can be freely defined by the user. For a detailed description please refer to [4].

Further studies are required which focus on the classification of material as conventional or radioactive waste, handling constraints in radioactive workshops, transport, etc. For these purposes, the calculation of nuclide inventories is required. The original code has been extended in version 2, introducing the calculation of nuclide inventories of compounds with subsequent convolution with either legal limits (Swiss exemption limits [5]) or various activity-to-dose conversion factors. This allows for the determination of the dominating contributors either to a compound's radiotoxicity or to its dose emission. At the same time, for a specific irradiation scenario the theoretical photon emission spectrum of an activated compound is calculated, neglecting self-shielding as the geometry of the real object is unknown. Furthermore, dominating photon energies that need to be considered for the shielding of radioactive material are highlighted. In addition, for a desirable relative attenuation factor (e.g. 1/10) the thickness for various shielding materials can automatically be determined, taking the full isotopic

mixture of the activated equipment into consideration. As this calculation is based on a relative attenuation factor, the self-shielding due to the object's actual geometry is implicitly taken into account.

Calculation of nuclide inventories

Nuclide inventories are a function of the material's chemical composition, the energy and the location of exposure in the accelerator as well as a defined irradiation and cooling period. The original concept of ActiWiz neither foresaw direct determination of nuclide inventories nor made them available to the user. Thus, the results calculated by the risk assessment model were directly based on the original FLUKA simulations, which already provided the activity of the various radioisotopes for the aforementioned parameters. Consequently, the user was restricted to the irradiation and cooling patterns that were directly available in ActiWiz. While this should satisfy most needs with respect to typical applications in radiation protection, there might be questions that could arise during specific studies that would require the determination of nuclide inventories for deviating or more complex irradiation and cooling patterns. This has led to the decision to develop and implement a dedicated isotope build-up and decay engine for ActiWiz, which uses the nuclide production source-terms of FLUKA for the irradiation scenarios described in [4], while providing the user with the flexibility to specify arbitrarily complex sequences of irradiation and cooling periods. In addition, nuclide production source terms from external sources can be used, which describe simulation scenarios and radiation environments beyond those already included in ActiWiz.

The production and decay of radioisotopes is described by linear first order kinetics which can be expressed as a series of coupled differential equations discussed originally by H. Bateman [6]. The quantity of a specific isotope is determined by a linear chain of parent and daughter nuclides which undergo first order production and decay phenomena. It can be understood as illustrated in Equation (1):

$$\frac{dN_i(t)}{dt} = -\lambda_i N_i(t) + \lambda_{i-1,i} N_{i-1}(t) + P_i \quad (1)$$

N_i denotes the quantity of the i^{th} member of the production/decay chain and λ_i being its decay constant. As the chains might branch into multiple sub-branches each progression from one generation to the next is connected with a branching fraction $b_{i,i+1}$ describing the partial branching from the parent of order i to the respective daughter of order $i+1$ [7]. Thus, a partial decay constant for the i^{th} species, considering branching, is defined as $\lambda_{i,i+1} = \lambda_i * b_{i,i+1}$. For the general description one cannot only restrict oneself to pure decay of isotopes. It is also important to consider their continuous production via the production rate P_i. Via the Laplace transforms $L\{N_i(t)\}=n_i(s)$ and $L\{N'_i(t)\}= s * n_i(s) - N_i(0)$, this system of differential equations can be transformed into a simple algebraic relation that can be solved for $n_i(s)$ by rearranging the terms as discussed in [8].

Operation of a particle accelerator can be seen as a sequence of time intervals during which the beam can either be present or switched off. Periods during which the particle beam is present will directly contribute to the build-up of radioactivity and thus will be referred to as "irradiation periods". During time spans without beam only radioactive decay will be observed and consequently they will be termed "cooling periods". However, one must also take into account that for example nuclides that could have been present at the beginning of an irradiation period will also decay during this time span. For accelerator applications an irradiation pattern typically consists of various consecutive irradiation sub-patterns, each of which comprise an irradiation period t_{irr}, resulting in the build-up of nuclides, followed by a cooling period t_{cool} during which only the decay of nuclides occurs. The resulting nuclide concentrations of such sub-patterns can be calculated by iterative solution of Equation (1) to the respective time span t_{irr} and t_{cool}, with appropriate selection of the associated factors $N_i(t)$ and $P_i(t)$.

In our definition an irradiation sub-pattern always consists of an irradiation period t_{irr} followed by a cooling period t_{cool}. Taking this into account, we can conduct a simple change of variable ($t = t_{irr} + t_{cool}$). As a consequence, the solution of the Bateman equations can be trivially extended to allow for calculating the respective nuclide concentrations for a pair of time periods, t_{irr} and t_{cool}, in a single step:

$$N_n(t) = \sum_{k=1}^{m}\sum_{i=1}^{n}\left[\left(\prod_{j=i}^{n-1}\lambda_{j,j+1}\right)\sum_{j=i}^{n}\left(\frac{N_i^k e^{-\lambda_j(t_{k,irr}+t_{k,cool})}}{\prod_{\substack{p=i\\p\neq j}}^{n}(\lambda_p-\lambda_j)} + \frac{P_i^k(1-e^{-\lambda_j t_{k,irr}})e^{-\lambda_j t_{k,cool}}}{\lambda_j\prod_{\substack{p=i\\p\neq j}}^{n}(\lambda_p-\lambda_j)}\right)\right] \quad (2)$$

This expression yields the nuclide concentration of the n^{th} isotope species in a decay chain after m consecutive irradiation patterns (consisting always of pairs of irradiation and cooling periods $t_{k,irr}$ and $t_{k,cool}$ for $k = 1…m$). It should be noted that possible initial concentrations of isotopes (N_i^k) are also taken into account during the treatment of the respective irradiation/cooling period indexed with k.

Detailed numerical and mathematical considerations

Evaluation of Equation (2) requires that some attention is paid to subtle mathematical as well as numerical aspects. On one hand the denominator $\prod_{p=i,p\neq j}^{n}(\lambda_p-\lambda_j)$ might yield zero for identical decay constants found at different levels of the decay chain. This is for example possible for the transmutation and decay of:

$$^{235}U \xrightarrow{(n,\gamma)} {}^{236}U \xrightarrow{(n,\gamma)} {}^{237}U \xrightarrow{\beta-} {}^{237}Np \xrightarrow{(n,\gamma)} {}^{238}Np \xrightarrow{\beta-} {}^{238}Pu \xrightarrow{(n,\gamma)} {}^{239}Pu \xrightarrow{\alpha} {}^{235}U.$$

Even if such physically closed loops are excluded in the data structures right from the beginning, as they might be of low significance for accelerator applications, they could be encountered as numerically closed loops if two decay constants cancel out due to insufficient numerical precision of the computer's floating point unit. A thorough and proper mathematical treatment of these cases can be found in [9,10]. However, in ActiWiz, for reason of simplicity and performance, an extremely simplified approach is implemented which ensures that such numerical cancellation does not occur. This is done by artificially modifying one decay constant as $\lambda = \lambda * (1+\varepsilon)$ with $\varepsilon << 1$ if the difference of two decay constants in the chain would evaluate to zero within floating point precision.

Another aspect which numerically could cause problems is the evaluation of $1 - e^{-\lambda t_{irr}}$ if the argument of the exponential function tends towards zero. The trivial approach to solve this situation is to replace the exponential with its Taylor series expansion which would result in $e^{-\lambda t_{irr}} \sim 1 - \lambda t_{irr}$. This simple approximation could also reveal non-obvious numerical problems when being applied to the whole term of $1 - e^{-\lambda t_{irr}}$, rather than just the exponential function. Detailed mathematical treatments of the numerical pitfalls of this specific case can be found in literature on numerical analysis. However, modern C++ compilers as well as some scientific computation libraries provide a function called *expm1()* which specifically handles the issue of calculating $e^x - 1$ in a numerically sound way for very small values of x. This function is used in our implementation. It should be noted that the actual algorithm of this function is implementation specific and thus, results could slightly vary from platform to platform. To the authors' current knowledge in most cases the chosen approach is based on Taylor series expansion to machine precision or polynomial interpolation like high-order Remez polynomials. Another important numerical aspect is the summation of the different terms of Equation (2). Keeping in mind that a computer provides finite precision in terms of floating point representation this sum can result in an accumulation of errors. A remedy would be the introduction of compensated summation like Kahan's algorithm [11]. Yet, calculations

with standard double precision floating point accuracy would still fail, an example being the decay process of 1 kg of ^{238}U over 100 years. Therefore, ActiWiz implements multi-precision arithmetics with a custom developed plugin data-type based on the MPRF library. As this wide topic is beyond the scope of this paper the interested reader is kindly referred to [12] for details.

Specific treatment of stable nuclides

As mentioned before, Equation (2) provides an analytic closed-form solution to the Bateman equations. Yet, some attention has to be paid during the implementation because the sub-expression describing the build-up of new nuclides:

$$\frac{P_i^k(1-e^{-\lambda_j t_{k,irr}})e^{-\lambda_j t_{k,cool}}}{\lambda_j \prod_{\substack{p=i \\ p\neq j}}^{n}(\lambda_p-\lambda_j)} \tag{3}$$

can become indeterminate $\left(\frac{0}{0}\right)$ if $\lambda_j = 0$, which is the case for stable nuclides. Commonly text-books on radiation physics address Bateman's equations in a simplified way and exclude the production term illustrated in Equation (3). Thus, they inherently avoid the need to address the problem of indeterminate terms. If the chain is not followed down to the last stable element or if only activity values (A = λN) instead of nuclide concentrations are of interest, this issue will most of the time go unnoticed as the activity of a stable isotope can directly be set to zero. Clearly, a numerical work-around can be found by artificially introducing an extremely small decay constant and thus approximating the calculation at the end of each decay chain. Yet, this somehow defies the idea of finding an accurate and generic solution that can be analytically calculated. Thus, we attempted to find a fully analytic solution which specifically treats the indeterminate case. The actual problem to be solved is given by:

$$\lim_{\lambda_j\to 0}\frac{P_i\left(1-e^{-\lambda_j t_{irr}}\right)e^{-\lambda_j t_{cool}}}{\lambda_j\prod_{\substack{p=i\\p\neq j}}^{n}(\lambda_p-\lambda_j)} = \lim_{\lambda_j\to 0}\frac{\frac{\partial}{\partial\lambda_j}\left(P_i\left(1-e^{-\lambda_j t_{irr}}\right)e^{-\lambda_j t_{cool}}\right)}{\frac{\partial}{\partial\lambda_j}\left(\lambda_j\prod_{\substack{p=i\\p\neq j}}^{n}(\lambda_p-\lambda_j)\right)} \tag{4}$$

A thorough mathematical treatise can be found in [13]. For reasons of conciseness only the final result will be shown. Consequently, for the full analytic solution which also circumvents indeterminate sub-terms for the calculation of stable nuclide concentrations one obtains:

$$N_n(t) = \sum_{k=1}^{m}\sum_{i=1}^{n}\left[\left(\prod_{j=i}^{n-1}\lambda_{j,j+1}\right)\sum_{j=i}^{n}\left(\frac{N_i^k e^{-\lambda_j(t_{k,irr}+t_{k,cool})}}{\prod_{\substack{p=i\\p\neq j}}^{n}(\lambda_p-\lambda_j)} + \begin{cases}\dfrac{P_i\left(1-e^{-\lambda_j t_{irr}}\right)e^{-\lambda_j t_{cool}}}{\lambda_j\prod_{\substack{p=i\\p\neq j}}^{n}(\lambda_p-\lambda_j)} & \lambda_j\neq 0\\ \dfrac{P_i\, t_{irr}}{\prod_{\substack{p=i\\p\neq j}}^{n}\lambda_p} & \lambda_j = 0\end{cases}\right)\right] \tag{5}$$

This analytic solution has been fully implemented in ActiWiz and can be used to calculate the time evolution of nuclide inventories for scenarios either directly included in ActiWiz, which are based on FLUKA calculations of generic cases, or external source terms originating from other Monte Carlo codes or measurements. Subsequent convolution with either legal limits (Swiss exemption limits, Swiss authorisation limits [5],

French exemption and clearance limits) or various activity to dose conversion factors (ambient dose equivalent, effective dose e(50) for inhalation and ingestion following ICRP 72) is provided. The code automatically identifies predominantly contributing isotopes and generates plots for gamma emission spectra (without correction of self-absorption) and the respective photon dose contribution. For the scenarios directly comprised by ActiWiz, a detailed analysis is carried out to identify the chemical element from which the respective nuclides are produced. The contribution is quantified which eventually allows for a sensitivity study of materials with respect to trace elements and impurities.

Shielding of activated material

At one point activated material typically needs to be separated from its surroundings and in addition may require transportation. In order to assess the required shielding thickness for these operations, one has to define the desirable attenuation that should be achieved and the shielding material to be used. The determination of the shielding dimensions can be done either by applying deterministic formulas or Monte Carlo simulations. Each of these approaches has its advantages as well as trade-offs. Monte Carlo simulations generally yield high precision as they take all secondary radiation effects into account, but they are very time consuming to set up and often entail considerable computation time. Deterministic assessment requires taking material and energy dependent attenuation and build-up factors into account. This can be done easily for simple cases (e.g. ^{137}Cs calibration source) where there is only one predominating energy-component and when the build-up is neglected for reasons of simplicity. However, in the environment of a particle accelerator one is usually confronted with activated material showing a broad energy spectrum of emitted radiation (mainly gamma radiation) that needs to be shielded (see Figure 1).

In general, the dose D caused by a point source at a certain distance d within a medium of thickness r can be expressed as:

$$D(d,r) = D(d = 1m, r = 0m)\, B(E,r) \frac{e^{-\mu(E)r}}{d^2} \tag{6}$$

with $\mu(E)$ describing the energy dependent attenuation coefficient and B being the dose build-up factor that in turn depends on the photon's energy as well as the shielding thickness. For shielding assessments the problem is usually formalised in view of a relative dose reduction (e.g. 1/10 of the original dose) for a given distance when placing a shielding material in between the radioactive object and the location of potential radiation exposure. Using the relative attenuation, the dependence on the distance between the source and the point of interest is implicitly considered. Therefore, Equation (6) can be re-written by introducing a relative dose-reduction factor A and a quantity C, denoting the relative contributions of the different photon energies to the total dose:

$$A = \sum_{i=1}^{n} C_i\, B_i(E_i, r) e^{-\mu_i(E_i)r} \tag{7}$$

In order to calculate the required shielding thickness to achieve the dose reduction factor A one would need to solve this equation for the variable r. The difficulty lies on one hand in the fact that the sum on the right might span over thousands of terms and that at the same time the build-up factor depends on the variable r as well. Using the logarithm to solve for r does not work as there is no simple mathematical expression for the logarithm of sums in contrast to the logarithm of products.

Figure 1. Exemplary photon emission spectrum of an activated electronic circuit board comprising 60176 different gamma lines originating from 1308 isotopes

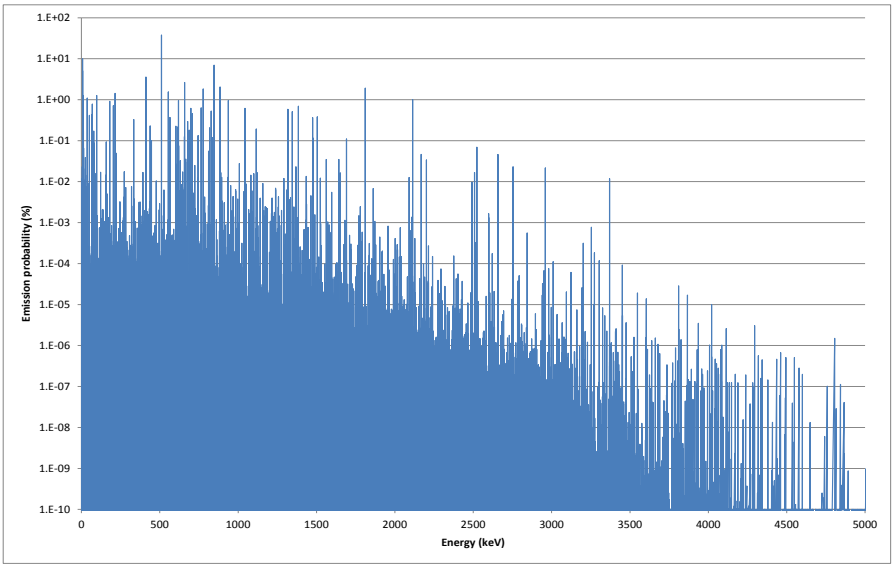

It is obvious that for such cases accurate assessment by deterministic methods requires the use of computational methods. One possible solution would be to first express the build-up factor B with an analytical approximation following the so-called "geometric progression form" as suggested in [14]. This expression is computationally rather complex and involves time consuming functions like the evaluation of the hyperbolic tangent. In order to save computation time for typical shielding materials like iron, concrete or lead the expression has been pre-calculated and tabulated [15] as a function of the energy as well as the so-called relaxation length R, which is equivalent to the mean-free path.

The solution implemented in ActiWiz generates specific build-up factor tables, which match the whole ensemble of photon energies emitted by the activated material. This is done on-the-fly by calculating two subsequent interpolations of tabulated build-up factors taken from [15]. The first interpolation is conducted with respect to the photon energy. It is followed by a second interpolation with respect to the relaxation length of a given photon in the shielding material. These tables are then used to express the build-up factors in Equation (7) as functions of the shielding thickness r only. The resulting expression is numerically solved for r by iterative evaluation and bisection based root-finding methods. The shielding materials available within ActiWiz currently comprise aluminum, concrete, iron, lead, water and tungsten. In addition to determining shielding dimensions for a desirable attenuation factor the user can also directly obtain graphs of attenuation curves as a function of the shielding thickness for the respective radionuclide mixture. Figure 1 shows an exemplary photon emission spectrum of an activated electronic circuit board which exhibits more than 60.000 discrete photon energies. In order to shield this equipment, an exemplary iron shielding (ρ = 7.8 g/cm^3) has been envisaged and the corresponding attenuation curve calculated by ActiWiz is shown in Figure 2. The curve contains 100 different data points and the calculation took about 1 second on a medium-level desktop PC (Intel i7-2600, 3.4 GHz), which can be considered as sufficiently fast for this rather complex example.

Figure 2. Exemplary attenuation curve of an iron shielding enclosing the activated electronic circuit board for which the photon emission spectrum illustrated in Figure 1 has been determined

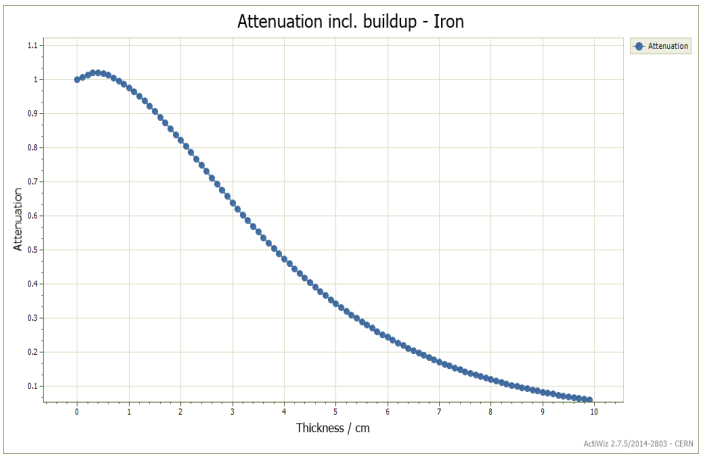

Benchmark of the shielding calculations

The actual performance of the calculations should not be judged only in terms of runtime but also in terms of accuracy and therefore, validation of the results is of highest importance. Comparisons of the estimates obtained by ActiWiz have been conducted with respect to Nucleonica [16] as well as the Monte Carlo code FLUKA. Nucleonica is a well-established toolkit used in the nuclear industry, which is based on internationally validated nuclear data. Within its wide selection of tools it contains a dosimetry and shielding calculator ("Dosimetry and Shielding++") which also uses a deterministic method to assess shielding dimensions. Therefore, the results can be directly compared to ActiWiz and the benchmark is eventually complemented by a comparison to a Monte Carlo based assessment conducted with FLUKA. In order to compare the different codes it has been decided to determine the shielding thickness required for an attenuation to 1/10 of the original dose rate.

Comparison of ActiWiz and Nucleonica

The selection comprised ^{137}Cs (dominant gamma line at 662 keV) as well as ^{60}Co (dominant gamma lines at 1.17 MeV and 1.32 MeV) as well as a complex nuclide mixture called "Fukushima" which is provided by Nucleonica on their web portal [16]. In order to increase the level of complexity in the comparison the nuclide mixture "Fukushima" has been used in two different scenarios. On one hand, the original nuclide set has been considered to be shielded and on the other hand, Nucleonica as well as ActiWiz independently calculated the time evolution of this mixture for a period of 1 month to also include daughter products originating from decay chains in the shielding assessment. The results of all comparisons are illustrated in Figure 3.

As can be seen in Figure 3, the results of both codes are in very good agreement. One has to keep in mind that most probably there are differences in the numerical algorithms that have been used in the two codes as well as in the nuclear data set of the gamma lines. Nucleonica uses the JEFF-3.1.1 library, whereas the gamma library used in ActiWiz was custom-built. It is primarily based on ENDF/B-VII.1, which has been found to be the most complete collection, containing information of over 70.000 gamma lines, and complemented, with information on missing radionuclides obtained from JEFF-3.1.1, JEF-2.2 and JENDL-FPDD2000. In total 101539 single gamma lines are contained in this merged data set. The most notable differences have been found in the comparison considering the "Fukushima" nuclide mixture including daughter products after one month of exemplary decay. One can see that these deviations are larger than the

comparison involving the "Fukushima" nuclide set without daughter products. Yet, perfect agreement is found also in this case for iron or concrete shielding. This suggests that there could be small differences in the data sets that are used to describe the respective decay chains or small deviations in the assumed material density as ActiWiz generally suggests lower values for uranium. However, the differences vary only between 3-6%, which can be considered as good agreement.

Figure 3. Ratio of the shielding thickness calculated by ActiWiz versus the results obtained from Nucleonica to reach 1/10 of the original dose for various materials and radiation sources

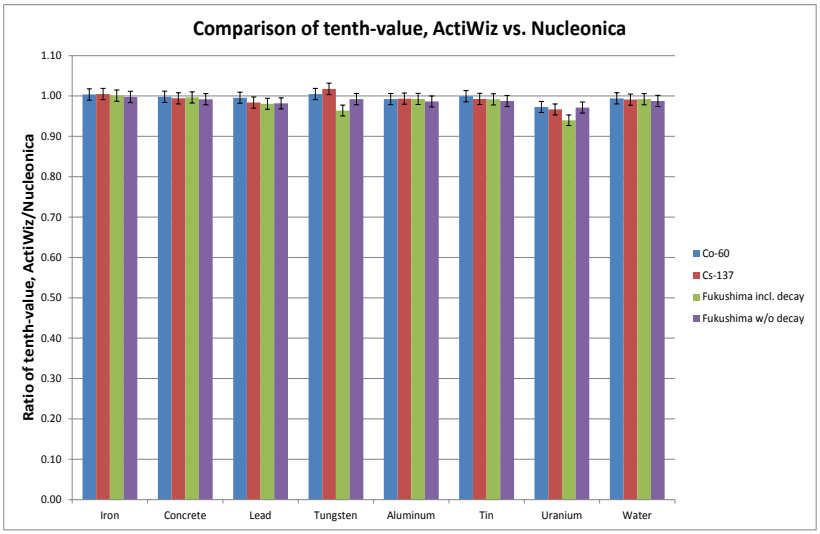

Comparison of ActiWiz, Nucleonica and FLUKA

In contrast to Monte Carlo simulations deterministic calculations of shielding, dimensions must account for the so-called radiation build-up effect in an approximated way. This correction should include indirect contributions due to in-scattering effects that usually can occur in scenarios involving massive shielding. These effects would increase the actual dose rate encountered at a detector in addition to line-of-sight contributions originating directly from the radiation source. It is important to keep in mind that the actual build-up depends on parameters like shielding thickness and extension, distance between shielding and source, distance between shielding and detector and the actual detector size. As the correction function utilised in deterministic assessments cannot fully account for all varieties of these details one can expect to have deviations from Monte Carlo simulations which are conducted for a specific geometric set-up. The actual situation that has been considered in the FLUKA Monte Carlo simulation is illustrated in Figure 4.

For typical shielding materials like iron, lead and concrete the tenth-value shielding thickness d, being pre-calculated with ActiWiz, has been used to calculate the dose attenuation for the given set-up with FLUKA. This result has then been extrapolated back to obtain an estimation for a FLUKA calculated tenth-value shielding thickness. The comparison to the tenth-values calculated by ActiWiz and Nucleonica is given in Table 1.

Figure 4. Set-up of the shielding calculation conducted with FLUKA

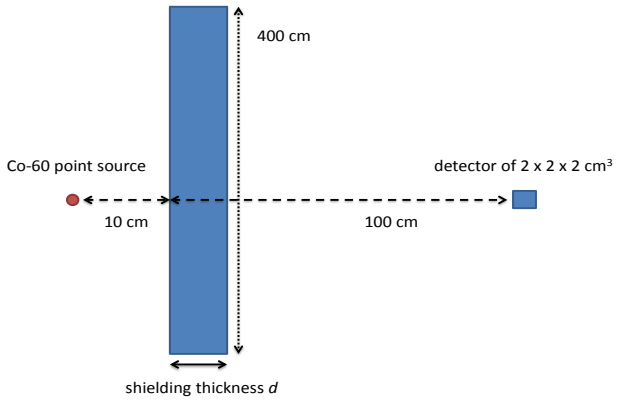

Table 1. Tenth-value dimension calculated by ActiWiz, Nucleonica and FLUKA for different materials

Material	ActiWiz/cm	Nucleonica/cm	FLUKA/cm	ActiWiz – FLUKA Δ/cm
Iron (ρ = 7.8 g/cm^3)	9.9	9.9	8.2 +/- 2%	1.7
Concrete (ρ = 2.4 g/cm^3)	30.5	30.5	26.0 +/- 2%	4.5
Lead (ρ = 11.3 g/cm^3)	5.0	5.0	4.6 +/- 3%	0.4

The uncertainty from the Monte Carlo simulation reflects solely the statistical fluctuations and does not consider any differences which could originate due to different nuclear data sets.

As shown in Table 1, the deterministic calculations of ActiWiz and Nucleonica would predict a slightly thicker shielding required for achieving an attenuation level of 1/10. The actual differences range from 0.4 cm of lead over 1.7 cm of iron to 4.5 cm of concrete, which is equivalent to 10-20% in terms of the respective total thickness. These deviations can be understood keeping in mind that the build-up factor in the deterministic calculations is approximated by a "one-size-fits-all" function, which conservatively tries to cover different geometric set-ups. As a consequence, the results might be slightly overestimated for some cases in contrast to a Monte Carlo simulation which can mimic the actual scenario by tracking particle trajectories through a full geometry. However, this flexibility and accuracy comes at the cost of speed and requires significantly more calculation time that can differ by several orders of magnitude. In general, the comparison between the deterministic solutions of ActiWiz and Nucleonica and the stochastic solution of FLUKA for a defined geometry yields reasonable agreement. In conclusion, the validation of the deterministic algorithms can be considered successful.

Summary and conclusions

The ActiWiz code has originally been developed at CERN for easy and quick assessment and comparison of the radiological hazard of materials used in the environment of high-energy accelerators. Due to its foundations on nuclide production terms, extensions have recently been developed which allow for expanding the scope of its application also to the field of operational radiation protection. An isotope build-up and decay engine has been developed to calculate nuclide inventories for arbitrary irradiation- and cooling period patterns. Automatic analysis of the dominating contributors to various quantities like radiotoxicity, clearance levels, photon dose-rate, gamma emission spectra etc. is

provided. The utilised initial nuclide inventories, including radioisotope production terms, can either originate directly from ActiWiz, from Monte Carlo codes like FLUKA, PHITS, MARS and MCNP or from gamma spectroscopy measurements. In this paper, details on the mathematical derivation of the implemented algorithms to calculate the time evolution of nuclide inventories are given, including also some numerical considerations.

Often activated material also needs to be transported. The appropriate shielding requirements, including photon dose build-up, can be calculated with ActiWiz within a few seconds even for large nuclide sets with many thousands of gamma lines. An overview of the implemented deterministic calculation method is provided and successful benchmark comparisons to another deterministic code (Nucleonica) as well as the FLUKA Monte Carlo code have been performed.

Acknowledgements

The authors would like to thank Stefan Roesler and Eduard Feldbaumer for stimulating discussions and the review of the Technical Notes which led to this paper. We would also like to express our gratitude to Joseph Magill from Nucleonica GmbH for fruitful discussions on the topic of shielding and Matthias Karacson for the meticulous review of this manuscript.

References

[1] H. Vincke, C. Theis (2013), "ActiWiz – optimizing your nuclide inventory at proton accelerators with a computer code", *Proceedings of the ICRS12 conference, 2012, Nara, Japan, Progress in Nuclear Science and Technology*.

[2] A. Fassò, A. Ferrari, J. Ranft, P. Sala (2005), "FLUKA: a multi-particle transport code", *CERN Yellow Report*, INFN/TC_05/11, SLAC-R-773.

[3] G. Battistoni et al. (2007), "The FLUKA code: Description and benchmarking", *Proceedings of the Hadronic Shower Simulation Workshop 2006, Fermilab 6--8 September 2006, M. Albrow, R. Raja eds.*, AIP Conf. Proc., 896, pp. 31-49.

[4] H. Vincke, C. Theis (2011), "ActiWiz: A computer code to model and assess radiological hazards of activated material", *CERN Technical Note CERN-DGS-2011-067-RP-TN*, CERN.

[5] suvaPro (2009), "Schweizer Strahlenschutzgesetz vom 22.3.1993 (StSG), Strahlenschutzverordnung vom 22.6.1994 (StSV), Stand 1.

[6] H. Bateman (1910), "Solution of a system of differential equations occurring in the theory of radioactive transformations", *Proc. Cambridge Philos. Soc. 15,* pp. 423-427.

[7] A. Koning et al. (2009), "The JEFF-3.1.1. nuclear data library", *JEFF Report 22*.

[8] K. Skrable et al. (1974), "A general equation for the kinetics of linear first order phenomena and suggested applications", *Health Physics, 27,* pp. 155-157.

[9] J. Cetnar (2006), "General solution of Bateman equations for nuclear transmutations", *Ann. Nucl. Energy* 33, pp. 640 – 645.

[10] R. Dreher (2013), "Modified Bateman solution for identical eigenvalues", *Annals of Nuclear Energy* 53, pp. 427 – 438.

[11] W. Kahan (1965), "Further remarks on reducing truncation errors", *Communications of the ACM 8 (1)*: 40, http://doi:10.1145/363707.363723, (1965).

[12] C. Theis, H. Vincke (2014), "Floating point considerations for ActiWiz 3", *CERN Technical Note,* CERN-RP-2014-016-REPORTS-TN, EDMS 1363729.

[13] C. Theis, H. Vincke (2014), "Addendum to the build-up and decay engine in ActiWiz", *CERN Technical Note,* CERN-RP-2014-017-REPORTS-TN, EDMS 1363771.

[14] D.K. Trubey (1988), "New Gamma-Ray Buildup Factor Data for Point Kernel Calculations: ANS-6.4.3 Standard Reference Data", ORNL-RSIC 49.

[15] ANSI/ANS, American National (1991), "Standard for Gamma-Ray Attenuation Coefficients and Buildup Factors for Engineering Materials", ANSI/ANS-6.4.3-1991.

[16] Nucleonica GmbH, Dosimetry and Shielding (2011), "Nucleonica Nuclear Science Portal (www.nucleonica.com)", Version 3.0.06, Karlsruhe, Germany.

A temporary storage for activated UCx targets at SPES

Lucia Sarchiapone, Demetre Zafiropoulos
Laboratori Nazionali di Legnaro, INFN, Italy

Abstract

SPES (Selective Production of Exotic Species) is a project of the INFN (Istituto Nazionale di Fisica Nucleare) for the production of radioactive ion beams, through direct irradiation of a fissile target with high-intensity proton beams. The irradiation of the uranium carbide target with protons at 40 MeV energy and 200 μA current during an irradiation cycle of two weeks causes an activity of approximately 10^{14} Bq. Less than 5% of the total activity is due to species of half-lives longer than one month. The replacement of the target takes place at each irradiation shift, ideally once per month, taking into account two weeks of irradiation and two weeks for the facility set-up. For the first years of operation, a temporary storage will host the exhausted targets. This work presents the evaluation of the residual dose rate due to the presence of several irradiated targets in order to design the needed shielding for the storage area and to allow the access nearby. The simulations have been performed with the FLUKA Monte Carlo code.

Introduction

SPES (Selective Production of Exotic Species) is an INFN project to develop a Radioactive Ion Beam (RIB) facility as an intermediate step towards EURISOL (European Isotope Separation On Line). The capability to obtain a RIB of interest for nuclear physics is supported by the presence at LNL (Laboratori Nazionali di Legnaro) of a superconducting linac, able to re-accelerate exotic ions at 8-13 MeV/u.

The RIB is a neutron-rich beam of fission fragments with a fission rate in the target of 10^{13} fissions per second, achieved through the interaction of a proton beam of 40 MeV energy and 0.2 mA current with a target of uranium carbide (production target) [1]. A 70 MeV-0.75 mA cyclotron, actually under construction by Best Cyclotron Systems, Inc. delivers the proton beam.

The production target is irradiated for 12 days and then replaced by a new one. A small area close to the irradiation bunker is being equipped to host up to 44 irradiated targets, conveniently located in lead boxes. Once this temporary storage is full, targets will be moved to their final destination as waste. The temporary storage area is not directly accessible but borders on a passageway classified as a controlled zone. This work presents the evaluation of the shielding thickness required in order to keep the ambient equivalent dose rate below 0.5 μSv/h in the accessible corridor. The evaluation has been performed with Monte Carlo simulations, using the FLUKA code [2,3].

Production target

The production target consists of multiple thin disks housed in a cylindrical graphite box. This geometry increases the body surface in order to optimise the target cooling. In fact,

the target in a low-pressure environment, the heat due to electromagnetic and nuclear interaction will be dissipated by radiative thermal transfer, directly proportional to the body surface. The disks have 40 mm diameter and 1 mm thickness.

Figure 1 shows the multifoil target as implemented in the Monte Carlo geometry in order to simulate the proton-induced fission process, including the graphite container and the dumping disks.

Figure 1. The SPES production target as implemented in the Monte Carlo geometry

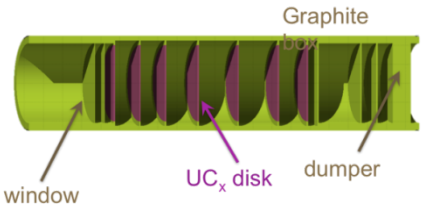

The irradiation of the target lasts 12 days with a total of 10^{21} protons on target per shift and 10^{19} fissions induced. At the end of the irradiation cycle, the radioactivity in the target amounts to around 1 kCi, whose distribution according to the half-life of the products can be seen in Figure 2.

Less than 3% of the total activity is due to species with half-life longer than 1 month and 2% longer than 10 years.

Simulation set-up

In order to simulate the storage of a target after an irradiation cycle, and to evaluate the gamma ambient equivalent dose rate only due to radioactive decay, the capability of FLUKA has been exploited to assign a material to a certain region during irradiation and to change material during decay.

In the present case the target has been placed in the lead box, as it will be performed after an irradiation for storing it, and located in the dedicated area of the storage (the green area in Figure 3, not the yellow one where the irradiation should take place). The volume between the target and the lead box is set to “blackhole” and the irradiation of the target with the proton beam is started. In this simulation phase, all the nuclear and electromagnetic interactions take place but secondary particles do not escape the system because as soon as they leave the target they meet the blackhole.

In this situation the target is activated but the surrounding materials are not, the irradiation is over and the volume between the target and the lead box is switched to air, so that the particles released during the decay can be transported outside and the dose rate in the area of interest can be evaluated.

Figure 2. Distribution of the target activation products as a function of the half-life

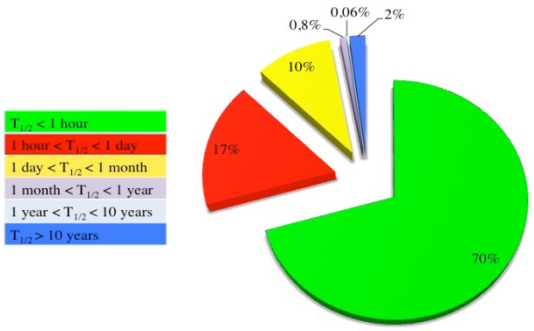

Figure 3. Layout of the SPES Facility (re-acceleration line not included)

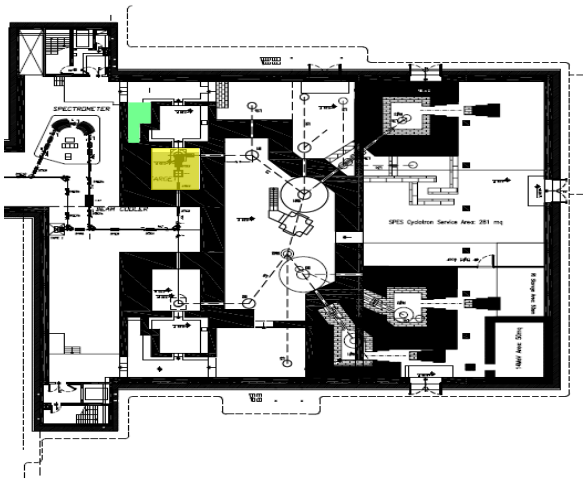

The irradiation bunker is highlighted in yellow and the storage area in green.

Results

The gamma dose rate in correspondence with the passageway is about 300 uSv/h (as indicated by the position of the man in Figure 4), and the photons contributing to this dose rate have an energy in the range of 0.3-3 MeV. In order to fulfill the radiation protection constraints for controlled areas (0.5 uSv/h), a standard concrete wall 70 cm thick must be provided. This allows a dose rate reduction of a factor 10^3 [4].

Furthermore, the configuration of the whole storage filled with targets was studied. To do this, 44 separate simulations were run, one for each target stored. Some preliminary considerations have to be clarified: before being placed in the storage, the irradiated target remains in its position for 14 days.

The targets will be automatically moved from the irradiation cave to the storage area. Once there, a lift will be able to place each target in a dedicated location in a rack.

After a few targets have been stored, their positions will be exchanged so that the furthest position from the passageway will always be free for the most active target in order to take advantage of the shielding effect by the other target boxes.

The results of this study are shown in Figures 5 and 6. All the available positions have been filled with targets, and the most active is in the furthest position. The dose rate in the passageway in this configuration is below 50 uSv/h, and a reduction of a factor 100 must be achieved. A standard concrete wall 50 cm thick will be sufficient to prevent a dose rate of 0.5 uSv/h where personnel can access.

After the first one or two irradiation cycles, shielding the exhausted targets with some empty lead boxes might be considered (they do not need to be prepared specially as they will be used for future targets). As shown in Figure 7, the dose rate at the desired position is about 50 uSv/h, similar to the "full rack" configuration and the shielding wall can be kept as thin as 50 cm.

Figure 4. Gamma dose rate (uSv/h) at the end of an irradiation cycle

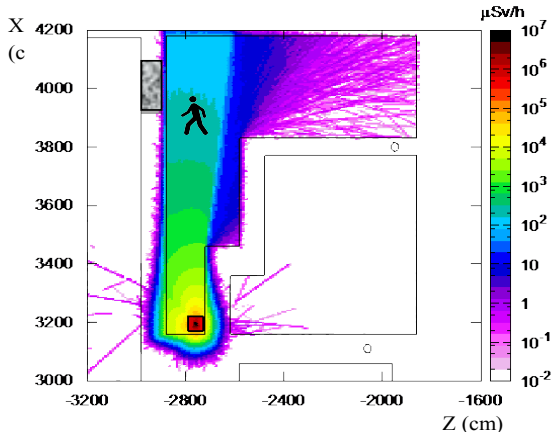

Figure 5. Gamma dose rate (uSv/h) due to 44 stored irradiated targets (aerial view)

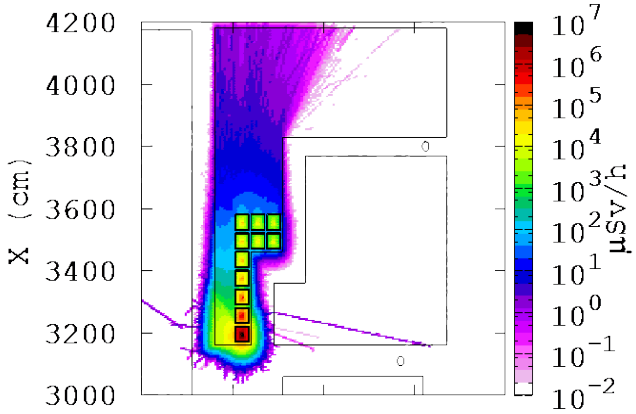

Figure 6. Gamma dose rate (uSv/h) due to 44 stored irradiated targets (side view)

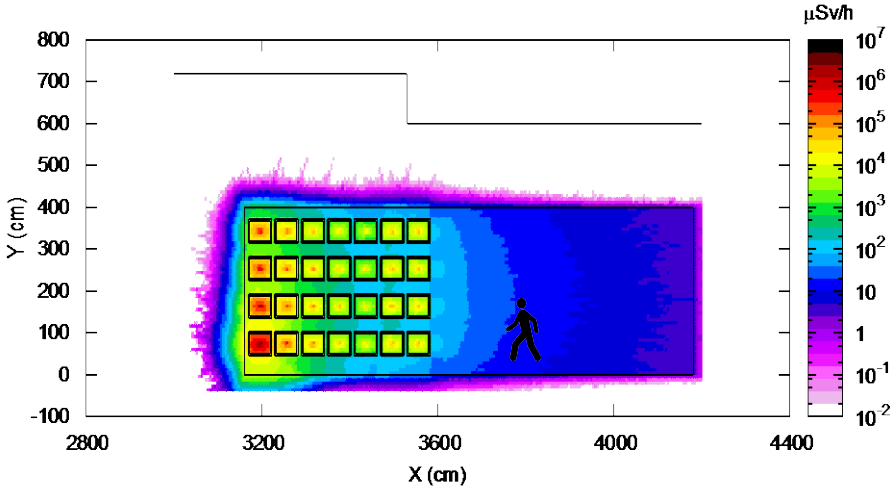

Figure 7. Gamma dose rate (uSv/h) at the end of an irradiation cycle

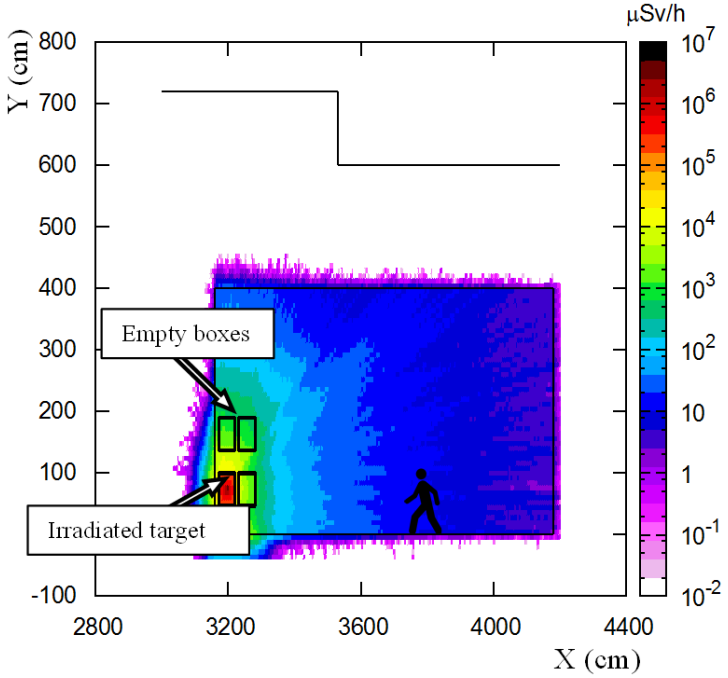

The irradiated target is shielded by some empty lead boxes (side view).

Conclusions

The schedule of the SPES project foresees the irradiation of an uranium carbide target for 12 days and a cooling time of two weeks before the start of a new irradiation cycle. The irradiated target is then placed in a lead box 2.5 cm thick and temporarily stored in a dedicated area close to the bunker, where a rack hosting up to 44 targets is installed.

Due to space restrictions, an accurate evaluation of the dose rate at a certain distance from the targets was needed in order to design an adequate shielding wall. The temporary storage, in fact, borders on a passageway with controlled access of personnel.

It has been seen that a single target, at the end of an irradiation cycle, causes a dose rate higher than 300 uSv/h at the distance of 6 metres. When the storage is completely filled with targets, the dose rate at 6 metres distance drops to less than 50 uSv/h, due to the fact that the targets shield each other.

Considering the full configuration as source term to design the shielding wall would cause an underestimation of the dose rate in the first operation cycle and this could lead to an overexposure of personnel passing through the corridor nearby. In order to keep both the wall thickness reduced and the dose rate as low as 0.5 uSv/h in controlled areas, it has been decided to shield the first irradiated target deposited in the storage with some empty lead boxes, taking advantage of the lead as shielding. In this scenario a concrete wall 50 cm thick will be sufficient to meet the radiation protection constraints in the corridor.

Acknowledgements

This work has been prepared together with the SPES Target Group, which we would like to acknowledge. They designed the storage rack and shared with us the details of the target handling system.

References

[1] G. Prete, A. Covello (2008) “SPES Technical Design Report”, INFN-LNL-223.

[2] G. Battistoni et al. (2007), “The FLUKA code: Description and benchmarking” *Proceedings of the Hadronic Shower Simulation Workshop 2006, Fermilab 6-8 September 2006, AIP Conference Proceeding* 896, 31-49.

[3] A. Ferrari et al. (2005), “FLUKA: a multi-particle transport code” CERN-2005-10, INFN/TC_05/11, SLAC-R-773.

[4] ICRP 15 (1969), “Protection against Ionizing Radiation from External Sources”, ICRP 21 (1971), “Data for Protection against Ionizing Radiation from External Sources”.

Shielding and activation studies for the ELI-beamlines project

Alberto Fasso[1], Anna Ferrari[1,2], Georg Korn[1], Roberto Versaci[1]
[1]ELI-Beamlines, Czech Republic
[2]Helmoltz-Zentrum Dresden-Rossendorf, Germany

Abstract

ELI-beamlines is one of the four pillars of the Extreme Light Infrastructure, a European ESFRI Project, for the next generation of high-energy and high-intensity lasers. It aims at the development of high-brightness sources of X-rays and the acceleration of proton, electron, and ion beams, to be used both for pure research and practical applications. Aiming at a proper radiation protection assessment, for both shielding and activation, extensive FLUKA simulations have been performed, taking into account the laser high repetition rates. The present work, which is the continuation of the calculations presented at SATIF-10, is the first one based on the design of the facility being constructed and on the updated experimental set-up.

Introduction to the ELI Project

The Extreme Light Infrastructure ELI project [1] is part of a European plan, by the European Strategy Forum for Research Infrastructures, ESFRI, to build a new generation of large research laser facilities. The main goal is to achieve ultra-short laser pulses of a few femtoseconds and power of 10 PW. ELI will be operated as a European Research Infrastructure Consortium, ERIC, and will have four facilities: the one whose construction status is the most advanced is ELI-Beamlines in the Czech Republic, the other facilities are ELI-Attosecond in Hungary and ELI-NuclearPhysics in Romania, plus a fourth facility whose location still has to be decided.

Due to the high intensities and short pulses, ELI-Beamlines will provide laser-driven particle beams of both protons having energy up to 3 GeV, and electrons having energy up to 50 GeV. This will allow investigation on a wide range of topics, including accelerator science, plasma physics, material science, etc.

Such energetic beams, which can have repetition rates up to 10 Hz, require a careful and precise assessment of possible radiation protection issues, including prompt dose radiation level in the experimental halls and activation of experimental devices.

We have assessed these issues evaluating the significant quantities by means of FLUKA simulations [2,3]. Also using simulations, we have started working on the modelling of some of the devices that will be installed on the beamlines. Here, we present the preliminary work on the beam dump for the E2 beamline and on the activation of various materials whose use is being envisaged.

Beamlines parameters and FLUKA model

The evaluation of the prompt dose level for each of the ELI's beamlines and for each operation mode would be a massive and very long task, therefore we have focused ourselves on those lines that would be of more concern from the radiation protection

point of view, because of the beam energy and of the repetition rate, namely ELIMAIA, LUX, and HELL, whose parameters of interest are reported in Table 1. Unfortunately, at the time this work started, the design of these lines was not completed, therefore, for the first round of simulations, very simplified models were used. These models did not account for the beam collimation before the dump, resulting in beams with very large divergence (up to 20 degrees). For each of the three beamlines, we have also used a single model for the beam dump which was not subject to any optimisation. For these cases, the dumps were modelled as cylindrical with an hole on the front face to contain the beam and reduce the backscattering, the front face was made of borated polyethylene, the core was made of graphite and was surrounded by iron; the dimensions were 1.3 m in radius and 4 m in length. Whenever no detailed information was available, conservative assumptions were made, therefore all the doors were removed and all the penetrations were empty.

Table 1 shows the parameters for the E2 beamline. This is the beamline whose development is in the most advanced state and for which the work for the optimisation of the beam dump has already started. The beam in E2 could be operated in a non-monochromatic mode, therefore, because of the presence of a spectrometer, the beam will be deflected over a large angle and the beam dump could not simply be a massive cylinder, but a more complex shape is required.

A very large FLUKA geometry is needed for all these simulations: the six experimental halls of ELI-beamlines will be located in the basement of the building, whose dimensions are roughly 80 m x 130 m x 8m. The model for a so large geometry has been prepared devoting particular care to the geometrical details of the penetrations. Each experimental hall will have many penetrations, mainly, but not only, due to the needs of the laser transport. Radiation escaping through the penetration could have effects in nearby rooms, which is one of the subjects of our investigations. A picture of the FLUKA model used for the simulations can be seen in Figure 1.

Table 1. Parameters of the beamlines considered for the simulations

Beamline	ELIMAIA	LUX	HELL	E2
Particles type	Protons	Electrons	Electrons	Electrons
Maximum energy	250 MeV	2 GeV	10 GeV	1 GeV
Repetition rate	1 Hz	10 Hz	1 Hz	10 Hz
Pulse charge	160 nC	1 nC	0.1 nC	500 pC
Particles per pulse	10^{12}	6.2×10^{9}	6.2×10^{8}	3.1×10^{9}

Figure 1. Three-dimensional view of the FLUKA model used for the simulations

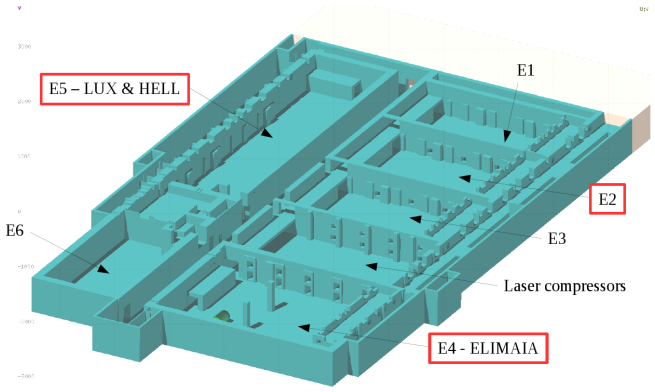

The experimental halls and laser compressor rooms are visible. The whole structure is made of concrete. A single dummy placeholder is used for additional service rooms. The building is oriented such that rooms from E1 to E4 are aligned on an axis pointing from east to west. This image and all the following, have been produced using the FLUKA graphical interface [4].

Prompt dose results

ELIMAIA beamline

The results of the ELIMAIA simulations have shown that neglecting the beam collimation before the beam dump, therefore having a very large hole on the front face of the dump, has two effects. First, it implies a large radial dimension of the shower generated inside the dump, second, it produces a large amount of backscattered particles. These effects are clearly indicated by the presence of three lobes in Figure 2, which shows the $H^*(10)$ value at the beam height, i.e. 1.3 m from the floor. The same pattern is also present in the simulations for LUX and HELL beamlines.

The experimental hall will not be accessible during beam operation (this holds for any beamline in ELI), therefore the high value of $H^*(10)$ is of limited concern. The laser compressor rooms, west of the E4 experimental hall, will not be accessible during operations either; this means that the radiation entering through the penetration is also of limited concern. The radiation levels in the control room (indicated in Figure 2 by a thick black line) are below 10^{-6} mSv per laser shot. Despite the large number of primaries simulated (148 millions protons), the statistical uncertainty on the $H^*(10)$ value inside the control room is quite high, nevertheless, the $H^*(10)$ pattern leaves us confident that the result is correct within an order of magnitude. We have made vows to achieve smaller uncertainties with future more detailed simulations.

To summarise, assuming 24 hours per day of operation (by large an overestimation of the beam time) at 1 Hz repetition rate, it will take 116 days to integrate 1 mSv, which is the yearly legal limit for the general public, and 2300 days to integrate 20 mSv, which is the yearly legal limit for personnel working in the controlled area.

It should also be noted that because of the penetration above the control room, a higher value of $H^*(10)$ is reached in the service room (with restricted access) behind the control room itself.

Figure 2. H*(10) in the E4 experimental hall and its surroundings during ELIMAIA beam operations at the beam height

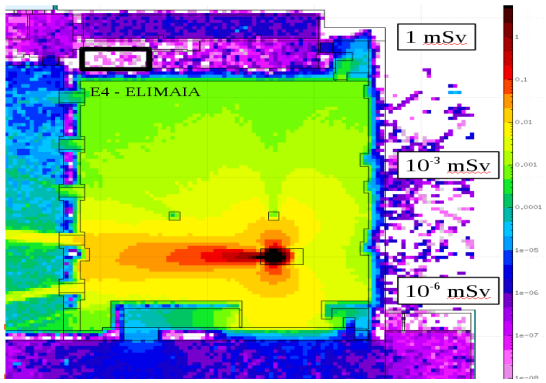

The normalisation is given per laser shot. The location of the control room is indicated by the thick black line. The beam is moving from west to east, i.e. from left to right in the picture.

LUX beamline

The simulation for the LUX beamline (52 millions primaries) has shown results similar to the ELIMAIA ones (see Figure 3). The presence of three lobes indicates that the impinging beam is too spread (backscattering and shower radial dimension). The particles accelerated by LUX are electrons of 2 GeV maximum and 10 Hz repetition rate, resulting in an estimate of 10^{-6} mSv per shot in the control room. Assuming 24 hours per day of operation (overestimate), this implies that, as for ELIMAIA, it will take 116 days to integrate 1 mSv and 2300 days to integrate 20 mSv. The considerations about the statistical significance of the ELIMAIA simulation results can be repeated also for the LUX beamline.

Figure 3. H*(10) in the E5 experimental hall and its surroundings during LUX beam operations at the beam height

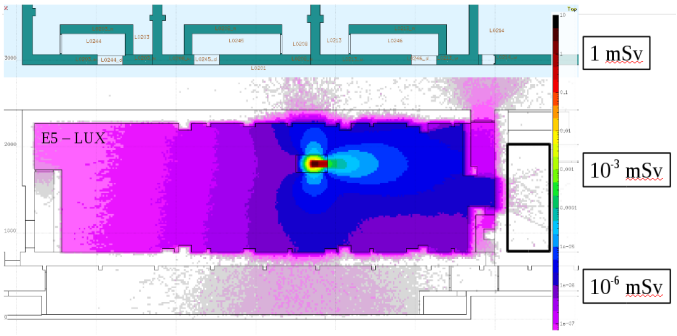

The normalisation is given per laser shot. The location of the control room is indicated by the thick black line. The beam is moving from east to west, i.e. from right to left in the picture.

HELL beamline

The results of the simulation for the HELL beamline, obtained with 10 million primaries and shown in Figure 4, are not too different with respect to those of LUX. Again, three lobes are present describing the same situation about backscattering and shower radial dimension. In this case, the particles accelerated are electrons of 10 GeV maximum and 1 Hz repetition rate. Because of larger distance between the beam dump and control room, 10^{-8} mSv per shot have been estimated in the control room. This implies that, always assuming an overestimate of 24 hours per day of operation, more than 11

thousands and more than 230 thousands days will be necessary to integrate 1 mSv and 20 mSv, respectively. The considerations made before about the statistical significance of the simulation results still hold.

Nevertheless, the simulations indicated an interesting feature of the HELL beamline. A high-energy electron beam can produce muons in the dump via photonuclear reactions. This phenomenon can raise some concerns about the radiological safety of the space outside the experimental hall located behind the dump. Once the experimental set-up of the beamline will be better defined, this problem will be assessed in more detail. To test the reliability of our simulations, we have started working on a benchmark of various Monte Carlo codes with the only experiment that has studied the muon production via photonuclear reaction available in literature [5]; for more details see S. Müller contribution to these proceedings [6].

Figure 4. H*(10) in the E5 experimental hall and its surroundings during HELL beam operations at the beam height

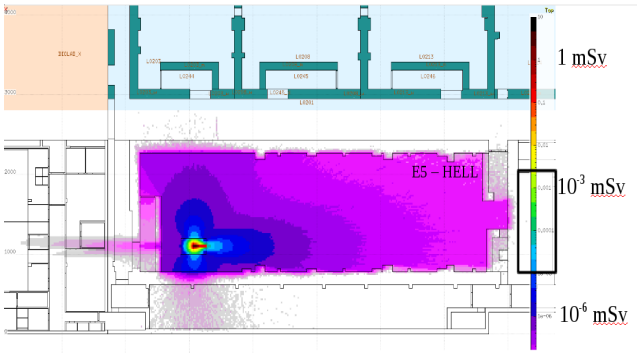

The normalisation is given per laser shot. The location of the control room is indicated by the thick black line. The beam is moving from east to west, i.e. from right to left in the picture.

E2 beam dump

The second part of our work has been devoted to the design of the beam dump for the E2 electron beamline. The beamline will be operated in two different modes: either at fixed energy with maximum beam energy of 1 GeV, or with a widespread momentum. The beamline will include a spectrometer, which, applied to particles of different momenta, will cause the beam to spread over a large angle. This point, together with the geometrical requirement to leave enough leeway for the experiments, implies the beam dump to be quite big (see Figure 5). As seen in Figure 6, two possible operation modes are presented: a beam with exponential energy spectrum having a low energy cut-off at 40 MeV and an almost monochromatic beam with an energy of (1 ± 0.05) GeV. It is evident that the deflected beam spans over a few metres length, requiring a very large dump.

Comparisons of the above operational modes are shown in Figures 6 and 7, which show the primary electron and all-particles fluences, and the ambient dose equivalent rates, H*(10). These plots, each obtained using many tenths of millions of primaries, show that the dump volume can be reduced and the material choice can be optimised in order to reduce the cost of the dump itself. The optimisation work continued after the SATIF-12 conference and the present working model costs about 25% of the one shown during the conference.

Figure 5. Three-dimensional (left) and horizontal (right) view of the working model of the dump for the E2 beamline

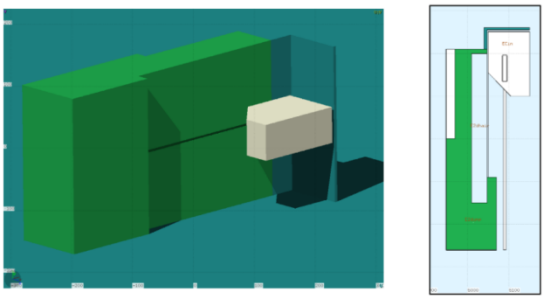

In the three-dimensional view, the experimental chamber and the slit to reduce the backscattering are visible. In the horizontal view are shown both the permanent magnet inside the experimental chamber and the x-rays beam pipe.

Figure 6. Comparison of primary electron particle fluences (arbitrary units) for the exponential and monochromatic operation modes (left), comparison of total particle fluences (arbitrary units) for the exponential and monochromatic operation modes (right)

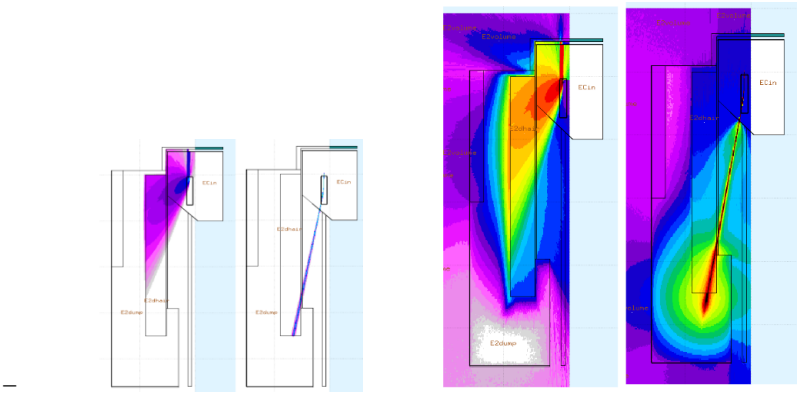

Figure 7. H*(10) in the E2 experimental hall and its surroundings during beam operations at the beam height in the case of exponential beam (left) and (right) of monochromatic beam

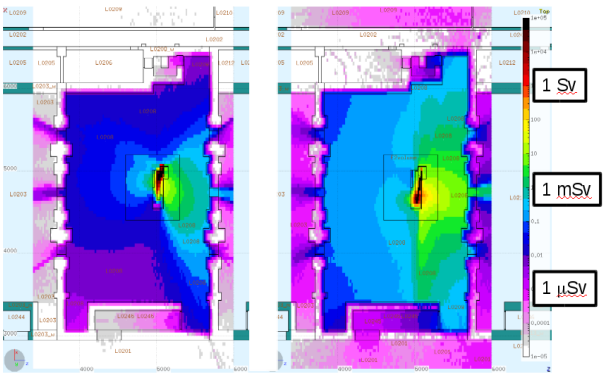

The normalisation is given per 4 hours of operation, which is assumed to be the standard duration of a day of operation.

Activation studies

An important point in the development of the experimental set-ups to be used at ELI, is the selection of the most suitable materials for the experimental chambers. For this purpose, we have started a massive campaign of simulation to study the activation of a wide range of materials irradiated by proton and electron beams of different energies, and prepare a database of material activation. As shown in Figure 8, the ambient dose was illustrated to be equivalent H*(10) at 30 cm from a steel slab irradiated for 1 day with 100 MeV proton beam, as a function of the slab thickness. Also, the activation is reduced if the slab is covered by an aluminium layer.

Figure 8. H*(10) at 30 cm from a steel slab irradiated for one day with a 100 MeV proton beam, after different cooling times and with and without a protective aluminium layer

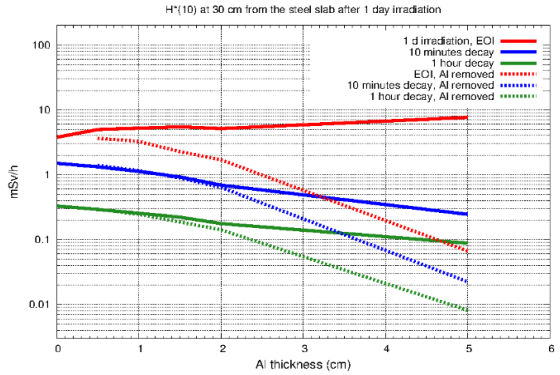

Conclusions

We have introduced the ELI-Beamlines project to the SATIF community. We have given an idea of the size of the project and of the amount of radiation protection work that will be required. We have shown the very first results obtained using the final model of the building. The next step will be to design the experimental set-ups and devices.

References

[1] M. Aleonard et al. (2011), "ELI-Extreme Light Infrastructure; Science and Technology with Ultra-Intense Lasers", *THOSS Media GbmH*, edited by G. A. Mourou, G. Korn, W. Sandner, J. L. Collier.

[2] G. Battistoni et al. (2007), "The FLUKA code: Description and benchmarking", *Proc. Of Hadronic Shower Simulation Workshop, Fermilab 2006*, AIP Conference Proceedins 896, pp. 31-49.

[3] A. Ferrari et al. (2005), "FLUKA: a multi-particle transport code", *CERN-2005-10, INFN/TC_05/11, SLAC-R-773*.

[4] V. Vlachoudis (2009), "FLAIR: A Powerful But User Friendly Graphical Interface For FLUKA", *Proc. Int. Conf. on Mathematics, Computational Methods & Reactor Physics (M&C 2009)*, Saratoga Springs.

[5] W. R. Nelson et al. (1974) "Muon Shielding Around High-Energy electron Accelerators. 2. Experimental Investigation", *Nucl. Instrum. Meth.*, 120, pp. 413-462.

[6] A. Fasso' et al. (2014) "Code intercomparison and benchmark for muon fluence and absorbed dose induced by 14 and 18 GeV electron beams after massive iron shielding", *SATIF-12 Proceedings*.

Comparison of radionuclide activity in the NuMI decay pipe to results from the MARS Monte Carlo

S.D. Reitzner
Fermi National Accelerator Laboratory, US

Abstract

The production of tritium is a radiological concern in the operation of accelerators as it has been shown to be relatively mobile; able to move from one medium to another. Tritium produced in shielding could transfer to the environment under the right conditions. Having a reliable inventory on the amount of tritium that will be produced in the shielding is therefore important. A method of inventory of the radionuclide production in shielding is presented. The activity from radionuclides other than tritium in shielding can be used to benchmark Monte Carlo codes on their accuracy on radionuclide production. The radionuclide activity in samples taken from the NuMI decay pipe shield has been measured and compared to the MARS results for the radionuclide distribution and production in a simple model of the NuMI beamline.

Introduction

Tritium is generated as a by-product of accelerator operation and is a significant radiation protection concern due to its inherent mobility. Whether in an elemental form (HT) or as tritiated water (HTO), tritium has been observed transmitting through materials such as concrete and steel [1-3]. With such mobility, great care must be taken to limit the pathways tritium can use to enter the environment from a beamline complex. Knowledge of the amount of tritium generated in shielding is important to gauge the tritium contamination potential of a beamline complex. Directly measuring the tritium activity in shielding is difficult due to the low beta endpoint energy (20 keV). Indirect methods are subject to inefficiencies in collecting the tritium. The mobility of tritium may result in a measured activity distribution not being reflective of the total tritium that was generated in that region. For future accelerator projects, estimating the amount of tritium that would be produced will be necessary in order to determine what order of tritium mitigation will be necessary.

As an alternative to a direct measurement of tritium activity in shielding, Monte Carlo methods can be employed. In concrete shielding, radionuclides such as ^{7}Be, ^{22}Na and ^{54}Mn are generated in significant quantities but generally remain fixed in place. The activities of these fixed radionuclides may be used to benchmark radiation transport codes for their utility in estimating tritium production in shielding. In this paper, the radiation transport code MARS15 [4,5] is used to demonstrate the utility of Monte Carlo methods for estimating radionuclide activity in concrete shielding. The data to which the MARS results will be compared is presented in the next section followed by the comparison of the data to the MARS results.

Data

In 2006 [6] and 2010, core samples were collected from the decay pipe shield in the Neutrinos at the Main Injector (NuMI) facility at the Fermi National Accelerator Laboratory for the purpose of assessing the tritium activity. The NuMI decay pipe is 675 m in length, has a diameter of 2 m and a shield thickness varying from 2.1 to 3.7 m. The shielding material is a controlled low strength material, also known as flowable fill, a low density concrete. The samples taken for the shielding activity studies were extracted from four different locations in the decay pipe shield. Three of the locations were selected to sample tritium activity at the upstream, downstream and middle of the decay pipe. The fourth location was selected to sample the tritium activity at a different shield thickness at the upstream location. A transition in the shield thickness from 2.86 m to 3.70 m occurs between the two upstream sample locations. At each location, several core samples were collected at different depths into the shield. The core samples were taken no deeper than 76 cm (30") from the outer surface of the shield.

Figure 1 shows the activity of the non-tritium radionuclides as a function of radius from the samples collected in 2010 from the upstream thin shield sample location. The location of the outer edge of the shield is at 286 cm in the figure. The fixed radionuclides, for the most part, have a purely exponential distribution in this region of the shielding. The rise in activity of ^{22}Na and ^{134}Cs near the shield outer surface is due to contamination. These nuclides being able to form water soluble salts are deposited in the outermost layers of the shield from water on the outer surface of the shield.

Figure 1. Activity as a function of radius for various radionuclides in the decay pipe shield

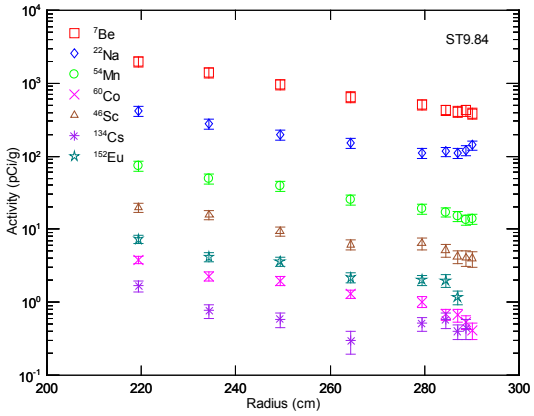

Figure 2 shows the raw tritium activity leached from the core samples as a function of radius for the 2006 (filled squares) and 2010 (open squares) data. The data was collected from the same location as the results shown in Figure 1. The 2006 data show a very pronounced increase in tritium activity at the outer edge of the shield. Large amounts of tritium from the target hall transfer into the moisture laden air and is transported down the decay pipe passageway. The tritium in the air can then transfer into the decay pipe shield. Between 2006 and 2010, dehumidifiers were installed in the target hall to control and collect the tritium that gets in the air. The result can be seen in the 2010 data, where the amount of tritium decreases at the edge of the shield. This figure illustrates the mobility of tritium in mediums like concrete.

Figure 2. Tritium activity in the decay pipe shield as a function of radius for the 2006 and 2010 core samples

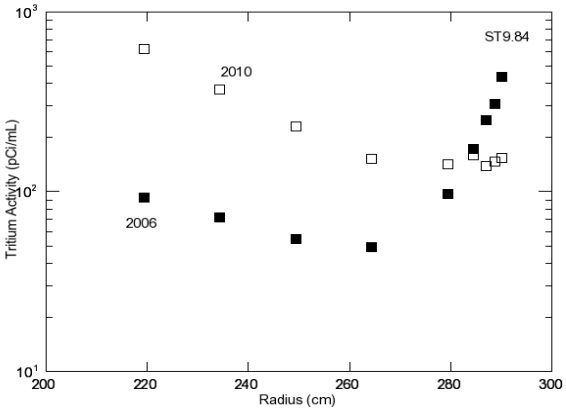

Analysis

The NuMI beam line was modelled using MARS15. Simplified geometry was used to model the shielding in the target hall and decay pipe while detailed geometry was used to model the magnetic focusing horns. The number of nuclides produced per proton was extracted from MARS at a radius greater than 1.7 m in the decay pipe shield. DETRA [7,8] was then used to calculate the radionuclide activity after 375 days, the number of days the 2006 decay pipe shield samples were collected after the start of NuMI operations. The data on the number of protons on target per day for NuMI was input into DETRA for the irradiation profile. In a separate MARS run, the decay pipe shield was subdivided into 3 m longitudinal and 0.2 m radial bins from which the star density distribution was extracted. The star density distribution was used to scale the activity in the decay pipe over a large volume to one representative of the activity seen in a location where a core sample was collected. Figure 3 compares the radial distribution of ^{7}Be activity estimated from MARS (crosses) to the activity seen at the upstream location (diamonds). For the MARS results, only the statistical uncertainties are shown. The ten-fold attenuation length extracted from MARS was found to be 96±4 cm, which is in agreement with the results from the data of 101±5 cm.

Figure 3. Comparison of activity of ^{7}Be as a function of radius between MARS and data

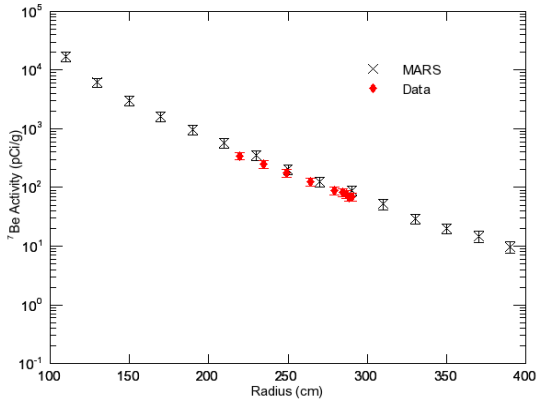

Table 1 shows the activity of the 2006 samples and the MARS predicted activity at the upstream location at a radius of 2.1 m. The results between data and MARS agree to within an error for all but tritium. To eliminate any geometrical effects on the results, Table 1 also lists the ratio of ^{7}Be to the other nuclides. For ^{7}Be/^{22}Na and ^{7}Be/^{54}Mn, the MARS results are in very good agreement with the data. MARS predicts a higher activity for ^{3}H but this is to be expected as not all of the tritium was leached from the core samples. Table 2 shows the predicted fraction of tritium leached (L_{3H}) from the various data sets assuming that MARS makes an accurate prediction of the tritium activity relative to the ^{7}Be activity. The average tritium leaching fraction for all data sets shown is 41%.

Table 1. The measured and predicted activity for various radionuclides found the decay pipe shield

Nuclide	Measured activity (pCi/g)	Predicted activity (pCi/g)	Data ^{7}Be/X	MARS ^{7}Be/X
^{7}Be	346±52	454±91	1	1
^{22}Na	79±12	111±21	4.4±0.9	4.1±0.7
^{54}Mn	19.7±3.0	25.1±5.0	17.6±3.7	18.1±3.4
^{3}H	57.0±0.9	229±46	6.0±0.9	2.0±0.4

Table 2. The estimated leaching fraction for tritium based on the predicted ^{3}H activity in MARS compared to the activity seen the core samples

Sample Location	Radius (m)	Year	^{7}Be/^{3}H from Data	Estimated L_{3H}
Upstream Thin	2.1	2006	6.0	0.33±0.09
Downstream	1.5	2006	8.0	0.25±0.07
Upstream Thin	2.1	2010	2.9	0.41±0.11
Upstream Thick	3.0	2010	1.8	0.66±0.17
Middle	3.0	2010	2.9	0.41±0.11
Downstream	1.5	2010	3.0	0.40±0.10

Conclusion

The agreement between MARS and the data from the NuMI decay pipe core samples on the values of the tenfold attenuation factor and the activities of ^{7}Be, ^{22}Na and ^{54}Mn demonstrate the utility of employing MARS in predicting the radionuclide activity in shielding. If the MARS prediction for the tritium activity is similarly accurate as the activity ratios of ^{7}Be/^{22}Na or ^{7}Be/^{54}Mn, then this implies that only 41% of the total tritium activity was collected from the core samples.

Acknowledgements

Support was provided by the US Department of Energy Contract No. DE-AC02-07CH11359.

References

[1] G.G. Eichholz, W.J. Park, and C.A. Hazin (1980), "Tritium penetration through concrete", *Waste Management*, 9, pp. 27-36.

[2] K. Furuichi, H. Takata, T. Motoshima, S. Satake, and M. Nishikawa (2006), "Study on behaviour of tritium in concrete wall", *J. Nucl. Mat.*, 350, pp. 246-253.

[3] G. Longhurst (2007), "Tritiated Water Interaction with Stainless Steel", Idaho National Laboratory Report, INL/EX-07-12584.

[4] N.V. Mokhov (1995), "The MARS Code System Users'Guide", Fermilab FN-625, http://www-ap.fnal.gov/MARS/m1514-manual.pdf.

[5] N.V. Mokhov, P. Aarnio, Yu.I. Eidelman, K.K. Gudima, A.Yu. Konobeev, V.S. Pronskikh, I.L. Rakhno, S.I. Striganov, and I.S. Tropin (2012), "MARS15 Code Developments Driven by the Intensity Frontier Needs", Fermilab-Conf-12-635-APC.

[6] B. Lundberg (2007), "Tritated water in the decay region: model comparisons to data", Fermilab Report, Projects Document 136-v4.

[7] P. Aarnio (1998), "Decay and transmutation of nuclides", CERN Technical Report CMS-NOTE-1998/086.

[8] A. Isotalo (2008), "Modifications to DeTra", Technical Report.

Activation products from copper and steel samples exposed to showers produced by 8 GeV protons lost in the Fermilab main injector collimation system

Bruce C. Brown, Nikolai V. Mokhov, Vitaly S. Pronskikh
Fermi National Accelerator Laboratory, Batavia, IL, US

Abstract

In conjunction with efforts to predict residual radiation levels in the Fermilab Main Injector, measurements of residual radiation were correlated with the time history of losses. Detailed examination suggested that the list of radioactive isotopes used for fitting was incomplete. We will report on activation studies of magnet steel and copper samples which we irradiated adjacent to the Fermilab Main Injector collimation system. Our results identified several additional radioactive isotopes of interest. The MARS15 studies using a simplified model are compared with measurements. The long half-life isotopes will grow in importance as operation stretches to a second decade and as loss rates rise. These studies allow us to predict limits on these concerns.

Introduction

In response to a demand for high-intensity operation of the Fermilab Main Injector to provide protons for producing neutrinos, an intense effort [1] to control activation due to beam loss has been carried out. While monitoring the activation and cool-down to allow planning for accelerator repairs and upgrades, we found that crude models [2] which acknowledge contributions from three radioactive isotopes of manganese were inadequate to explain some detailed measurements [3]. Using an available HPGe spectrometer, we have measured the isotopes produced in a copper sample and a sample of the magnet lamination steel when activated near the collimation system. We have constructed a simplified model in MARS [4] to explore the activation in two locations with two different momentum spectra.

Studies of activation history

Using measurements of residual radiation at a series of 126 (later 142) locations identified by bar coded tags, a simple fitting procedure provided a formula for radiation cool-down sufficient for planning work in the accelerator enclosure. The recorded beam loss at a nearby beam loss monitor, weighted by the half-life of the isotope considered, is used in a linear model to fit the residual radiation measurements. A typical result is shown in Figure 1.

Figure 1. Simple fit to residual radiation

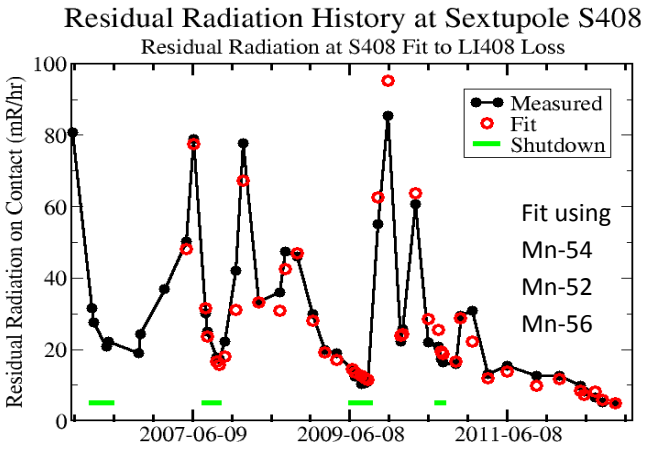

Figure 2. Secondary collimator showing monitoring locations

Activation measurements with Copper and steel tags

During machine down-time, cool-down studies using Geiger counters (see Figure 2) measured the residual radiation [3] for times from one to many days. As more detailed studies showed that the fit required half-life values intermediate between ^{52}Mn (5.59 days) and ^{54}Mn (312 days), we initiated a study of activation employing an available high purity Germanium (HPGe) spectrometer[1]. This system had been employed for monitoring using Al Tags, as shown in Figure 2 [5]. 1.5 inch tags of pure Cu and of steel from the magnet laminations were fabricated. These were placed on the side (left photo of Figure 2) and at the downstream end (right photo of Figure 2) of the third secondary collimator in the MI300 straight section [6]. Lost proton beam which was captured by this collimator produced a spectrum of electromagnetic and hadronic secondaries, which activates materials in the area. Samples were placed and removed during available access times and delivered to the Fermilab Radiation Analysis Facility (RAF) for measurement. Activation times were varied and smaller samples were prepared to allow measurements with a limit of 1 mR/hr at the HPGe spectrometer.

[1] Ortec GEM Series P-type High Purity Germanium detector. The crystal diameter is 56.4 mm and the length is 43.6 mm. The detector resolution at 1332 keV is ~2 keV and the relative efficiency is ~20%. Ortec GammaVision 32 v6.08 analysis software is used.

Decay correction for activation measurements

Analysis of activation measurements usually rely on the "activation formula" [7] (Equation 1), which assumes a uniform activation rate. MARS calculations assume a uniform activation so, for a specific isotope, one can apply the activation formula to translate the results to the desired activation and cool-down time.

$$S_A(t_c)(pCi/gm) = \frac{N_A \sigma_I}{3.7\times10^{-2} A_T} \frac{d\phi}{dt}(1-e^{-\frac{ti}{\tau_I}})e^{-\frac{tc}{\tau_I}} \qquad (1)$$

where SA is the activation of isotope I, NA is Avogadro's number, AT is the nucleon number for the isotope I, σI is the cross-section for production of isotope I and ϕ is the fluence of activating particles, τI is the lifetime (corresponding with the half-life t1/2), ti is the time of activation and tc the time allowed for cool-down. The measurements were corrected for decay during activation using reading from a nearby Beam Loss Monitor (BLM) which was recorded every Main Injector cycle (typically 2.2 seconds) which allowed accounting for the details of beam intensity and beam loss variations [6]. Activation was reported in the "instantaneous" activation limit for which ϕ = ti dϕ/dt in the limit ti $\rightarrow$ 0. Measurement results from RAF are corrected to receipt of the sample (tc=0). Equilibrium activation is of interest for long-term exposure. In this case, one assumes (tc=0) and takes the limit ti >> t1/2.

Figure 3. Toy model for MARS simulation (beam from left)

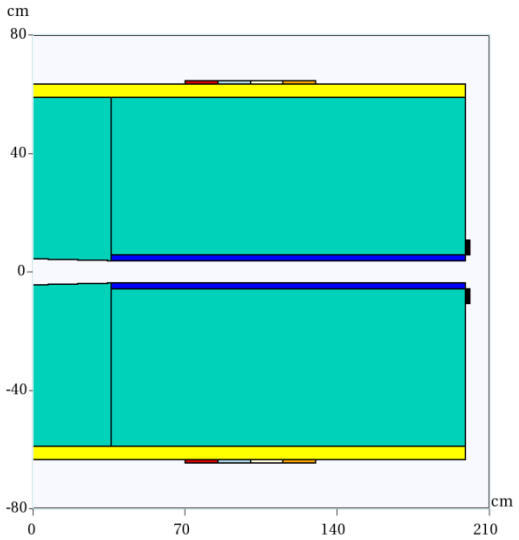

MARS15 model and collimator details

A complete model of the collimation system has been constructed in MARS [4], but for this study we employ a simplified geometry ("toy model") which supports the essential features while requiring much less computation. The toy collimator model (see Figure 3) employs a ~200 cm long cylinder with a 3.8 cm inner bore radius and a 63.5-cm outer radius. The first 36 cm of the inner bore are tapered from 4.4 cm at the entrance to 3.8 cm. The collimator main body in the model is made of the yoke steel (green), with a stainless steel (blue) inner and a marble (yellow) outer layer. The 1.25×1012 p/s proton beam strikes the inner surface of the bore at the end of the tapered part (30 cm from the entrance to the collimator). The "shielded" samples are placed onto the outer surface of the marble

layer, and the "unshielded" ones near the exit at the downstream end of the collimator. All the samples are cylinders.

The two sample locations provide different spectra for the activating secondaries. The tapered upstream in both model and real collimator is intended to intercept all losses in a short longitudinal region. The side (shielded) location is similar for the model and measurements. The downstream (unshielded) location in the collimator is activated by the losses at the end of the tapered region as well as by small losses near the downstream end of the collimator. As a result, the toy model will provide a more energetic (harder) spectrum of secondaries but is not intended as a careful representation of the measurement configuration.

Figure 4a. Gamma spectra from HPGe spectrometer (490 to 820 keV spectrum)

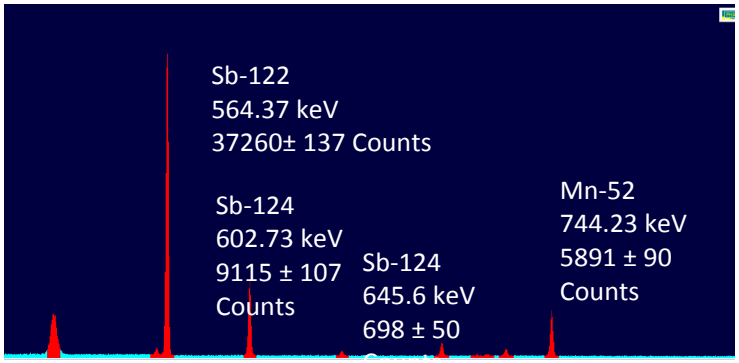

Figure 4b. Gamma spectra from HPGe spectrometer (1000 to 1325 keV spectrum)

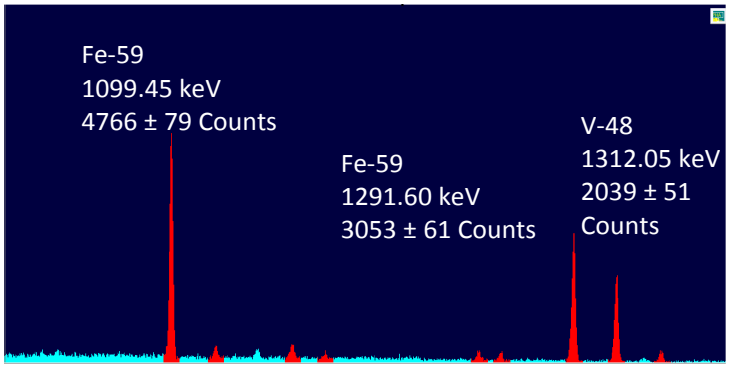

Results of measurement and simulation

To explore the distribution of isotopes produced in this activation study, we recognise that the normalisation and spectra are imperfectly reproduced in the "toy model" MARS simulation. We choose to normalise to dominant isotopes for each sample using ^{64}Cu for the copper sample and ^{54}Mn for the Fe and yoke steel samples. The ^{54}Mn dominates the activation after a few days and for the "shielded" location, the measurements of three samples agree to 1.2% when normalised to the half-life weighted BLM reading. Figure 4

shows a part of the spectra for one steel sample. Using the analysis software, the results for each measured isotope were obtained using multiple gamma lines when available. These were combined using known branching fractions and corrected for decay from the sample removal time. Using these results and the half-life weighted BLM reading, results are tabulated for the ratio of activation over BLM reading corrected to the instantaneous exposure limit [6]. These values were then corrected to the 30-day exposure with 2-hour decay condition to match the choice used in the MARS calculations. Measurements and MARS calculation results (shielded or unshielded exposures separately) were normalised to ^{64}Cu (copper samples) or ^{54}Mn (steel). Results are shown in the figures below. The Main Injector yoke lamination steel had a 0.3% by weight of antimony (Sb). Activation of this to ^{122}Sb and ^{124}Sb was measured. This was not included in the MARS simulations. Further studies will be required.

Figure 5. Steel activation normalised to ^{54}Mn with 30-day exposure, 2-hour cool-down (upper figure) shielded location, (lower figure) unshielded location

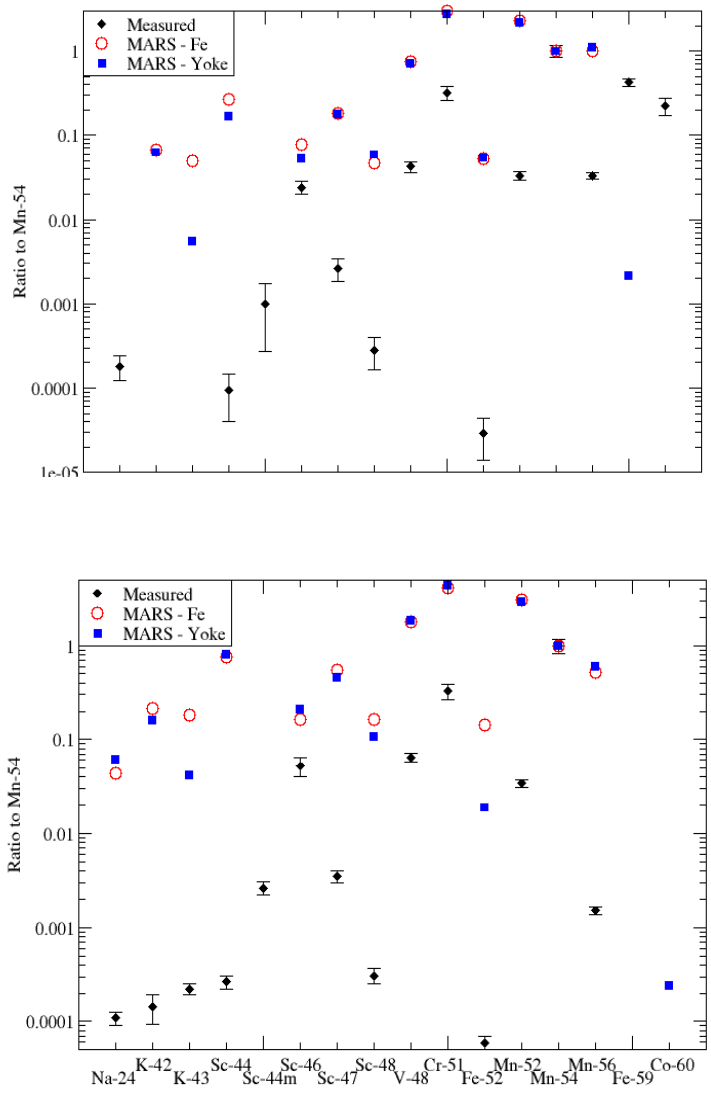

Figure 6. Copper activation normalised to ^{64}Cu with 30-day exposure, 2-hour cool-down (upper figure) shielded location, (lower figure) unshielded location

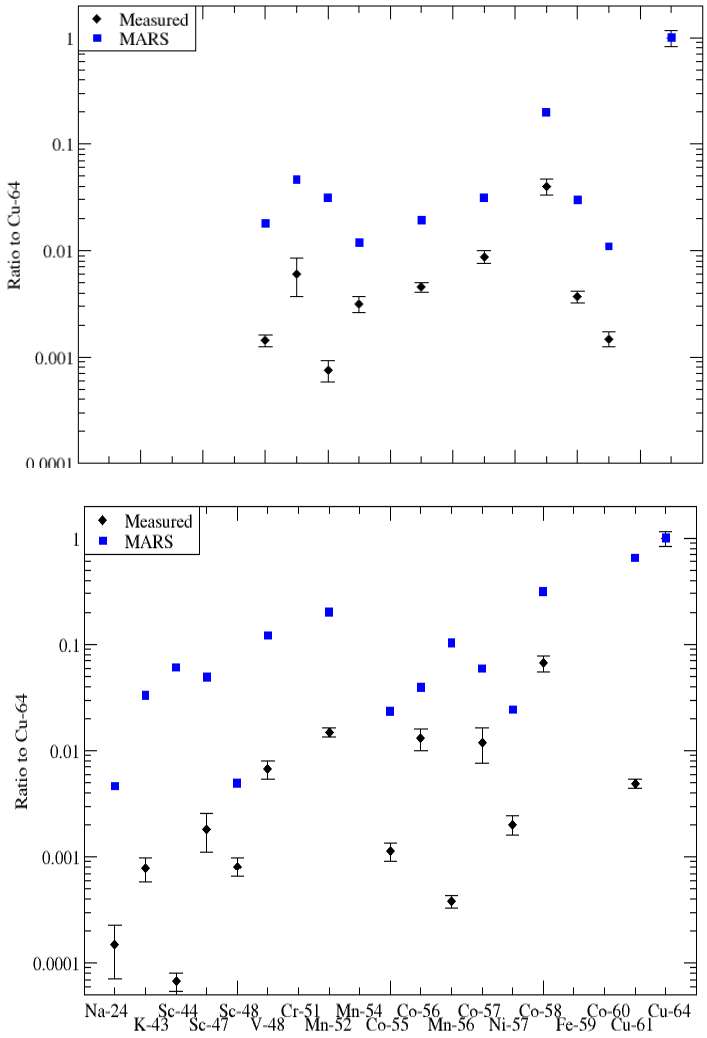

Conclusions

It should be noted that the relative abundance of radioactive isotopes produced in this secondary flux is not precisely predicted by the current toy model MARS simulation. The measurements have identified isotopes which contribute to the observed activation. We find that using the ^{59}Fe or ^{51}Cr half-life for the weighted fit contributes to the shape in ways which will not impact planning for tunnel work radiation limits.

Acknowledgements

Fermi National Accelerator Laboratory is operated by Fermi Research Alliance, LLC under Contract No. DE-AC02-07CH11359 with the United States Department of Energy. Special thanks are due to Vernon Cupps, Meka Francis, Gary Lauten and Matt Quinn for assistance in exposing the samples, measuring the activation and aiding in presentation of the results.

References

[1] B.C. Brown et al. (2013), "The Fermilab Main Injector: high intensity operation and beam loss control", Phys. Rev. ST Accel.Beams, 7, 071001.

[2] B.C. Brown, G.H. Wu (2010), "Measuring Correlations Between Beam Loss and Residual Radiation in the Fermilab Main Injector", *Proceedings of the 46th ICFA Advanced Beam Dynamics Workshop on High-Intensity and High-Brightness Hadron Beams* (HB2010), pp. 391-394.

[3] A.J. Safavi (2010), "Comparison of Short Term Cooldown Data for MI Collimator C307 Near Beam and Beside Marble Shielding", Fermilab Beams-doc-3717-v1 and subsequent detailed studies (unpublished).

[4] http://www-ap.fnal.gov/MARS/.

[5] Bruce C. Brown (2012), "Analysis Procedures for Al Activation Studies", Fermilab Beams-doc-3980-v2.

[6] Bruce C. Brown (2012), "Activation of Steel and Copper Samples in the Main Injector Collimator Region", Fermilab Beams-doc-4046-v2.

[7] M. Barbier (1969), "Induced Radioactivity", John Wiley and Sons, Inc. P.15, Equation 3.9.

New results on the beam-loss criteria for heavy-ion accelerators

Peter Katrík[1,2], Edil Mustafin[1], Dieter H.H. Hoffmann[1,2], Ivan Strašík[1], Márius Pavlovič[3]
[1]GSI Helmholtzzentrum für Schwerionenforschung GmbH, Germany
[2]Technische Universität Darmstadt, Germany
[3]Slovak University of Technology in Bratislava, Slovak Republic

Abstract

Activation of high-energy heavy-ion accelerators due to beam losses is a serious issue for accelerator parts like collimators, magnets, beam-lines, fragment separator targets, etc. The beam losses below 1 W/m are considered as tolerable for "hands-on" maintenance in proton machines. In our previous studies, the FLUKA2008 code has been used for establishing a scaling law expanding the existing beam-loss tolerance for 1 GeV protons to heavy ions. This scaling law enabled specifying beam-loss criteria for projectile species from proton up to uranium at energies from 200 MeV/u up to 1 GeV/u. FLUKA2008 allowed nucleus-nucleus interactions down to 100 MeV/u only. In this work, we review our previous results and extend activation simulations to lower energies with the help of the new FLUKA version, namely FLUKA2011. It includes models for nucleus-nucleus interactions below 100 MeV/u. We also tried to expand the scaling law to lower energies. This, however, needs further studies, because the heavy-ion-induced nuclide composition starts deviating from the proton-induced nuclide composition at energies below 150 MeV/u.

Introduction

Activation of accelerator components and their environment due to the beam losses during normal machine operation is not negligible. It is important to diminish them as much as possible; even they can never be totally eliminated. Activation of the accelerator components has an impact on hands-on maintenance of the machine and high level of residual activity may lead to access restrictions in some machine areas [1-3]. Beam losses may also damage or reduce lifetime of radiation-sensitive components of the accelerator. They also may alter material properties such as strain resistance, magnetic susceptibility, break-down voltage, etc., which influences proper functioning of accelerator elements made of these materials. Quantification of the residual activity can provide a key to specify tolerable beam losses and/or to optimise the choice of the construction materials. Analysis of the activation products (nuclides, their life-times and characteristics of the emitted radiation) is necessary in order to calculate the "cooling" time needed to keep the personnel exposure below radiation safety limits after the accelerator shut-down.

The lost beam particles interact with construction materials of the accelerator in several ways. The most important interactions are high-energy inelastic hadron interactions, neutron capture and photonuclear reactions. Important sources of activation are protons, neutrons and target fragments. Previous activation experiments and measured depth-profiles of residual activity pointed secondary particles as the main source of activation [4-7]. The FLUKA2008 calculations confirmed that the target fragments were the dominant source of activation in the case of high-energy heavy ions. They are produced independently from the projectile mass [7]. However, the projectile

fragments can play an increased role in the case of lower beam energies. This contribution should depend on the projectile species.

A set of activation experiments and Monte Carlo simulations have been performed at GSI Helmholtzzentrum für Schwerionenforschung GmbH Darmstadt in the frame of preparation works for the FAIR (Facility for Antiproton and Ion Research) project [8]. The paper presents new simulation results obtained with FLUKA2011.2b.5. The new simulations were used to revise the previous beam-loss criteria [4]. The main difference between the old and new simulations concerns the energy threshold for the nucleus-nucleus interactions, which is below 100 MeV/u in FLUKA2011.2b.5 [9,10].

A summary of the previous studies

One of the first attempts to set a beam-loss criterion for high-energy heavy ions was based on FLUKA2008 simulations validated with dedicated activation experiments [4-7]. Those simulations were done for two target geometries representing a beam-pipe and a bulky target (see Figure 1). Stainless steel and copper were chosen as target materials frequently used for magnet yokes, coils, etc. Target activation was simulated for different projectiles (^{1}H, ^{4}He, ^{12}C, ^{20}Ne, ^{40}Ar, ^{84}Kr, ^{132}Xe, ^{197}Au and ^{238}U) at different energies from 200 MeV/u up to 1 GeV/u. The activities were normalised to the unit beam power of 1W delivered permanently during 3 months. The activity was calculated at several time points from the beginning of irradiation, through the end of irradiation up to 10 years after the end of irradiation. Results of the simulations were cross checked with experimental data [11-14]. Analysis of the simulated data showed that partial relative activities of the nuclides with dominating contribution to the total activity practically did not depend on the projectile mass. Generally, the total induced activity depended on energy and mass of the projectiles, as well as on the composition of the target material [4]. The total induced residual activity decreased with increasing projectile mass and with decreasing projectile energy [5-7].

Figure 1. Geometrical model of a beam-pipe (upper) and a bulky target (lower) irradiation [4]

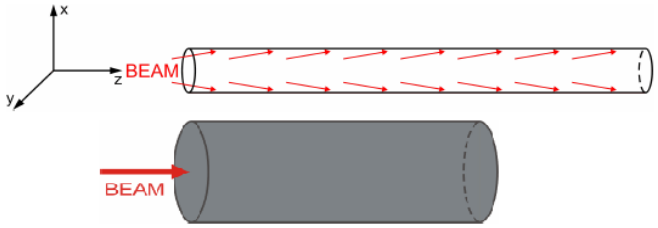

Results based on the FLUKA2008 simulations

Simulations of the beam-pipe activation showed that normalised activity induced by uranium ions was about 12 times lower at 1 GeV/u, 23 times lower at 500 MeV/u, and almost 75 times lower at 200 MeV/u compared to 1 GeV protons. Therefore, the tolerable beam losses for uranium beam could be 12 W/m at 1 GeV/u, 23 W/m at 500 MeV/u, and 75 W/m at 200 MeV/u. The same results were obtained from calculated effective-dose rates [4].

The normalised activity induced by uranium ions in the bulky target was about 5 times lower at 1 GeV/u, 12 times lower at 500 MeV/u, and almost 60 times lower at 200 MeV/u compared to 1 GeV protons. Therefore, the tolerable beam losses for uranium beam could be 5 W/m at 1 GeV/u, 12 W/m at 500 MeV/u, and 60 W/m at 200 MeV/u.

Influence of the 100 MeV/u interaction threshold of FLUKA2008

Independent simulations were performed by another Monte Carlo code – SHIELD that takes into account production of radioactive nuclides by primary ions with energies down

to zero [15]. Discrepancy between FLUKA and SHIELD was less than 8% at higher beam energies, but 25% at 200MeV/u ^{238}U ions [4]. This is why it is motivating to revise the simulations with the new version of FLUKA (FLUKA2011) that calculates the nucleus-nucleus interactions below 100 MeV/u.

Monte Carlo simulations by FLUKA2011

It was necessary to use the same settings and physical models as used before to study differences between the two versions of FLUKA. The evaporation model with heavy-fragment evaporation was used. Emission of the high-energy light fragments through the coalescence mechanism was activated. The heavy-ion transport with nuclear interactions was switched on. Low-energy neutron transport was simulated down to thermal energies (10^{-5} eV) and residual nuclei from low-energy neutron interactions were scored [4]. The simulations were performed with the same projectile species. The range of the beam energies was expanded to 25 MeV/u – 1 GeV/u. In this paper, we concentrate on the results for a bulky target made of copper.

Tolerable beam losses

Tolerable beam losses have been defined at the 7th ICFA Workshop on High-intensity Brightness Hadron Beams [3] for uncontrolled proton-beam losses at energies above 100 MeV. To allow hands-on maintenance of accelerator components without unreasonable constraints after 100 days of using the machine, dose-rate levels should be below 1 mSv/h (measured 30 cm from the component surface). This corresponds to the beam losses of about 1 W/m along the beam enclosure [3]. The main goal of our study is to scale the proton beam-loss criterion to heavy-ion machines.

First, a list of nuclides with the biggest contribution to the total activity has been created for each simulation. Examples of graphical representation of the partial relative activities 1 day after the end of irradiation are shown in Figures 2 through 6. Figure 2 reproduces the previous data obtained with FLUKA2008 [4], whereas Figures 3 through 6 show the recent data obtained with FLUKA2011. The partial relative activities are almost the same for all nuclides independently from the projectile mass at energies from 1 GeV/u down to 150 MeV/u. This suggests that radioactive nuclides are produced mostly by secondary particles.

However, the partial relative activities are no longer identical at energies below 150 MeV/u (see Figure 6). There are nuclides produced by some projectile species that are not produced by other projectile species at all. Different nuclide composition must have an influence on the decay-curve of the total residual activity.

Important comparison is between Figure 2 and Figure 3 representing the results from two different versions of FLUKA. The nuclide inventory shows the same list of nuclides produced in the bulky target. However, FLUKA2011 gives smaller partial relative activities for the most dominating nuclides than FLUKA2008. For example, there is a difference of 5% in the case of ^{64}Cu.

Figure 2. Partial relative activities induced in copper bulky target one day after the end of irradiation by different projectiles at 1 GeV/u obtained by FLUKA2008 [4]

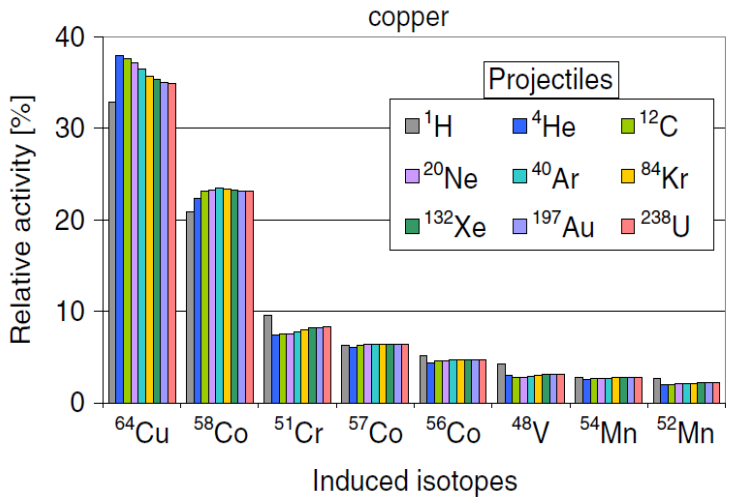

Figure 3. Partial relative activities induced in copper bulky targets one day after the end of irradiation by different projectiles at 1 GeV/u obtained by FLUKA2011

Figure 4. Partial relative activities induced in copper bulky targets one day after the end of irradiation by different projectiles at 500 MeV/u obtained by FLUKA2011

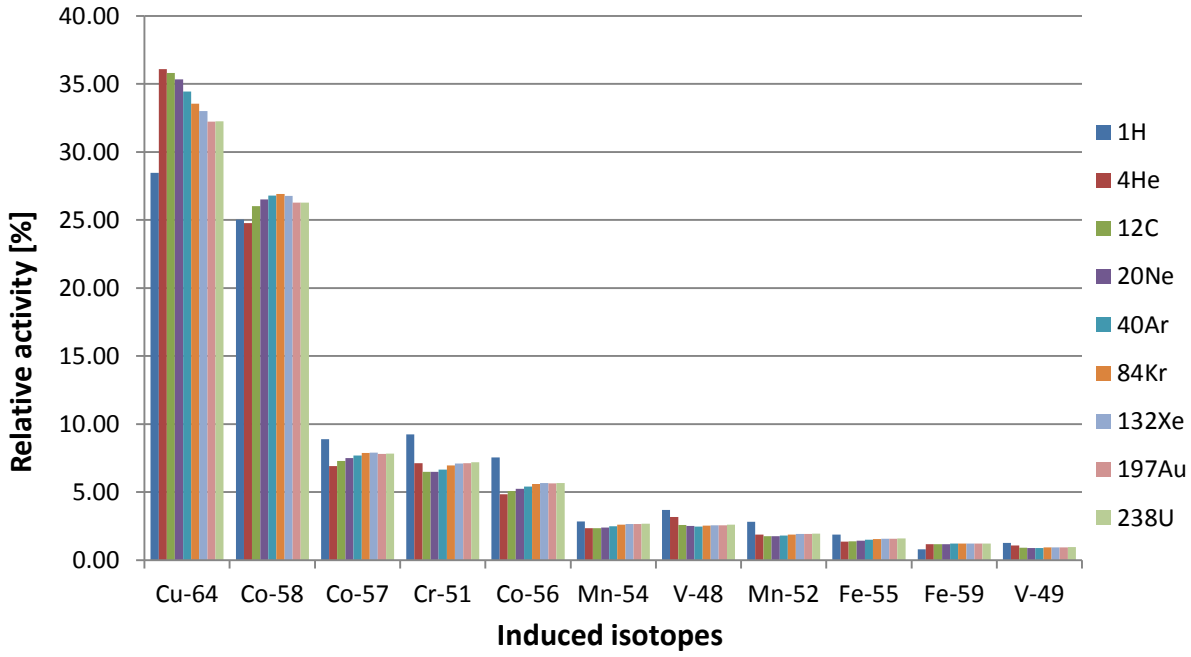

Figure 5. Partial relative activities induced in copper bulky targets one day after the end of irradiation by different projectiles at 150 MeV/u obtained by FLUKA2011

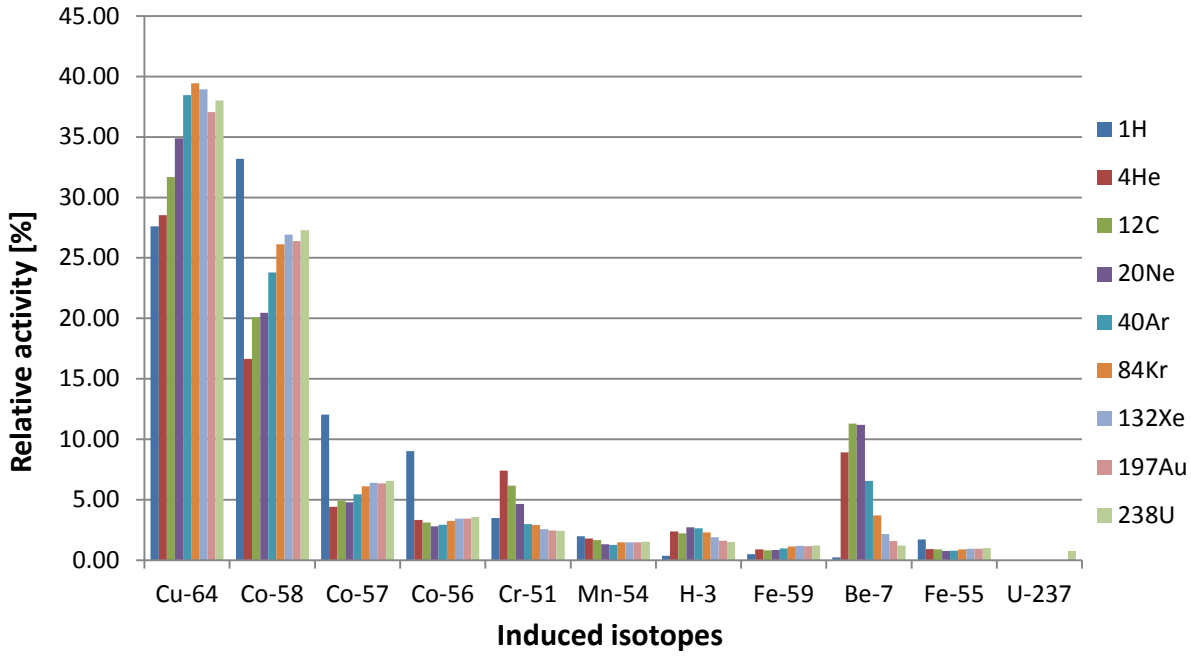

Figure 6. Partial relative activities induced in copper bulky targets one day after the end of irradiation by different projectiles at 25 MeV/u obtained by FLUKA2011

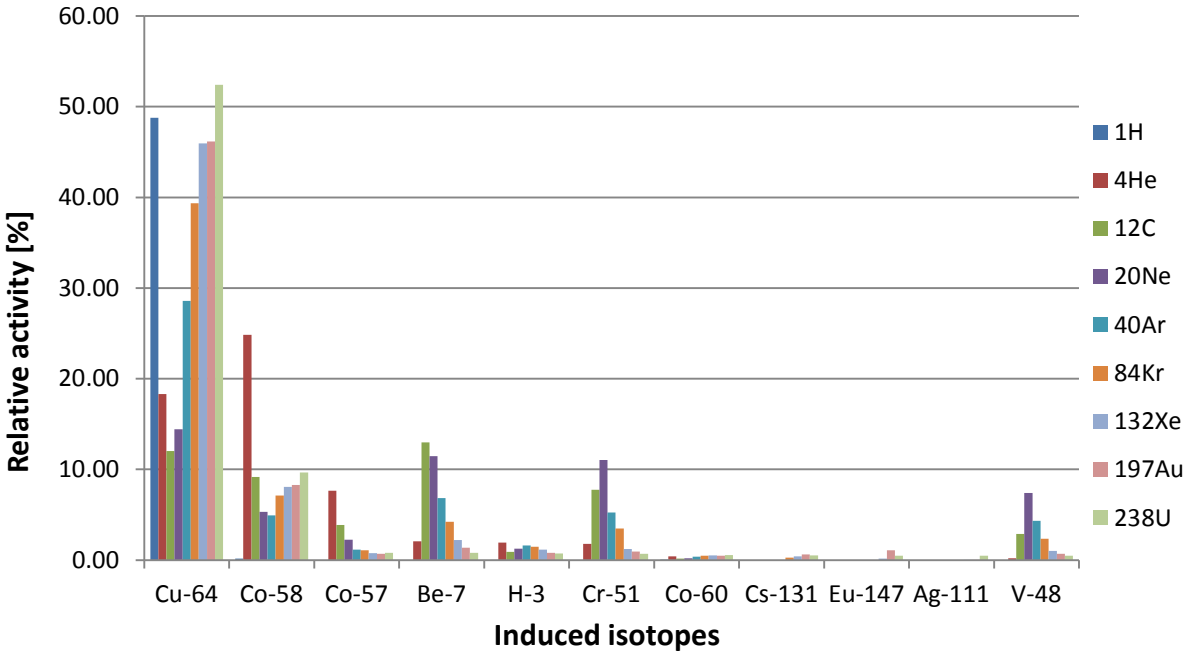

Time evolution of the induced activity

Time evolution of the induced activity is important for establishing a scaling law between the proton and heavy-ion beam-loss criteria. Figures 7 through 10 show the time evolution of the induced activity, A_t, normalised by the activity at the end of irradiation, A_{eoi}. If there is no big difference in the time evolution of the activities induced by different beams (which is a matter of the nuclide composition), a generic curve can be created by averaging the individual curves. The generic curve is representing the time evolution of the induced activity independently from the primary beam particles. It can be subdivided into two parts: (1) an increase of the activity during permanent irradiation = activation part, (2) a decrease of the activity after the end of irradiation = decay part.

Similarly to the nuclide inventory, there are no significant differences in the time evolution of the induced activity for beam energies from 1 GeV/u to 150 MeV/u. However, this is no longer true for energies below 150 MeV/u. Individual curves start deviating from each other shortly after the start of irradiation as well as after the end of irradiation. They do not follow the generic curve, either (see Figure 10). It seems that a reliable universal scaling law cannot be found for energies below 150 MeV/u.

Figure 7. Time evolution of the induced activity in copper bulky target irradiated by different projectiles at 1 GeV/u (GC – the generic curve)

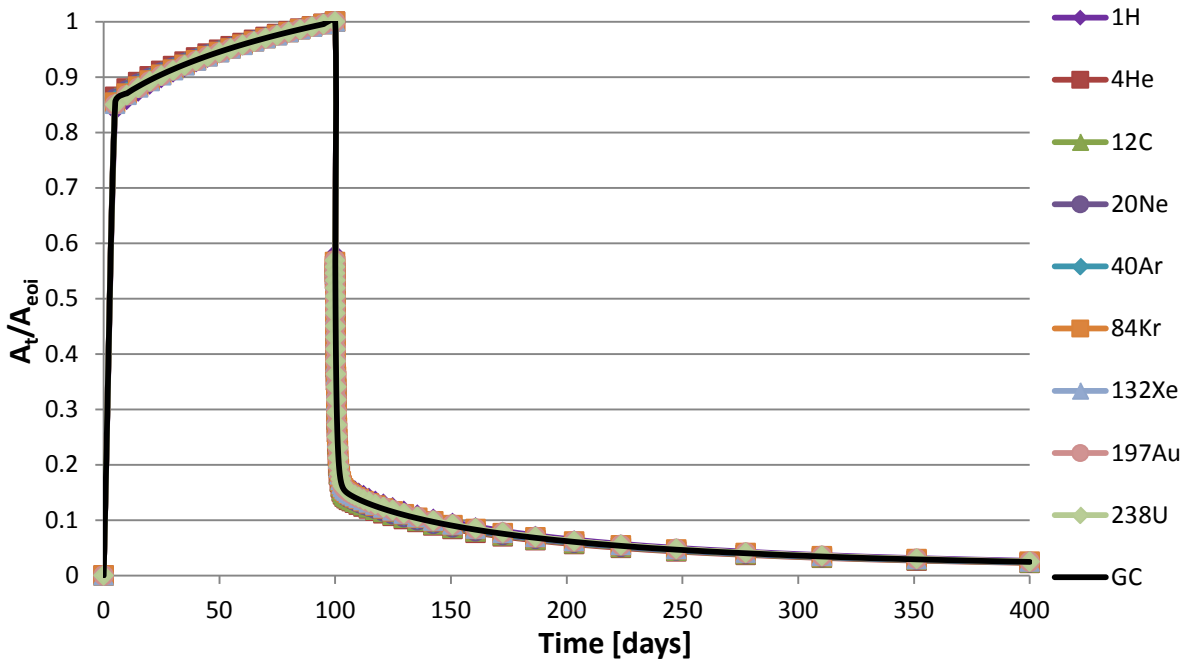

Figure 8. Time evolution of the induced activity in copper bulky target irradiated by different projectiles at 500 MeV/u (GC – the generic curve)

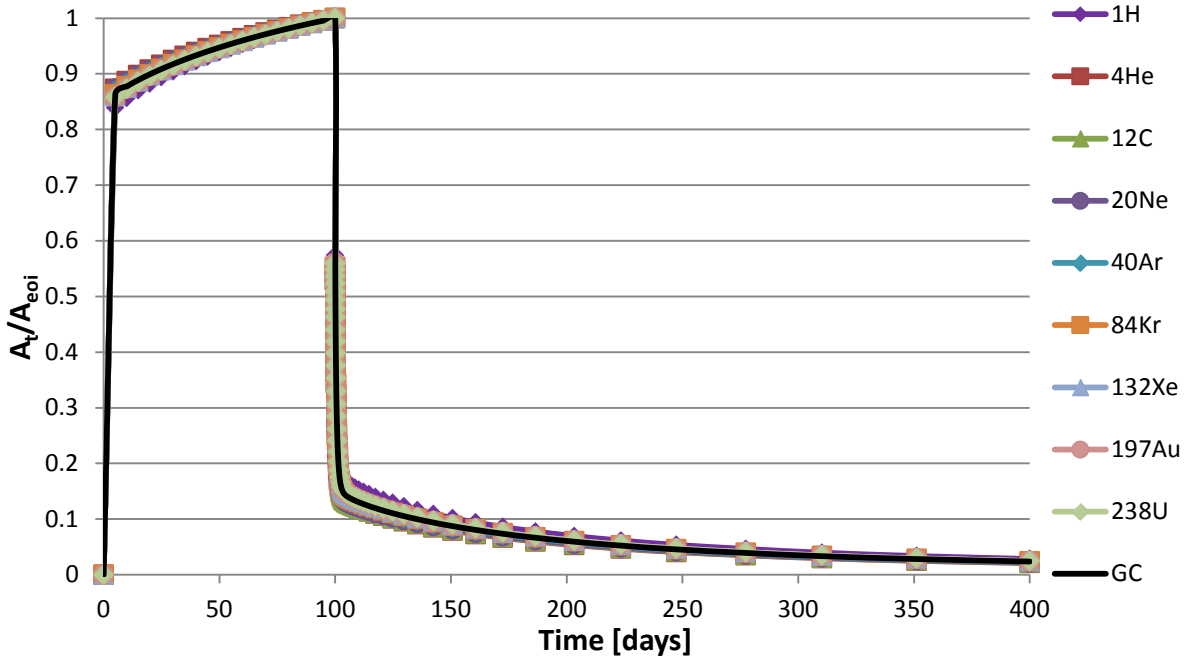

Figure 9. Time evolution of the induced activity in copper bulky target irradiated by different projectiles at 150 MeV/u (GC – the generic curve)

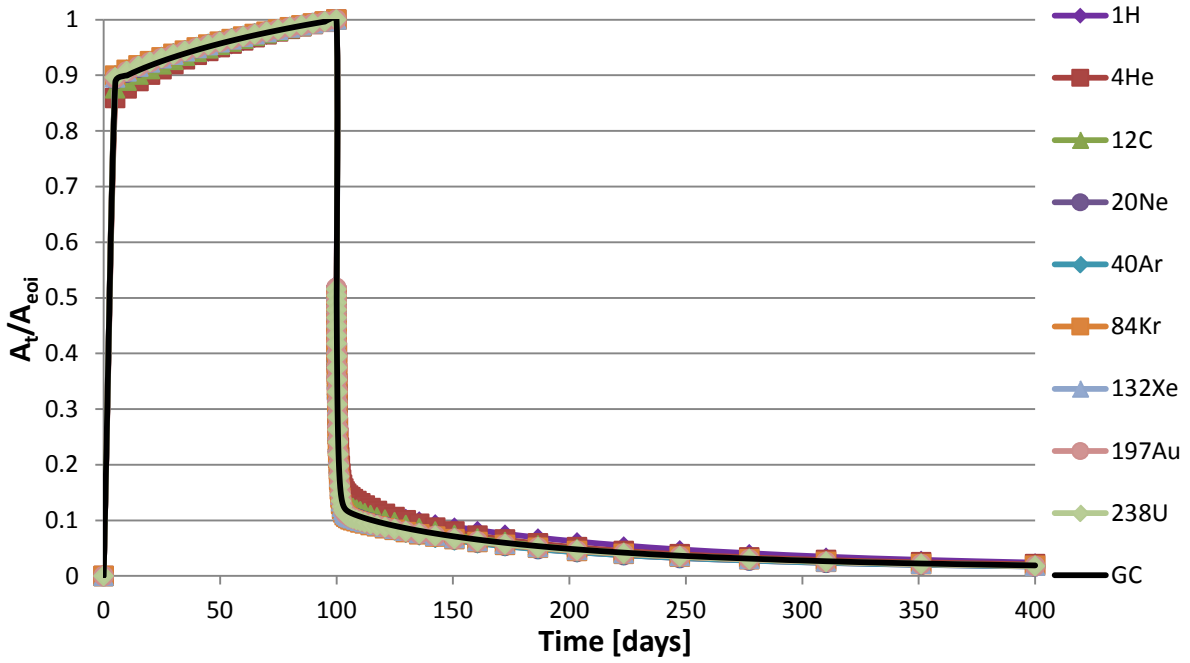

Figure 10. Time evolution of the induced activity in copper bulky target irradiated by different projectiles at 25 MeV/u (GC – the generic curve)

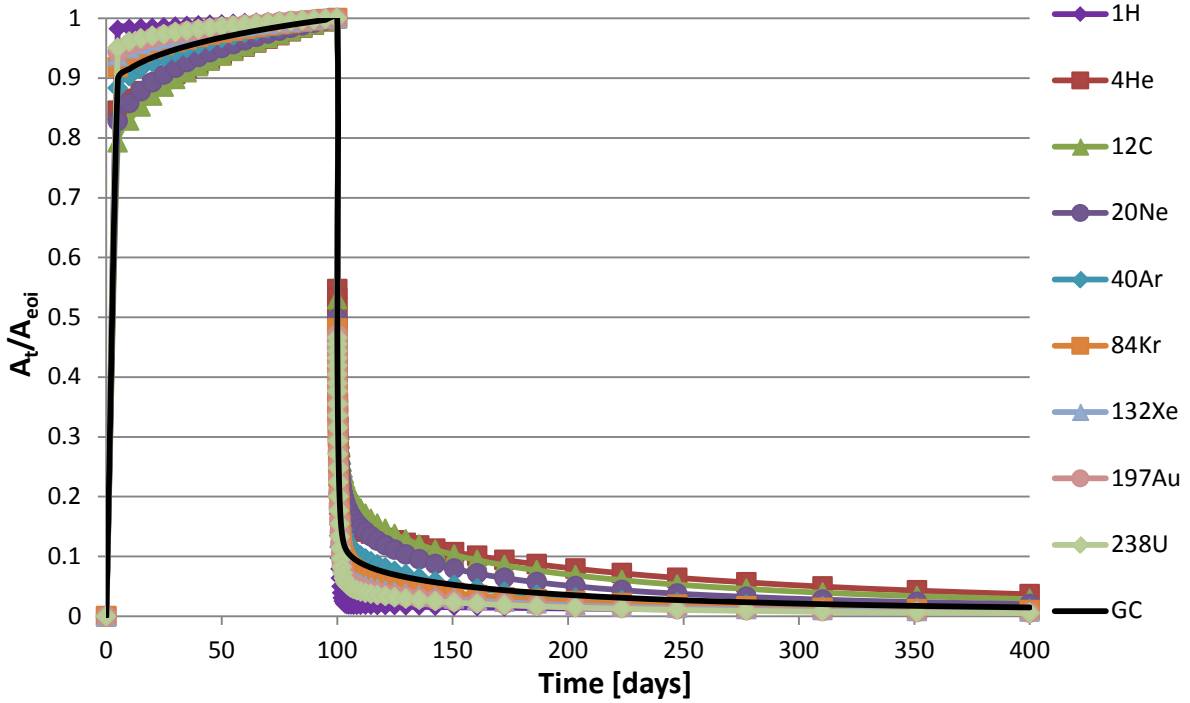

The scaling law for beam-loss tolerance

The previous studies revealed the following: (1) the induced-nuclide inventory does not strongly depend on the projectile species, (2) time evolution of the induced activity correlates to a generic curve, and (3) the total activity induced by 1 W/m of beam losses (the normalised activity) decreases with increasing ion mass and decreasing energy. The scaling factor can therefore be expressed as the ratio of the normalised activity induced by 1 GeV protons, A_p(1 GeV), to the normalised activity induced by the particles of interest at given energy, A_i(E).

Our recent study verified the previous findings for the copper bulky target irradiated by heavy-ion beams with energies above 150 MeV/u. For comparison, Figure 11 reproduces the data from the previous studies based on FLUKA2008 [4], whereas Figure 12 shows new data based on FLUKA2011. The lower threshold for the nucleus-nucleus interactions in FLUKA2011 leads to higher induced activities due to the increased contribution from projectile fragments. As a consequence, the tolerable beam losses derived from FLUKA2011 are lower compared with the losses derived from FLUKA2008. As an example, they are 40 W/m for uranium beam at 200 MeV/u according to FLUKA2011 instead of, 60 W/m according to FLUKA2008. Tolerable beam losses based on the FLUKA2011 simulations are collected in Table 1.

The situation becomes more complicated at energies below 150 MeV/u. In this case, the activation is driven by the target – as well as the projectile fragments. The contribution from the projectile fragments depends also on the primary beam parameters. Different nuclide composition leads also to different time evolution of the induced activity, which does not comply with a generic curve. A reliable universal scaling law is no longer possible.

Figure 11. Scaling factor for the tolerable beam losses as a function of ion mass – FLUKA2008

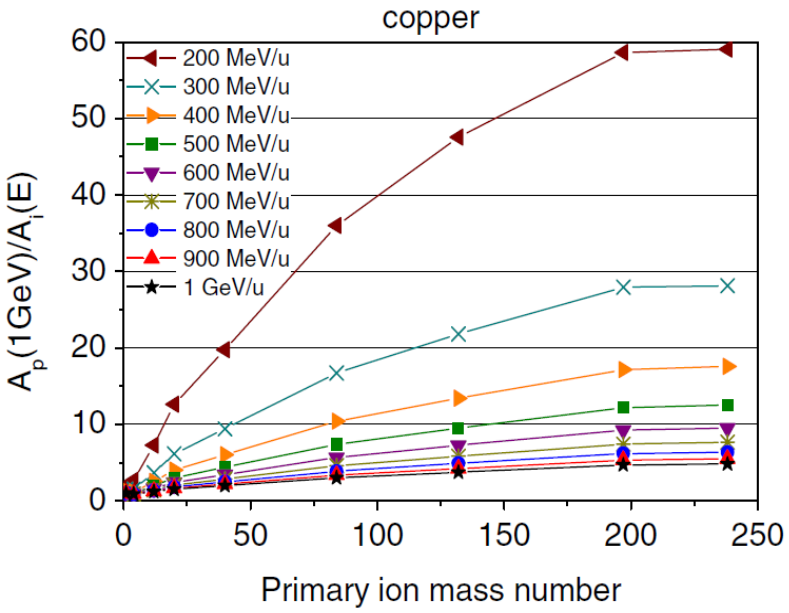

Figure 12. Scaling factor for the tolerable beam losses as a function of ion mass – FLUKA2011

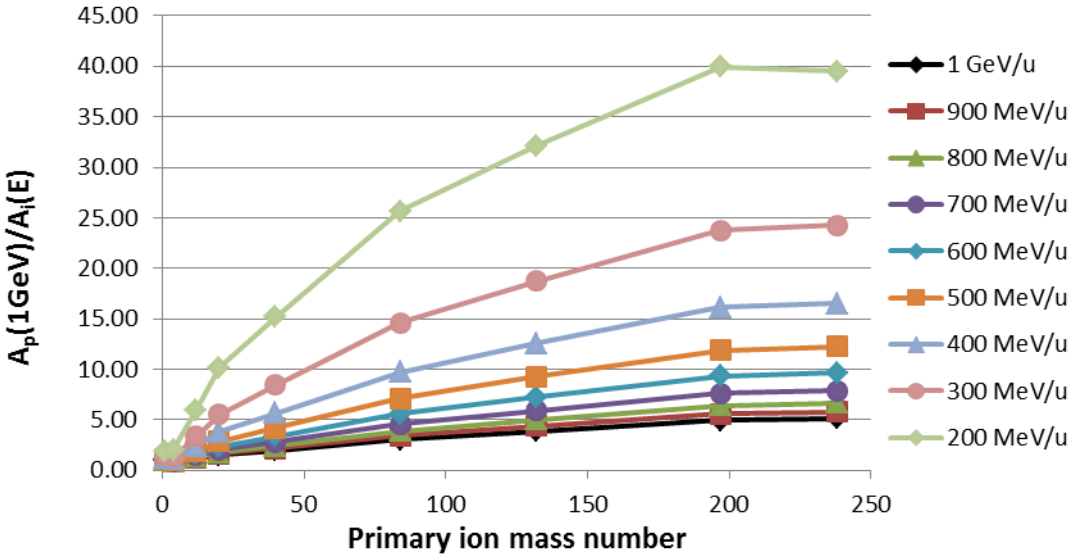

Table 1. Tolerable beam losses according to FLUKA2011

Energy Ion [MeV/u]	Tolerable beam loses for different ion beams at different energies, [W/m]												
	1000	900	800	700	600	500	400	300	200	150	100	50	25
^{1}H	1.00	1.01	1.02	1.05	1.09	1.16	1.28	1.49	1.90	2.25	~~2.81~~	~~4.17~~	~~8.51~~
^{4}He	0.87	0.87	0.87	0.88	0.91	0.97	1.09	1.33	1.98	2.85	~~4.61~~	~~9.31~~	~~19.86~~
^{12}C	1.18	1.23	1.30	1.42	1.59	1.88	2.37	3.35	5.96	9.76	~~17.12~~	~~35.28~~	~~74.36~~
^{20}Ne	1.51	1.61	1.77	2.00	2.34	2.86	3.77	5.54	10.15	16.39	~~28.33~~	~~60.41~~	~~138.25~~
^{40}Ar	1.97	2.17	2.42	2.79	3.34	4.19	5.63	8.42	15.17	23.08	~~37.29~~	~~76.62~~	~~194.25~~
^{84}Kr	3.03	3.39	3.88	4.58	5.57	7.10	9.69	14.60	25.67	36.69	~~54.69~~	~~107.10~~	~~254.56~~
^{132}Xe	3.85	4.34	4.99	5.89	7.23	9.24	12.59	18.71	32.10	43.74	~~62.94~~	~~116.75~~	~~261.93~~
^{197}Au	4.92	5.56	6.41	7.58	9.29	11.88	16.15	23.75	39.92	52.88	~~73.26~~	~~124.72~~	~~262.71~~
^{238}U	5.12	5.77	6.63	7.84	9.61	12.21	16.50	24.25	39.49	51.59	~~70.07~~	~~113.18~~	~~245.72~~

The strikethrough values correspond to the primary beam energies where the scaling law is not reliable.

Conclusion

Generally, our results confirmed that the energy-threshold for nucleus-nucleus interactions does have an influence on activities calculated by FLUKA. At high beam energies (above 150 MeV/u), the scaling law can be applied, but the simulations based on FLUKA2011 lead to lower tolerable beam losses compared to FLUKA2008. For example, they are 40 W/m for uranium beam at 200 MeV/u according to FLUKA2011 instead of

60 W/m according to FLUKA2008. At energies below 150 MeV/u, the energy-threshold for nucleus-nucleus interactions becomes even more important, because the contribution from the projectile fragments to the total induced activity increases. Since this contribution depends on projectile species (mass), the universal scaling law cannot be applied or – at least – becomes less reliable and must be checked/refined by simulating the corresponding dose-rates induced by low-energy beams.

Acknowledgements

This work was prepared at GSI Darmstadt and partially supported by the BMBF project 05P12RDFN6.

References

[1] A. H. Sullivan (1992), "A Guide to Radiation and Radioactivity Levels Near High Energy Particle Accelerators", *Nuclear Technology Publishing*, Chap. 4, pp. 93.

[2] L. Ulrici et al. (2006), "Radionuclide characterization studies of radioactive waste produced at high-energy accelerators", *Nucl. Instrum. Methods Phys. Res.*, Sect A 562, pp. 596-600.

[3] N.V. Mokhov, W. Chou (2000) "Proceedings of the 7th ICFA Mini-Workshop on High Brightness Hadron Beams", *Fermi National Accelerator Laboratory*, pp. 51-61.

[4] I. Strašík et al. (2010), "Residual activity induced by heavy ions and beam-loss criteria for heavy-ion accelerators", *Phys. Rev. ST Accel. Beams 13*, 071004, pp. 1-10.

[5] E. Mustafin et al. (2003), "Influence of electronic stopping power on the total neutron yield of energetic heavy ions", *Nucl. Instrum. Methods Phys. Res.*, Sekt. A 501, pp. 553-558.

[6] I. Strašík et al. (2009), "Simulation of the residual activity induced by high-energy heavy ions", *Nuclear Technology 168*, p. 643.

[7] I. Strašík et al. (2008), "Residual activity induced by high-energy heavy ions in stainless steel and copper", *Proceedings of EPAC08, Genoa, Italy*, pp. 3551-3553.

[8] P. Spiller et al. (2013), "Status of the SIS100 heavy ion synchrotron project at FAIR", *Proceedings of the 4th International Particle Accelerator Conference IPAC'13*, Shanghai, China.

[9] G. Battistoniet et al. (2007), "Proceedings of the Hadronic Shower Simulation Workshop 2006", Fermilab, Illinois, pp. 31.

[10] A. Fasso et al. (2005), Reports No. CERN-2005-10, No. INFN/TC_05/11, No. SLAC-R-773.

[11] V.Chetvertkova et al. (2011), "Activation of aluminum by argon: Experimental data and simulations", *Nuclear Instruments and Methods in Physic Research B 269,* pp. 1336.

[12] I. Strašík et al. (2010), "Experimental study and simulation of the residual activity induced by high-energy argon inos in copper", *Nuclear Instruments and Methods in Physic Research B 268*, pp. 573.

[13] E. Mustafin et al. (2009), "Ion irradiation studies of construction materials for high-power accelerators", *Radiation Effects & Defects in Solids 164,* pp. 460.

[14] A. Fertman et al. (2007), "First results of an experimental study of the residual activity induced by high-energy uranium ions in steel and copper", *Nuclear Instruments and Methods in Physic Research B 260*, pp. 579.

[15] A.V.Dementyev, N.M. Sobolevsky (1999), "SHIELD – universal Monte Carlo hadron transport code: scope and applications", *Radiation Measurements 30*, pp. 553-557.

Po-production in lead: Calculation and measurement on SINQ-samples (PSI)

Daniela Kiselev[1], Tobias Lorenz[1], Yong Dai[1], Jean-Christophe David[2], Dorothea Schumann[1], Michael Wohlmuther[1]
[1]Paul Scherrer Institut, Switzerland
[2]CEA-Saclay, France

Abstract

The Paul Scherrer Institut operates a MW-class spallation source, SINQ, using the 590 MeV proton beam delivered by the ring cyclotron, HIPA. The target of the spallation source consists of a bundle of lead filled metal tubes (Cannelloni). Five lead samples were extracted from a rod in the target centre close to the beam entrance window from SINQ target-4, which had been in operation since 2000/2001 and received a total integrated beam charge of about 10 Ah. The lead was radiochemically investigated and the activities of several isotopes could be measured. Special attention was paid to Po as it has β^+*/*ε*emitting isotopes with considerable half-lives and the element can show – depending on the experimental conditions - distinct volatility properties. A much larger amount of the Po isotopes* ^{208}*Po (2.9 y),* ^{209}*Po (102 y) and* ^{210}*Po (138 d) was found in the samples compared to the prediction obtained with available cross-section models in the particle transport code MCNPX. In particular, the amount of* ^{210}*Po measured more than 10 years after the target operation is by far too large to be explained by direct production from Bi impurities in the lead. This implies another reaction mechanism not considered in the standard INC (Intranuclear Cascade) and evaporation models. Therefore, a recently improved INC and evaporation model, the Liège intranuclear-cascade model (named INCL) coupled to the de-excitation model ABLA07 was implemented into MCNPX2.7.0. INCL4.6/ABLA07 is one of the most accurate models to describe spallation reactions as an inter-comparison done under the auspices of IAEA demonstrated. In this contribution, preliminary results of the nuclide inventory calculated with MCNPX using INCL4.6/ABLA07 and Bertini-Dresner are presented and compared to the experimental data.*

Introduction and motivation

The Paul Scherrer Institut (PSI) operates the High Intensity Proton Accelerator (HIPA), which delivers a continuous proton beam with energy of 590 MeV and a current of up to 2.4 mA. The protons are produced in a compact electron cyclotron resonance (ECR) source [1], which is located in the Crockcroft-Walton. The 870 keV protons are subsequently accelerated in two cyclotrons called injector2 and ring. In the first step, injector2 accelerates the protons to 72 MeV. From there they are injected to the ring cyclotron and finally extracted with an energy of 590 MeV. On their way to the spallation source SINQ, they pass two graphite targets Target M and Target E used for meson production. The latter one has a thickness of 40 mm, which leads to a reduction of the beam energy to 575 MeV as well as beam loss. Due to multiple scattering at Target E, an extended collimator system follows to shape the beam. Including the beam loss at Target E, the beam intensity drops by 30%. In normal operation, the beam is guided to SINQ, where it is fully stopped. The purpose of SINQ is to deliver a high flux of thermal and cold

neutrons for e.g. material research. The neutrons are produced in lead, which is packed into about 350 tubes called cannelloni. Today, the cladding consists of zircaloy. Zircaloy absorbs fewer neutrons than steel, which was used formerly. The cannellonis are cooled by D_2O and surrounded by a safety shroud from AlMg3. To date, SINQ is the most powerful continuous spallation neutron source in the world.

Figure 1. Sketch of the lower part of SINQ target-4 with the safety hull, (left) sketch of the beam profile on the first row of cannellonis (right)

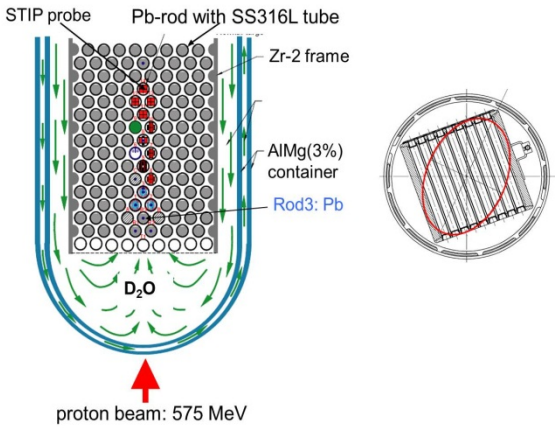

Each SINQ target is irradiated for 2 years. After that it has to be replaced to avoid failure due to radiation damage. The target is highly activated with dose rates around 10 Sv/h after 1 year cooling time in the SINQ target storage. Therefore, it has to be disposed as radioactive waste. The STIP(SINQ Target Irradiation Programme – a research programme aimed to study material properties after high-power proton und neutron exposure) samples, which often contain other materials than lead, are used for post-irradiation examination. They are removed by remote-handling via manipulators in the service cell ATEC. For disposal, the SINQ target is put into a steel container, which is filled with lead-bismuth eutecticum (LBE) for safety reasons. Before the SINQ target can be disposed as radioactive waste, the authorities require – in addition to other documentation – the complete nuclide inventory with radioactive isotopes of half-lifes larger than 60 days. The complete nuclide inventory can only be provided by calculations. For the evaluation of nuclide inventories of directly irradiated components the particle transport Monte Carlo programme MCNPX [2] is used at PSI. The calculated nuclide inventories have to be at least partially validated by comparison with experimental data, i.e. specific activities of relevant isotopes. Particularly interesting are isotopes with are highly radiation hazardous like α-emitters and volatile elements. Some of these isotopes have to be extracted first by radiochemical methods before their activities can be measured. Isotopes with high energetic photons, which are particularly damaging to the human body, are of interest as well. Since MCNPX is also used for other purposes at PSI, it is important to have an estimate of the reliability and uncertainty of its predictions.

Figure 2. Double Gaussian beam distribution from MCNPX, (left) proton flux distribution along Rod3 (right)

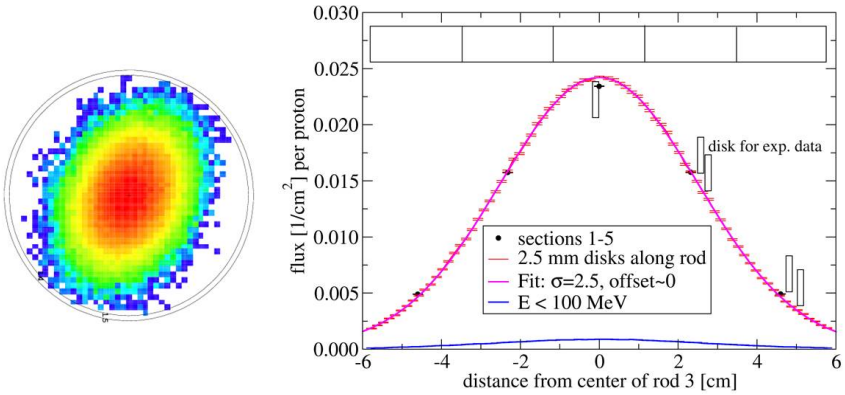

The locations of the sample disks and the partitioning of the rod as used in MCNPX are also shown.

For this purpose, a cannelloni filled with lead was removed from the centre of the second filled row of SINQ target-4. This cannelloni is called Rod3 (see Figure 1). Next to Rod3, left and right as well as downstream, STIP samples were located (see Figure 1). Rod3 was also equipped with a thermocouple, which indicated an operation temperature of 550 +/-30 K, close to but lower than the melting temperature of lead of 600.6 K. Target-4 was in operation in 2000 and 2001, where it received 10.03 Ah protons. The cannellonis of target-4 were still made of stainless steel 316L. The target holder itself had a quadratic cross-section of about 14 cm x 14 cm and was about 40 cm long. The shape of the proton beam on the target window had in good approximation a double Gaussian profile. Since Rod3 is from the centre of the target, the flux distribution of the protons and secondary particles is symmetric along the rod with respect to its centre (see Figure 2). Because Rod3 is located in the second row, the protons are mainly high-energetic and resemble the Gaussian profile of the beam. As expected, the neutron flux distribution is wider than the proton distribution and does not vanish close to the end caps of the rod. For further examination with radiochemical methods, the lead bar of Rod3 was cut into a few disks, each 1.5 mm thick, which later were subdivided. The specific activities of 17 isotopes were measured in five disks. The locations of the disks relative to the centre of Rod3 are indicated in the plot of the proton flux distribution in Figure 2. The activities of the γ-emitters ^{60}Co, ^{101}Rh, ^{102m}Rh, ^{125}Sb, ^{133}Ba, ^{172}Hf, ^{172}Lu,^{194}Hg, ^{207}Bi were detected by a High Purity Germanium detector (HPGe) [3]. The α-emitters ^{146}Sm, ^{148}Gd, ^{150}Gd, ^{208}Po, ^{209}Po, ^{210}Po had first to be chemically separated and then were measured by an α-analyst spectroscopic system from Canberra using the GENIE-2000 software [4]. The amount of very long-lived isotopes ^{36}Cl and ^{129}I had to be measured by Accelerator Mass spectrometry (AMS) at the ETHZ Hönggerberg after chemical separation for a suitable ion source. The distribution of the specific activities along the rod follows the proton flux distribution for all isotopes – except for two, ^{36}Cl and ^{125}Sb. This suggests another or additional reaction mechanism in addition to the spallation by protons. When the activity of ^{210}Po was determined 10.5 y after end of beam (EOB), it was surprisingly high – much higher than predicted by the available calculations at the time. With a half-life of only 138 d simple back-scaling of activities to EOB would result in an enormous activity of 1.2 10^{13}Bq/g. The measurement was repeated after 1 additional year. The activity of ^{210}Po was almost as high as 1 year ago in the first measurement. This discrepancy triggered the following work.

In this report it will be shown how the nuclide inventory is obtained using MCNPX coupled to build-up and decay codes in general. The post-analysis, necessary before comparing to the experimental results, will be shortly explained. Reaction mechanisms leading to the production of Po-isotopes will be discussed and supported by extracted production cross-sections. As the physics cross-section models implemented in MCNPX2.7.0 could not explain the high activity of ^{210}Po, a new physics model, INCL4.6/ABLA07, was

implemented in MCNPX2.7.0. The most important features of INCL4.6/ABLA07, particularly the improvements compared to the older version INCL4.2/ABLA, which is still a model choice in MCNPX2.7.0, will be listed. Finally, the calculated activities using the default model in MCNPX2.7.0 as well as INCL4.6/ABLA07 will be compared to experimental data.

Nuclide inventory by MCNPX

MCNPX can transport all kind of particles, protons, neutrons, pions up to heavy nuclei. Nuclear reactions of these particles have to be handled by physics models, when no cross-section tables are available. Physics models are necessary, since there is no exact theory for the strong interaction yet. Most physics models use, for the SINQ energy range, the microscopic picture of an intranuclear cascade (INC) followed by evaporation or fission. In the first step, the INC, the energy transferred by the primary particle is dissipated in the nucleus to several nucleons by nucleon-nucleon collisions. The INC proceeds until the dissipated energy falls below a specified value, related to the depth of the nuclear potential well, or a stopping time has been reached. The typical duration of the intranuclear cascade is 10^{-22} seconds. During the INC, high energetic particles might be emitted in forward direction by direct reactions, i.e. high-energy transfer from the primary particles to a constituent of the nucleus. If the INC is not able to give a thermalised remnant nucleus, it is followed by a preequilibrium phase. When the INC (with or without a preequilibrium step) is finished, the nucleus is left in an excited state with defined excitation energy and an angular momentum. The number of protons and neutrons residing in the nucleus is usually already less than in the target nucleus, as some particles might have been already emitted. When the excitation energy is high enough, low energetic particles, often neutrons but also light ions and photons, are emitted isotropically at low kinetic energy. This is called evaporation and leads to the reduction of the excitation energy until no particle can be emitted anymore. Depending on the conditions and on the remaining nucleus, fission is a competitive reaction channel.

The INC model BERTINI [5,6] has for years been the default choice in MCNPX for neutrons and protons of energy less than 3.5 GeV. The BERTINI model, which uses a pre-equilibrium step by default, is coupled to the evaporation code of Dresner [7]. The DRESNER code is based on Weisskopf´s statistical model. Fission, if possible, is handled by the RAL code [8]. Since BERTINI can handle only protons and neutrons, reactions containing light ions up to 1 GeV are handed over to ISABEL [9].

In addition to BERTINI and ISABEL, MCNPX2.7.0 contains the Cascade Exciton Model CEM3.03 [10] and INCL4.2/ABLAV3p. CEM is able to emit light ions and clusters up to ^{28}Mg. INCL4.2 has several known shortcomings. For instance, the model cannot form clusters in the cascade state and reaction cross-sections below 100 MeV are severely underestimated. In addition, the version ABLAV3p [11], could only emit neutrons, protons and ^{4}He. Tritons are missing, which means that the tritium content is always underestimated using ABLAV3p. Therefore, INCL was upgraded to INCL4.6 [13] and ABLA to ABLA07 [14]. The new INCL4.6 treats neutrons, protons, pions, deuterons, tritons, ^{3}He and α-particles, i.e. reaction cross-sections are provided for reactions with these particles as projectiles. At the same time, INCL4.6 is also able to emit such particles as well as light fragments up to a mass number of 8 during the intranuclear cascade phase. This is done by forming these clusters by coalescence in phase space. ABLA07 itself is able to generate neutrons, protons, deuterons, tritons, ^{3}He, α-particles as well as intermediate mass fragments (IMF) by break-up, fission or evaporation. A drawback of the new physics model INCL4.6/ABLA07 is that no information of the production of metastable nuclei in the residual state is available. The fraction, which is devoted to the metastable partner, is needed not only for the calculation of metastable nuclei but also for the ground state. This fraction is subtracted from the number of ground state nuclei and therefore reduces its activity. To take this into account, the fractions of metastables produced were taken

from the MCNPX default choice. Previously, comparison with measured radioisotope activities provided good results with it, also for metastables like ^{108m}Ag.

In the following work, a comparison of the activities obtained with the MCNPX default physics model and INCL4.6/ABLA07 as well as with data has been made. Since INCL4.6/ABLA07 is not available in one of the officially released versions of MCNPX or MCNP, it was implemented in MCNPX2.7.0 as a replacement for INCL4.2/ABLA. The implementation was performed in such a way that the code runs on several CPU´s in parallel. The final version will be sent to RSICC as a patch (MW) to comply with the regulations for the use of the MCNPX source code. In our upgraded version of MCNPX2.7.0, the production rates obtained from the physics models are not written to the histp-file but appended to the MCNPX output file. Otherwise the histp-file would become dramatically large, which finally would limit the number of primary particles in the simulation. This method is similar to a previous patch for MCNPX2.5.0 included in the CINDER1.05 package from the NEA Data Bank [15]. This package contains also the so-called activation script [16], which simplifies the coupling of the output of MCNPX and decay- and build-up codes to proceed finally to the activities. The decay- and build-up code CINDER1.05 [17] was used in this report and was checked using FISPACT-2007 [18] with EAF-2007 [19].

For neutrons of E<20 MeV, the physics models are not evoked but rather tabulated cross-sections ENDF/B-VI are applied. Therefore, their production rates are not written to file instead the neutron flux up to 20 MeV in each cell is recorded. The neutron flux is later folded by production cross-sections provided by CINDER1.05 or EAF-2007.

The geometrical model used for the calculations in MCNPX is shown in Figure 3. The geometry of the full SINQ monolith, which is available as MCNPX input, was limited to the necessary parts to speed up the Monte Carlo simulation. This is the target with some D_2O (in turquoise) around and part of the steel dump to account for backscattered neutrons. All STIP probes with their different material compositions were modelled as they have a significant influence e.g. on the neutron flux in the SINQ target. The presence of all STIP probes reduces the neutron flux by ca. 20%. To further reduce the computation time to reach sufficient statistics, Rod3 was divided into 5 parts only, one central to the beam. Each part is 2.32 cm long. With disks of 1.5 mm thickness, as they were used in the radiochemical examination, the required statistics could not be reached on a reasonable timescale. The subdivision into five cells, which are much larger than the disks, means that the nuclide inventory calculated is an average over the region of the cell. Moreover, the positions of the experimentally investigated disks do not coincide with the centres of the cells, as shown in Figure 2. In addition, the calculated nuclide inventory was corrected by a factor obtained from the ratio of the proton flux in the disk and in the corresponding cell. This procedure is justified as the radioactive isotopes under consideration are produced mainly by protons – except for the Po isotopes. It turned out that tritons and alphas follow closely the spatial flux distribution of protons along the rod. As expected, tritons and alphas are produced by high energetic protons.

For the results presented in this work, the high performance cluster ROSA in Lugano, Switzerland, was used for the calculations with INCL4.6/ABLA07. To calculate the activities 86016 CPU*h, it was only necessary to count the runs. The total number of primary particles was 3.3 10^9. Other runs like the calculation of the particle fluxes or using pure Pb, are not included in this line-up. These additional simulations amount in about the same order of CPU*h as given above. As MCNPX with the default choice of INC and evaporation models runs much faster, the calculations could be performed on the smaller parallel cluster MERLIN available at PSI. 2.4 10^9 primary particles were collected from different runs in 4704 CPU*h.

Figure 3. Full (reduced) geometrical model used in MCNPX, (left) zoom into the target area (right)

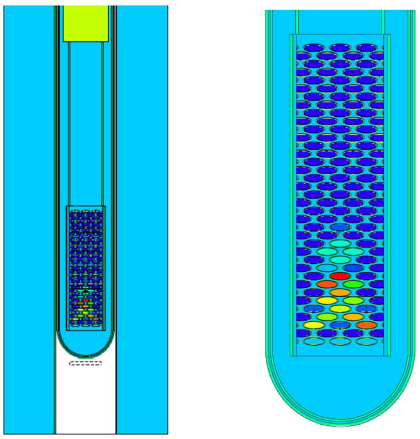

Po-isotopes: Production mechanisms and comparisons of the activities

Using the MCNPX default choice as described above the three relevant Po-isotopes, ^{208}Po, ^{209}Po, ^{210}Po are almost exclusively produced from the Bi impurity in the lead. Since these production mechanisms were known at the design state of SINQ, lead with a low Bi impurity is used. Still, the abundance of Bi in the SINQ lead is 220 ppm [20]. Since Bi has only one stable isotope, ^{209}Bi, the relevant production channels are as follows

^{209}Bi(p,2n)^{208}Po

^{209}Bi(p,n)^{209}Po

^{209}Bi(p,γ)^{210}Po, ^{209}Bi(n,γ)^{210}Bi $\rightarrow$ ^{210}Po

For the ^{210}Po production clearly the n-capture is the dominant reaction mechanism and leads to a large activity of the order of MBq/g ^{210}Po in the lead of the SINQ target after end of operation. ^{210}Bi decays with a half-life of 5 min into ^{210}Po. According to the MCNPX default physics model no other reaction mechanism leads to a significant contribution. Since ^{210}Po has a half-life of 138 d, the ^{210}Po activity should be well below 1 Bq/g after 10 years cooling time. This prediction is in strong disagreement with the recent measurement performed at PSI [4]. Therefore, other reaction mechanisms were considered. The double n-capture on ^{208}Pb is negligible, particularly since ^{209}Pb has a half-life of 3 h and the neutron fluxes in the SINQ target are moderate. Nevertheless, the reaction channel is considered in the Cinder1.05 library. A promising reaction mechanism is ^{208}Pb(t,p)^{210}Pb, where ^{210}Pb decays with a half-life of 22 years to ^{210}Bi, which almost instantaneously decays into ^{210}Po. As described above INCL4.6 is able to simulate reactions with tritons as well as to produce tritons as secondary particles from the proton nuclear reaction, which is a prerequisite. The triton energy spectrum as well as its cross-sections on ^{208}Pb to ^{210}Pb was explicitly calculated with INCL4.6 and MCNPX default settings. The comparison is shown in Figure 4. The tail to higher energies of the triton spectrum obtained by INCL4.6 is striking compared to MCNPX default. This is surely a consequence of the new feature in INCL4.6 to emit high energetic tritons during the INC phase. In spite of this, the peak at about 20 MeV is a bit higher. The low energetic tritons are mostly produced by evaporation, i.e. ABLA07. A more dramatic difference is seen in the triton production cross-section for ^{210}Pb. On the linear scale, the result from MCNPX2.7.0 default cannot be seen as it is 4 orders of magnitude lower. The cross-section from INCL4.6 is of the order of 20 mbarn at its maximum, at 25 MeV. It is concentrated in a small band of +/- 5 MeV around the maximum. Therefore, the high energetic tritons do

not contribute much to the production cross-section of ^{210}Pb. A triton energy distribution as obtained by MCNPX default using the INCL4.6 cross-section would lead to about a factor 2 to 3 lower production rate only.

Figure 4. Triton flux obtained with the two physics models in MCNPX

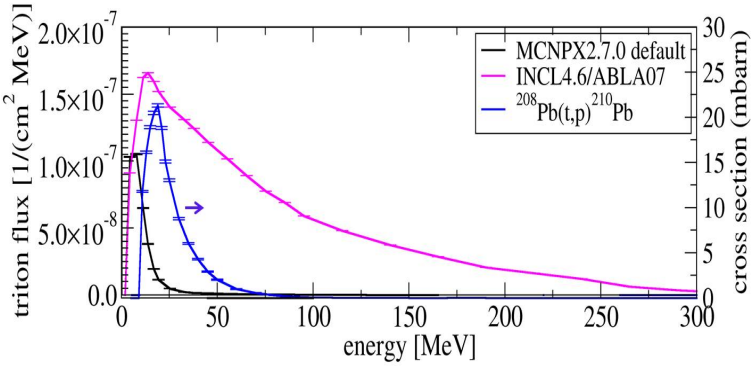

Blue curve: Cross-section for the reaction ^{208}Pb(p,t)^{210}Pb (right axis).

The time dependence of the ^{210}Po specific activity is shown in Figure 5 for the central part of Rod3. It illustrates and confirms the considerations above. Using MCNPX default the ^{210}Po activity simply decays with its half-life of 138 d. 7-8 years after end of operation the decay curve slows down. After 9 years the activity is completely determined by the decay of ^{210}Pb, which is produced in very small quantities by MCNPX with default settings. However, the measured ^{210}Po activity after 10.5 years is about 5 orders of magnitude larger than obtained with MCNPX default. The new implemented physics model INCL4.6/ABLA07 leads to a production of ^{210}Pb in a much larger amount. It was obtained by folding the calculated triton spectrum with the corresponding production cross-section depicted in Figure 4. However, the statistics for the reaction channel was still unsatisfactory. Nevertheless, the ^{210}Pb production rate calculated with MCNPX plus INCL4.6/ABLA07 agreed within a factor of less than 2 in all 5 cells of Rod3 with the one obtained by folding. Already after 3 years the activity of ^{210}Po is in radioactive balance with ^{210}Pb, which is about 5 orders of magnitude larger than calculated with MCNPX default.

Figure 5. Predicted time dependence of ^{210}Po after end of beam (EOB) using the two physics models and comparison to the experimental data point

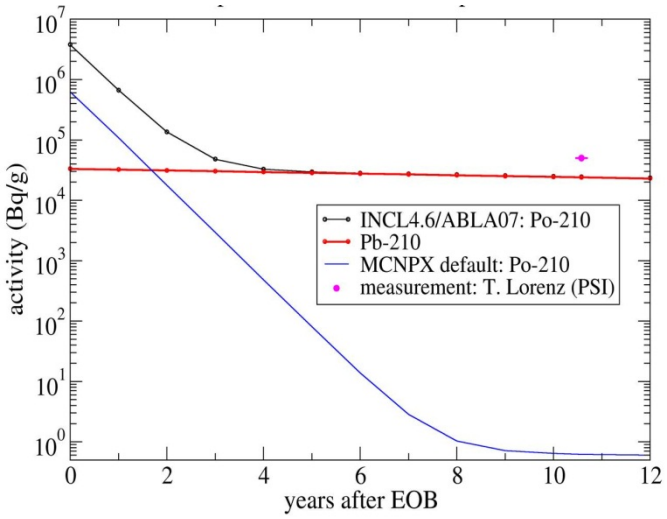

Figure 6. Ratio of simulated and measured activities, averaged over the different measured locations, 10.5 y after EOB

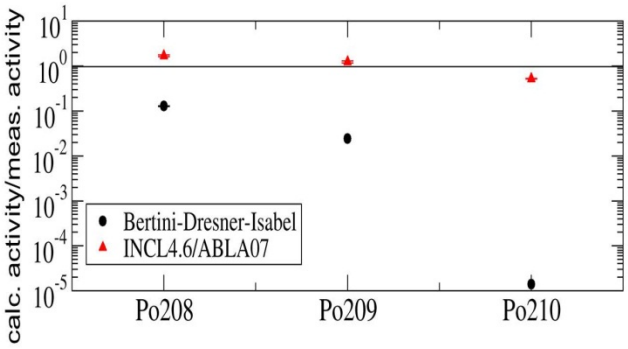

The specific activities of ^{210}Po, ^{208}Po and ^{209}Po, obtained with INCL4.6/ABLA07, are remarkable close to the experimental data points (see Figure 6). The comparison to the data is made at the measurement date, about 10.5 years after end of operation. The results depicted in Figure 6 were averaged over the different measurement locations. The time dependent behaviour of ^{208}Po and ^{209}Po was also checked. It corresponded to a pure decay, i.e. no other isotopes are contributing to it.

It should be noted that the ^{210}Po activity just after end of operation is about 5 times larger using INCL4.6/ABLA07 compared with MCNPX default (see Figure 5 at 0 years). This contribution cannot result from the Bi impurity, since the same tabulated neutron cross-sections were used in MCNPX applying the two physics models, which leads to the same neutron flux spectra below 20 MeV. A test run with pure Pb confirmed this assumption. In addition, the production of ^{208}Po and ^{209}Po is also increased by a factor of 10 and 100, respectively. This is clearly seen in Figure 6, when compared with the results from MCNPX default. This means that the Bi impurity is not the main source of the Po production anymore. It contributes about 20% to the ^{210}Po activity in the first years before ^{210}Po is produced via ^{210}Pb. Bi only contributes only 10% and 1% to the production of ^{208}Po and ^{209}Po, respectively. The reaction channels, which produce the Po isotopes from the stable Pb isotopes are driven by alphas this time. In Figure 7, the ^{208}Po production cross-section is shown for alpha particles on three Pb isotopes ^{206}Pb, ^{207}Pb, ^{208}Pb. The cross-sections obtained by INCL4.6/ABLA07 are 4 to 5 orders of magnitude larger than extracted from MCNPX default simulations. Two sets of experimental data [21-22] are in very good agreement with the predictions of INCL4.6/ABLA07. If one compares the cross-sections from ISABEL for the three Pb isotopes relative to each other, they show at least the same order as the ones from INCL4.6/ABLA07.

Figure 7. ^{208}Po production cross-section by alpha reaction on Pb isotopes

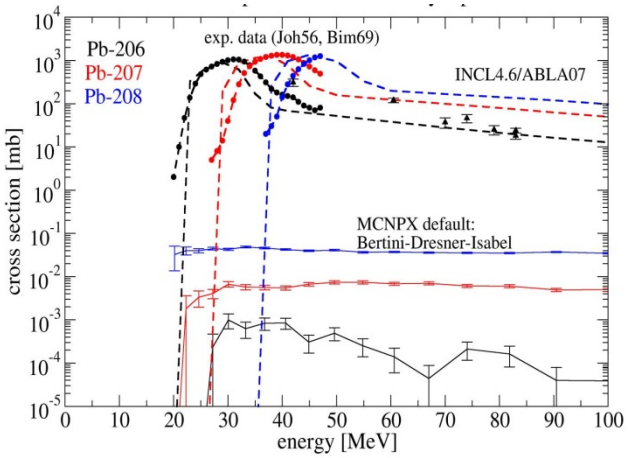

Figure 8 shows the spatial distribution of the calculated Po activities along the rod using INCL4.6/ABLA07 in logarithm scale and the spatial distribution is compared to the data. The error bars of the calculation are purely statistical. They result from the statistical error of the production rate calculations. As expected from the reaction mechanisms and keeping in mind that the spatial flux distribution of tritons and alphas are very similar, the calculated spatial distributions of the activities of the three Po isotopes are very similar and follow the proton flux distribution. The comparison to the experimental data is satisfactory and is a significant improvement compared to MCNPX default.

Figure 8. Spatial distribution of the three Po isotopes along Rod3

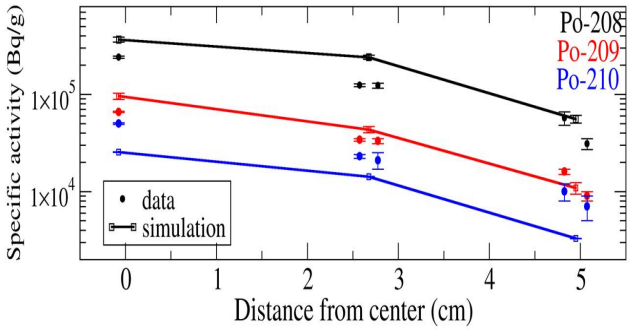

Comparison of the results obtained with INCL4.6/ABLA07 and measurement.

Comparison of the calculated and measured activities for the remaining isotopes

In addition to Po, the activities of 12 γ-emitters and two long-lived isotopes were measured at different positions along Rod3. The isotopes were already listed above. Since it is not feasible to show all comparisons in detail in this report, first a comparison of the spatial distributions along Rod3 for the activities obtained with INCL4.6/ABLA07 and MCNPX default was made. This would allow observing large differences and might suggest different production mechanisms. As can be seen in Figure 9, the variation of the ratio of the activities calculated with INCL4.6/ABLA07 and MCNPX default is between 0.2 and 2.5. In most of the cases, MCNPX default predicts larger activities. For most of the

isotopes, the distribution of the activities is the same, i.e. the ratio is roughly constant. The largest difference appears for ^{36}Cl and ^{148}Gd. Far from the centre of Rod3, INCL4.6/ABLA07 predicts almost a factor two larger activity of ^{36}Cl. As this isotope showed a broader spatial distribution in the measurement, it will be investigated in more detail below.

Figure 9. Ratio of activities obtained by MCNPX using INCL4.6/ABLA07 and BERTINI-DRESNER-ISABEL

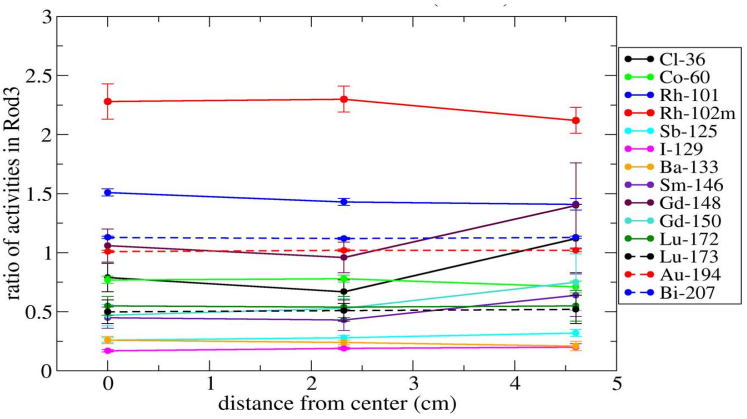

Figure 10. Comparison of the calculation using the two physics models to the measured activities of the remaining isotopes

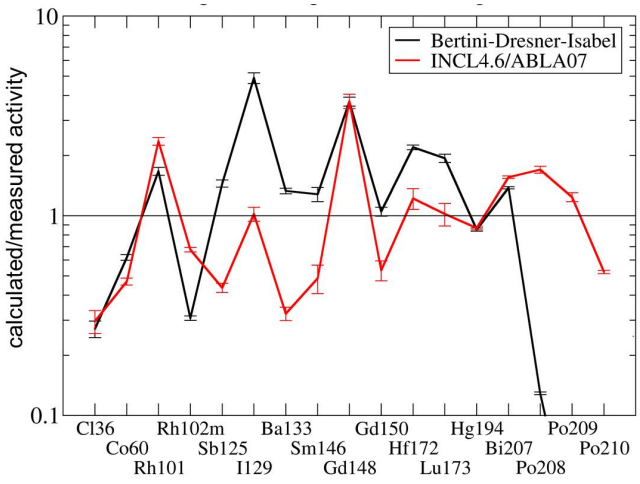

A comparison with the experimental data is shown for both physics models in Figure 10. The ratio of the calculated to measured activities is the weighted average over the results obtained at the measured locations. The experimental data, which are spatially close to each other, were averaged first. Excluding the Po-isotopes in the following discussion, the deviation of the calculated activity to the measured one is less than a factor of four for both physics models. The largest deviations appear for ^{36}Cl and ^{102m}Rh. The prediction for ^{102m}Rh could be improved by INCL4.6/ABLA07 by a factor 2. A significant improvement can also be noted for ^{129}I. On the other hand, ^{133}Ba is worse predicted than in MCNPX default. Altogether both physics models show a similar behaviour and agreement.

In Figure 11, a detailed comparison for ^{36}Cl activity is presented as a function of the position in Rod3. The experimental data seems to be quite independent of the position. There is some spread of the data and the uncertainties are larger compared to other isotopes. This is due to the difficult preparation and measurement via AMS. As already mentioned, both physics models predict similar ^{36}Cl activities. At the centre of Rod3, they both match well with the measurement. The disagreement becomes obvious when compared with the data at the tail of Rod3. In the simulation, ^{36}Cl is produced by spallation only, mainly from Pb, as the elemental composition of Pb used in MCNPX contains no Cl. Therefore the spatial distribution of the calculated activity follows the proton flux distribution. INCL4.6/ABLA07 slightly deviates from this at the outer region of Rod3. However, the reason why Cl is not in the material composition of Pb, is that it could not be measured in [20]. The method used is ICP-OES, i.e. inductively coupled plasma optical emission spectroscopy. Via n-capture on Cl ^{36}Cl is produced. Therefore elemental Cl would certainly broaden the spatial distribution of the activity along Rod3, since the neutron flux distribution is much broader and particularly has much more strength at the tail of the rods. Therefore some Cl was added to the material composition defined in MCNPX using INCL4.6/ABLA07 and its effect studied. It turned out that a tiny fraction of 0.5 ppm Cl is enough to match quite well the measured activities (see Figure 11). It seems that even less (about a factor 2) might be sufficient to explain the trend of the data.

Figure 11. Spatial distribution of the ^{36}Cl activity comparing calculations and measurement

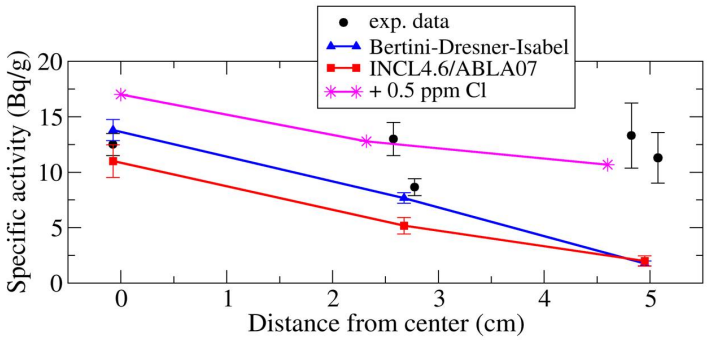

Figure 12. Spatial distribution of the ^{125}Sb activity comparing calculations and measurement

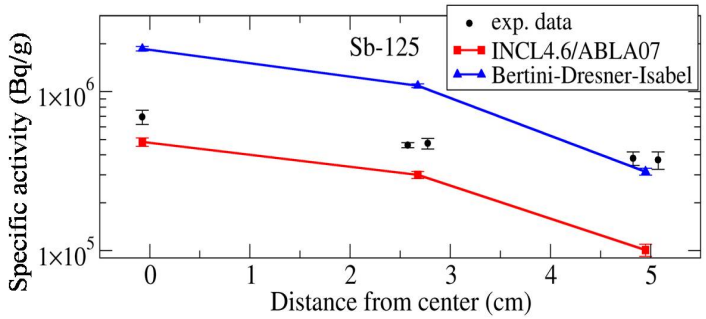

A similar trend of the data is observed for ^{125}Sb. The results are shown at the date of measurement in November 2011 in Figure 12. The results from both physics models follow the shape of the proton distribution. The difference between them is a factor 3 whereas the experimental data are somehow in between the two predictions. Similar to the case of ^{36}Cl, we looked deeper into possible reaction mechanisms with a neutron

involved as the primary particle to broaden-up the spatial distribution. Two ideas came up. Neutron capture on ^{124}Sn leads to ^{125}Sn, which decays with a half-life of 2.8 y to ^{125}Sb. This process is driven by low-energy neutrons and is included in the Cinder1.05 library. The abundance of Sn in the material definition of Pb is 100 ppm. However, the isotope fraction for ^{124}Sn is only 5%. A second possibility would be double neutron capture on ^{123}Sb. The interim state has a half-life of only 60 d, which reduces the probability of a second neutron capture. In order to determine the contribution to the ^{125}Sb production for both reaction mechanisms, both elements, Sn and Sb, were removed from the Pb composition. It turned out that their contribution to ^{125}Sb production is negligible. Since the reaction mechanisms described above strongly depend on the corresponding cross-sections in the build-up and decay code, the analysis was performed also with FISPACT-2007 using EAF-2007. There were no additional contributions to the production of ^{125}Sb in agreement with CINDER1.05. The discrepancy between the measured data and the calculation is not solved yet.

Summary and outlook

Knowledge of the nuclide inventory of highly activated components is important to make provisions during operation in case of an accident as well as for the later disposal as radioactive waste. The nuclide inventory is provided by calculations and therefore needs to be validated by measurements. In the spallation target-4 of SINQ at PSI, the activities of 17 isotopes were measured at positions in the lead material of one cannelloni, which is located central and close to the proton beam entrance window. Ten years after the end of operation of the target, a 5 orders of magnitude, a larger activity was measured for ^{210}Po compared with predictions from the calculations available at this time (MCNPX with default physics model). In addition, ^{210}Po decayed much slower than expected. This led to the conclusion that ^{210}Po is fed by ^{210}Pb, which can be produced by tritium reaction on ^{208}Pb. As the cross-section for this reaction is negligible for the default physics model in MCNPX, BERTINI-DRESNER-ISABEL, a new intranuclear cascade model INCL4.6 plus the evaporation/fission code ABLA07 was implemented in MCNPX2.7.0 in a way to allow for parallel computation and to avoid huge data output (histp-file). Good agreement with the measured ^{210}Po activity as well as the ^{208}Po and ^{209}Po activities was found using INCL4.6/ABLA07. The spatial distribution along the rod is well reproduced, too. The ^{208}Po and ^{209}Po, ^{210}Po activities were also a factor 10, 100 and 5 higher than predicted with MCNPX default. Reactions with alphas on the lead isotopes leading to ^{208}Po, ^{209}Po, ^{210}Po were not accounted for properly in the previous calculation. This means that all Po-isotopes are mainly produced from lead and not from the Bi impurity as predicted by MCNPX default choice.

For the remaining isotopes, differences between BERTINI-DRESNER-ISABEL and INCL4.6/ABLA07 are less than a factor 5. The largest deviation from the data is observed for ^{36}Cl. The measured activities of ^{36}Cl and ^{125}Sb show along the rod a much flatter distribution than the calculations, which follow the shape of the proton beam. This suggests reactions with low energetic neutrons which are more evenly distributed due to isotropic evaporation from the nuclei. The material definition used for the calculation does not contain Cl, because it could not be detected with ICP-OES. The addition of 0.5 ppm Cl considerably improved the agreement with the data. Although ^{125}Sb can also be produced by neutrons from ^{124}Sn or ^{123}Sb, the contribution is small according to the calculation. No reaction mechanism was found to explain the flat distribution of the measured activity for ^{125}Sb.

As interest in comparing the measured Po data with other codes was great during the workshop, a benchmark will be organised involving all state-of-the-art codes FLUKA [23], GEANT[24], MARS [25] and PHITS [26] in addition to MCNPX2.7.0. PHITS already uses INCL4.6/ABLA07 by default and A. Ferrari has a private version of FLUKA with INCL4.6/ABLA07 for testing [27]. The benchmark will be performed first on a simplified toy model, a lead block surrounded by D_2O, to avoid large running times (still the

computer power needed is considerable) and the additional time to code the detailed geometry. A comparison with MCNPX using INCL4.6/ABLA07 will be made with other physics models available in MCNPX2.7.0. In particular, ISABEL will be used as INC model not invoking BERTINI to check, if the coupling between BERTINI and ISABEL has an influence on the treatment of reactions with tritons and alphas. Y. Yariv is working on an improved version, ISABEL2. For this, a comparison of the cross-sections for the relevant reaction channels will be made.

On the experimental side, there is on-going work to measure the spatial distribution of the activities of several isotopes in three more rods from the same SINQ target-4. One rod will be in the fourth filled row not in a central position, the other one is roughly in the centre of the target in a central position. The last rod is located in the last row and in the outermost position. Therefore, additional interesting data for comparisons will become available.

Acknowledgements

This work was supported by a grant from the Swiss National Supercomputing Centre (CSCS) under project PSI. Part of the calculations was performed at the HPC Merlin4 cluster at PSI.

References

[1] C. Baumgarten, A. Barchetti, H. Einenkel, D. Goetz, P.A. Schmelzbach (2011), "A compact electron cyclotron resonance proton source for the Paul Scherrer Institute's proton accelerator facility", *Rev. Sci. Instrum.*, 82[5], 053304.

[2] D.B. Pelowitz (2011), "MCNPX user's manual – version 2.7.0", LA-CP-11-00438.

[3] T. Lorenz, Y. Dai, D. Schumann (2013), "Analysis of long-lived radionuclides produced by proton irradiation in lead targets –γ- Measurements", *Radiochim. Acta*, 101[10], pp. 661-666.

[4] T. Lorenz, Y. Dai, D. Schumann, A. Türler (2014),"Proton-induced Polonium Production in Lead", *Nucl. Data Sheets*.

[5] H.W. Bertini (1963), "Low-Energy Intranuclear Cascade Calculation", *Phys. Rev.,* 131, pp. 1801-1821.

[6] H.W. Bertini (1969), "Intranuclear-Cascade Calculation of the Secondary Nucleon Spectra from Nucleon-Nucleus Interactions in the Energy Range 340 to 2900 MeV and Comparisons with Experiment", *Phys. Rev.,* 188, pp. 1711-1730.

[7] L. Dresner(1981), "EVAP-A Fortran Program for Calculating the Evaporation of Various Particles from Excited Compound Nuclei", *Oak Ridge National Laboratory report ORNL-TM-7882*.

[8] F. Atchison (2007), "A treatment of medium-energy particle induced fission for spallation-systems' calculations", *Nucl. Instr. Meth.* B, 259, pp. 909-932.

[9] Y.Yariv, Z.Fraenkel (1979), "Intranuclear cascade calculation of high-energy heavy-ion interactions", *Phys. Rev. C*, 20, pp. 2227-2243; dito (1981),"Intranuclear cascade calculation of high energy heavy ion collisions: Effect of interactions between cascade particles", *Phys. Rev. C*, 24,pp. 488-494.

[10] S.G. Mashnik, A.J. Sierk (2012), "CEM3.03 User Manual", *LANL Report LAUR-12-01364*, Los Alamos, US.

[11] J.-J. Gaimard, K.-H. Schmidt (1991), "A reexamination of the abrasion-ablation model for the description of the nuclear fragmentation reaction", *Nucl. Phys. A*, 531, pp. 709-745.

[12] A.R. Junghans, M. de Jong, H.-G. Clerc, A.V. Ignatyuk, G.A. Kudyaev, K.-H. Schmidt (1998), "Projectile-fragment yields as a probe for the collective enhancement in the nuclear level density", *Nucl. Phys. A*, 629, pp. 635-655.

[13] A. Boudard, J. Cugnon, J.-C. David, S. Leray, D. Mancusi (2013), "New potentialities of the Liège intranuclear cascade model for reactions induced by nucleons and light charged particles", *Phys. Rev. C*, 87, p. 014606.

[14] A. Kelić, M.V. Ricciardi, K.-H. Schmidt (2008), "ABLA07 – Towards a Complete Description of the Decay Channels of a Nuclear System from Spontaneous Fission to Multifragmentation", *IAEA INDC(NDS)-0530*, pp. 181–222.

[15] CINDER1.05, NEA-databank CCC-0755, https://rsicc.ornl.gov/, http://www.oecd-nea.org/tools/abstract/detail/CCC-0755/.

[16] F.X. Gallmeier et al. (2007), "An Environment using Nuclear Inventory Codes in Combination with the Radiation Transport Code MCNPX for Accelerator Activation Problem", *Proc. of the 8th Int. Topical Meeting on Nuclear Applications and Utilization of Accelerators*, Pocatello, US, p. 207.

[17] W.B. Wilson et al. (1995), "Recent Developments of the CINDER'90 Transmutation Code and Data Library for Actinide Transmutation Study", *Proc. GLOBAL'95 Int. Conf. on Evaluation of Emerging Nuclear Fuel Cycle Systems*, Versailles, France.

[18] R. Forrest (2007), "FISPACT-2007: User manual", *UKAEA FUS 534*, UKAEA.

[19] R. Forrest, J. Kopecky, and J.-C. Sublet (2007), "The European Activation File: EAF-2007 neutron-induced cross section library", *UKAEA FUS 535*, UKAEA.

[20] R. Keil (1999), "Chemical analysis of lead from SINQ target 4", *Analysis No. 7129*, PSI.

[21] R. Bimbot, H. Jaffrezic, Y. Le Beyec, M. Lefort, A. Vigny-Simon (1969), "Étude du mécanisme des réactions nucléaires induites par particules α de haute énergie I. Réactions 206Pb(α,xn)210-xPo", *J. de Physique,* 30[7], pp. 513–520.

[22] W. John (1956),"Excitation Functions for (α,xn) Reactions on Lead", *Phys. Rev.,* 103, pp. 704-713.

[23] G. Battistoni, S. Muraro, P.R. Sala, F. Cerutti, A. Ferrari,S. Roesler, A. Fasso, J. Ranft (2007), "The FLUKA code: Description and benchmarking", *AIP Conference Proceeding 896*, pp. 31-49.

[24] S. Agostinelli et al. (2003), "Geant4 - A Simulation Toolkit", *Nucl. Instr. & Meth. A*, 506, pp. 250-303.

[25] N.V. Mokhov (2010), "Recent Mars15 developments: nuclide inventory, DPA and gas production" ,*Fermilab-Conf-10-518-APC*.

[26] T. Ogawa, S. Hashimoto, T. Sato, K. Niita (2014), "Development of gamma de-excitation model for prediction of prompt gamma-rays and isomer production based on energy-dependent level structure treatment", *Nucl. Instr. Meth. B*, 325, pp. 35-42.

[27] A. Ferrari, private communication during the SATIF-12 workshop.

Activation by 2.25 and 3.36 GeV electrons: Comparison of measurements with FLUKA calculations

George Kharashvili, Pavel Degtiarenko
Jefferson Lab, Newport News, Virginia, US

Abstract

Activation of materials impacted by GeV electron beams at particle accelerator facilities is of great importance for the purposes of radiation protection as well as decommissioning. In order to measure common material activation in the beginning and well inside an electromagnetic cascade, Al, Cu, Nb, Pb, and stainless steel foils (0.01 – 0.1 mm) were placed upstream and downstream of 1.25 cm thick tungsten alloy plates and irradiated by 2.25 and 3.36 GeV electron beams. Gamma spectroscopy analysis of each foil was then performed using high purity germanium detectors. The measured activities were compared to the values calculated using FLUKA Monte Carlo code. A good overall agreement was shown for the foils placed inside well-developed cascades, while activation in the beginning of the cascades was generally underestimated. The underestimation was corrected by the introduction of a simplified model of electronuclear interaction based on the equivalent photon approximation.

Introduction

One of the most important concerns of radiation safety programmes at high-energy electron accelerator facilities is induced radioactivity. It typically presents the most significant source of occupational exposure and must also be considered from the points of view of environmental impact, material disposal, and facility decommissioning [1]. Most radioactivity at electron accelerators is produced by the photonuclear reactions and by the secondary radiation, such as neutrons. However, in thin targets (thicknesses of less than a few percent of a radiation length) the electronuclear interaction is a significant source of activation.

The purpose of this work was to measure activation of commonly used metals in the beginning and in the middle of electromagnetic showers produced by GeV electrons and to compare the measurement results with the values predicted using FLUKA Monte Carlo code [2]. FLUKA is widely used to calculate radionuclide inventories produced by the photonuclear reactions and by the interaction of secondary particles, but does not currently include the electronuclear interaction mechanism.

Opportunity to irradiate samples presented itself when a nuclear physics experiment was designed to measure the proton's transverse spin structure function g^{p}_{2} planned to terminate 2.25 and 3.36 GeV electron beams on a specially designed tungsten alloy dump. Two stacks of Al, Cu, Nb, Pb, and type 316L stainless steel foils were placed in special cartridges on the face of the dump, separated from each other by a 1.25 cm thick tungsten alloy plate. The front foils were irradiated by early stages of electromagnetic showers and the back foils saw well-developed cascades.

Activated foils were then analysed in series of gamma spectroscopy measurements using high-purity germanium detectors. The measurement results were compared to FLUKA calculations. Both 2.25 and 3.36 GeV irradiations were modelled twice: first using the standard FLUKA distribution and then by introducing a simplified model of the electronuclear interaction based on the equivalent photon approximation [3].

Methods and materials

The sample irradiation took place at Jefferson Lab's experimental Hall A during the g^{p}_{2} experiment. Two separate irradiations used 2.25 and 3.36 GeV electron beams with 2 cm diameter circular rastering.

After passing through a liquid ammonia target, the electrons were bent in magnetic field and exited the target chamber through a 0.58 mm thick Al window with 6^0 and 4^0 angles, respectively. Then they travelled through 18 cm of helium gas and were incident on the first stack of foils, followed by a 1.25 cm thick HD17 tungsten alloy plate (90% W, 6% Ni, 4% Cu) and the second stack of foils. One cm downstream from the back foils, the beams were absorbed by a 10 cm long HD17 dump surrounded with lead shielding. Schematic representation of the experimental set-up is presented in Figure 1 and the irradiation profile in Figure 2. The two stacks consisted of 0.1 mm Al, 0.1 mm Cu, 0.1 mm Nb, 0.05 mm Pb, and 0.1 mm steel 316L, and 0.01 mm Al, 0.01 mm Cu, 0.01 mm Nb, 0.025 mm Pb, and 0.025 mm steel 316L foils, respectively.

Several hours after the end of each irradiation, the foils were transported to the radioanalytical laboratory where series of gamma spectroscopy analysis were performed during the following 3 months. The foils were analysed using high-purity germanium detectors and GENIE-2000 software [4]. The absolute detector efficiency for each sample was calculated using ISOCS™ software [5]. Each foil was counted 4 to 7 times with count times varying from 10 minutes to 24 hours. The short counts taken relatively soon after the irradiation were used to measure the short-lived radioactivity, while the longer counts taken later in time were used to measure the long-lived radionuclides. The pulse height spectra were thoroughly analysed, including the use of specially compiled nuclide libraries, performing cascade corrections, and various quality control and quality assurance techniques.

Figure 1. Schematic representation of the experimental set-up

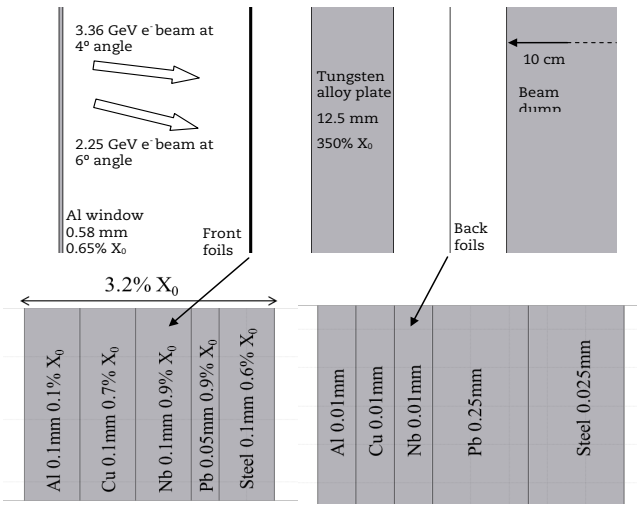

Figure 2. Irradiation profile

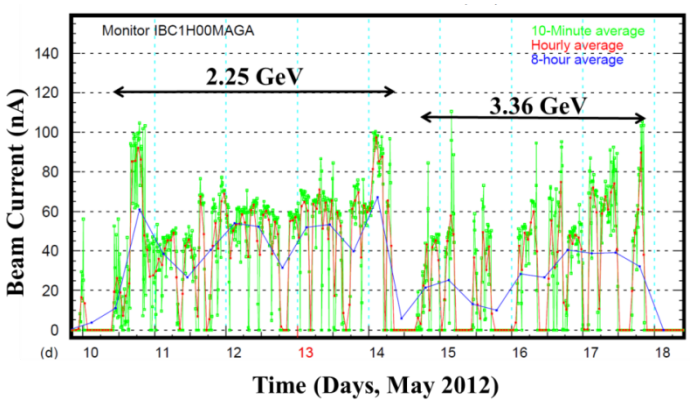

Detailed models of the foil irradiations were created using FLUKA. Radionuclide inventories were calculated for the decay times corresponding to the gamma spectroscopy measurements. The first set of FLUKA calculations modelled interaction of monoenergetic electron beams with the targets, hence not taking into consideration the electronuclear interaction mechanism. In the second set of the calculations, a FLUKA source routine was used to introduce a simplified model of the electronuclear interaction based on the equivalent photon approximation [3].

Results

The comparisons of measured activities to the values calculated using FLUKA are presented in Figures 3-12. Figures 3, 5, 7, 9, and 11 present the comparisons with the main FLUKA distribution results, not including the electronuclear interactions. Figures 4, 6, 8, 10, and 12 present the results that include the electronuclear correction introduced in FLUKA via the source routine.

^{91m}Nb in Figures 7 and 8 and ^{202m}Pb in Figures 9 and 10 are not shown. Production of these metastable states of Nb and Pb isotopes was overestimated by factors of 4.2 and 4.4 on average in the back foils. In the front foils, they were overestimated by factors of 1.2 and 2.2 on average. The addition of the electronuclear model changed these values to 1.7 and 3.8, respectively.

Figure 3. Comparison of Al activation with FLUKA calculation

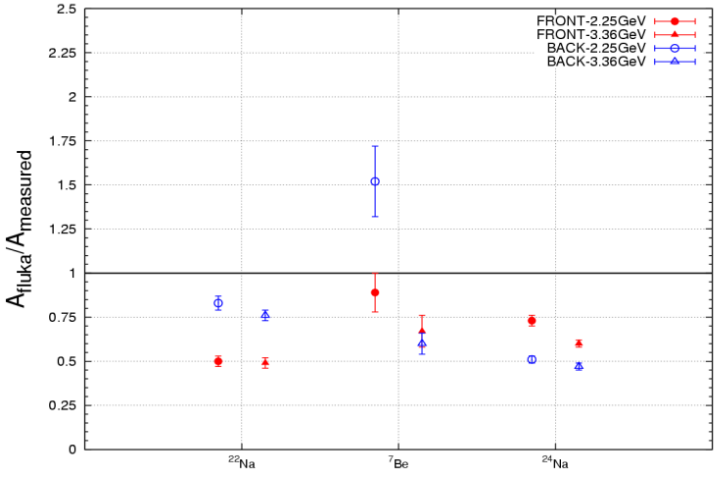

Figure 4. Comparison of Al activation with FLUKA calculation performed using a source routine accounting for the electronuclear interaction

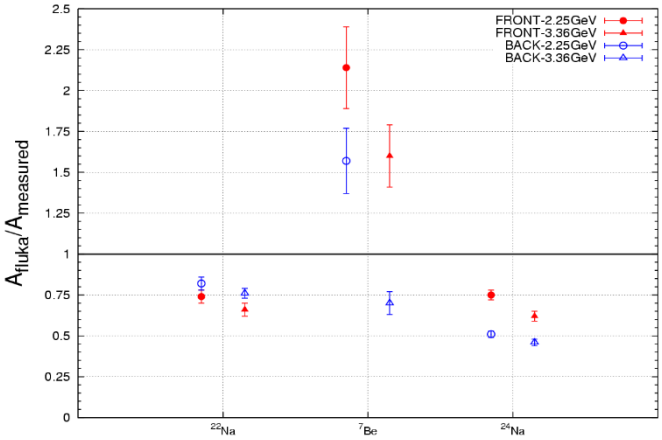

Figure 5. Comparison of Cu activation with FLUKA calculation

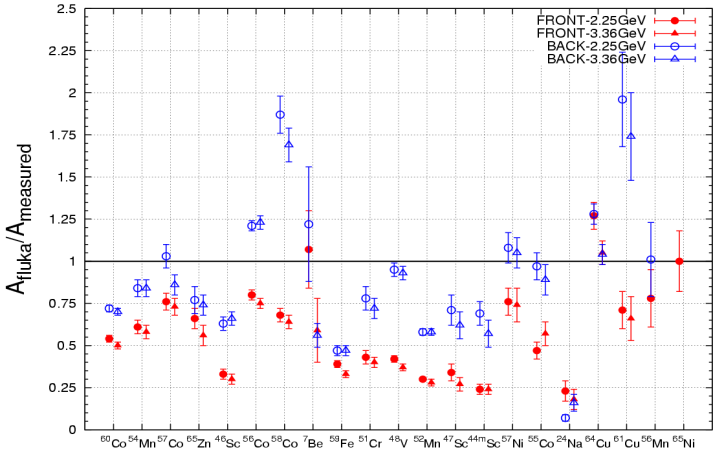

Figure 6. Comparison of Cu activation with FLUKA calculation performed using a source routine accounting for the electronuclear interaction

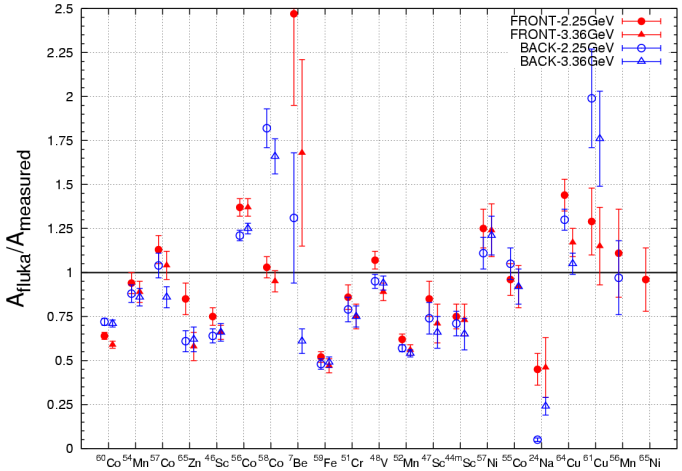

Figure 7. Comparison of Nb activation with FLUKA calculation

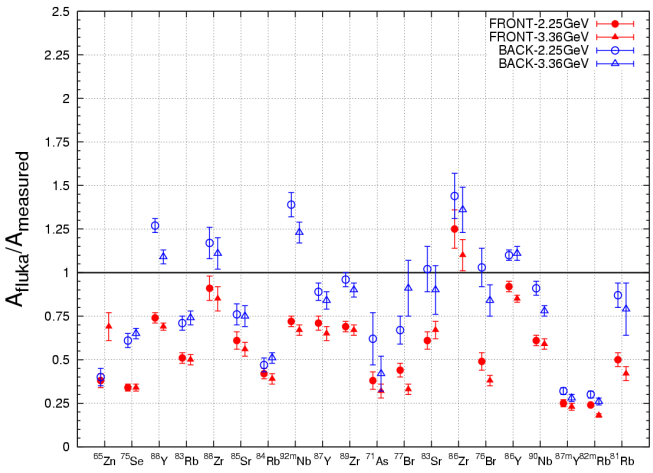

Figure 8. Comparison of Nb activation with FLUKA calculation performed using a source routine accounting for the electronuclear interaction

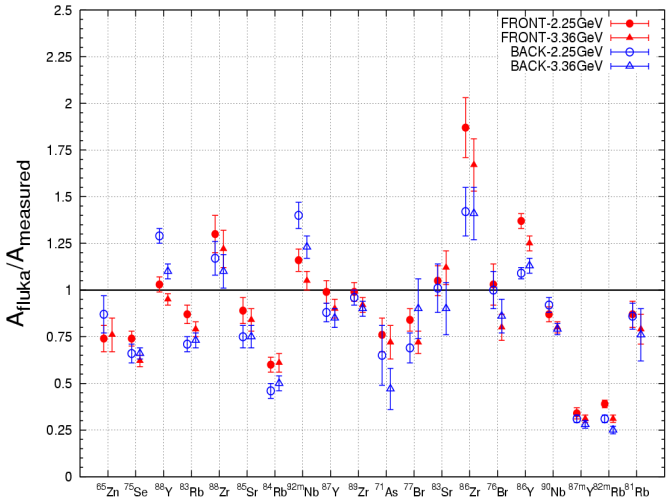

Figure 9. Comparison of Pb activation with FLUKA calculation

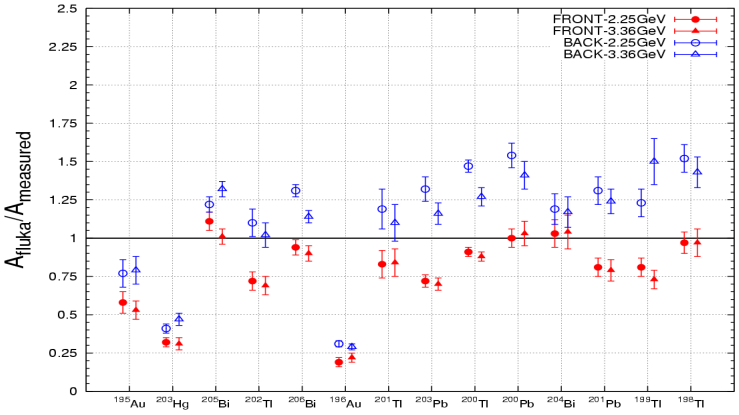

Figure 10. Comparison of Pb activation with FLUKA calculation performed using a source routine accounting for the electronuclear interaction

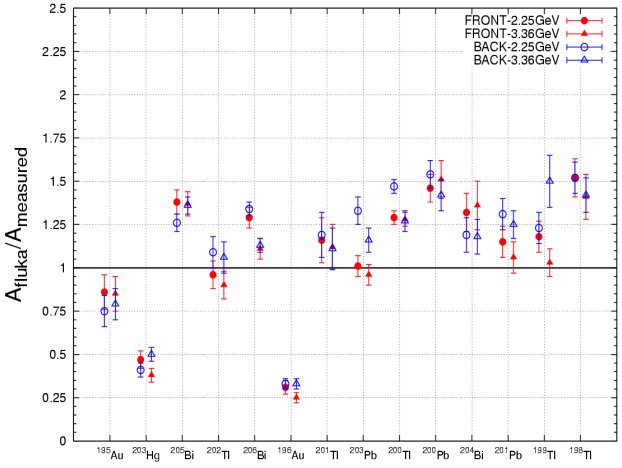

Figure 11. Comparison of steel 316L activation with FLUKA calculation

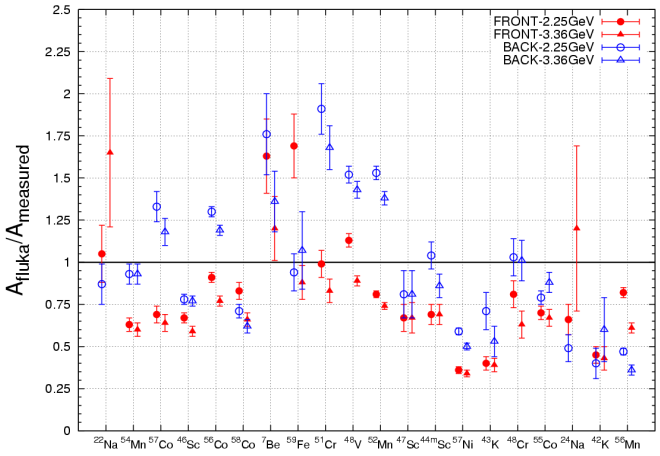

Figure 12. Comparison of steel 316L activation with FLUKA calculation performed using a source routine accounting for the electronuclear interaction

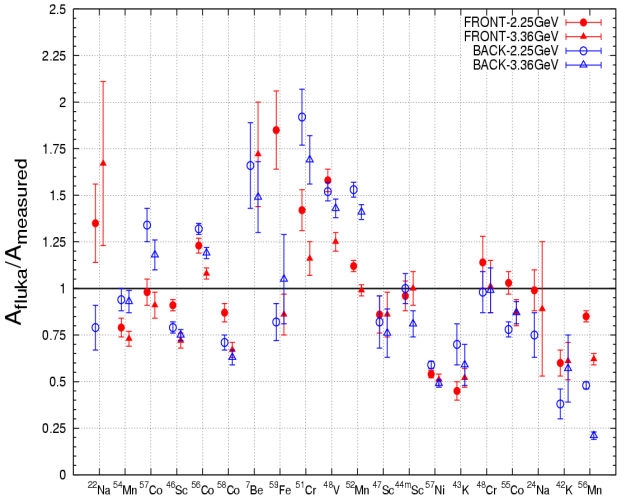

Conclusions

Activation of Al, Cu, Nb, Pb, and stainless steel foils in the beginning and in the middle of the electromagnetic showers produced by 2.25 and 3.36 GeV electron beams was measured. Results were compared to FLUKA calculations performed with and without a source routine written to account for the electronuclear interactions.

A good overall agreement of FLUKA with the experiment was demonstrated in the back foils, which were exposed to well-developed electromagnetic showers. Exceptions were ^{91m}Nb and ^{202m}Pb, which were overestimated 4 – 4.5 times. The overestimation of these isomers may be attributed to the simplistic approach of equal sharing used in FLUKA. The present models do not distinguish between ground state and isomeric states and instead evenly populate them.

A systematic underestimation of activation in the front foils was observed when the electronuclear interactions were not considered. The introduction of the model based on the equivalent photon approximation corrected the underestimation for the majority of the detected radionuclides.

Acknowledgements

The authors would like to thank Alberto Fassò, Vashek Vylet, Adam Hartberger, David Hamlette, Keith Welch, Maya Keller, Jixie Zhang, Alan Gavalya, Ed Folts, Karl Slifer, J. P. Chen, and g2p collaboration for their contributions. This work was supported by the US Department of Energy under contract number DE-AC05-06OR23177s.

References

[1] A. Fassò, M. Silari, L. Ulrici (1999), "Predicting Induced Radioactivity at High Energy Accelerators", *SLAC-PUB-8215*, Ninth International Conference on Radiation Shielding, Tsukuba, Japan.

[2] G. Battistoni, S. Muraro, P.R. Sala, F. Cerutti, A. Ferrari, S. Roesler, A. Fassò, J. Ranft (2007), "The FLUKA code: Description and benchmarking", *Proceedings of the Hadronic Shower Simulation Workshop 2006,* Fermilab 6-8 September 2006, M.Albrow, R. Raja eds., AIP Conference Proceeding 896, pp. 31-49.

[3] P. Degtiarenko, G. Kharashvili (2014), "Contribution of the Direct Electronuclear Processes to Thin Target Activation", *SATIF-12 Proceedings*.

[4] Canberra Industries, Inc., GENIE-2000 Gamma Analysis S501 V3.2.2.

[5] Canberra Industries, Inc., GENIE-2000 ISOCS S573 V4.2.1.

Session III: Radiation Shielding

Chair: Hideo Hirayama and Vashek Vylet

SNS shielding analyses overview

Irina Popova, Franz Gallmeier, Erik Iverson, Wei Lu, Igor Remec
Oak Ridge National Laboratory, US

Abstract

This paper gives an overview of on-going shielding analyses for Spallation Neutron Source. Currently, most of the shielding work is concentrated on the beam lines and instrument enclosures to prepare for commissioning, save operation and adequate radiation background in the future. There is on-going work for the accelerator facility. This includes radiation-protection analyses for radiation monitors placement, designing shielding for additional facilities to test accelerator structures, redesigning some parts of the facility, and designing test facilities to the main accelerator structure for component testing. Neutronics analyses are required as well to support spent structure management, including waste characterisation analyses, choice of proper transport/storage package and shielding enhancement for the package if required.

Introduction

The Spallation Neutron Source (SNS)[1] currently operates at 1.2-Megawatt (MW) proton beam power incident on a mercury target, with a proton beam energy of 1 GeV and a repetition rate of 60 Hz. The facility is still ramping up the power to reach the design goal of 1.4MW on target. SNS consists of accelerator system, target system, and a world-class suite of neutron scattering instruments to benefit material, life-science and fundamental physics research.

The SNS accelerator is powered by an H- beam, which transfers after acceleration into proton beam and consists of the linear accelerator (linac), the high-energy-beam-transfer line (HEBT), the accumulator ring and the ring-to-target-beam-transfer line (RTBT). The high-energy neutrons resulting from the proton initiated spallation reactions in the mercury target are converted to thermal and cold neutrons by one ambient water and three supercritical hydrogen moderators placed above and below the target. The thermalised neutrons are directed to the neutron scattering instruments through neutron beam lines. There are 18 beam lines, 6 of which serve two instruments each, so the facility is able to accommodate 24 instruments. Currently, 17 instruments are operating, two additional instruments are in or near the commissioning stage.

Although the facility is completed and in operation, there is still a wide range of demands for shielding analyses. During accelerator operation, some parts of the facility are redesigned and improved, and neutronics optimisations are an important part of the process. Linac access way redesign is on-going work. Additional facilities for test purposes for accelerator structures are being built and require shielding. Recently, a linac cryomodule RF test facility and an RFQ test stand were constructed. A conceptual study for standalone electronics irradiation station for single-event effects in avionic and ground based systems is in preparation to scope out the feasibility and cost. Shielding requirements are a huge factor in the construction cost. The neutron scattering instruments USANS and Corelli will be commissioned soon, which require extensive

work on beam line and instrument enclosure shielding. The neutron imaging instrument VENUS is currently being designed; also their shielding is an integral part of the instrument and a large cost factor. Another large area of neutronics/shielding work is the prediction of isotope composition for spent structures from accelerator and target facilities in order to do waste characterisation analyses and to develop proper transport and storage containers such as spent proton beam window and target modules, neutron beam line shutters and neutron beam collimators and spent accelerator components.

Methods and codes

Radiation transport calculations for shielding design and radiation protection analyses are performed mainly with the Monte Carlo code MCNPX version 2.6.0 [1] with realistic three-dimensional geometric description for all facility components and support structures. The MCNPX code simulates the particle transport of hadrons, continuous energy loss of charged particles in matter, elastic and nonelastic hadron interactions, secondary particle generation (here mainly gamma ray and neutrons) and their transport. Geometry splitting is applied to force particles towards the outside of the shielding for deep penetration calculations. MCNPX calculations are usually run on multiprocessor computers in the parallel mode. For beam line analyses applications, an in-house version is used with a neutron mirror guide option, permitting the thermal and cold neutron transport in the neutron guides to be adequately modelled.

Effective dose rates are obtained by folding neutron and gamma ray fluxes with flux-to-dose conversion coefficients, which are taken from standardised SNS neutron and gamma ray flux-to-dose conversion factors libraries [2]. For scoring the neutron and gammas dose rates, two types of tallies are generally used – surface and mesh tallies.

Analyses are performed in three steps for residual dose calculations for the parts of facility, and for developing storage/transport containers for extracted irradiated structures. In the first step, reaction rates in the requested structures were calculated using MCNPX. In the second step, isotope production rates are fed into the Activation Script [3]. This script provides the interface between MCNPX and the transmutation codes CINDER'90 [4], ORIHET3 and SP-FISPACT. CINDER'90 is usually applied to obtain the time dependence of the isotope build-up and decay for given locations according to the provided operational scenario. From the transmutation code outputs, gamma ray decay spectra and gammas ray power are extracted. In the third step, the extracted gamma spectra are formatted into source descriptions for MCNPX to perform decay gamma ray transport calculations.

For the radionuclide inventory analyses, steps one and two are applied, and then isotope concentrations are extracted from the transmutation code outputs for structural accelerator materials, water and soil.

Beam line shielding

Most of the shielding work is concentrated on the neutron beam lines. Neutron beams are contaminated by a large fraction of fast neutrons with energies up to the driving proton energy. The fast neutrons can be attenuated by choppers making use of the pulsed beam structure, the discrimination of fast and thermal neutrons by time of flight, and by curved neutron guides. In either way the neutron flight paths have to be packed into heavy thick shielding that needs to be custom tailored to each specific instrument including the neutron guides, choppers, sample environments, detectors and beam stops. Each beam line requires elaborative work to design shielding because of differences in the viewing moderator (which means different sources), the size of neutron beam pipe, neutron optics, distance between sample position and moderator, and differences in the nominal conditions of operation. Guidelines for the SNS neutron beam line shielding

calculations [2] provide standards for the beam line and instrument enclosure analyses. Beam line shielding analyses are logically divided into two sets:

- analysis of the incident beam line;
- analysis of the instrument cave or enclosure, including the neutron beam stop.

Beam line and instrument shielding analyses are performed using source terms describing the neutron in scattering into the beam lines starting at about one metre distance from the moderator faces.

Beam line specific neutron and gamma source terms [5] were generated for beam lines depending on which moderator beam line faces. The source terms were built by taking into account the neutron in-leakage into the core vessel insert opening.

Incident beam line shielding

Neutron beam lines at SNS can be straight (allowing passage of fast and high-energy neutrons) or curved (relying on neutron optics to transport slow neutrons). All beam lines have primary shutters within the shielding monolith. Many beam lines also have secondary shutters, either to allow multiple instruments to use a single primary shutter or to permit more rapid personnel access to the instrument sample area.

Beam line shielding should limit dose rates to 0.25 mrem/h at 30 cm distance from accessible shielding surfaces for at least the following conditions:

- white beam (all choppers open or removed);
- any single chopper, slit, secondary shutter, or other beam obstruction expected to affect shielding closed or in place;
- dual beam lines (e.g., POWGEN and MANDI) must consider both source terms, or if one beam line is not built out, it must be shown to be adequately blocked.

The secondary shutter must be designed for dual beam lines in order to provide independent work of the beam lines as a safety feature. The criterion for the design is to assure that a total dose rate at the sample position and/or the end of the neutron guide of less than 2 mrem/hour when the primary shutter is open, secondary shutter closed, and all choppers are open or removed.

Figure 1 gives an example for the straight beam line shielding design, beam line 17, the SEQOUIA instrument shielding. The beam guide is tapered towards the sample position from 9.567 x 11.43 cm to 5.042 x 5.455 cm at sample position, which is 20 m from the moderator face. Numbers on the bottom show distance from the moderator to components of the beam line. Figure 2 shows the dose rates along the flight path for beam line 17, the SEQOUIA instrument, when T0 chopper is open and when T0 shopper is parked in a closed position. This beam line is straight and its sample is positioned 20 m from the moderator. Black lines represent the beam line geometry on all the figures. Dotted lines represent cavities for the choppers. The beam line model starts at 100 cm from the moderator and extends to 1709 cm from moderator. Lines after 1709 cm from the moderator represent the front portion of the instrument enclosure shielding. Shielding around the beam line guide is 15 cm of steel followed by high-density concrete with varying height depending on the distance from the moderator.

Figure 1. SEQOUIA beam line layout

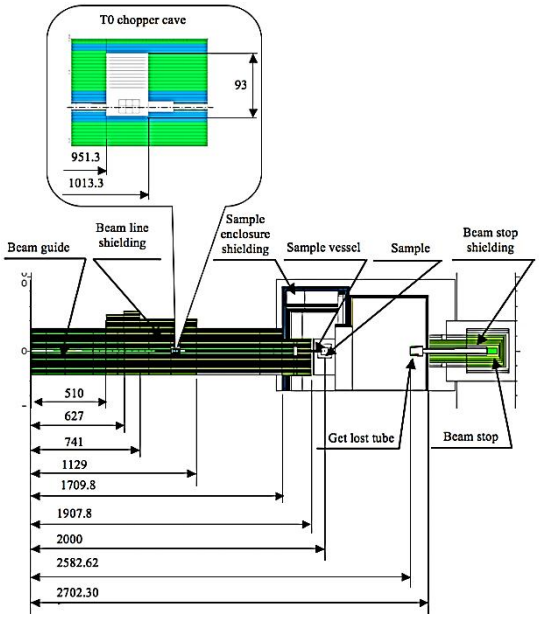

Figure 2. Dose rate map in elevation view of SEQOUIA beam line, T0 chopper is open and T0 chopper is closed, mrem/h (dimensions in cm)

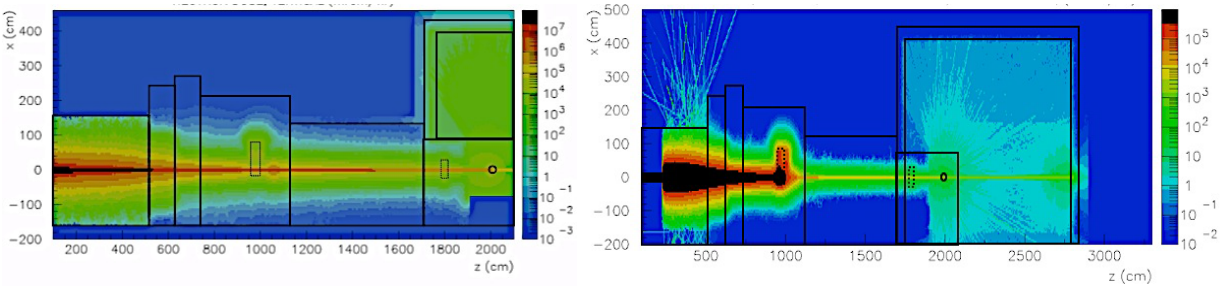

Shielding analyses for the curved beam lines are more challenging, especially when beam pipe aperture is small. Figure 3 gives an example for the curved beam line shielding design, beam line 11b, the MANDI instrument. Red numbers show height of the shielding from the beam centreline and numbers on the bottom show distance from the moderator. Beam guide opening at position 28.5 m from the moderator is 1.214 cm by 1.531 cm. The beam line model starts at 100 cm from the moderator and extends to 2620 cm from moderator. Lines after 2620 cm from the moderator represent the front portion of the instrument enclosure shielding. Beam line curvature radius is 1200 m, and line of sight is lost at about 1550 cm from the moderator. Material for the beam line shielding changes along the beam line. From the target monolith to the 1020 cm position from the moderator, the shielding material is high density concrete. There is a slab of steel shielding inside the high-density concrete above the first/second chopper cavity, which is 55 cm high and goes through the whole shielding in width. From a 1020 cm position from the moderator to a 2620 cm position from the moderator beam line shielding is regular concrete. Figure 4 shows the dose rates along the flight path for beam 11b, MANDI instrument in elevation and horizontal view. Because MANDI instrument is a dual beam line, a second shutter is required as a safety measure. A secondary shutter from borated carbon neutron absorber followed by 2 cm of the steel was designed. The secondary

radiation field is well mitigated by the beam line shielding, when the shutter is in a closed position. Also the in-beam dose rate predicted in the instrument enclosure with the secondary shutter closed meets the dose rate design criterion for all analysed cases.

Figure 3. MANDI beam line layout (dimensions in cm)

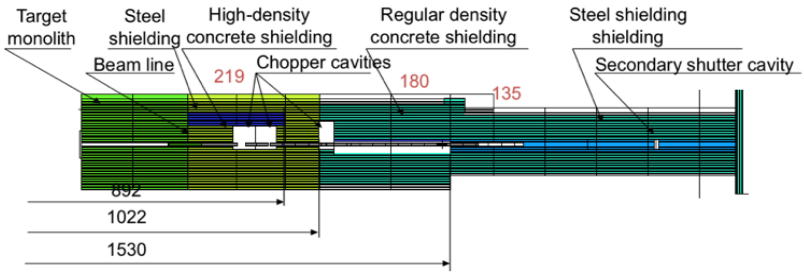

Figure 4. Dose rate map in elevation and horizontal view of MANDI beam line, mrem/h

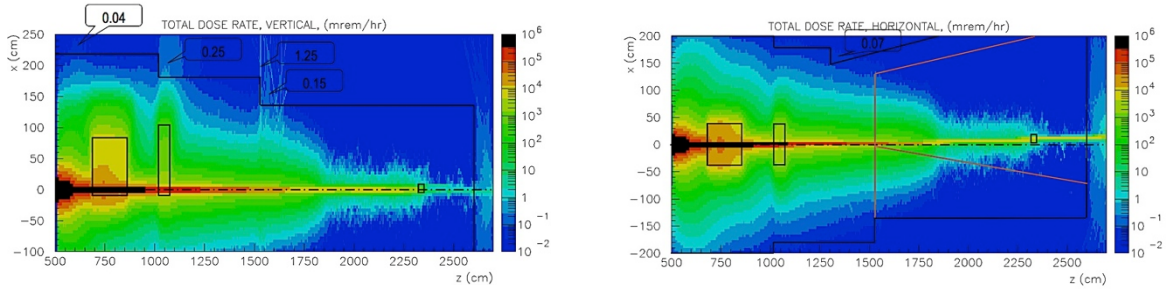

Instrument cave/enclosure shielding

The instrument enclosure shielding analyses will include two separate analyses: the beam stop and the enclosure shielding design. Enclosure shielding is designed for the "normal operation" beam conditions (beam with limited energy bandwidth) in case an area monitor activates the closing of the shutter in case of elevated dose rates. Otherwise accident-case beam conditions are considered such as a white unobstructed beam running into the piece of equipment or the worst case samples. Both polyethylene and steel samples are used for those analyses. The beam stop shielding must be designed for the white unobstructed beam with no sample inserted.

Figure 5. VENUS enclosure layout in elevation and horizontal view

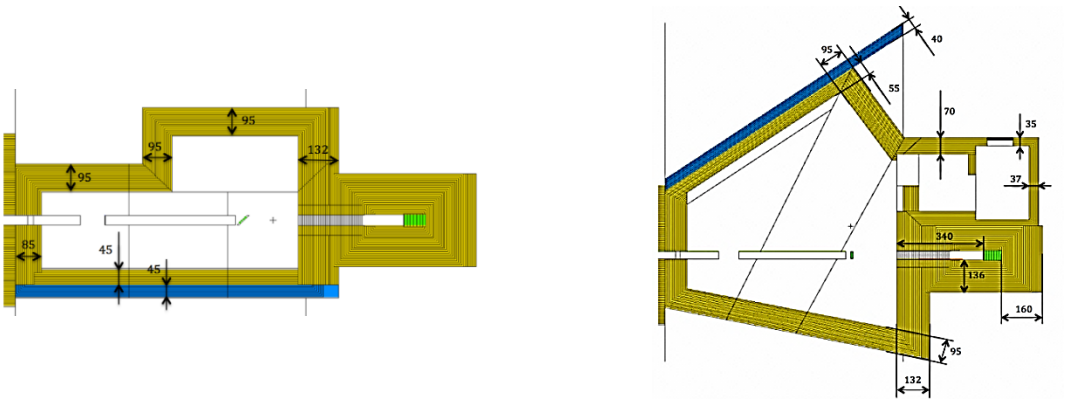

Figure 5 gives an example of shielding design for enclosure for beam line 12, VENUS instrument in elevation and horizontal view. This instrument set-up requires the thickest instrument enclosure compared to all the other SNS instruments because of large beam opening at the sample position – about 21 cm in diameter near the sample position at 2000 cm from the moderator. The suggested thickness of the enclosure is 95 cm of high density concrete. This work is still on-going. Figure 6 shows the dose rate map of VENUS instrument enclosure in elevation and horizontal view.

Figure 6. Dose rate map in elevation and horizontal view of VENUS instrument enclosure, mrem/h

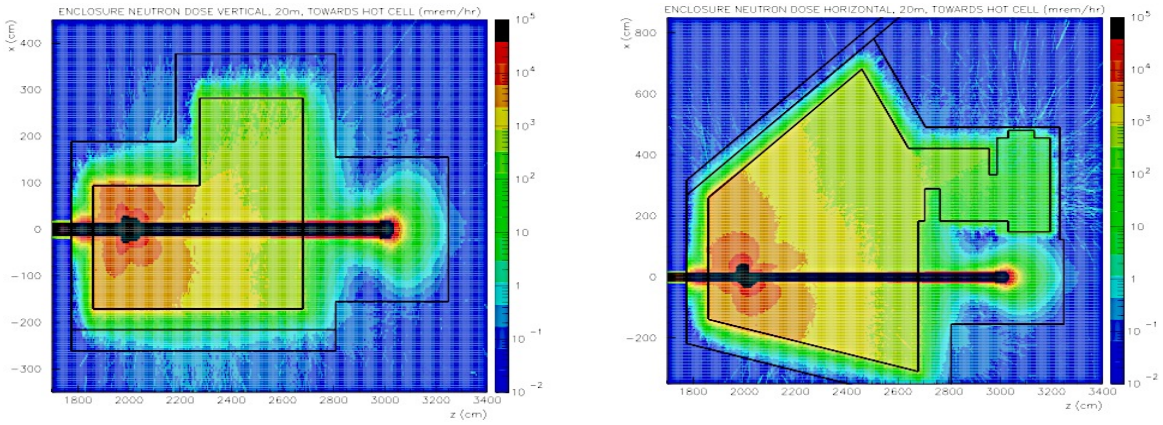

Accelerator facility shielding aspects

The accelerator facility has been in operation since 2006, however, it is still necessary to perform neutronics work. The scope of work to support accelerator facility includes:

- radiation-protection analyses for radiation monitor placement;
- shielding for additional facilities to test accelerator structures (linac cryo-module RF and RFQ test stands, Integrated test stand facility for accelerator front-end);
- neutronics optimisation for redesign and improved components (Linac access way redesign, HEBT momentum dump redesign).

Radiation protection analyses

Extensive work has been completed to summarise the response of the area radiation monitors ("chipmunks") to the maximum possible accidental beam spill around the accelerator facility and to evaluate whether any beam-spill accidents would be detected by at least two chipmunks. Analyses for the dose rates at the chipmunks were performed based on the maximum possible accident of a full beam spill for each considered accelerator section. The location of the accident was considered to be in the closest possible position to the chipmunk. As an example, Figure 7 summarises chipmunk readings in case of a possible maximum beam spill in the ring section of the accelerator. The coloured dot shows the location of the beam spill at a thick target or the centre of the beam spill on the beam pipe assuming a Gaussian distribution. The coloured dot shows the location of the beam spill; the coloured numbers near each chipmunk show the dose rate measured at the chipmunk in mrem/h. The colour of the number refers to the dose rate measured by the chipmunk when the spill appears in the place marked with the same colour. Chipmunk locations are marked by the letter R. Analyses show that the existing chipmunk locations are satisfactory to measure any elevated dose rate from accident conditions in the accelerator and that there is overlapping response - if one

detector fails other detector will identify beam loss. Maximum dose rates in occupied areas are calculated to be approximately 110 rem/h in the ring section.

Figure 7. Dose rate at chipmunks at the ring section of accelerator, mrem/h

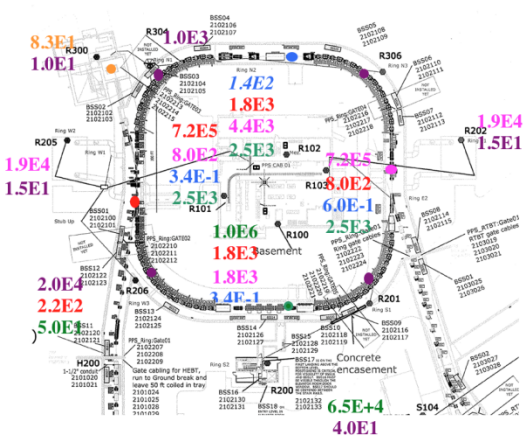

Linac test stands

Test pit for RF cryo-module cavities is an example of linac test stands shielding design. This facility is an underground construction with concrete lining with varying thickness inside the pit. In order to ensure safe operation from radiation protection point of view, a cover, which will be placed over the pit, needed to be designed as radiation shield of varying RF conditions. Figure 8 shows configuration of test pit facility modelled in MCNPX geometry language. Source for shielding analyses to design pit cover is an electron beam, which hits the end plate of cryo-module and generates gamma emission. Analyses were performed for the most conservative possible source – an electron energy of upcoming beam is 20MeV, and electron current is 200nA.

Figure 8. Layout of the pit with the cover in elevation views (dimensions in cm)

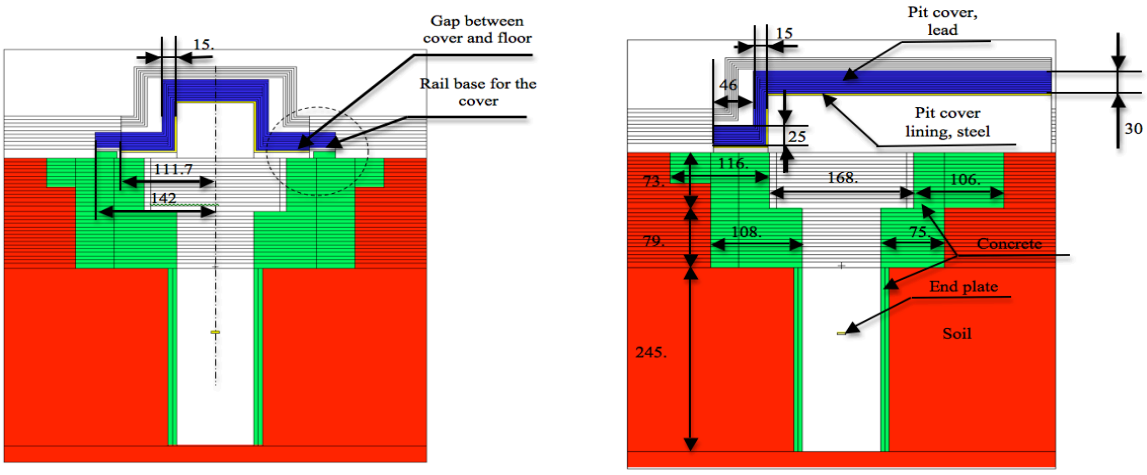

Figure 9 shows the dose rate map in the vicinity of the test pit facility in 2 elevation views. Analyses show that with the present configuration (Figure 8) there are some areas with slightly elevated dose rates. It has been suggested that elevated dose rates should be mitigated by putting lead bricks in locations of elevated dose rates.

Figure 9. Dose rate map in elevation views for test pit facility, mrem/h

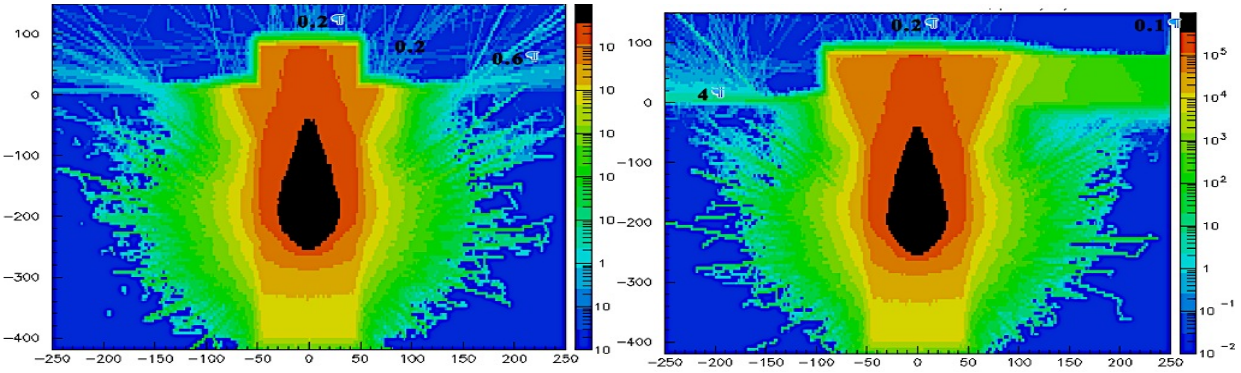

Neutronics optimisations for redesigned and improved components

Some of the existing accelerator structures are replaced for various reasons such as facilitating access to the tunnel or replacing old components with newer and better performing ones. Extensive work has been performed to redesign the momentum beam stop in Linac-to-Ring transfer line and the accelerator tunnel front-end door.

The accelerator tunnel starts in the front-end building. The front wall of the accelerator tunnel contains an access for moving Linac equipment and supplies in and out of the tunnel. This access is closed by the so-called plug door, which provides with 90 cm thick concrete, the same shielding as the surrounding tunnel walls. The plug door is very heavy and difficult to handle. In order to make it more manageable a door with lighter weight was designed.

A full-scale model of the front-end of the accelerator and first accelerating sections was built for these simulations. First, source terms near the front end inside the tunnel were calculated based on measured beam losses during normal operations. Then scaling calculations were performed to figure out the proper amount of materials for the door, which were resulted in 2.5 cm of steel followed by 10 cm of 5% borated polyethylene followed by 2.5 cm of steel. The area in the front of the accelerator tunnel is a radiation controlled area, the door was designed so that the dose rate outside the front accelerator wall would not exceed 5 mrem/h.

Neutronics analyses for waste management

Components are replaced when they reach their end-of-life due to radiation-induced material damage or burn-up, or because of mechanical failure. During operation, these components, especially those in proximity to the target, are exposed to a radiation environment and build up significant activity during their service lifetime. All these components must be safely removed, placed in a container/package for storage, and ultimately transported off-site for disposal.

Target system facility

Target vessel, proton beam window (PBW), inner reflector plug (IRP) and core vessel insert (CVI) plugs are routinely scheduled to be replaced in maintenance periods following the facility operation periods about twice a year. Target and proton beam window are replaced to avoid material embrittlement. Estimated allowable peak damage of the steel and inconel structures is 10 dpa.

IRP is expected to be replaced in 2016. The process for the determination of right box/package has started. CVI plugs are temporary constructs and are replaced, when a

beam line is opened up, a full beam line shutter and actual optics components are installed. At present, we have two CVI plugs being prepared to be transported off-site.

The most time consuming analyses are required for target vessel disposal. The SNS target vessel contains the liquid mercury target in the in-beam area of the target station. The target vessel is exposed to a severe radiation environment and builds up significant activity during its service lifetime. The target vessel is routinely replaced as it approaches its estimated life-time, or if it prematurely fails. Based on the estimated radionuclide inventory for full beam power (2MW) for 5000 h operations, as well as the size and weight of the target vessel, it was decided to use the TN-RAM cask or equivalent for off-site transport to a waste disposal facility. Figure 10 shows the MCNPX model of target station for target vessel for transport calculations. Figure 11 shows the MCNPX model for typical configuration of spent target inserted in liner and TN-RAM cask. The radionuclide inventory for the target vessel includes three components: the target vessel, 200 g of activated mercury dispersed in the target, and 10% of the mercury radionuclide inventory (other than mercury, gold and noble gas isotopes) deposited on mercury exposed steel piping.

In order to simplify analyses and avoid errors arising from manual preparation of calculations, the Perl script TARGET_DISPOSAL was created to run these analyses. This script uses reaction rates in the target vessel and in the mercury calculated by MCNPX, and stored in the output and runs ACTIVATION_SCRIPT, for transmutation analyses to produce the radionuclide inventory and gamma source terms. Then, the script prepares the decay gamma source definition for MCNPX photon transport calculations for the target vessel inside a liner and also for the target vessel inside the liner inside the transport cask. For analyses of residual dose rates, next-event point and ring detectors are applied, as well as dose rate mesh tallies, to allow for dose rate contours in and around liner and cask geometries. After completion of the transport analyses, the script automatically generates a final report. As an example, Figure 11 shows a typical configuration for spent target inserted in the liner and TN-RAM cask modelled in MCNPX geometry language and dose rate contours in and around the TN-RAM cask loaded with the liner and the SNS spent target #8 after 202 days decay. Target #8 module had a service lifetime of approximately 0.97 years in which it accumulated slightly more than 3744 MWh proton beam energy at 1GeV proton energy.

Figure 10. MCNPX model for target vessel and proton beam window transport calculations

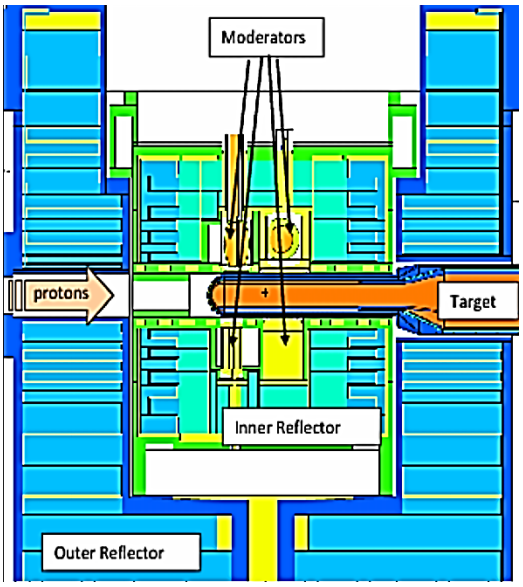

Figure 11. MCNPX model for typical configuration of spent target inserted in the liner inside TN-RAM cask and dose rates map around this configuration, mrem/h

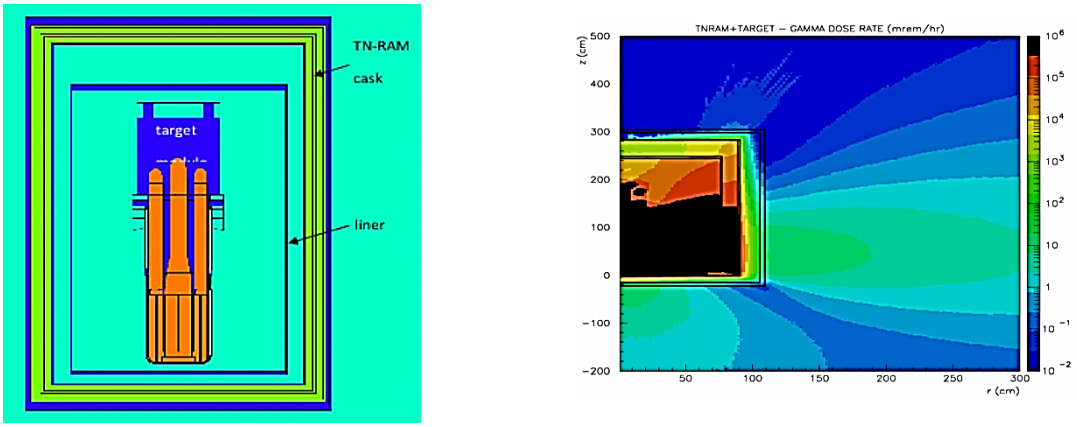

Accelerator system facility

Temporary storage casks for accelerator spent structures are designed under the criterion, that the dose rate outside the container will not exceed 5 mrem/h at 30 cm distance from the container surface and are already designed for: HEBT momentum beam stop, RTBT harp and ring injection dump (RID).

According to the accelerator operations plan, the beam stop core and window assemblies of the existing RID will be removed when they have reached their end-of-life. Both parts are expected to be highly activated because the RID receives the highest losses in the accelerator facility, 5% of the accelerator beam power (100kW). Shielding above these two assemblies has to be removed to allow access, and will be placed into temporary storage containers while the beam stop core and window assemblies are removed and reinstalled. Two container configurations for each assembly were suggested. The first configuration assumes use of a lead container whereas the second configuration assumes use of a steel container, but reinforced with lead. Figure 12 shows dose rate distribution for beam stop assembly lead container as an example. The container has variable thickness around the RID assembly.

Figure 12. Dose rates map inside and outside the beam stop assembly lead container, mrem/h

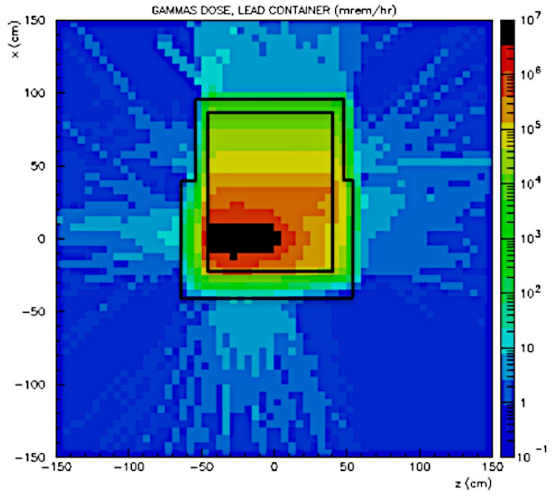

Conclusions

Neutronics work is in full swing for the SNS facility, meeting demands on shielding work for neutron beam line in preparation for their commissioning and to ensure their safe operation; providing support for accelerator components to help redesign parts and system and to do shielding design for test stands; providing support for radiations protection analyses for radiation monitors placement and performance; and providing analyses to support waste management of spent components.

Acknowledgements

Work performed at Oak Ridge National Laboratory is managed by UT-Battelle, LLC, under contract DE-AC05-00OR22725 for the US Department of Energy.

References

[1] C D. Pellowitz, ed. (2008), "MCNPX User's Manual, Version 2.6.0," LA-CP-07-1473, Los Alamos National Laboratory, Los Alamos, New Mexico.

[2] I. Popova (2009), Flux to Dose Conversion Factors, SNS-NFDD-NSD-TR-0001, R00.

[3] F.X. Gallmeier, M. Wohlmuther (2008), Activation Script Version 1.0 User Guide, ORNL-TM-2008/031, Oak Ridge National Laboratory.

[4] W.B. Wilson, S.T. Cowell, T.R. England, A.C.Hayes, P. Möller (2007), A Manual for Cinder'90 Version 07.4, LA-UR-07-8412, Los Alamos National Laboratory, Los Alamos.

[5] F. Gallmeier (2005), Source Terms for Neutron Beam Line Shielding and Activation Calculations, SNS-107030700-DA0002-R00, Oak Ridge National Laboratory.

Evaluation of SNS beamline shielding configurations using MCNPX accelerated by ADVANTG

Joel M. Risner[1], **Seth R. Johnson, Igor Remec, Kursat B. Bekar**
Oak Ridge National Laboratory, US

Abstract

Shielding analyses for the Spallation Neutron Source (SNS) at Oak Ridge National Laboratory pose significant computational challenges, including highly anisotropic high-energy sources, a combination of deep penetration shielding and an unshielded beamline, and a desire to obtain well-converged "nearly global" solutions for mapping of predicted radiation fields. The majority of these analyses have been performed using MCNPX with manually generated variance reduction parameters (source biasing and cell-based splitting and Russian roulette) that were largely based on the analyst's insight into the problem specifics. Development of the variance reduction parameters required extensive analyst time and was often tailored to specific portions of the model phase space.

We previously applied a developmental version of the ADVANTG code to an SNS beamline study to perform a hybrid deterministic/Monte Carlo analysis and showed that we could obtain nearly global Monte Carlo solutions with essentially uniform relative errors for mesh tallies that cover extensive portions of the model with typical voxel spacing of a few centimetres. The use of weight window maps and consistent biased sources produced using the FW-CADIS methodology in ADVANTG allowed us to obtain these solutions using substantially less computer time than the previous cell-based splitting approach. While those results were promising, the process of using the developmental version of ADVANTG was somewhat laborious, requiring user-developed Python scripts to "drive" much of the analysis sequence. In addition, limitations imposed by the size of weight-window files in MCNPX necessitated the use of relatively coarse spatial and energy discretisation for the deterministic Denovo calculations that we used to generate the variance reduction parameters. We recently applied the production version of ADVANTG to this beamline analysis, which substantially streamlined the analysis process. We also tested importance function collapsing (in space and energy) capabilities in ADVANTG. These changes, along with the support for parallel Denovo calculations using the current version of ADVANTG, give us the capability to improve the fidelity of the deterministic portion of the hybrid analysis sequence, obtain improved weight-window maps, and reduce both the analyst and computational time required for the analysis process.

Introduction

Shielding analyses for the Spallation Neutron Source (SNS) at Oak Ridge National Laboratory (ORNL) have typically been performed using MCNPX [1] with limited variance reduction (source biasing and cell-based splitting and Russian roulette) that was largely based on the analyst's insight into the problem specifics. Development of the variance reduction parameters required extensive analyst time and was often tailored to specific portions of the model phase space. The cell-based splitting parameters, which were not energy dependent, also added considerable complexity to the model geometry, as many surfaces and cells were added solely to define splitting parameters, not to describe actual geometric details. These additional surfaces and cells not only required significant analyst time to develop but also slowed the particle tracking process.

Over the past several years, ORNL has pioneered the development and application of hybrid transport methods, which utilise "moderate fidelity" discrete ordinates transport calculations to generate variance reduction parameters (weight windows and consistently biased sources) that can significantly accelerate Monte Carlo simulations. These hybrid methods have been incorporated into the MAVRIC sequence (which employs the Monaco Monte Carlo code) in the SCALE code system [2] and into the ADVANTG code [3], which generates weight windows and biased sources that can be used in MCNP [4] and MCNPX.

In a previous unpublished study, we applied a developmental version of ADVANTG to an SNS beamline study. We showed that we could substantially reduce the computational time required to achieve acceptable relative errors for specific regions of interest in the model, and furthermore, that we could obtain nearly global Monte Carlo solutions with essentially uniform relative errors for mesh tallies that cover extensive portions of the model. While those results were promising, the process of using the developmental version of ADVANTG was somewhat laborious, reducing the potential for other users to readily apply ADVANTG to applications of this type. In the current study, we applied the production version of ADVANTG, which will soon be released through the Radiation Safety Information Computational Center, to analyse radiation levels for several configurations of SNS beamline 1B. Our results again demonstrate the effectiveness of the hybrid methodology, and with this new production version of ADVANTG, the analysis process is substantially improved.

The SNS beamline 1B model

The MCNPX model that we used for this study is based on a model that has been used to evaluate dose rates for beamline 1B (BL-1B), which contains the Nanoscale-Ordered Materials Diffractometer (NOMAD) experimental arrangement. A plan view of this model at the elevation of the centreline of BL-1B is shown in Figure 1. For this study, we consider three scenarios: a "white" source (neutron energies up to 300 MeV) with an open beamline, a low-energy source (primarily neutron energies from 0.009–8.17 eV) with an open beamline, and a white source with the secondary carousel rotated to a closed position. The low-energy source represents the normal operating condition for locations downstream of the T0 chopper. The white source represents an accident condition in which none of the choppers are in operation.

Figure 2 shows details of the model in the vicinity of the T0 chopper when the secondary carousel is in the open position. Figure 3 shows the same configuration for a model in which cell-based splitting and Russian roulette are used for variance reduction. Both the spatial extent of the splitting cells and the importances assigned to each of those cells require significant amounts of analyst time and experience with the model to develop. Because these cells and importances are dependent on the model geometry, the source characteristics, and the location and extent of the desired tallies, they must be developed specifically for each scenario that is analysed. Furthermore, the cell-based

importances are not energy dependent, so a single set of importances is assigned to all energies for each particle type of interest.

Generation of weight windows and biased sources using ADVANTG

For the hybrid analysis of BL-1B, we applied the Forward-Weighted Consistent Adjoint Driven Importance Sampling (FW-CADIS) methodology in ADVANTG. In the FW-CADIS approach, ADVANTG first discretises the MCNP (or MCNPX) model based on a user-supplied spatial mesh. A deterministic forward calculation is then performed using the spatially discretised model, a user-specified multigroup cross-section library, and user-specified angular quadrature data. This forward calculation is used to generate an estimate of the flux or response of interest throughout the model phase space. For this analysis, the response of interest was the total (neutron plus photon) dose rate. An adjoint source corresponding to the Monte Carlo tallies of interest is then constructed based on the deterministic forward solution, with the adjoint source magnitude in each spatial cell being the inverse of the response, and the adjoint source spectrum being the response function of interest (e.g. the flux-to-dose-rate conversion factors). An adjoint deterministic calculation is then performed to generate particle importances as a function of space and energy. Monte Carlo target weights and a consistently biased Monte Carlo source are then constructed from the importance values. Details of the FW-CADIS method can be found in [3,5].

ADVANTG includes six coupled (neutron/photon) multigroup cross-section libraries, but they all have an upper neutron energy limit of approximately 20 MeV. For these beamline evaluations we required a library with neutron energies up to 300 MeV. We used a collapsed version of the HILO2K library [6] with 33 neutron groups (with an upper energy of 300 MeV) and 11 photon groups for the scenarios with the high-energy source and a collapsed HILO2K library with 5 neutron groups and 11 photon groups for the low-energy source scenario.

The neutron source for the accident condition (the white source) is located 1 m from the moderator and is modeled as a plane source 12 cm high and 10 cm wide. The angular distribution is described with two angular bins, one from 0° to 1° and one from 1° to 2° with respect to the beamline axis. We used an auxiliary Python script in ADVANTG to define this anisotropic surface source for use with the Monte Carlo uncollided flux option in Denovo. This anisotropic source feature may be fully integrated in a future release of ADVANTG. The uncollided flux approach generates an accurate first-collision source which significantly reduces ray effects in the forward transport calculation. For the low-energy source (the normal operating condition), a plane source is located in the T0 chopper cavity and represents the neutrons that are transmitted through the T0 chopper. We used P_3 scattering, the default step characteristics spatial differencing scheme, and a Lobatto quadrature set with 16 “polar” angles and a triangular arrangement of azimuthal angles. Lobatto quadrature is not one of the standard options in Denovo, but it is ideally suited to this application because it provides a quadrature ordinate along the Z-axis, which, in our geometry modelling, is the axis of the BL-1B beamline. Use of the Lobatto quadrature for this application is essential, as it avoids the significant variation in target weights in the “near end” of the beamline (i.e. near the source location at 1 m) that occurs when a level symmetric S_{16} quadrature is used. This effect is illustrated in Figure 4, where target weights are shown along the beamline axis for four neutron energy groups from the deterministic calculation. Applying the weight windows developed using the S_{16} quadrature results in very poor tally convergence of the MCNPX simulation, as particles are split excessively before they have had any interaction as they are transported down the beamline.

MCNPX results

We generated weight windows and biased sources using ADVANTG for the three scenarios noted above: an open beamline with a white source, an open beamline with a low-energy source, and a white source in a configuration in which the secondary carousel is closed. We then used those weight windows and biased sources in MCNPX simulations. For the first two cases, we provide comparisons to earlier MCNPX calculations that employed cell-based splitting and rouletting. For the third case, we show only the ADVANTG results to illustrate the effectiveness of the hybrid approach in generating high-quality variance reduction parameters when significant model changes are made.

Figures 5 and 6 show mesh tally plots of the total dose rate and associated relative errors for a horizontal plane at the elevation of the beamline axis. The red contour lines on each plot are at 0.25 mrem/hr. The region outlined in blue in Figure 5 represents the "region of interest" for the original calculation, which is the portion of the model for which the cell-based splitting and rouletting parameters were developed to reduce the relative error. The hybrid results in Figure 6 show a very well-converged solution, with relative errors well under 10% over most of the solution space. The only locations for which the convergence is somewhat poor are at the beam stops for both beam lines. The beam stops are often evaluated separately, and it may be appropriate to do so with the hybrid method as well. Figures 7 and 8 show mesh tally plots for a vertical plane perpendicular to the BL-1B axis at the location of the sample position in the NOMAD detector vessel. The MCNPX run time for the original calculation was approximately 5000 CPU hours. The hybrid case used approximately 190 CPU hours for the deterministic calculations to generate the variance reduction parameters and approximately 1000 CPU hours for the MCNPX simulation.

Figures 9 through 12 show mesh tally results at the same locations as Figures 5 through 8, but for calculations with the low-energy neutron source at the T0 chopper location. Note that these results are used only for evaluation of dose rates downstream of the T0 chopper (i.e., locations beyond ~1620 cm on the Z-axis of the model). The hybrid solution again provides nearly uniform relative errors at all downstream locations except for the beam stop regions. The MCNPX run time for the original calculation was approximately 1300 CPU hours. The hybrid case used approximately 60 CPU hours for the deterministic calculations to generate the variance reduction parameters and approximately 480 CPU hours for the MCNPX simulation.

Finally, Figure 13 illustrates the total dose rate and associated relative errors for a vertical mesh tally along the BL-1B axis using the white source with the secondary carousel shutter rotated to the closed position. For the original cell-based splitting and rouletting analysis (which is not shown here), extensive model changes were required to construct splitting and rouletting regions that differed substantially between the open-shutter and closed-shutter geometries. For the hybrid case we simply applied a coordinate transformation to rotate the carousel shutter, made a simple refinement of the spatial mesh perpendicular to the beamline over the extent of the secondary shutter, and then ran the ADVANTG sequence to generate variance reduction parameters for this new configuration. No additional analyst time was required, and the variance reduction parameters again provided well-converged mesh tallies in almost all locations. This hybrid calculation used approximately 180 CPU hours for the deterministic calculations to generate the variance reduction parameters and approximately 1000 CPU hours for the MCNPX simulation.

Figure 1. Horizontal cut of the SNS beamline 1B (BL-1B) MCNPX model at the elevation of the centreline of BL-1B

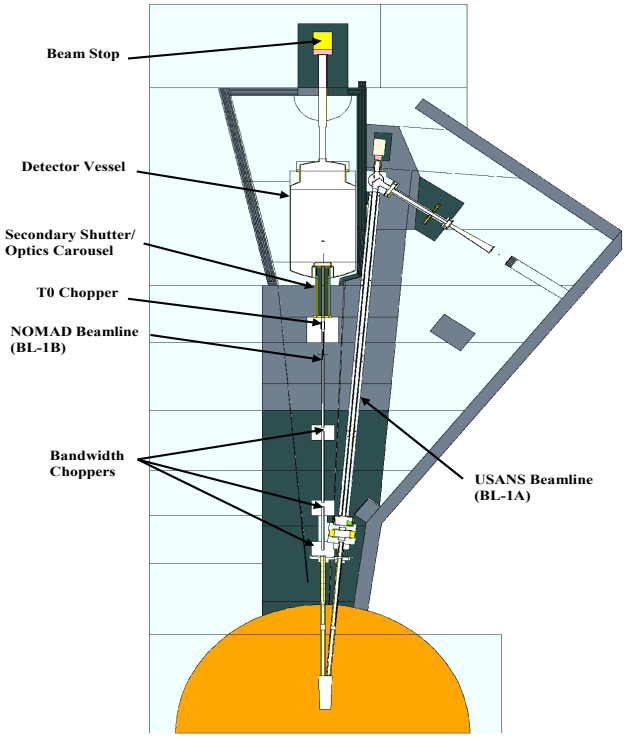

Figure 2. Horizontal cut of the SNS beamline 1B model in the vicinity of the secondary shutter

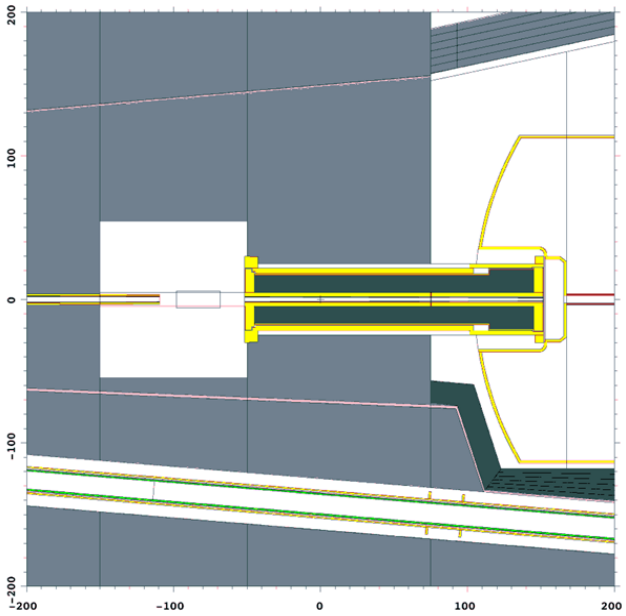

Figure 3. Horizontal cut of the SNS model in the vicinity of the secondary shutter with additional geometry details that are used only for cell-based splitting and rouletting

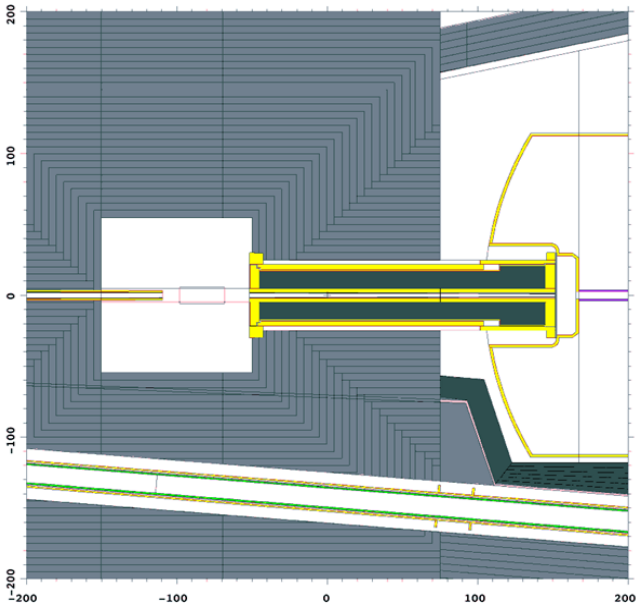

Figure 4. Neutron target weights along the beamline axis for four neutron energy groups using Lobatto-16 and level symmetric S_{16} quadrature

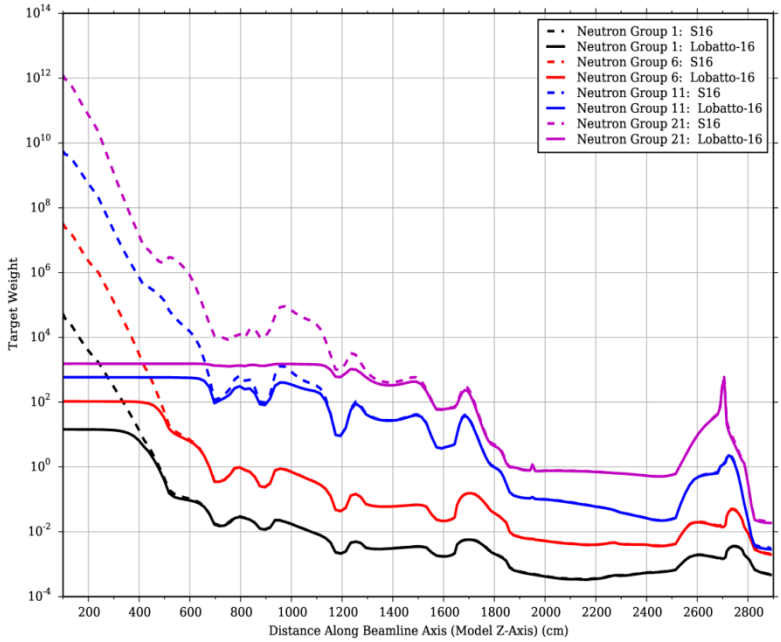

Note the significant variation in target weights along the "near end" of the beamline when the S_{16} quadrature is used. Use of the S_{16} target weights results in poor tally convergence in the MCNPX simulation.

Figure 5. Total (neutron plus photon) dose rates and associated relative errors at the elevation of the centreline of SNS beamline 1B for the MCNPX cell-based splitting and rouletting solution with the white source

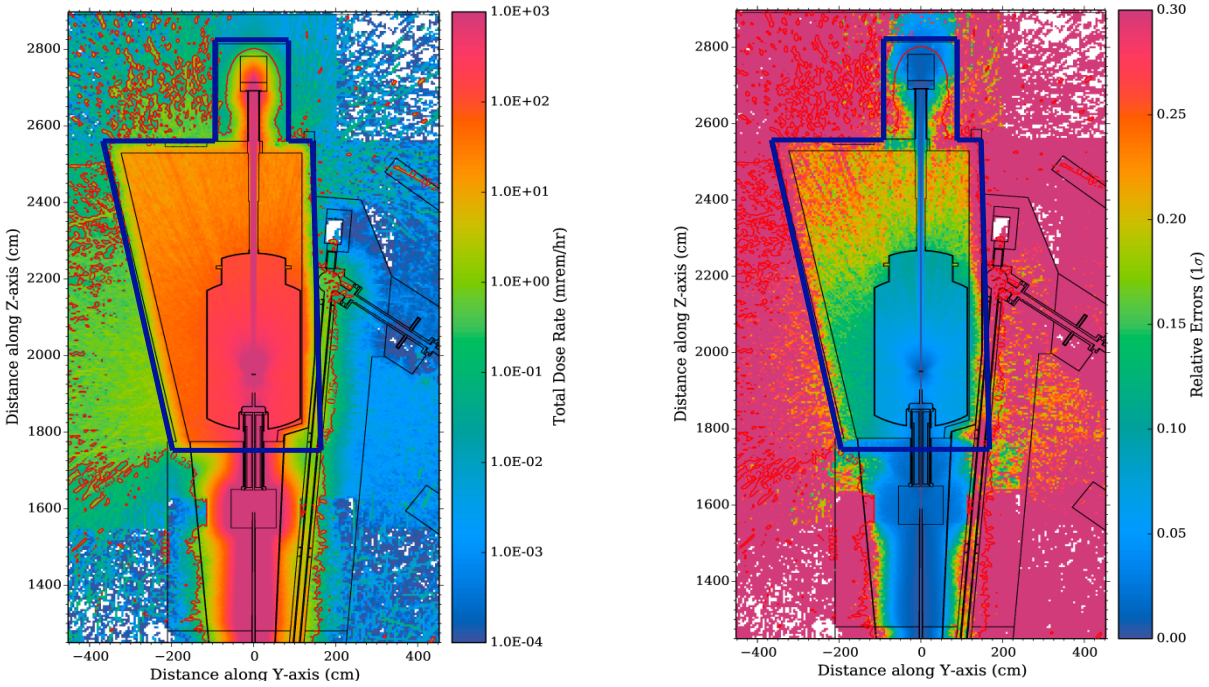

The “region of interest” for the calculation is outlined in blue.

Figure 6. Total (neutron plus photon) dose rates and associated relative errors at the elevation of the centreline of SNS beamline 1B for the hybrid ADVANTG/MCNPX solution with the white source

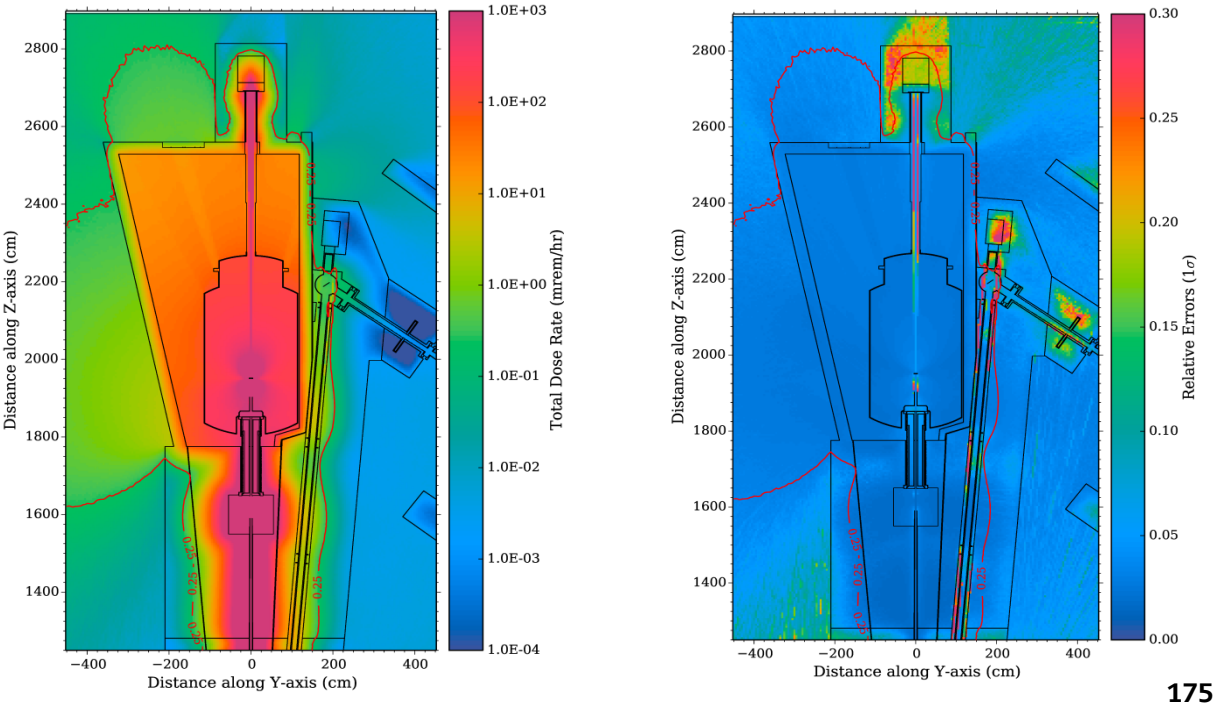

Figure 7. Total (neutron plus photon) dose rates and associated relative errors for a vertical mesh tally perpendicular to the SNS BL-1B axis for the MCNPX cell-based splitting and rouletting solution with the white source

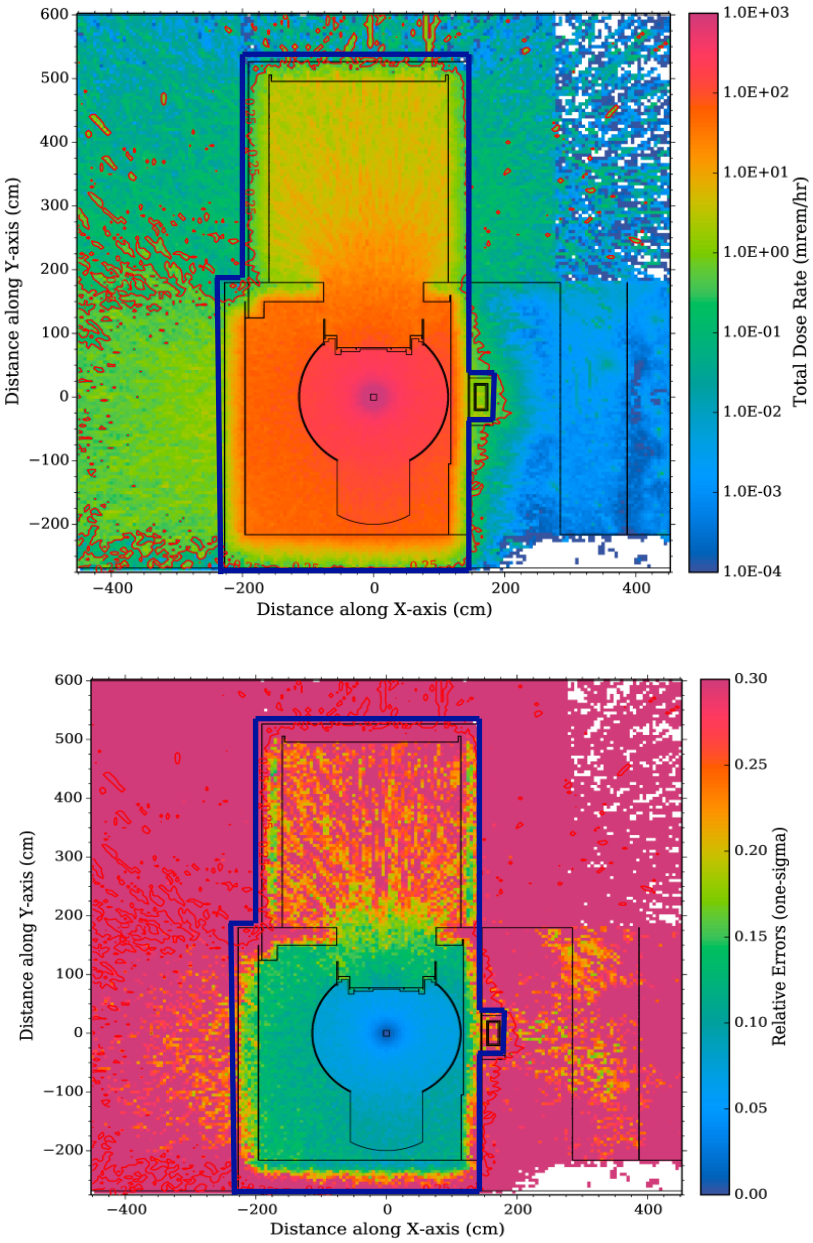

The “region of interest” for the calculation is outlined in blue.

Figure 8. Total (neutron plus photon) dose rates and associated relative errors for a vertical mesh tally perpendicular to the SNS BL-1B axis for the hybrid ADVANTG/MCNPX solution with the white source

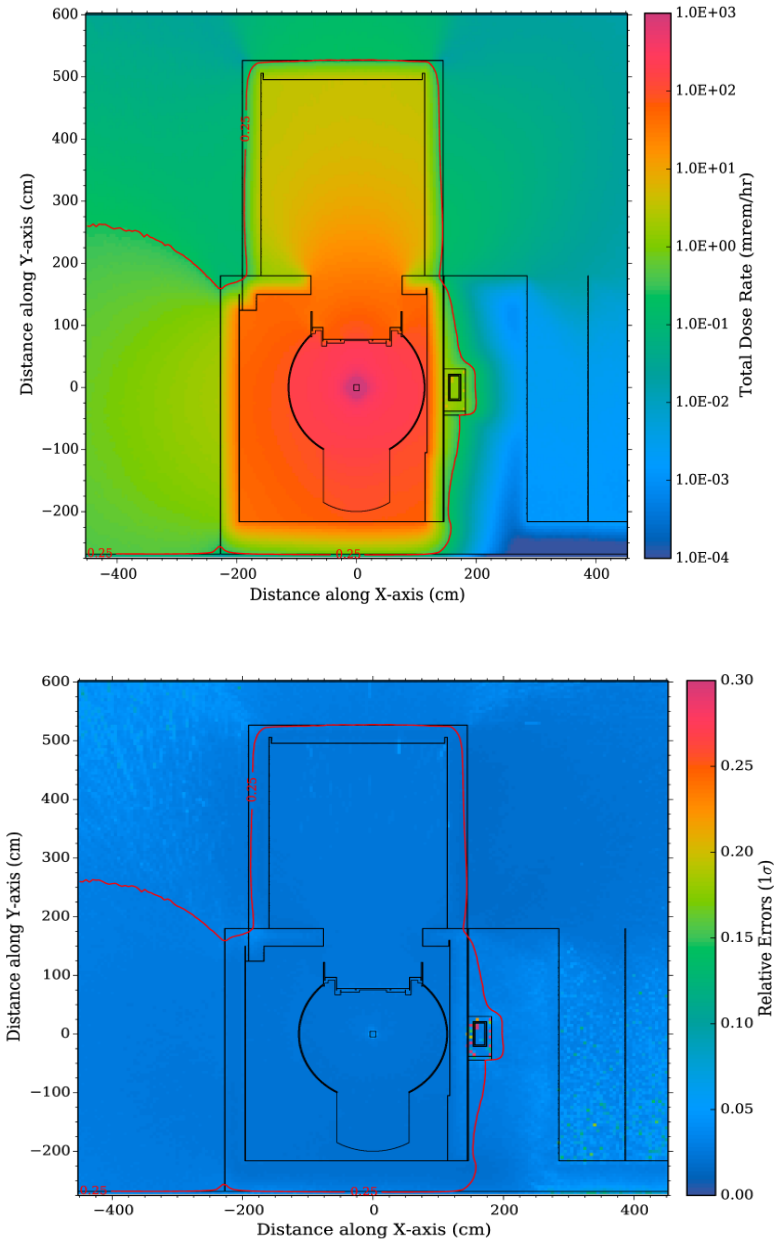

Figure 9. Total (neutron plus photon) dose rates and associated relative errors at the elevation of the centreline of SNS beamline 1B for the MCNPX cell-based splitting and rouletting solution with the low-energy source

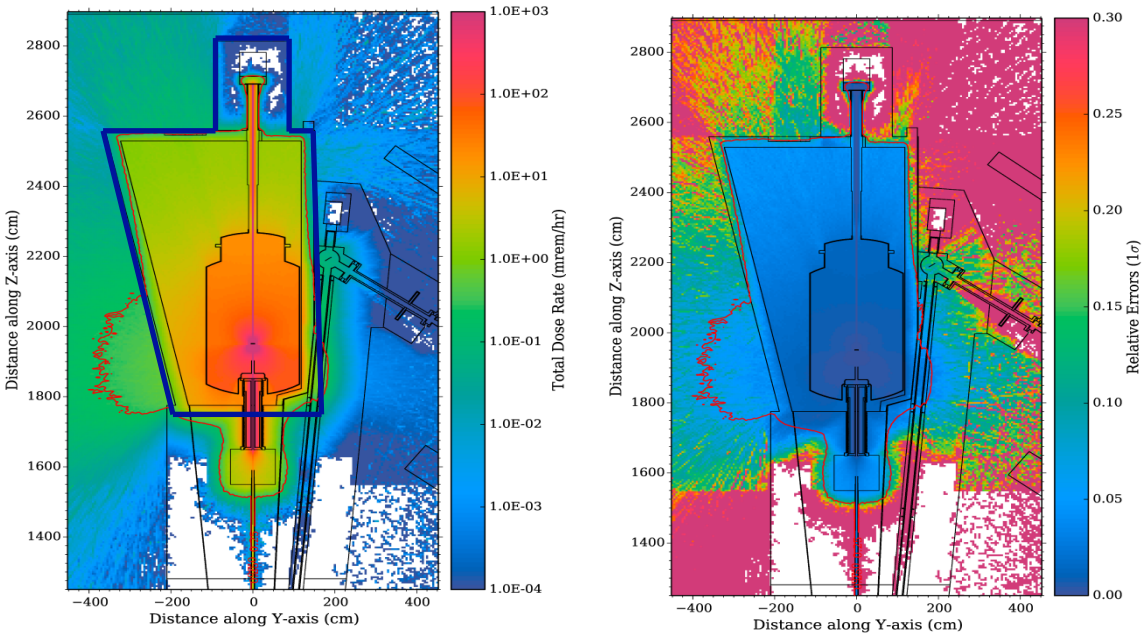

The “region of interest” for the calculation is outlined in blue.

Figure 10. Total (neutron plus photon) dose rates and associated relative errors at the elevation of the centreline of SNS beamline 1B for the hybrid ADVANTG/MCNPX solution with the low-energy source

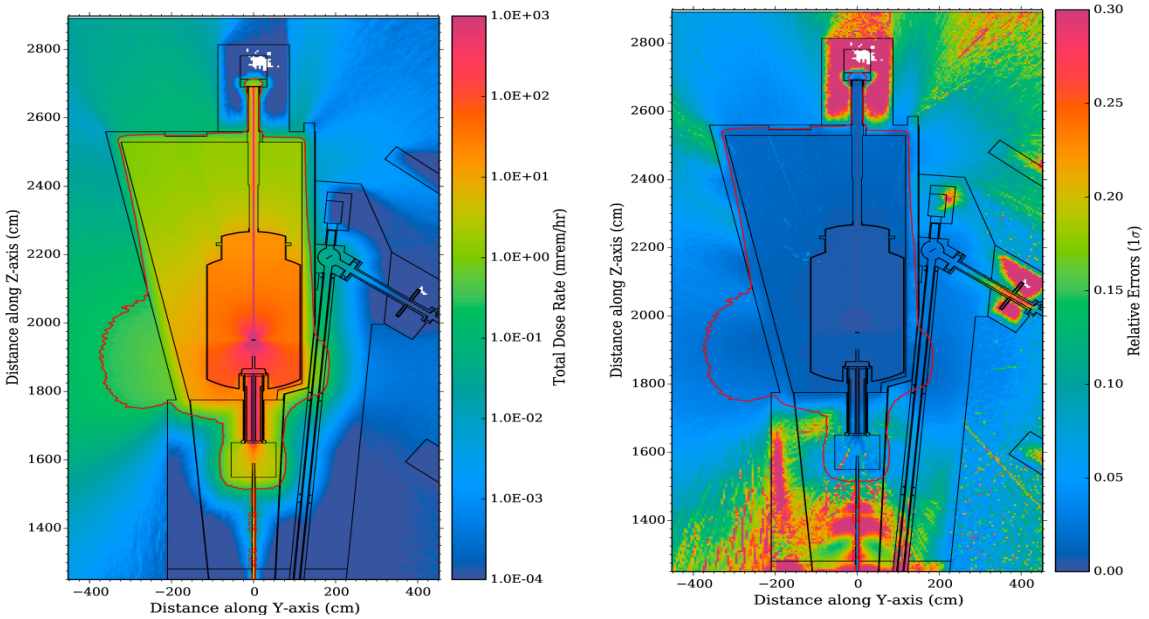

Figure 11: Total (neutron plus photon) dose rates and associated relative errors for a vertical mesh tally perpendicular to the SNS BL-1B axis for the MCNPX cell-based splitting and rouletting solution with the low-energy source

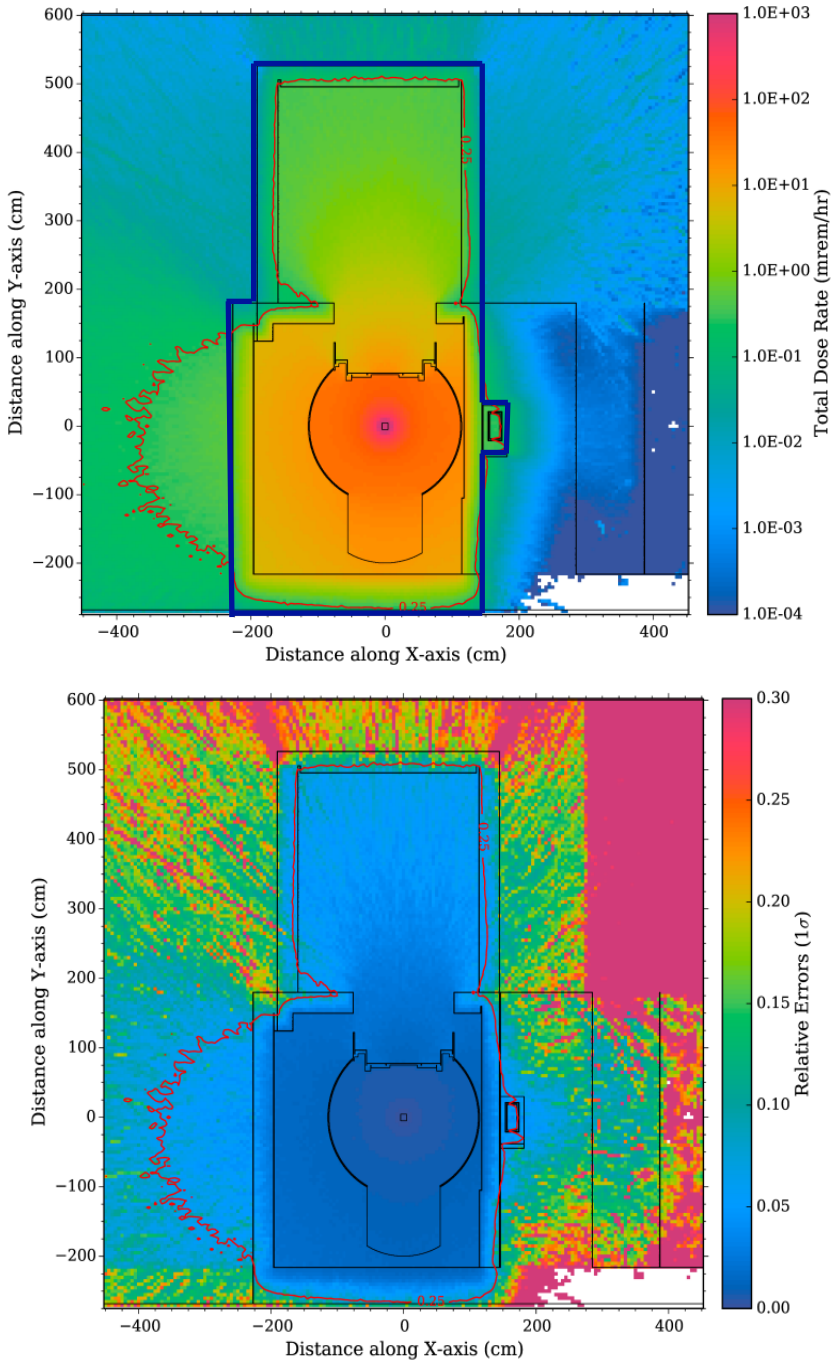

The “region of interest” for the calculation is outlined in blue.

Figure 12. Total (neutron plus photon) dose rates and associated relative errors for a vertical mesh tally perpendicular to the SNS BL-1B axis for the hybrid ADVANTG/MCNPX solution with the low-energy source

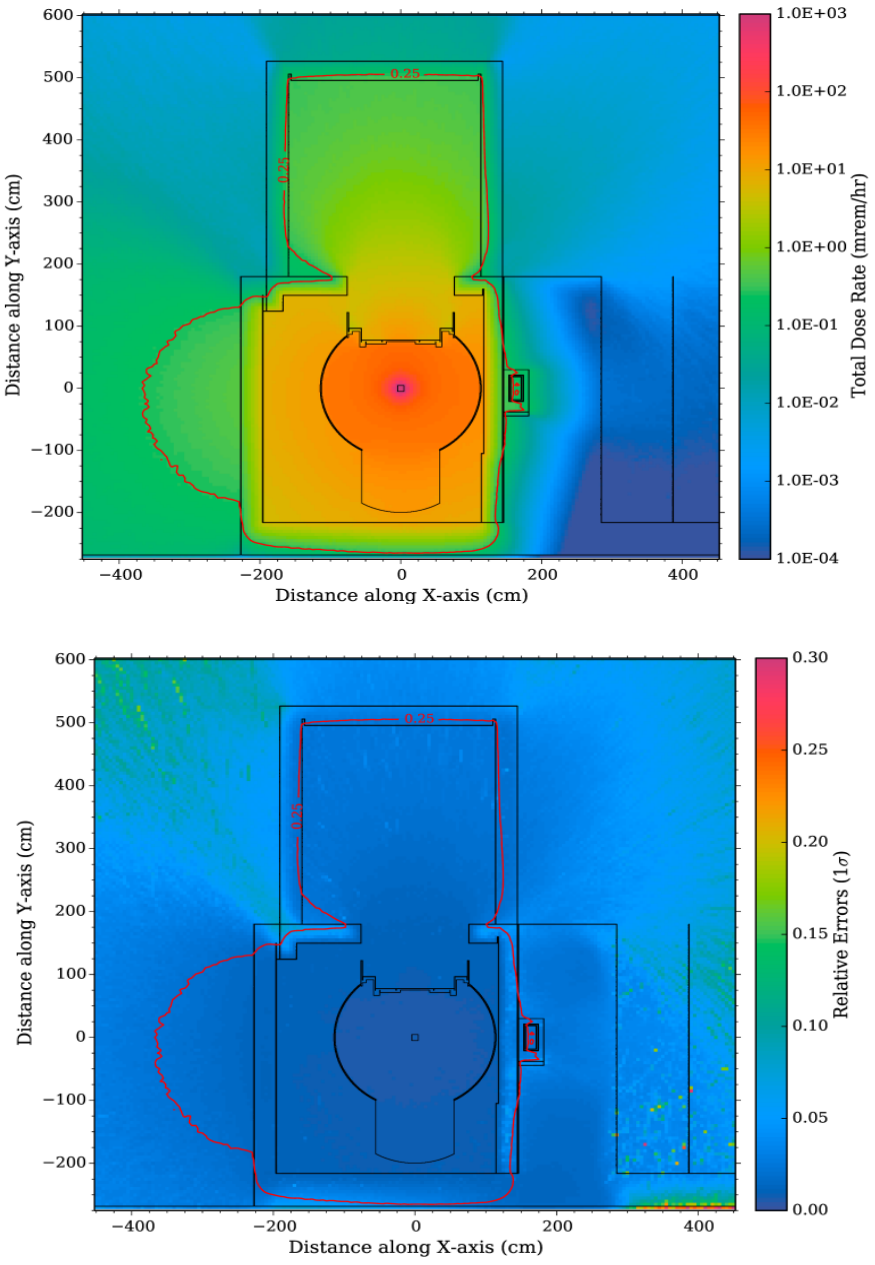

Figure 13. Total (neutron plus photon) dose rates and associated relative errors for a vertical mesh tally at the centreline of SNS beamline 1B for a hybrid ADVANTG/MCNPX solution with the white source and the secondary carousel closed

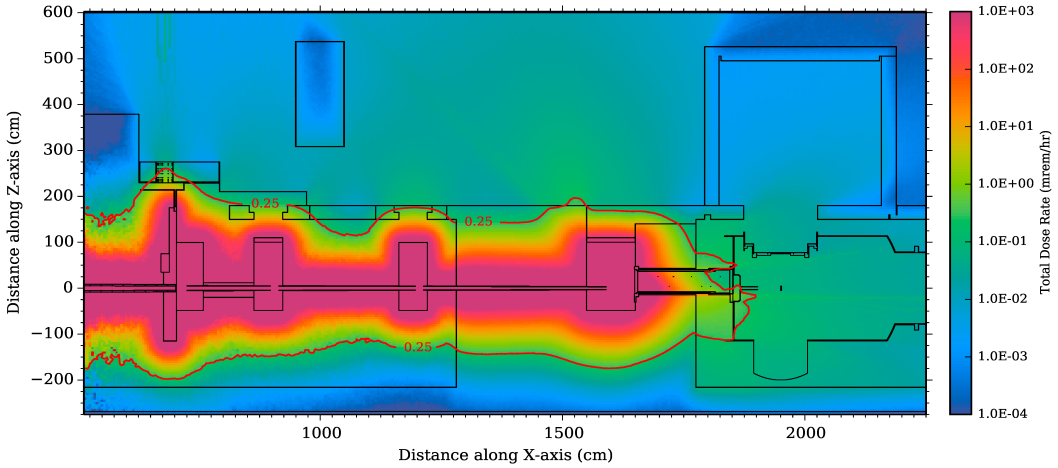

Summary and conclusions

We have applied the ADVANTG code to perform a hybrid deterministic/Monte Carlo analysis of SNS beamline models using several combinations of beamline geometry and source energy distributions. In previous calculations that employed cell-based splitting and rouletting, each of those source/geometry combinations required extensive analyst time to modify the geometry description and develop corresponding splitting and rouletting parameters. By using the FW-CADIS hybrid method in ADVANTG, we were able to generate weight windows and consistently biased sources with very little additional analyst time required for each scenario. In addition to saving analyst time, the variance reduction parameters generated by ADVANTG provided well-converged nearly global solutions and did so with substantial reductions in the required MCNPX computational time. We also demonstrated the importance of using an appropriate quadrature for this type of application, in which particle transport is dominated by streaming along the beamline axis. For the BL-1B geometry, the use of Lobatto quadrature was crucial to the generation of weight windows that can be used with no additional user modifications. We also noted that the convergence of the ADVANTG-accelerated MCNPX calculations is somewhat poor in the beam stop area. This is probably due to target weight variations that cause rouletting followed by splitting along the beamline axis just prior to the beam stop. A separate analysis of the beam stop (rather than the essentially global approach that we used) may be a better technique for this region.

References

[1] D.B. Pelowitz, editor (2005), *MCNPX User's Manual Version 2.5.0*, LA-CP-05-0369, Los Alamos National Laboratory, Los Alamos, New Mexico.

[2] ORNL (2011), *SCALE: A Comprehensive Modeling and Simulation Suite for Nuclear Safety Analysis and Design*, ORNL/TM-2005/39, Version 6.1, Radiation Safety Information Computational Center at Oak Ridge National Laboratory as CCC-785, Oak Ridge, Tennessee.

[3] S.W. Mosher et al. (2013), *ADVANTG – An Automated Variance Reduction Parameter Generator*, ORNL/TM-2013/416, Oak Ridge National Laboratory, Oak Ridge, Tennessee.

[4] X-5 Monte Carlo Team (2003), *MCNP – A General Monte Carlo N-Particle Transport Code, Version 5. Volume I: Overview and Theory*, LA-UR-03-1987, Los Alamos National Laboratory, Los Alamos, New Mexico.

[5] J.C. Wagner, D.E. Peplow, S.W. Mosher (2014), "FW-CADIS Method for Global and Regional Variance Reduction of Monte Carlo Radiation Transport Calculations", *Nucl. Sci. Eng.*, 176(1), pp. 37-57.

[6] R.A. Lillie, F.X. Gallmeier (2000), "HILO2K: A Coupled Neutron-Photon Transport Cross-Section Library for Neutron Energies up to 2000 MeV", *Fourth International Topical Meeting on Nuclear Applications of Accelerator Technology, American Nuclear Society,* Washington, DC.

Shielding calculations with MCNPX at the European spallation source

Riccardo Bevilacqua, Lali Tchelidze, Günter Muhrer, Eric Pitcher
European Spallation Source, Lund, Sweden

Abstract

The European Spallation Source (ESS) is a collaboration of 17 European partner countries established to project, build and operate the world's most powerful neutron source in Lund, Sweden. The construction of the facility started in 2014, and ESS is expected to produce the first neutrons in 2019. Monte Carlo calculations are required to design the appropriate shielding needed to guarantee the radioprotection of the workers and of the public. We present here the results obtained with the MCNPX radiation transport code for front-end building of the 2 GeV proton linear accelerator. We have modelled the RFQ, the MEBT and the DTL components of the accelerator, and we have calculated the dose contribution to the water-cooling room, adjacent to the front-end building, as a function of several shielding solutions. We show that 80% of the contribution to the neutron and gamma dose comes from the first three tanks of the DTL, and that a 1 m ordinary concrete shielding wall is necessary to guarantee a prompt dose below 3 μSv/h in the areas accessible during operation.

Introduction

The European Spallation Source (ESS) will be the world's most powerful neutron source. The facility was expected to be built in Lund, Sweden, and the construction phase was expected to start in 2014; we expect to produce the first neutrons in 2019.

At ESS, protons will be linearly accelerated up to 2 GeV and neutrons will be produced by the interaction of a 5 MW beam with a rotating tungsten target. The baseline of the ESS facility is described in detail in the Technical Design Report [1]. Monte Carlo calculations were performed at ESS as part of the design effort, in order to guarantee appropriate shielding for the radioprotection of the ESS workers, the visiting scientists and the public. We present here calculations relative to the warm section of the ESS linac, where proton energies are available up to 90 MeV. The MCNPX code is widely used for shielding calculations at accelerator facilities around the world allowing the transport of all relevant particles. Nuclear interactions may be described by both models, experimental data and evaluated cross-sections.

Geometry of the front-end building area

The aim of this work was to design the shielding of the front-end building (FEB) of the ESS linear accelerator. In the baseline design of the ESS facility, the FEB will be located below the ground surface, and will be covered by a 5 m thick berm. The berm thickness will be the same for the whole length of the accelerator tunnel, and has been calculated to account for 1 W/m proton beam losses along the linac [2]. There is no planned shielding separating the FEB from the linac tunnel, and no access will be allowed in the FEB during operation of the accelerator.

Access to the FEB – with beam off – should be guaranteed from the adjacent water-cooling room (WCR), after a certain cooling time for activation of the accelerator components (activation is not discussed in this work). According to the ESS baseline requirements, the WCR has been designated as a radiation supervised area with a maximum allowed prompt dose of 3 μSv/h during operation of the accelerator.

As a reference, we note that at the SNS facility a 80 cm thick ordinary-concrete wall has been installed immediately upstream the Drift Tube Linac (DTL) [3,4]. There, the FEB is designed as an accessible area during operation, with a prompt dose limit of 2.5 uSv/h. However, at SNS the beam energy at the tunnel entrance is 2.5 MeV, whereas at ESS the maximum proton energy in the FEB is 3.6 MeV.

Accelerator components

We have modelled three components of the warm section of the proton linear accelerator: the Radio Frequency Quadrupole (RFQ), the Medium Energy Beam Transport (MEBT) and the normal conducting DTL. The first two components are located in the front-end building, whereas the DTL is located in the first section of the accelerator tunnel. A schematic drawing of the ESS linac is presented in Figure 1. Our work did not include the ion source and the Low Energy Beam Transport (LEBT), since the energies of the protons in these components (up to 75 keV) are below the threshold for neutron production in copper: 2.167 MeV for ^{65}Cu(p,n) and 4.215 MeV for ^{63}Cu(p,n).

Figure 1. The ESS linear accelerator

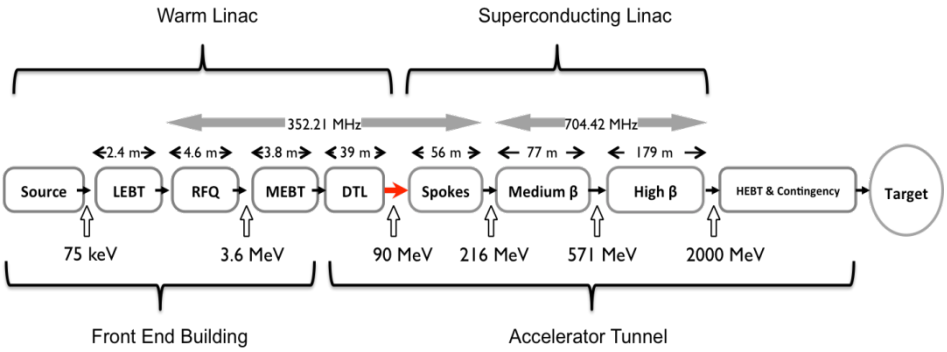

RFQ

The RFQ accelerates the 75 keV protons from the LEBT up to 3.6 MeV. We have modelled the RFQ taking in account the actual design of the section orthogonal to the proton beam line. In the MCNPX model, the RFQ was built with Cu in its natural isotopic composition. Cooling water channels were also included in the model, in the actual position of the RFQ design. To account for the modularity of the RFQ design, we have reduced the materials density according to the actual design. The RFQ is 461.1 cm long and has a diameter, averaged along its length, of 28.8 cm. The eight cooling water channels have diameters of 2.0 cm (four outer channels) and 1.0 cm (four inner channels).

Figure 2 shows the section of the MCNPX model of the RFQ. The orange material is Cu, the blue corresponds to the eight water channels, the green material is the air in the FEB. In our model, we have assumed ideal vacuum inside the RFQ (white material Figure 2).

We have simulated a point-like loss of the proton beam on the internal tips of the RFQ. In our calculations, we have assumed a loss of 1 W/m, and the maximum proton energy available in the RFQ, which corresponds to 3.6 MeV. Hence, since the RFQ has a length of 461.1 cm, we have normalised our results for a loss of 4.6 W. To account for different scenarios, we have simulated the proton beam loss for each of the four internal

tips and at different positions along the length of the RFQ. However, due to the 2.167 MeV threshold for the ^{65}Cu(p,n) reaction, neutrons can be produced in the RFQ only in the last section of its length.

Figure 2. Section of the MCNPX model of the RFQ

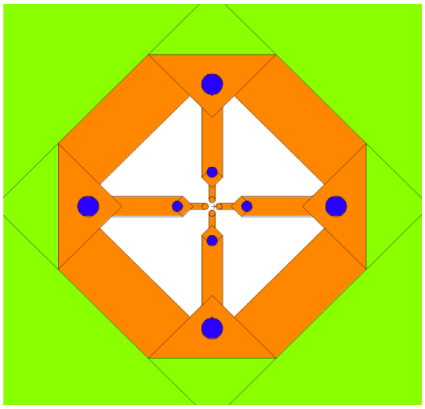

MEBT

We have accounted for three scenarios of proton beam losses in the MEBT: the protons impinging on three sets of collimators, the protons diverted on the beam chopper dump and a point-like loss in the MEBT beam pipe. Since there is no acceleration in the MEBT, all the protons have an energy of 3.6 MeV, which is the exit kinetic energy from the RFQ.

In the MEBT, there are three sets of collimators, each composed by four elements, orthogonal to the proton beam line. Each component of the collimator consists in a 2 mm graphite absorber coupled to 20 mm of Cu for heat dissipation. To account for the cooling water channels in the Cu elements, we have modelled a uniform medium composed by 85% Cu and 15% water. The MEBT chopper dump consists in a graphite absorber 2 mm thick, and a thicker layer of Cu (10 mm). The dump is tilted at 5 degrees, and has a transverse size of 200 X 50 mm^2. The beam pipe was modelled as a 1.6 mm thick stainless steel (316L) tube. The MCNPX geometry used in these calculations is presented in Figure 3.

We modelled the beam loss on each collimator as a Gaussian beam of 3.6 MeV protons depositing 1% of the full current (62.5 mA) on all the four elements, the jaws being opened at 3 sigma from the beam centre (corresponding to 1.70 X 10^{14} protons/second). The size of the beam was respectively 2 X 3 mm^2, 3 X 3.6 mm^2 and 2.6 X 1 mm^2 at the position of the first, second and third collimator. The beam loss on the MEBT chopper dump was modelled as a Gaussian beam of 3.6 MeV protons, impinging orthogonally on the graphite absorber (5.68 X 10^{14} protons/second). Finally, we modelled a point-like 4 W beam loss on the beam pipe (7.0 X 10^{12} protons/second), and at an incident angle of 0.1 radians.

Since the range of 3.6 MeV in 1.7 g/cm^3 graphite is 0.135 mm, all the incident protons are stopped in the graphite absorbers, both in the collimators and in the chopper dump. The neutron production threshold for ^{12}C is 19.6 MeV, hence neutrons can be produced only via the ^{13}C(p.xn) reaction with threshold 3.2 MeV. In the MCNPX model of the problem, we assumed the natural isotopic composition of carbon, accounting for 98.9% ^{12}C, and 1.1% ^{13}C.

Figure 3. MCNPX model of the MEBT chopper dump, (left) one of the collimators and the beam pipe (right) and section of the chopper dump

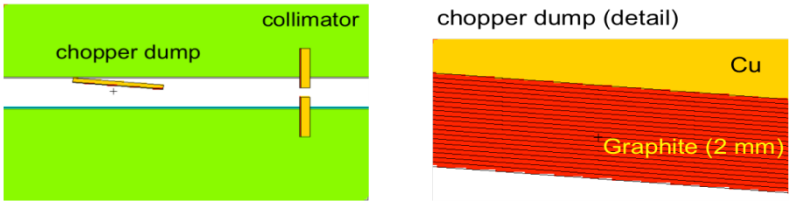

A digression on $^{13}C(p,xn)$

There is no ENDF/B-VII proton data library available for ^{13}C, however, these cross-section data are included in the – TALYS based – TENDL library [5]. The data in the TENDL library are delivered both in ENDF format and in ACE format, to be used in MCNPX calculations. We have observed that, whereas the TENDL ACE files behave as expected above 4 MeV, the 3.2 MeV threshold for the $^{13}C(p,xn)$ reaction is not correctly represented (Figure 4). This seems to be due to the fact that the conversion to the ACE file for this reaction data was performed in steps of 1 MeV [6]. Moreover, we have observed a large discrepancy between the TENDL-2011 and TENDL-2013 cross-sections near threshold, independently from the used library format. Finally, as we can observe in Figure 4 (right panel) in the TENDL-2013 ACE file, the partial $^{13}C(p,xn)$ cross-section at 4 MeV is higher than the total p + ^{13}C reaction cross-section.

Figure 5 shows the MCNPX calculations for the neutron production yield from a thick target of ^{13}C, for incident proton energies from 3.6 MeV to 6 MeV. The calculations were performed using respectively the MCNPX built-in model, the TENDL-2011 data and the TENDL-2013 data for the $^{13}C(p,xn)$ reaction. These results were compared with the experimental yields from Bair et al. [7], which are available in the EXFOR database, for proton energies above 4 MeV. We observe that at 5 MeV and at 6 MeV, the three sets of calculations agree with the experimental data. At 4 MeV, both TENDL-2011 and TENDL-2013 give results consistent with the data from Bair et al. whereas the MCNPX model overestimates the neutron production yield. At lower energies, the three sets of data give discrepant results. In the present shielding calculations, we decided to use the built-in MCNPX model to account for the $^{13}C(p,xn)$ reaction: this choice is both conservative, since the model gives higher yields, and consistent, given the discussed shortcomings relative to the TENDL ACE files (Figure 4).

Figure 4. Total p + ^{13}C and partial $^{13}C(p,xn)$ cross-section data as included in the ACE version of the TENDL-2011 (left panel) and TENDL-2013 (right panel) nuclear data files

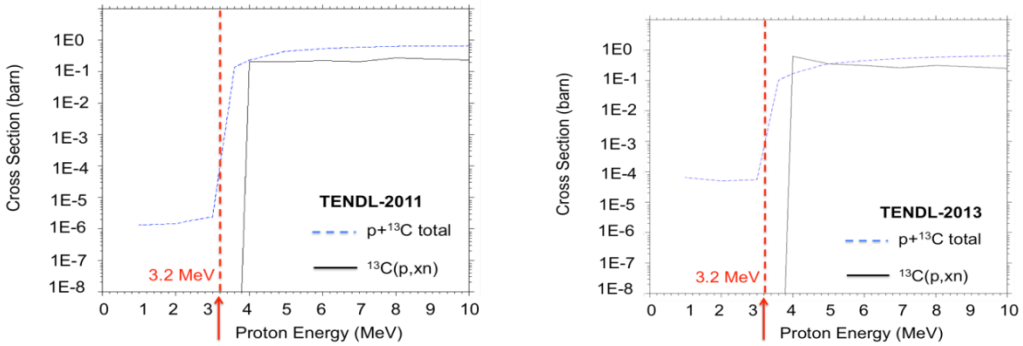

The threshold at 3.2 MeV for the $^{13}C(p,xn)$ reaction is indicated in both plots.

DTL

The DTL is composed of five independent tanks. Table 1 lists the technical information about each of these tanks. The 3.6 MeV protons entering the DTL are accelerated up to 90 MeV over a length of 40 meters. In the MCNPX calculations we followed the ESS design requirements and assumed a beam loss of 1 W/m, however, preliminary results show that the expected average total power loss over the 40 metres of the DTL will account for 0.25 W [8].

We modelled the DTL as presented in Figure 6. Each tank was designed as a vacuum stainless steel beam pipe, with a 50 μm internal coating of Cu. The cells were not modelled independently, but their average length was computed and divided by the total length of each tank: this number was then used as scaling factor for the density of the materials included in the MCNPX geometry. In the ESS DTL design, each second cell is occupied by a Sm_2Co_{17} permanent magnet, which was included in the Monte Carlo simulations. The free cells will be either empty, or will contain steerers and beam diagnostic instruments; since these instruments and their position were not identified yet, in the present study we have assumed all the free cells to be empty. To account for the Sm_2Co_{17} magnet, we included the actual transverse geometry, and reduced the material density along the beam direction accordingly to the actual volumes.

We performed independent calculations for each DTL tank. The 1 W/m proton beam loss was modelled as protons impinging on the internal Cu drift tube (with internal radius ranging from 10 to 12 mm, see Table 1), at an angle of 0.01 radians with respect to the beam direction. In the present work, we assumed a discrete source term: each tank was divided into ten sections (c.a 70 cm each), and the protons with the maximum energy for a specific section were transported from the most upstream position in that section. For each source position, the protons were equally distributed at eight equally spaced angles – on the plane normal to the beam direction. The number of protons per second was calculated for the maximum kinetic energy in each of the 10 sections/tanks.

Figure 5. Neutron production yield from a thick ^{13}C target, calculated with the MCNPX code using the built-in MCNPX model (squares), the TENDL-2011 data (triangles) and the TENDL-2013 data (diamonds)

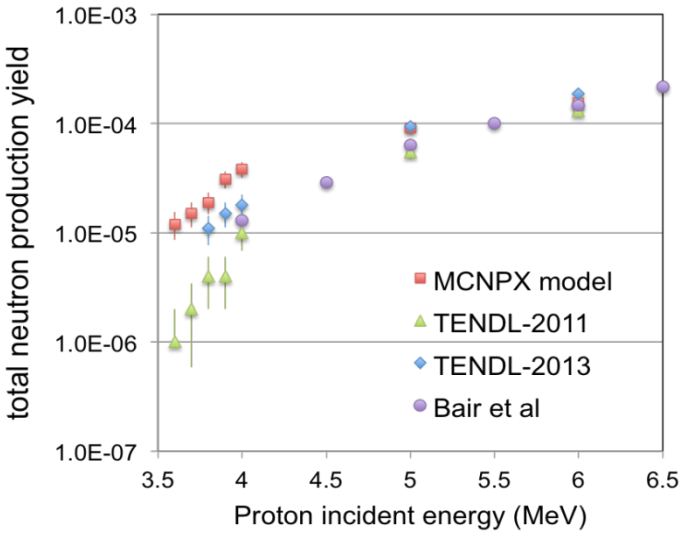

MCNPX results are compared with experimental data by Bair et al. [6] (circles).

DTL's Faraday cup

In the present work we also simulated the Faraday cup placed at the end of the first DTL tank, 7.62 m downstream the linac tunnel. The Faraday cup was modelled as a 1 mm carbon foil, followed by a 5 mm carbon absorber at a distance of 20 mm; the foils were placed in a stainless steel housing, 5 mm thick. The Faraday cup is designed to absorb a beam pulse of 10 μs, at a repetition rate of 14 Hz and full current (62.5 mA). The protons impinging on the Faraday cup have a kinetic energy of 21 MeV. Four other Faraday cups will be placed at the downstream end of each of the remaining DTL tanks, however, they were not modelled as part of this work.

Table 1. DTL parameters for each tank

Parameter	Tank 1	Tank 2	Tank 3	Tank 4	Tank 5
Cells per tank	61	34	29	26	23
Accelerating field (MV m^{-1})	3.00	3.16	3.07	3.04	3.13
Bore radius (mm)	10	11	11	12	12
Number of modules	4	4	4	4	4
Length (m)	7.62	7.10	7.58	7.85	7.69
Beam output energy (MeV)	21.29	39.11	56.81	73.83	89.91

Figure 6. MCNPX model of the DTL

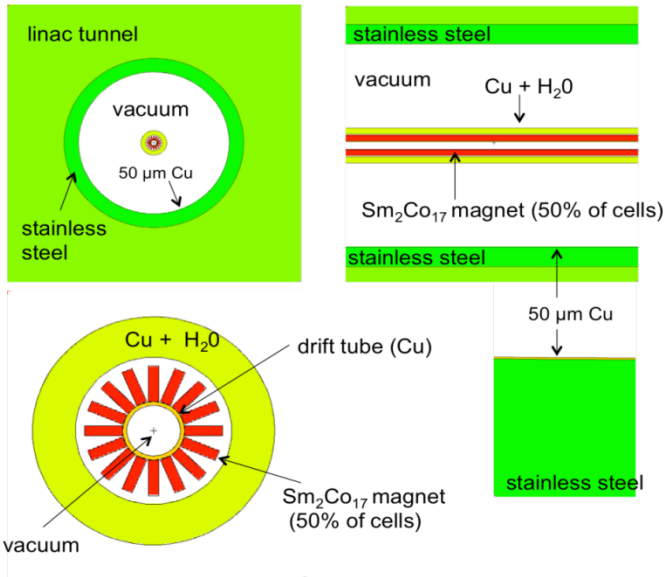

Scaled material densities account for the discrete DTL cells structure. Each second cell will contain a Sm_2Co_{17} permanent magnet. Eventual diagnostic instruments in the free cells were not taken into account.

Results

We have calculated the prompt neutron and gamma doses given by the beam losses on the MEBT's beam pipe, collimators and chopper dump, on the RFQ tips, on each of the five DTL tanks and on the Faraday cup at the end of the first DTL tank. These doses were reported at the door of the WCR, accessing the FEB: this location is the one offering the least shielding, and our MCNPX calculations confirmed that this location was the hottest point in the WCR.

We have considered two shielding geometries, with the constrain that – to allow maintenance of the FEB equipment – the access between FEB and WCR should be at least 3 m wide and 2.50 m high. The first geometry (Figure 7, left panel) consists in a corridor, parallel to the linac, extending for the full length of the FEB; the corridor is 3 m wide, 20 m long, and it is defined by two ordinary concrete walls. The access is guaranteed by two doors (not providing radiation shielding), at the opposite extremes of the corridor. Calculations were performed for 40 cm thick shielding walls and for 1 m thick walls. The second geometry (Figure 7, right panel) consists in a labyrinth, 3 m wide, with three legs, respectively, 9 m, 7 m and 9 m long, and walls 1 m thick.

Figure 7. Front-end building (FEB) and water-cooling room (WCR), with the shielding geometries: (left panel) corridor with 40 cm thick shielding walls (right panel) and labyrinth with 1 m thick shielding walls

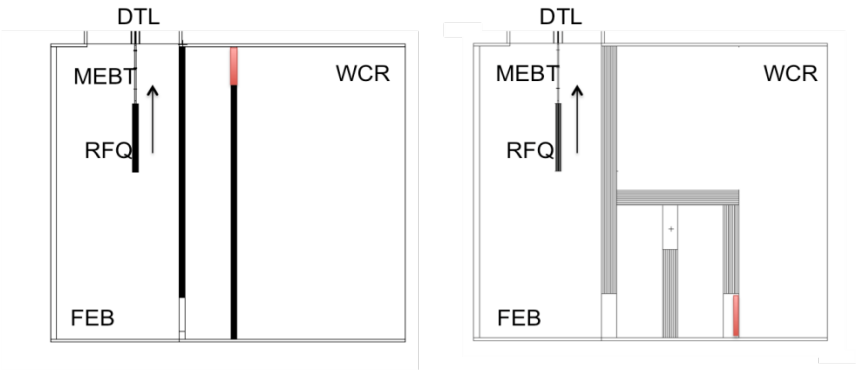

The corridor configuration with 1 m thick shielding walls is not shown in the figure. The doses reported here were calculated at the entrance door (red cell). The arrow indicates the direction of the proton beam.

Figure 8. DTL tanks contribution to the neutron and gamma prompt dose in the WCR for the corridor configuration and the labyrinth configuration

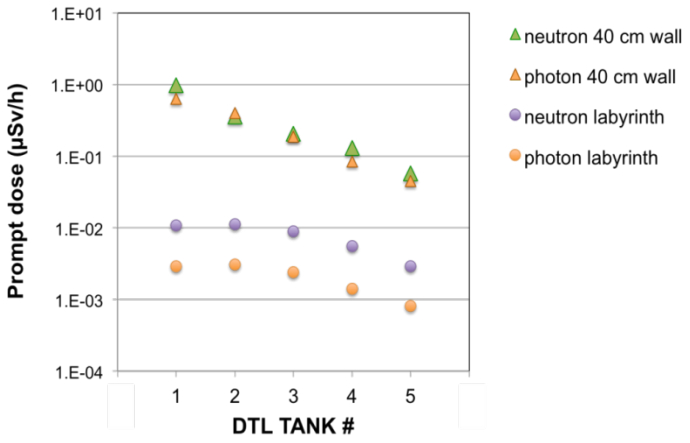

Dose contribution from MEBT and RFQ

Calculations for the MEBT and RFQ were conducted only for the first geometry (corridor), with 40 cm thick shielding walls. In this configuration the main contribution to the prompt neutron dose to the WCR from the MEBT came from the 4 W point-like loss on the stainless steel beam pipe, and accounted for 0.08 μSv/h. When calculating the contribution from the MEBT collimators and chopper dump, we observed that MCNPX did not produce any neutrons when transporting 10^7 protons: this is due to the fact that the Coulomb stopping power on graphite is much higher than the probability of undergoing nuclear interaction. To estimate an upper limit for the dose from these two components of the MEBT, we have assumed that 10^{-7} protons per source particle could reach the Cu inside the collimators and the dump. Even under this assumption, the neutron dose contribution to the WCR accounted for less than 10^{-8} μSv/h.

The maximum neutron dose rate contributed by the RFQ was 0.13 μSv/h, assuming a 4.6 W point-like loss and 3.6 MeV protons. This is a very conservative assumption, since protons are accelerated in the RFQ from 75 keV up to 3.6 MeV, along its 4.6 length, and only protons above the 2.167 MeV threshold in ^{63}Cu may contribute to the neutron production. The range of 3.6 MeV protons in Cu is 46 μm, hence they cannot reach the cooling-water channels in the RFQ, where neutrons might be eventually produced via the ^{18}O(p,xn) reaction (threshold 2.575 MeV).

Dose contribution from DTL

For the corridor configuration of the shielding (Figure 7, left panel), with 40 cm walls, the prompt neutron dose in the WCR from the five tanks of the DTL was 1.97 μSv/h, and the prompt gamma dose was 1.43 μSv/h. Hence, our calculations showed that the DTL contribution to the prompt dose in the WCR was one order of magnitude larger than the combined contribution given by the MEBT and the RFQ. In this configuration, the total prompt dose exceeds the 3 μSv/h limit for the WCR.

In the labyrinth configuration (Figure 7, right panel), the prompt dose from the DTL was 0.0396 μSv/h and 0.0107 μSv/h, respectively for neutrons and gammas. Given the reduction by a factor 50 of the prompt neutron dose, and by more than a factor 100 of the prompt gamma dose contributed by the DTL tanks, we assumed that in this configuration the dose contribution from the MEBT and the RFQ were negligible. However, we can account for the fact that the MEBT and the RFQ increase the total dose by 10%. The resulting total prompt dose of 0.055 μSv/h is well below the required 3 μSv/h limit.

In Figure 8, we compare the contribution to the dose from each tank of the DTL, for the two configurations described in Figure 7. We observe that for the corridor configuration with 40 cm walls, the gamma and neutron dose contributions were equivalent, whereas in the labyrinth configuration the gamma dose is consistently lower (by a factor 3) than the neutron contribution. From the neutron and gamma flux maps, we observed that the largest contribution to the dose was coming from neutron penetration through the shielding wall. A MCNPX calculation for the corridor configuration and 1 m thick shielding walls showed that the neutron dose from DTL tank 1 reduced from 0.98 μSv/h to 0.016 μSv/h, and the gamma dose reduced from 0.68 μSv/h to 0.022 μSv/h; now the main contribution was given by radiation streaming through the corridor. The labyrinth configuration further reduced these values to 0.011 μSv/h and 0.003 μSv/h, respectively for neutrons and gammas. The large reduction in gamma dose is due to the three-leg geometry vs. the single-leg design of the corridor configuration.

Dose contribution from DTL's Faraday cup

We have finally calculated the dose contribution given by the proton beam on the Faraday cup at the downstream end of the first DTL tank. The prompt neutron dose was 0.0042 μSv/h and the gamma dose 0.0013 μSv/h. These results were obtained for the

labyrinth configuration, and are consistently lower than the dose given by 1 W/m loss in the first three tanks of the DTL.

Conclusions

We have modelled the components of the ESS warm linac where protons have kinetic energies above the neutron production thresholds, and we have designed the shielding for the FEB to guarantee supervised access to the neighbouring WCR. Our calculations showed that the first three tanks of the DTL contribute to 80% of the total prompt dose in the WCR, and that the optimal shielding configuration is a labyrinth with 1 m thick concrete walls. The MEBT and the RFQ do not contribute significantly to the dose, compared to the DTL.

Acknowledgements

We acknowledge the input received from Franz Gallmeier (SNS) for the DTL calculations. This work was completed with the collaboration of Benjamin Cheymol, Renato de Prisco, Carl-Johan Hårdh, Giobatta Lanfranco and Aurélien Ponton at ESS, who provided information about the linac components and the geometry of the FEB.

References

[1] "Technical Design Report" (2013), *European Spallation Source*, Editor Steve Peggs, ESS-2013-001, Lund, Sweden.

[2] L. Tchelidze (2014), "ESS Linac Shielding Strategy and Calculations", ESS-0007143.

[3] F.X. Gallmeier (2001), "Calculations of Operational and Residual Doses for the SNS Linac", *Fifth International Topical Meeting on Nuclear Applications of Accelerator Technology*, ANS.

[4] F.X. Gallmeier (2002), "Shielding the Backstreaming Radiation in the Linac Tunnel originating in the Operational Beam Losses", SNS-106100200-TR0059-R00.

[5] A.J. Koning, D. Rochman (2012), "Modern Nuclear Data Evaluation With The TALYS Code System", *Nuclear Data Sheets* 113, 2841.

[6] A. Koning (2014), ESS, private communication.

[7] J.K.Bair, P.D.Miller, B.W.Wieland (1981), "Neutron Yields from the 4-12 MeV Proton Bombardment of 11B,13C and 18O as Related to the Production of 11C,13N and 18F", Applied Radiation and Isotopes, Vol.32, p.389, UK.

[8] R. de Prisco, ESS, private communication.

Towards the next generation RIB facility using the ISOL method: Radiological protection and shielding challenges*

P. Vaz[1], R Luís[1], Y. Romanets[1], J.C. David[5], A. Dorsival[2], D. Ene[5], I. F. Goncalves[1], Y. Kadi[2], C. Kharoua[2], S. di Maria[1], F. Negoita[4], R. Rocca[2], L. Tecchio[3], V. Vlachoudis[2], J. Vollaire[2]

[1]IST, Grupo de Protecção e Segurança Radiológica, Centro de Ciências de Tecnologias Nucleares, Bobadela LRS, Portugal

[2]CERN, European Laboratory for Particle Physics, Geneva, Switzerland

[3]INFN-LNL - Legnaro (PD), Italy

[4]NIPNE - - Magurele, Romania

[5]CEA - Saclay, DSM/IRFU/SPHN, France

Abstract

Over the last decade, the importance of evolving towards the construction of Radioactive Ion Beam (RIB) facilities has gained considerable interest and support from the Nuclear Physics community (at large). Projects like the EURISOL (EURopean Isotope Separation On-Line Radioactive Ion Beam) Design Study paved the way for the investigation of scientific, technological and engineering studies of the next generation facility for the production of RIBs using the ISOL (Isotope Separation On-Line) method, two to three orders of magnitude more intense than the ones currently available at other facilities. At the same time, upgrade studies were undertaken at the existing facilities such as SPIRAL-2 at GANIL and ISOLDE at CERN, among others, in order to fill the gap between the existing facilities and the future EURISOL facility. The HIE-ISOLDE project stands for the on-going High Intensity and Energy upgrade of the ISOLDE facility at CERN.

Computational studies with the state-of-the-art Monte Carlo codes FLUKA and MCNPX pinpointed severe constrains in the shielding design and in the dose rate assessment of these facilities due to activation of the structural materials and the high intensity of the proton beams impinging on the spallation targets. These translate into dose-rate values that impose careful shielding assessment and consideration of radiation safety issues, should a technical intervention be needed, in a routine situation/maintenance or following an accident with the need to replace or fix damaged components.

In this paper the dose-rate mapping, activation studies of structural components, the shielding design of the above installations HIE-ISOLDE and EURISOL are described. Discrepancies between the Monte Carlo simulation results and the experimental data (measurements) obtained at ISOLDE are presented. The analysis of eventual limitations in the Monte Carlo modelling and simulation of these complex and sophisticated installations are performed, from the geometry, materials and available cross-sections data viewpoints.

* The full paper being unavailable at the time of publication, only the abstract is included.

Radiation protection study for the HIE-ISOLDE project at CERN

Sandra Giron, Joachim Vollaire
CERN, DGS/RP, Switzerland

Abstract

The HIE-ISOLDE project will expand the physics programme at the ISOLDE Facility at CERN with the possibility to post-accelerate a large variety of radioactive ion beams to energies well below and significantly above the Coulomb barrier. While this project contains three major elements: higher energies, improvements in beam quality and higher beam intensities, the most significant improvement is the replacement of the current post-accelerator (REX) by a new superconducting linear accelerator delivering ions of energy up to 10 MeV/u. This energy upgrade leads to new radiological hazards such as neutron emission when the post-accelerated beams at energies above the Coulomb barrier interact with beam intercepting devices or the vacuum chamber walls in case of beam loss. The new superconducting cavities installed will also be a strong source of X-rays due to electron field emission.

A review of the operating parameters of similar facilities allowed us to conclude that X-rays emitted by the cavities would drive the shielding requirements for the post-accelerator. In this context, systematic measurements of the X-ray levels were performed during RF cavity tests to evaluate the radiation source term. FLUKA simulations allowed the assessment of shielding requirements and geometry of the tunnel hosting the superconducting cavities, as well as evaluation of the maximum neutron dose rates expected in the event of beam losses. Activation of the machine components was also estimated, allowing the determination of the future waste classification due to beam-induced activation.

Introduction

The ISOLDE Facility at CERN is mainly dedicated to nuclear physics studies. At ISOLDE, Radioactive Ion Beams (RIB) are produced and post-accelerated up to 3 MeV/u. The HIE-ISOLDE (High Intensity and Energy ISOLDE) project will expand the nuclear physics programme at the ISOLDE Facility at CERN, by upgrading the ion beam energy and intensity, as well as the beam quality. New radiological hazards are expected after the energy upgrade of the facility, which require new mitigation measures to be integrated in the project.

In the first part of this paper, the HIE-ISOLDE Facility is presented, as well as radiation protection hazards related to the future post-accelerator. The procedure followed to determine the radiation source term, by comparison to similar facility and through X-ray measurements, is then described. The results of FLUKA simulations for X-ray dose rates, neutron emission due to beam losses and material activation are also reported. The technical shielding design chosen and the different mitigation measures required to deal with the different radiological hazards are presented.

The HIE-ISOLDE project at CERN

HIE-ISOLDE is a project aiming to improve the performances and capabilities of the ISOLDE Facility at CERN with an increase in the accelerated beam energy and intensity as well as with an improvement of the beam quality. The installation of the necessary hardware will take place in three stages between 2014 and 2018.

The ISOLDE Facility

The current ISOLDE Facility [1] allows RIBs with masses ranging from He to U to be produced and accelerated at energies ranging from 300 keV/u to 3 MeV/u. The proton beam delivered by the PS Booster (PSB) with an energy of 1 or 1.4 GeV and an intensity of 2 µA is used to produce spallation, fragmentation or fission reactions in the ISOLDE target. The radioactive ions are then extracted by diffusion and by ionisation processes. The General Purpose Separator (GPS) and the High Resolution Separator (HRS) allow the isotopic separation, selection and distribution of the beam to the experimental areas. The presence of a post-accelerator in one of the experimental beam line allows RIBs to be accelerated up to 3 MeV/u.

Figure 1. General layout of the ISOLDE experimental hall

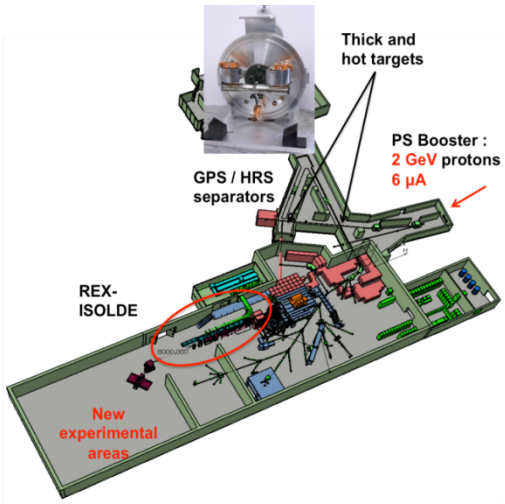

The HIE-ISOLDE upgrade

The HIE-ISOLDE project consists of three different upgrades of the facility [2]. First, the intensity upgrade is related to the replacement of PSB injector, linac2, by linac4 (~ 2017) and the energy increase of the PSB from 1.4 GeV to 2.0 GeV. Following this upgrade, proton beams received at ISOLDE will reach 2 GeV and 6 µA on ISOLDE production targets, which requires a completely new target design and the consolidation of the ISOLDE target area [3]. Second, due to a new RFQ cooler and buncher, a better mass resolving power to select the ions of interest for the experiments will be achieved, improving the ion beam quality. Finally, the most significant upgrade of the facility is the replacement of the existing Radioactive ion beam EXperiment (REX) linac by a superconducting linac consisting of 32 superconducting cavities. It will allow the ion beam to be accelerated up to 10 MeV/u, which is above the Coulomb barrier for most target/projectile combinations. The new radiation hazards introduced by the replacement of the post-accelerator are studied in this paper.

Radiation protection issues in the experimental hall

Radiation protection hazards

The different radioactive hazards associated with the construction of a new post-accelerator are the risks due to the implanted radioactive or volatile radioactive ions, the X-ray emitted by the superconducting RF cavities or the prompt neutron dose when the beam impinges on a target along its path.

The use of RIB involves a risk of external exposure: beam losses in normal operation of the machine may lead to the build-up of strong gamma-ray emitters (e.g. ^{7}Be, ^{74}As, ^{88}Y, ^{121}Te, ^{125}I...) in the vacuum pipe or vacuum chamber. Moreover, the production of volatile radiotoxic isotopes represents a risk of internal exposure during intervention requiring the opening of the vacuum chamber, in particular by alpha-emitters (e.g. ^{148}Gd, Po, daughters of ^{228}Ra/Th, etc.). As these risks already exist at ISOLDE, the same precautionary measures will apply at HIE-ISOLDE: beam intensity reduction and expiration duration limitation during isotopic collection, gamma monitoring and RP supervision and the use of appropriate protective equipment while opening vacuum chambers.

The replacement of the REX-ISOLDE post-accelerator by a new superconducting linac made of 32 superconducting RF cavities involves the emission of X-rays. These cavities are made of Cu and covered by a thin Nb deposit [5]. During the sputtering process, defects or dust can appear at the surface of the cavity, which will emit electrons during RF operation. These electrons, accelerated by the accelerating field, lead to bremsstrahlung X rays. However, as the intensity of X-rays emitted depends on the cleanliness and surface state of the cavity, measurements are required to evaluate expected dose rates during operation.

The possibility of accelerating ions above the Coulomb barrier induces the possibility of neutrons being produced during beam losses. The intensities expected for characteristic RIB used for experiments and stable beams used for beam tuning are presented in Table 1.

Table 1. Characteristic ion beam intensities at HIE-ISOLDE [4]

Beams	A/Q	Energy (MeV/u)	Intensity (ppA[1])	Comment
RIB	2	19.8	< 1	RIB (limit case)
Ne5+	4	11.3	1	Stable pilot beam
N4+	3.5	12.6	5	Stable pilot beam
He2+	2	19.8	10	Stable pilot beam
Ne5+	4	11.3	200	High intensity stable beam

In order to evaluate the main radiological hazards, HIE-ISOLDE was compared to similar facilities such as ISAC2 in TRIUMF (RIB accelerated up to few pnA intensity) [6] and ALPI in Legnaro (stable ion beams) [7], which both use superconducting accelerating structures. The HIE-ISOLDE intensity is lower by a factor 100 to 1000 as compared to ISAC2, while neutron dose rates due to ion beam losses are expected to be below 1 µSv/h. Since X-ray dose rates emitted by superconducting cavities measured at ALPI reached up 360 mSv/h at contact [8], X-rays are the main hazards at HIE-ISOLDE.

[1] ppA: particle pico-ampere; 1 ppA is equivalent to 6.25 10^{6} particles/s.

Constraints and challenges

The main constraint of the HIE-ISOLDE post-accelerator is its location in the experimental hall, close to experimental area and users (see Figure 2). In order to keep the current classification of the experimental hall as supervised radiation area (ambient dose rate below 3 µSv/h for permanent workplaces), a shielded enclosure will be built around the future post-accelerator. The design objective for parasitic X-rays was set to 1 µSv/h behind the shielding.

Figure 2. Location of the HIE-ISOLDE post-accelerator in the experimental hall close to experimental areas

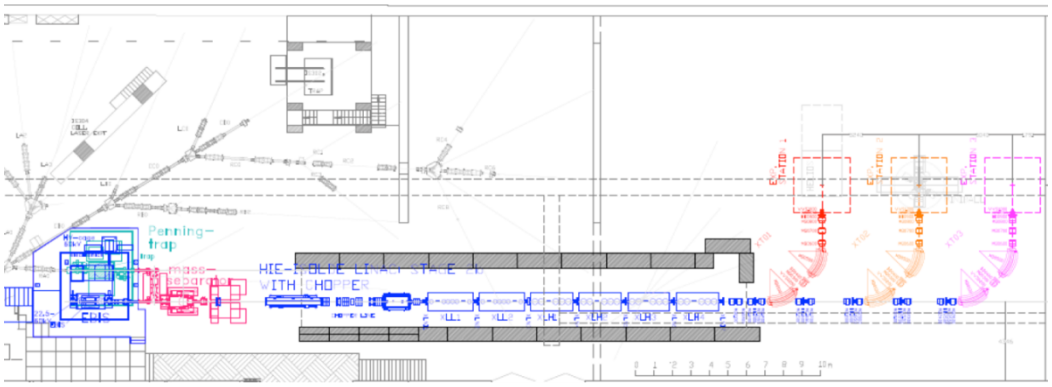

In addition, several penetrations in the bulk shielding are needed to integrate the required services to the post-accelerator, such as high voltage, RF, He supply and exhaust. In order to comply with these constraints, the shielding was designed in close collaboration with the team in charge of civil engineering.

The main challenge for the specification of the shielding was the definition of the source term. The bremsstrahlung X-rays come from electrons removed from the defects of the cavity, which are accelerated and hit the cavity surface during RF operation. Since this emission depends on the surface state of the cavity, no theoretical and systematic source term can be derived and direct measurements are required to determine the X-ray intensity emitted by the cavities.

Source term evaluation: X-ray measurements and FLUKA simulations

X-ray dose rates have been measured on contact with the cryostat during RF tests on several prototype cavities, using a 30 cm^3-ionisation chamber placed at the height of the beam pipe. The Monte Carlo code FLUKA [9,10] was then used to perform simulations of the cavity test bench, allowing the determination of the rate at which electrons are removed from the cavity surface.

There are three different modes of operation for RF cavities. The first one is quality factor measurement, corresponding to normal operation of the accelerator. The second is “normal” conditioning, preliminary step to normal operation, which consists of the excitation of the cavity by a strong RF power to overcome the multipactor barrier. The last mode of operation, called He processing, is a specific conditioning where He is sent to the cavity and transformed into plasma after excitation by a strong RF power [12]. This procedure allows emission sites to be cleaned and removed, but involves the emission of a large amount of X-rays. The maximum dose rates measured during RF tests for these three modes of operation are presented in Table 2. The maximum dose rate was measured during He processing and reached 350 mGy/h. Weighting factors for electrons and X rays being wR=1, a source term of 350 mSv/h was used for shielding calculations.

Table 2. Maximum dose rates measured on contact with the cryostat contact at the beam pipe level [11]

Beams	Normal operation	Standard conditioning	Conditioning by He processing
Maximum dose rate measured at cryostat contact (mGy/h)	20	20	350

In order to evaluate the electron removal rate, dose rates around the cryostat were simulated with FLUKA. Considering the maximum RF field strength and the length of the cavitiy, the maximum energy that a parasitic electron can reach in a HIE-ISOLDE cavity is 900 keV. In order to be conservative, it was considered that all the electrons reach an energy of 900 keV. Using the measured dose rate level of 350 mSv/h at the position of the ionisation chamber, the electron emission rate could be derived. This intensity for one cavity, 1.5e14 e-/s, was later used to normalise FLUKA simulations of the post-accelerator (see Radiation Protection study, X dose rates). The results of the simulation for the test area cryostat with a single cavity are presented in Figure 3.

Figure 3. Simulation of dose rate distribution around the cryostat during RF tests

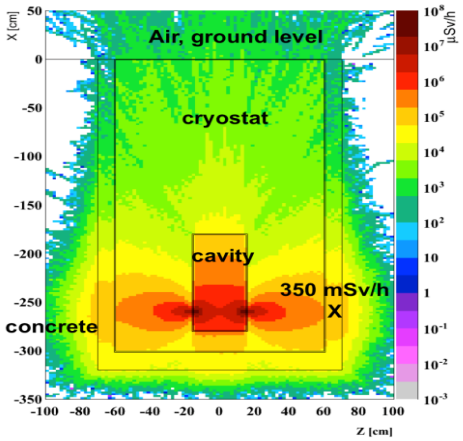

Radiation protection study

As a first step, the bulk shielding was determined using the measured dose rate levels and the attenuation coefficient for 900 keV photons. Then, FLUKA simulations were performed to validate the shielding thicknesses and identify possible weak points considering the different openings and chicanes required for services (RF, HV, He supply, etc.) integration. The dose rate levels in the vicinity of the beam line due to the ion beam interaction were also evaluated. Finally, residual dose rates and material activation were also estimated with consideration of the very short cooling time after operation.

Shielding thickness evaluation

The shielding thickness was first determined analytically, using Equation (1):

$$x = \frac{\ln(H_0/H^*(10))}{\ln 10} x_{1/10} \qquad (1)$$

where H_0 is the equivalent dose rate before attenuation, $H^*(10)$ the equivalent dose rate after attenuation and $x_{1/10}$ the tenth-value layer for a given material in cm^{-1}. The source term H_0 was evaluated to 350 mSv/h and the target design value was fixed to $H^*(10) = 1$ µSv/h for X-rays. The equivalent thicknesses obtained for different shielding materials are given in Table 3.

Table 3. Equivalent shielding thicknesses for different materials

Beams	Concrete	Iron	Lead
Thickness (cm)	80.5	26.8	13.4

FLUKA simulations

The HIE-ISOLDE post-accelerator geometry was implemented in FLUKA as 6 stainless-steel cryomodules containing each 5 low-beta or 6 high-beta cupper cavities. Shielding geometry has been defined in close collaboration with the team in charge of service integration. The bulk shielding is 80 cm concrete. Chicanes have been implemented on the concrete roof for RF cables, as well as in iron chimneys to reduce the dose rates expected on the top of the shielding. However, some cables cannot be bent and some vertical penetrations go straight through the shielding. A general view of the shielded enclosure is presented in Figure 4.

Figure 4. Shielding geometry of the future HIE-ISOLDE post-accelerator

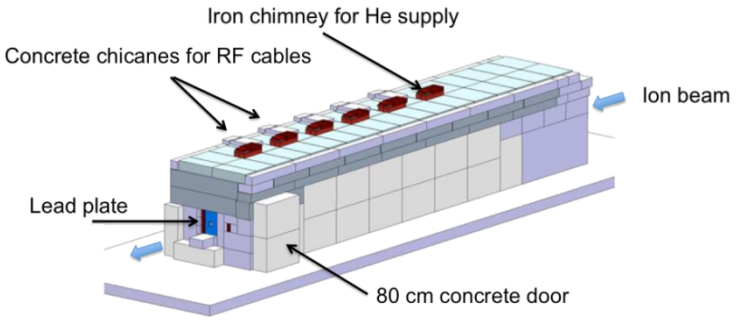

X-ray dose rates

For X-ray dose rates calculations, 32 electron emission sites distributed in each cavity with the maximum possible energy (600 keV for low-beta cavities and 900 keV for high-beta cavities) were used as primary particles (see Figure 5). The electron emission rate considered was deduced from measurements and simulations of the test cryostat (see Source term evaluation) considering the He processing phase, which is our worst-case scenario. While the 32 cavities are considered in this study, in practice only a single cryomodule (6 cavities maximum) should be conditioned at the same time. Moreover, this operation will take place only once a year for a few days. During normal operation or normal conditioning, dose rates are expected to be at least 10 times lower.

Inside the tunnel, dose rates can reach up to 300 mSv/h between two cryomodules and 30 mSv/h on top of a cryomodule during He processing of the whole post-accelerator. Outside the bulk shielding (accessible areas), the target design value of 1 µSv/h is achieved (see Figure 5, right). Due to the many penetrations on the roof of the shielding, dose rates out of chimneys reach up to 300 µSv/h (see Figure 5, left). As a consequence, access to the roof will be forbidden during RF operation, unless acceptable dose rates are measured during operation.

Figure 5. Dose rate distribution around the post-accelerator during He processing; (left) horizontal cut at beam height; (right) vertical cut at beam position

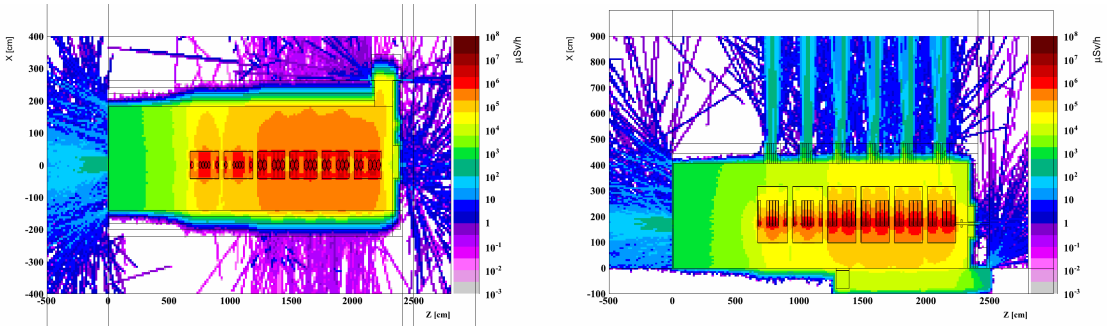

Neutron dose rates from ion beam losses

To estimate neutron dose rates expected in the event of ion beam losses due to beam intercepting devices, FLUKA simulations were performed for the most constraining case of stable beams during machine settings. Both losses in a beam dump and losses at a grazing angle in a magnet vacuum chamber were considered, but only the first study is presented here, as the results obtained were similar.

Dose rate distribution around a Cu dump irradiated by a-11.3-MeV Ne^{5+} beam with an intensity of 4 ppA is presented in Figure 6 (left). At 1 m and 90 degrees from the beam dump, dose rate is a few µSv/h. The case of He at 19.8 MeV/u presented in Figure 6 (right) is a very specific case and will be authorised with additional mitigation measures. For beam settings with intensity leading to dose rates higher than few µSv/h at 1 m and 90 degrees of a beam intercepting devices, small exclusion areas will be implemented around the beam loss point during the duration of the tuning period.

Figure 6. Dose rate distribution for a 11.3 MeV Ne beam impinging on a copper dump (left) and dose rate profiles at 1 m and 90 degrees for 1 ppA ion beams (right) in the event of a total ion beam loss

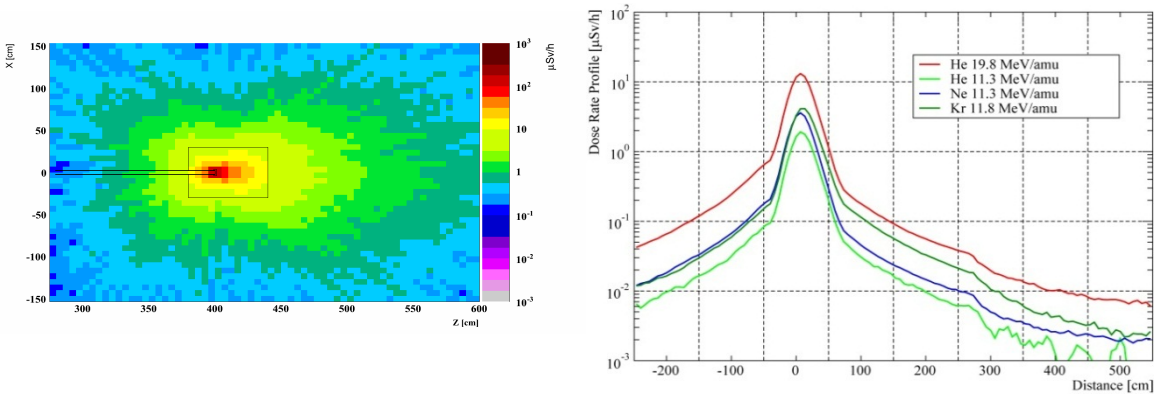

Residual dose rates

Residual dose rates due to ion beam losses have been estimated around a Cu beam dump and a magnet after different of cooling times at the end of the use period of the post-accelerator. As shown in Figure 7, residual dose rate distribution after 1s cooling time around the beam dump is already well below 1 µSv/h at 40 cm from the dump.

Figure 7. Residual dose rate around a beam dump after one-second cooling time

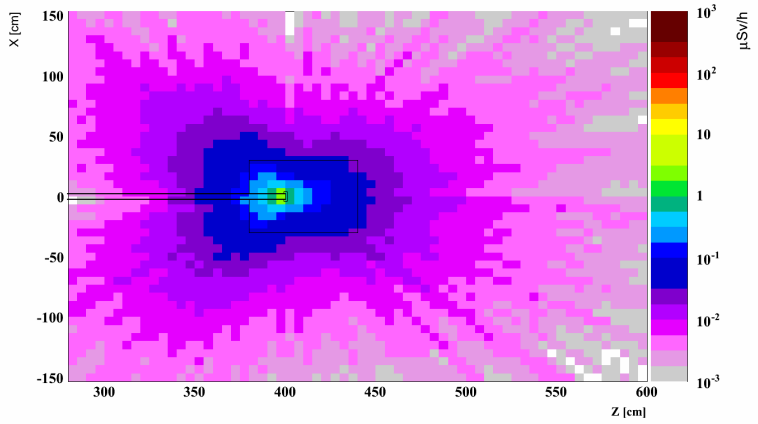

Material activation and radioactive waste

The radionuclide inventory has been calculated after 30 years of operation and one year of cooling time for a Cu beam dump and a magnet, considering a total beam loss during the whole period. The case of a loss occurring in a dipole magnet is presented here. The magnet coil is made of copper cooled with demineralised water and the yoke of iron. The activities after one year of cooling time of the radionuclides produced in copper and iron are shown in Table 4 and compared with the exemption limits used at CERN for the design of new facilities [13]. The design limits are conservative as compared to the ones specified in the corresponding Swiss legislation [14]. As a mixture of radionuclides is present in material activated during accelerator operation, the following sum rule [12] [13]:

$$\sum_{i=1}^{n} A_i/LE_i < 1$$

applies (with A_i the activities of the radionuclides of artificial origin and LE_i the corresponding exemption limits). Following the sum rule, materials containing a specific radionuclide activity of artificial origin smaller than one are exempted from further regulatory control. This is the case for irradiated materials at HIE-ISOLDE, as presented in Table 4. In addition, it was also concluded that no radionuclides produced in circulating cooling water or water activation are expected in HIE-ISOLDE magnets. The same conclusion was drawn for the beam dump study. As a consequence, activation of beam line components during beam tuning period or physics is considered negligible and the waste characterisation after the facility decommissioning will depend on the implantation of RIBs in the concerned equipment.

Table 4. Dipole activation after 30 years of operation and one-year cooling time

Material	Nuclide	$T_{1/2}$	LE_i (Bq)	A_i (Bq)	A_i / LE_i	$\sum_{i=1}^{n} \frac{A_i}{LE_i}$
Copper	^{63}Ni	100.1 y	7E+04	1.9E+01 ± 1.35%	2.7E-04	1.19E-01
	^{60}Co	5.3 y	1E+02	1.1E+01 ± 3.58%	1.1E-01	
	^{3}H	12.3 y	1E+05	5.0E-01 ± 13.71%	5.0E-06	
Iron	^{55}Fe	2.7 y	3E+04	7.9E+01 ± 1.24%	2.6E-03	1.30E-01
	^{54}Mn	312.5 d	1E+02	1.3E+01 ± 2.14%	1.3E-01	

Conclusion

The first step of the HIE-ISOLDE, which corresponds to the energy increase of the post-accelerated beam delivered by the ISOLDE Facility at CERN, is underway and will allow new opportunities for nuclear physics experiments. However, the energy upgrade, allowing beams to be accelerated above the Coulomb barrier and consisting of the replacement of the REX post-accelerator by a superconducting linac, involves new radiological hazards such as neutron and X-ray emission.

After the identification of X-rays as the main radiological hazards of the future post-accelerator by comparison with similar facilities, a radiation source term of 350 mSv/h at 1.4e14 pps (electron) was derived from measurements and FLUKA simulations. Then, FLUKA simulations validated shielding thickness and design by considering the worst-case scenario for radiation emissions (maximum electron energy, He conditioning of all cavities at the same time). In that configuration, no access will be authorised on the roof of the shielding during RF operation. The concrete shielding blocks have already been installed in the HIE-ISOLDE experimental hall.

In the event of energy loss during machine tuning with stable ion beams, dose rates could locally reach values above the limit. Small exclusion limits around the beam intercepting devices should be installed during that short period of time.

No specific measures concerning residual dose rates due to beam induced activation are necessary, as the expected dose rates 1s after cooling are already at background levels due to the low beam intensity. Activation of material after 30 years of operation should be negligible 1 year after cooling time, and no water or air activation is expected.

Acknowledgements

A Marie Curie Early Training Network Fellowship of the European Community's Seventh Programme under contract number PITN-GA-2010-264330-CATHI has supported this research project. Thanks are due to the HIE-ISOLDE collaboration at CERN and external partners such as TRIUMF and INFN Legnaro for supporting this study.

References

[1] A. Herlert (2010), "The ISOLDE Facility", *Nuclear Physics News,* Vol. 20, Iss.4

[2] M.A. Fraser et al. (2012), "Status of the HIE-ISOLDE project at CERN", *Proceedings of HIAT 2012,* pp. 175-181.

[3] R. Catherall et al. (2013), "An overview of the HIE-ISOLDE Design Study", *NIM B Vol. 317 Part B*, pp. 204-207.

[4] D. Voulot, "Specification of the sources of radiation and maximum beam intensities and energies at the HIE-ISOLDE linac", HIE-O-FS-0001, CERN EDMS document 1223228, v.5.

[5] N. Jecklin et al. (2013), Niobium Coatings for the HIE-ISOLDE QWR Superconducting Accelerating Cavities, SRF2013, Paris.

[6] L. Moritz (2005), "TRIUMF - ISAC II Safety Report".

[7] G. Fortuna et al. (1990), "The ALPI project at the Laboratori Nazionali di Legnaro", *NIM A,* Vol. 287, Iss. 1-2, pp. 253-256.

[8] INFN Legnaro (2013), private communication.

[9] G. Battistoni et al. (2007), "The FLUKA code: description and benchmarking", *AIP Conference Proceedings*, 896, pp. 31-49.

[10] A. Ferrari et al. (2005), "FLUKA: a multi-particle transport code", *CERN-2005-10*, INFN/TC 05/*11*, SLAC-R-773.

[11] S. Giron, "Results of measurements performed at CERN on HIE-ISOLDE prototypes", CERN EDMS document 1235259.

[12] W. Venturini Delsolaro et al. (2013), Nb Sputtered Quarter Wave Resonators for the HIE-ISOLDE, SRF2013, Paris.

[13] S. Roesler, C. Theis (2009), "Exemption and Clearance of Material at CERN", *Operation Radiation Protection Rule*, CERN EDMS 942170 v.5.

[14] Conseil Fédéral Suisse, (Etat le 1er janvier 2014) "Ordonnance du 22 juin 1994 sur la Radioprotection (ORaP)".

[15] CERN's Director General (2006), "CERN Safety code F".

Radiation safety design of super KEKB factory

Toshiya Sanami
High Energy Accelerator Research Organisation (KEK), Japan

Abstract

The SuperKEKB factory, which was scheduled to start operation early 2015, is an electron-positron collider designed to produce an 80×10^{34}-1/cm^2/s luminosity, which is 40 times greater than the KEKB factory. Built to investigate CP violation and "new physics" beyond the Standard Model, the facility consists of a 7-GeV electron/3.5-GeV positron linac, a 1.1-GeV positron damping ring, beam transport, and a 7-GeV electron/4-GeV positron collider. To meet this level of luminosity, the collider will be operated with a small beam size and a large crossing angle at the interaction point. According to particle tracking simulations, beam losses under these conditions will be 35 times more than those previously operated. To help optimise shielding configurations, leakage radiation and induced activity are estimated through empirical equations and detailed Monte-Carlo simulations using MARS15 code for the interaction region, beam halo collimators, emergency pathways, ducts, forward direction tunnels, and positron production target. Examples of shielding strategies are presented to reduce both leakage dose and airborne activity for several locations in the facility.

Introduction

The SuperKEKB factory – an electron-positron collider – is designed to produce a luminosity of 80×10^{34} 1/cm^2/s, 40 times greater than its predecessor, the KEKB factory. Built to investigate CP violation and "new physics" beyond the Standard Model [1], the facility consists of a 7-GeV electron/3.5-GeV positron linac, a 1.1-GeV positron damping ring, beam transport, and a 7-GeV electron/4-GeV positron collider. To attain this luminosity, the collider will operate with a small beam size and a large crossing angle at the interaction point. According to particle tracking simulations, beam losses under these conditions will be 35 times more than those previously given. Leakage radiation and induced activity are estimated through empirical equations and detailed Monte-Carlo simulations using MARS15 for the interaction region, beam halo collimators, emergency pathways, ducts, forward direction tunnels and positron production target, to aid shield design optimisation.

This paper describes examples of shielding strategies used to reduce both leakage dose and concentration of airborne activity around several parts of the facility.

Figure 1. Schematic drawing of the super KEKB factory

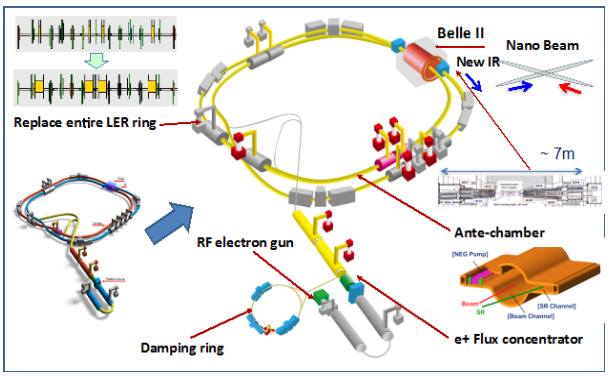

Design specifications

Figure 1 shows a schematic of the SuperKEKB factory, together with a device upgrade plan. The SuperKEKB factory uses a 3-km-long circular tunnel, at a depth of 10 m underground. The ring has four straight and four curved sections. Three of the straight sections have RF cavities to accelerate the electrons and positrons; the fourth is designated as the interaction region (IR) where particle collisions take place.

To achieve higher luminosity, various hardware devices were replaced, including the electron gun, the flux concentrator to enhance positron production, the 3-km-long beam chamber, and the magnets of the low energy ring (LER) for positrons, and an upgrade in IR design and for the detector (Belle2). A damping ring was newly installed to improve the positron beam emittance.

Table 1 lists the design specifications for the SuperKEKB factory along with those of the previous KEKB factory for comparison. SuperKEKB commissioning will proceed in three stages, named phases 1–3. Phase-1 operations will start in 2015 with vacuum scrubbing and injection beam tuning. On completion of phase 1, phase 2 will start with collision tuning, the Belle2 detector with operations, anticipated to begin within 5 months. Phase 3 operations will then start with a physics run. The target luminosity in phase 3 is 80×10^{34} 1/cm^2/s, which is 80 times greater than the design value for the KEKB factory.

Table 2 summarises beam loss estimations obtained from particle tracking simulations. Beam losses are caused by three processes, namely beam-gas interaction, radiative-Bhabha, and Touschek. Beam-gas interaction occurs between the remaining gas molecules and circulating beam particles. It is roughly proportional to the beam current and the level of vacuum. Beam loss from radiative-Bhabha originates from energy losses from electron-positron interactions at the interaction point; the amount is proportional to luminosity.

Beam loss from Touschek stems from scattering within the bunches of the beam, and is related to beam size. From KEKB to SuperKEKB, all three losses will increase because of the increases in the beam current and luminosity, and the decreased beam size.

Table 1. Design specifications for the KEKB and SuperKEKB

	KEKB	SuperKEKB phase1	SuperKEKB phase1	SuperKEKB phase2
Beam energy and current	LER 3.5 GeV/2.9 A HER 8 GeV/1.2 A	LER 4 GeV/1 A HER 7 GeV/1 A	LER 4 GeV/1.8 A HER 7 GeV/1.3 A	LER 4 GeV/3.6 A HER 7 GeV/2.6 A
Target luminosity	$1x10^{34}$	0	$1x10^{34}$	$80x10^{34}$
Duration	11 years from 1998	5 months from 2015	5 months after 9-month shut-down (Belle2 install)	After 3-month shut-down (VXD install)
Operation mode	Physics run	Injection tuning Vacuum scrubbing without Belle2	Collision tuning with limited number of cavities, without VXD	Physics run

As shown in Table 2, beam loss increases step-by-step with increasing beam current and luminosity. In phase 3, the total number of particles lost from the beam is over 30 times greater than for KEKB. Finally, the total beam loss power rises to nearly 500 W. Secondary radiation should be shielded properly to mitigate radiation leakage and lower the concentration of airborne activity.

Table 2. Beam losses at KEKB and SuperKEKB

unit [10^9 pps]	Beam life				Injection and abort	Total
LER HER	Ring uniform (Beam gas)	Arc uniform (Touschek)	Collimator local	IR RBB		
KEKB	0.53 0.01	0.98 0.65	5.44 0.71	1.43 1.44	15.2 6.12	24 9
Super KEKB Phase1	4.36 0.937	0 0	0 0	0 0	4.68 3.86	9 5
Super KEKB Phase2	16.95 0.67	31.25 31.30	233.5 80.0	1.13 0.83	69.1 24.9	351 138
Super KEKB Phase3	33.90 1.33	62.5 62.6	467.0 160.0	90.4 66.2	138 49.8	792 340

Airborne activity and leakage dose using empirical equations

From the beam loss estimations listed in Table 2, induced air activity and leakage dose were deduced using empirical equations. Our goal in shielding design was for less than 20 μSv/h for controlled areas, 1.5 μSv/h for the supervised areas, and 0.2 μSv/h for general areas. Concentrations of airborne activity should be less than the limits for release air that are determined according to chemical composition.

For estimation of airborne activities, Swanson's specific activity was used with a 2-m average path length of above 20 MeV photon in air. Beam losses at dumps were not taken into account for this estimation because electron/positron powers are fully absorbed within them. Sixteen air condition units (two units for each section) were assumed for this estimation. Table 3 lists typical results for the ratio of the estimated concentration of

airborne activity to the release limit, DAQpa, for air conditioning units in the curved and straight sections, and IR. The concentration of airborne activity was obtained using the saturated activity for ^{3}H, ^{7}Be, ^{11}C, ^{13}N, ^{15}O, ^{41}Ar [2] and their limits. The table contains the ratios for when the collimators are totally shielded (shown in the last row, "Phase3 WO col."). The values are useful in revealing how much reduction there is when shielding against radiation leakage is placed around the collimators.

As shown in the results, releasing air from the curved sections is difficult even with the collimators perfectly shielded. Such releases are only possible in the straight sections. To achieve this scenario, we need to consider collimator shielding.

For the IR, the concentration of airborne activity can exceed the release limit because of the large beam loss from radiative-Bhabha.

Table 3. Ratio of the estimated concentration of airborne activity to the release limit (DAQpa)

	Arc	Straight	IR
KEKB	0.56	0.02	0.07
Phase1	0.05	0.02	0.02
Phase2	8.43	0.51	1.10
Phase3	16.83	1.17	8.96
Phase3 WO col.	1.89	0.44	7.20

Table 4. Estimated dose rates on the floor of the IR experimental hall

	L side	R side
KEKB	0.12 μSv/h	0.17 μSv/h
Phase1	0.01 μSv/h	0.05 μSv/h
Phase2	0.15 μSv/h	0.64 μSv/h
Phase3	9.37 μSv/h	40.3 μSv/h

Leakage dose was estimated using Jenkins formula for the bulk shielding wall [3]. Mao's equation [4] with transfer rate obtained by a Monte Carlo *N*-particle calculation [5] was used for the duct-streaming problem. The skyshine radiation dose at the site boundary was estimated using the Thomas equation [6].

Table 4 summarises estimated dose rates on the floor of the IR experimental hall for both sides of the detector. As many users would like to access the hall during beam operations, the dose rate must be below the supervised-area limit of 1.5 μSv/h. According to beam loss scenarios, radiative-Bhabha beam loss is a contributing factor to dose rates. Additional shielding should be placed to mitigate the dose rate increase.

Detailed Monte-Carlo simulations

As shown in previous sections, additional shielding should be considered against beam losses from the collimators and the IR hall. For this purpose, three-dimensional Monte-Carlo simulations were performed using MARS15 code [7,8]. An extended geometry description, GEOM.INP, was used to configure the IR hall, tunnel, detector, and beam line devices such as chamber, magnet, and collimator.

Figure 2 shows the plan view of the beam line model in IR hall for simulations. The straight section including the IR hall has nine collimator losses and one radiative-Bhabha loss. To simulate the collimator losses, their structure and material, i.e. a 5-mm Ta tip head supported by a copper block, were modelled. For radiative-Bhabha losses, energy and particle counts from beam loss obtained from tracking simulations were embedded in a user routine of the MARS code. The electron and positron beams were injected with a 1-mrad grazing angle onto the collimator tip and inner surface of the beam pipe. Beam chamber, dipole and quadrupole magnets were modelled and placed to consider their effect.

Separated runs for each collimator and radiative-Bhabha beam losses were performed to identify the largest contribution of beam loss to the IR hall. The results showed that radiative-Bhabha in the positron ring gives the largest contribution.

Figure 2. Beam line, detector and the IR hall model for simulation

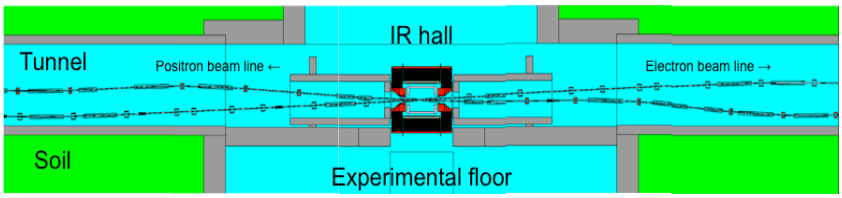

Figure 3 shows the plan view of the IR hall and the calculation result of dose rates under the original condition. Three leakage paths inducing airborne radioactivity and dose rate increases in the IR hall floor were identified: (1) un-shielded radiation along the beam duct, (2) directly through the machine-detector interface, and (3) indirectly through the gap between the tunnel and the IR hall. Four supplemental shields/modifications were designed to suppress dose rates and airborne activity on the IR hall floor; these are: (1) Lead cover surrounding the beam chamber to stop photons; (2) extended wall to completely cover the machine-detector interface part; (3) concrete and polyethylene caps to close small gaps around the detector; and (4) extended wall to cover the gap between the tunnel and the IR hall. Figure 4 shows the plan view of the IR hall and the calculation result of dose rate with the updated geometry. Dose rates on the IR hall floor were reduced to less than 1 μSv/h, which would allow access to supervised areas.

In addition, to mitigate skyshine doses at the site boundary, additional 45-cm-thick concrete on top of the concrete shields covered the beam lines.

For collimator loss, the same methodology was followed to reduce airborne activity. Figure 5 shows the plan view for simulations of the beam-line model including a collimator. The collimator, beam pipes, and magnets were modelled to describe the spread of secondary radiation in downstream air. The total length of the beam line was 40 m.

Figure 3. Plan view of the IR hall (left) and the calculation result of dose rate (right) with original condition

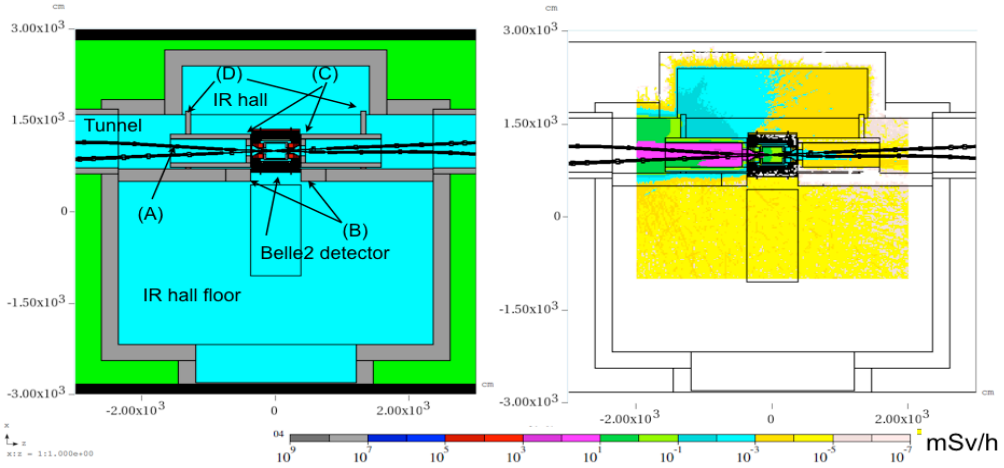

Figure 4. Plan view of the IR hall (left) and the calculation result of dose rate (right) with updated condition

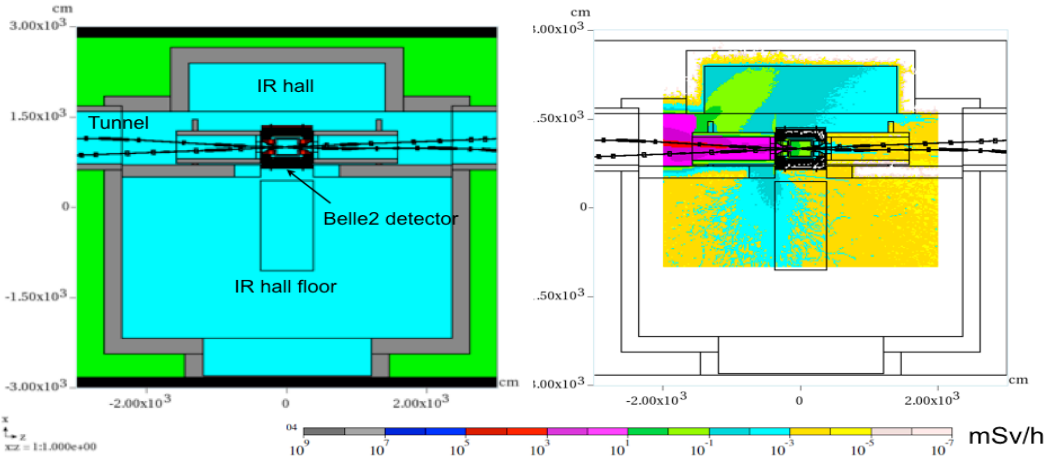

The electron and positron beams were injected onto the collimator tip with 1-mrad grazing angle. All radiation produced was transported down to 20 MeV, which is close to the reaction threshold for airborne activity generation, except for ^{41}Ar.

Figure 6 shows calculation results for a photon flux of energies above 20 MeV for the original design (upper panel) and with supplemental shield (lower panel) composed of 5-cm lead around the beam line. From the upper panel, a significant photon passes through the air. In contrast, a reduction of order greater than two in magnitude is seen in the result with lead (lower panel). Further work is required to optimise the lead block thickness and length covered ahead of beam-line maintenance work.

Figure 5. Beam line model of collimator for simulation

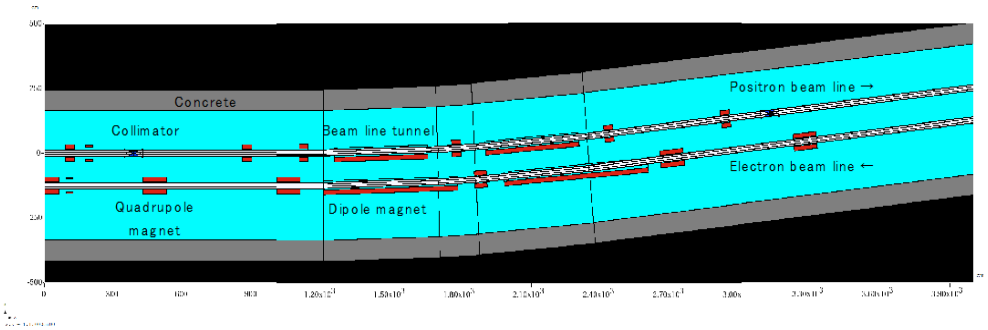

Figure 6. Photon flux above 20 MeV for original configuration and with 5 cm lead

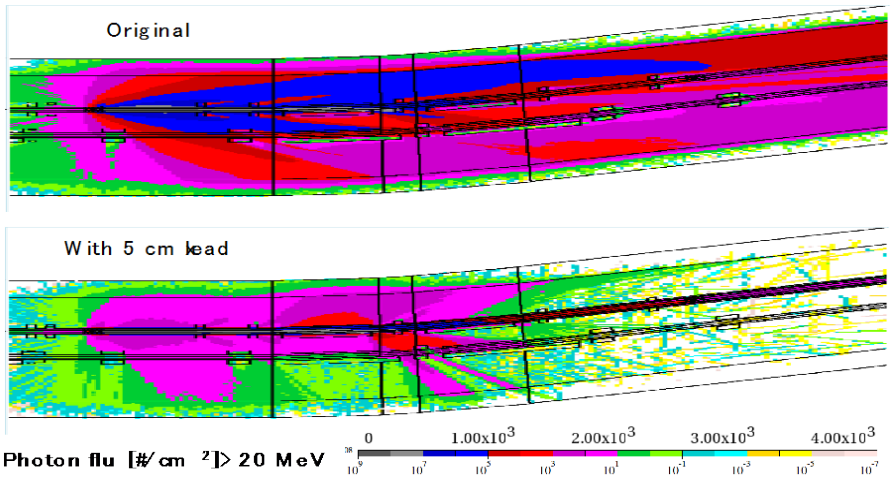

Conclusion

Following beam loss scenarios calculated from beam tracking simulations, various radiation safety designs at the SuperKEKB factory are being developed. Bulk shield thickness and concentrations of airborne activity were estimated along the entire ring and in the IR hall. To design supplemental shielding, several locations in accessible areas, which could exceed legal limits in regard to airborne activity and dose rate, were modelled in a detailed Monte Carlo study. The supplemental shields reduced both activity and dose, however, further work is required to optimise their configurations.

References

[1] Y. Ohnishi et al. (2013), "Accelerator design at SuperKEKB", *Prog. Theor. Exp. Phys.* 03A011.

[2] W.P.Swanson (1979), "Radiological safety aspects of the operation of electron linear accelerators", IAEA technical reports series No.188.

[3] T.M.Jenkins (1979), Nucl.Instrm.Meth. 159, 265.

[4] X. Mao, K. Kase, W.R.Nelson (1996), Health Phys. 70, 207.

[5] MCNP-A general Monte-Carlo N-Particle Transport Code Version 4A (1993), J.F.Briesmeister Ed., LA-12625-M Manual.

[6] N.V. Mokhov (2003), “Status of MARS Code”, Fermilab-Conf-03/053.

[7] N.V. Mokhov, K.K. Gudima, C.C. James, et al. (2004), “Recent Enhancements to the MARS15 Code”, Fermilab-Conf-04/053; http://www-ap.fnal.gov/MARS/.

Section IV: Medical Accelerators

Chair: Vladimir Mares

Neutron therapy in the 21st century

Thomas K. Kroc[1], James S Welsh[2]
[1]Fermi National Accelerator Laboratory, Batavia, Il, US
[2]Northern Illinois University, DeKalb, Il, US

Abstract

The question of whether or not neutron therapy works has been answered. It is a qualified yes, as is the case with all of radiation therapy. But, neutron therapy has not kept pace with the rest of radiation therapy in terms of beam delivery techniques. Modern photon and proton based external beam radiotherapy routinely implements image-guidance, beam intensity-modulation and 3-dimensional treatment planning. The current iteration of fast neutron radiotherapy does not. Addressing these deficiencies, however, is not a matter of technology or understanding, but resources.

The future of neutron therapy lies in better understanding the interaction processes of radiation with living tissue. A combination of radiobiology and computer simulations is required in order to optimise the use of neutron therapy. The questions that need to be answered are: Can we connect the macroscopic with the microscopic? What is the optimum energy? What is the optimum energy spectrum? Can we map the sensitivity of the various tissues of the human body and use that knowledge to our advantage? And once we gain a better understanding of the above radiobiological issues will we be able to capitalise on this understanding by precisely and accurately delivering fast neutrons in a manner comparable to what is now possible with photons and protons?

This presentation will review the accomplishments to date. It will then lay out the questions that need to be answered for neutron therapy to truly be a 21st century therapy.

Introduction

Fermilab's first director, Robert Wilson, first proposed hadron therapy in 1946 [1]. Fast neutron therapy began in the United States through a series of grants in the early 1970s from the National Cancer Institute to approximately eight facilities around the country [2]. In most cases, each facility was an add-on to an existing physics laboratory and used the beam and beam energy peculiar to that facility. Interest in offering neutron therapy at Fermilab grew out of a presentation by Louis Rosen, of the Los Alamos Scientific Laboratory, at the 1971 Particle Accelerator Conference and subsequent discussions among Chicago area physicians and physicists [3].

After Rosen's talk, local physicians and physicists began discussions to start hadron therapy in the Chicago area. Prof. Lester Skaggs of the University of Chicago and the Argonne Cancer Hospital organised these discussions looking into protons, ions, and pions. It is unclear what caused the shift from these particles to neutrons, but on 7 September 1976, the first patient was treated at the Cancer Therapy Facility, later named the Neutron Therapy Facility (NTF), at Fermilab with neutrons.

Why neutrons?

The primary reason supporting the use of neutrons for therapy is their relative biological effectiveness (RBE). For the neutron energies supplied by the NTF beam, 1/3 less dose is required to achieve the same clinical effect with neutrons as is required with conventional photons. However, this is not the complete story as there is probably no clinical advantage to using such a beam if the final outcome were exactly the same as with photons. Certain tumours are classified as being radioresistant. They respond very poorly to conventional photon therapy. In these cases, neutrons are more effective, beyond just the factor of three in RBE (see Table 1) [4]. A partial explanation is that conventional radiation therapy relies on the creation of oxygen free radicals to provide the lethal effect. Radioresistant tumours tend to be hypoxic which inhibits the creation of radicals. Neutrons on the other hand do not rely on radicals and therefore are less dependent on the oxygenation of the tumour. But even this does not completely explain a neutron's RBE. Other mechanisms are at underway that are not completely understood.

In addition to fast neutron therapy, a new opportunity is appearing, neutron capture therapy (NCT). This is a binary therapy where a neutron absorbing agent is attached to a drug that is preferentially taken up by tumour cells. When exposed to neutron radiation, the agent absorbs a neutron and undergoes a radioactive decay. The energetic by-products of the decay provide a localised boost of dose to the tumour area in addition to the dose from the neutron radiation itself. The two agents presently being investigated are boron-10 (BNCT) and two isotopes of gadolinium, 155 and 157, (GdNCT).

Table 1. Review of the loco-regional rates for malignant salivary gland tumours treated with radiation therapy

Fast Neutrons			
Authors	Number of Patients	Loco-regional control (%)	
Saroja *et al.* (1987)	113	71	(63%)
Catterall and Errington (1987)	65	50	(77%)
Battermann and Mijnheer (1986)	32	21	(66%)
Griffin *et al.* (1988)	32	26	(81%)
Duncan *et al.* (1987)	22	12	(55%)
Tsunemoto *et al.* (1989)	21	13	(62%)
Maor *et al.* (1981)	9	6	(67%)
Ornitz *et al.* (1979)	8	3	(38%)
Eichhorn (1981)	5	3	(60%)
Skolyszewski (1982)	3	2	(67%)
Overall	310	207	(67%)

Low-LET Radiotherapy Photon and/or Electron beams and/or Radioactive Implants			
Authors	Number of Patients	Loco-regional control (%)	
Fitzpatrick and Theriault (1986)	50	6	(12%)
Vikramet *et al.* (1984)	49	2	(4%)
Borthne et al. (1986)	35	8	(23%)
Rafla (1977)	25	9	(36%)
Fu *et al.* (1977)	19	6	(32%)
Stewart *et al.* (1968)	19	9	(47%)
Dobrowsky *et al.* (1986)	17	7	(41%)
Shidnia *et al.* (1980)	16	6	(38%)
Elkon *et al.* (1978)	13	2	(15%)
Rossman (1975)	11	6	(54%)
Overall	254	61	(24%)

Table 3 from IAEA-TECDOC-992, "Nuclear data for neutron therapy: Status and future needs", December 1997, p.12.

The Fermilab set-up

At Fermilab, the neutron beam is produced by bombarding a beryllium target with protons. The Neutron Therapy Facility is located at approximately a third of the length of the proton linac used as the injector for Fermilab's High Energy Physics programme. As the linac pulses at 15 Hz, a fast 58° dipole magnet can divert linac pulses into the NTF beam line. A second 32° dipole magnet completes the 90° bend. Quadrupole magnets maintain the focus of the beam in the 12 foot long beam line and direct the beam onto the target. At the point where the beam is diverted from the linac, the proton energy is 66 MeV. The beryllium target is 49 MeV thick or 2.21 cm and is 2.5 cm in diameter (see Figure 1). It is backed by 0.05 cm of gold and placed in an aluminium holder which is

0.32 cm thick in the beam direction. The latter two elements ensure that all the protons have ranged out so that only photons and neutrons escape the target.

A primary collimator of steel with a conical opening of 7.5° is immediately downstream of the target assembly. This followed by a transmission chamber which is used to monitor the flux of neutrons generated. The neutrons then enter the therapeutic collimator assembly. This contains interchangeable collimators of either a concrete/polyethylene matrix or polyurethane that have various rectangular openings. The proper choice of one of these collimators determines the size of the field to be used for treatment. These collimators are 78 cm long. To better conform the outline of the neutron field to the shape of the tumour to be treated, blocks, 20 cm long, made from low carbon steel are placed in the opening of the collimator.

Figure 1. NTF target and collimation

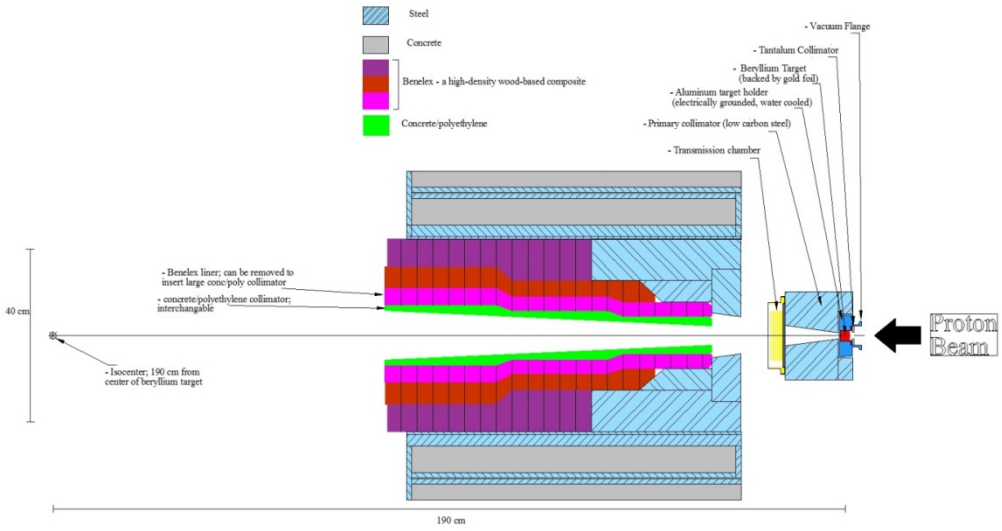

While the beam is fixed in the horizontal plane, treatment is able to be delivered in an isocentric manner by moving the patient. The patient either stands or sits on an immobilisation platform that rotates in front of the beam opening. The platform can translate along, and transversely to, the beam axis allowing the placement of the tumour above the centre of rotation of the platform. This allows the tumour to be irradiated from multiple angles throughout the treatment while remaining fixed at the isocentric distance of 190 cm.

A matter of scale

While trying to understand how neutrons, and all radiation for that matter, truly interact to cause their damage, one is faced with the drastic range of distance scale involved. This is apparent in both conducting physical measurements and in simulations. Macroscopic measurements, with distance scales of centimetres or millimetres are easily achievable in both cases.

The conventional wisdom is that linear energy transfer (LET), in the context of double-strand breaks in the DNA, is the key to understanding the killing power of neutrons. This wisdom, in effect, assumes that LET is a linear value that can somehow be varied over orders of magnitude with an optimum value at 100 keV/µm. This value of LET happens to match well with the distance scale of the double helix of DNA. Despite a criticism that will be mentioned shortly, this means that we need to understand the interactions of fast neutrons and matter on a distance scale of a few nanometres. This is

in contrast with the distance scale of BNCT where the range of fission products of the boron atom is 7.3 µm and 4 µm for the alpha and lithium ions respectively, whereas the range of the Auger electrons from gadolinium decay is again a few nanometres.

The connection to chemistry and biology

It is becoming apparent that simple DNA breakage is not sufficient in understanding the killing power of ionising radiation. A broader understanding of the ways ionising radiation can disrupt cellular processes is needed [5]. We previously mentioned RBE as a factor in determining the need for neutron therapy along with LET and double-strand breaks. However, this understanding, particularly of LET, is not completely adequate for describing the impact of neutrons. Radiobiologist Shirley Lehnert provides this critique of LET: "LET is a simplistic way to describe the quality of different types of radiation since it fails to address the size of the individual energy-loss events that occur along the track of a particle".[1] Understanding "the size of the individual energy-loss events" could very well be the key in understanding the difference between photon, neutron, and light-ion initiated events. Simulations of the radiation/matter interactions on scales comparable to the biological processes involved will be necessary to truly understand and exploit ionizing radiation.

The role of simulations

In this paper we only report on our own efforts in simulating the NTF beam. MCNPX [6] was chosen because of past experience with the style of input format used in operating the code. Very early on we had the benefit of comparing some initial results with GEANT 4 [7,8] and that work served to validate our initial efforts and give us some assurance that we were operating the code correctly (Figure 2).

Figure 2. Comparison of MCNPX and GEANT4 results showing proton energies after passing through beryllium and gold of target assembly

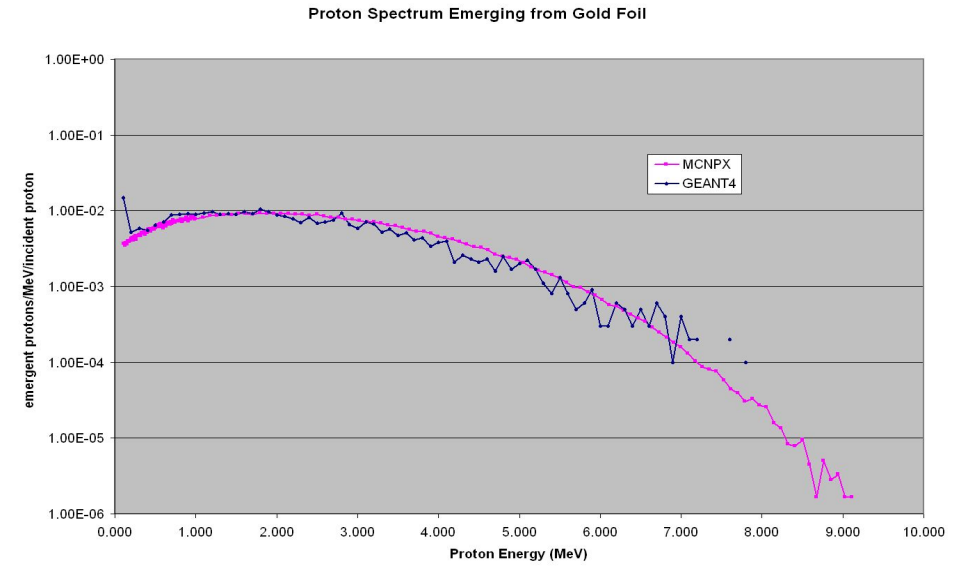

[1] Page 16 of [5].

Our work with MCNPX has been useful in understanding the macroscopic evolution of the neutron energy as it passes through the system. Much of our work has been focused on finding ways to moderate our fast neutron beam so that it is better suited to NCT. We have tried various filtration schemes to try to maximise the production of epithermal neutrons (Figure 3). This figure shows the neutron energy spectrum at the exit of the clinical collimation system (yellow). After exiting the collimator the beam is then simulated to pass through either 10 cm of lead (purple) or 10 cm of tungsten (dark blue). Alternately, the figure shows the results of the neutron passing through alternating 1 cm thicknesses of lead and tungsten, with a total of 5 cm each (cyan). The goal of this work is to generate a neutron spectrum that retains enough penetrating power to reach deep tumours and yet moderate in energy as they pass through tissue so that the energy is low enough for capture once they encounter the enhancing compound in the tumour. However, we are not able to see what happens at scales smaller than a few millimetres.

Figure 3. Simulation of neutron spectra leaving collimator system (input spectra) and after passing through 4 cm of lead and/or tungsten to optimise neutron production in epithermal range

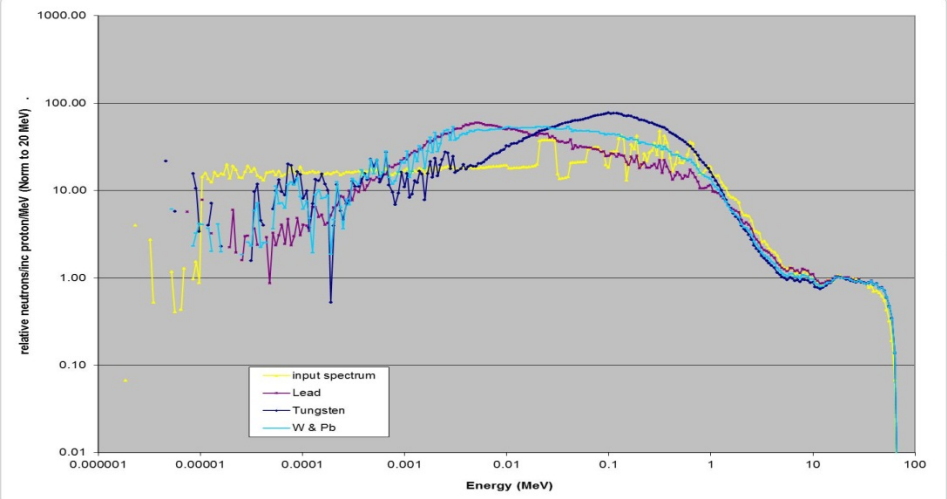

Figure 4. The 1/e attenuation distance of mono-energetic neutrons striking A150 plastic

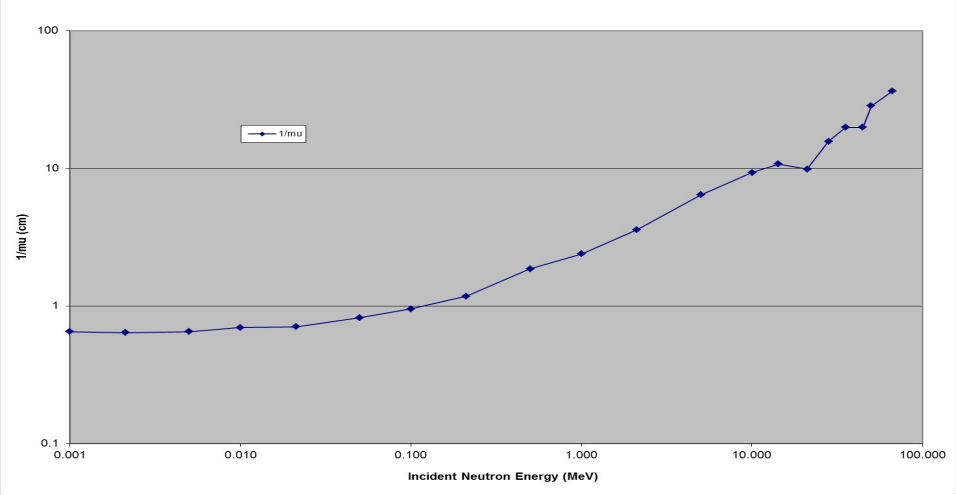

As mentioned above, a challenge in NCT is having enough penetrating power to reach deep tumours. Figure 4 shows the range of neutrons of various initial energies (Figure 4). This shows that neutrons with initial energies below 100 keV cannot contribute to a clinical dose at depth. This has implications for both fast neutron therapy and NCT. For fast neutron therapy, it would be advantageous to remove these neutrons from the incident beam as they only contribute to higher risk for complications. For NCT, it places a limit on the lower edge of the energy spectrum that we hope will moderate, as it penetrates tissue, to near thermal energies by the time they reach the tumour.

Future needs

There are many applications waiting for accurate simulations of the interaction of radiation with matter at the nanometer level. Physics, chemistry and biology can all benefit from this development. The effective treatment of cancer and other diseases need an understanding of the magnitude and type of interactions that occur. Are certain chromosomal structures more or less susceptible to damage? What kind of radiation induces this damage? How do the interactions of the recoil fission products of BNCT interact differently than the dense Auger electron shower of GdNCT? Do fast neutrons produce different secondary ionizing radiation depending on their energy?

Once answered, this knowledge can be entered into optimisation routines for treatment planning systems. Instead of plotting dose deposition, actual killing power can be visualised. Target structures can be enhanced and sensitive tissues can be avoided. Then we will truly have a 21st century therapy.

Acknowledgements

Fermilab is operated by Fermi Research Alliance, LLC under Contract No. De-AC02-07CH11359 with the US Department of Energy.

References

[1] R.R. Wilson (1946), “Radiological use of fast protons”, Radiology, 47(5), pp. 487-491.

[2] S. Zink, J. Antoine, F.J. Mahoney (1989), “Fast neutron therapy clinical trials in the United States”, *American Journal of Clinical Oncology*, 12(4), pp. 277-282.

[3] Consider use of NAL linac, booster for cancer therapy, The Village Crier, 4(1), pp. 1-2.

[4] “Nuclear data for neutron therapy: status and future needs”, IAEA-TECDOC-992, December 1997, p. 12.

[5] S. Lehnert (2008), “Biomolecular action of ionizing radiation”, Taylor & Francis, ISBN 978-0-7503-0824-3.

[6] D.B. Pelowitz (2011), “MCNPX User’s Manual, 2.7.0”, LA-CP-11-00438.

[7] S. Agostinelli et al. (2003), “GEANT4 – a simulation toolkit”, *Nuc. Inst. Meth. In Phys. Res.*, A 506, pp. 250-303.

[8] J. Allison et al. (2006), “GEANT4 developments and applications”, *IEEE Trans. Nuc. Sci.*, 53(1), pp. 270-278.

Session V: Status of Codes and Data Bases

Chair: Alfredo Ferrari

New developments in FLUKA

F. Cerutti[1], R. Engel[2], A. Fedynitch[1], A. Ferrari[1], A. Mairani[3], A. Mereghetti[1], S. Roesler[1], P.R. Sala[4], P. Schoofs[1], G. Smirnov[1], V. Vlachoudis[1]
[1]CERN, European Laboratory for Particle Physics, Switzerland
[2]KIT, Institut für Kernphysik, Karlsruhe Institute of Technology, Germany
[3]Unità di Fisica Medica, Fondazione CNAO, Italy
[4]INFN, Italy

Abstract

The FLUKA Monte Carlo code is extensively used at CERN for all beam-machine interactions, radioprotection calculations and facility design for forthcoming projects. Such needs require the code to be consistently reliable over the entire energy range (from MeV to TeV) for all projectiles (the full suite of elementary particles and heavy ions). Outside CERN, among various applications worldwide, FLUKA serves as a core tool for the HIT and CNAO hadrontherapy facilities in Europe. Medical applications further impose stringent requirements in terms of reliability and predictive power, which demands constant refinement of nuclear models and continuous code improvement. This paper presents the latest developments implemented in FLUKA.

Introduction

FLUKA [1,2] is a general purpose tool for calculations of particle transport and interactions with matter, covering an extensive range of applications spanning from proton and electron accelerator shielding to target design, calorimetry, activation, dosimetry, detector design, accelerator-driven systems, cosmic rays, neutrino physics and radiotherapy. Sixty different particles plus heavy ions can be transported by the code. The energy range covered for hadron-hadron and hadron-nucleus interaction is from threshold up to 10000 TeV, while electromagnetic and μ interactions can be dealt with from 1 keV (100 eV for photons) up to 10000 TeV. Nucleus-nucleus interactions are also supported up to 10000 TeV/n. Neutron transport and interactions below 20 MeV down to thermal energies are treated in the framework of a multi-group approach, with cross-section data sets developed for FLUKA starting from standard evaluated databases (mostly ENDF/B-VII, JENDL and JEFF).

Transport in arbitrarily complex geometries, including magnetic fields, can be accomplished using the FLUKA combinatorial geometry. A suitable voxel geometry module allows modelling properly CT scans or other detailed 3D representations of humans, typically for dosimetry or therapy planning purposes.

The code has the ability to run either in fully analogue mode, or in biased mode exploiting a rich variety of variance reduction techniques.

FLUKA is jointly developed by the European Laboratory for Particle Physics (CERN), and the Italian National Institute for Nuclear Physics (INFN) in the framework of an international collaboration. The approach to hadronic interaction modelling adopted in FLUKA has been described in several papers [3,4]. In short, hadron-nucleon inelastic collisions are described in terms of resonance production and decay up to a few GeV.

At higher energies, a model based on the Dual Parton Model [5] (DPM) takes over. Hadron-nucleus (h – A) interactions as modelled in FLUKA can be schematically described as a sequence of the following steps:

- Glauber-Gribov cascade and its high energy collisions;
- (Generalised)-intranuclear cascade;
- pre-equilibrium emission;
- evaporation/fragmentation/fission and final de-excitation.

Some of the steps can be omitted by design depending on the projectile energy and identity. Nucleus-nucleus collisions are treated by three different models depending on the energy range; details about the nuclear models can be found in [6] and references therein.

The simulation of the electromagnetic cascade in FLUKA is very accurate, including the Landau-Pomeranchuk-Migdal effect and a special treatment of the tip of the bremsstrahlung spectrum. Electron pairs and bremsstrahlung are sampled from the proper double differential energy-angular distributions improving the common practice of using average angles. In a similar way, the three-dimensional shape of the electromagnetic cascades is reproduced in detail by a rigorous sampling of correlated energy and angles in decay, scattering, and multiple Coulomb scattering. Tabulations for pair production, photoelectric and total coherent cross-sections as well as for atomic form factor data are based on the EPDL97 [7] photon cross-section library.

Bremsstrahlung, direct pair production and muon photo-nuclear interactions by muons are modelled according to state-of-the-art theoretical description and have been checked against experimental data.

Transport of charged particles is performed through an original Multiple Coulomb scattering algorithm [8], supplemented by an optional single scattering method.

Multiple scattering, taking into account nuclear form factors, is applied also to heavy ion transport. Up-to-date effective charge parametrisations have been employed, and straggling of ion energy loss is described in “normal” first Born approximation with the inclusion of charge exchange effects.

LHC and future high-energy projects

LHC successfully ran up to 8 TeV cms with record luminosity, providing, as a by-product, plenty of data of relevance for machine protection, shielding, and other applications.

Comparisons with p-p (and Lead-Lead) event generators have shown areas where improvements are required, with the exception of EMD results for Pb-Pb interactions, where predictions are remarkably accurate.

Model improvements are becoming critical, for the new LHC run at 7+7 TeV, where quenching margins will be much lower, for the forthcoming High Luminosity LHC upgrade (HL-LHC), and for the (hypothetical) Future Circular Collider, a 100 km ring hosting a proton-proton (50+50 TeV) collider and an electron-positron (up to 175+175 GeV) one.

Electro Magnetic Dissociation (EMD)

The beam loss and collimation efficiency estimates at the LHC depend directly on predictions of the yields of fragments close in mass and charge to the initial ions. The distribution of magnetic rigidity (about 1%) of the fragments results in their being selectively lost in different places along the machine. One or both colliding nuclei can break-up in the high-intensity electromagnetic fields involved in ultraperipheral collisions without direct overlap of nuclear densities. At relativistic energies the Lorentz

contracted Coulomb fields of colliding nuclei can be represented as swarms of virtual photons. Absorption of equivalent photons by a nucleus leads to its excitation followed by various de-excitation processes via emission of neutrons, protons, mesons and even light nuclear fragments. Such photo-nuclear reactions are given the collective name electromagnetic dissociation of nuclei. FLUKA employs its internal nuclear interaction generator, PEANUT, in order to describe photo-nuclear reactions induced by both real and virtual photons. Electromagnetic dissociation has been implemented in this framework [9]. Comparisons of the results of simulations with data give very satisfactory results. As an example, Figure 1 shows the inclusive single and double neutron emission from 30 GeV/n to √s=2.76 TeV/n. Nuclear fragmentation and electromagnetic dissociation of ions which occur in the LHC collimation system produce fragments close in mass and charge to beam ions. The fragments have similar magnetic rigidity and, therefore, remain close to the beam trajectory in the LHC ring for a long distance from the interaction point. This is primarily true for fragments created in electromagnetic dissociation of beam ions, as shown in Figure 2.

Figure 1. Electromagnetic dissociation and nuclear cross-sections for Pb-Pb collisions as a function of the effective relativistic γ factor

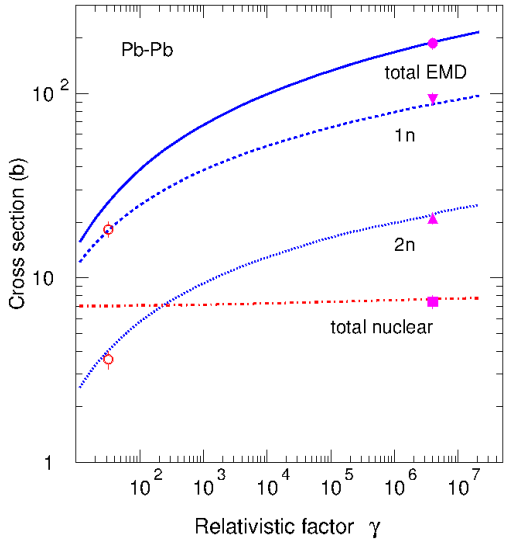

The results of calculations of the total EMD cross-section and partial cross- sections in 1n and 2n channels are shown by solid, dashed and dotted lines, respectively. Total nuclear cross- section calculated in the DPMJET-III [13] model is shown by dot-dashed line. Results from the ALICE collaboration [10] for the total EMD and nuclear cross-sections are shown by the full circle and full box, respectively. The measurements for 1n and 2n channels are shown by open circles [11] and full triangles [10].

Improvements to Phojet/Dpmjet

For heavy ion interactions above 5 GeV/n, as well as for hadron-hadron and hadron-nucleus interactions above 20 TeV FLUKA interfaces to DPMJET-III [13], the nuclear framework around the PHOJET [16,17] event generator for hadron-hadron, photon-hadron and photon-photon collisions. Comparisons with LHC *pp* data at √s=7 TeV showed discrepancies in the description of charged particle multiplicities. A satisfactory data agreement could be achived by using an improved treatment of multiple parton interactions and fragmentation. Further developments are on-going, in particular regarding elastic scattering, where an approach based on the JLL model [14] has been selected. The dip-bump structure is generated trough interference of terms associated with a two-component Pomeron, 2 effective Reggeons and an Odderon contribution. The model can be expressed in a simple analytic form, thus allowing for efficient MC sampling. The small number of free parameters ensures that extrapolations up to very

high energies stay reasonable. Once tuned to experimental data sets this model provides very good results from as low as √s=15 GeV up to √s=7 TeV, corresponding to a laboratory momentum as high as $2.6 \cdot 10^4$ TeV/c. Using a single set of parameters, the preliminary model reproduces the available measurements from the ISR to the latest data from the TOTEM experiment [18,19] at the LHC, as shown in Figure 3.

Figure 2. Cross-sections for the production of the heaviest fragments in electromagnetic dissociation of 2750 GeV/n Pb nuclei on ^{12}C target as a function of the momentum-to-charge ratio normalised to that of the main circulating beam

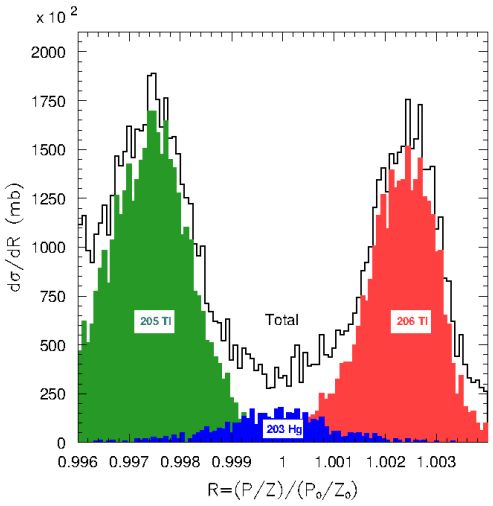

Figure 3. Elastic cross-section for proton-proton and proton-antiproton scattering at different centre of mass energies [GeV]

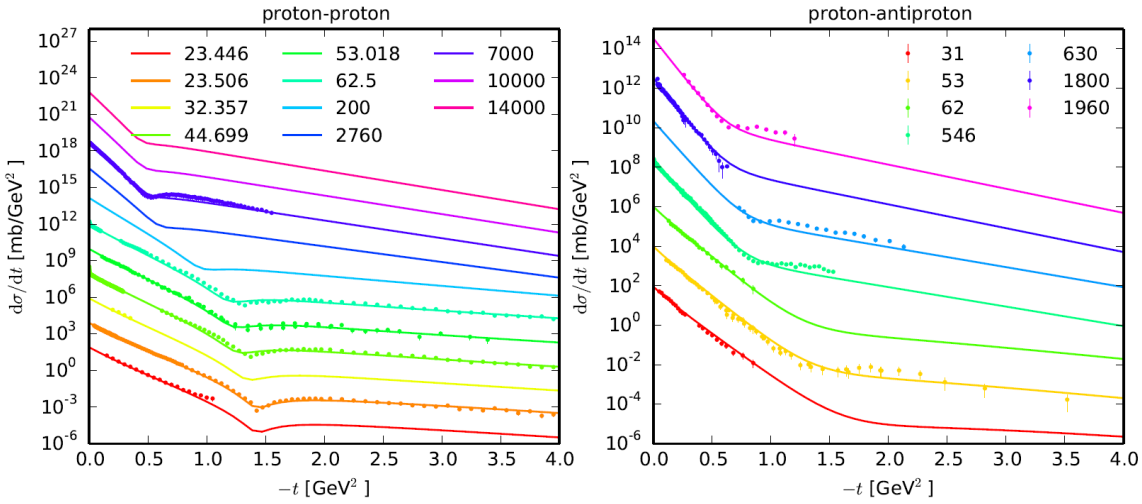

Lines are simulated results and points are experimental data [15]. Energy sets are multiplied by an increasing power of ten.

Synchrotron radiation

Synchrotron radiation is a limiting issue for possible future high energy e^+e^- circular colliders, like the proposed FCCee at CERN. The ability to easily compute synchrotron radiation emission is an obvious advantage for these studies, as well as for all calculations related to synchrotron radiation sources.

Sophisticated low-energy photon transport including polarisation effects and full account for bound electron effects has been available in FLUKA for several years [20]. Recently, a new dedicated source for SR radiation has been added to the collection of ready-to-use options in FLUKA. It includes sampling from the appropriate photon spectrum, polarisation as a function of the emitted photon energy, proper angular distribution. Arbitrary orientation of the emitting particles with respect to an external magnetic field can be treated, as well as the emission along accelerator arcs and helical paths.

Crystal channeling

Charged particles entering a crystal close to some preferred direction can be trapped in the electromagnetic potential well existing between consecutive planes or strings of atoms. This channeling effect can be used to extract beam particles if the crystal is bent beforehand. Crystal channeling is becoming a reliable and efficient technique for collimating beams and removing halo particles. At CERN, the installation of silicon crystals in the LHC is under scrutiny by the UA9 [21] collaboration with the goal of investigating if they are a viable option for the collimation system upgrade.

Figure 4. Distribution of angular deflections given by a strip crystal to 400 GeV protons

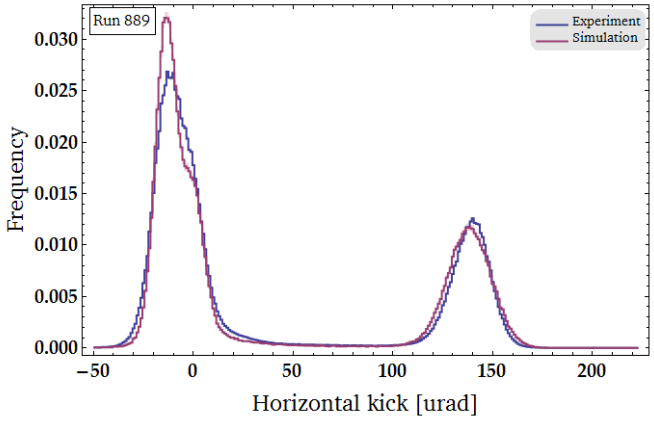

Results from the simulation, using FLUKA model for channeling, are shown in red and compared to the UA9-H8 [24] experiment conducted at CERN, in blue.

A new Monte Carlo model of planar channeling has been developed from scratch [22] in order to be implemented in the FLUKA code. Crystal channels are described through the concept of continuous potential taking into account thermal motion of the lattice atoms and using Molière screening function. The energy of the particle transverse motion determines whether or not it is trapped between the crystal planes while single Coulomb scattering on lattice atoms can lead to dechanneling. Volume capture and reflection applying to quasi-channeled particles are also modelled. Similarly to dechanneling, single scattering is used to determine the occurrence of volume capture. The parameters of the crystals, such as torsion or miscut, are described as well. Work is on-going on the implementation of a reduced energy loss for channeled particles. This model has been succesfully benchmarked [22] against data taken by the UA9-H8 experiment with a 400 GeV/c proton beam. An example of the results is shown in Figure 4, where the

experimental distribution of deflected protons downstream the crystal compares nicely to the simulation.

Spin and parity effects

All nuclear interaction models, including those generated by ions, share parts of the common PEANUT framework. In particular, all nuclear fragments, irrespective of the originating reaction, are de-excited through the same evaporation/fragmentation and gamma production chain. The final steps of the reaction include evaporation in competition with fission and gamma de-excitation.

The FLUKA evaporation model, which is based on the Weisskopf-Ewing approach, has been continuously updated over the years, with the inclusion, for instance, of sub-barrier emission, full level density formula, analytic solution of the emission widths, evaporation of nuclear fragments up to $A \leq 24$. As a result, the code can be reliably used for the prediction of induced radioactivity and residual dose in most of the cases of interest for radioprotection. However, spin/parity dependent evaporation (Hauser-Feshbach) is still too complex to be implemented in MC codes in the energy range of interest for FLUKA applications. Furthermore, it is difficult to keep track of the total angular momentum and parity evolution of the system during the cascade and pre-equilibrium stages, particularly at medium/high energies. As a consequence, isomer production with respect to ground state production cannot be reliably computed. Similarly, individual level population and the subsequent gamma emission are hard to predict.

The first attempts to enforce spin/parity conservation in PEANUT targeted the Fermi break-up part in cases when initial conditions are well defined. Statistical evaporation of excited low mass fragments is unsuitable due to the relatively few, widely spaced levels. Therefore, alternative de-excitation mechanisms are employed for these light (typically $A \leq 16$) residual nuclei in most Monte Carlo (MC) codes. A popular choice for this calculations is the Fermi Break-up model [25,26], where the excited nucleus is supposed to disassemble in one single step into two or more fragments, possibly in excited states, with branching given by plain phase space considerations.

However, the basic formulation of Fermi Break-up implicitly assumes that the fragment emission occurs in L=0 and neglects whichever consideration of the initial spin and parity state, J^{π}, of the excited nucleus. If the initial J^{π} is known, suitable modifications must be applied in order to account for it, in particular:

- The minimum orbital momentum L_{min} compatible with J^{π} and the spins and parities of the emitted particles must be computed.
- The spin factor S_n must be restricted to the spin projections compatible with an emission with L_{min}.
- In case $L_{min} > 0$, a suitable centrifugal barrier must be added to E_{Coul}.

Figure 5 shows the example of the improvement due to the inclusion of spin/parity considerations, where the calculated excitation curve for $^{12}C(\gamma, n)^{11}C$, a reaction for which $J^{\pi} = 0^{+}$ in the GDR energy range, is compared with experimental data before and after their application. This reaction is of special relevance for underground experiments, particularly those using liquid scintillators, where photons produced by high-energy muons penetrating through the underground rock can produce ^{11}C and neutrons which represent a background.

Recently, work has started also for standard evaporation at low excitations, together with the implementation of the MLO (Modified Lorentzian) model for the competition between particle evaporation and γ emission. As an example, Figure 6 shows good agreement in the prediction of the excitation function for double neutron emission after

photon absorption on gold. A perfect application for this new treatment is the EMD process described beforehand, because the initial state after the virtual photon absorption has definite spin and parity.

Developments of interest for hadrontherapy monitoring

FLUKA is routinely used at the CNAO and HIT hadron therapy centres for the generation of Treatment Planning System (TPS) databases and for TPS verification. It is also used as a research tool, for instance for the investigation of new beams and new methods for therapy monitoring. The latter research field is also the scope of the ENVISION/ENTERVISION European programmes. ^{16}O (p, x) ^{15}O and ^{12}C(p, x)^{11}C are the most important reactions for in-vivo or off-line PET (Positron Emission Tomography) monitoring of proton therapy [27]. These reactions can proceed through the emission of either independent nucleons or deuterons. A reliable prediction of these channels, particularly at energies typical of the Bragg peak region for protons, is critical. Composite ejectiles like d, t, ^{3}He, and α can be reasonably described by coalescence algorithms during the IntraNuclear Cascade and pre-equilibrium stages. All possible combinations of unbound nucleons and/or light fragments are checked at each stage of system evolution and a figure-of-merit evaluation based on phase space "closeness" at the nucleus periphery is used to decide whether a light fragment is formed rather than not. This approach works reasonably well at medium/high energies: It has been recently extended up to Intermediate Mass Fragments of mass A ≤10 [28]. However, at energies below a few tens of MeV, coalescence is increasingly ineffective in reproducing experimental data. Recently, a direct deuteron formation mechanism following the first *pn* or *np* elementary interaction has been implemented in FLUKA which greatly improved the predictive power for reactions like (p,d). Examples outlining the effectiveness of the new approach can be found in [30]. Another promising technique for in-vivo hadrontherapy monitoring relies on the detection of prompt photons emitted following nuclear interactions by the beam particles. FLUKA capabilities in this aspect have been recently enhanced, as described in [30,31].

Figure 5. ^{12}C(γ,n)^{11}C cross-sections as computed with FLUKA2013.0 (red, upper curve), and FLUKA2011.2 (blue curve) compared with data retrieved from the EXFOR [29] library

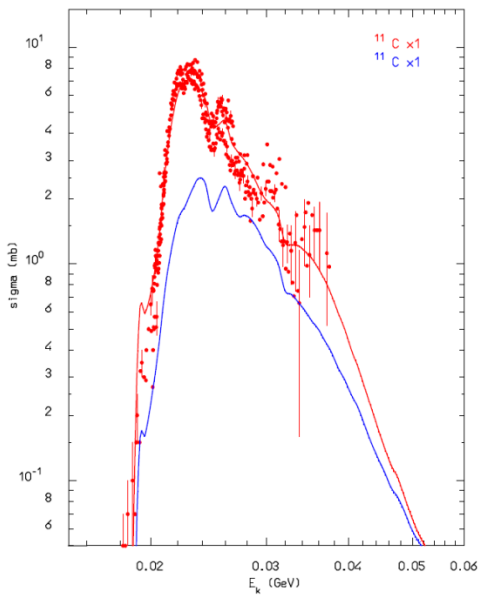

Figure 6. Cross-section for the production of ^{195}Au from photon absorption on ^{197}Au, as a function of the incoming photon energy

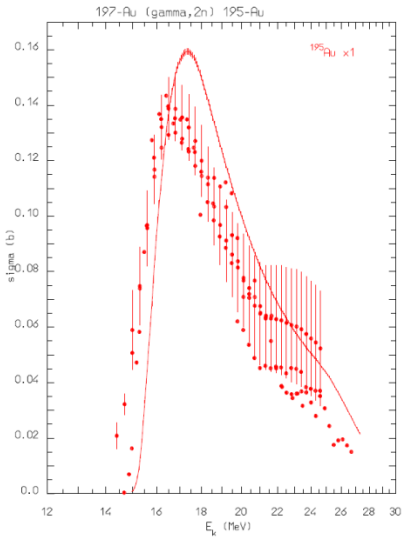

Dots: experimental data [29], line: FLUKA simulation.

Technical advancements

Besides its physics capabilities, FLUKA is also becoming an increasingly flexible and user-friendly tool.

The LineBuilder

The FLUKA geometry allows for easy replication of basic structures, as well as rotations, translations and scaling of selected elements. These features were exploited to develop the "LineBuilder" (LB) tool, now essential for any LHC related simulation. The LineBuilder consists of a database of accelerator components and of an assembler of geometries. The actual beam lines are automatically generated through direct use of machine optics files, thus ensuring protection against wrong settings of the beam line, e.g. misplacements, wrong orientations, mismatches in magnetic fields and collimator apertures. An example of LB results, as visualised by Flair is shown in Figure 7.

Figure 7. Example of beam line geometry generated with the LB package

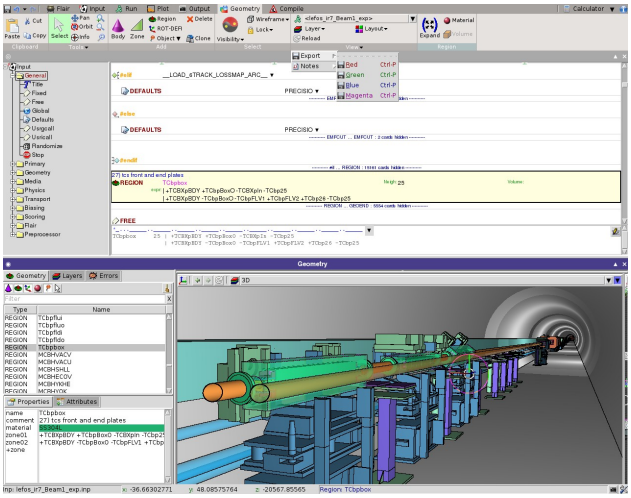

Coupling with SixTrack

Machine protection is a multi-disciplinary field, based on radiation-matter interaction and particle dynamics in accelerators: Typical Monte Carlo results (energy deposition, particle fluence, signals in monitors...) are affected by multi-turn effects, namely particles that interact but stay within the accelerator acceptance and reappear in the same place after one or even more turns. On the other hand, particle scatterings in intercepting devices may cause beam losses far away from the interaction point. This interplay between Monte Carlo and accelerator transport is now accurately accounted for with the recent coupling [32] between FLUKA and SixTrack. SixTrack is a 6D transport code routinely used for single particle tracking in high energy circular machines (e.g. LHC and RHIC), especially for dynamic aperture and collimation studies. FLUKA and SixTrack run independently at the same time, communicating with each other. One or more portions of the accelerator lattice are covered by FLUKA, the rest by SixTrack. The two codes exchange particles at run-time through a network port, by means of a dedicated communication protocol (C/C++). The advantages of this coupling are more accurate predictions, relying on the best of the two codes, self-consistency, limited human intervention.

Flair: graphical user interface

Flair [33] is a user-friendly graphical interface for FLUKA Monte Carlo transport code. It provides an Integrated Development Environment (IDE) for all stages of FLUKA simulations, from building an error- free input file, debugging, creation of user-written routines, execution, status monitoring, data processing and plot generation. Its use greatly enhances the productivity of users and provides a less steep learning curve for beginners. Flair includes real-time geometry visualisation and graphical editing, both with two-dimensional cross-section cuts and with three-dimensional projections. To facilitate the use of FLUKA for medical applications, flair integrates intuitive PET scanner geometry generator and importing routines for processing DICOM [34] files. DICOM is a non-proprietary data interchange protocol used in medicine. 3D CT scans, MRI, PET dose maps, as well dose distribution from the treatment planning systems all use the DICOM format to exchange their information. Flair is able to import the DICOM files (see Figure 8) and convert them in FLUKA voxel geometries.

Figure 8. Three-dimensional rendering of a CT scan converted by Flair into the FLUKA voxel geometry

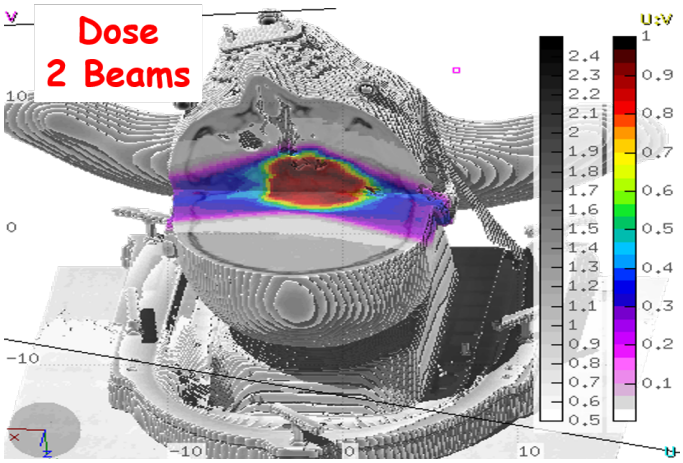

Simulated dose delivery with a two-beam proton treatment is superimposed to the geometry.

Conclusions

The FLUKA code is used for a variety of applications at CERN and elsewhere. Some of the recent improvements have been described, together with examples showing the improved results when compared with experimental data.

Acknowledgments

This research project was partially supported by ENVISION, which is co-funded by the European Commission under FP7 Grant Agreement N. 241851.

References

[1] A. Ferrari, P.R. Sala, A. Fassò, J. Ranft (2005), "FLUKA: a multi-particle transport code", CERN-2005-10, INFN/TC_05/11, SLAC-R-773.

[2] G. Battistoni et al. (2007), *AIP Conference Proceedings* 896, p. 31.

[3] A. Ferrari, P.R. Sala (1998), "The Physics of High Energy Reactions", *Proceedings of Workshop on Nuclear Reaction Data and Nuclear Reactors Physics*, Design and Safety, A. Gandini, G. Reffo eds., Trieste, Italy, April 1996, 2, p.424.

[4] G. Battistoni et al. (2006), *Proceedings of 11th International Conference on Nuclear Reaction Mechanisms*, Varenna, Italy, 12-16 June 2006, E. Gadioli ed., p. 483.

[5] A. Capella, U. Sukhatme, C-I. Tan, J. Tran Thanh Van (1994), *Phys. Rep*. 236, p. 225.

[6] F. Ballarini et al. (2007), *Adv. Space Rad*. 40, p. 1339.

[7] D.E. Cullen et al. (1997), "EPDL97: The Evaluated Photon Data Library, '97 Version", UCRL– 50400, Vol. 6, Rev. 5.

[8] A.Ferrari, P.R. Sala, R.Guaraldi, F.Padoani (1992), Nucl. Instr. and Meth. B 71, p. 412.

[9] H.H. Braun et al. (2014), Phys. Rev. ST Accel. Beams 17, 021006.

[10] B. Abelev et al. (2012), *Phys. Rev. Lett.* 109, 252302.

[11] M. B. Golubeva (2005), *Phys. Rev. C* 71, 024905.

[12] T. Sjöstrand, S. Mrenna and P. Skands (2006), *JHEP* 5 p. 26.

[13] S. Roesler, R. Engel, J. Ranft (2001), "The Monte Carlo event generator DPMJET-III", *Proceedings of the MonteCarlo 2000 Conference*, Lisbon, October 23–26 2000, A. Kling, F. Barão, M. Nakagawa, L. Távora, P. Vaz eds., Springer-Verlag Berlin, p. 1033.

[14] L.L. Jenkovszky et al. (2011), *Int. Jour. Mod. Phys.* A26 p.4755.

[15] J.R. Cudell: http://www.theo.phys.ulg.ac.be/ cudell/data/.

[16] R. Engel (1995), *Z. Phys.* C66, p. 203.

[17] R. Engel, J. Ranft (1996), *Phys. Rev.* D54, p. 4244.

[18] "The TOTEM Collaboration" (2011), *EPL* 96, 21002.

[19] "The TOTEM Collaboration" (2011), *EPL* 95, 41001.

[20] T. T. Bohlen, A. Ferrari, V. Patera and P. R. Sala (2012), *JINST* 7) P07018.

[21] http://home.web.cern.ch/about/experiments/ua9.

[22] P.J. Schoofs (2014), Monte Carlo Modeling of Crystal Channeling at High Energies, These Ecole polytechnique federale de Lausanne EPFL, nr. 6046.

[23] P. Schoofs, F. Cerutti, A. Ferrari, G. Smirnov (2013), *Nucl. Instr. and Meth. in Phys. Res. B*, 309, p. 115.

[24] M. Pesaresi et al. (2011), *JINST* 6 P04006.

[25] E. Fermi (1950), *Prog. Theor. Phys.* 5, p. 1570.

[26] M. Epherre and, E. Gradsztajn (1967), *J. Phys.* 28, p. 745.

[27] K. Parodi, A. Ferrari, F. Sommerer, H. Paganetti (2007), *Phys. Med. Biol.* 52 p. 3369.

[28] A. Boudard et al. (2013), *Phys. Rev.* C87, 014606.

[29] http:www-nds.iaea.org/exfor/.

[30] A. Ferrari et al. (2013), "The FLUKA Code: Developments and Challenges for High Energy and Medical Applications", Proc. of ND2013, in press.

[31] G. Battistoni et al. "Modeling prompt photon emission with FLUKA".

[32] A. Mereghetti et al. (2013), "SixTrack-Fluka active coupling for the upgrade of the SPS scrapers", *Proceedings of IPAC2013*, Shangai, China, 2013.

[33] V. Vlachoudis (2009), *Proc. of Int. Conf. on Math,* Comp Meth & Reactor Physics,Saratoga Springs, NY, http://www.fluka.org/flair.

[34] National Electrical Manufacturers Association (1996), NEMA Standard Publications PS 3.

Modelling proton-induced reactions at low energies in the MARS15 code

Igor L. Rakhno[1], Nikolai V. Mokhov[1], Konstantin K. Gudima[2]
[1]Fermi National Accelerator Laboratory, Batavia, Illinois, US
[2]Institute of Applied Physics, National Academy of Sciences, Cisineu, Moldova

Abstract

In order to describe nuclear reactions by low-energy projectiles in the Monte Carlo code MARS15, an implementation of both the ALICE code and the TENDL evaluated nuclear data library is presented. In addition, comparisons between results of modelling and experimental data on reaction cross-sections and secondary particle distributions are shown.

Introduction

Correct prediction of secondary particles, both neutral and charged ones, generated in proton-nucleus interactions below a few tens of MeV is required for various applications. The latter include, among other things, radiation studies for front-end of many proton accelerators, energy deposition studies for detectors, radiation damage calculations, etc. Cascade models of various flavours fail to properly describe this energy region (see Figure 1). Therefore, we opted to use the TENDL library developed by the Nuclear Research and Consultancy Group [1]. The evaluated data is provided in the ENDF/B format in the energy range from 1 to 200 MeV, and the library has been updated regularly since 2008. In addition, a much more time-consuming approach utilised in a modified code ALICE [2] was also considered. For both options, the energy and angle distributions of all secondary particles are described with the Kalbach-Mann systematics. The following secondaries are considered: gammas, neutrons, protons, deuterons, tritons, ^{3}He and ^{4}He. The energy and angular distributions of all generated residual nuclei – including unstable ones – are accounted for as well.

Various comparisons with experimental data for both options are presented. The corresponding processing and modelling software was written in C++, which provides substantial flexibility with respect to the computer memory used. In addition, the initialisation of the required evaluated data is performed dynamically whenever the modelling code encounters a nuclide not accounted for yet. The latter feature enables us to significantly reduce the amount of requested memory for extended systems with large number of materials.

Figure 1. Calculated and measured [3] neutron production cross-section for aluminium at low incident proton energies

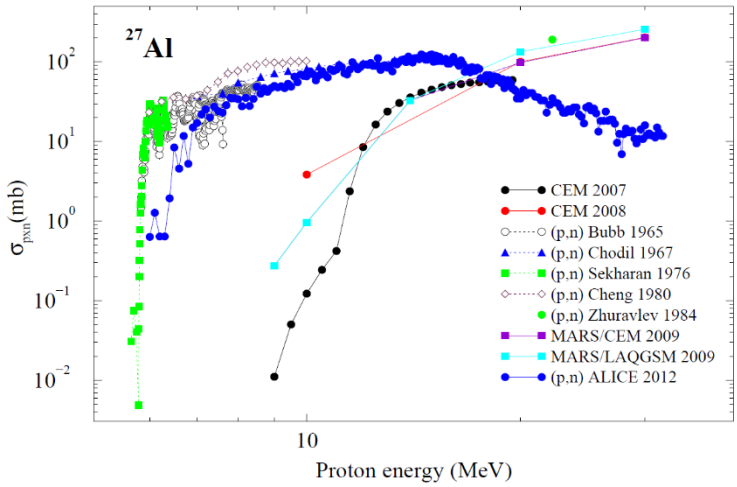

Details of the implementation and formalism

TENDL library

The TALYS-based evaluated nuclear data library (TENDL) contains data for direct use in both basic physics and applications, and has been updated annually since 2008. The evaluations were performed for practically the entire periodic table except for hydrogen and helium. The range for projectile kinetic energies is from 1 to 200 MeV. The library contains data for both stable and unstable target nuclei – all isotopes which live longer than 1 second were taken into account. At present, the list includes about 2400 isotopes.

The TENDL library contains data not only for protons as projectiles, but also for light ions (d, t, ^{3}He, ^{4}He), neutrons and gammas. In the current implementation, the data for protons and light ions are used when modelling low-energy reactions in MARS15 code [4,5]. It should also be noted that only inelastic collisions are taken into account. In other words, for every interaction the following information is extracted from the library: (i) total inelastic cross-section; (ii) energy and angular distributions of all the above mentioned secondary particles and residual nuclei; (iii) yields of all the secondaries.

The TENDL library is a collection of files in both ENDF/B and ACE format. We opted to use the source – ENDF/B format – because it is more user friendly, which is a very important feature at the development and debugging stages. At the same time, there is little difference between the two formats with respect to storage requirements.

ALICE code

An alternative approach – using an event generator – was explored as well. For this purpose, the nuclear model code ALICE [2] based on a hybrid model of pre-compound decay, Weisskopf-Ewing evaporation and Bohr-Wheeler fission models was employed. It was re-designed in order to be used as an event generator for nucleon, photon and heavy-ion nuclear reactions at incident energies from 1 to 20-30 MeV matching CEM and LAQGSM at energies above 20-30 MeV in MARS15. Currently, this option looks much more time consuming, but potentially it can offer some advantages for applications where the accuracy of full exclusive modelling is of major importance, e.g. when modelling a detector performance.

Kalbach-Mann systematics

Nowadays, continuum energy-angle distributions of secondary particles generated in low energy interactions are described mostly with the Kalbach-Mann systematics [6] represented by Equation (1).

$$f(\mu_b, E_a, E_b) = 0.5 * f_0(E_a, E_b)\left[\frac{a}{\sinh(a)}\left[\cosh(a\mu_b) + r(E_a, E_b)\sinh(a\mu_b)\right]\right] \quad (1)$$

where $a = a(E_a, E_b)$ is a parametrised function, $r(E_a, E_b)$ is the pre-compound fraction as given by the evaluator, μ_b is cosine of scattering angle, E_a and E_b are energies of incident projectile and emitted particle, respectively, and $f_0(E_a, E_b)$ is total probability of scattering from E_a to E_b integrated over all angles. The function $a(E_a, E_b)$ depends mostly on the emission energy, and there is also a slight dependence on particle type and the incident energy at higher values of E_a.

Comparisons between experimental data and results of modelling

Reaction cross-sections

Comparisons between calculated and measured reaction cross sections for several light and medium target nuclei are shown for incoming protons in Figures 2 through 5 and for incoming deuterons in Figure 6.

Figure 2. Calculated (ALICE, TENDL) and measured [3] single neutron production cross-section on ^{65}Cu

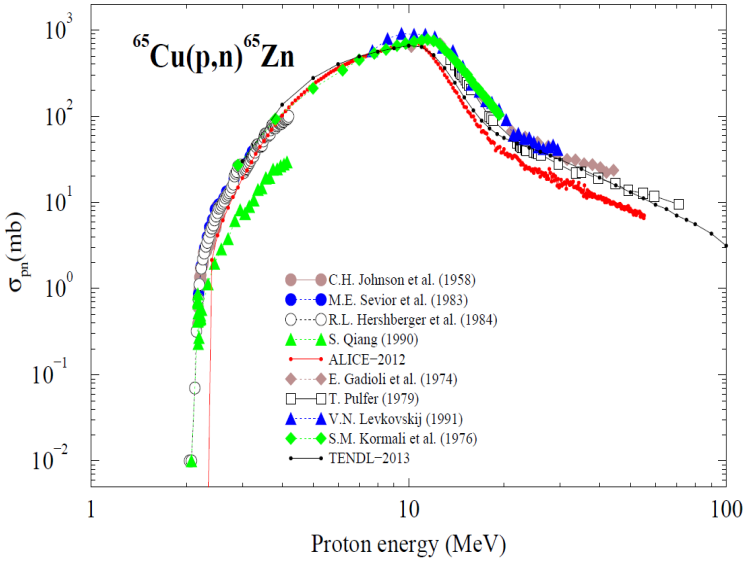

Figure 3. Calculated (ALICE, TENDL) and measured [3] neutron production cross-section on ^{65}Cu

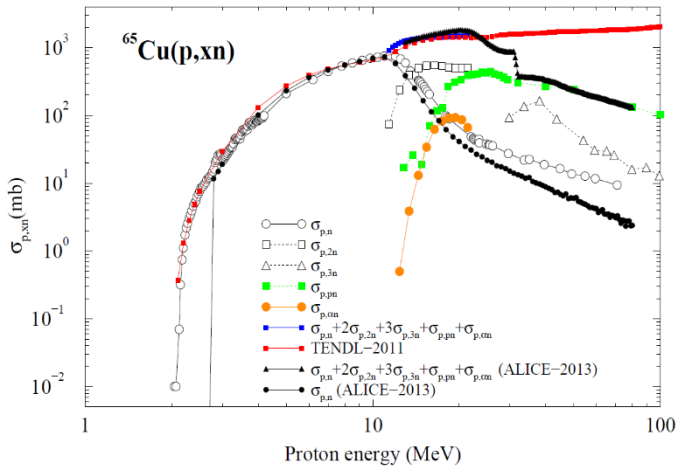

Figure 4. Calculated (red and black lines - TENDL) and measured [3] neutron production cross-section on Al and Ti nuclear targets

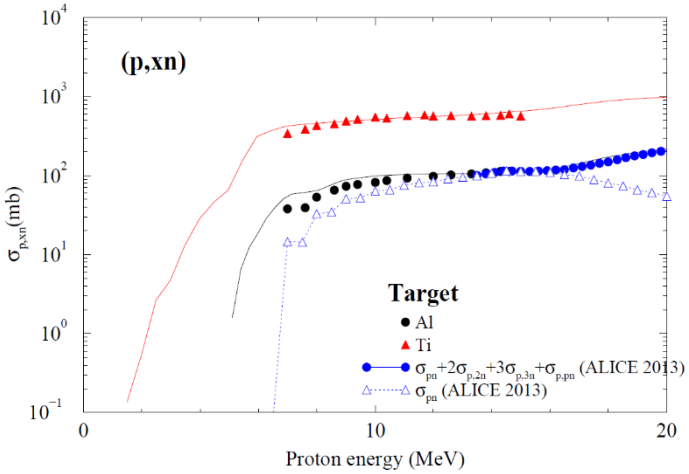

Figure 5. Calculated (lines - TENDL) and measured [7-8] reaction cross-sections on ^{93}Nb

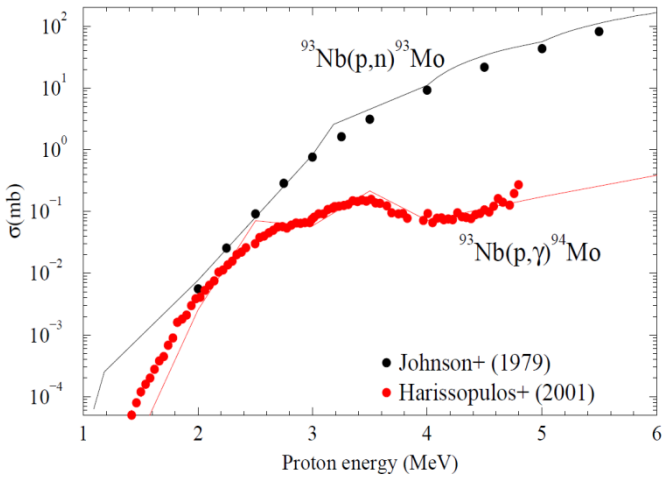

Figure 6. Calculated (lines - TENDL) and measured (circles [9] and triangles [10]) deuteron-induced reaction cross-sections on ^{93}Nb

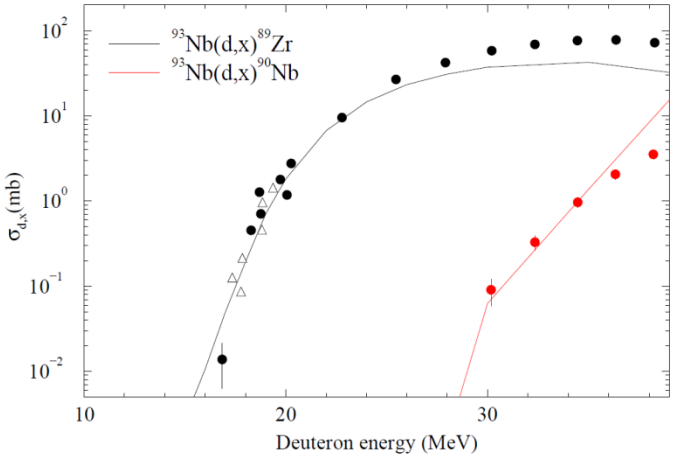

Energy distributions of secondary particles

Energy spectra of secondary neutrons are shown in Figures 7 through 9. As shown in Figure 7, at low secondary energies – where the major neutron emission takes place – the TENDL library provides rather reliable predictions for energy distributions. At the same time, at very low projectile energies – about 10 MeV and lower – the library does not reproduce the significant nuclear structure effects observed in the experimental data (see Figure 9). However, for high-energy applications, the accuracy provided by the TENDL library is quite adequate.

Angular distributions of secondary particles

Angular distributions of secondary neutrons are shown in Figures 10 and 11. It should be noted that both the library and the ALICE-based generator can reproduce the general features of the angular distributions well: close to isotropic distributions at low emitted neutron energies and forward-peaked fistributions at higher secondary energies. The observed numerical agreement between calculations and experimental data in these two cases of medium and heavy nuclei is also rather good.

Transition region

In order to provide smooth transition between the low-energy region described, e.g. with the TENDL evaluated data library and higher energies where cascade models work well, several cases were studied (see Figures 12 through 14).

Figure 7. Calculated (solid lines – TENDL) and measured [3] energy distributions of secondary neutrons

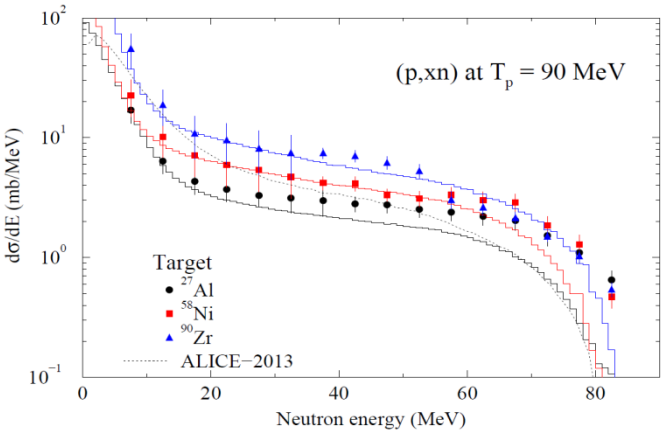

Figure 8. Calculated (lines – TENDL) and measured [3] energy distributions of secondary neutrons

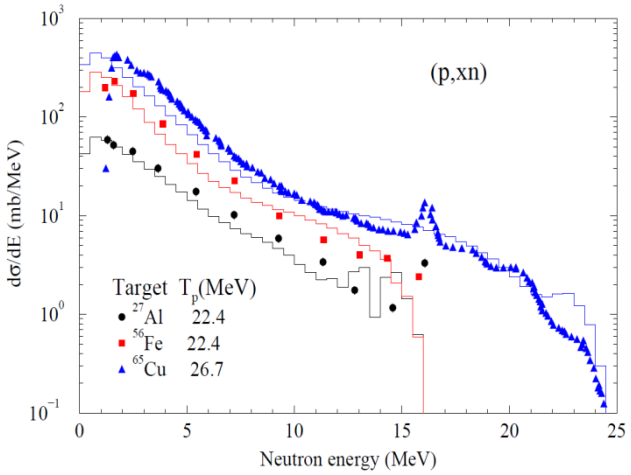

Figure 9. Calculated (lines – TENDL) and measured [3] energy distributions of secondary neutrons

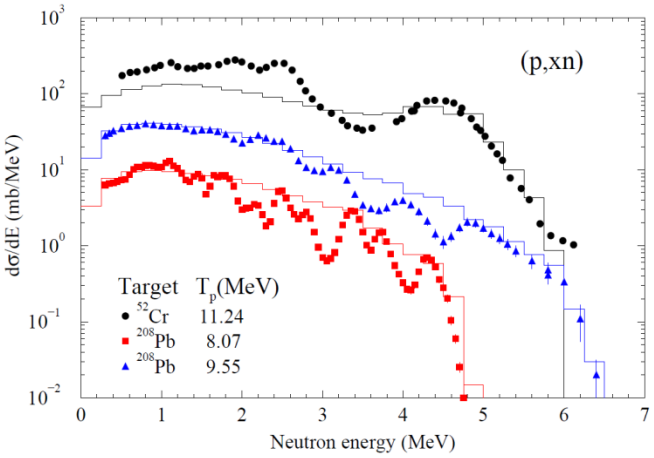

Figure 10. Calculated (solid lines – TENDL) and measured [3] angular distributions of secondary neutrons from ^{65}Cu

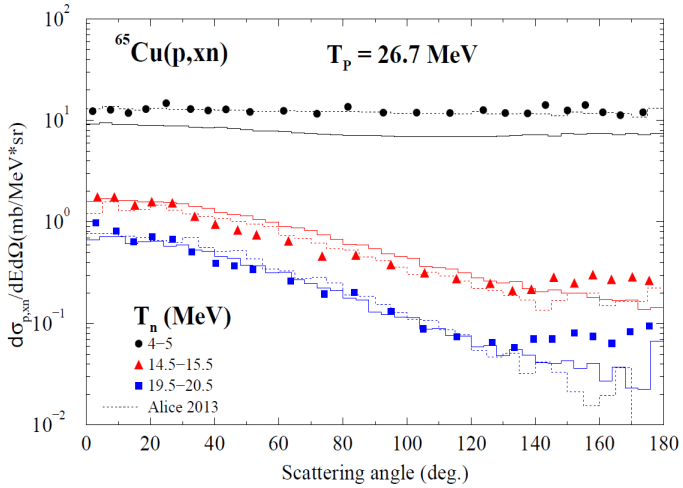

Figure 11. Calculated (solid lines – TENDL) and measured [3] angular distributions of secondary neutrons for ^{107}Ag

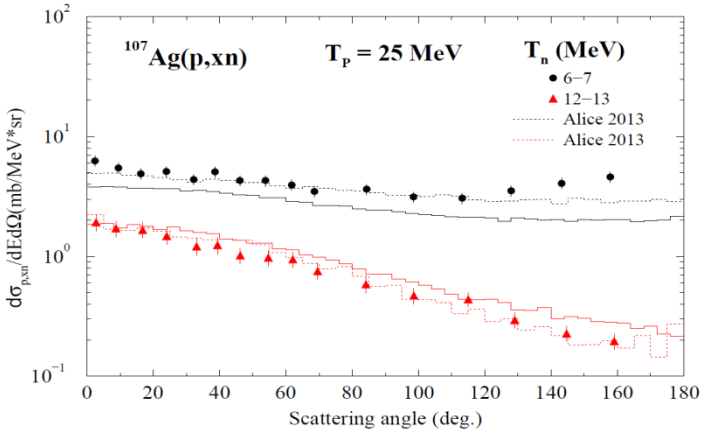

Figure 12. Calculated (lines – TENDL) and measured [6] angular distributions of secondary deuterons and α-particles from 27Al (projectile/ejectile energies are given in MeV)

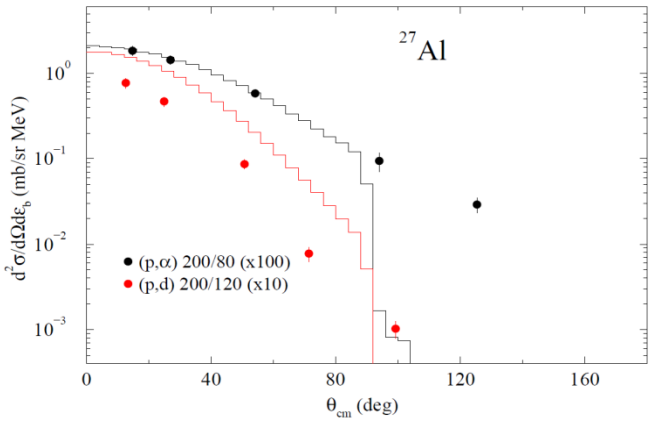

Figure 13. Calculated (lines – TENDL) and measured [6] angular distributions of secondary deuterons and α-particles from ^{62}Ni (projectile/ejectile energies are given in MeV)

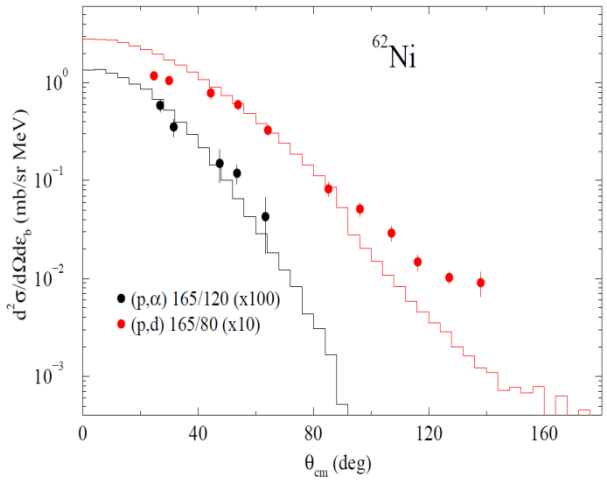

Figure 14. Calculated (lines – TENDL) and measured [6] angular distributions of secondary protons for light, medium and heavy target nuclei (projectile/ejectile energies are given in MeV)

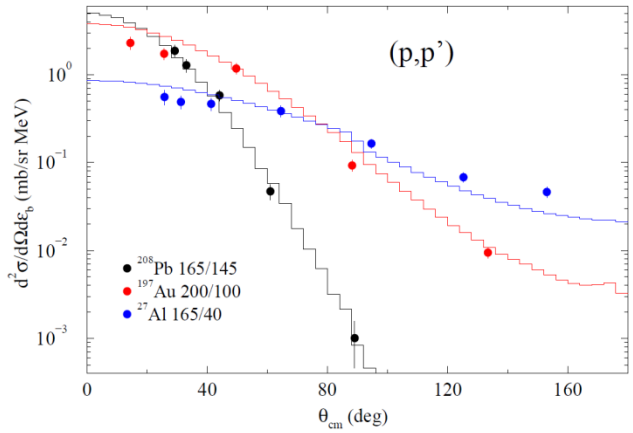

The transition region between low energies described with TENDL library and higher energies can be very broad because the library provides a good description of experimental data up to projectile energy of 200 MeV. At the same time, the transition region is expected to be dependent on target mass number because, in general, the quality of the Kalbach-Mann systematics gets worse with decreasing target mass number (see Figure 12). Work on the proper description of the transition region between low and higher energies is currently in progress.

Acknowledgements

This work was supported by Fermi Research Alliance, LLC, under contract No. DE-AC02-07CH11359 with the US Department of Energy.

References

[1] A. J. Koning et al. (2013), "TENDL-2013: TALYS-based evaluated nuclear data library"; http://www.talys.eu/tendl-2014/.

[2] M. Blann et al. (2011), "ALICE2011, Particle Spectra from HMS Precompound Nucleus Decay", *Package ID USCD1238/05*; http://www.oecd-nea.org/tools/abstract/list.

[3] Experimental Nuclear Reaction Data (EXFOR); http://www.nndc.bnl.gov/exfor/exfor.htm.

[4] N.V. Mokhov (1995), "The MARS code system user's guide", *Fermilab-FN-628;* http://www-ap.fnal.gov/MARS.

[5] N.V. Mokhov, S.I. Striganov (2007) "MARS15 overview", *Proc. Of Hadronic Shower Simulation Workshop, Fermilab, September 2006, AIP Conf. Proc. 896,* pp. 50-60.

[6] C. Kalbach (1988), "Systematics of continuum angular distributions: Extension to higher energies", *Phys. Rev.*, C37, pp. 2350-2370.

[7] C.H. Johnson et al. (1979), "(p,n) reactions for 89<A<130 and an anomalous optical model potential for sub-Coulomb protons", *Phys. Rev.*, C20, pp. 2052-2071.

[8] S. Harissopulos et al. (2001), "Cross section measurement of the ^{93}Nb(p,γ)^{94}Mo reaction at E_p=1.4-4.9 MeV relevant to the nucleosynthetic *p* process", *Phys. Rev.*, C64, pp. 055804-1 – 055804-9.

[9] F. Tarkanyi et al. (2007), "Production of longer lived radionuclides in deuteron induced reactions on niobium", *Nucl. Inst. Meth.*, B255, pp. 297–303.

[10] M. Avrigeanu et al. (2013), "Low-energy deuteron-induced reactions on ^{93}Nb", *Phys. Rev.*, C88, pp. 014612-1 – 014612-24.

Session VI: Code Benchmarking and Inter-comparison

Chair: Robert Grove

Inter-comparison of particle production

Hideo Hirayama, Toshiya Sanami
KEK, High Energy Accelerator Research Organisation, Japan

Abstract

In accordance with the discussions at SATIF-11, inter-comparison was performed on neutron production by 1, 10 and 100 GeV protons from thick targets of Al, Cu and Au. This paper presents a comparison of the neutron angular spectrum and fluence above 20 MeV provided by six groups.

Introduction

A series of inter-comparisons among various computer codes concerning the attenuation of medium- and high-energy neutrons inside iron and concrete shields occurred from SATIF-3 to SATIF-10 [1-8]. We observed a large difference in the neutron spectra from inter-comparisons among codes deep inside iron and concrete, particularly for mono-energetic neutrons in the high-energy region, as shown in Figure 1.

To study the reason for this difference, at SATIF-11 we proposed new inter-comparison studies on the neutron production from simple targets by high-energy protons among codes and models used.

The problems to be calculated were sent to all participants. The results from six groups were sent to the organiser. This paper presents a comparison among the 6 groups, as well as the future themes that result from this inter-comparison.

Figure 1. Neutron spectra at 4 m inside iron for 1GeV neutrons

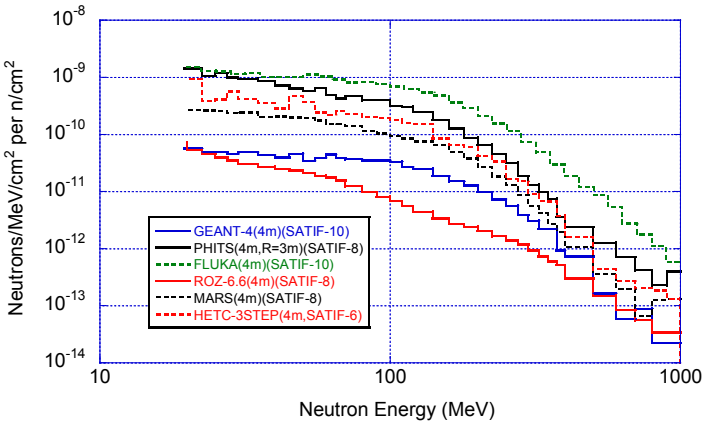

Problems for an inter-comparison

Incident particle

Pencil beam of protons used with the following energies:

- (a) 1 GeV;
- (b) 10 GeV;
- (c) 100 GeV.

Target materials and their sizes

The target geometry was a cylinder. Source protons were incident on the centre of the cylinder bottom. The target detector distance from the centre of the cylinder was 500 cm.

- (a) Al: length = 40 cm, diameter = 4.0 cm and density = 2.7 g/cm^3;
- (b) Cu: length = 16 cm, diameter = 1.6 cm and density = 8.63 g/cm^3;
- (c) Au: length = 10 cm, diameter = 1.0 cm and density = 19.3 g/cm^3.

Quantities to be calculated

The neutron spectrum above 20 MeV in n/MeV/sr/proton at 15, 30, 45, 60, 90, 120, and 150 degrees with an angular width of ± 0.5 degrees was calculated.

Summary of contributors

Six groups sent their results to the organiser. Table 1 lists the participants, the names of the computer codes, the database and the physical model used.

Table 1. Summary of contributors

Name of participants and organizations	Code	Data Base	Physical model
Lucia Sarchiapone and Demetre Zafiropoulos (INFN)	FLUKA 2011[9,10]	Physical Models and Event generators inside the FLUKA code	
Stefan Roesler (CERN)	FLUKA Version 2011.2b.5 [9,10]		Peanut model
Toshiya Sanami (KEK)	MARS 1514 [11-14]	Original MARS	LAQGSM
Norihiro MATSUDA (JAEA) and PHITS development team	PHITS [15,16]	Original (PHITS)	INCL4.6(<3GeN)+JAM(>3GeV)+GEM
Koi, Tatsumi (SLAC)	Geant4 v10.00.p01 (use "Shielding" physics list) [17,18]		BERT style cascade up to 5GeV and from 4 GeV Fritof (FTF) string model
Irina Popova (ORNL)	MCNPX version 2.7 [19]	ENDF7	default
			CEM03

The results were sent by Dr. Sarchiapone and Dr. Zafiropoulos for all cases. Unfortunately, their results used the old model for the 10 and 100 GeV cases. Therefore, only the 1 GeV results were included in this inter-comparison.

Figure 2. Neutron angular spectra from the Al target

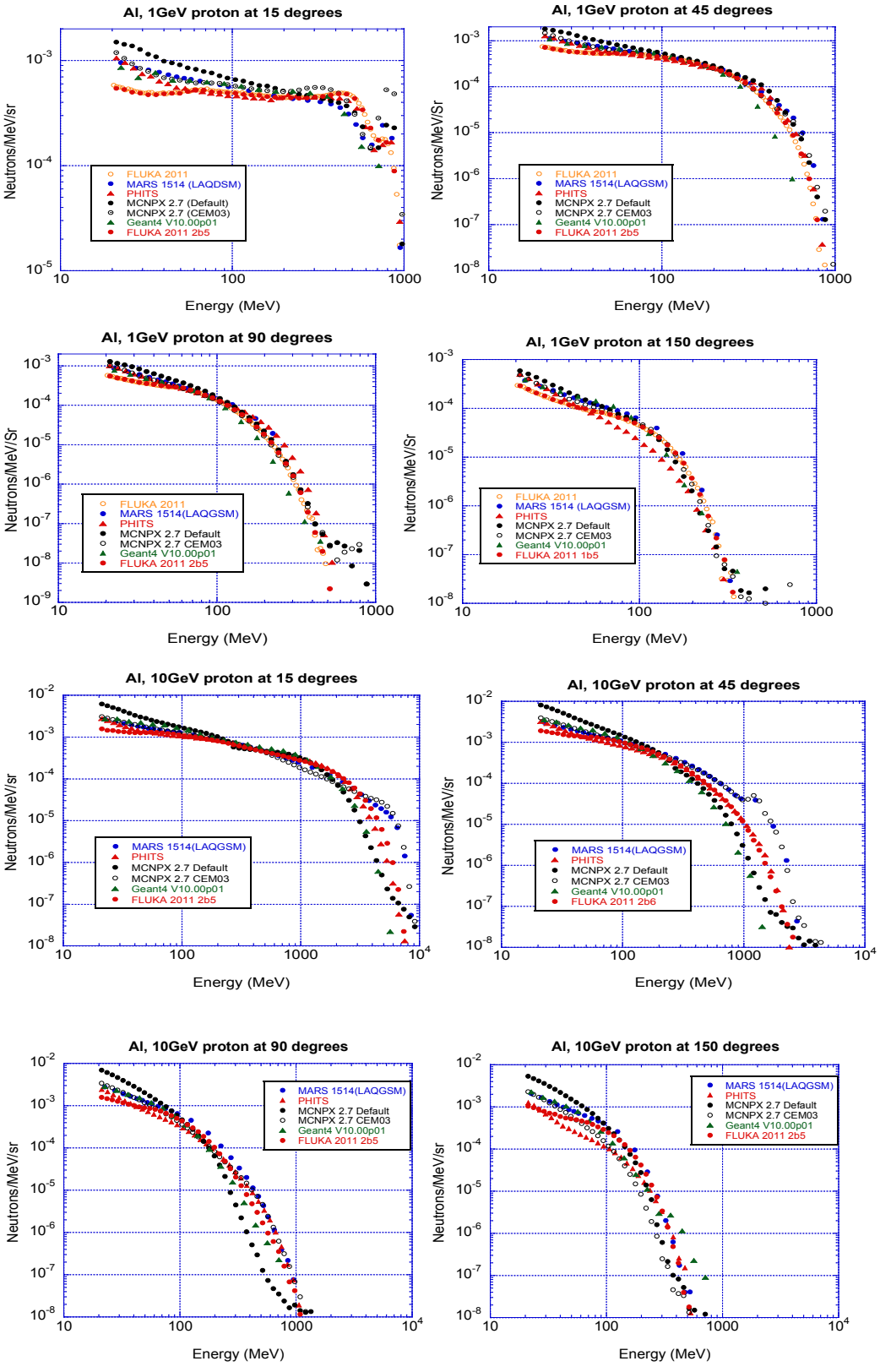

Figure 2. Neutron angular spectra from the Al target (continued)

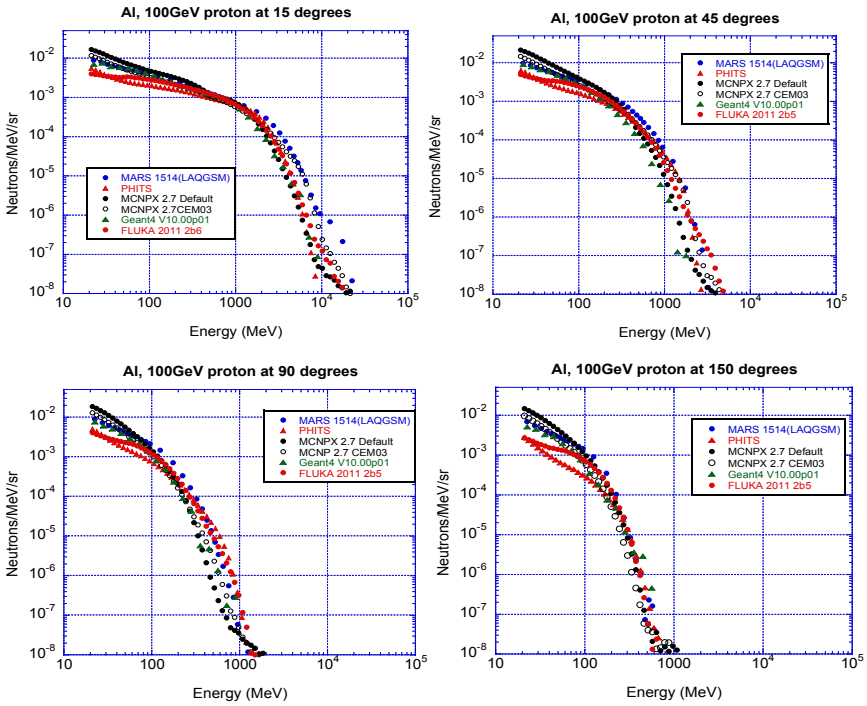

Figure 3. Neutron angular spectra from the Cu target

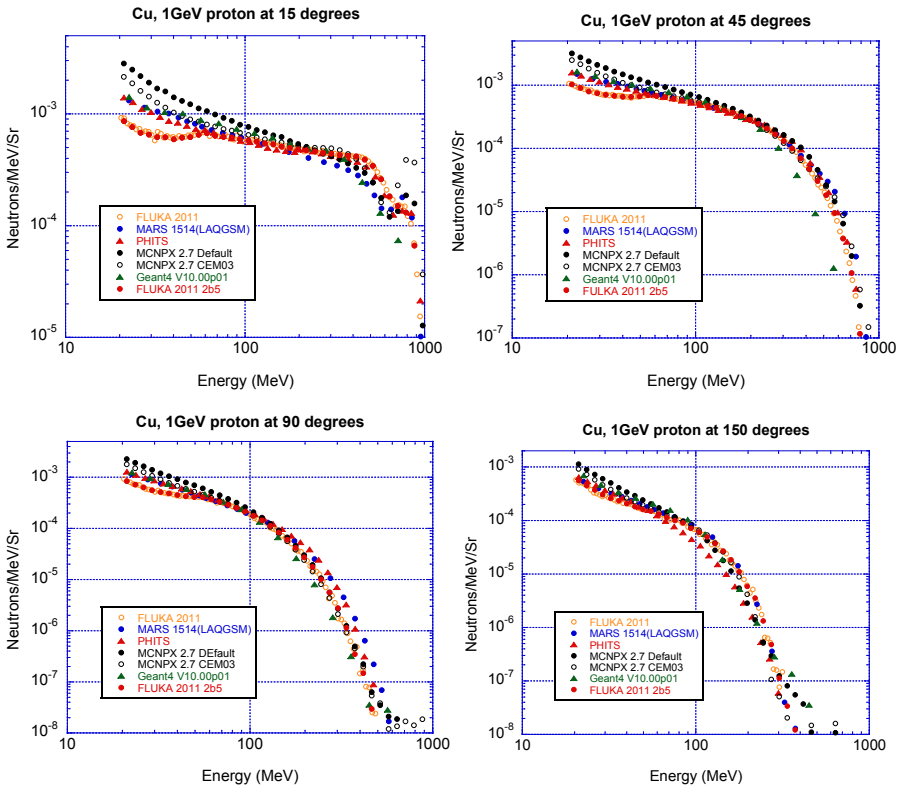

Figure 3. Neutron angular spectra from the Cu target (continued)

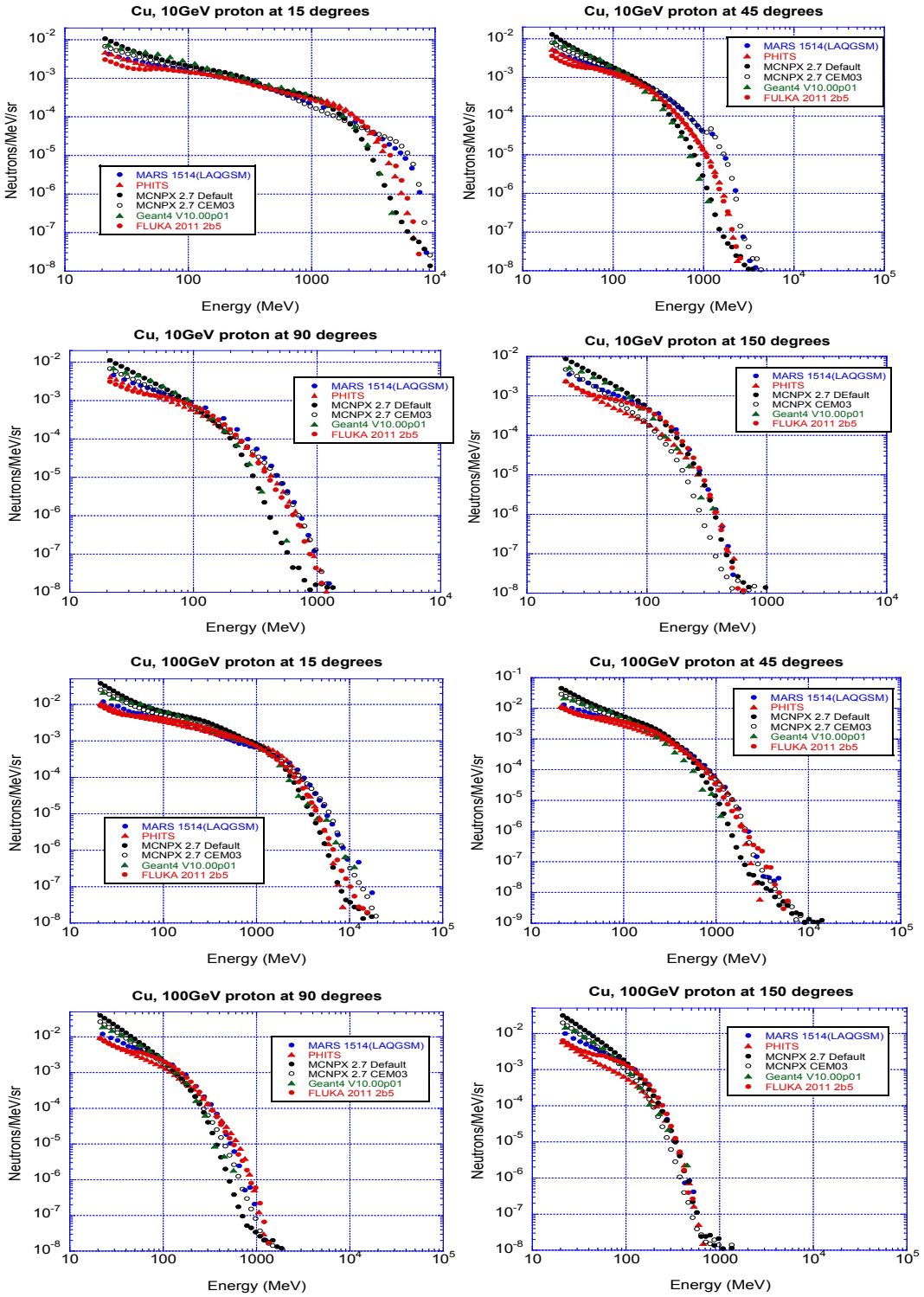

Figure 4. Neutron angular spectra from the Au target

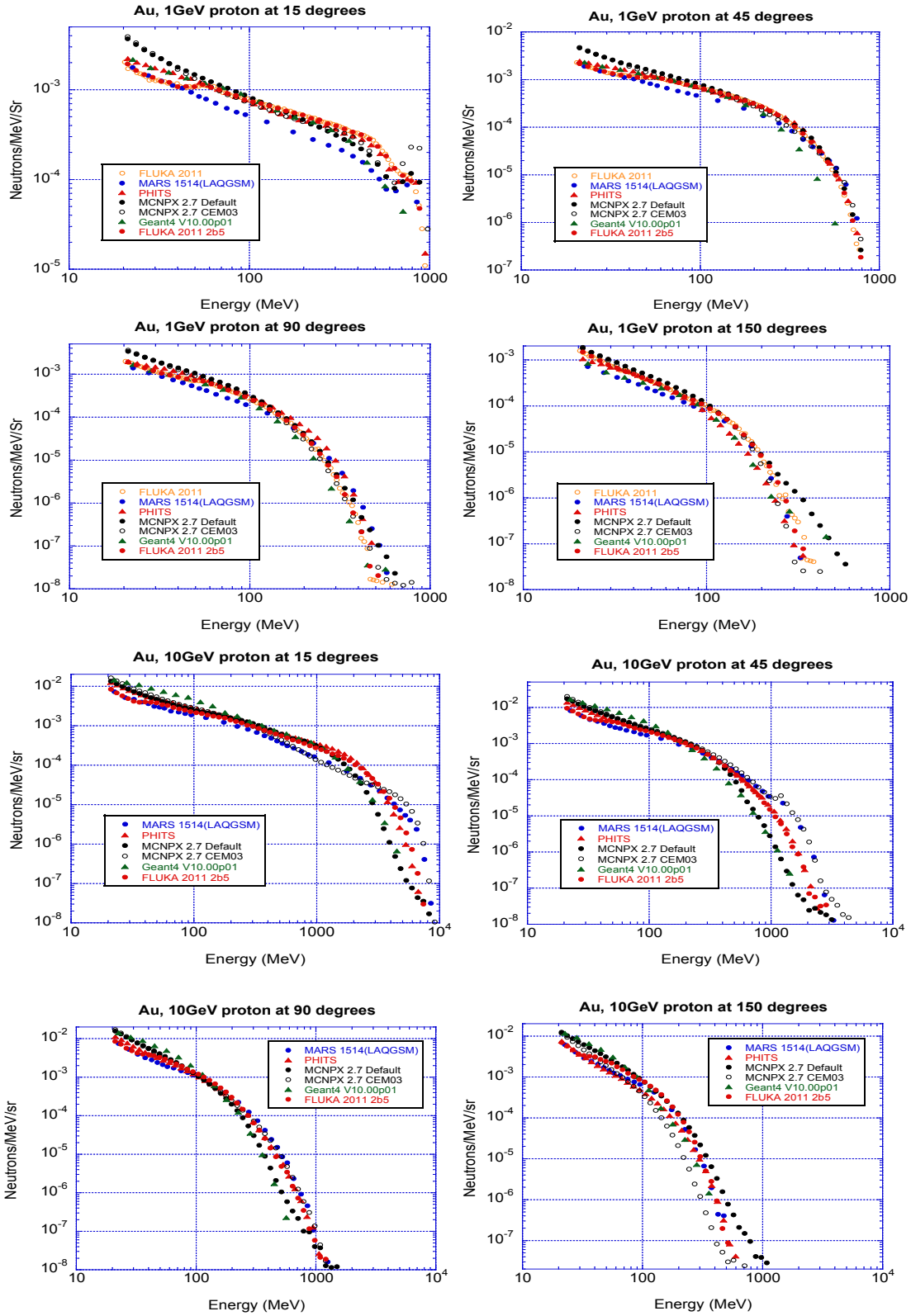

Figure 4. Neutron angular spectra from the Au target (continued)

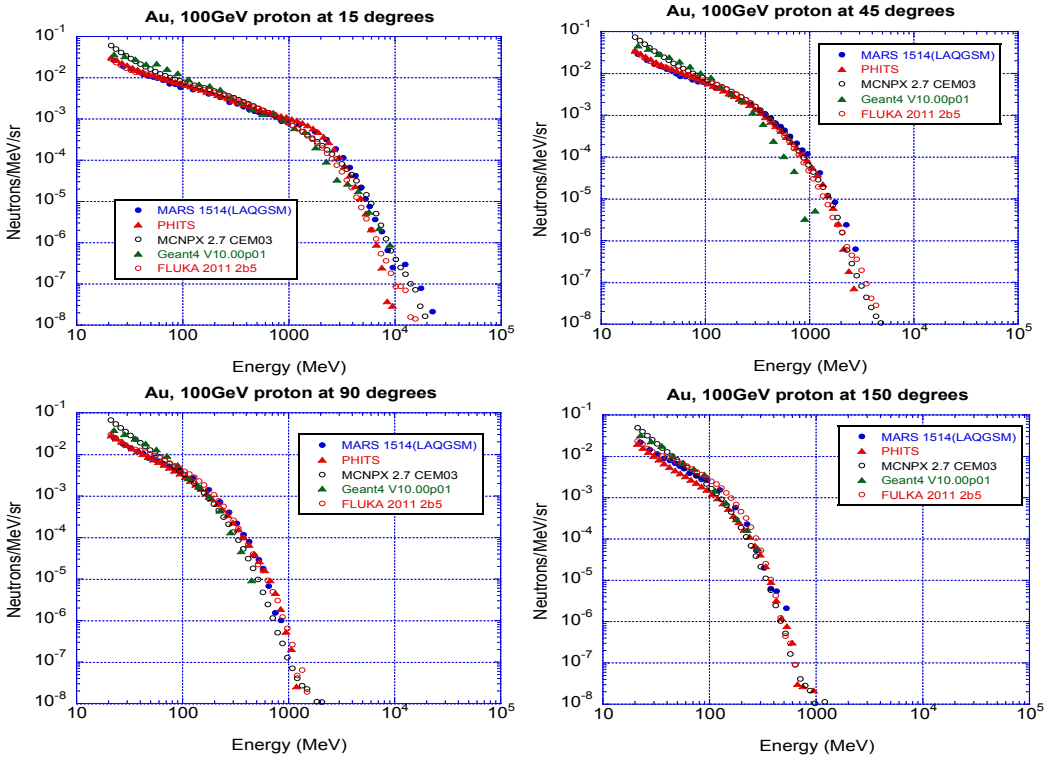

Figure 5. Neutron angular fluence above 20 MeV from the Al target

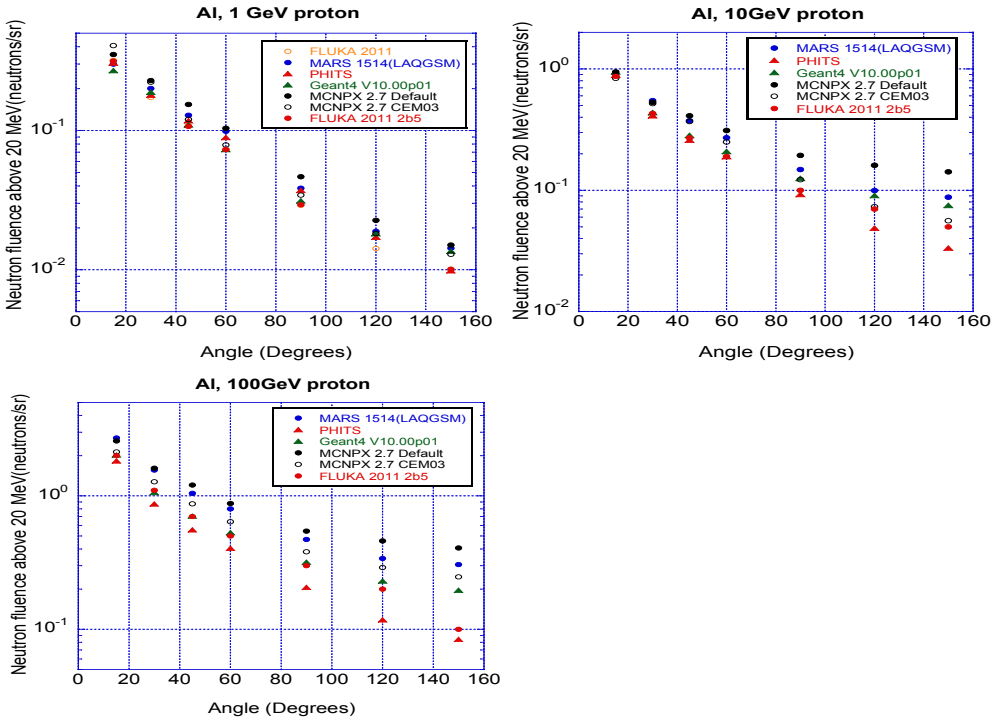

Figure 6. Neutron angular fluence above 20 MeV from the Cu target

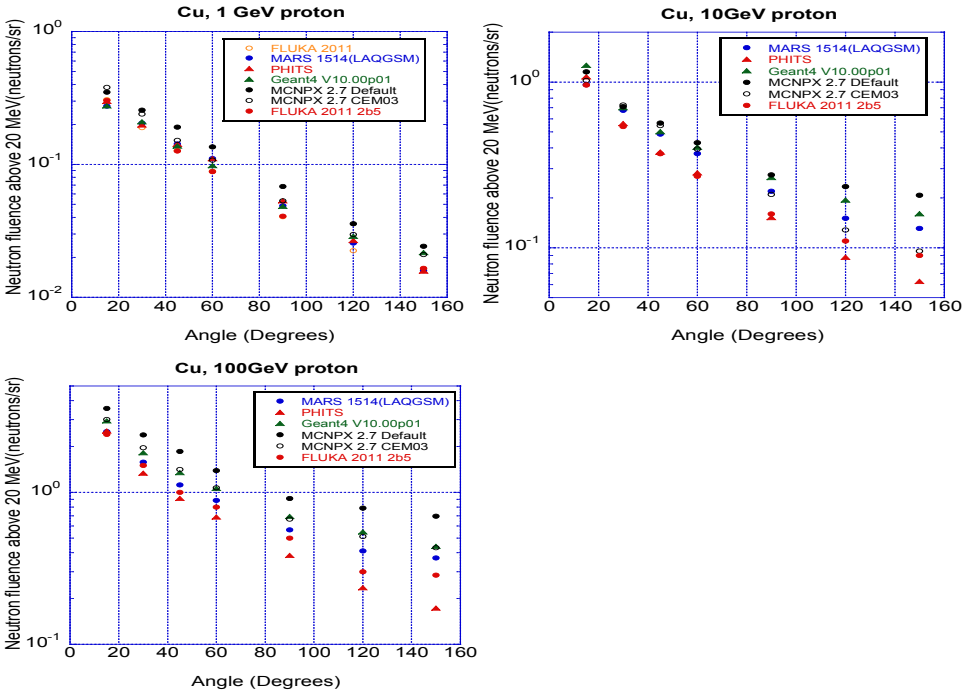

Figure 7. Neutron angular fluence above 20 MeV from the Au target

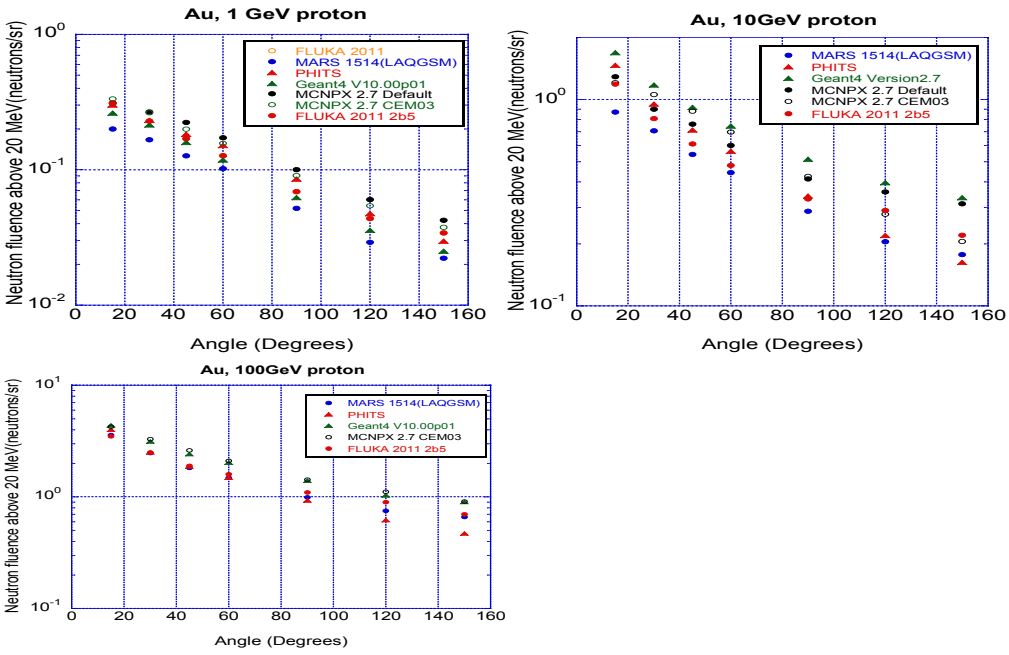

Results and discussions

Neutron angular spectra and fluence above 20 MeV

Figures 2 through 4 show the comparison of neutron angular spectra at 15, 45, 90 and 150 degrees for Al, Cu and Au, respectively. Figures 5 through 7 show the comparison of neutron fluence above 20 MeV.

Summary

From the comparison of spectra, the following results can be summarised:

- Differences among codes and models used are larger than expected.
- Differences at 15 degrees for 1 GeV are less than a factor of 3.
- The relation among codes and models used changes at several hundreds of MeV, except at 15 degrees for a 1 GeV proton. For example, the result of MCNPX(default) is the largest below 200 MeV at 15 degrees for 10 GeV protons on Al target and the smallest below 200 MeV. Differences in this energy region range between a factor of 2 and a factor of 5.
- Differences above this energy region become larger. The maximum differences are about a factor 10 and over a factor 100 and an order of 100 for 1, 10 and 100 GeV protons, respectively.
- Differences depend on the model used from the results of MCNPX with two production models.

From the comparison of fluences, the following results can be summarised:

- Fluence above 20 MeV mainly reflects differences below several hundred MeV.
- Differences among codes and models used do not depend on an angle for 1 GeV protons within a factor 1.5, 1.5 and 1.9 for Al, Cu and Au, respectively.
- Differences increase with increasing angle for 10 and 100 GeV protons within a factor of 5, 4 and 1.9, for Al, Cu and Au, respectively.

Future themes

As a next step, it will be necessary to study the following themes: (a) add angles of 0 and 180 degrees for spectral comparisons; (b) compare the total energy fluence at each angle; (c) compare the spectra with experimental results, particularly around 10 GeV and (d) present results using different models that can be used for each code.

References

[1] H. Hirayama et al. (1998), "Inter-comparison of the Medium-Energy Neutron attenuation in on and Concrete", *Shielding Aspects of Accelerators, Targets and Irradiation Facilities (SATIF-3)*, Tohoku University 12-13 May, 1997, pp.185-195, OECD/NEA, Paris.

[2] H. Hirayama et al. (1999), "Inter-comparison of the Medium-Energy Neutron attenuation in Iron and Concrete (2)", *Shielding Aspects of Accelerators, Targets and Irradiation Facilities (SATIF4)*, Knoxville, Tennessee, US, 17-18 September, pp.143-154, OECD/NEA, Paris.

[3] H. Hirayama et al. (2001), "Inter-comparison of the Medium-Energy Neutron attenuation in Iron and Concrete (3)", *Shielding Aspects of Accelerators, Targets and Irradiation Facilities (SATIF-5)*, Paris, France, 18-21 July, 2000, pp.189-201, OECD/NEA, Paris.

[4] H. Hirayama et al. (2003), "Inter-comparison of the Medium-Energy Neutron attenuation in Iron and Concrete (4)", *Shielding Aspects of Accelerators, Targets and Irradiation Facilities (SATIF6)*, SLAC, US, 10-12 April, 2002, pp.173-182, OECD/NEA, Paris.

[5] H. Hirayama et al. (2005), "Inter-comparison of the Medium-Energy Neutron attenuation in Iron and Concrete (5)", *Shielding Aspects of Accelerators, Targets and Irradiation Facilities (SATIF7)*, Sacavém, Portugal 17-18 May, 2004, pp.117-126, OECD/NEA, Paris.

[6] H. Hirayama et al. (2010), "Inter-comparison of the Medium-Energy Neutron attenuation in Iron and Concrete (6)", *Shielding Aspects of Accelerators, Targets and Irradiation Facilities (SATIF8)*, Pohang Accelerator Laboratory, Republic of Korea, 22-24 May, 2006, pp.237-250, OECD/NEA, Paris.

[7] H. Hirayama et al. (2010), "Inter-comparison of the Medium-Energy Neutron attenuation in Iron and Concrete (7)", *Shielding Aspects of Accelerators, Targets and Irradiation Facilities (SATIF9)*, ORNL, Tennessee, US, 21-28 April, 2008, pp.261-274OECD/NEA, Paris.

[8] H. Hirayama et al. (2010), "Inter-comparison of the Medium-Energy Neutron attenuation in Iron and Concrete (8)", *Shielding Aspects of Accelerators, Targets and Irradiation Facilities (SATIF10)*, CERN, Geneva, Switzerland, 2-4 June, 2010, pp.217-234, OECD/NEA, Paris.

[9] G. Battistoni, S. Muraro, P.R. Sala, F. Cerutti, A. Ferrari, S. Roesler, A. Fasso`, J. Ranft (2007), "The FLUKA code: Description and benchmarking", *Proceedings of the Hadronic Shower Simulation Workshop 2006*, Fermilab 6-8 September 2006, M.Albrow, R. Raja eds., *AIP Conference Proceeding* 896, pp.31-49.

[10] A. Ferrari, P.R. Sala, A. Fasso, J. Ranft (2005), "FLUKA: A multi-particle transport code", CERN-2005-10, INFN/TC_05/11, SLAC-R-773.

[11] N.V. Mokhov (1995), "The Mars Code System User's Guide", Fermilab-FN-628.

[12] O.E. Krivosheev, N.V. Mokhov (2000), "MARS Code Status", *Proceedings of Monte Carlo 2000 Conference*, Lisbon, 23-26 October, 2000, pp. 943.; Fermilab-Conf-00/181.

[13] N.V. Mokhov (2003), "Status of MARS Code", Fermilab-Conf-03/053.

[14] N.V. Mokhov, K.K. Gudima, C.C. James et al. (2004), "Recent Enhancements to the MARS15 Code", Fermilab-Conf-04/053; http://www-ap.fnal.gov/MARS/.

[15] T. Sato, K. Niita, N. Matsuda, S. Hashimoto, Y. Iwamoto, S. Noda, T. Ogawa, H. Iwase, H. Nakashima, T. Fukahori, K. Okumura, T. Kai, S. Chiba, T. Furuta, L. Sihver (2013), "Particle and Heavy Ion Transport Code System PHITS, Version 2.52", *Journal of Nuclear Science and Technology,* 50:9, pp.913-923.

[16] K. Niita, T. Sato, H. Iwase, H. Nose, H. Nakashima, L. Sihver (2006), "PHITS-a particle and heavy ion transport code system", *Radiation Measurement,* 41, pp.1080-1090.

[17] S. Agostinelli et al. (2003), "Geant4 – A Simulation Toolkit", *Nuclear Instruments and Methods in Physical Research A*, 506, pp.250-303.

[18] IEEE Transactions on Nuclear Science 53 No. 1 (2006), pp.270-278.

[19] D.B. Pelowitz (2011), "MCNPX User's Manual, Version 2.7.0", *Report LA-CP-11-00438*, Los Alamos National Laboratory, Los Alamos, New Mexico.

Code inter-comparison and benchmark for muon fluence and absorbed dose induced by an 18 GeV electron beam after massive iron shielding

Alberto Fassò[1], Alfredo Ferrari[2], Anna Ferrari[3], Nikolai V. Mokhov[4], Stefan E. Müller[3], Walter Ralph Nelson[5], Stefan Roesler[2], Toshiya Sanami[6], Sergei I. Striganov[4], Roberto Versaci[1]

[1]ELI Beamlines, Czech Republic
[2]CERN European Organisation for Nuclear Research, Switzerland
[3]Institute of Radiation Physiscs, Helmholtz-Zentrum Dresden-Rossendorf, Germany
[4]Fermi National Accelerator Laboratory, US
[5]SLAC National Accelerator Laboratory (retired), US
[6]KEK High Energy Accelerator Research Organisation, Japan

Abstract

In 1974, Nelson, Kase and Svenson published an experimental investigation on muon shielding, using the SLAC high-energy linac [1]. They measured muon fluence and absorbed dose induced by a 18 GeV electron beam hitting a copper/water beamdump and attenuated in a thick steel shielding. In this paper, the authors compared the results with the theoretical models available at the time. In order to compare their experimental results with present model calculations, we use the modern transport Monte Carlo codes MARS15, FLUKA2011 and GEANT4 to model the experimental set-up and run simulations. The results will then be compared between the codes and with the SLAC data.

Introduction

It has been stressed recently [2] that a good understanding of muon photoproduction by high-energy, high-intensity beams of photons or electrons is crucial in the shielding design for future beam facilities like the ELI beamlines facility in Prague [3]. The same holds for upcoming projects at LCLS (SLAC) and the planned ILC in Japan. The underlying question is how well the theoretical models for photoproduction of muons in current transport codes used for shielding design represent experimental data. We have therefore prepared benchmark calculations using the codes MARS15, FLUKA2011 and GEANT4 in order to compare them to data from an experiment performed in 1974 at the Stanford Linear Accelerator Center in California. This will also lead to a code intercomparison concerning the implementation of muon photoproduction models in the different codes.

The experiment

In 1974, Nelson, Kase, and Svenson carried out an experimental investigation at SLAC to study the muon fluence and absorbed dose induced by an 18 GeV electron beam hitting a copper/water beamdump [1]. In the vicinity of a nucleus, the electrons produced bremsstrahlung photons in the beamdump, which subsequently led to muon pair photoproduction. The muons were produced within 6 radiation lengths in the beamdump (corresponding to 22.23 cm), and were subsequently attenuated by thick blocks of

shielding iron. The lateral distribution of the muon fluence and the absorbed dose were measured by positioning detectors perpendicular to the incident electron beam axis in four narrow gaps (gap A, gap B, gap C, gap D) between the iron shielding blocks. The muon fluence was detected using 400 μm thick nuclear track emulsion plates, which were read out by microscopes after the exposure. Thermoluminescent dosimeters were used to register the absorbed dose. In addition, two scintillation counters determined the exposure and also cross-checked the muon fluence measurements. The geometry of the set-up allowed performing measurements at vertical angles from 0 to 150 milliradians. Within this range, it is ensured that the direct flight paths from the muon production point in the beam dump to their detection are completely contained in the iron shielding. To protect the detectors against background radiation, the gaps A, B and C were covered with lead blocks on the side and on top. Gap D, which is the furthest away from the muon production point, was left exposed.

The authors compared their experimental results to the theoretical formulation derived in [4]. It was found that the muon fluence and absorbed dose were accurately predicted by the theory for polar angles below 30 milliradians, while for larger angles, the theoretical prediction underestimated both fluence and dose by an order of magnitude or more.

Transport codes

In 2007, a first comparison [5] was undertaken of the experimental data with the modern transport codes MARS [6-10] and FLUKA [11] [12]. Together with the observations made in the shielding design for the ELI beamlines facility in Prague [3], this inspired the idea to repeat the comparison with the newest versions of the two codes, and also include the GEANT4 [13][14] toolkit as a third transport code into the comparison.

MARS15

The MARS code is a general-purpose, all-particle Monte Carlo simulation code. It contains established theoretical models for strong, weak and electromagnetic interactions of hadrons, heavy ions and leptons. Most processes can be treated either exclusively (analogously), inclusively (with corresponding statistical weights) or in a mixed mode. There are several options for the geometry, with "extended" or ROOT-based [15] modes as the most commonly used ones. Photoproduced muons are included in the MARS code in two ways:

- An exclusive muon generator based on the Weizsäcker-Williams approximation using algorithms based on the work of [16]. Only coherent photomuon production is simulated. This generator is used as the default generator for muon production.
- An inclusive muon generator based on the calculation of the lowest-order Born approximation in [17] [18] for targets of arbitrary mass, spin and form factor as well as arbitrary final states.

Both models give practically identical results for photon energies larger than 10 GeV. At lower energies, a precise description of the nuclear form factors becomes important. MARS supports two options for the description of the nuclear density for the inclusive muon generator: the original Tsai power-law mode and a symmetrised Fermi function. Angular and momentum distributions of muons produced by bremsstrahlung photons of 18 GeV electrons in copper simulated with the inclusive and the exclusive generator are in close agreement. The Weizsäcker-Williams approximation is therefore adequate for the benchmark in question.

FLUKA2011

FLUKA is a fully integrated particle physics Monte Carlo simulation package containing implementations of sound and modern physical models. A powerful graphical interface

(FLAIR [19]) facilitates the editing of FLUKA input, execution of the code and visualisation of the output. Photomuon production in FLUKA is implemented in the Weizsäcker-Williams approximation using the formalism of [17] [18]. Only coherent photomuon production is simulated.

GEANT4.10

The GEANT4 toolkit is the successor of the series of GEANT programs for geometry and tracking developed at CERN. It is based on object-oriented software technology. GEANT4 represents a set of software tools from which the user needs to program his own application. The implementation of muon pair production is described in [16] and is based on the work in [20].

The geometry of the experiment has been modelled using the three codes based on information from [1] [21]. Vertical views of the resulting geometries can be seen in Figure 1 (MARS), Figure 2 (FLUKA) and Figure 3 (GEANT4). Figure 1 also indicates the location of the beamdump and the gaps in which the detectors were placed in the experiment. The electron beam is coming from the left and hit the beamdump. While the geometries in Figures 1-3 still show some minor differences concerning dimensions and material between the different codes, a consistent geometry was defined at the SATIF-12 workshop, which will be used in upcoming simulation campaigns with all three codes.

Scoring and simulation parameters

In order to score the results with the different transport codes and compare with the experimental results, the following scorers were defined:

- The muon fluence in the 4 gaps normalised to the integrated electron charge on the beam dump (in μ/cm^2/Coulomb).
- The absorbed dose in the 4 gaps normalised to the integrated electron charge on the beam dump (in rad/Coulomb). To simulate the dose deposition in the thermoluminescent dosimeters, thin layers of LiF (500μm thickness) are placed in each gap.
- Several double-differential scorers in energy and angle for muons crossing the copper-water intersections over approximately 6 radiation lengths in the beamdump allow cross-checking the implementation of muon photoproduction in the different codes.

For MARS, scoring distributions are obtained via post-processing using PAW. FLUKA scoring distributions are obtained from the built-in scorers and post-processing is performed using FLAIR [20]. With GEANT4, a mixture of built-in scoring and ROOT histograms [15] is used.

The following simulation parameters and configuration options are used in the simulations:

- MARS (used version: MARS15 2014):
  - Generation and transport thresholds were set at 2 GeV in the beamdump, at 1 GeV in the shielding upstream, and at the following values elsewhere: 0.001 eV for neutrons, 1 MeV for muons, heavy ions and charged hadrons, 0.1 MeV for photons, and 0.2 MeV for electrons.

- FLUKA (used version: FLUKA2011.2b.6):
  - Defaults for precision simulations are used;
  - Production and transport thresholds for electrons and photons are set to 100 keV and 10 keV, respectively;
  - Full simulation of muon nuclear interactions and production of secondary hadrons switched on;
  - Production of secondaries for muons and charged hadrons switched on (100 keV threshold).
- GEANT4 (used version: GEANT4.10p1):
  - Basic physics list with quark gluon string and Bertini models is used, with parameters for electromagnetic physics tuned for high precision;
  - Additional process for gamma conversion to muons switched on for photons;
  - Additional process for muon-nucleus interactions switched on for muons;
  - Range threshold for gamma, electron, positron, proton: 700 μm.

Preliminary results

To date, preliminary results exist only for FLUKA-based simulations. Simulation campaigns with MARS and GEANT4 are in progress, but no results are available yet. Figure 4 shows the muon fluence registered in the four gaps for data (black triangles) compared to the FLUKA simulation (red squares) with 5 million simulated events. The agreement between the simulated and experimental data sets is quite good. The same holds for Figure 5, in which the absorbed dose is plotted for data and FLUKA simulation (same symbols and colorcodes as in Figure 4 apply), with the exception of gap D, where the lack of lead shielding in the experiment leads to a constant off-set in the data for angles above 60 milliradians, which was already noted in [1]. In particular, it can be concluded that both in Figures 4 and 5, an underestimation of both fluence and dose for angles above 30 milliradians, as reported in [1], is not observed. The simulations in Figures 4 and 5 were performed using cast iron with a density ρ=7.0 g/cm^3 for the material of the shielding blocks. Due to the fact that the exact density of the material used to construct the shielding blocks is not known at the moment, additional simulations were performed using steel with a density of ρ=7.6 g/cm^3 as shielding material. The corresponding results for gap A are shown in Figures 6 (muon fluence) and 7 (absorbed dose). A clear effect of the different materials is visible only for muon fluence at angles <60 milliradians, with steel giving a lower value for muon fluence than iron. For larger angles and for the absorbed dose, the effect is masked by the current statistical uncertainties of the simulations.

Figure 1. Geometrical model of the experimental set-up using MARS15

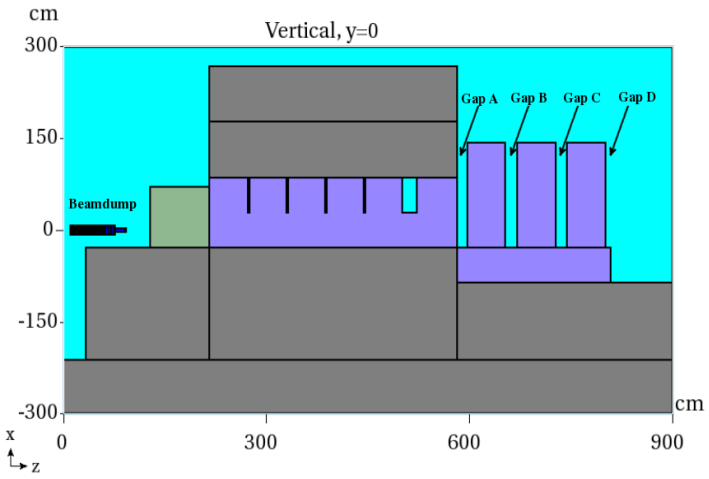

Figure 2. Geometrical model of the experimental set-up using FLUKA2011

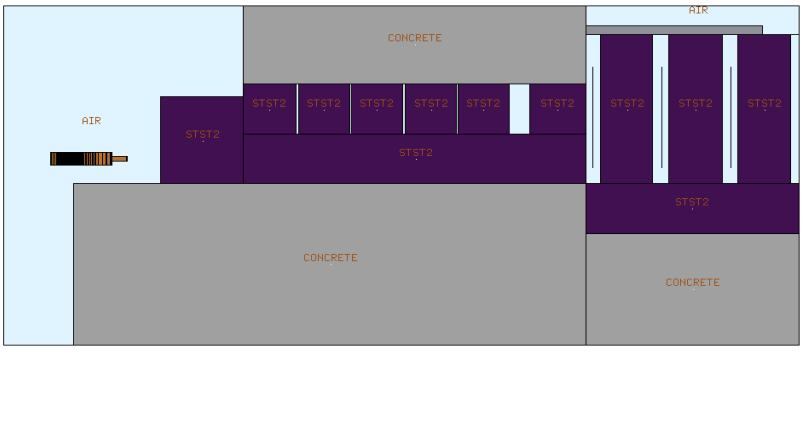

Figure 3. Geometrical model of the experimental set-up using GEANT4.10

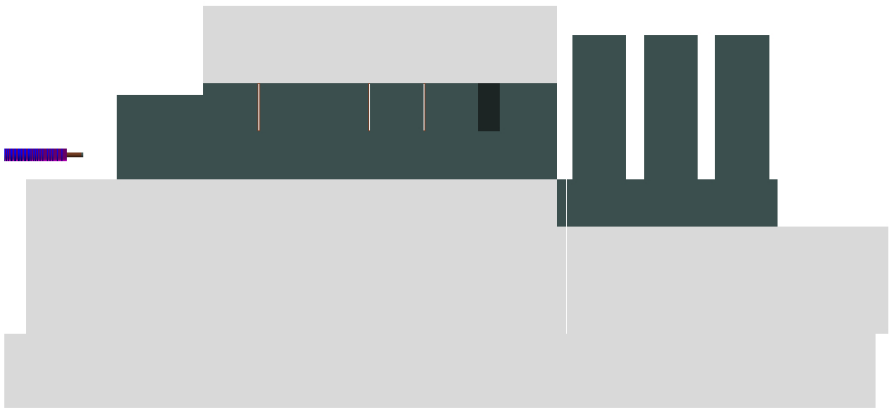

Figure 4. Preliminary results for muon fluence in gap A-D for FLUKA simulation compared to data

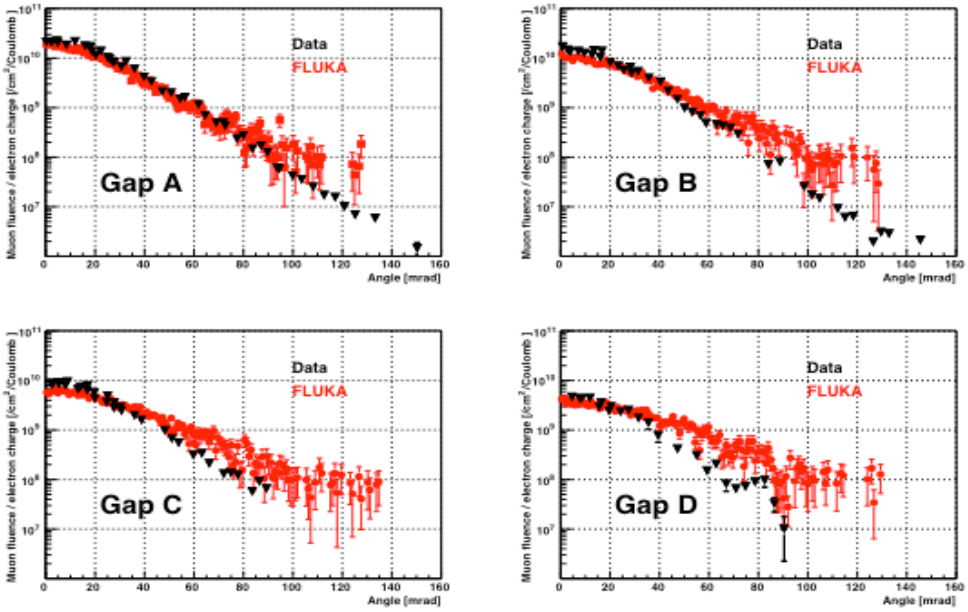

Figure 5. Preliminary results for absorbed dose in gap A-D for FLUKA simulation compared to data

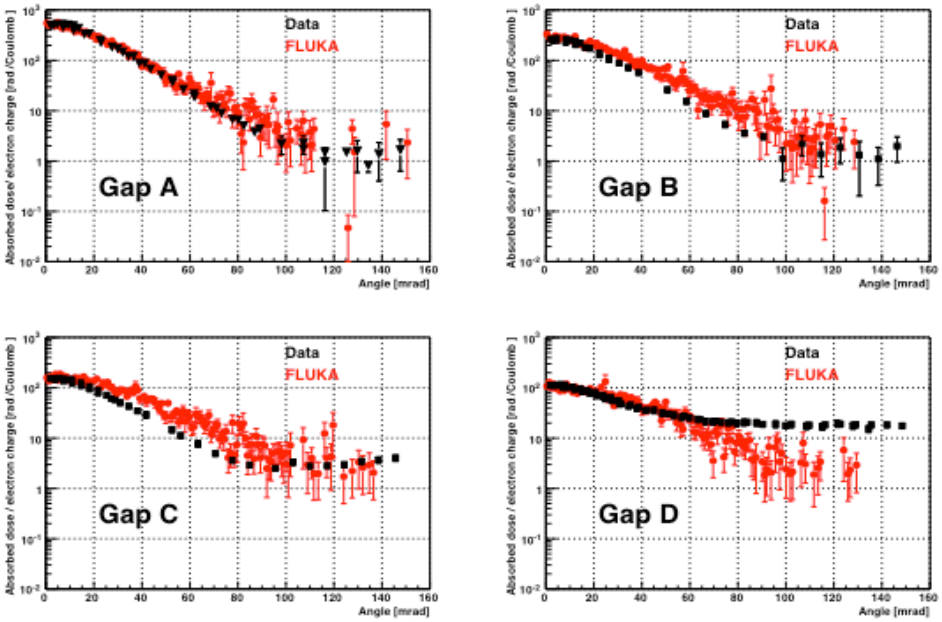

Figure 6. Preliminary results for muon fluence in gap A for FLUKA simulations and data

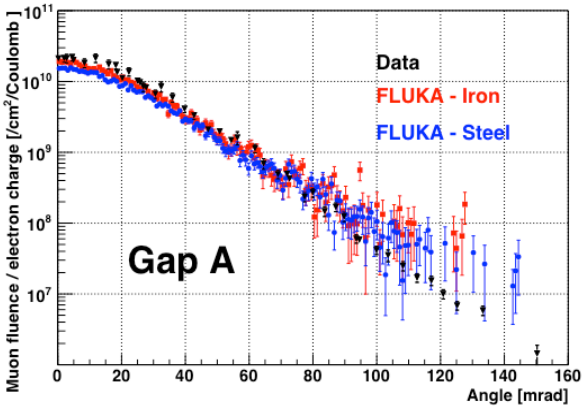

Figure 7: Preliminary results for absorbed dose in gap A for FLUKA simulations compared to data

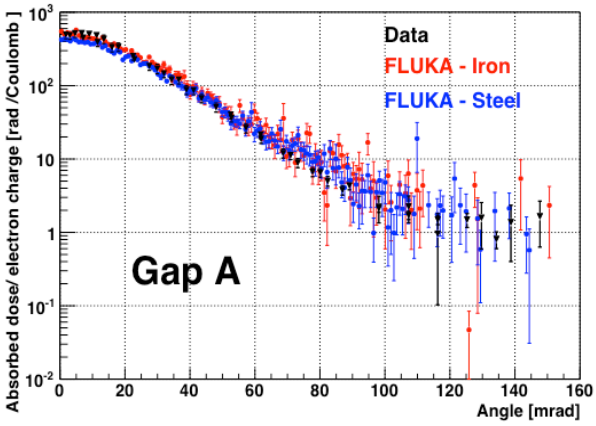

Summary and conclusions

Based on the experimental results on muon production by an 18 GeV e- beam hitting a copper-water target reported by Nelson, Kase and Svensson, the Monte Carlo transport codes MARS, FLUKA and GEANT4 have been used to model the experimental conditions. First preliminary results on muon fluence and absorbed dose have been produced with FLUKA. The agreement between the simulated results and the experimental values is quite promising. Results with the Monte Carlo transport codes MARS and GEANT4 are expected to follow soon. Some uncertainties about actual geometry and material composition still exist. The original logbooks of the experiment, which are currently being retrieved, may be of help here. Further refinement of the simulations together with consistency checks will allow comparing the implementation of muon production and transport in the different Monte Carlo codes.

References

[1] W.R. Nelson, K.R. Kase, G.K. Svensson (1974), "Muon Shielding Around High-Energy electron Accelerators, Part 2. Experimental Investigation", *Nucl. Instrum. Meth.* 120, pp. 413-429.

[2] R. Versaci (2015), SATIF-12 Proceedings.

[3] M. Aleonard et al. (2011), "ELI-Extreme Light Infrastructure; Science and Technology with Ultra-Intense Lasers", THOSS Media GmbH, edited by G.A. Mourou, G. Korn, W. Sandner, J.L. Collier.

[4] W.R. Nelson, K.R. Kase (1974), "Muon Shielding Around High-Energy electron Accelerators. Part 1. Theory", *Nucl. Instrum. Meth.* 120, pp. 401-411.

[5] N.V. Mokhov, W.R. Nelson, T. Sanami (2007), "Code benchmark of muon flux after a several meters of iron from 14 and 18 GeV electron induced reactions in forward direction", *SLAC Radiation Physics Note* RP-07-15.

[6] N.V. Mokhov (1995), "The Mars Code System User's Guide", Fermilab-FN-628.

[7] O.E. Krivosheev, N.V. Mokhov (2000), "MARS Code Status", *Proc. Monte Carlo 2000 Conf.* p. 943, Lisbon, October 23-26, 2000; Fermilab-Conf-00/181.

[8] N.V. Mokhov, K.K. Gudima, C.C. James et al. (2004), "Recent Enhancements to the MARS15 Code", Fermilab-Conf-04/053.

[9] N.V. Mokhov, S.I. Striganov (2007), "MARS15 Overview", *Proc. of Hadronic Shower Simulation Workshop,* Fermilab, September 2006, AIP Conf. Proc. 896, pp. 50-60.

[10] http://www-ap.fnal.gov/MARS/.

[11] G. Battistoni, S. Muraro, P.R. Sala, F. Cerutti, A. Ferrari, S. Roesler, A. Fassò, J. Ranft (2007), "The FLUKA code: Description and benchmarking", *Proceedings of the Hadronic Shower Simulation Workshop 2006*, Fermilab 6-8 September 2006, M. Albrow, R. Raja eds., AIP Conference Proceeding 896, pp. 31-49.

[12] A. Ferrari, P.R. Sala, A. Fassò, J. Ranft (2005), "FLUKA: A multi-particle transport code", CERN-2005-10, INFN/TC_05/11, SLAC-R-773.

[13] S. Agostinelli et al. (2003), "GEANT4: A simulation toolkit", *Nucl. Instrum. Meth.* A506, pp. 250-303.

[14] J. Allison et al. (2006), "Geant4 developments and applications", *IEEE Transactions on Nuclear Science* 53 No.1 pp. 270-278.

[15] R. Brun, F. Rademakers (1997), "ROOT – An Object Oriented Data Analysis Framework", *Nucl. Instrum. Meth.* A 389, pp. 81-86.

[16] H. Burkhardt, S.R. Kelner, R.P. Kokoulin (2002), "Monte Carlo Generator for Muon Pair Production", CERN-SL-2002-016 (AP).

[17] Y.S. Tsai (1974), "Pair production and Bremsstrahlung of charged leptons", *Rev. Mod. Phys.* 46, pp. 815-851.

[18] Y.S. Tsai (1977), "Pair production and Bremsstrahlung of charged leptons (erratum)", *Rev. Mod. Phys.* 49, pp. 421-423.

[19] V. Vlachoudis (2009), "FLAIR: A Powerful But User Friendly Graphical Interface for FLUKA", *Proc. Int. Conf. on Mathematics*, Computational Methods and Reactor Physics, Saratoga Springs.

[20] S.R. Kelner, R.P. Kokoulin, A.A. Petrukhin (1995), "About cross section for high-energy muon bremsstrahlung", *Moscow Phys. Eng. Inst.* 024-95.

[21] W.R. Nelson, private communication.

Validating PHITS for heavy ion fragmentation reactions

Reginald M. Ronningen
Facility for Rare Isotope Beams (FRIB)
Michigan State University, East Lansing, US

Abstract

The performance of the Monte Carlo code system PHITS is validated for heavy-ion transport capabilities by performing simulations and comparing results against experimental data from heavy-ion reactions of benchmark quality. These data are from measurements of isotope yields produced in the fragmentation of a 140 MeV/u ^{48}Ca beam on a beryllium target and on a tantalum target. The results of this study show that PHITS performs reliably.

Introduction

The Facility for Rare Isotope Beams (FRIB) is being designed and established at Michigan State University as a DOE Office of Science national user facility for the study of nuclear structure, reactions, and astrophysics [1]. FRIB consists of a driver linac for the acceleration of stable heavy-ion beams, followed by a fragmentation separator and a stopped beam/ReAccelerating facility (ReA) [1]. Stable heavy-ion beams having >200 MeV/u at beam powers up to 400 kW will be used to produce rare isotopes by in-flight fragment separation in the fragmentation separator. Selected rare isotopes will be stopped and reaccelerated. Beginning in the Electron Beam Ion Trap (EBIT) charge state booster, beams from ReA3 will range in energy from 0.3 to 6 MeV/u. The maximum energy is 3 MeV/u for heavy nuclei such as uranium, and 6 MeV/u for ions having A<50. All rare isotope beams that can be produced by fragmentation or in-flight fission with sufficient intensity can be reaccelerated.

To support design and operations, the performance of the Monte Carlo code system PHITS [3] is validated for heavy-ion transport capabilities by performing calculations of rare isotope yields and comparing results against experimental data from heavy-ion reactions of benchmark quality [4]. The calculations have been compared to measurements of isotope production cross-sections from the fragmentation of a 140 MeV/u ^{48}Ca beam on a beryllium target and on a tantalum target [4]. The results of these comparisons can be used to suggest possible code improvements. Simulations were carried out using recent introduction of PHITS version 2.52 updated to version 2.64 of the PHITS code system, with comparisons to previous studies [7] using PHITS version 2.13.

Motivation

The first motivation of our study is that predictions of radionuclide distributions and residual radioactivity are especially important in determining inventories for facility licensing and for operational health physics and radiation protection purposes. These predictions can be obtained from Monte Carlo simulations that describe rare isotope production from the most important processes of spallation, fragmentation and fission

processes, followed by activation calculations of residual radioactivity build-up and decay. For safe operations it is important that calculations are accurate.

As an example, the rare isotope beam of ^{32}Mg (86 ms half-life) is possible for study at ReA. Although its half-life is very short, its decay includes beta-delayed neutron emission branches to daughters having half-lives much larger than the assumed typical irradiation time (here taken as 7 days). A summary of relevant decay properties of ^{32}Mg and its daughters are given in Table 1.

Table 1. ^{32}Mg parent, daughter half-lives and decay modes

Parent Nucleus	Parent Half Life	Decay Mode	Daughter Nucleus
$^{32}_{12}$Mg	86 ms	β- : 100.00 % β-n : 5.50 %	$^{32}_{13}$Al, $^{31}_{13}$Al
$^{32}_{13}$Al	33.0 ms	β- : 100.00 % β-n : 0.70 %	$^{32}_{14}$Si, $^{31}_{14}$Si
$^{31}_{13}$Al	644 ms	β- : 100.00 %	$^{31}_{14}$Si
$^{32}_{14}$Si	153 y	β- : 100.00 %	$^{32}_{15}$P
$^{31}_{14}$Si	157.3 m	β- : 100.00 %	$^{31}_{15}$P stable
$^{32}_{15}$P	14.262 d	β- : 100.00 %	$^{32}_{16}$S stable

The time evolution of a 10^6 ion/s beam of ^{32}Mg and daughter activities deposited in a stainless steel stopping target was calculated using DCHAIN-SP 2001 [8] and is shown in Figure 1. After the 7 day irradiation is stopped, the total activity is nearly constant at ~ 150 Bq for 10 years, owing to the long half-life of Si-32 that decays to ^{32}P. The extremity dose rate resulting from this activity is about 0.01 mGy/h, the level of which is important for health physics and radiological protection purposes. This result underscores that reliable calculations of rare isotope yields, in this case that of ^{32}Mg, are important for safe operations planning at a rare isotope beam facility.

Figure 1. Activity in a stopping stainless steel target as a function of time from a 7-d irradiation by a 10^6 pps ^{32}Mg beam

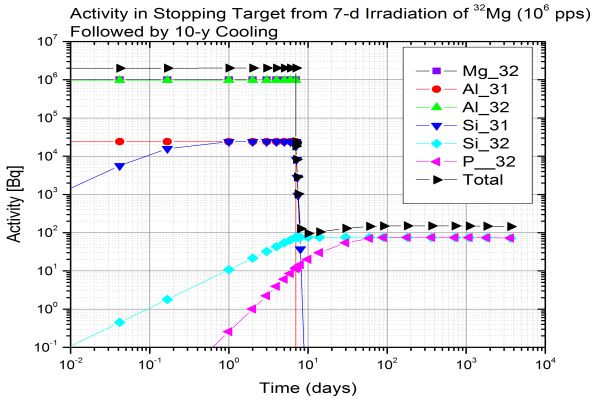

The total activity is the sum of activities from the decays of ^{32}Mg and its daughters.

The second motivation is to validate the default value of the "switching time" t_{sw} used in the JQMD model [9] within PHITS. The JQMD model treats dynamical processes in nucleus-nucleus collisions, e.g. direct and non-equilibrium reactions that form highly excited fragments. Later in the time evolution of these systems, the statistical model GEM [10] is used to describe statistical processes, e.g. decays of the fragments by fission and evaporation. Within PHITS simulations, the JQMD calculations of dynamical processes are stopped, excited nuclei are created, and results transferred to GEM for decay in a statistical way at the "switching time" specified by the parameter *nqtmax*. This parameter is necessary because of two-step nature of the calculations. The default value in PHITS is 150 fm/c (one fm c-1 is 3.3 x 10-24 s). Beginning with PHITS version 2.13, the parameter *nqtmax* can be set externally. We found previously [7] that calculations using 100 fm/c better described the heavy-ion fragmentation production cross-sections at 140 MeV/u (see Figure 2). Subsequently, Iwamoto et al. [11] used values for t_{sw} of 50, 100, and 150 fm c-1 to generate neutron energy spectra for comparison against experimental data [12] from 6.25 MeV amu-1 and 10 MeV amu-1 C-12 ions and 10 MeV amu-1 O-16 ions incident on a thick copper target. The shape of neutron energy spectra was compared with experimental data near the evaporation component. The slope is especially sensitive to the evaporations stage and thus to t_{sw}. Iwamoto et al. concluded that 100 fm/c is preferred over 150 fm/c to best describe the neutron energy spectra. Thus, establishing the best setting for the parameter nqtmax apparently will help serve to obtain the most reliable sets of calculated fragment production cross-sections and neutron energy spectra.

Figure 2. Comparisons of experimental fragmentation production cross-sections for sulphur isotopes from 140 MeV/u ^{48}Ca incident ion reactions with a Be target to calculations using PHITS versions 2.11 and 2.12 with the switching time parameter *nqtmax* set to 150 (default), 130, and 100 fm/c

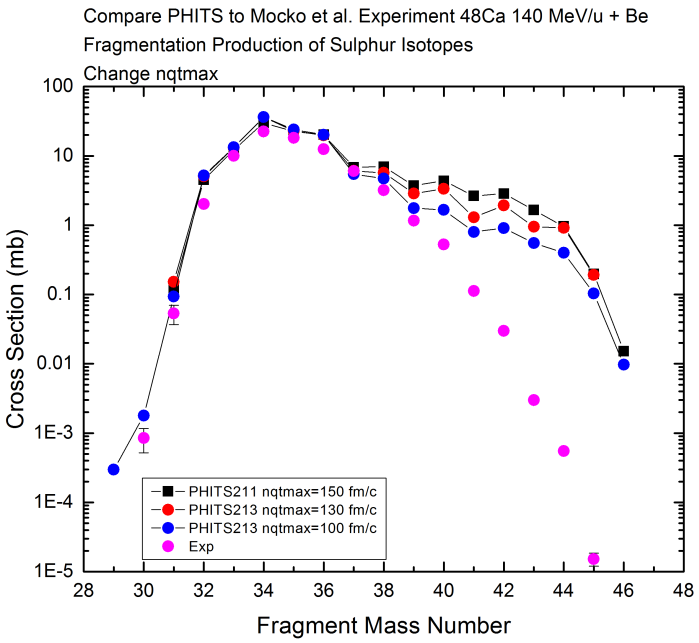

Figure 3. Neutron energy spectra using switching times 50, 100 and 150 fm/c for 10 MeV amu-1 C-12 incident ion reactions with a thick copper target

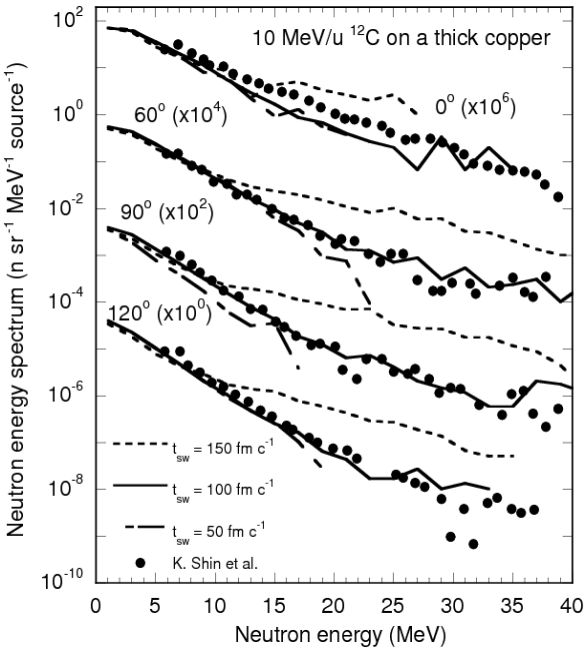

Fragment production calculations

Our studies were carried out on the isotope production cross-sections from projectile fragmentation reactions [4] using the ^{48}Ca beams at 140 MeV/u on beryllium and tantalum targets at the Coupled Cyclotron Facility at the National Superconducting Cyclotron Laboratory at Michigan State University. We performed calculations using PHITS version 2.64 to obtain fragmentation production cross-sections for those systems, and compared them with the measured values. Comparisons are made to previous calculations performed using PHITS version 2.13 [7].

The physics models used in the calculations, in addition to the JQMD model, were the INCL4.6 model [13] for light particle production and the Kuratoma model for calculating the total reaction cross-sections of nucleon–nucleus and nucleus–nucleus interactions [14]. The latter is set by parameters *icrhi* = 2 and *icxsni* = 1. The production cross-sections were obtained using the T-YIELD tally in PHITS. The *axis* = *dchain* option was used, which provides a table of isotope production sorted by element. The *unit* = 1 option was chosen, providing the production per beam particle. To convert the production to cross-section, the tally's multiplicative factor "*factor*" was set to $\frac{10^{27} mb-cm^{-2} \times target\ atomic\ mass}{Avogadro's Number \times target\ areal\ density}$. The target sizes and areal densities were taken from [4].

Results and discussion

Figure 4 shows the experimental measurements of cross-sections for phosphorus isotopes produced by 140 MeV/u ^{48}Ca incident ion reactions with a Be target compared to calculations by PHITS versions 2.13 and 2.64 with nqtmax = 100 fm/c and version 2.64 with nqtmax = 150 fm/c. Both versions significantly overpredict the data for the larger mass numbers. As observed previously [7], agreement between data and calculations is improved with nqtmax = 100 fm/c compared to the default value of 150 fm/c. Also, version 2.64 provides better agreement with the data than does version 2.13. The same

conclusions are reached for the measurements taken with the Ta target, as shown in Figure 5.

Figure 4. Comparisons of experimental fragmentation production cross-sections for phosphorus isotopes from 140 MeV/u ^{48}Ca incident ion reactions with a Be target to calculations using PHITS versions 2.13 and 2.64 with the switching time parameter *nqtmax* set to 150 (default) and 100 fm/c

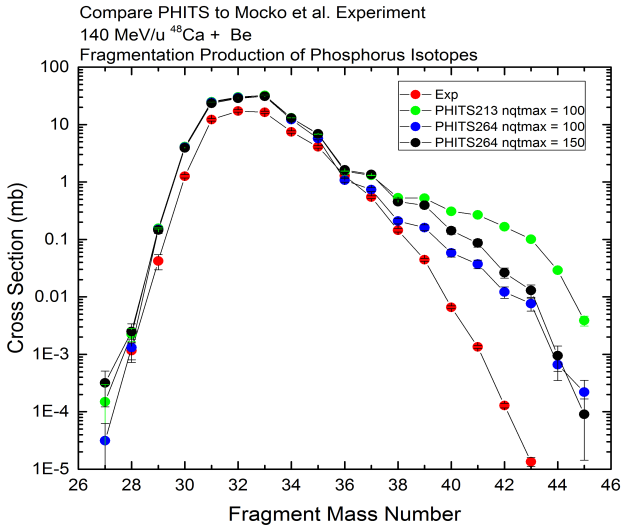

Figure 5. Comparisons of experimental fragmentation production cross-sections for phosphorus isotopes from 140 MeV/u ^{48}Ca incident ion reactions with a Ta target to calculations using PHITS versions 2.13 and 2.64 with the switching time parameter *nqtmax* set to 100 fm/c

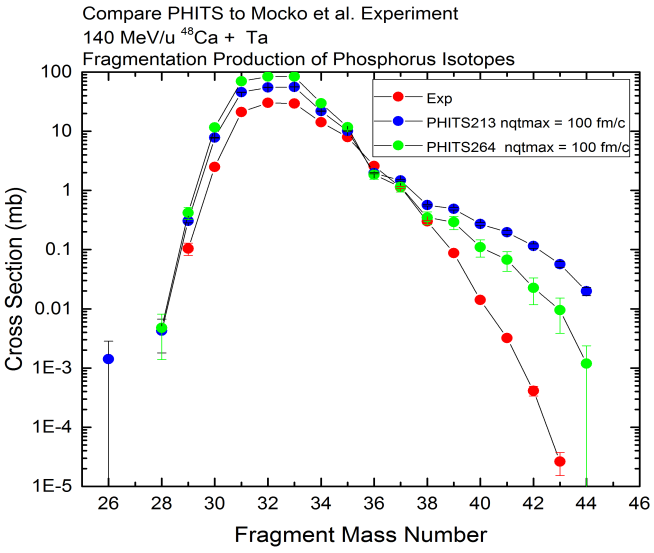

Focusing on production of lighter fragments, comparisons were made between data and calculations for the production of carbon isotopes. Figures 6 and 7 show the results for the Be target and the Ta target, respectively. In these cases, no clear choice can be made between the code versions or between the values of *nqtmax* for the values studied. It is noted that the calculations slightly under predict the data from the Be target for the larger mass numbers and that there is good agreement with data from the Ta target for both versions.

Figure 6. Comparisons of experimental fragmentation production cross-sections for carbon isotopes from 140 MeV/u ^{48}Ca incident ion reactions with a Be target to calculations using PHITS versions 2.13 and 2.64 with the switching time parameter *nqtmax* set to 100 and 150 fm/c

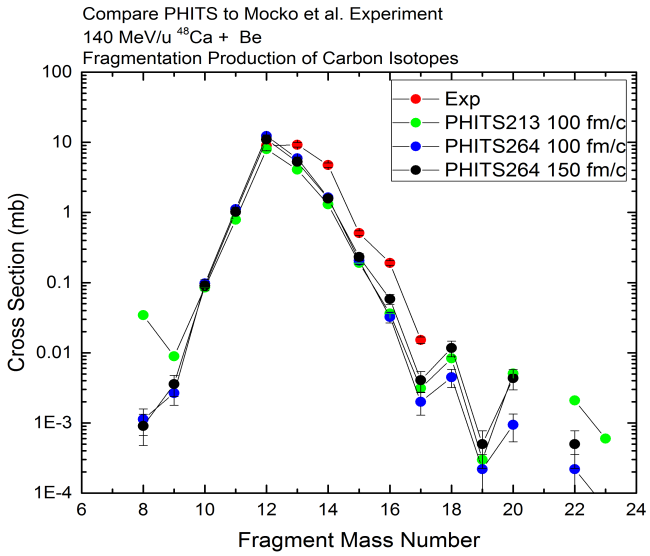

Figure 7. Comparisons of experimental fragmentation production cross-sections for carbon isotopes from 140 MeV/u ^{48}Ca incident ion reactions with a Ta target to calculations using PHITS versions 2.13 and 2.64 with the switching time parameter *nqtmax* set to 100 fm/c

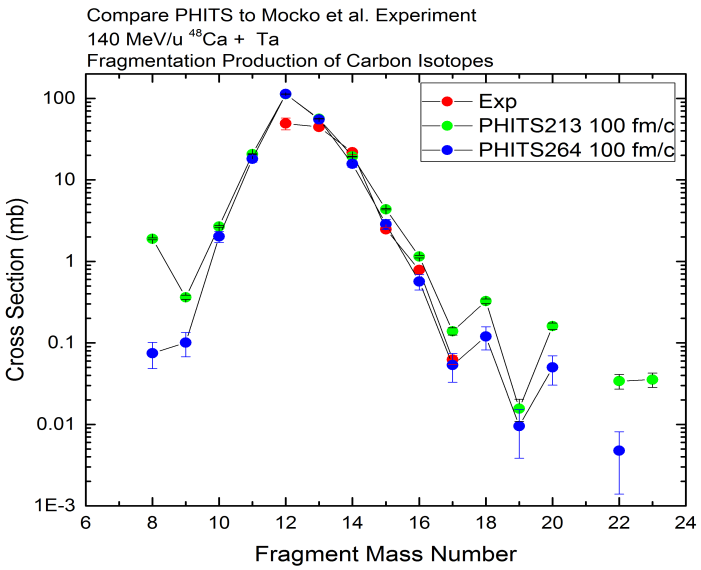

Focusing on production of the heaviest measured fragments, comparisons were made between data and calculations for the production of titanium isotopes. Figures 8 and 9 show the results for the Be target and the Ta target, respectively. It is noted that the calculations underpredict the data from the Be target and overpredict the data from the Ta target, and that no clear choice can be made between the code versions or between the values of *nqtmax* for the values studied.

Figure 8. Comparisons of experimental fragmentation production cross-sections for titanium isotopes from 140 MeV/u ^{48}Ca incident ion reactions with a Be target to calculations using PHITS versions 2.13 and 2.64 with the switching time parameter *nqtmax* set to 100 and 150 fm/c

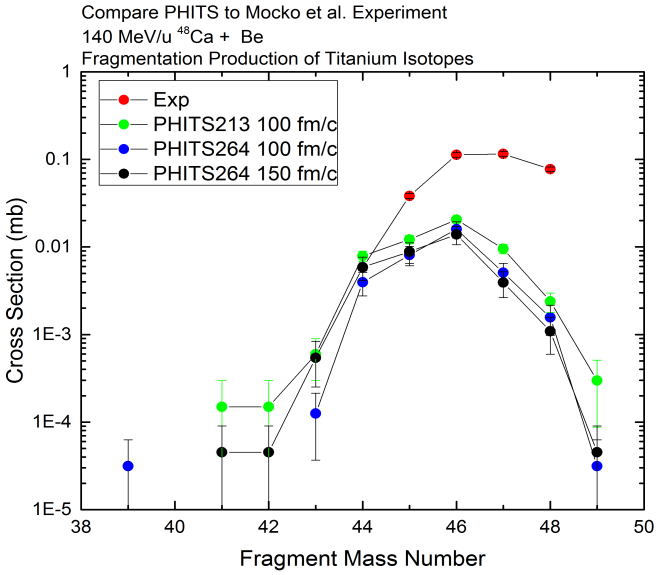

Figure 9. Comparisons of experimental fragmentation production cross-sections for titanium isotopes from 140 MeV/u ^{48}Ca incident ion reactions with a Ta target to calculations using PHITS versions 2.13 and 2.64 with the switching time parameter *nqtmax* set to 100 fm/c

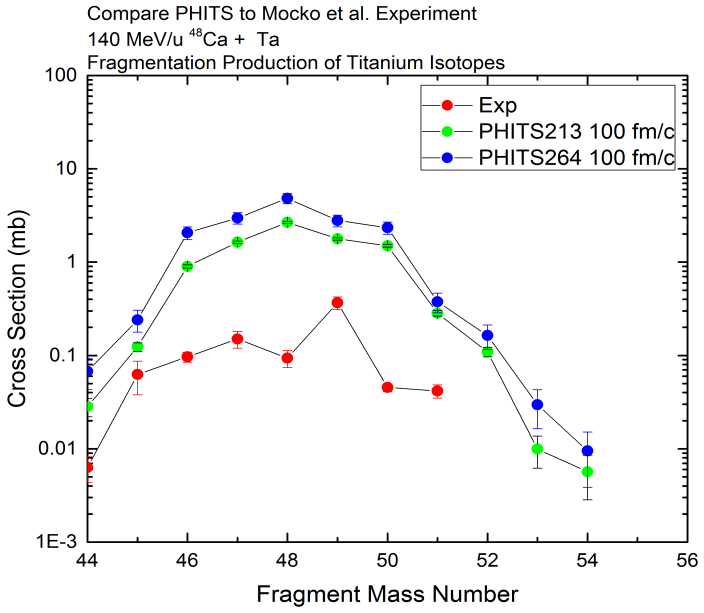

Summary

Reliable calculations of rare isotope yields are important for safe operations planning at FRIB and other rare isotope beam facilities. The recent introduction of PHITS version 2.52 updated to version 2.64 contains many new models and other improvements. Our study of fragment production cross-sections is limited in scope, but the impact of those improvements is evident in that we have found that version 2.64 performs better than version 2.13. In this study, we have found that comparisons to data are improved using the switching time parameter *nqtmax* = 100 fm/c rather than the default value of 150 fm/c. We plan to continue our tests, to provide performance feedback to the PHITS authors and to solicit suggestions from them on improving our calculations.

Acknowledgements

This material is based upon work supported by the US Department of Energy Office of Science under Cooperative Agreement DE-SC0000661, the State of Michigan and Michigan State University. Michigan State University designs and establishes FRIB as a DOE Office of Science National User Facility in support of the mission of the Office of Nuclear Physics.

References

[1] J. Wei et al. (2013), "Progress at MSU towards a Facility for Rare Isotope Beams", *Proceedings of PAC2013,* pp. 1453-1457, Pasadena, CA, US.

[2] O. Kester et al. (2010), "Rea3 – The Rare Isotope ReAccelerator at MSU", LINAC2010, Tsukuba, Japan; D. Leitner et al. (2013), "Status of the Rare Isotope Reaccelerator Facility REA", PAC2013, Pasadena, CA, US.

[3] T. Sato et al. (2013), "Particle and Heavy Ion Transport Code System PHITS", Version 2.52, *J. Nucl. Sci. Technol.* 50[9], pp. 913-923.

[4] M. Mocko et al. (2006), "Projectile fragmentation of Ca40, Ca48, Ni58, and Ni64 at 140 MeV/nucleon", *Phys. Rev*. C 74, pp. 054612-1 – 054612-11.

[5] M. Mocko et al.(2007), "Projectile fragmentation of Kr^{86} at 64 MeV/nucleon" *Phys. Rev*. C 76, pp. 014609-1 - 014609-6.

[6] S. Lukyanov et al. (2009), "Projectile fragmentation of radioactive beams of Ni^{68}, Cu^{69}, and Zn^{72}", *Phys. Rev*. C 80, pp. 014609-1 – 014609-6.

[7] R.M. Ronningen (2007), "Validation of Heavy Ion Capabilities in PHITS", *Hadronic Shower Simulation Workshop*, edited by M. Albrow and R. Raja, American Institute of Physics Conference Proceedings 896 (Melville, NY), pp.71-80.

[8] T. Kai et al. (2001), "DCHAIN-SP 2001: High energy particle induced radioactivity calculation code", JAERI-Data/Code 2001-016, Japan Atomic Energy Research Institute.

[9] K. Niita et al. (1995), "Analysis of the(N,xN') reactions by quantum molecular dynamics plus statistical decay model", *Phys. Rev*. C 52, pp. 2620-2635.

[10] S. Furihata (2000), "Statistical analysis of light fragment production from medium energy proton-induced reactions", *Nucl Instrum Meth* B 171, pp. 251–258.

[11] Y. Iwamoto, R.M. Ronningen, K. Niita (2010), "Estimating Neutron Dose Equivalent Rates from Heavy-Ion Reactions around 10 MeV amu^{-1} using the PHITS Code", *Health Physics* 98, pp. 591-596.

[12] K. Shin, K. Miyahara, E. Tanabe,Y. Uwamino (1995), "Thick-target neutron yield for charged particles", *Nucl. Sci. Eng.* 120, pp.40-54.

[13] J. Cugnon, A. Boudard, S. Leray, D. Mancusi (2011), "New Features of the INCL4 Model for Spallation Reactions", *J. Korean Phys. Soc.* 59, pp. 955-958.

[14] K. Iida, A. Kohama, K. Oyamatsu (2007), "Formula for proton–nucleus reaction cross section at intermediate energies and its application", *J. Phys. Soc.* pp. 76, Japan.

Shielding benchmarks for Geant4 version 10

Tatsumi Koi on behalf of Geant4 collaboration
SLAC National Accelerator Laboratory, US

Abstract

Geant4 is a toolkit for the simulation of the passage of particles through matter. To show its capability in the shielding area, we have submitted Geant4 results for the "Inter-comparison Problems of Neutron Attenuation" to SATIF organisers since 2006. Version 10 is the latest and major update of Geant4 and has been publicly available since December 2013. We have validated the version against shielding benchmarks that were proposed in the past inter-comparison projects and obtained good agreement between measurements. A newly introduced INCL++ based physics list shows promising physics performance, however, it requires more CPU resources than others. The version supports multi-threaded application and multi-threading performance was tested with the SATIF-12 inter-comparison project. Computing time of same calculation is measured changing the number of threads used in calculation. The time decreased along with increase of number of thread. Power law index of -0.9 was obtained for the fitted curve. We also measured memory consumption and found that 80% of memory was shared among threads at initialisation time. Using multi-threaded application makes it easy to use full CPU resource of modern machines with less amount of memory.

Introduction

The Geant4 toolkit [1][2] provides a complete set of class libraries for Monte Carlo simulations of particle interactions in matter. It is used in many research fields and to demonstrate its capability in radiation protection and shielding calculations, we have participated in the "Inter-comparison" project since SATIF8 [3-5]. Utilising outputs from the project, we have developed a physics list of Geant4, dedicated to shielding application. The physics list is called as "Shielding" and it has been included in releases of Geant4 since version 9.4. Users can easily apply it in their shielding applications.

Geant4 version 10 is publicly available since December 2013 and it is the first major update of Geant4 in 7 years. Because it is a major update, there are many new features. Some of the new features relevant to shielding applications are described in the next section. Shielding benchmarks using Geant4 10.00 will be shown in the following section, as well as comparisons to thick target measurements. Supporting multi-threaded application is one of most important feature of this version. We will show the performance of multi-threaded application that we use for submitting the "inter-comparison" project of SATIF-12. Finally, we will give conclusions of shielding benchmarks for Geant4 version 10 from physics and computing performance views.

Geant4 version 10

Geant4 version 10 is the latest version of Geant4. Since this is a major update, many new features have been added to the release. However, there have been some discontinued features and also interface changes. As a result, user code may need to be modified. Some of the new features and updates of version 10 will be described.

Support for multi-threaded Geant4 applications is one of the key features of this version. Clock up of CPU becomes difficult for a decade and these days improvement in computing performance mainly comes from an increase in the number of CPU cores. Multi-threaded application enables the easy use of the entire CPU resource of the machine easily. Another advantage of multi-treaded applications is the possible usage of shared memory among threads. Using such shared memory for unchanged objects in simulations like geometry, physics table etc. reduces the total memory expenditure. Reducing memory consumption becomes important especially in many-core CPUs. We will show performance of an example of multi-threaded application in a later section.

Concerning physics developments, the Fritiof (FTF) model has been extended to handle nucleus-nucleus collisions from 3 GeV per nucleon and above. Geant4 now provides interaction models for almost all energy regions and species of Galactic Cosmic Ray. This will be beneficial to users of space applications. G4Nuclide Table has been introduced for collaboration work among models in the production of isomer and its decay. State data of the table are derived from ENSDF database. The Gheisha-like parameterised models LEP/HEP have been removed and more sophisticated models have been provided to replace them. New physics lists making use of the INCL++, a C++ version of the INCL cascade model, have been introduced. Choice of cross-section data set for various particles in reference physics lists has been improved in the two public releases immediately following the SATIF-11 meeting. Now most reference physics lists use a selection of data-sets similar to the shielding physics list.

Benchmarks for shielding applications

The first benchmark uses data from the BNL AGS shielding experiment [6]. In this experiment, 2.83 GeV and 24 GeV proton beam irradiate a mercury target. Secondary neutron fluences in the shielding material of concrete and iron were measured through activation of Bi samples embedded in the shielding. This measurement was employed in the inter-comparison projects at SATIF-9 and SATIF-10. The reaction rates of ^{209}Bi(n,4n)^{206}Bi and ^{209}Bi(n,6n)^{204}Bi were provided by the coordinator of the inter-comparison and the same reaction rates are used in our benchmark. Figure 1 shows the result of Geant4 version 10 with the shielding physics list. The agreement between simulation and measurement is very good especially in iron shielding. We performed the same benchmark with other reference physics lists in Geant4 version 10. The result with FTFP_INCLXX physics list, which uses INCL++ as cascade model, is shown in Figure 2. The agreement of FTFP_INCLXX in concrete shielding is even better than the shielding physics list that uses the Bertini-like cascade model. We also compare computing performances across the reference physics lists. Figure 3 shows the result. FTFP_INCLXX and QGSP_INCLXX, both of which use the INCL++ as cascade model, and require more CPU resource than other physics lists. The INCL physics lists expended most CPU time, followed by shielding. However, the shielding list is slow mainly because the high precision neutron model is used for low-energy neutron transport. The remaining reference physics lists tested were faster.

The second benchmark was a comparison against measurements of neutron production double differential cross-sections induced by protons bombarding a thick target. The configuration of this benchmark is similar to the problem of “Inter-comparison” project of SATIF-12. The benchmark result from FTFP_BERT, QGSP_BIC and FTFP_INCLXX physics lists are shown in Figure 4 with measurement of Ishibashi et al. [7]. The main difference

among these physics lists is the cascade model used (Bertini-like, Binary cascade and INCL++). There are some differences in predicted cross-sections especially at high-energies, however; all three physics lists well reproduce the measurement in general. Because the target was a short disk perpendicular to the beam axis, strong attenuation at 90 degree was expected and observed in the simulation. However, this was not observed in the measurement.

All calculations in this section were performed with Geant4.10.00.p01.

Figure 1. Validation of result of shielding physics list to BLN AGS experiment

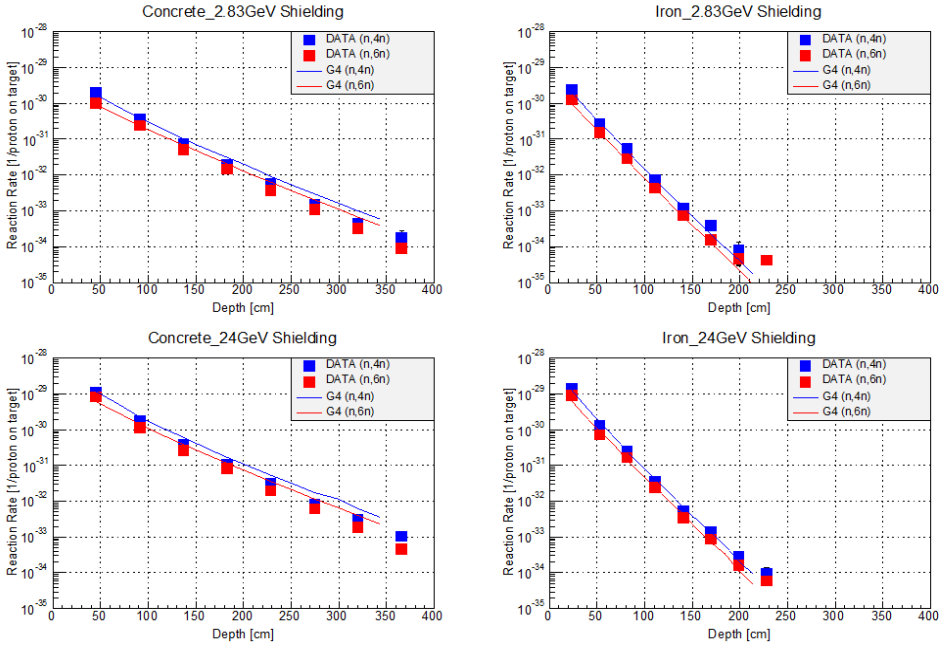

Figure 2. Validation of result of FTFP_INCLXX physics list to BLN AGS experiment

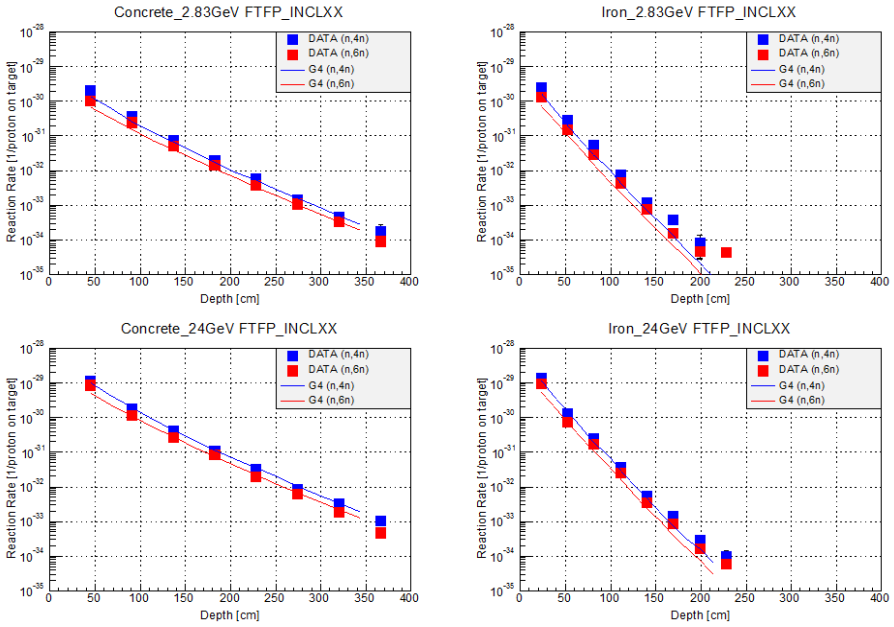

Testing performance of multi-threaded application

In this section, we demonstrate the performance of the multi-threaded application. Performance testing was performed with a multi-threaded application which we submitted to the "inter-comparison" project of SATIF-12. It calculates double differential neutron production cross-sections induced by protons on thick target. We used 100 GeV primary protons on thick gold target. The application was run on a machine consisting of two Intel Xenon E5620 CPU operating at 2.4 GHz. Each CPU has 4 cores; therefore a total of 8 physical cores were available. The machine has a 48GB memory and the OS is 64 bit version of Red Hat Enterprise Linux 6.3. The application was built using the Multi-threaded version of Geant4.10.00.p01 library and the GCC 4.4.7 compiler. We ran an application of 16k events changing the number of threads from 1 up to 8. We measured the total calculation time and memory consumption just after the initialisation phase of the calculation.

Figure 5 shows a decrease in calculation time vs the number of threads. A power law function was fitted to the result. The resulting power law index was -0.90. The index would be -1 in an ideal case. The calculation time included both initialisation and post-processing of calculation.that were basically running on single thread. The index was systematically risen by them, therefore we consider that the power law index of -0.90 in total is reasonably good. Memory consumption of the application was measured and single thread application uses 370 MB just after initialisation and 290 MB of them are shared in multi-threading calculation. Therefore, 80% of consumed memory was shared among threads. We also confirmed that the physical result of an eight-thread calculation is equivalent to the result for a single thread.

Figure 3. CPU performance among reference physics lists

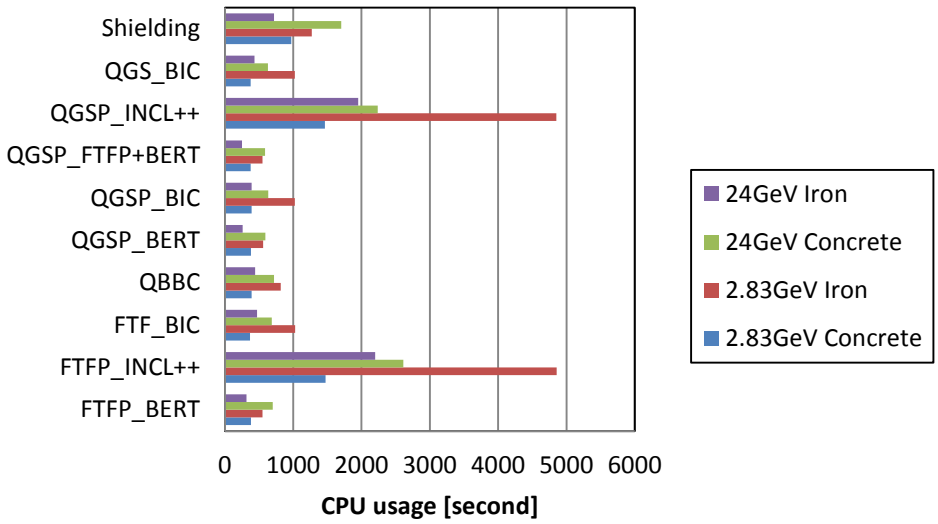

Figure 4. Validation among reference physics lists of (a) FTFP_BERT (b) QGSP_BIC and (c) FTFP_INCLXX to double differential neutron production cross-section

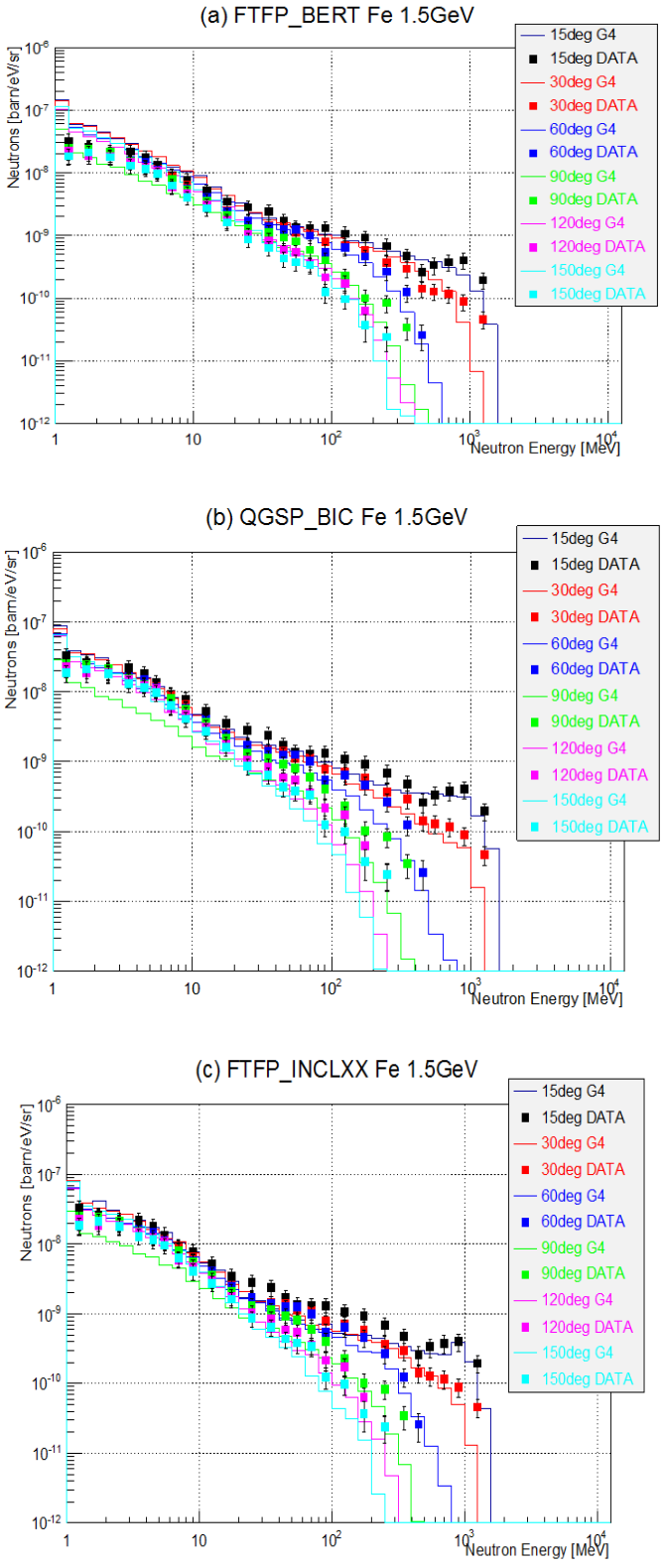

Figure 5. Multi-threading performance

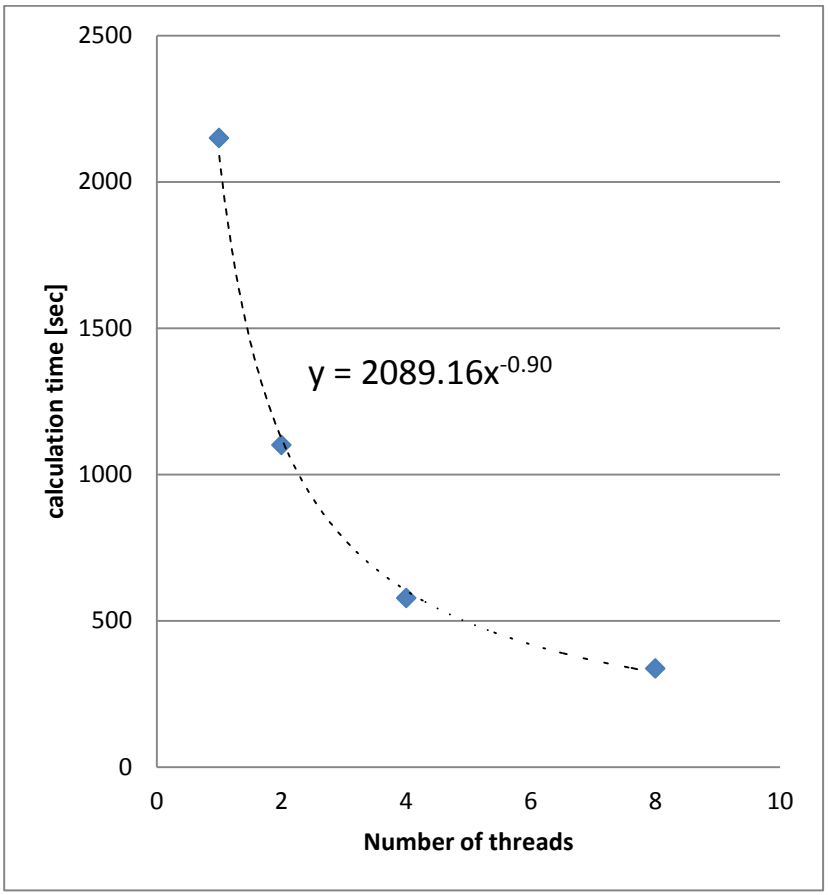

Conclusions

We validated the performance of the Geant4 version 10 for shielding applications through the problems of SATIF "inter-comparison" projects. Neutron fluxes of BNL AGS experiment were well reproduced by calculation of Geant4 version 10 with the shielding physics list. A newly introduced FTFP_INCLXX physics list also gave good agreement and even better in the case of concrete absorbers. INCLXX physics lists show promising physics performance, however, they require more CPU resources than others. Double differential neutron production cross-sections are also compared across reference physics lists. All three cascade models (Bertini-like, Binary and INCL++) that are employed in reference physics lists show reasonable agreements to data. Multi-threaded applications are supported on the Geant4 version 10. Multi-threading performance and memory consumption were tested with application for SATIF-12 inter-comparison. Power law index of -0.90 is obtained for multi-threading performance and 80% of memory consumption was shared at initialisation time. Physically equivalent results were obtained from single and eight threads calculations. Multi-threaded application easily enables use of full CPU power of machine with smaller amounts of memory.

References

[1] S. Agostinelli, et al. (2003), "Geant4: a Simulation Toolkit", *Nucl. Instrum. Meth.* A 506 250.

[2] J. Allison et al. (2006), "Geant4 Developments and Applications", *IEEE Transactions on Nuclear Science* 53 No. 1, 270-278.

[3] H. Hirayama et al. (2006), "Inter-comparison of the Medium-Energy Neutron attenuation in Iron and Concrete (6)", *Proceedings of the Shielding Aspects of Accelerators, Targets and Irradiation Facilities – SATIF8*, Pohang Accelerator Laboratory, Republic of Korea, pp. 237-250.

[4] H. Hirayama et al. (2008), "Inter-comparison of the Medium-Energy Neutron attenuation in Iron and Concrete (7)", *Proceedings of the Shielding Aspects of Accelerators, Targets and Irradiation Facilities – SATIF9,* OECD/NEA, pp. 261-274, ORNL, US.

[5] H. Hirayama et al. (2010), "Inter-comparison of the Medium-Energy Neutron attenuation in Iron and Concrete (8)", *Proceedings of the Shielding Aspects of Accelerators, Targets and Irradiation Facilities – SATIF10*, OECD/NEA, pp. 217-233. CERN, Switzerland.

[6] N. Matsuda et al. (2008), "Analyses of Benchmark Problems for the Shielding Design of High Intensity Proton Accelerator Facilities"*, JAEA-Technology* 2008-030.

[7] K. Ishibashi et al. (1997), "Measurement of Neutron- production Double-differential Cross Sections for Nuclear Spallation Reaction Induced by 0.8, 1.5 and 3.0 GeV Protons", *J. Nucl. Sci. Technol.*, 34, 529-537.

Poster Session

Comparison between PHITS and beam physics codes calculations in support of FRIB dipole magnet design

Dali Georgobiani, Marc Hausmann, Mauricio Portillo, Reginald Ronningen
Facility for Rare Isotope Beams (FRIB), Michigan State University, US

Abstract

The Facility for Rare Isotope Beams (FRIB) at Michigan State University will use projectile fragmentation and induced in-flight fission of heavy ion primary beams at energies of 200 MeV/u and higher and at a beam power of 400 kW to generate rare isotope beams for experimental studies in nuclear physics. The production of rare isotope beams during FRIB operations creates a high-radiation environment for the fragment pre-separator superconducting magnets. Therefore, detailed studies of the proposed magnet designs and shielding by both beam physics and radiation transport codes are necessary. We study the radiation power deposition into the 30-degree bending dipole magnet located in the FRIB fragment pre-separator using both the radiation transport code PHITS[1] and the beam physics codes COSY[2] and LISE++[3]. Preliminary results from these approaches are in reasonable agreement. The results of our calculations are important to magnet design.

Introduction

The 400 kW heavy-ion primary beam impinges on the production target located in the target assembly, as shown in Figure 1. A part of the beam reacts with the target and produces rare isotopes as reaction products. The reaction products and the remainder of the primary beam are transported through the post-target shield, three focusing quadrupole magnets, and the sextupole-octupole magnet before reaching the first 30-degree dipole magnet. There they spatially separate into different beam components. Figure 1 shows these major beamline components of the FRIB hot cell pre-separator. The beam dump intercepts the primary beam and the undesired fragments are stopped by associated fragment catchers. If the primary beam and the undesired fragments do not stop in these locations, the potential to cause damage exists. Magnetic field settings for very neutron-rich light rare isotopes lead to large deflections of the primary beam in the dipole, as well as beam focusing conditions that can cause unwanted beam losses. When the primary beam with the residual power of ~300 kW approaches the magnet aperture limit, the accuracy of the simulation becomes important. The primary beam has a certain power density and spatial distribution, while the reaction products have parameters differing from the parameters of the primary beam. The path region for the beam should be wide enough to avoid losses; however, ample shielding is required to minimise radiation heating of the helium cryostat that keeps the superconducting coils cold. The method used here addresses the necessary issues.

Figure 1. An engineering drawing of an elevation view of the FRIB hot cell pre-separator

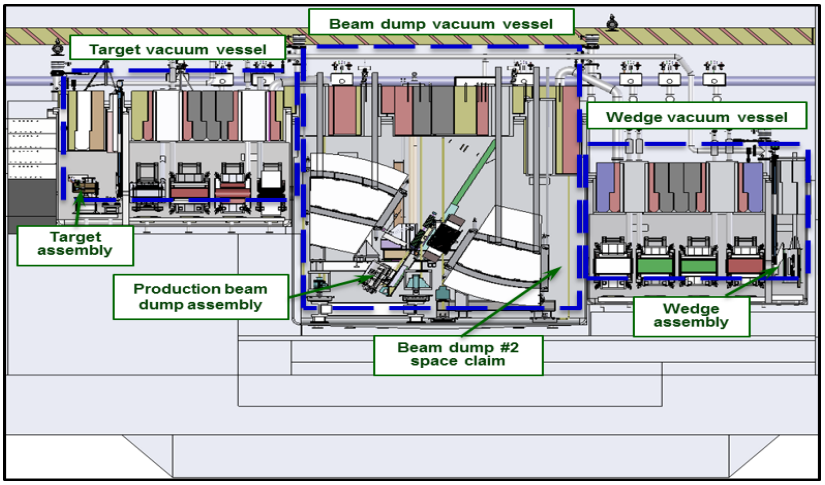

The pre-separator consists of target, beam dump, and wedge vacuum vessels, containing the beam line components: the target assembly, the post-target magnet shield, beam focusing quadrupoles, beam bending dipoles, the beam dump, sextupole-octupoles, and the wedge assembly.

Calculation input and methodology

Beam parameters and code inputs

The radiation transport code PHITS [1] and beam optics codes COSY [2] and LISE^{++} [3] results are compared to validate the codes against each other. The code COSY is used to calculate the maps and optimise the beam transport conditions throughout the system. The maps are calculated to fifth order and the focusing conditions are optimised by varying quadrupoles, sextupoles and octupoles. The maps are then transferred to the code LISE++ which uses the maps for beam transport calculations, and in addition, can do Monte Carlo simulation of the beam particle interactions with matter. This includes the reaction products in the target, but only accounts for charged particles in their ground state; i.e. neutrons, gammas, pions and other secondary particles are not accounted for.

Each of these codes has certain strengths and weaknesses in the context of this work. The COSY maps used by LISE^{++} include the magnet fringe fields, whereas PHITS uses a hard edge approximation and first order simulation of trajectories. LISE^{++} uses beam-matter interaction models that have been frequently tested for the energy regime being considered here. The PHITS code system has the advantage that it tracks events that happen when a particle is lost to the surrounding components in the beam line, such as energy loss and further production which is used to account for activation and damage in the material. On the other hand, LISE^{++} simply ignores effects after a beam particle is lost any aperture in the beamline.

The calculations used for this study focus only on an ^{18}O beam incident on a 2.48 g/cm^2 graphite target at a beam energy of 200 MeV/u and 400 kW of beam power. The magnet fields are optimised to transport a beam of 8 T-m beam rigidity with the product ^{8}He. We use COSY to minimise unwanted losses yet maintain good transmission throughout the separator for ^{8}He. This production setting is expected to give the largest deflection of the primary beam to the bottom side of the dipole. Best match between available models for angular and energy straggling is selected between PHITS and LISE++ in order to make fair side by side comparisons of the straggling effects.

Table 1 presents angular and energy straggling, energy loss, and reaction product models used in LISE^{++} and PHITS calculations. Table 2 shows the comparison of the angular and energy straggling RMS values calculated for the primary beam and a selected

set of fragments. Table 3 compares the average energies of the primary beam calculated after the target. For the purpose of these studies, we find that RMS values calculated after the target for both the primary beam and fragments, as well as average energies, are in reasonable agreement.

Table 1. Angular and energy straggling, energy loss, and reaction product models used in LISE^{++} and PHITS calculations

Model setting	LISE^{++}	PHITS
Angular straggling	ATIMA [4]	ATIMA
Energy straggling	ATIMA	ATIMA
Energy loss	ATIMA	SPAR [6]
Reaction products	Tarasov Model [5]	JAM [7], QMD [8], BERTINI [9]

Table 2. Angular (a-rms) and energy straggling (E-rms) RMS values calculated with LISE^{++} and PHITS for the primary beam and fragments

	LISE^{++}	PHITS	LISE^{++}	PHITS
Beam or Fragment	a-rms [mrad]		E-rms [MeV]	
^{18}O (primary)	3.2	5.1	4.3	4.9
^{16}O	24	15	83	62
^{12}C	35	26	113	100
^{13}N	32	26	105	99

Table 3. Average energy of the primary beam after the target

LISE^{++}	PHITS
E average [MeV]	
2920	2914

Dipole mechanical design and radiation transport models

Mechanical design drawings of the 30-degree bending dipole magnet used to develop the model used in the radiation transport calculations are presented in Figure 2 (panels **a** and **b**). The area of focus in the lower exit corner of the dipole is shown in panel **a** (red circle). Panel **c** depicts a part of the radiation transport model used in the calculations. The radiation transport model supports calculations of losses to all critical components, including the surrounding shielding in the hot cell. Here, the first 30-degree bending dipole, beam dump, sextupole-octupole, and the second 30-degree bending dipole are shown. Most unwanted particles are stopped by the beam dump. A fraction of the beam is lost directly to the bottom blocker and consists mostly of secondary products generated from the primary beam at the target.

Figure 2. Mechanical design drawings of the 30-degree bending dipole (panels a and b) and radiation transport model of the dipole and surrounding beam line components (panel c)

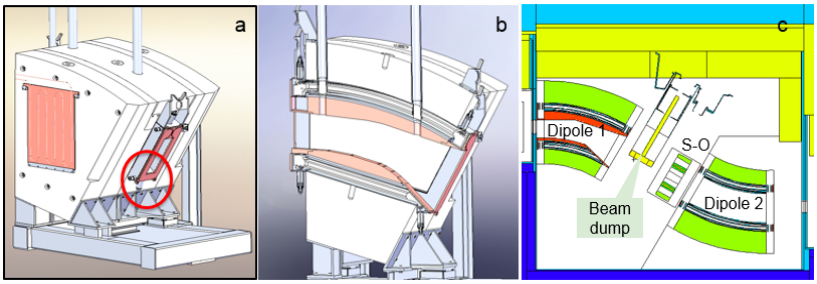

Red circle (panel a) shows the area where the beam hits the dipole in this particular beam setting scenario. Beam blockers optimised to minimise power loss into coils and cryostats are shown in panel b (light pink parts) and in panel c (red parts).

Results of calculations

Beam optics

Beam transport comparisons between LISE^{++} and PHITS results have been performed for reaction products. As an example, beam envelopes for ^{12}C fragments calculated are presented in Figure 3. The similarity in trajectories indicates that the beam optics and the fragment distributions are similar in both calculations.

Figure 3. Beam envelopes for ^{12}C fragments from target for PHITS (top) and LISE^{++} (bottom)

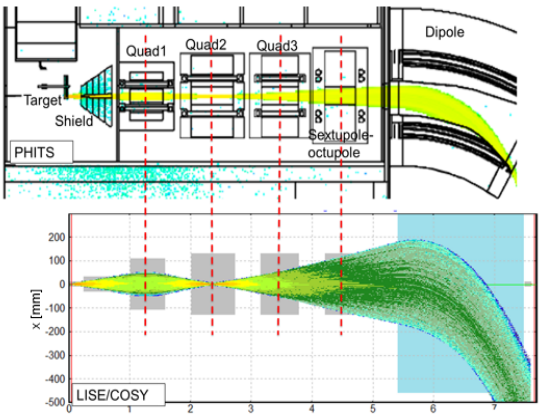

LISE^{++} x-values are in beam co-ordinates; therefore, the dipole bend curvature is not imposed Gray areas in the bottom plot correspond to the apertures of the quadrupoles.

Flux maps and power deposition into the beam blockers

Flux maps from LISE++ and from PHITS calculations are shown in Figure 4. Power deposition to the lower blocker was extracted for each calculation. For losses at the bottom blocker, we obtain 3 kW from LISE^{++} and 2.1 kW from PHITS. The lower value can be explained by the smaller angular spread of reaction products using the ATIMA model within PHITS. The flux distributions are similar and the results of the power deposition calculations are in reasonable agreement.

Figure 4. Flux maps from (left) LISE^{++} and (right) PHITS

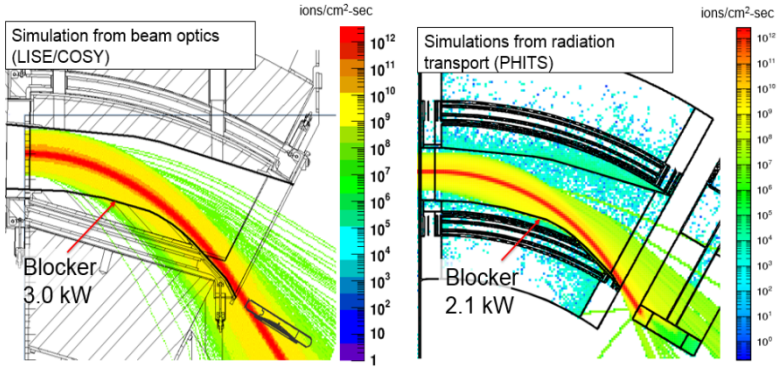

Both the primary beam ^{18}O and reaction products are presented.

Conclusions

The radiation transport code PHITS - with selected settings for straggling and energy loss parameters, as well as its fragment production model was validated against beam optics codes LISE++/COSY to support operational flexibility at FRIB. Beam interference conditions in surrounding components were identified and resolved as follows:

- increasing width of dipole exit window opening so that primary beam clears magnet hardware safely;
- adding top and bottom beam blockers inside of dipole gap to stop intense fragments near the primary beam and reduce the radiation heat load to cryostat;
- optimising the blocker shape to minimise direct beam losses while maintaining adequate shielding;
- developing beam optics settings to minimise losses to all surrounding dipole components;
- calculating induced thermal losses with PHITS to aid in the design of water and helium cooling.

Flux maps from both codes show similar flux distributions. Power deposition to the lower blocker are found to be in reasonable agreement. The radiation transport design is also used in evaluating lifetimes of critical components as well as induced activation.

Summary

Radiation transport (PHITS) and beam optics (LISE^{++}/COSY) codes have been used to calculate beam and fragment distributions, as well as power deposition at the first 30-degree bending dipole magnet located in the FRIB preseparator. Good agreement between the two code systems has been demonstrated. The results from this study provide the design requirements for this magnet in terms of the beam conditions. The current design supports the requirements for future operations for the FRIB project.

Acknowledgements

DG would like to express her gratitude to the SATIF-12 organisers for their hospitality. This material is based on work supported by the US Department of Energy Office of Science under Cooperative Agreement DE-SC0000661, the State of Michigan and Michigan State University. Michigan State University designs and establishes FRIB as a DOE Office of Science National User Facility in support of the mission of the Office of Nuclear Physics.

References

[1] T. Sato, K. Niita, N. Matsuda, S. Hashimoto, Y. Iwamoto, S. Noda, T. Ogawa, H. Iwase, H. Nakashima, T. Fukahori, K. Okumura, T. Kai, S. Chiba, T. Furuta, L. Sihver (2013), "Particle and Heavy Ion Transport Code System PHITS, Version 2.52", *J. Nucl. Sci. Technol.* 50:9, 913.

[2] K. Makino, M. Berz (2005), "COSY INFINITY Version 9", *Nucl. Instr. and Meth. Phys. Res.* A 558, 346-350.

[3] O.B. Tarasov, D. Bazin (2008), "LISE^{++}: Radioactive beam production with in-flight separators ", *Nucl. Instr. and Meth. Phys. Res.* B 266, 4557-4664.

[4] web-docs.gsi.de/~weick/atima/.

[5] O.B. Tarasov (2004), "Analysis of momentum distributions of projectile fragmentation products", *Nucl. Phys.* A 734, 536.

[6] T.W. Armstrong, K.C. Chandler (1973), "A Fortran program for computing stopping powers and ranges for muons, charged pions, protons, and heavy ions", ORNL-4869, Oak Ridge National Laboratory, US.

[7] K.Y. Nara, N. Otuka, A. Ohnishi, K. Niita, S. Chiba (1999), "Relativistic nuclear collisions at 10 A GeV energies from p+Be to Au+Au with the hadronic cascade model", *Phys. Rev.* C 61, 024901.

[8] K. Niita, S. Chiba, T. Maruyama, H. Takada, T. Fukahori, Y. Nakahara, A.Iwamoto (1995), "Analysis of the (N,xN) reactions by quantum molecular dynamics plus statistical decay model", *Phys. Rev.* C 52, 2620.

[9] K. Niita, H. Takada, S. Meigo, Y. Ikeda (2001), "High-energy particle transport code NMTC/JAM", *Nucl. Instr. Methods* B 184, 406.

Contribution of the direct electronuclear processes to thin target activation*

Pavel Degtiarenko, George Kharashvili
Jefferson Lab, Newport News, US

Abstract

Contribution of the direct inelastic interactions of electrons with nuclei to the neutron production and to the material activation radiation source terms may become significant or even critical in certain conditions at high-energy electron accelerators. At Jefferson Lab's CEBAF accelerator, these processes are often responsible for the significant portion of the radiation source terms in the experimental Halls. New experimental data on thin nuclear target activation by the few-GeV electron beams recently obtained at JLab help to evaluate the contribution of the direct electronuclear processes to thin target activation. A model description of the process based on the Equivalent Photon Approximation method, the corresponding Monte Carlo simulation algorithm, and the (limited and simplified) method of implementing these processes in the FLUKA code are presented.

Introduction: Thin targets in electron beams

The ability to evaluate material activation by the electron beams at High Energy Electron Accelerators is a practical necessity serving the purposes of evaluating radiation environment, planning work, decommissioning efforts.

Thin targets present a special class in such evaluations, due to the need to take into account not only nuclear interactions of real photons, but also the direct electronuclear interactions. Impact of these processes may be considered negligible in descriptions and simulations of fully developed electromagnetic or hadronic particle cascades in thick targets and beam dumps. However, in the cases of electron beam interactions in targets thinner than a few percent of a radiation length, the direct electronuclear processes become significant.

Beam interactions in vacuum windows, experimental targets, air gaps, residual gasses in the beam lines – all serve as examples in which electronuclear processes may dominate.

Electronuclear processes

At transfers of sufficiently high-energy and momentum electrons can scatter off parts of the target nucleus. In the processes of quasielastic electron scattering electrons interact directly with weak-bound nucleons or nuclear fragments and may knock them out of the nucleus. The deep inelastic scattering processes generally leave enough excitation energy to break up the target nucleus.

In direct electronuclear processes, electrons break up the nucleus without the need to produce real bremsstrahlung photons to invoke subsequent photonuclear reactions.

The electronuclear reactions are therefore direct one-stage reactions with their rates linearly dependent on the target thickness as opposed to the two-stage photonuclear reactions, dependent on the target thickness quadratically. For sufficiently thin targets the electronuclear reactions will therefore constitute a dominating term in hadron production.

Figure 1 illustrates the relative importance of the electro- and photoproduction in thin targets, as a function of the target thickness. Electroproduction starts to dominate neutron production in thin targets at thicknesses below approximately 4% radiation length.

Figure 1. Neutron yields or target activation by the high-energy electron beams, in arbitrary units, as a function of target thickness in radiation lengths

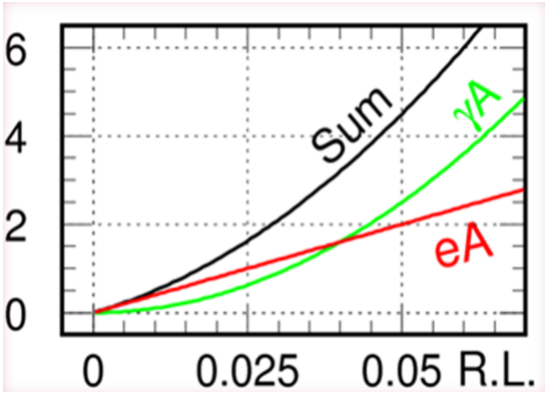

The relative importance of electronuclear and photonuclear (bremss.) contributions to the GDR neutron yield was evaluated as $Y_{total}/Y_{bremss} = (1 + 0.04/T)$ in [1] (T is the target thickness in Radiation Lengths).

Simulation tools

The algorithm for Monte Carlo simulation of the electronuclear reactions was first implemented in 1995 [2]. Since that time the simulation tool based on GEANT3 has been successfully used at JLab in the radiation background calculations. The electronuclear processes have since been implemented in Geant4 (in 2000-2001) and in MARS (around 2003).

The algorithm is based on implementation of the equivalent photon approximation (EPA) method as described in [3]. More details, discussion, and the description of the algorithm can be found in [4]. The electromagnetic interaction of fast charged particles with nuclei can be reduced to the effective interaction of equivalent flux of photons distributed with density $n(\omega)$ on a frequency spectrum. Figure 2 illustrates the connection between the two processes, showing in (a) the interaction of the incident charged particle (for example, electron) with the target nucleus via the dominating one-photon exchange mechanism, which can be related with (b) the interaction of real photons of the same energy with the same target.

Figure 2. Diagrams for electroproduction (a) and photo-absorption (b)

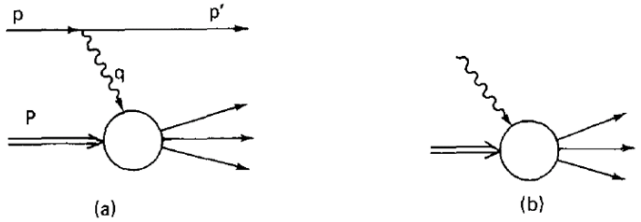

The brief description of the EPA algorithm for electrons as originally implemented within the GEANT3 Monte Carlo Simulation code is as follows:

- At each step of the simulated cascade, the electron is represented as carrying a collinear flux of equivalent photons distributed according to dn(ω) (Equation 6.17b of [3]) in the range of ω from the threshold energy E_{thr} up to the electron energy E_e.
- One "virtual" equivalent photon is generated with an energy ω_v in accordance with the spectrum dn(ω).
- The distance to the next nuclear interaction point of this photon (considered as real) is generated according to its photonuclear cross section, multiplied by the flux factor (the total flux is obtained by integrating dn(ω) from E_{thr} to E_e).
- If this generated point happens to be the closest among all of the electron interaction candidates at the step, then the photon interaction is generated, producing secondary particles and the electron is continuing in the cascade with decreased energy. If other electron interaction process wins, then the virtual equivalent photon is discarded.

Foil activation experiment at JLab

To observe and characterise the contribution of the direct electronuclear processes we have conducted the experiment on foil activation by high-energy electron beams at 2.3 and 3.4 GeV [5]. The schematic of the foil activation set-up is shown in Figure 3. After passing through the experimental target, the electron beam was bent in magnetic field, crossed thin aluminum exit window and was then directed into the set of test metal foils of different materials: aluminum, copper, niobium, lead, and stainless steel. These front foils were subject to mostly direct electron beam, with a small addition of gammas produced in the exit aluminum window. As a reference point to these measurements, we used a symmetric set of back test foils positioned downstream of the first set, and after a thick (1.25 cm) tungsten plate. All parameters of the irradiation were recorded, and after the runs all test foils were analysed using methods of gamma spectroscopy to measure amounts of the various radioactive isotopes produced. Detailed data on multiple isotopes are presented in [5]. For the pupose of this work, only a few representative and most reliably measured isotopes are used.

Figure 3. Schematic of the thin foil activation experiment at JLab, together with the diagram for the simplified model of equivalent photon approximation describing the electronuclear interaction contribution to foil activation

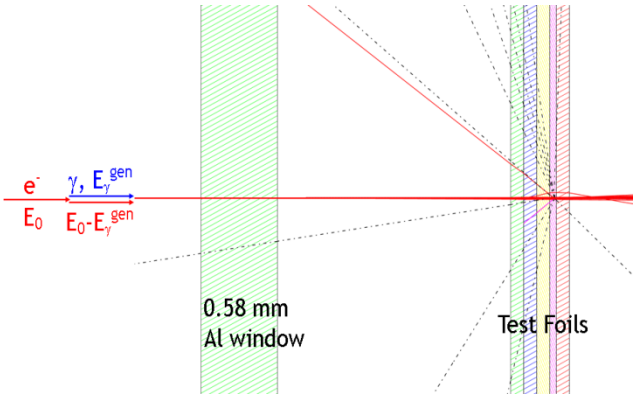

Comparison between the front set of foils and the back set of foils allows evaluating the contribution of the direct electronuclear mechanism of isotope production. The front set is irradiated directly by the beam electrons, and also by the small number of real photons produced in the aluminum exit window, plus by the photons returning from the tungsten block. The foils in the back set are placed inside a well-developed electromagnetic cascade in tungsten, where the real photonuclear reactions dominate.

Simplified electronuclear algorithm for FLUKA

The mechanism of real photonuclear reactions is implemented in FLUKA [6], thus the irradiation of the back foils can be simulated using the code, and can be used as a reference. To model the activation of the front set of foils, we have introduced the simplified model of direct interaction of beam electrons with target nuclei, implemented as a FLUKA user routine.

In this method, equivalent photons with correct energy spectrum are added as real photons to the beam electrons in proportion, conserving energy, as illustrated in Figure 3. The method approximates the general EPA algorithm for Monte Carlo simulations in the simple case of a thin target set at the beam entry point. Because of the energy conservation, the subsequent electromagnetic cascade is practically not disturbed.

Figure 4. FLUKA/Measurement ratios in the front foil set with eA *Off*

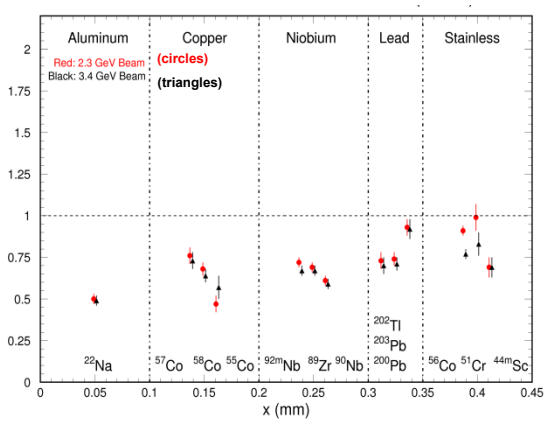

Figures 4 through 7 present the results of comparison between the measurements of the selected isotopes' production in different materials, and the FLUKA model simulations, both without („eA Off") the electronuclear algorithm, and with it ("eA On"). The results are presented as ratios FLUKA/Measurement (Figures 4,5), and the "ratios of ratios" (Figures 6,7), that is the ratios of the FLUKA/Measurement values between the front and the back set of foils. The abscissa is shown as the cumulative thickness of the five foils in mm as they were installed in the set. The radioactive isotopes selected for comparison are indicated at the bottom of the plot, corresponding to the foil placement. The 2.3 and 3.4 GeV data sets are distinguished by the symbols and colours.

Figure 5. FLUKA/Measurement ratios in the front foil set with eA *On*

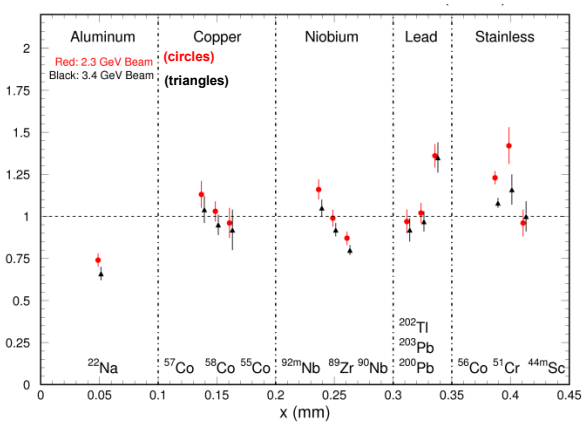

Overall comparison of the measurements with FLUKA simulations for the selected isotopes generally shows a very good agreement (within 25%) for the back foil set as discussed in [5], both in "eA Off" and "eA On" simulations. In the front foils, without the direct electronuclear production contribution the simulation is systematically lower than measurements by 25-50%. Adding the direct electronuclear production removes this systematic difference.

"Ratio of Ratios" plots (see Figures 6,7) allow removing part of a systematic difference between the FLUKA model and the measured data, which might be expected to be the same for the front and the back set of foils, demonstrating more clearly the necessity to introduce direct electroproduction mechanism in the Monte Carlo simulation code.

Figure 6. Ratio of FLUKA/Measurement ratios in the front foil set to the back foil set, with eA *Off*

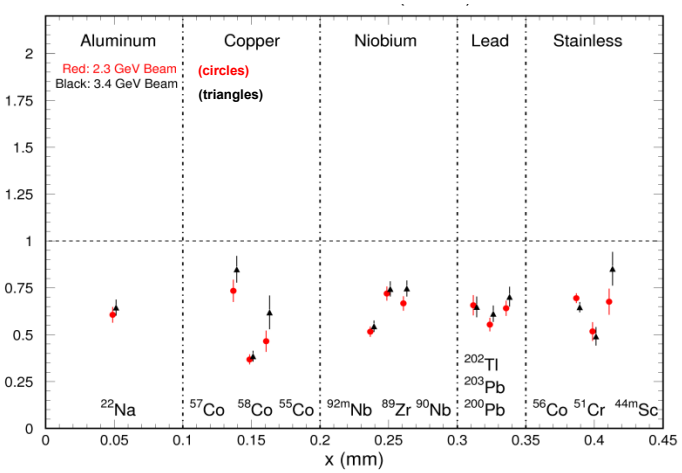

Figure 7. Ratio of FLUKA/Measurement ratios in the front foil set to the back foil set, with eA *On*

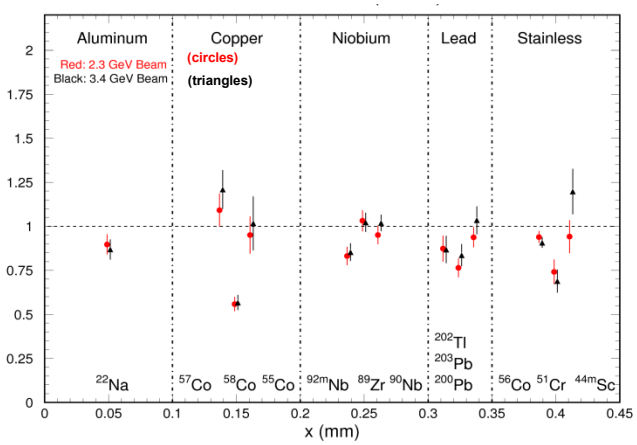

Summary and conclusions

Radioactive isotope production by 2.3 and 3.4 GeV electron beams in thin metal foils made of aluminium, copper, niobium, lead, and stainless steel has been measured in two characteristic placements of the foils near the beam dump absorber. One set of the foils was placed directly on the beam at the dump entrance, in an attempt to observe activation processes due to the direct interactions of high-energy electrons with nuclei. The second set was placed around the maximum of the E-M shower in the body of the dump as a reference point, where the dominant contribution to the nuclear disintegration processes comes from the real photons in the well-developed electromagnetic cascade. The concentration of the radioactive isotopes after irradiation was measured using the methods of gamma spectroscopy, and then compared with the results of realistic simulation of the setup using FLUKA Monte Carlo.

The comparison indicated that FLUKA in the standard configuration reproduces well radioisotope production in the second set of the foils in the maximum of E-M cascade. At the same time, it underestimates by 25-50% the production in the first set, which is subject to the direct electron beam impact. By introducing the simplified model of direct interaction of beam electrons with the target nuclei, we were able to reproduce the observed increase in the isotope production. Thus we report strong experimental evidence for the need to include the direct electronuclear production model in the standard set of Monte Carlo simulation tools. Important applications of such calculation tool would include material activation and neutron source term evaluations in high-energy electron beam interactions with thin vacuum windows, experimental targets, air gaps in the beam lines, etc.

Acknowledgements

We thank Vashek Vylet and all staff at the Radiation Control Department at Jefferson Lab for their support of this work and useful discussions.

References

[1] X. Mao, K.R. Kase, W.R. Nelson (1996), SLAC-PUB-6628.

[2] P. Degtyarenko, G. Stapleton (1995), SARE-2, CERN.

[3] V.M. Budnev, I.F. Ginzburg, G.V. Meledin, V.G. Serbo (1975), Physics Reports 15, no.4, 181-282.

[4] P. Degtiarenko (2012), "Electronuclear Interactions in FLUKA", *2nd FLUKA Advanced Course and Workshop* – Vancouver, Canada.

[5] G. Kharashvili, P. Degtiarenko (2015), "Activation by 2.25 and 3.36 GeV electrons – comparison of measurements with FLUKA calculations",*SATIF-12 Proceedings*.

[6] A. Ferrari, P.R. Sala, A. Fasso`, J. Ranft (2005), CERN-2005-10, INFN/TC_05/11, SLAC-R-773.

Energy production demonstrator for megawatt proton beams

Vitaly S. Pronskikh[1], Nikolai V. Mokhov[1], Igor Novitski[1], Sergey I. Tyutyunnikov[2]
[1]Fermi National Accelerator Laboratory, Batavia, US
[2]Joint Institute for Nuclear Research, Dubna, Russian Federation

Abstract

A preliminary study of the Energy Production Demonstrator (EPD) concept - a solid heavy metal target irradiated by GeV-range intense proton beams and producing more energy than consuming - is carried out. Neutron production, fission, energy deposition, energy gain, testing volume and helium production are simulated with the MARS15 code for tungsten, thorium, and natural uranium targets in the proton energy range 0.5 to 120 GeV. This study shows that the proton energy range of 2 to 4 GeV is optimal for both a ^{nat}U EPD and the tungsten-based testing station that would be the most suitable for proton accelerator facilities. Conservative estimates, not including breeding and fission of plutonium, based on the simulations suggest that the proton beam current of 1 mA will be sufficient to produce 1 GW of thermal output power with the ^{nat}U EPD while supplying < 8% of that power to operate the accelerator. The thermal analysis shows that the concept considered has a problem due to a possible core meltdown; however, a number of approaches (beam rastering, in the first place) are suggested to mitigate the issue. The efficiency of the considered EPD as a Materials Test Station (MTS) is also evaluated in this study.

Introduction

In this contribution we are considering a possibility for high-energy proton beams to be applied to build a demonstrator of energy production. The neutron production by proton accelerators was studied in the US in the 1960s (for example, [1]). In the 1970s an uranium target was considered by R.R. Wilson [2] for the Energy Doubler's 100 to 1000 GeV proton beams. A number of experimental [3-6] and simulation [7-9] studies have later been undertaken employing heavy metal and fissile targets. Most of the recent studies were devoted to the lead-bismuth liquid targets surrounded by blankets [10-11]. In this work, a solid target concept is considered.

Neutron production and fission

We extend previous studies encompassing the 0.5 to 120 GeV proton energy range and simulating energy deposition in solid targets explicitly using the MARS15 code [12-13]. The model used in this work is shown in Figure 1. It is a 60-cm radius and 110-cm long cylindrical target with a 10-cm diameter, and a 35-cm long beam entrance channel. Target and hole dimensions were chosen to keep the neutron leakage at the level of a few percent in the entire energy range (see Figure 2). The simulated proton beam is uniform and parallel, 10 cm in diameter.

Figure 1. MARS15 model of the tungsten, thorium and uranium target

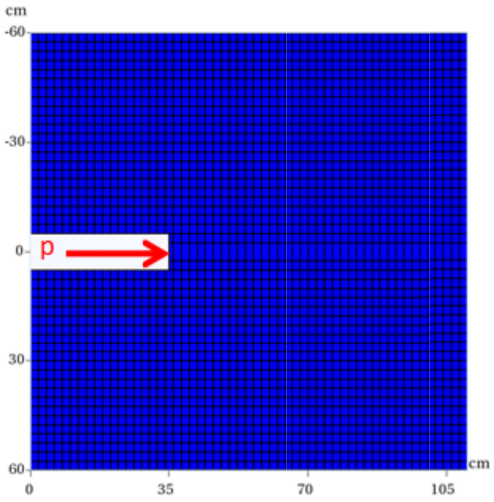

Three target materials – tungsten, natural uranium, and thorium – were studied. These are the good neutron producers as well as quite abundant and representative of heavy fissile material. In the course of simulations, the CEM and LAQGSM event generators were invoked in MARS15 in order to determine outcomes of the hadron-nuclei interactions in the range (~few MeV – 8 GeV, for negative pions 0 – 8 GeV). Above 8 GeV, for all interactions the MARS15 inclusive model is invoked. Figure 3 gives the number of neutrons generated in the target in all possible processes per incident proton and per GeV beam energy (i.e. energy cost of neutrons).

For all the three target materials, these distributions show that the optimal energy for neutron production is between 2 and 4 GeV. The absolute number of neutrons per fission (Figure 4) is in agreement or slightly higher than in other studies for uranium [2], [8], and higher than for thorium [9]. Another difference is that many other studies report the optimal energy to be close to 1 GeV, while our simulations reveal the optimum at 2-4 GeV. This difference is most probably due to the fact that we use the latest version of LAQGSM generator for high-energy spallation, which has recently been modified to incorporate a more detailed physics processes description [13] in the range 1 - 10 GeV based on a better adjustment of the model to all available differential data.

Figure 2. Leakage from the uranium target surface

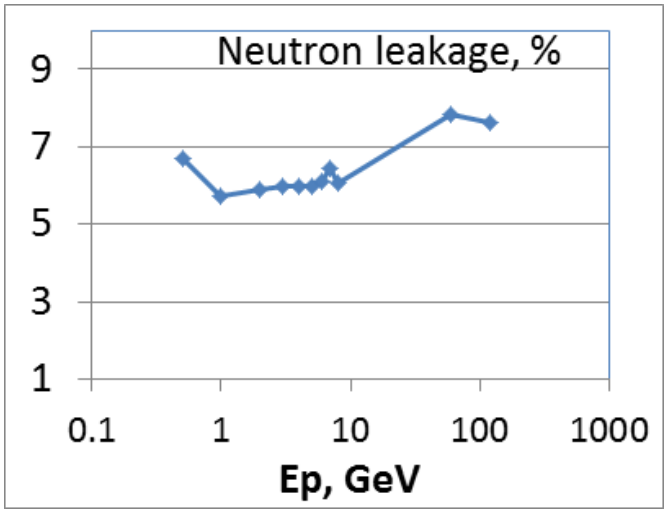

Figure 3. Number of neutrons released per one proton per GeV in the target

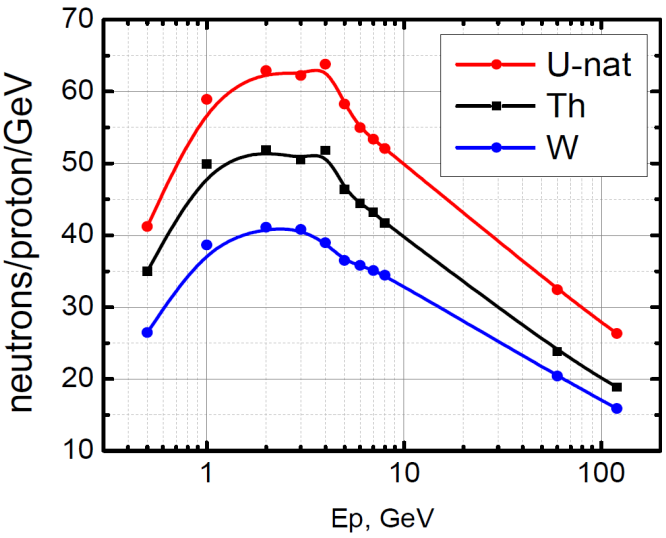

Most fissions in the uranium target (see Figure 4) also occur in the above energy range, suggesting that a significant part of the neutrons are created in fission. In the case of the tungsten target the fission has a peak at 1 GeV, but its contribution is smaller by three orders of magnitude. This explains the neutron surplus of ~20 neutrons in the uranium target as compared to the tungsten one.

Figure 4. Number of fissions in the target per GeV proton energy

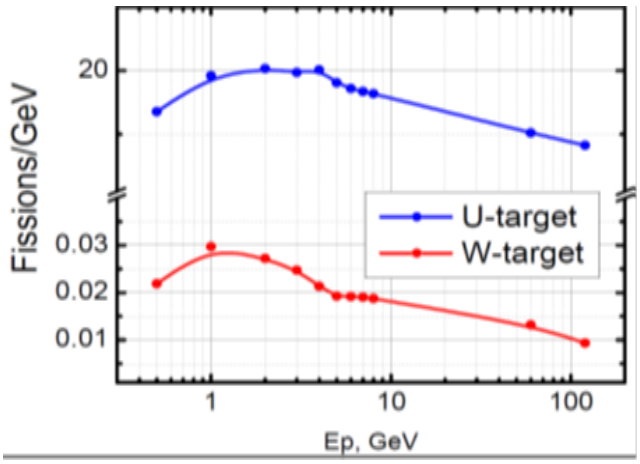

Energy production

Figure 5 shows energy multiplication, which is the ratio of the energy deposited in the target to that of the primary beam impinging on it. It has a peak in the same 1-4 GeV range as above for ^{nat}U because the factor is > 1 due to fission in the target. The fission cross-section for tungsten is by orders of magnitude smaller than that for ^{238}U. That is why the energy gain for tungsten is less than 1, and that material cannot serve efficiently for the energy production. The energy deposition in the thorium target is also much lower. Energy deposited in the target per neutron produced in it (see Figure 6) is the quantity that shows the energy production efficiency as compared to neutron production efficiency at particular beam energy. This quantity has a minimum between 2 and 4 GeV for both ^{nat}U and W; energy deposition in all processes in the target per one produced

neutron is up to 6 times higher the ^{nat}U target than in the W one. Note that for this quantity, the differences between its value at the optimal proton energy of 3 GeV and at minimal (0.5 GeV) and maximal (120 GeV) energies studied are about 15 %, making that difference not a very significant factor.

Figure 5. Energy multiplication in the target

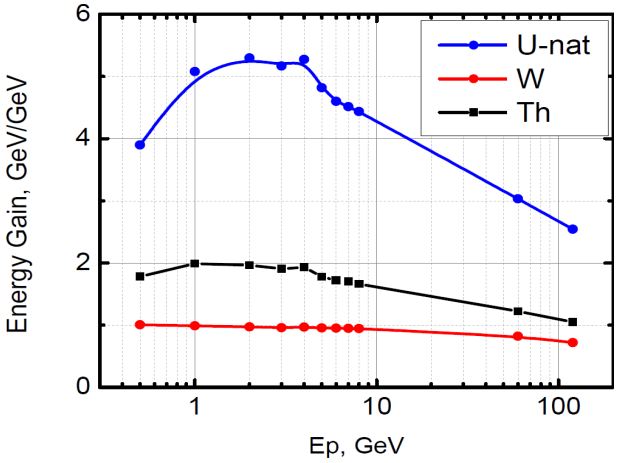

Figure 6. Energy released in the target per GeV proton energy

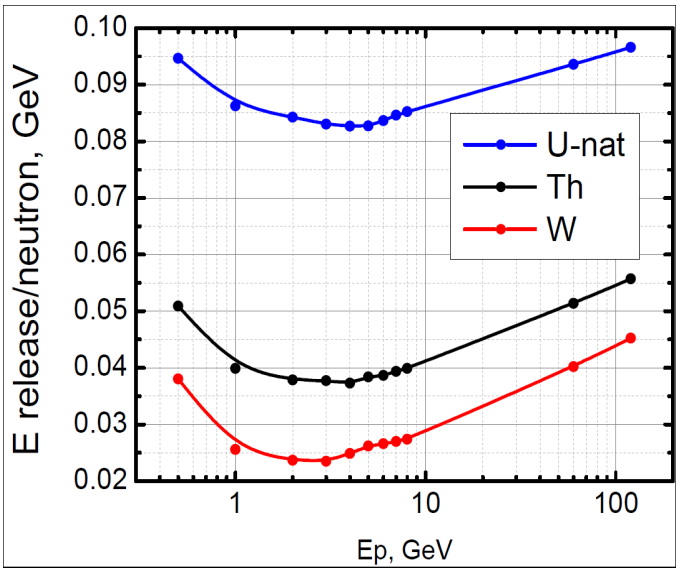

Radiation damage and materials test station

The efficiency of the studied target as a Materials Test Station (MTS) is also evaluated here (see [11] for the discussion of a liquid target concept proposed for that purpose). The aim of MTS is to maximise the DPA radiation damage and gas production in order to load the samples under study in the hottest location in the target. Figure 7 shows the target volume with DPA > 20 yr^{-1} (at the beam intensity of $6.25 \cdot 10^{15}$ p/s), which is one of the reference numbers used to evaluate the MTS performance [11]. For both target materials such a quantity has an optimum around 2-3 GeV.

Figure 7. Testing volume in the target with DPA > 20 /yr per E_p

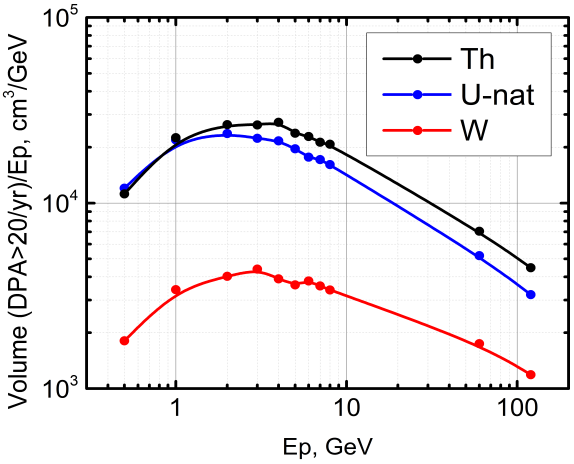

One of the key quantities to estimate radiation damage in a target or a reactor unit is the peak helium production expressed in units of appm/DPA per GeV beam energy (i.e. the energy cost of the gas production) (see Figure 8). It has a peak between 1 and 3 GeV; the helium production per unit energy grows faster than DPA up to 2 GeV, after which the growth of the energy becomes slightly slower. Figure 8 indicates that the gas/damage/E_p ratio is highest (has the lowest cost) at lower energies between 0.5 and 4 GeV, while at 120 GeV it is two orders of magnitude less efficient. In absolute numbers, the helium production per DPA per E_p is a factor of 7 less for the ^{nat}U than for W target. For tungsten it is at the level of a typical fusion reactor and slightly less than for a spallation neutron source, like SINQ. For the ^{nat}U target at 1 to 3 GeV it is at the level of a fission reactor on fast neutrons. The behaviour of the curve in Figure 8 above 8 GeV remains the same even if the LAQGSM model is used in that range instead of the inclusive one, for example, the appm/DPA value at 120 GeV drops by ~20%.

Figure 8. Peak helium production in the target, appm/DPA

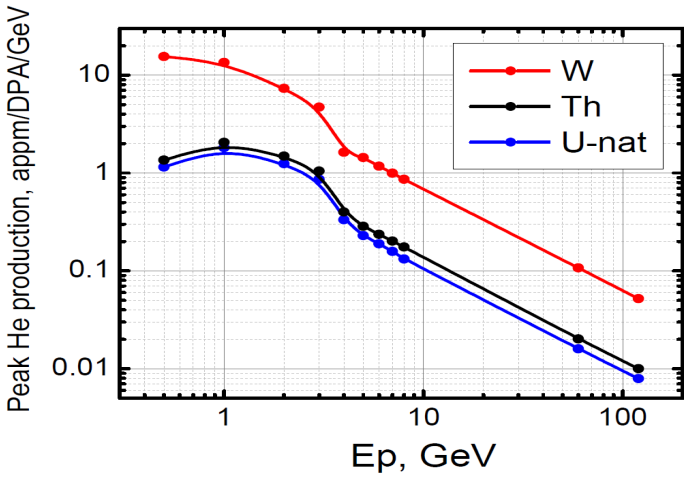

Thermal output power

In order to use the target station in the energy production mode, so that the energy release in the target was higher than the energy used by accelerator, the following condition (1) should be satisfied:

$$\mathbf{P = P_{rel} - P_0 - P_{acc} \leq 0} \quad (1)$$

where P is the potential power produced by the station, P_{rel} is the power released in the target, P_0 is the power needed to run the accelerator in the idle mode, P_{acc} is the power fed to the RF system to accelerate protons.

It was estimated [2] that the proton intensity required at the tevatron energies was obtained taking P0 to be 20 MW, and Pacc = b· N·E, where b = 2. It is assumed that Prel is equal to 0.2 a·N·E, where 0.2 is the energy released per fission in GeV, and a ≈ 60 neutrons per fission, N is the proton beam intensity, and E is the proton energy. The latter is an estimate of the energy released in fission assuming that neutron production is constant and each neutron is captured by uranium leading to the production of plutonium. A more detailed approach relevant to the accelerator-driven energy production calculations is described in [14]. In that approach, the thermal output power of an energy station can be described by Equation (2):

$$\mathbf{P_0^{th} = I \cdot E_p \cdot G} \quad (2)$$

where I is the proton beam current (mA), E_p is the proton beam energy (GeV), and G is the energy gain.

Figure 9. Energy gain G

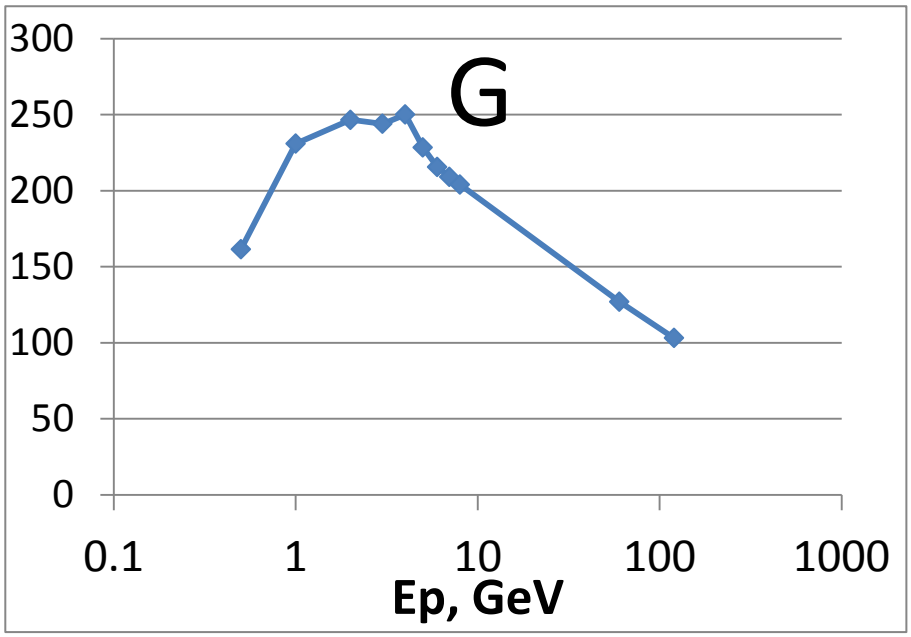

The energy gain (see Figure 9) is the key quantity, a high value of which in a system allows a significant increase in the output power as compared to the proton beam power provided that the target is capable of an efficient neutron multiplication. The energy gain is described by Equation (3) as follows:

$$G = \frac{\chi_s \cdot \varphi^* \cdot k_{eff} \cdot E_f}{\nu \cdot (1 - k_{eff})} \quad (3)$$

where χ_s is the number of neutrons leaving the target and entering the blanket in target-blanket ADS; in this case, the whole target (a "full absorption" target) serves its own blanket and both the neutron multiplication and energy production take place in its entire media and that is why in our case χ_s was taken to be equal to the number of neutrons produced per proton in the target (see Figure 3). The other quantities in the equation above were assumed to have the following values: k_{eff} = 0.98 (a typical number assumed for ADS), φ^*=1, neutron importance (can be larger than 1 if other neutron sources than fission exist in the system; in this case a conservative assumption is made), the number of fissions per neutron ν was taken to be 2.5, and E_f=0.2 GeV is the energy released per one fission.

Figure 10 gives the proton beam current required for a natural uranium target described in this work to produce 1 GW of thermal output power (Equation 1). It indicates that in the optimal energy range (assuming 4 GeV beam energy) one needs 1 mA of proton beam power to produce 1 GW output power; it requires more than 10 mA below 1 GeV, and it is at the level of 80μA for a 120-GeV beam.

Another important quantity is the fraction of the thermal output power required to support the accelerator operation. It is defined [14] by Equation (4):

$$f = \frac{1}{G \cdot \varepsilon \cdot \eta} \quad (4)$$

where ε is the electric to beam power conversion efficiency, 0.4, and η is the thermal to electric power conversion efficiency, 0.45. Figure 11 shows the f dependence on the beam energy. The optimal beam energy (defined by the energy gain G) is also between 2 and 4 GeV.

Figure 10. Beam current for 1 GW output power

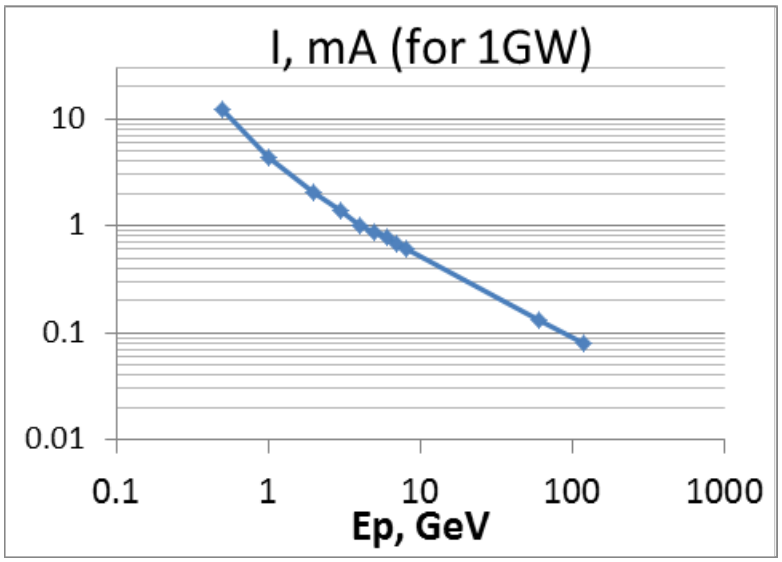

Figure 11. Fraction of the output power required to operate the accelerator

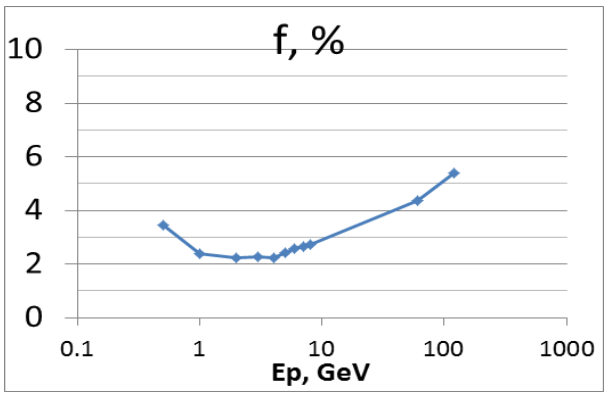

Thermal analysis

A thermal analysis using the ANSYS code has been carried out in order to determine the feasibility of such a target from the point of view of heat removal. The simplest cooling scheme with the cooling lines indicated by the yellow colour is shown in Figure 12. The heat map was calculated with MARS15 for a E_p= 3 GeV proton beam with the current I_p= 0.5 mA. The bunched beam was assumed to have the following parameters (similarly to those used in [11]): the bunch duration is $4 \cdot 10^{-11}$ s, the interval between bunches is $6.08 \cdot 10^{-8}$ s. The thermal analysis showed that during the first 100 s of irradiation, the target core will melt (see Figure 13). The hot spot is highly localised due to a small beam diameter as well as a low thermal conductivity of the natural uranium.

To explore the possibility of mitigating the overheating and a core meltdown issue, the beam rastering to the radius of 30 cm (instead of 5 cm) was applied to the model, and the temperature distribution in the target was studied. Figure 14 shows that the peak temperature dropped by an order of magnitude (to 3100° C) compared to the initial model. The core temperature vs time curve plotted in Figure 15 indicates that 3100° C will be reached in approximately 200 s. This temperature is still higher than the melting temperature of natU, however, it is a significant decrease relatively to R=5 cm, which suggests that further beam rastering combined with scanning and adding more cooling lines can help keep the temperature within the limits.

Figure 12. A simple water cooling scheme

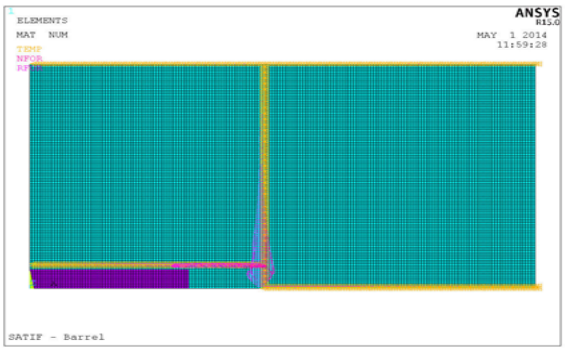

Yellow lines – water cooling lineswith T=20° C.

Figure 13. Temperature distribution in the target after 100 s of irradiation with R= 5 cm beam

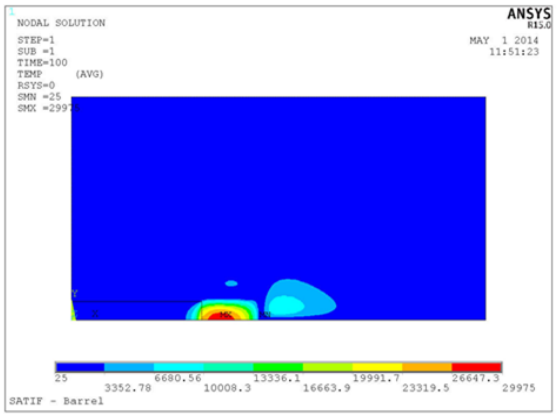

Figure 14. Temperature distribution in the target with the beam rastered to 30 cm in radius

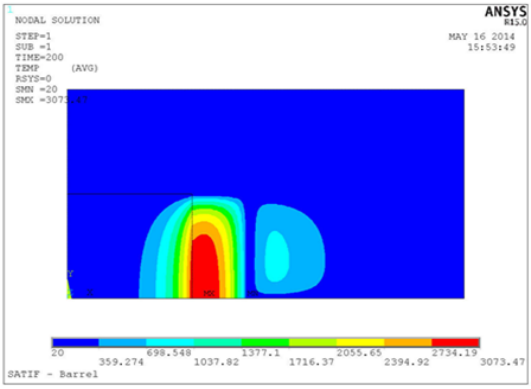

Figure 15. Peak core temperature as a function of time for the beam rastered to R = 30 cm

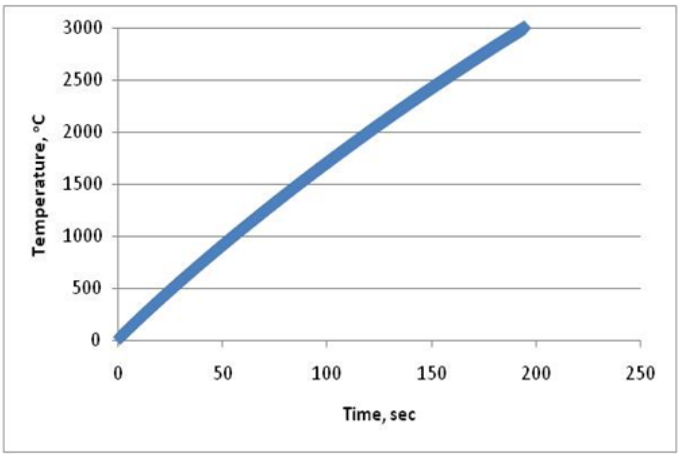

Benchmark target

Simulations carried out in this work suggested target dimensions sufficient to keep the neutron leakage within 5-7 % so that the target could perform as a full absorption one in the energy range studied. A cylindrical target with similar dimensions (R = 60 cm, L = 100 cm) was built about 20 years ago in JINR, Dubna (see Figure 16). Potentially, this target can be employed to benchmark neutron production predictions made in this work as well as the isotope production and fission rates. In principle, these studies could engage proton or deuteron beams of the Nuclotron accelerator of the JINR LHEP (the energy range available 0.5 - 4 AGeV, beam power ~3 W). These beams could also be used in the ADS targetry instrumentation and radiation protection research. However, for higher energy range experiments as well as for heat production studies at least an order of magnitude more beam power is required.

Figure 16. The 21-tonne prototype ^{nat}U target

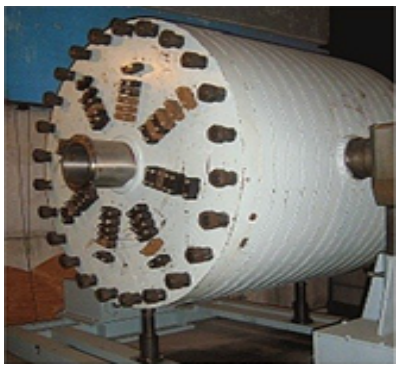

Conclusions

MARS15 simulations and ANSYS thermal studies of solid ^{nat}U, Th, and W "full absorption" targets have been performed in this work. Target dimensions were optimised to keep the neutron leakage below 8% of the total number of neutrons produced in the target in the 0.5-120 GeV energy range. The studies reveal that in order to maximise neutron production, energy deposition, energy gain, and radiation damage, the optimal energy range is 2 to 4 GeV (not 1 GeV as reported in a number of earlier works). It was shown that in the optimal energy range, the 1-mA proton beam current is sufficient to attain the 1-GW thermal output power in the case that the ^{nat}U target is used in an ADS reactor; the fraction of the output power required to operate the accelerator in the entire energy range under scrutiny amounts to not higher than 6%.

Thermal analysis indicated that the beam on the target core would lead to a fast overheating and core meltdown. However, encouraging results were obtained by rastering the beam in a 30-cm radius (the peak temperature dropped by a factor of 10). This is a possible direction for further target optimisation work. Suggested experiments with a similar existing target are able to provide data for benchmarking the simulation results discussed in this work.

References

[1] A. Weinberg (1966), *Proc. Int. Conf. Isochr. Cycl.*, Tennessee, US.

[2] R.R. Wilson (1976), *Very Big Accelerators as Energy Producers*, FERMILAB-FN-0298.

[3] R.G. Vassilkov et al. (1978), At. Energy, V. 44 (4), 1978 (In Russian).

[4] S. Andriamonje et al. (1995), Phys. Lett. B 348, pp. 697–709.

[5] R. Brandt et al. (1999), Rad. Meas. V. 31 (1), pp. 497 – 506.

[6] J. Adam et al. (2005), Proc. Int Conf. Nucl. Data for Sci. Tech., AIP Publishing, V. 769 (1), pp. 1560 – 1563.

[7] R.R. Fullword (1972), LANL Report LA-4789-UC.

[8] V.S. Barashenkov et al. (1974), At. Energy V. 37, p. 475, (In Russian).

[9] S.R. Hashemi-Nezhad et al. (Ann. Nucl. Ener. V. 38, pp. 1144 – 1155.

[10] H. Ait Abderrahim et al. (2010), *Nucl. Phys. News*, 20:1, p. 24 – 28.

[11] D. Wootan, D. Asner (2012), PNNL Report PNNL 21134.

[12] N.V. Mokhov et al. (1995), Fermilab Report Fermilab-FN-628; N.V. Mokhov et al. AIP Conf. Proc. 896, pp. 50-60 (2007); http://www-ap.fnal.gov/MARS/.

[13] N.V. Mokhov et al. (2014), *Progr. Nucl. Sci. Tech.*, vol. 4, pp. 496-501.

[14] M. Salvatores et al. (1997), *Nucl. Sci. Eng.* V. 126, pp. 333 – 340.

Energy deposition studies for the LBNE beam absorber

Igor L. Rakhno, Nikolai V. Mokhov, Igor S. Tropin
Fermi National Accelerator Laboratory, Batavia, Illinois, US

Abstract

Results of detailed Monte Carlo energy deposition studies performed for the LBNE absorber core and the surrounding shielding with the MARS15 code are described. The model of the entire facility that includes a pion-production target, focusing horns, target chase, decay channel, hadron absorber system – all with corresponding radiation shielding – was developed using the recently implemented ROOT-based geometry option in the MARS15 code. This option provides substantial flexibility and automation when developing complex geometry models. Both normal operation and accidental conditions were studied. Various design options were considered, in particular the following: (i) filling the decay pipe with air or helium; (ii) the absorber mask material and shape; (iii) the beam spoiler material and size. Results of detailed thermal calculations with the ANSYS code helped to select the most viable absorber design options.

Introduction

The Long-Baseline Neutrino Experiment (LBNE) at Fermilab provides the world's highest-intensity neutrino beam for the US programme in neutrino physics [1]. The corresponding incoming proton beam power can ultimately be as high as 2.3 MW, and the underground beam absorber at the end of the decay channel with related infrastructure operates with little or no maintenance for about 20 years. Such a combination of long operation time and high deposited power imposes strict limitations on the design of the absorber. In this paper, both normal operation and accidents are studied. All the calculations described below were performed with the MARS15 Monte Carlo computer code [2-3].

Normal operation and accidents

Normal operation

At normal operation, the 120-GeV proton beam delivered to the target will ultimately have 1.6×10^{14} proton/pulse with a 1.33 second time interval between the pulses. The average beam power on the target will be equal to 2.3 MW. The beam shape at this location is described by Gaussians with $\sigma_x = \sigma_y = 1.3$ mm and $\sigma_{x'} = \sigma_{y'} = 17$ μrad. The beam is tilted down by 101 mrad.

Accidents

The development of credible accident scenarios usually requires separate investigations. At this stage, we studied only a "target disappears" scenario which, in a sense, represents the most severe case in terms of power deposited in the absorber core. Accident scenarios with a misbehaved beam will be developed and studied later. Such scenarios

will be useful, for example, in order to determine if cooling channels, located at some distance from the absorber core centre, can withstand such accidents.

Unified computer model

The elevation views of the entire MARS model and several fragments – target hall, target chase and absorber hall – are shown in Figures 1, 2 and 3. The absorber model shown in Figure 2 represents one of the most recent design options with a beam spoiler. Figure 3 shows that a great deal of attention was paid to tiny details in order to follow the design specifications as close as possible. The colour code used in the Figures implies that light blue and grey colours usually refer to air and concrete while the meaning of the other colours depends on the problem studied.

Figure 1. Elevation view of the entire unified model

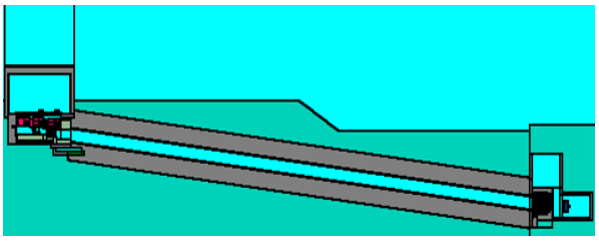

Figure 2. Elevation view of the leftmost (target hall, top) and rightmost (absorber, bottom) fragments of the entire computer model

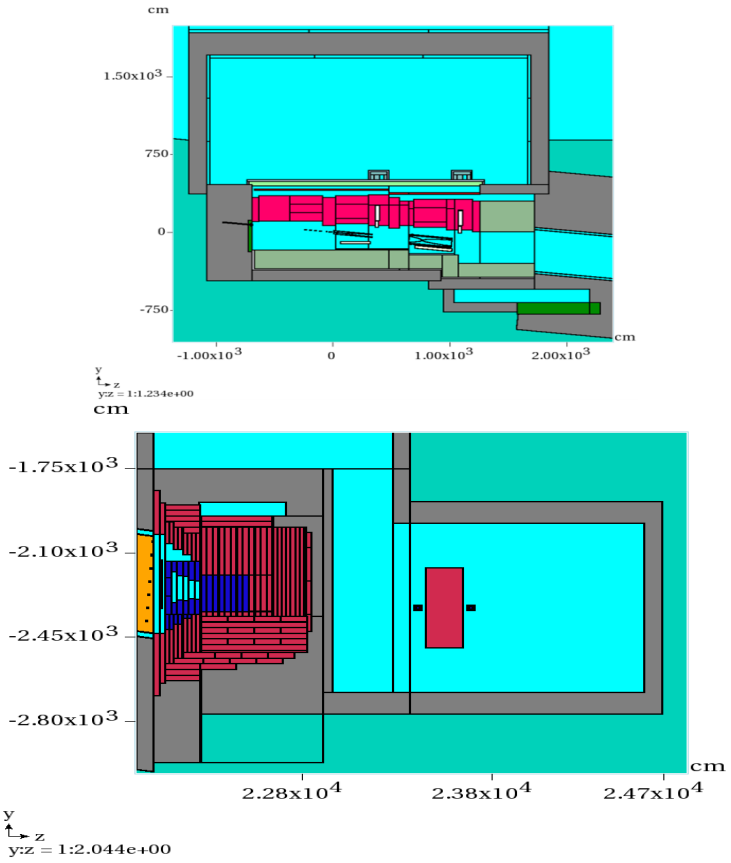

Figure 3. Two fragments of the target chase model

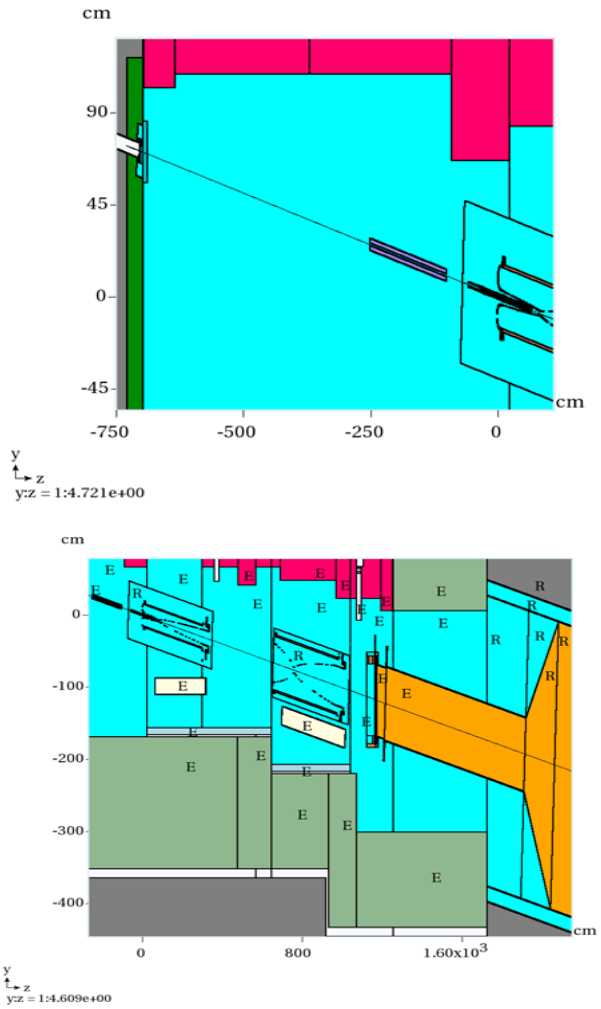

Source term

The incoming beam for the absorber was calculated with the MARS15 code in the exclusive mode using the LAQGSM hadron generator. Interactions in both the target and decay channel were taken into account so that one can predict the effect due to replacement of the air with helium in the decay pipe. Four different cases were considered: normal operation and an accident for both the air and helium as a filling gas in the decay pipe. The calculated distributions of the source term across the beam pipe cross-section are shown in Figures 4 and 5. The area with major energy deposition in the absorber core is expected to be confined within a two-foot in radius. And due to reduced scattering on helium in the decay pipe, the helium case is more severe in terms of peak deposited energy for both normal operation and accidents. At the same time, the accident case allows for simplified analytical calculations for the beam window, and at the end of the decay pipe, the beam can be represented with a Gaussian, as shown in Figure 6.

Power density distributions

The calculated deposited power for normal operation with helium in the decay pipe is shown in Table 1. More detailed power density distribution for the aluminium core is shown in Table 2. The calculated deposited power density distributions for normal operation are shown in Figure 7. With helium the peak power density is higher by about 30% compared with air.

Figure 4. Calculated particle and energy flux (arbitrary units) for normal operation (left) with air (right) and helium in the decay pipe

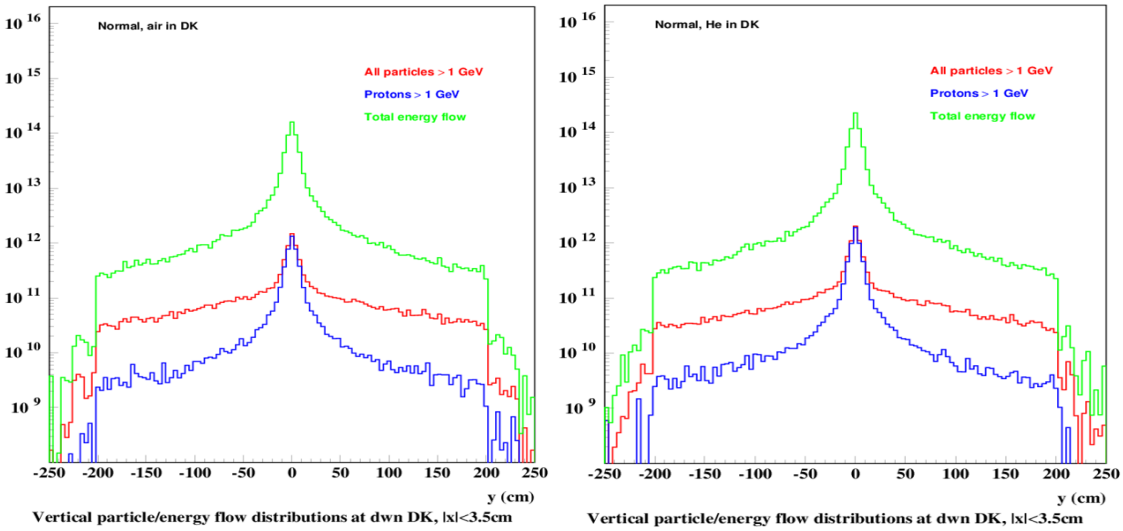

Figure 5. Calculated particle and energy flux (arbitrary units) for accidents with air (left) and helium (right) in the decay pipe helium (right) in the decay pipe

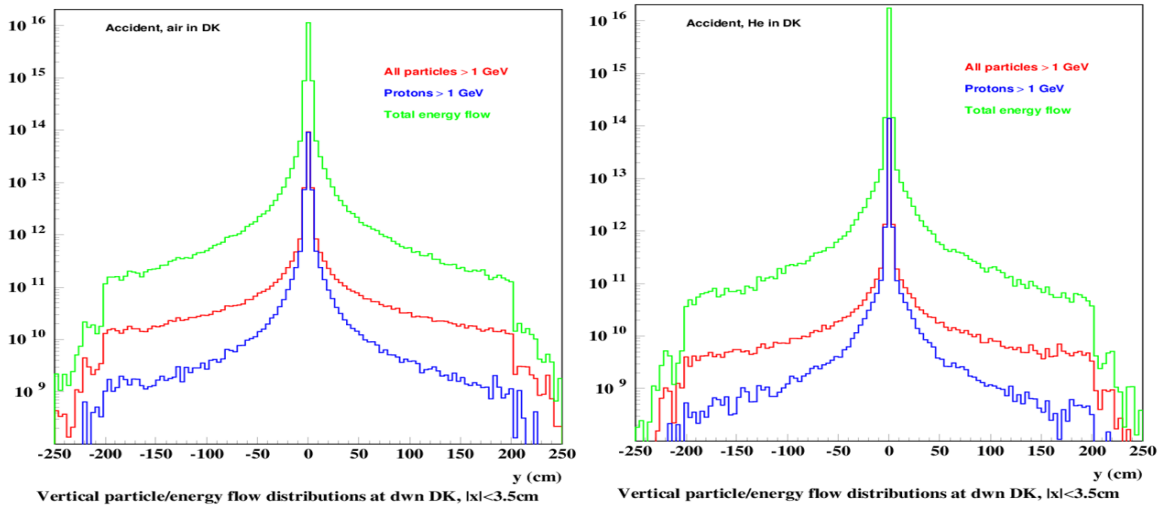

Figure 6. Gaussian fit (lines) to incoming source calculated with MARS15 code (circles)

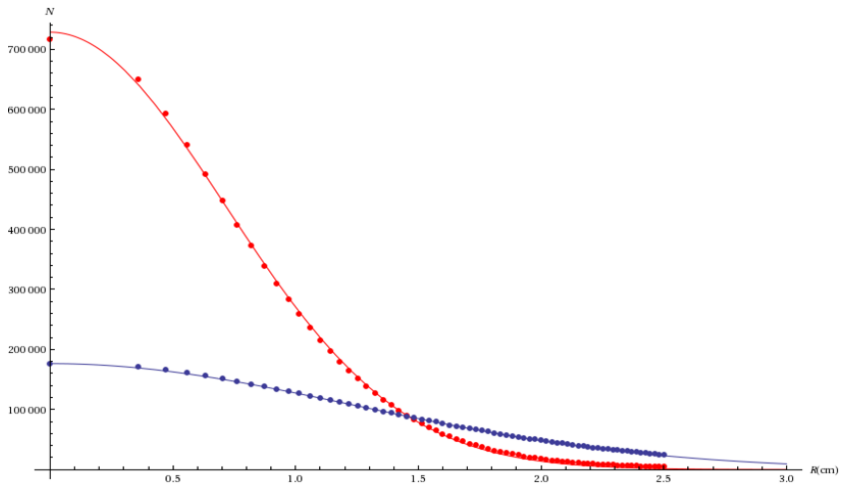

The data are for the "target disappears" accident scenario with air (blue) and helium (red) in the decay pipe. Protons with energies above 110 GeV were considered. Normalisation is arbitrary.

Table 1. Integral power (kW) deposited in the elements of the LBNE absorber in the case of normal operation with helium

Element	Without spoiler	Single Al spoiler	Three Al spoilers
First spoiler		12.6	12.5
Aluminium mask	168.4	180.7	181.0
Aluminium core	289.8	271.7	269.3
Steel core 1	24.6	16.6	19.8
Steel core 2	8.6	5.7	6.9
Steel core 3	3.5	2.4	
Steel core 4	1.5	1.1	
Steel shielding	238.3	235.5	243.3
Total	734.6	726.2	732.7

Neutron energy cut-off is 100 keV.

As a result of the Monte Carlo modelling, very detailed power density distributions for the hottest regions in the absorber core are provided for the subsequent thermal and stress analysis with the ANSYS code. At present, several options are under investigation that have the potential of providing reduced peak power density in the case of helium compared to the initial estimate of 2.4 mW/cm^3. According to extensive ANSYS studies performed for this case, the normal operation with helium at the temperature in the aluminium core not exceeding 100°C can be expected.

Table 2. Integral power (kW) deposited in aluminium core of the LBNE absorber in the case of normal operation with helium

Aluminium block number	Without spoiler	Single Al spoiler	Three Al spoilers
1	26.9	42.8	42.5
2	45.0	53.7	23.9
3	54.2	50.8	20.6
4	50.7	41.6	42.0
5	41.5	31.7	15.1
6	31.7	23.2	36.3
7	23.3	16.5	32.0
8	16.7	11.6	25.0
9			18.6
10			13.4
Total	289.8	271.7	269.3

Neutron energy cutoff is 100 keV.

Figure 7. Calculated power density distributions for normal operation (left) with air (right) and helium in the decay pipe

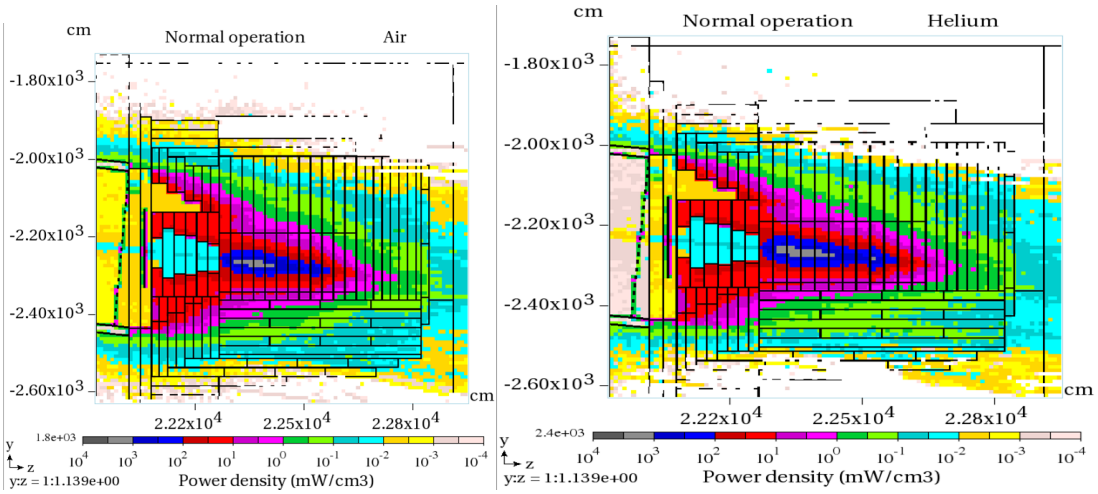

Acknowledgements

This work was supported by Fermi Research Alliance, LLC, under contract No. DE-AC02-07CH11359 with the US Department of Energy.

References

[1] M. Bishai et al. (2012), "LBNE Long-Baseline Neutrino Experiment", Conceptual Design Report, *LBNE-doc-5235-v9. Fermilab*, pp. 1-83, US.

[2] N.V. Mokhov (1995), "The MARS code system user's guide", *Fermilab-FN-628; http://www-ap.fnal.gov/MARS*.

[3] N.V. Mokhov, S.I. Striganov (2007) "MARS15 overview", *Proc. Of Hadronic Shower Simulation Workshop, Fermilab, September 2006, AIP Conf. Proc. 896*, pp. 50-60.

Shielding design for the LBNE decay pipe

S. Diane Reitzner
Fermi National Accelerator Laboratory, US

Abstract

The Long Baseline Neutrino Experiment (LBNE) is being designed to deliver a high intensity neutrino beam from Fermilab to a detector 1300 km away in South Dakota. The neutrino beam will be produced from the decays of pions and kaons generated from a 120 GeV proton beam incident on a 95 cm long graphite target. The pions and kaons will decay in flight in the 200 m decay pipe downstream of the two magnetic focusing horns. The operation of this proposed beamline will generate radionuclides in the soil surrounding the beamline complex which may leach into the groundwater resources. Sufficient shielding will therefore be required to maintain the concentration of the radionuclides in the ground water resources, over the lifetime of the facility, below the environmental regulatory limits. This paper presents an estimate of the minimum decay pipe shielding required to maintain the radionuclide concentrations in the ground water below the regulator limits. A 30-year operation period of the LBNE beamline at a 2.3 MW beam power is assumed.

Introduction

The proposed LBNE project [1] is planned to deliver a beam of neutrinos to a detector located 1300 km away in South Dakota. The operation of this beamline has the potential to activate the soil and water in its vicinity. As the beamline is angled 102 mrad downward with respect to the plane of the accelerator, this will result in the hadron absorber being located at the soil rock interface, which, in turn, will increase the potential of contaminating the ground water with radionuclides. The focus of this document is on the soil and water activation in the vicinity of the 200 m long decay pipe. Detailed within are the calculations used to estimate the amount of decay pipe shielding required to maintain the concentration of radionuclides that can be leached into the aquifers to be below the Federal and State regulatory standards for drinking water.

Regulatory standards

The Federal Ground Water Regulatory standards [2-4] require that the radionuclide concentrations in water meet the following requirement:

$$\sum_i \frac{C_i}{C_{\max,i}} \leq 1 \qquad (1)$$

where C_i is the concentration of the i^{th} radionuclide and $C_{max,i}$ is the derived concentration standard, the maximum concentration allowed for a single radionuclide. The purpose of this regulatory standard is to limit the dose the general public receives from drinking water to be under 4 mrem per year [2].

Of particular concern are the ^{3}H and ^{22}Na radionuclides given their long half-lives and copious production in earth shielding used at accelerator facilities [5]. For ground water, the Federal derived concentration standards for ^{3}H and ^{22}Na are 20 pCi/mL [2,3] and 0.4 pCi/mL [4], respectively. All other radionuclides are either too short-lived or are produced in such insignificant quantities that they will be effectively undetectable when appropriate shielding is applied for ^{3}H and ^{22}Na.

The State of Illinois regulations requires [6] that no degradation of the waters of the State resources should occur. To satisfy this requirement, the LBNE Project aims to have sufficient shielding in place so that the concentrations of radionuclides that do leach into the ground water are below the levels defined as detectable by Federal standards. Having enough shielding to just satisfy the Federal regulatory standards will not be sufficient and could be interpreted as a violation of the State of Illinois standard. The limits of detectability for ^{3}H and ^{22}Na are 1 pCi/mL and 0.04 pCi/mL, respectively. At the limit of detectability, the sum of the concentration ratios becomes:

$$\frac{C_{^{3}H}}{C_{\max,^{3}H}} + \frac{C_{^{22}Na}}{C_{\max,^{22}Na}} = \frac{1}{20} + \frac{0.04}{0.4} = 0.15 \qquad (2)$$

To push the concentration levels down below the limits of detectability, the LBNE Project has adopted the following standard for the sum of concentration ratios:

$$\sum_{i} \frac{C_i}{C_{\max,i}} \leq 0.1 \qquad (3)$$

Simulation

The MARS Monte Carlo simulation code [7,8] is used to determine the concentrations of the ^{3}H and ^{22}Na radionuclides in the soil which is in the immediate vicinity of the decay pipe. Included in the simulation are various beam line elements such as the target and focusing horns along with the shielding. The reference design for LBNE neutrino beam line is described in the CDR [1]. Unlike the reference design where the decay pipe shield cross-section is box shaped, the MARS model has cylindrical shaped shielding, of 3 m thickness, for ease of calculation. The result provides a more conservative estimate for the radionuclide concentrations if the outer diameter of the shielding is equal to the lateral dimensions of the reference design. Figure 1 shows the full MARS model of the neutrino beam line.

Figure 1.The LBNE beamline geometry as modelled in the MARS simulation code

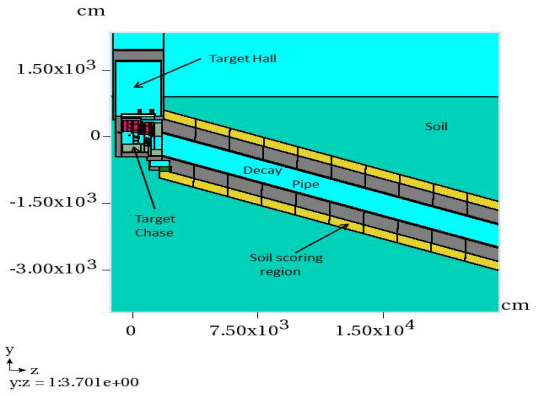

An exponential function is used to describe the radial source term in the soil and concrete for a 3 m thick shield. These source terms are then used to extrapolate the results to other shield thicknesses. The decay pipe shield is subdivided into ten 20-m sections longitudinally and fifteen 20-cm thick subsections radially. The soil immediately outside the decay pipe is likewise subdivided into ten 20-cm thick scoring regions.

Radionuclide concentration

Fermilab has adopted the concentration model [9] to determine the amount of radionuclides produced by an accelerator facility that may propagate into the ground water system. In this model, the concentration of the i^{th} radionuclide is:

$$C_i = \frac{N_p K_i L_i S_{av}}{1.17 \times 10^6 R_{vol}} \{1 - e^{-t_{irr}/\tau_i}\} \quad (4)$$

where N_p is number of incident protons on target per year, K_i is the number of radionuclides produced per star (inelastic interaction), L_i is the fraction of radionuclides that are leachable, S_{av} is the average star density per proton on target over the volume which contains 99.9% of the stars, R_{vol} is the ratio of the volume of water which will leach 99% of the leachable nuclides to the volume of material from which they are leached, t_{irr} is the irradiation time, and τ_i is the mean lifetime of the radionuclide. The factor 1.17×10^6 in the denominator scales the units from Bq to pCi and seconds to years.

The average star density in each of the longitudinal and radial bins in the concrete and soil were extracted to determine the source terms for each longitudinal subdivision of the decay pipe. Figure 2 shows star density distribution per proton for the longitudinal subsections located 50 m into the decay pipe in the concrete and soil. The data points are the MARS results while the solid and dashed lines show the fitted source terms for the concrete and soil respectively. Note that the slope for the soil is shallower than that for the concrete due to the soil's lower density.

Figure 2. The average star density distribution in concrete (black squares) and soil (blue circles) as a function of radius

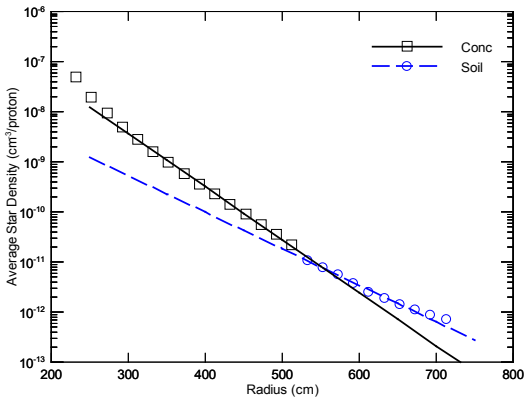

The values for the nuclide production per star (K_i) for ^{3}H and ^{22}Na were calculated using MARS running in MCNP [10] mode. Hadron interactions in MARS were modelled exclusively using the LAQGSM2012 [11,12] model. Table 1 lists the input values for the concentration model parameters.

Table 1. Input parameter list for the concentration model

Parameter	Value
N_p	2.5×10^{21} protons/year
K_{3H}	$(2.9\pm0.3)\times10^{-2}$ ^{3}H/star
K_{22Na}	$(2.6\pm0.2)\times10^{-2}$ ^{22}Na/star
L_{3H}	1.0
L_{22Na}	0.15±0.05
$R_{vol,3H}$	0.90±0.06
$R_{vol,22Na}$	1.88±0.13
τ_{3H}	17.8 years
τ_{22Na}	3.8 years

The radionuclide concentrations that are leached into the water are calculated using Equation 4 for multiple shield thickness ranging from 2 m to 16 m. Figure 3 shows the sum of the concentration ratios as a function of shield thickness. The minimum shield thickness averaged over all longitudinal subsections was found to be 549±10 cm, which satisfies Equation 3.

Figure 3. The sum of concentration ratios as a function of shield thickness

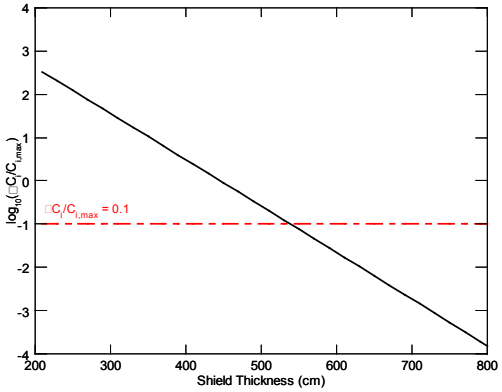

The use of a square shaped shield cross-section reduces the average star density in a fixed area of the soil by a factor of 0.88. This correction will reduce the minimum shield thickness by 5 cm. Figure 4 shows the minimum shield thickness as a function of longitudinal position (z) corrected for the shape of the shield cross-section. The blue line in the figure is the conservative value for the average minimum shield thickness. The conservative value of 559 cm is the sum of the uncorrected the average minimum shield thickness (549 cm) and the 1σ uncertainty (10 cm). As can be seen in Figure 4, the conservative average shield thickness is greater than the corrected shield thickness calculated for any individual longitudinal subsection. This demonstrates that uncertainties in the calculation are unlikely to result in detectable levels radionuclides in the ground water.

Figure 4. Minimum thickness as a function of longitudinal distance for a square shielding cross-section

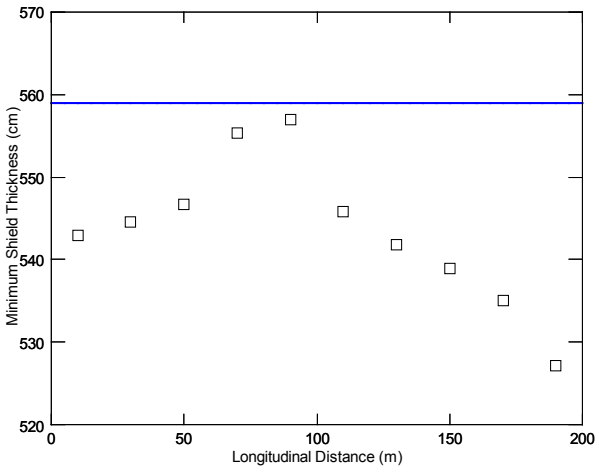

Summary

To eliminate any degradation of the water resources by the operation of the LBNE beamline, sufficient shielding must be in place to reduce the concentrations of ^{3}H and ^{22}Na radionuclides that can potentially be transmitted to the groundwater to be below detectable levels. Applying sufficient shielding to maintain radionuclide concentrations in the ground water to be below 10% of the Ground Water Regulatory Standard should be sufficient. The average minimum shield thickness was found to be 549±10 cm. Adding the 1σ uncertainties to this value gives a final result of 559 cm for the decay pipe shield thickness.

Acknowledgements

Support was provided by the US Department of Energy Contract No. DE-AC02-07CH11359.

References

[1] The LBNE Collaboration (2013), "Long-Baseline Neutrino Experiment (LBNE) Project", Conceptual Design Report, http://lbne.fnal.gov/papers.shtml.

[2] United States Code of Federal Regulations (1976), "National Primary Drinking Water Standard for Beta- and gamma- Emitting Radionuclides", Title 40, Part 141.16.

[3] United States Code of Federal Regulations (2000), "National Primary Drinking Water Regulations; Final Rule", Title 40, Parts 9, 141, and 142.

[4] US. Department of Energy (2011), "Radiation Protection of the Public and the Environment", DOE Order 458.1.

[5] Borak et al. (1972), "The underground migration of radionuclides produced in soil near high energy proton accelerators", *Health Physics*, 23, pp. 670-687.

[6] Illinois Pollution Control Board, "Title 35: Environmental Protection, Subtitle C: Water Pollution, Chapter I Pollution Control Board", Illinois Administrative Code.

[7] N.V. Mokhov (1995), "The MARS Code System Users'Guide", Fermilab FN-625, http://www-ap.fnal.gov/MARS/m1514-manual.pdf.

[8] N.V. Mokhov, P. Aarnio, Yu.I. Eidelman, K.K. Gudima, A.Yu. Konobeev, V.S. Pronskikh, I.L. Rakhno, S.I. Striganov, I.S. Tropin (2012), "MARS15 Code Developments Driven by the Intensity Frontier Needs", Fermilab-Conf-12-635-APC.

[9] J.D. Cossairt, A.J. Elwyn, P. Kesich, A. Malensek, N. Mokhov, A. Wehmann (1999), "The Concentration Model Revisited", Fermilab Environmental Protection Note-17, http://esh-docdb.fnal.gov/cgi bin/RetrieveFile?docid=2166;filename=E_P_%20Notei%2017.pdf;version=1.

[10] J. Briesmeister (1993), "MCNP – A General Monte Carlo n-Particle Transport Code", Los Alamos Report LA-12625-M.

[11] S.G. Mashnik et al. (2008), "CEM03.03 and LAQGSM03.03 Event Generator for the MCNP6, MCNPX and MARS15 Transport Codes", LANL Report LA-UR-08-2931, arXiv:0805.0751 v1 [nucl-th].

[12] N.V. Mokhov, K.K. Gudima, S.G. Mashnik, I.L. Rakhno, S.I. Striganov (2004), "Towards a Heavy-Ion Transport Capability in the MARS15 Code", Fermilab Report CONF-04/052.

Modified Moliere's screening parameter and its impact on multiple coulomb scattering

Sergei Striganov
Fermi National Accelerator Laboratory, US

Abstract

The Moliere approximation of elastic Coulomb scattering cross-sections plays an important role in accurate description of multiple scattering, non-ionisation energy, DPA radiation damage etc. The cross-section depends only on a single parameter that describes the atomic screening. Moliere calculated the screening angle for the Tomas-Fermi distribution of electrons in atoms. In this paper, the screening parameter was recalculated using a more accurate atomic form-factor obtained from the self-consistent Dirac-Hartree-Fock-Slater computations. For relativistic particles, the new screening angle can differ from the Moliere approximation by up to 50%. At the same time, it is rather close to other independent calculations. At low energies, the new screening angle is different for positrons and electrons. The positron screening parameter is much larger than the electron one for heavy nuclei at energies of ~Z keV. The impact of the screening angle on particle transport and calculated quantities is discussed.

Introduction

The Moliere's approximation of the elastic Coulomb scattering cross-section plays an important role in an accurate description of the multiple scattering. The cross-section depends only on a single parameter that describes the atomic screening. Moliere [1] calculated the screening angle using Tomas-Fermi model. Since the Tomas-Fermi model is statistical, for light element it cannot provide a high accuracy of calculation. More precise results can be obtained within the Hartree-Fock approach. It takes into account individual properties of atoms – in particular, their shell structure. Salvat et al. [2] proposed a simple analytical approximation for the atomic screening functions depending on five parameters which are determined from the results of Dirac-Hartree-Fock-Slater calculations. In this study we recalculate Moliere screening angle using this approximation. The impact of new values of screening parameters on Moliere's theory prediction is considered.

Moliere screening angle

Using Salvat et al. approximation [2], the atomic form factor can be written as:

$$F_a(q) = \sum_{i=1}^{3} A_i \alpha_i^2 / (\alpha_i^2 + q^2), \qquad (1)$$

where $\boldsymbol{q}$ - momentum transfer. After tedious algebra, one finds that in the Born approximation the Moliere "screening angle" reads:

$$\chi_{HF}^{B} = m_e \alpha \chi_0 / p$$
$$\ln \chi_0 = \sum_{i=1}^{3} A_i (\ln \alpha_i - 0.5) + 2A_1A_2(\alpha_2^2 \ln \alpha_2 - \alpha_1^2 \ln \alpha_1)/(\alpha_2^2 - \alpha_1^2) + \quad (2)$$
$$2A_1A_3(\alpha_3^2 \ln \alpha_3 - \alpha_1^2 \ln \alpha_1)/(\alpha_3^2 - \alpha_1^2) + 2A_2A_3(\alpha_3^2 \ln \alpha_3 - \alpha_2^2 \ln \alpha_2)/(\alpha_3^2 - \alpha_2^2) - 0.5$$

where $\boldsymbol{p}$ – projectile momentum, α – fine structure constant, $\boldsymbol{m_e}$ – electron mass. Figure 1 presents the screening parameter χ_o calculated using Equation (2) and parameters obtained in [2].

Figure 1. Screening parameter χ_o in Born approximation

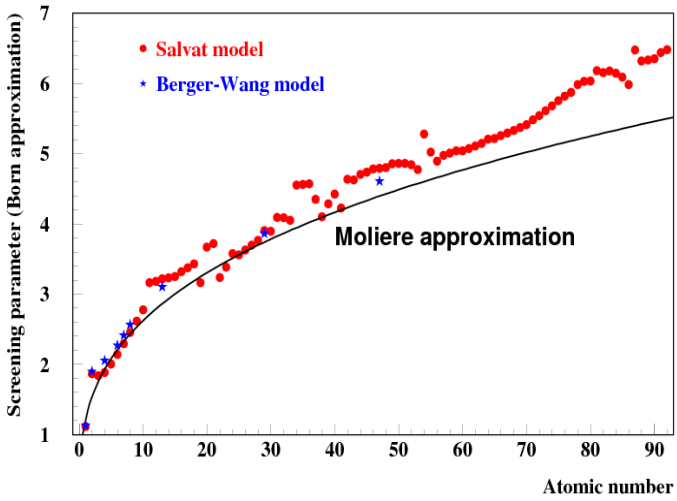

For the determination of the screening angle, Moliere [1] uses his own calculation of the single scattering by a Tomas-Fermi potential. Berger and Wang [3] calculated the correction to Moliere's approximate formula using a modern version of Moliere's method and Hartree-Fock potential. In Figure 1, we compare the screening parameter calculated using different atomic form factors in Born approximation. One can see that the models based on Hartree-Fock form factors are in good agreement. HF screening parameter is larger than Moliere's one, but the difference exceeds 20% for helium only.

The Coulomb correction is the difference between the values of parameters calculated in the eikonal approximation and in Born approximation. An exact formula for the differential cross-section in terms of an integral is given in Moliere's paper [1], but his final evaluation of integral is numerical and only approximate. Recently, Kuraev et al. [4] have found an exact solution in the ultra-relativistic limit. Their result reveals significant deviation from Moliere's approximation for sufficiently heavy elements.

Fernandez-Varea et al. [5] proposed an accurate formula for elastic Coulomb scattering based on the Hartree-Fock atomic form factor for electrons/positrons with energies larger Z keV. This cross-section is used in the popular PENELOPE code [6] for simulation of the multiple Coulomb scattering. To improve an agreement with precise partial wave calculation they introduced a correcting factor $t(\beta,Z)$ which can be considered as estimate of Coulomb correction. Note that the above mentioned correction factor depends on particle charge. It can be shown that in the small angle approximation the screening angle reads

$$\chi_{HF} = \chi_{HF}^{B} \cdot t(\beta, z) \quad (3)$$

In the ultra-relativistic limit difference between positive and negative particle is not large. As shown in Figure 2, the "Coulomb correction" calculated according to Equation (3) is close to results of Dubna group [4], but at large Z is lower than Moliere Coulomb correction by about 10%.

Figure 2. Coulomb correction in ultra-relativistic limit

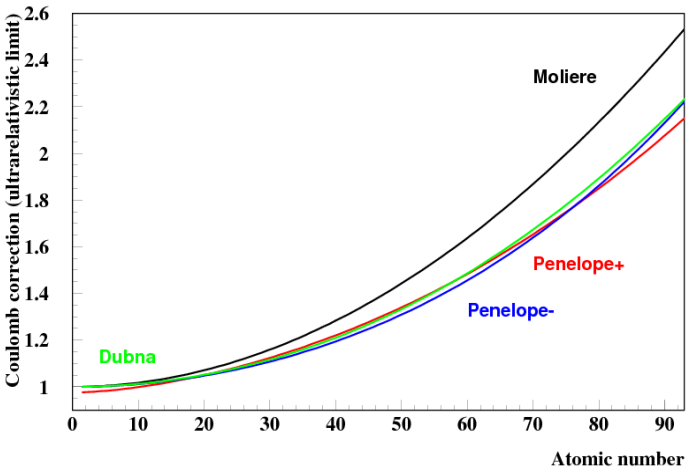

Figure 3 presents a comparison of the screening parameters calculated by different approaches for ultra-relativistic particles. The most prominent difference is seen for low-Z nuclei. HF screening angle squared is larger than Moliere one for heavy nuclei by ~20%.

Seltzer [7] has compared the transport cross-section obtained using Moliere approach and exact phase shift calculations. He found that agreement can be generally improved by making a strictly empirical adjustment to Moliere's screening angle. Seltzer's correction significantly decreases the screening angles for electrons at low energies as approach proposed by Fernandez-Varea et al. [5].

Figure 3. X^2_{HF}/X^2_M in ultra-relativistic limit

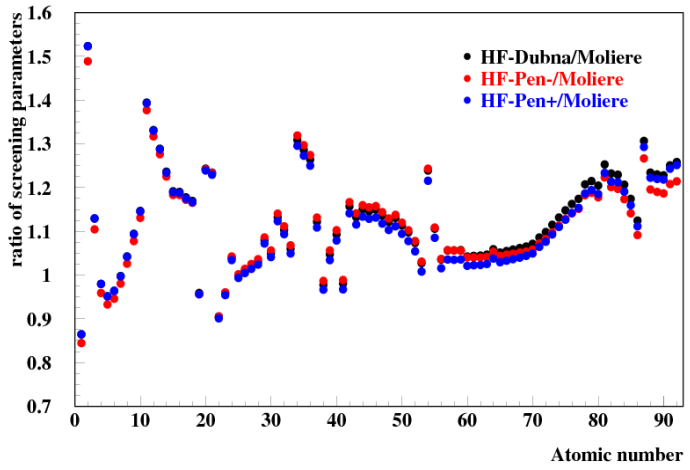

Figure 4 shows the energy dependence of the screening angle calculated by the different approaches. It is seen that Seltzer model [7] is close to Penelope correction [5] for electrons. For positive particles Moliere and Penelope results are rather similar also. Note that at low energies, Coulomb correction for positive particles is much larger than for negative.

Figure 4. Energy dependence of Coulomb corrections

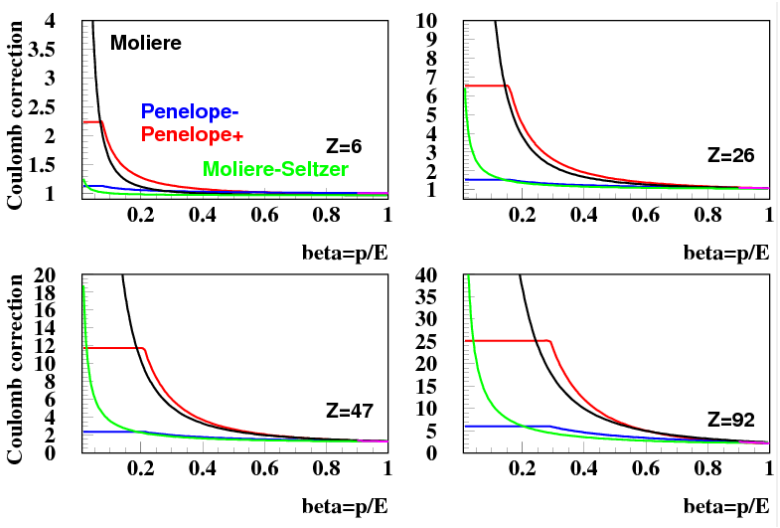

For energies less than Z keV, the accuracy of Penelope correction factor [5] progressively deteriorates. However, the Penelope approximation still yields reasonable results for electron/positron second transport cross-section if the correction factor $t(\beta,Z)$ is evaluated using the value of velocity β corresponding to a kinetic energy E_c=0.25Z when $E<E_c$ [5].

The energy dependence of the screening angle is shown in Figure 5. It is seen that the new screening parameter (3) is very different from Moliere's one for slow particles especially for heavy nucleus.

Figure 5. Energy dependence of X^2_{HF}/X^2_M

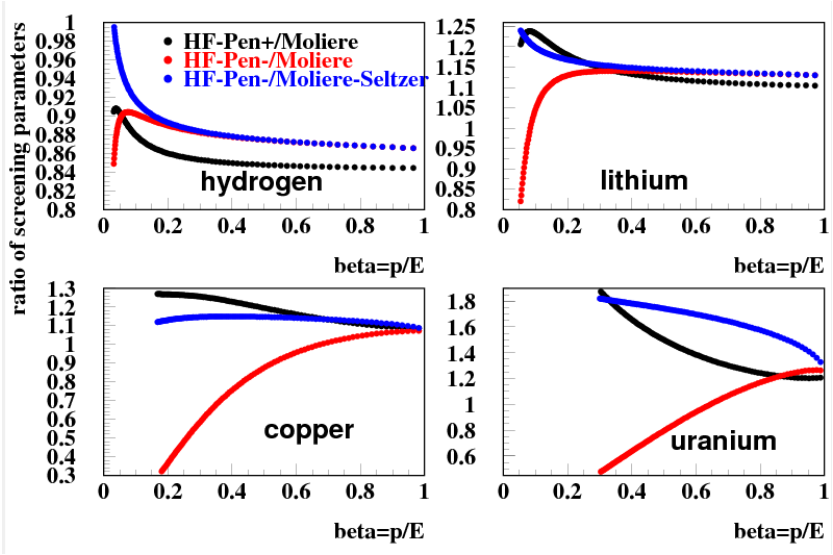

Sensitivity of the angular distribution width to screening angle

In Moliere theory the angular distribution depends only on a single parameter B. It is defined by transcendental equation:

$$B = \ln B - 0.1544 + \ln \Omega; \quad \Omega = \frac{\chi_c^2}{\chi_M^2} \tag{4}$$

Ω is mean number of scattering events that occur in thickness z. An approximative interpolation solution of Equation (4) reads [8]:

$$B = 1.153 + 2.583 \log_{10} \Omega \tag{5}$$

Now, we can estimate sensitivity of parameter B to value of screening angle:

$$\frac{B_{HF}}{B_M} = 1 + \frac{\ln(\chi_{HF}^2 / \chi_M^2)}{1.027 + \ln \Omega} \tag{6}$$

For large thickness even a large error in the definition of the screening parameter does not change prediction of Moliere theory. It should be noted that Moliere theory can be applied for foil thickness corresponding to large number of scatterings only, Ω>100.

Using Equation (4) we can predict the ratio of the angular distribution width calculated by Moliere prescription and more precise Hartree-Fock screening angle (3). Figure 6 shows the thicknesses where the ratio reaches 2% and 3% for relativistic particles. If one needs to know the angular distribution parameters with precision about 3%, new screening angle (3) should be used for rather low thicknesses, usually less than 1 g/cm2. If the better accuracy is needed, the newly defined values of the screening parameter can improve the quality of calculation at the larger thickness also.

Figure 6. Three percent and two percent thicknesses for positive and negative projectiles

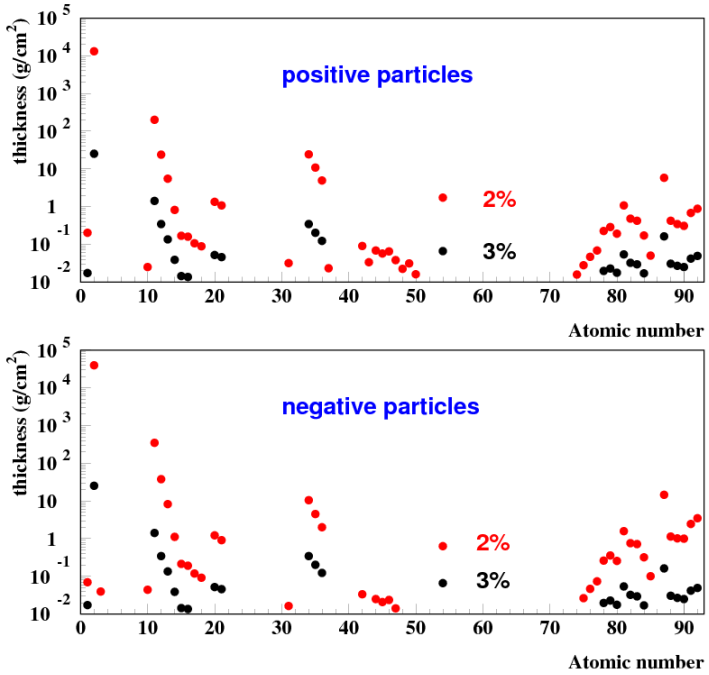

Conclusion

Moliere's screening angle was recalculated using a precise approximation of the partial wave differential cross-section [5]. Our results are in close agreement with other estimates [3,4,7]. The deviation from Moliere approximation [1] could reach factor 2 at lower energies. The new screening angle depends on the particle charge. Positron screening angle is about 5 times larger than electron's one in large Z material and low momentum. Because of the generally logarithmic dependence of the angular distribution width on the screening parameter the ultimate effect of using more precise screening model is small. The accuracy of experiment to date (a few percent) is not enough to resolve difference between Moliere's and our approaches. But the angular distribution after very thin foils (see Figure 6) is predicted more accurately with newly defined screening parameter (3).

Acknowledgements

Work was supported by Fermi Research Alliance, LLC, under contract DE-AC02-07CH11359 with the US Department of Energy.

References

[1] G. Moliere (1948), "Theorie der Streuung schneller geladener Teilchen II. Mehrfach- und Vielfachstreuung", *Z. Naturforsch.*, 3a, pp. 78-97.

[2] F. Salvat, J.D. Martinez, R. Moyol, J. Parellada (1987), "Analytical Dirac-Hartree-Fock-Slater screening function for atoms (Z=1-92)", *Phys. Rev.*, A36, pp. 467-474.

[3] M.J. Berger, R. Wang (1988), "Multiple-Scattering Angular Deflections and Energy-Loss Stragling", *Monte Carlo transport of Electrons and Photons, eds. T.M. Jenkins, W.R.Nelson, A. Rindi (Plenum Press, New York)*.

[4] A. Tarasov, O. Voskresenskaya (2012), "An Improvement of the Moliere-Fano multiple scattering theory", *arXiv:1107.5018 [hep-ph]*.

[5] J.M. Fernandez-Varea, R. Moyol and F. Salvat (1993), "Cross sections for elastic scattering of fast electrons and positrons by atoms", *Nucl. Meth.*, B82, pp. 39-45.

[6] F. Salvat, J.M. Fernandez-Varea, J. Sempau (2011), "PENELOPE-2011: A Code System for Monte Carlo Simulation of Electron and Photon Transport", *OECD NEA Data Bank/NSC DOC(2011)/5*.

[7] S.M. Seltzer (1988), "An Overview of ETRAN Monte Carlo Methods", *Monte Carlo transport of Electrons and Photons, eds. T.M. Jenkins, W.R.Nelson, A. Rindi (Plenum Press, New York)*.

[8] W.T. Scott (1963), "The Theory of Small-Angle Multiple Scattering of Fast Charged Particles", *Rev. Mod. Phys.*, 35, pp. 231-313.

Radiation safety study for conventional facility and siting pre project phase of International Linear Collider

Toshiya Sanami, Syuichi Ban, Shin-ichi Sasaki
High Energy Accelerator Research Organisation (KEK), Japan

Abstract

The International Linear Collider (ILC) is a proposed high-energy collider consisting of two linear accelerators, two dumping rings, electron and positron sources, and a single colliding hall with two detectors. The total length and CMS energy of the ILC will be 31 km and 500 GeV, respectively (and 50 km and 1 TeV after future upgrade). The design of the ILC has entered the pre-project phase, which includes site-dependent design. Radiation safety design for the ILC is on-going as a part of conventional facility and siting activities of the pre-project phase. The thickness of a central wall of normal concrete is designed to be 3.5 m under a pessimistic assumption of beam loss. The beam loss scenario is under discussion. Experience and knowledge relating to shielding design and radiation control operational work at other laboratories are required.

Introduction

The International Linear Collider (ILC) is a proposed high-energy collider consisting of two linear accelerators, two dumping rings, electron and positron sources, and a single colliding hall with two detectors. The total length and CMS energy of the ILC will be 31 km and 500 GeV, respectively (and 50 km and 1 TeV after future upgrade). In 2013, a technical design report (TDR) of the ILC was published and a Japanese candidate site for the ILC was determined to be the Kitakami area. The project has moved from the design phase to the pre-project phase, which includes detailed design of the accelerator, research and development for cost-effective production, site study and conventional facility and siting (CFS) designs. It is intended that CFS design in the pre-project phase will determine not only the actual design of the accelerator tunnel and related infrastructure but the design of the tunnel structure, beam dump housing, local shield for the positron production target, ventilation, cooling water circulation and drainage; therefore, many radiation safety studies need to be performed. The KEK Radiation Science Center will conduct these studies in response to a request from ILC project management. This paper outlines the ILC status and on-going topics of related radiation safety studies including the determination of the required thickness of the separation shielding wall according to design criteria.

Figure 1. Schematic view of the ILC [1]

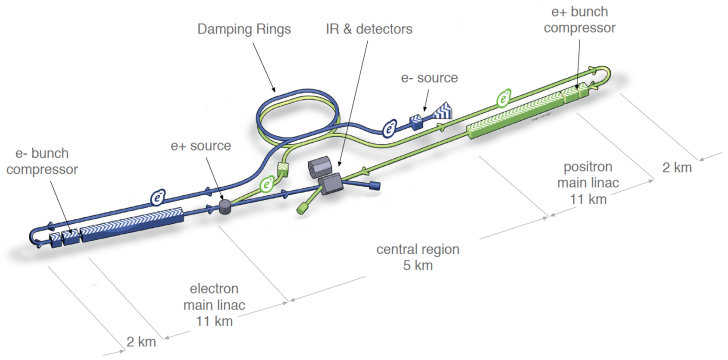

ILC accelerator layout and beam power

Figure 1 is a schematic view of the ILC [1]. In the ILC, polarised electrons are generated by a radio-frequency gun and accelerated to 5 GeV (e-source in the figure). The 5-GeV electrons are injected to the damping ring (DR) to reduce their emittance. The electrons are then extracted from the ring and fed to the main linac (ML) through the ring-to-main-linac apparatus (RTML). The ML accelerates the electrons to 250 GeV. The 250-GeV electrons are fed to the interaction region (IR) through a beam delivery system (BDS) after passing through an undulator section to generate photons for positron production. The positrons are delivered to the IR with energies of 250 GeV through the DR, RTML, ML and BDS as for the electrons. The interaction point is located at the centre of the detector hall, which accommodates two detectors. The remaining electrons and positrons after the IR are absorbed by the large water dump. Table 1 gives the beam power parameters. For the baseline design, the maximum power is 10.5 MW. It is anticipated that, after several years of operation, the luminosity and energy will be upgraded depending on the results obtained.

CFS pre-project phase

A TDR of the ILC was published in 2013. The TDR describes the technical design of each accelerator component with an integration plan for a non-specified site [1]. Several model sites in Japan, the United States and Europe, were described in the TDR. The model sites have two different topographies of (1) a flat surface and (2) a mountainous surface, with different tunnel structures.

In October 2013, a candidate site in Japan was constructed in the Kitakami area, which has mountainous topography. The tunnel design of this site has two separated regions in a single tunnel. Figure 2 shows a map of the candidate site with the elevation cross-section. The site is located in the northeast of Japan, about 700 km from Tokyo. The accelerator design, especially the CFS design, has to be updated in consideration of the actual site conditions of the candidate site in Japan.

The ILC-CFS team has a five-year plan that has phases for basic planning, basic design and detailed design. The goal of this plan is to prepare a detailed drawing of the entire site in preparation for construction. The plan includes a topographical survey, geological survey and environmental impact assessment. In the first step, basic planning, the ILC-CFS team intends to determine the IR location, total accelerator length and standard cross-sections of the tunnel. This will require several studies on not only accelerator integration but also radiation safety. The KEK Radiation Science Center (KEK-RC) will conduct this study in response to a request from ILC project management. KEK-RC starts information exchange to address radiation safety issues in the ILC-CFS pre-

project phase, and will raise several discussion points relating to the design constraints of the ILC accelerator.

Figure 2. Map of the ILC candidate location [1]

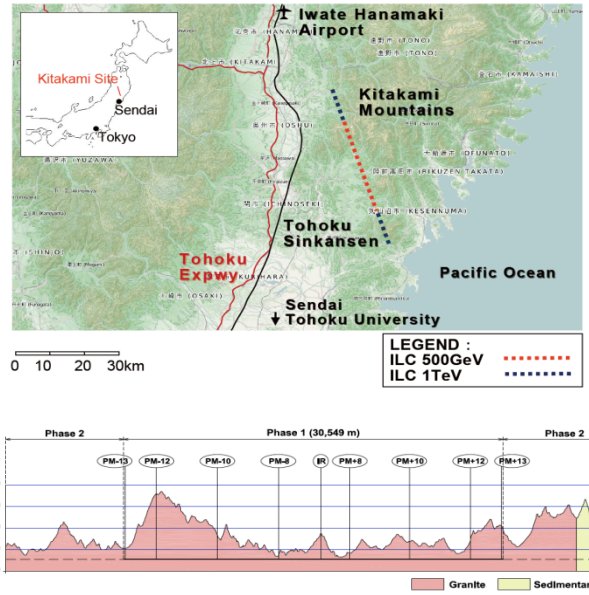

Table 1. Beam power parameters

		Baseline	Luminosity upgrade	TeV upgrade
Centre-of-mass energy	E_{CM} GeV	500	500	1000
Collision rate	Hz	5	4	4
Bunch population	N x10^{10}	2	2	2
Number of bunches	n_b	1312	2625	2450
Beam power	MW	10.5	21.0	27.2

Central shield

Because of the mountainous topography, the construction of surface buildings and vertical shafts at reasonable cost will be limited. Thus, power sources such as klystrons should be installed in the ML tunnel and accelerator column. The geology in the Kitakami area allows us to construct a tunnel with a rather large cross-section at an affordable cost and in a short construction period employing the New Austrian Tunnelling method [1].

Figure 3. ML tunnel cross-section [1]

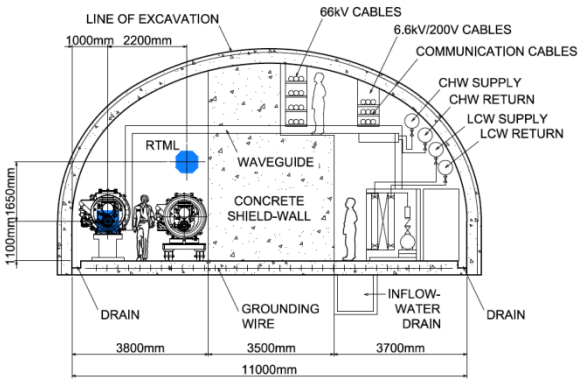

In terms of machine operation, radiation control and emergency evacuation, it is preferable to divide the tunnel area into two regions by introducing a central shield. Furthermore, if one of the regions is accessible during beam operation, the beam operation time could be lengthened since maintenance work could be done in parallel to the beam operation. Figure 3 shows a schematic drawing of the ML cross-section. The sizes of the accelerator and klystron sides are fixed owing to the equipment size and required space of installation, and the thickness of the central shield thus determines the tunnel size. The ML length is 2 × 11 km, and thus, even a small difference in the wall thickness notably affects the tunnel construction cost. The central shield should be designed by making reasonable assumptions.

To design a shielding wall, an assumption of beam loss and a policy of area classification are required. The beam loss for this design during normal operation has not yet been identified. The beam loss would be very small since the beam size is very small (a few microns) in comparison with the aperture of the accelerator column (7 cm). In addition, dark current induced by the acceleration field should be taken into account. Beam loss of 1 W/m is assumed as a tentative value for normal loss. Beam loss for a length of 1 m, 1 W, is considerably smaller than (by a factor of 10^{-7}) the maximum power given in Table 1. Because the dose rate limit for the accessible radiation control area is of the order of 10 μSv/h, if the thickness of the central shield was determined according only to normal loss, a dose rate of 10 μSv/h /10^{-7} = 100 Sv/h would be observed behind the shield for a full-beam-loss accident.

Figure 4. Dose rate as a function of concrete thickness

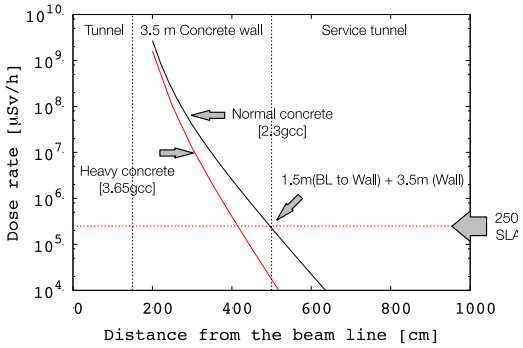

To avoid this situation, beam-loss scenarios and protection devices should be evaluated carefully, and subsequent agreement on the maximum credible loss would then allow design work to move forward. This process is currently underway for the ILC. The SLAC National Accelerator Laboratory has a design guideline for similar conditions that says the shield must be designed to reduce the dose rate to 250 mSv/h for maximum credible beam loss. Figure 4 shows the calculated dose rate as a function of shield thickness for maximum credible beam loss of 18 MW, obtained using the Jenkins formula. The figure shows that at least 350 cm of concrete is required to limit the dose rate to 250 mSv/h.

According to Japanese law, there is no guideline to follow in designing the shielding thickness for a situation of system failure. Therefore, it would be reasonable to determine the thickness required to limit the dose to the maximum allowable for personnel, 50 mSv/year and 100 mSv/5 years. To determine the thickness according to the annual integral dose, a reliable accident scenario is required for the failure rate, beam termination device, time required to turn off the beam and operation recovery procedure.

Conclusion

An outline and the current status of the ILC were described. The design of the ILC has entered the pre-project phase, which includes site-dependent design. The radiation safety design of the ILC is on-going as a part of CFS pre-project phase activities. The thickness of a central wall of normal concrete is designed to be 3.5 m under a pessimistic assumption of beam loss. The beam loss scenario is under discussion. Experience and knowledge relating to shielding design and radiation control operational work at other laboratories are required.

Reference

[1] "ILC Technical Design Report" (2013), http://www.linearcollider.org/from-design-to-reality/downloads.html.